

**The Education, Scholarships, Apprenticeships and Youth Entrepreneurship Programme
– EEA Grants 2014-2021**

Project No: 18-Cop-0041

Project Title: *Cooperation and partnership strategy for the enhancement of the education quality of strategic master Chemistry of Advanced Materials in line with Green Chemistry requirements – Green Chemistry of Advanced Materials*

E-BOOK OF MASTER THESIS



UNIVERSITY OF
BUCHAREST

VIRTUTE ET SAPIENTIA

FACULTY OF CHEMISTRY

MSc. Thesis

Master student: MIHAI BORDEIAȘU

Thesis Advisor:

Assist. Prof. DELIA-LAURA POPESCU, PhD

2021



UNIVERSITY OF
BUCHAREST
VIRTUTE ET SAPIENTIA

FACULTY OF CHEMISTRY
DEPARTAMENT OF INORGANIC CHEMISTRY

MSc. Thesis

**Cu(II)-based Metal-Organic Frameworks
with Kagomé Layers**

Master: Chemistry of Advanced Materials

Master student: MIHAI BORDEIAȘU

Thesis Advisor:

Assist. Prof. DELIA-LAURA POPESCU, PhD

June – July, 2021

Contents

Introduction	2
Chapter I. Theoretical Aspects	4
I.1. Porous Coordination Polymers	4
I.2. Structural features and physical properties of PCPs	5
I.2.1. Building blocks for PCPs	5
I.2.2. Dimensionality and structural motifs	6
I.2.3. Porosity and Flexibility	8
I.3. Applications of PCPs	9
I.3.1. Catalysis	9
I.3.2. Gas storage	11
I.3.3. Ion exchange/sorption	16
Chapter II. Experimental Part	17
II.1. Synthesis of Cu-based PCPs with Kagomé layers	17
II.2. Characterization of Cu-based PCPs with Kagomé layers	18
II.2.1. Structural characterization.....	18
II.2.2. Spectral characterization	22
II.2.3. Thermal stability	25
II.3. Applications of Cu-based PCPs with Kagomé layers.....	27
II.3.1. Anion-exchange studies	27
II.3.2. Adsorption properties.....	33
Conclusions	36
Acknowledgements	37
Materials and Instrumentation	37
References	39
Appendix	43
A. Powder X-ray diffractograms of compounds 1, 3-6.....	43
B. Elemental analysis	45
C. FTIR spectra of compounds 1-6.....	46
D. Powder X-ray diffractograms after N ₂ sorption.....	49

Introduction

Modern society faces great climate changes that affect both the environment and the everyday lifestyle of individuals. One of the main issues is the greenhouse effect exerted by different gases generated from human activity, most notably from burning of fossil fuels, production and transport of coal, natural gas, and oil, during treatment of wastewater as well as from livestock and agricultural practices. Of the greenhouse gases, carbon dioxide (CO₂), methane (CH₄), nitrous oxide (N₂O), and fluorinated gases such as hydrofluorocarbons (HFCs), perfluorocarbons (PFCs), sulfur hexafluoride (SF₆), and nitrogen trifluoride (NF₃) have the most pronounced effect, according to the United States Environmental Protection Agency (EPA). CO₂ is the most abundant, representing approximately 76% of the total greenhouse gases [1].

Studies have shown that for the 1959–2019 period, 19% of the total CO₂ emissions were caused by land-use change while the rest of 81% came from fossil emissions. Global fossil CO₂ emissions have increased every decade, from an average 11 billion tons CO₂ per year in 1960s to an average of 35 billion tons CO₂ per year during 2010–2019, with a maximum of 36.44 billion tons in 2019. The annual fossil CO₂ emissions during this period are presented in Figure 1. In contrast, CO₂ emissions from land use, land-use change, and forestry have remained relatively constant, at around 5 billion tons/year over the past half-century [2]. In 2020, the values decreased, reaching approximately 34 billion tons from fossil emissions, while for land-use change emissions it reached 5.8 billion tons [1].

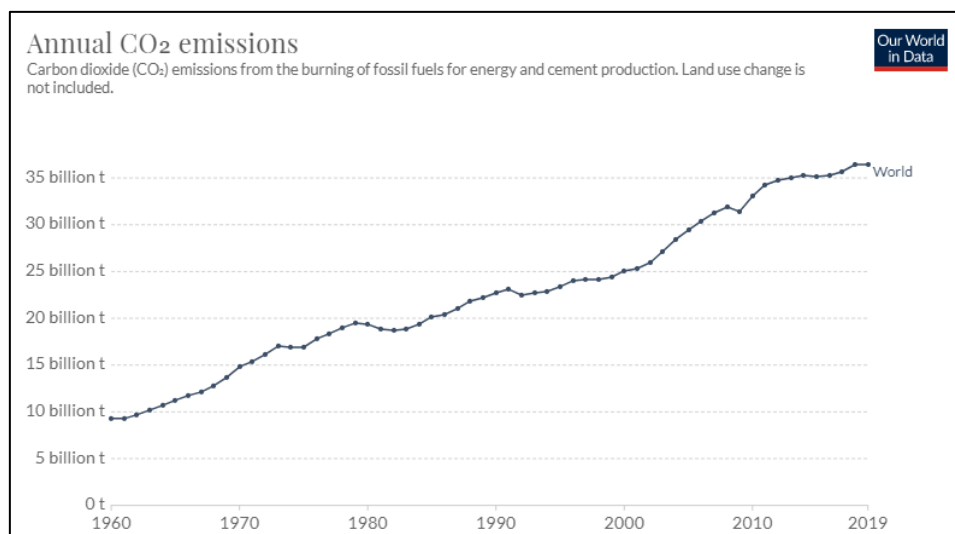


Fig.1. Annual fossil CO₂ emissions during 1960–2019

Source: <https://ourworldindata.org>

To overcome the large amount of greenhouse gases emitted into the atmosphere, old technologies have been updated and new methods are being developed to decrease the amount produced during certain processes.

For CO₂ capture and storage, different physical, chemical and even biological methods of sequestration have been implemented. The ocean and geological storage [3], as well as direct mineral carbonation [4] are among the most used methods. The storage relies on the injection of carbon dioxide into the ocean, at depths higher than 1000 meters and into porous rock formations, while the mineral carbonation aims to create stable carbonates such as magnesite (MgCO₃) and calcite (CaCO₃). Biological methods focus around phytoplankton and microalgae which utilizes dissolved CO₂ in photosynthesis for generation of storage carbon sugars [5]. Besides these approaches, carbon dioxide can also be used as raw material in the synthesis of new compounds such as porous coordination polymers, were it would be fixed as carbonate linking different metal ions into an extended structure [6].

The present dissertation focus on the synthesis of Cu-based porous coordination polymers with different bipyridine-based ligands through direct fixation of atmospheric carbon dioxide into the structure and the characterization of the obtained compounds through the use of single-crystal and powder X-ray diffraction, along with spectroscopic techniques, such as FTIR and UV-Vis in solid state.

Our main aim is to obtain a series of compounds that would combine both physical and chemical methods for carbon dioxide sequestration: the chemical fixation into the structure and furthermore, the physical adsorption of carbon dioxide into the pores of the obtained coordination polymers.

The thesis is structured into two main chapters, the former presenting a general overview of porous coordination polymers, their structural features and physical properties, as well as their applications in the fields of catalysis, gas storage and ion exchange. The second chapter comprises the experimental results of the research and is divided into three parts: the synthesis of Cu-based coordination polymers, their structural and spectral characterization, where some unique features are revealed, and the possible applications of these compounds in gas storage and anion-exchanges.

Chapter I. Theoretical Aspects

I.1. Porous Coordination Polymers

Porous coordination polymers (PCPs), most commonly known as Metal-Organic Frameworks (MOFs), are a class of porous materials formed by self-assembly of metal ions or clusters and bridging ligands, whether it is an organic or organometallic ligand, or a coordinative compound with free coordination sites, yielding to an infinite structure characterized by high regularity, tunable pore sizes, large surface area and adjustable internal surface properties [7-9].

A great advantage of these compounds is their diversity as there can be obtained a large variety of coordination polymers depending on the nature of the building blocks and their properties which have a major impact on PCPs topology, defining the final structure. Thus, PCPs may be tuned for a targeted application from the synthesis stage.

Due to their structural characteristics, which lead to versatile architectures, porous coordination polymers are used in different applications (Figure I.1-1.), such as adsorption, separation and storage of gases, heterogeneous catalysis, drug delivery and sensor technology, magnetism, luminescence, water treatment, production of composite resins and fuel cells [10,11]. As a result, the number of published articles related to MOFs has increased greatly in the last 20 years, reaching almost 8000 publications in 2019 [11].

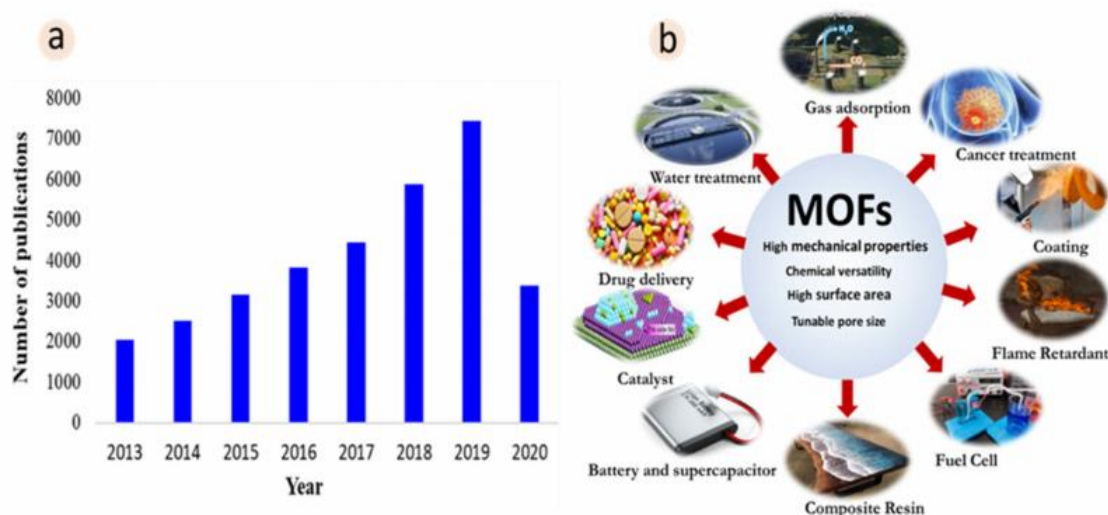


Fig.I.1-1. (a) number of publications related to MOFs in the period of 2013 to 2020, (b) various applications of MOFs

Source: Mashhadzadeh, A.H., Taghizadeh, A., Taghizadeh, M., Munir, M.T., Habibzadeh, S., Salmankhani, A., Stadler, F.J., Saeb, M.R., J. Compos. Sci., 4(2) (2020), 75:88.

The general strategy of synthesis for MOFs is to use a divergent ligand that has at least two donor atoms which can form a linking bridge between metal ions or clusters, as it can be observed in Figure I.1-2. Building blocks are brought together in liquid phase, using the solvent as a medium to induce the self-assembly process that generates the framework, the reaction usually taking place at room temperature or under hydro/solvothermal conditions [10,12]. There are several factors which influences the synthesis, part of which derive from the assembly units and are detailed in the following subchapter.

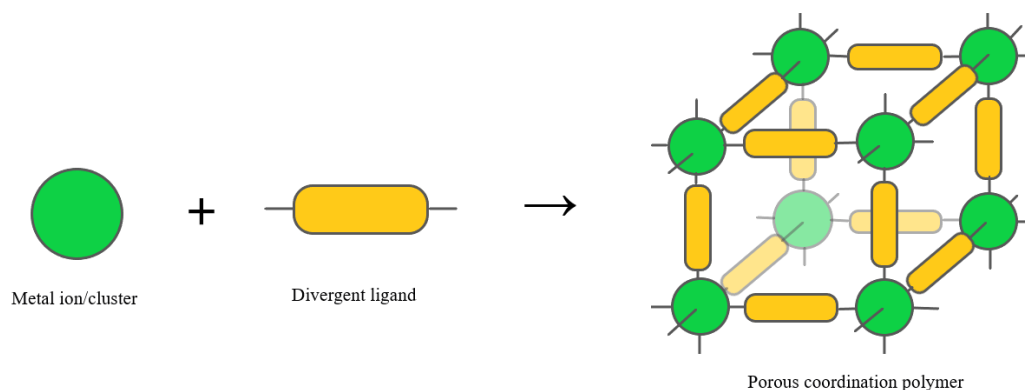


Fig.I.1-2. Schematic representation of the strategy for synthesis of PCPs

I.2. Structural features and physical properties of PCPs

I.2.1. Building blocks for PCPs

The building blocks of coordination polymers are usually classified in *connectors* (metal ions or clusters) and *linkers* or *spacers* (bridging ligands) [13]. Connectors have different shapes and sizes, depending on the stereochemistry of the metal ion (e.g., linear, angular, T-shape, trigonal-planar, tetrahedral), its size, chemical hardness/softness [14], influencing the dimensionality and structural motifs of the obtained coordination polymer. The tetrahedral and octahedral geometries are widely used because of their tendency to form 3D architectures, but also because they can generate other different geometries through the use of blocking ligands.

Linking groups have to be multidentate exo-type ligands in order to obtain the extended network of the coordination polymer. Important features of linkers include charge, the most common being the neutral (Figure I.2.1-1.) and anionic (Figure I.2.1-2.) ligands, as well as the shapes, lengths and sizes of the core, the overall rigidity of the ligand, and orientation of the donor groups [13,14].

Besides the building blocks, auxiliary components such as counter ions, nonbonding guests or template molecules are present in the structure of the final compound [12]. The void

space within the structure is occupied by guest molecules, usually solvent molecules and/or counter ions, provided by the metal salt which will also satisfy the charge balance. The formation of weak non-covalent interactions within the final packing of the solid provides further stability to the compound.

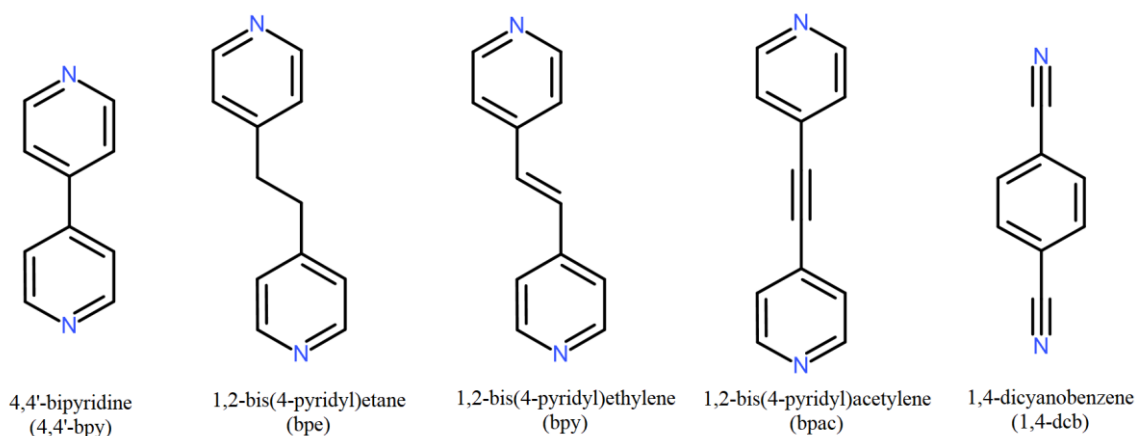


Fig.I.2.1-1. Common neutral ligands (adapted)

Source: Robin, A.Y., Fromm, K.M., *Coord. Chem. Rev.*, 250(15-16) (2006), 2127:2157

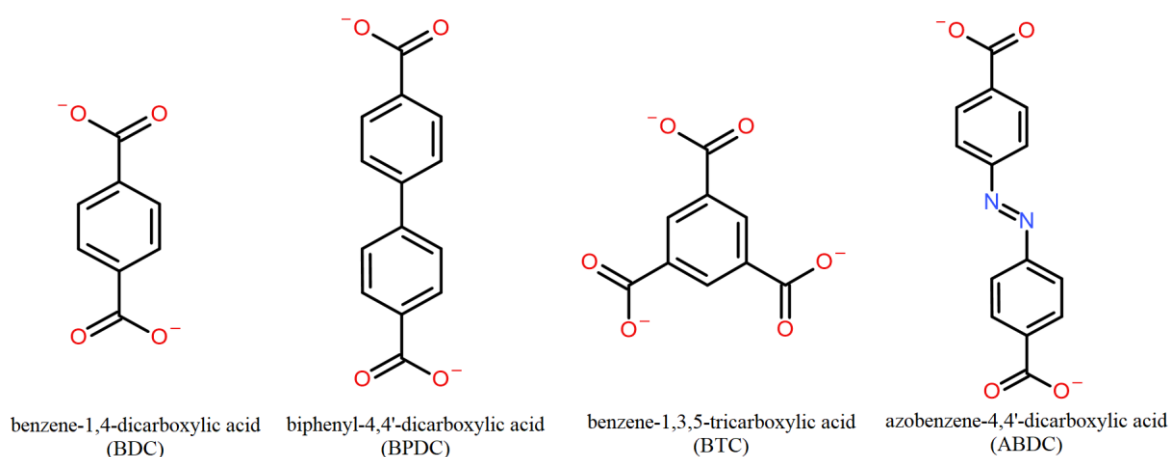


Fig.I.2.1-2. Common anionic ligands (adapted)

Source: Robin, A.Y., Fromm, K.M., *Coord. Chem. Rev.*, 250(15-16) (2006), 2127:2157

I.2.2. Dimensionality and structural motifs

The dimensionalities of the PCPs depend on how the building blocks are organized in the structure, mainly on how the metal atoms coordinate the ligands considering that most ligands have a rod-like structure. The stereochemistry of the metal atoms has an important role in the formation of 1D or 2D coordination polymers or 3D frameworks and is a function of the coordination number characteristic to the metal [13]. In certain coordination systems, the counter anions, introduced additionally to the system or provided by the metal salt, have a

higher influence on the arrangement of the building blocks and control the resulting architectures [15,16]. Therefore, a way to control the dimensionality, as well as the structural motifs of a coordination polymer is by using the proper metal salt.

Structural motifs describe the arrangement of metal atoms and organic ligands within the structure of the coordination polymers, based on the stereochemistry of the metal and the number of coordinated ligands. As such, for 1D motifs, the metal atom is coordinated by two divergent ligands, leading to infinite chains, while in the 2D motifs there are three or four ligand molecules coordinated to the metal ion which expand on two directions. 3D motifs are formed using four or six ligands depending on the geometry of the metal which in most of the cases is tetrahedral or octahedral [17]. As shown in Figure I.2.2-1., the most common motifs for 1D PCPs are: linear, zigzag, double chain, helix, ladder, fish bone, and railroad; for 2D – honeycomb, brickwall, herringbone, bilayer; and for 3D – diamondoid, octahedral, and NbO net.

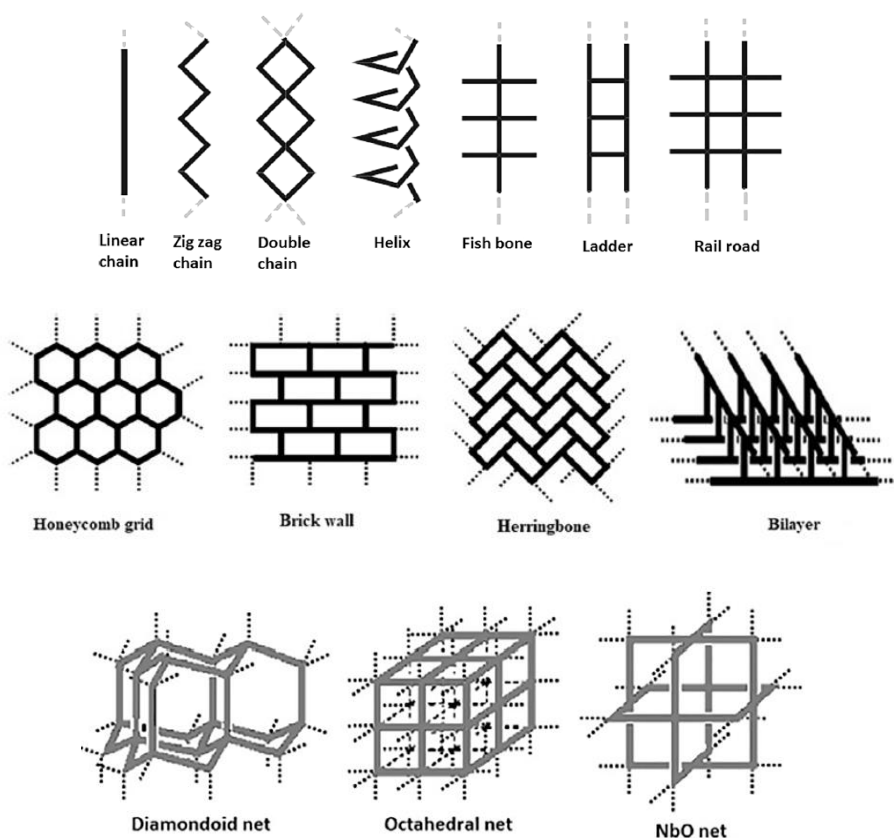


Fig.I.2.2-1. 1D (top), 2D (middle) and 3D (bottom) motifs of coordination polymers
Source: Ghosh, A., Hazra, A., Mondal, A., Banerjee, P., *Inorg. Chim. Acta*, 488 (2019), 86:119

I.2.3. Porosity and Flexibility

Porosity is essential in designing high performance materials mainly for storage, due to the empty space that is formed, but also for catalysis, because it provides a high surface area which is important for the catalytic process. Another application determined by porosity is separation; coordination polymers can be used in separation processes in the same fashion as zeolites. Due to its importance for previously mentioned applications, many studies have focused on increasing the porosity limit while maintaining the robustness of the polymer [18].

The easiest control of the pore size can be obtained by varying the length of ligands within the same type of network [9]. For large pore sizes however, it may be possible for the structure to collapse in the absence of a guest molecule or at its removal. At the same time, the catenation effect may occur, in which interpenetrating structures are formed in order to minimize the free space in the packing of the constituent particles in solids. A selection of pore structure in a series of different MOFs is illustrated in Figure I.2.3-1.

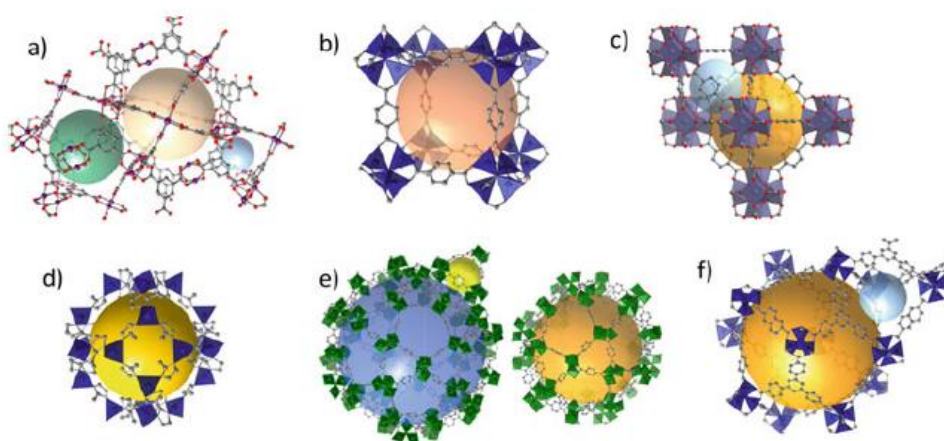


Fig.I.2.3-1. Pore structures in HKUST-1 (a), MOF-5 (b), UiO-66 (c), ZIF-8 (d), MIL-101 (e), DUT-6 (f)

Source: Bon, V., Senkowska, I., Kaskel, S., Chapter 6: Metal-Organic Frameworks in Nanoporous Materials for Gas Storage, Green Energy and Technology, (2019), 137:172.

Flexibility is the property of porous coordination polymers to reversibly change their structure upon applying external stimuli, such as: guest molecules, heat, an electro-magnetic field, giving an advantage to these compounds over the other porous materials (zeolites and activated carbon). Guest molecules are the main factor that influences flexibility of PCPs, and can be classified into - rotation of bridging ligands (a), shape fitting response (b) or interpenetration (c) [19], as can be seen in Figure I.2.3-2.

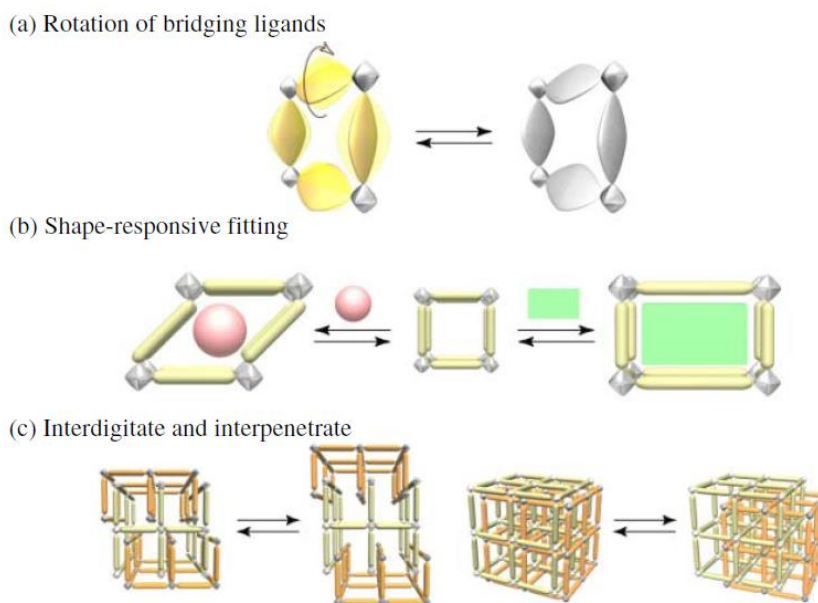


Fig.I.2.3-2. Schematic representation of PCPs flexible property

Source: Bureekaew, S., Shimomura, S., Kitagawa, S., Sci. Technol. Adv. Mater., 9(1) (2008), 014108

I.3. Applications of PCPs

Given their unique intrinsic properties, PCPs have found a wide variety of domains where they can be applied. Starting from areas that rely on their porosity, such as adsorption and separation, catalysis and even biomedical field, to applications focused on the metal ions properties like magnetism and luminescence. The usage of PCPs in the fields of catalysis and gas storage is presented below.

I.3.1. Catalysis

PCPs are used in catalysis due to their unique features and, although these compounds do not expose many coordinatively unsaturated metal sites, which could act as active catalytic sites, alternatives are used to prepare PCP-based type catalysts. Amongst these, the most accessible are: the use of functional organic sites [20], incorporation of nanocatalysts [21], or the structural modification in order to add unsaturated coordinative metal sites [22]. Also, post-synthetic modifications may be used in order to tune coordination polymers for catalysis or to create PCP-based catalysts.

Functional organic sites

Hasegawa *et al.* underlined the importance of functional organic sites in catalytic processes by using a tridentate ligand containing amide groups to develop a Cd(II) PCP-

based catalyst for Knoevenagel condensation reactions [20]. The synthesized compound, $\{[\text{Cd}(4\text{-btapa})_2(\text{NO}_3)_2] \cdot 6\text{H}_2\text{O} \cdot 2\text{DMF}\}_n$, where 4-btapa = 1,3,5-benzene tricarboxylic acid tris[N-(4-pyridyl)amide], consists of octahedral Cd^{2+} ions coordinated by six different ligand molecules. The arrangement of connectors and linkers generates six-membered ring composed of three octahedral Cd(II) and three 4-btapa units which interpenetrates to form 3D channels in the crystalline structure. The extended structure of $\{[\text{Cd}(4\text{-btapa})_2(\text{NO}_3)_2] \cdot 6\text{H}_2\text{O} \cdot 2\text{DMF}\}_n$ is presented in Figure I.3.1-1.

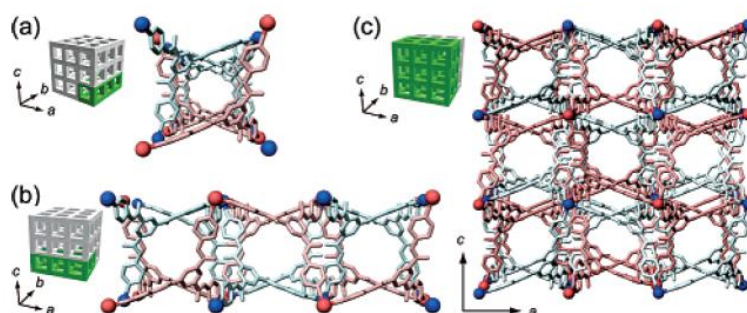


Fig.I.3.1-1. 3D crystal structure of $\{[\text{Cd}(4\text{-btapa})_2(\text{NO}_3)_2] \cdot 6\text{H}_2\text{O} \cdot 2\text{DMF}\}_n$

Source: Hasegawa, S., Horike, S., Matsuda, R., Furukawa, S., Mochizuki, K., Kinoshita, Y., Kitagawa, S., *J. Am. Chem. Soc.*, 129(9) (2007), 2607:2614

The amide functional group has two types of hydrogen-bonding sites: the electron acceptor $-\text{NH}$ and the electron donor $-\text{C}=\text{O}$ parts which are working as interaction sites with the substrate during the catalytic process. The Knoevenagel condensation reaction was performed using the benzaldehyde and three methylene compounds (malononitrile, ethyl cyanoacetate and cyano-acetic acid *tert*-butyl ester) with the Cd(II) PCP-based catalyst. The result revealed that the reaction takes place within the channels and not on the surface of the catalyst. High conversion values are obtained for substrates close to the dimensions of the channels, $4.7 \times 7.3 \text{ \AA}$, as the substrate molecules have to fit into the channels for the reaction to proceed [20].

Nanocatalysts

When incorporating metal nanoparticles, the coordination polymers act as support, but also as a template because the walls of PCPs framework apply constraints, restricting the growth and yielding to a uniform size distribution of the nanoparticles. El-Shall *et al.* conducted a study in which they incorporated Pd, Cu and Pd-Cu nanoparticles, respectively,

into MIL-101, a chromium-based metal-organic framework for the catalytic oxidation of carbon monoxide [21].

MIL-101 supported nanocatalysts were obtained using two methods based on the simultaneous activation of the pores and the rapid chemical reduction of the metal precursors using hydrazine and microwave irradiation. The first method consists in addition of metal nitrate to an aqueous dispersion of MIL-101, followed by the addition of hydrazine and heating with microwave irradiation. In the second method, the MIL-101 was stirred in the nitrate solution, separated by centrifugation, and then it was redispersed in water following the addition of hydrazine and heating with microwave irradiation [22]. Higher loadings of nanoparticles were obtained using the first method.

Unsaturated coordinative sites

To use unsaturated coordinative metal sites, supplementary anchor points are required in the structure of the ligand that can coordinate to metal ions. The desired active metal site must not be involved in the formation of the framework and should have space available for interaction with the substrate molecules. In this regard, bridging ligands with acidic or basic functional groups, such as carboxylic or sulfonic and amine group, respectively, are a good choice in the synthesis of such compounds [22]. Chen *et al.* obtained a chromium-based porous coordination polymer having unsaturated chromium ions by using an isophthalic acid ligand modified with sulfonic groups. The compound was used as an acid catalyst to transform glucose into 5-hydroxymethylfurfural (HMF) in a biomass recovery process due to the fact that is representing a renewable and sustainable alternative to fossil resources. The catalyst was prepared using a hydrothermal method by self-assembly of monosodium 5-sulfoisophthalate with metal ions and high conversion values were reported [23].

I.3.2. Gas storage

Due to their adsorption properties, porous coordination polymers were rapidly recognized as gas storage and separation materials. Kitagawa *et al.* were the first to report the methane adsorption in 1997-2000, using three-dimensional frameworks build from 4,4'-bipyridine linkers and M(II) = Co, Ni, Zn connectors. In 2003, the first hydrogen storage measurements performed on isorecticular MOF-5 and IRMOF-8 were reported by Yaghi *et al.* [9,24].

PCPs exhibit high gravimetric and volumetric storage capacity and also a stronger interaction with the gas molecules [24], which gives an advantage to these compounds over

other porous materials. However, the most important feature for a higher uptake of gas molecules is the pores size, influencing the gas storage at both high and low pressures [9]. When the pore dimension is closer to the size of the gas molecules a stronger interaction will be formed which will lead to a better adsorption of the guest into the pores.

On the background of heavy industrialization and chemicals production, which in turn have negative effects on both the environment and society (i.e. high atmospheric pollution, consumption of resources and the increase of the ever-present greenhouse effect) a better control or even a decrease of these effects is mandatory. This can be achieved with the use of metal organic frameworks to alleviate the greenhouse effect caused by the carbon dioxide, to control the toxic gases, such as carbon monoxide, ammonia, and hydrogen sulfide and to widespread the clean energy through the use of energy-related gases (hydrogen and low molecular weight hydrocarbons) [25].

Carbon dioxide storage

Large amounts of carbon dioxide are released during the combustion of fossil fuels for the energy production. PCPs separate and capture the carbon dioxide from the gas mixture based on the different interaction of gas molecules with the frameworks.

CO₂ capture using PCPs are performed in the following situation: post-combustion capture, pre-combustion capture, oxy-fuel combustion, and direct capture from air. In the post-combustion capture, carbon dioxide is absorbed at low pressure, usually atmospheric pressure, while in the pre-combustion, captured of fuels must first undergo decarbonation and the carbon dioxide is adsorbed at high pressures (5-40 bars) in order to obtain zero CO₂ during the combustion step. Oxy-fuel combustion implies the use of nearly pure O₂ and will result in almost completely CO₂ generated gas, after the removal of water, thus facilitating the capture step [25].

De *et al.* synthesized two isostructural porous coordination polymers using a linear tetracarboxylic acid ligand, decorated with amino groups, and zinc or copper nitrates, respectively. The Cu-based MOF proved to be more stable and allows the removal of the solvent molecules leading to a high porous surface and thus, becoming a good candidate for hydrogen, methane, and carbon dioxide adsorption. The porous structure of Cu-MOF is illustrated in Figure I.3.2-1. The CO₂ adsorption and desorption isotherms at 0 and 25 °C revealed that the CO₂ adsorption capacity of Cu-MOF reaches the values of approximately 90 cm³g⁻¹ and with the decrease of temperature the adsorbed CO₂ volume increases reaching almost 200 cm³g⁻¹ at 0 °C [26].

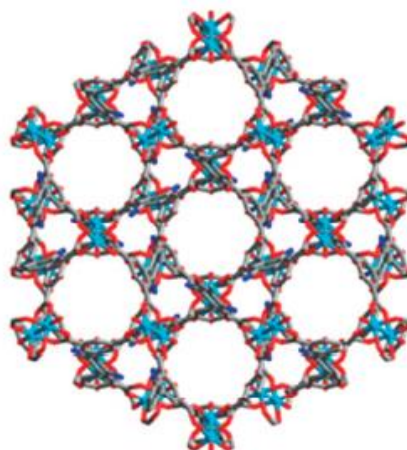


Fig.I.3.2-1. Structure of Cu-based MOF for CO₂ adsorption

Source: De, D., Pal, T.K., Neogi, S., Senthilkumar, S., Das, D., Gupta, S.S., Bharadwaj, P.K.,
Chem. Eur. J., 22(10) (2016), 3387:3396

Hydrogen storage

Hydrogen is an excellent alternative for coal and gasoline because of its ultrahigh gravimetric combustion heat and benign combustion products. At the same time, hydrogen could improve the environment if it would be used as fuel for automobiles. Two techniques are exploited for the hydrogen storage with the use of porous coordination polymers: cryo-temperature storage which implies the retaining of hydrogen in a tank filled with PCPs at usually 77 K, relatively low pressure (below 100 bars), and room-temperature storage. Because of the weak interactions of the PCPs with the surface at room temperature, hydrogen adsorption does not work efficiently [25]. The structure of MOF-177, a compound used for hydrogen storage, is presented in Figure I.3.2-2.

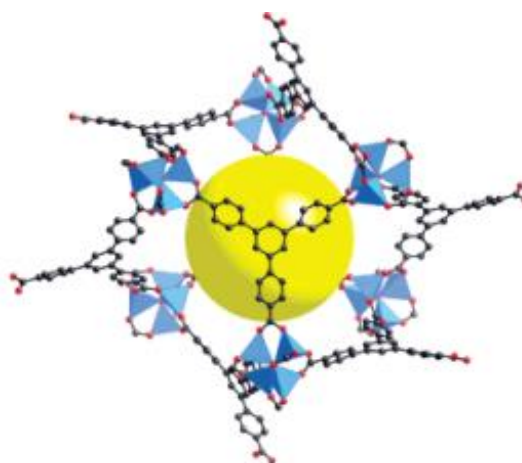


Fig.I.3.2-2. Structure of MOF-177

Source: Saha, D., Deng, S., Tsinghua Sci. Technol., 15(4) (2010), 363:376.

Hydrocarbons storage

Hydrocarbons adsorption by porous coordination polymers takes place via van de Waals interactions between the hydrocarbons and the frameworks and also uses of the flexibility of the PCPs for a better uptake depending on the hydrocarbon concentrations [25]. Besides hydrogen, methane is another fuel alternative due to its low carbon emission and thermal efficiency and also because of its abundance, being the major component of natural gas [28]. Due to its potential, many studies focused on the methane adsorption using different PCP architectures.

Acetylene is the simplest alkyne and is widely used as gas for oxy-acetylene welding and metal cutting and is a key starting material for electronic materials, as well as in manufacturing of various fine chemicals, such as vinyl chloride and methyl acrylate [28].

Jiang *et al.* reported the synthesis of MOF materials based on the Zn_4O cluster, benzene-1,3,5-tri- β -acrylic acid (H_3BTAC) ligand and a series of functionalized benzene dicarboxylic acids (H_2DBC) linkers. The structure of MOF-905, one of the compounds used can be observed in Figure I.3.2-3. These compounds were used for methane adsorption at both low and high pressure and room temperature. The results shown methane uptake between $7.7\text{-}11.0\text{ cm}^3\text{g}^{-1}$ at low pressure (1.1 bar) and an increase of the loading capacity of approximately 39 times at high pressure (80 bar), the highest value obtained being $310\text{ cm}^3\text{g}^{-1}$ [29].

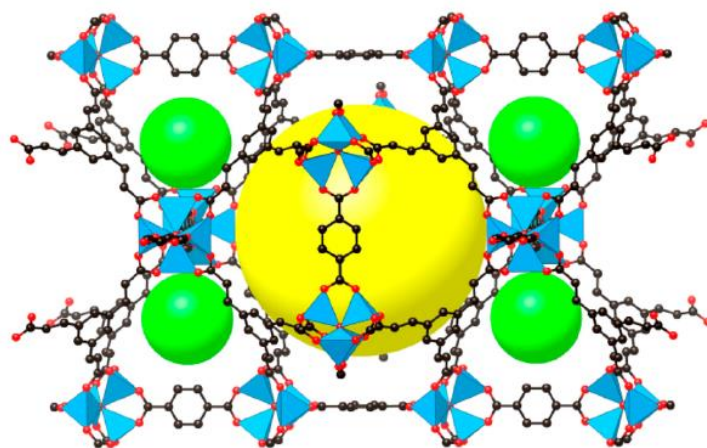


Fig.I.3.2-3. Structure of MOF-905 with the octahedral (yellow) and tetrahedral (green) cages

Source: Jiang, J., Furukawa, H., Zhang, Y.-B., Yaghi, O.M., *J. Am. Chem. Soc.*,
138(32) (2016), 10244:10251

Yuan *et al.* obtained a porous coordination polymer based on copper clusters and isophthalate ligands that show high acetylene uptake at ambient conditions. An interesting feature of this compound is the pore distribution which defines three types of nanocages with

pore diameters of 15, 12 and 8 Å, respectively. The acetylene adsorption test revealed a very good uptake at room temperature, around $220 \text{ cm}^3\text{g}^{-1}$ and maximum uptake of $280 \text{ cm}^3\text{g}^{-1}$ achieved at 0°C [28].

Toxic gases storage

The separation and storage of toxic gases, such as carbon monoxide (CO), nitrogen oxides (NO, NO₂), ammonia (NH₃), sulfur dioxide (SO₂), and hydrogen sulfide (H₂S) are related to human health and chemical production [25].

Leroux *et al.* obtained a Cd-based porous coordination polymer with piridinium carboxylate ligands (Figure I.3.2-4.). The compound has tetrameric building blocks that generate hexagonal channels in the final structure of the compounds. The adsorption tests had shown a high ammonia uptake at room temperature, reaching a maximum of 22.8 mmol/g at 900 hPa that corresponds to 0.39 g of ammonia per 1 g of compound [30].

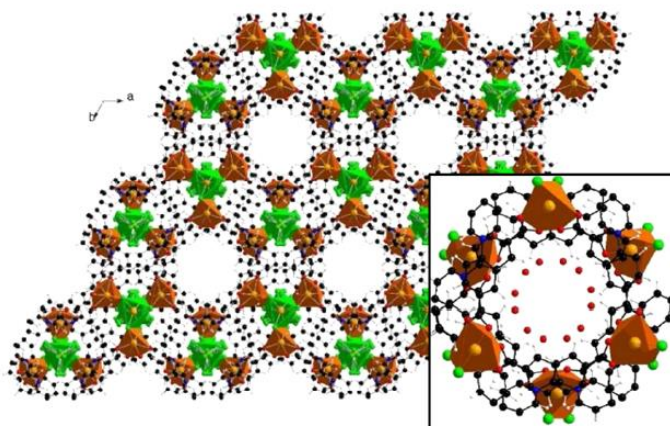


Fig.I.3.2-4. General view of Cd-based PCP showing hexagonal channels

Source: Leroux, M., Mercier, N., Allain, M., Dul, M.-C., Dittmer, J., Kassiba, A.H., Bezverkhyy, I., *Inorg. Chem.*, 55(17) (2016), 8587:8594

Belmabkhout *et al.* developed a series of isostructural metal-organic framework with square-octahedral topology (soc-MOF), using azobenzene tetracarboxylic acid (ABTC) linking groups and different oxo-centered trinuclear metal cluster ($M = \text{In}^{3+}, \text{Fe}^{3+}, \text{Ga}^{3+}, \text{Al}^{3+}$). The general structure of the $\{[\text{M}_3\text{O}(\text{ABTC})_6]\}_n$ compounds can be seen in Figure I.3.2-5. The gas adsorption was performed for carbon dioxide, different hydrocarbons with low molecular weight and hydrogen sulfide. The results revealed that H₂S exhibits high affinity towards the Ga-based compound, which can be explained by the favorable binding to the exposed and coordinatively unsaturated M^{3+} open metal sites [31].

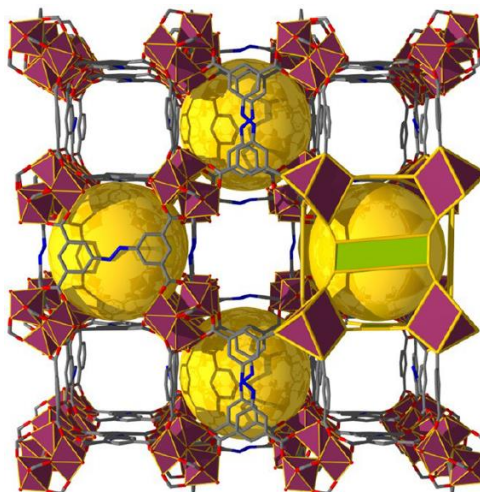


Fig.I.3.2-5. Structure of $\{[M_3O(ABTC)_6]\}_n$ compounds

Source: Belmabkhout, Y., Pillai, R.S., Alezi, D., Shekhah, O., Bhatt, P.M., Chen, Z., Eddaoudi, M., J. Mater. Chem. A, 5(7) (2017), 3293:3303

I.3.3. Ion exchange/sorption

This application relies on the MOFs property to interact with external chemicals, notably ionic species, and is usually implemented in water treatment, as most pollutants are heavy metals ions (Hg^{2+} , Pb^{2+} , Cd^{2+}) or anionic species (CrO_4^{2-} , CN^- , NO_3^- , ClO_4^- etc).

Conventional material, such as organic resins and inorganic materials (zeolites and layered double hydroxides – LDHs), have been investigated for their ion-exchange properties but each of them suffers from different drawbacks: in the case of organic resins - poor regeneration, relatively low thermal and chemical stability and for LDHs or zeolites - slow sorption kinetics and limited selectivity. In this regard, MOFs that exhibit ion-exchange/sorption properties may be considered as a next-generation of materials because it combines a highly-ordered porous structure, which is not typical for organic resins, and a large variety of binding groups that are not present in traditional inorganic ion exchangers [32].

Ion-exchanging MOFs are designed to work mostly as anion-exchangers and their synthesis employs the use of neutral polytopic organic ligands like DABCO (1,4-diazabicyclo[2,2,2]octane) and poly-pyridines [32], by combining these neutral ligands with polycarboxylate compounds [33] or through the use of ligands that possess both neutral and anionic points for coordination to metal ions. Other methods employ the post-synthetic ligand or metal ion exchanges [34] which can be used for tuning neutral MOFs for ion-exchange or enhancing MOFs that have an ionic framework.

Chapter II. Experimental Part

II.1. Synthesis of Cu-based PCPs with Kagomé layers

Three-dimensional Cu-based porous coordination polymers were obtained using $\text{Cu}(\text{BF}_4)_2 \cdot 6\text{H}_2\text{O}$ or $\text{Cu}(\text{ClO}_4)_2 \cdot 6\text{H}_2\text{O}$ salts and different exo-bidentate bipyridine-based ligands, such as: 1,2-bis(4-pyridyl)ethylene (bpe), 1,2-bis(4-pyridyl)ethane (bpe), and 4,4'-azopyridine (azopy).

In the first part of the synthesis, 1 mmol of bipyridine-based ligand was dissolved in a mixture of methanol and water, then it was added over a methanolic solution containing 1 mmol of Cu(II) salt. The resulting mixture was magnetically stirred for 30 minutes at room temperature, forming a blue/purple suspension or orange in the case of azopyridine, due to the intense color of the ligand.

During the second step, several drops of aqueous ammonia (25%) is added dropwise to the mixture yielding a clear dark blue solution (brown, when azopyridine is used) which is then stirred for another 10 minutes at room temperature. The synthesis of Cu-based porous coordination polymers is depicted in Figure II.1-1.

The final solution undergoes a slow evaporation process during which atmospheric carbon dioxide is directly fixed into the structure as carbonate (CO_3^{2-}) due to the basic conditions provided by ammonia. After several days, small blue-purple crystals are formed except in the case of azopyridine where brown crystals are formed after 2-3 weeks.

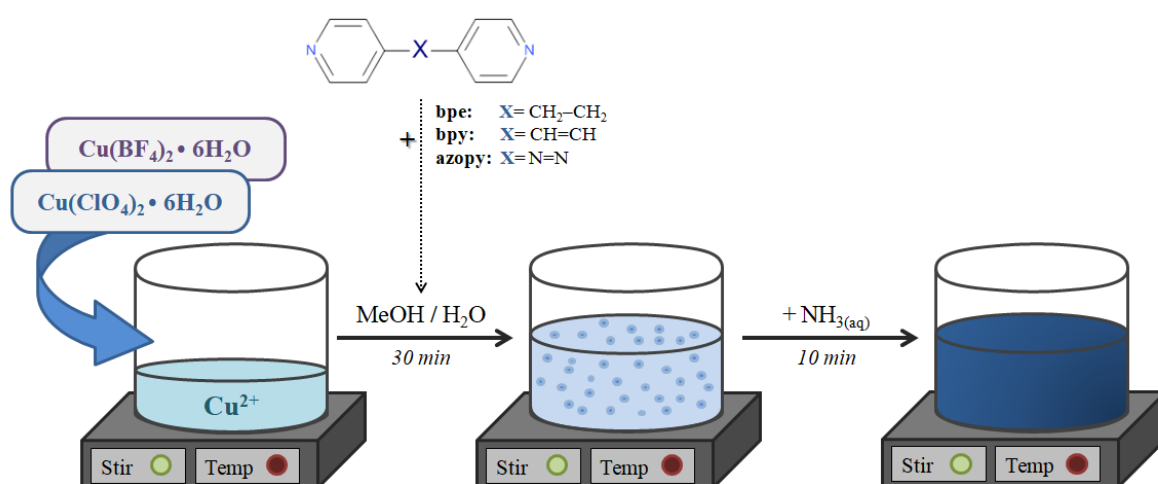


Fig.I.1-1. Synthesis of Cu-based porous coordination polymers

II.2. Characterization of Cu-based PCPs with Kagomé layers

II.2.1. Structural characterization

Single crystal X-ray diffraction revealed that all compounds crystallize in a hexagonal system, belonging to P-6 space group, and share the general formula $\{[\text{Cu}_3(\text{CO}_3)_2(\text{L})_3](\text{Y})_2\}_n$, where L = bipyridine-based ligand and Y = ClO_4^- or BF_4^- anions. In total, six isostructural compounds were obtained: L = bpy, Y = ClO_4^- (**1**), L = bpy, Y = BF_4^- (**2**), L = bpe, Y = ClO_4^- (**3**), L = bpe, Y = BF_4^- (**4**), L = azopy, Y = ClO_4^- (**5**), L = azopy, Y = BF_4^- (**6**). The crystallographic data of compounds **1**, **2**, **3**, and **6** are given in Table II.2.1-1.

Table II.2.1-1. Crystallographic parameters for **1**, **2**, **3** and **6**

Compound	(1)	(2)	(3)	(6)
Formula	$\text{C}_{38}\text{H}_{30}\text{Cl}_2\text{Cu}_3\text{N}_6\text{O}_{14}$	$\text{C}_{38}\text{H}_{30}\text{B}_2\text{Cu}_3\text{F}_8\text{N}_6\text{O}_6$	$\text{C}_{38}\text{H}_{36}\text{Cl}_2\text{Cu}_3\text{N}_6\text{O}_{14}$	$\text{C}_{32}\text{H}_{24}\text{B}_2\text{Cu}_3\text{F}_8\text{N}_{12}\text{O}_6$
Formula mass / g mol^{-1}	1056.20	1030.92	1062.25	1036.87
Crystal system	Hexagonal	Hexagonal	Hexagonal	Hexagonal
Space group	P-6	P-6	P-6	P-6
$a/\text{Å}$	9.297(5)	9.275(3)	9.396(1)	9.279(6)
$c/\text{Å}$	13.364(8)	13.371(4)	13.296(2)	12.961(7)
$V/\text{Å}^3$	1000.4(1)	996.2(7)	1016.6(3)	966.6(1)
$\rho/\text{g cm}^{-3}$	1.753	1.718	1.735	1.781
T/K	293(2)	293(2)	293(2)	293(2)
Z	1	1	1	1
Goodness of fit (S)	1.105	1.105	1.106	1.604
R	0.0413	0.0422	0.0876	0.1064
wR	0.1068	0.1108	0.2323	0.3264

The Cu-based porous coordination polymers consists of 2D $[\text{Cu}_3(\text{CO}_3)_2]^{2+}$ layers in the crystallographic *ab*-plane, which act as secondary building units (SBU) that are further linked one to another by the bipyridine-based ligands along the *c*-axis, yielding to a 3D pillared-layer framework of Cu atoms with mixed anionic and neutral ligands, as it can be observed in Figure II.2.1-1. Disordered ClO_4^- or BF_4^- anions are positioned along the *c*-axis and neutralize the remaining charge of the framework.

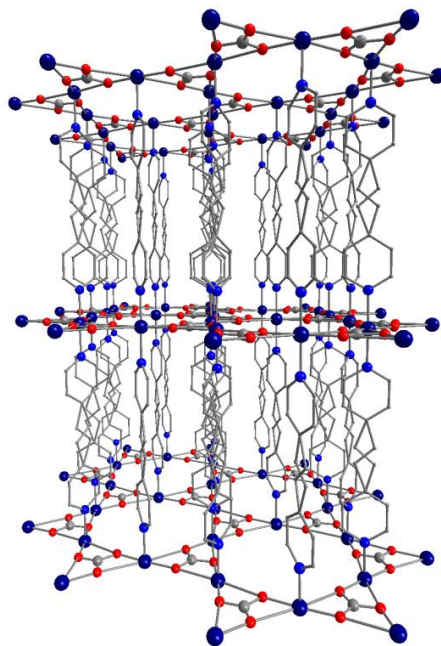


Fig.II.2.1-1. Structure of $\{[\text{Cu}_3(\text{CO}_3)_2(\text{L})_3](\text{Y})_2\}_n$
H atoms and counter ions were omitted for clarity.

Each Cu(II) center has a coordination number of six, displaying an octahedral geometry with disordered vertices as a result of the Jahn–Teller effect. The coordination environment of Cu(II) atoms (illustrated in Figure II.2.1-2.) is satisfied by four oxygen atoms from two crystallographically independent CO_3^{2-} anions, of which two occupy the apex positions of the octahedron and the other two form the basis of the octahedron together with two nitrogen atoms from two different bipyridine-based ligands. The specific bond lengths between the metal ion and donor atoms are in the range of 1.959(7) – 2.739(8) Å, while the specific angles vary between 51.5(1) – 131.8(2) degrees. These values differ in each compound and are detailed in Table II.2.1-2 and Table II.2.1-3.

CO_3^{2-} anions act as tridentate tris-chelated ligands and connect three different Cu(II) atoms through μ_2 -oxo bridges in a planar trigonal arrangement. These trigonal units build up a perfectly planar $\text{Cu}(\text{CO}_3)$ layer with hexagonal arrangement in the crystallographic *ab*-plane, known in the literature as Kagomé layer, and is presented in Figure II.2.1-2. The Jahn–Teller axes of the Cu(II) centers lie in the plane of the Kagomé layer, leading to a concerted rotation of each carbonate unit from its regular orientation [6]. The angles have a slightly variation in the synthesized compounds, being in the 171.0(1) – 175.3(3) degrees range for Cu–O(1)–Cu angles and 172.2(3) – 179.1(2) for Cu–O(2)–Cu angles, respectively. The ClO_4^- or BF_4^- anions are in symmetry-related disorder and occupy the hexagonal pores of the Kagomé planes, as well as the void spaces between the bipyridine-based pillars.

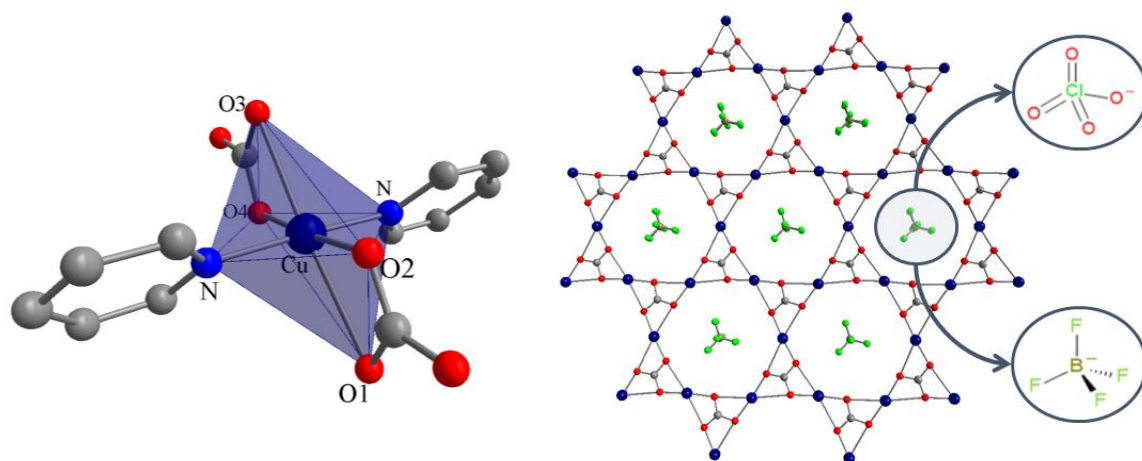


Fig.II.2.1-2. Coordination environment of Cu(II) and Kagomé layer in $\{[\text{Cu}_3(\text{CO}_3)_2(\text{L})_3](\text{Y})_2\}_n$ with counter anions in the hexagonal pores

Table II.2.1-2. Specific bond lengths in compounds **1**, **2**, **3** and **6**

Bond	Length (Å)			
	1	2	3	6
Cu – O(1)	2.739(8)	2.721(6)	2.720(1)	1.995(3)
Cu – O(2)	1.959(7)	1.959(7)	1.974(1)	2.599(4)
Cu – O(3)	2.655(8)	2.650(5)	2.643(1)	2.505(2)
Cu – O(4)	1.970(6)	1.968(7)	2.080(2)	2.505(3)
Cu – N	1.999(5)	1.998(5)	2.000(1)	1.965(8)

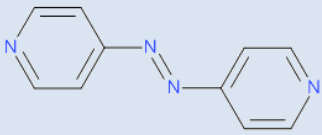
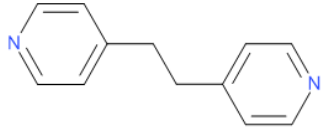
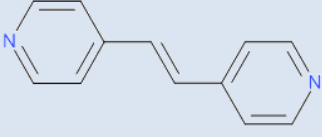
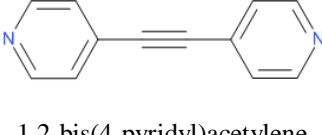
Table II.2.1-3. Specific angles in compounds **1**, **2**, **3** and **6**

Atoms	Angle (°)			
	1	2	3	6
O(1) – Cu – O(2)	52.3(2)	53.1(2)	55.4(5)	59.1(1)
O(2) – Cu – O(3)	120.6(2)	120.5(2)	130.5(6)	123.1(1)
O(3) – Cu – O(4)	55.3(2)	54.9(2)	51.8(8)	51.5(1)
O(1) – Cu – O(4)	131.8(2)	131.4(2)	123.1(7)	126.2(1)
O(2) – Cu – N	89.8(1)	90.0(1)	90.0(3)	92.8(6)
O(4) – Cu – N	90.2(1)	90.0(1)	90.0(3)	87.4(4)
O(1) – Cu – N	89.2(1)	89.2(1)	91.0(3)	89.7(5)
O(3) – Cu – N	90.8(1)	90.8(1)	89.0(3)	90.3(5)

The overall size of the coordination polymers is determined by the sizes of the 2D $[\text{Cu}_3(\text{CO}_3)_2]^{2+}$ layers as well as the distances between them. The size of the layer is a function of the amount of CO_2 that is fixed into the structure as this is a key factor in obtaining the Kagomé layers and may be correlated with the amount of connectors, since the SBU layers have a ratio between Cu^{2+} and CO_3^{2-} ions of 3:2.

The interlayer distance (Table II.2.1-4) provides information about the void space within the channels and is directly dependent on the length of the linkers. As expected, the distance increases from 12.960 Å to 13.603 Å with the increase of the spacer length between the two pyridyl rings. The highest value is obtained in the case of 1,2-bis(4-pyridyl)acetylene due to the linear arrangement of this molecule [6]. For 1,2-bis(4-pyridyl)ethylene and 1,2-bis(4-pyridyl)ethane ligands, the variation is given by the flexibility/rigidity of the spacer with the latter providing a shorter interlayer distance due to compression movements.

Table II.2.1-4. Interlayer distances in $\{[\text{Cu}_3(\text{CO}_3)_2(\text{L})_3](\text{Y})_2\}_n$

Ligand	Distance (Å)
 4,4'-azopyridine	12.960 (for BF_4^-)
 1,2-bis(4-pyridyl)ethane	13.296 (for ClO_4^-)
 1,2-bis(4-pyridyl)ethylene	13.365 (for ClO_4^-) 13.371 (for BF_4^-)
 1,2-bis(4-pyridyl)acetylene	13.606 (for ClO_4^-) [6]

Powder X-ray diffraction (PXRD) analysis was employed for characterization of the compounds in terms of crystalline phase purity. Each sample was grounded and then exposed to Cu-K α radiation at room temperature, in the 5 – 35 degrees range of 2θ . The X-ray powder diffractogram of compound **2** is presented in Figure II.2.1-3. All diffraction peaks observed in the powder XRD pattern are well defined, indicating a good crystallinity of the probe. It can be observed that the experimental pattern of diffraction corresponds with the theoretical one, generated from the crystallographic information file (cif), thus showing the purity of the crystalline phase. The intense peak obtained at 22 degrees of 2θ is due to preferential arrangement of crystallographic planes which occurs during the grounding of the sample. This diffraction pattern was obtained in all synthesized compounds thus showing the phase purity for this family of isostructural MOFs. Diffractograms of the other compounds are attached in Appendix (section A, Figures A1 – A5).

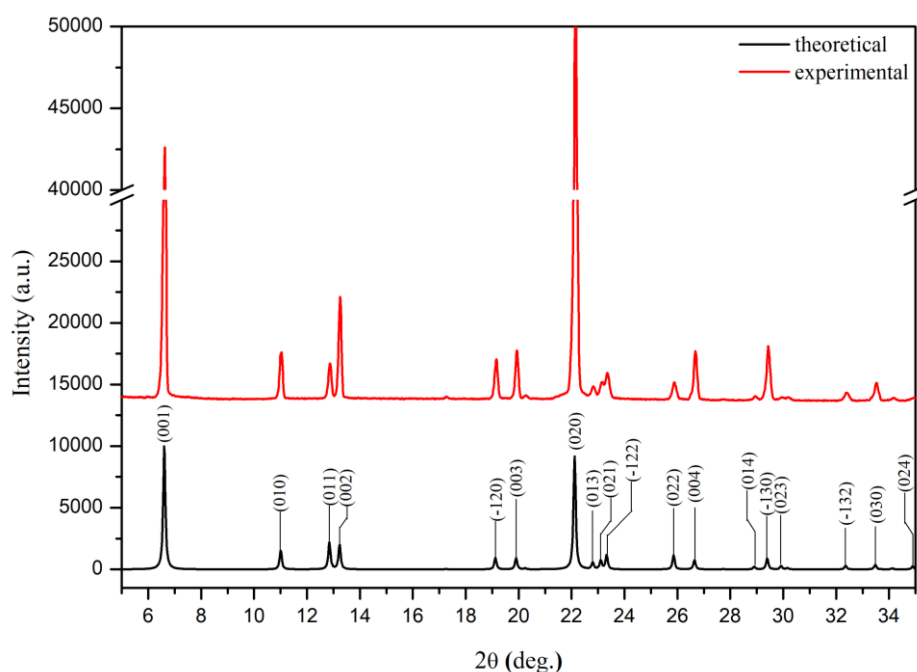


Fig.II.2.1-3. Powder XRD pattern of compound **2**

II.2.2. Spectral characterization

The infrared spectra (all IR spectra are included in the Appendix, section C, Figures C1 – C6) were recorded in the 4000 – 400 cm^{-1} range and it has been observed that all synthesized compounds follow the same pattern of peaks with very few variations, which explains the structural similarities of the compounds as well as the type of existing bonds. Around 1450, 1032 and 871 cm^{-1} one strong and two medium peaks appear and characterize

the bridging carbonate within the Kagomé layers. The bipyridine-based ligands are described by a series of peaks: two weak peaks in the 3100 – 3000 cm⁻¹, a medium one in the 1625 – 1610 cm⁻¹ range, two weak peaks in the 1350 – 1230 cm⁻¹ range, and a weak (in the case of compounds 5 and 6) peak around 1426 cm⁻¹.

BF₄⁻ anions are characterized by a strong peak in the 1100 – 1050 cm⁻¹ range. The infrared spectra of coordination complexes **1**, **3**, and **5** show two intense bands, at around 1100 and 630 cm⁻¹ attributed to the presence of the ClO₄⁻ anions. These bands are assigned to the anti-symmetric stretching and anti-symmetric bending vibration mode, respectively [35]. The former band is split with a poorly defined maximum showing the deformation from Td symmetry [36]. At low wavenumbers metal – donor atoms bonds may be identified, in the present compounds the stretching vibration modes of Cu–O and Cu–N bonds have a medium peak around 560 cm⁻¹ and weak peaks around 440 cm⁻¹, respectively. The characteristic vibrations for each compound are given in Table II.2.2-1.

Table II.2.2-1. Characteristic vibrations (cm⁻¹) of {[Cu₃(CO₃)₂(L)₃](Y)₂]_n

Bonds	Compounds					
	1	2	3	4	5	6
ν C–H	3099 (w)	3102 (w)	3098 (w)	3101 (w)	3100 (w)	3103 (w)
	3051 (w)	3053 (w)	3050 (w)	3053 (w)	3049 (w)	3051 (w)
			1235 (w)	1236 (w)		
ν C=N	1617 (m)	1617 (m)	1619 (m)	1620 (m)	1609 (m)	1609 (m)
	1450 (s)	1451 (s)	1443 (s)	1444 (s)	1450 (s)	1450 (s)
ν CO ₃	1032 (m)	1031 (m)	1034 (m)	1033 (m)	1031 (m)	1030 (m)
	871 (m)	873 (m-s)	840 (m)	875 (m)	862 (m)	862 (m)
ν N=N	–	–	–	–	1426 (w)	1427 (w)
ν C=C	1354 (w)	1355 (w)	1346 (w)	1347 (w)	1330 (w)	1331 (w)
	1254 (w)	1255 (w)				
ν ClO ₄ ⁻	1090 (s)	–	1087 (s)	–	1084 (s)	–
	623 (m)		669 (m)		623 (m-w)	
ν BF ₄ ⁻	–	1056 (s)	–	1054 (s)	–	1064 (s)
ν Cu–O	556 (m)	557 (m)	546 (m)	547 (m)	557 (m)	578 (m)
ν Cu–N	437 (w)	435 (w)	447 (w)	434 (w)	445 (w)	435 (w)

The UV-Vis spectra of the Cu(II)-based compounds were recorded in solid state in the 200 – 850 nm range and are presented in Figure II.2.2-1. As it can be observed, all compounds share the same pattern of electronic transitions, with three main absorption maxima. At higher energy values (250 – 270 nm range) are the $\pi \rightarrow \pi^*$ transitions of the bipyridine-based ligands. The ligand-to-metal charge transfer (LMCT) can be assigned to the transition bands in the 360 – 385 nm range and probably involves the oxygen donor atoms of the carbonate.

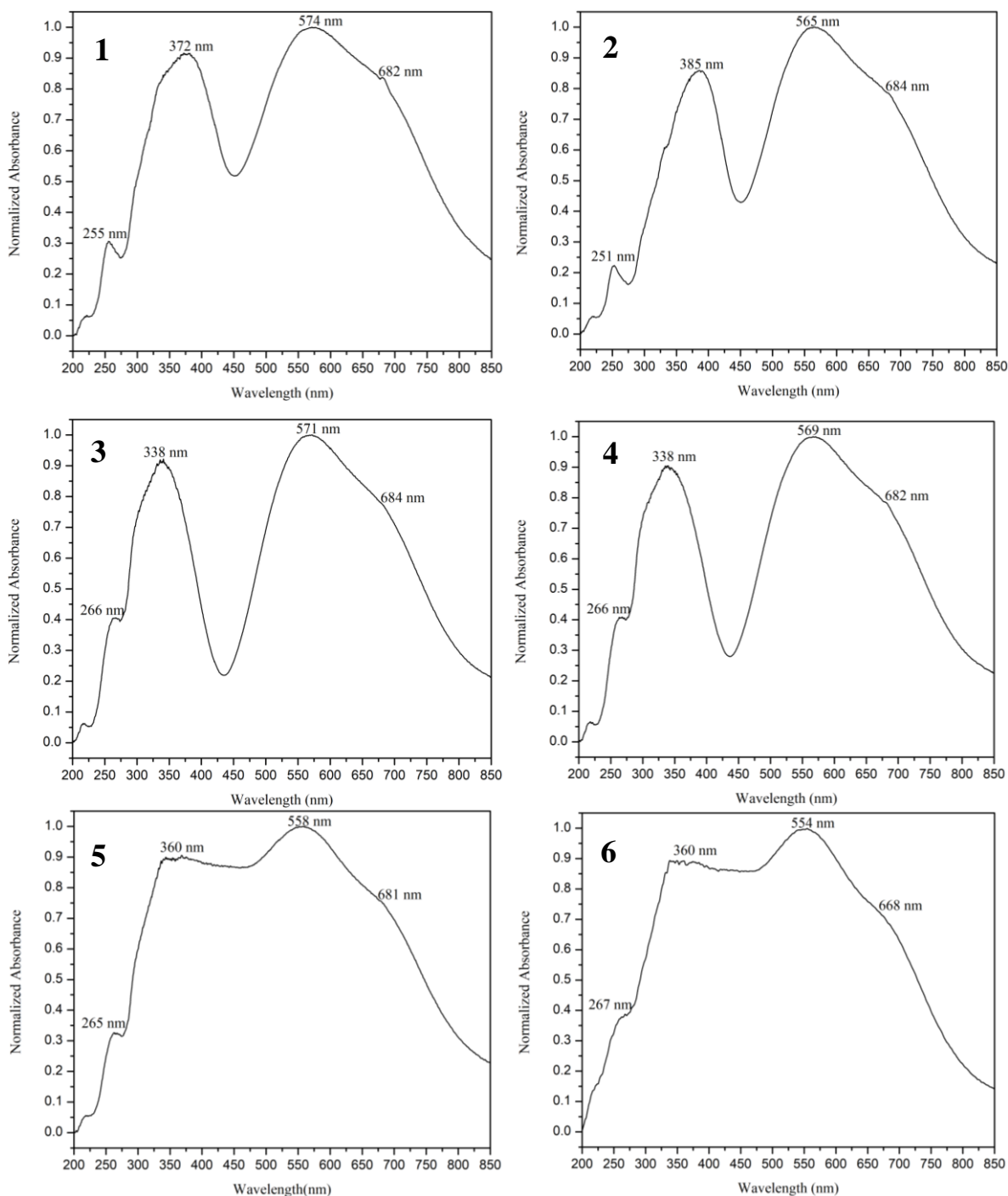


Fig. II.2.2-1. UV-Vis spectra of the obtained compounds

The wide bands in the 550 – 580 nm range can be attributed to the specific d–d transitions of Cu(II) and the shoulder around 680 nm may be explained by the Jahn–Teller distortion of the Cu(II) octahedral geometry. The large width of the bands assigned to the d–d transitions is due to the overlap of the absorption of $d_{xy} \rightarrow d_{x^2-y^2}$, $d_{z^2} \rightarrow d_{x^2-y^2}$ and $d_{xz,yz} \rightarrow d_{x^2-y^2}$ transitions which are possible for the species with square-planar or distorted octahedral stereochemistry [37].

The electronic spectra for compounds **5** and **6** are not well defined because of the presence of coloured azopy ligand which determines a brown color of the crystals and, therefore, a high absorption capacity exhibited by the compound, as can be seen in the last two (**5** and **6**) spectra in Fig.II.2.2-1.

II.2.3. Thermal stability

The thermogravimetric analysis (TGA) was performed in order to determine the thermal stability of the compounds and the results are presented in Figure II.2.3-1. It can be observed that, for compounds **1**, **3**, and **5**, the thermal decomposition is carried out in one major sharp process, similar to a total combustion, due to the presence of explosive perchlorate anions and then is followed by a broader process that continues to 600 °C. The weight loss for these compounds is 86.95%, 91.46%, and 89.12%, respectively, and the residual mass corresponds to a mixture of CuO and Cu.

For the compounds with tetrafluoroborate anions (**2**, **4**, and **6**), the thermal decomposition is carried out in two subsequent steps with a total weight loss of 65.75%, 77.07% and 61.77%, respectively. As the thermogravimetric analysis was performed in an inert atmosphere (N₂) the residual mass for these compounds could be a mixture of CuO, Cu and carbon ash. The nature of the residual products will be investigated in the future.

The relatively high stability of these Cu-based MOFs is given by a series of weak interactions that span over the whole structure, hydrogen bonds and electrostatic interactions established between counter anions and the cationic framework. The CH– π interactions are formed between the aromatic rings of the organic ligand, as presented in Figure II.2.3-2. (green dotted lines), and have distances in the 2.93 – 2.99 Å range. Although these interactions are quite weak, it provides an increased stability to the 3D framework through their number and position, spreading throughout the structure.

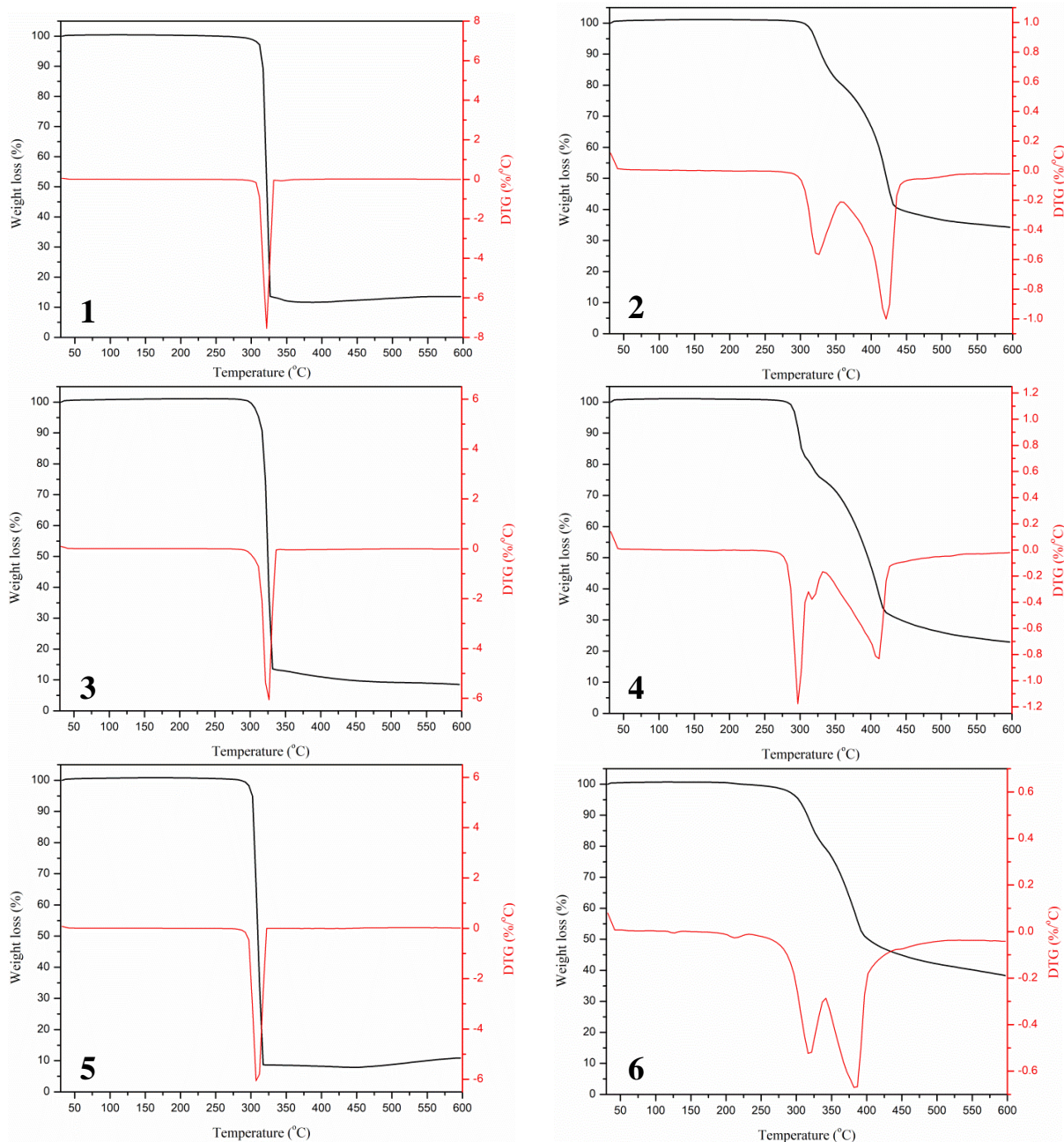


Fig.II.2.3-1. TGA and DTG curves of the obtained compounds

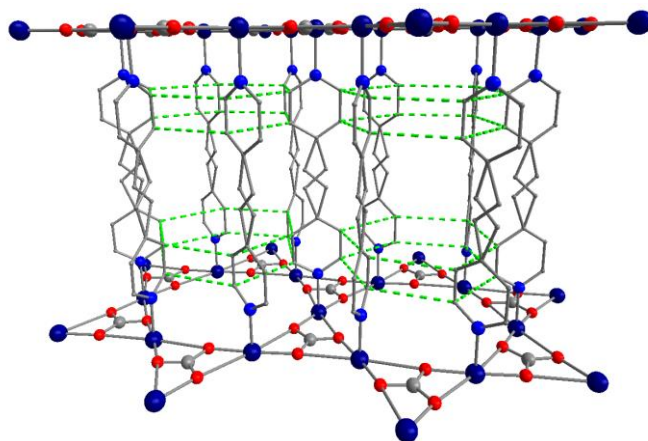


Fig.II.2.3-2. CH— π interactions in $\{[\text{Cu}_3(\text{CO}_3)_2(\text{L})_3](\text{Y})_2\}_n$

II.3. Applications of Cu-based PCPs with Kagomé layers

II.3.1. Anion-exchange studies

MOFs that contain guest anions in the pores can undergo ion exchange. By immersion of the solids in the solution of other anion source, the guest anions of the MOFs can be exchanged with external ones. In 1990 was first reported an anion-exchange process in MOFs which happened at solid–liquid interface [38].

As revealed by crystal structure analyses, ClO_4^- and BF_4^- counter anions in the obtained MOFs are loosely bound, through weak noncovalent hydrogen bonds, to the cationic structures of the Cu-based coordination polymers. Therefore, anion exchange properties of the obtained compounds have been investigated in aqueous solutions of the appropriate salts and monitored by FT-IR and UV-Vis spectroscopies. The position of the anions along the hexagonal channel is illustrated in Figure II.3.1-1.

In this study, to investigate the anion-exchange the following categories of anions (which possess geometry and charge similarities or differences in comparison to ClO_4^- and BF_4^- ions) were employed: 1) anions with the same geometry and charge (permanganate – MnO_4^-), 2) anions with the same geometry and different charge (chromate – CrO_4^{2-}), and 3) anions with different geometry and the same charge (hexafluorophosphate – PF_6^- , nitrate – NO_3^-). At the same time, the influence of the concentration of the anion solutions on the ion-exchange process was monitored.

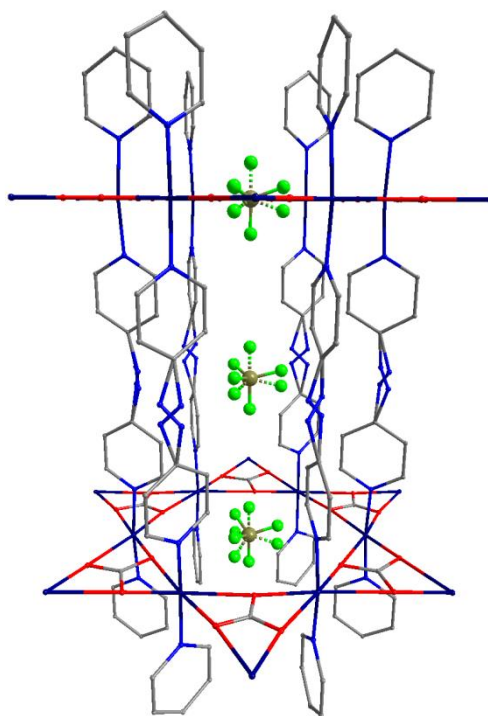


Fig.II.3.1-1. Hexagonal channels along *c*-axis in $\{[\text{Cu}_3(\text{CO}_3)_2(\text{L})_3](\text{Y})_2\}_n$

Low concentration of anions

Given the strong oxidizing power of MnO_4^- and CrO_4^{2-} , low concentration solutions of these anions were used in order to highlight both possible anion-exchanges and other modifications that may occur in the compounds. In this regard, 5 mg of each synthesized compound, in the solid state, were immersed in 0.1 mM aqueous solutions of MnO_4^- and CrO_4^{2-} , respectively. After three days, visual changes have been observed only in the case of the compounds containing the bpy ligand, **1** and **2**, where the pink MnO_4^- solution turned to a yellow-brown clear solution and the immersed blue-purple crystals have acquired a brownish shade. In the CrO_4^{2-} samples no changes occurred, the solution and crystals maintained the initial colours.

FTIR spectra of **1** immersed in MnO_4^- and CrO_4^{2-} solutions were recorded and are presented in Figure II.3.1-2. These two spectra are identical to the spectrum of initial **1** (Figure II.3.1-2.C). As it can be observed, there is no peak around 900 and 885 cm^{-1} that could be assigned to MnO_4^- and CrO_4^{2-} vibrations. Also, no major changes in the wavenumbers of ClO_4^- peaks (around 1100 and 620 cm^{-1}) are present, thus concluding that no anionic exchange occurs at low concentrations.

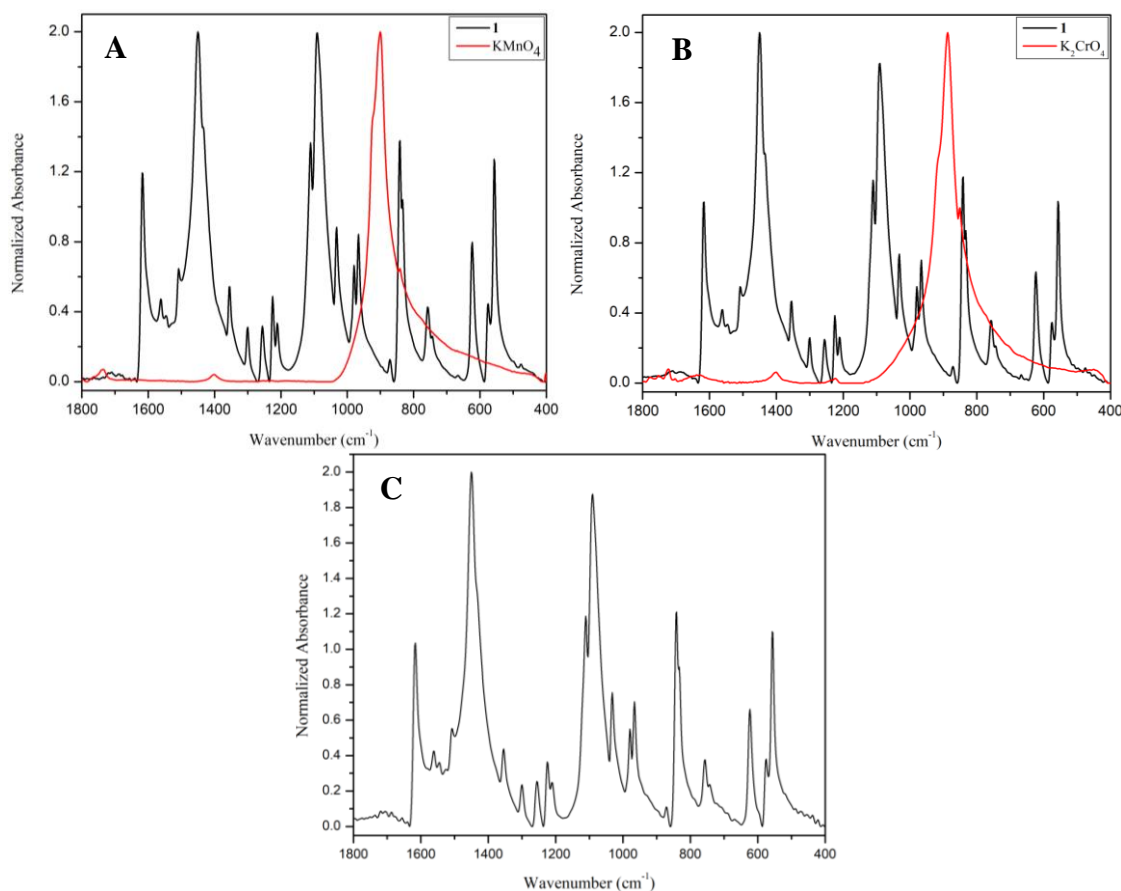


Fig.II.3.1-2. FTIR spectra of **1** immersed in 0.1 mM KMnO_4 (A) and 0.1 mM K_2CrO_4 (B) solutions and initial spectrum of **1** (C).

The brown colour obtained for the KMnO_4 samples may be explained by the presence of colloidal manganese oxide [39] formed during the oxidation of bpy ligand with KMnO_4 . Since no oxidation conditions were provided to the system (heat or high concentration of oxidizing agent), the ligand was partially oxidized at the C-C double bond, probably forming a vicinal diol. We assume that this oxidation step is a typical mild oxidation of alkenes with Baeyer Reagent; the equation of the chemical reaction is presented in Figure II.3.1-3.

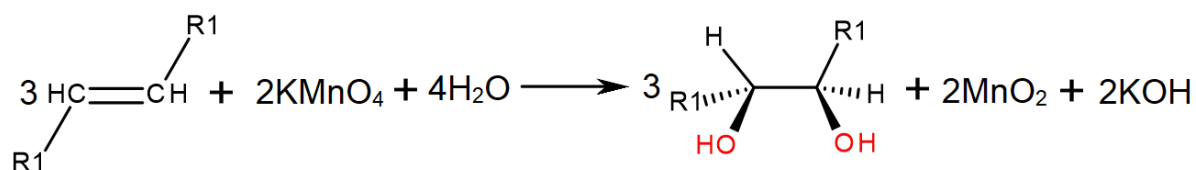


Fig.II.3.1-3. Oxidation of the ethylene derivate ligand to vicinal diol with Baeyer Reagent

The UV-Vis spectra were recorded for both solution and solid for complementary characterization. In Figure II.3.1-4 is presented the UV-Vis spectrum of the yellow-brown solution of immersed **1** and compared with the spectrum of pure KMnO_4 solution at the same concentration. It can be observed that the characteristic region of Mn(VII) in the 500-575 nm range is missing in the probe. At the same time, an increase of the wide band absorbance in the UV region is occurring.

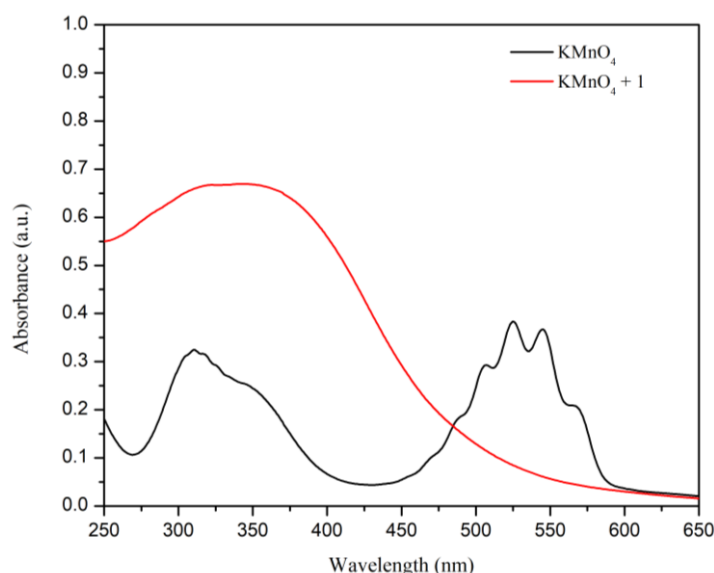


Fig.II.3.1-4. UV-Vis spectra on aqueous solutions of KMnO_4 (0.1 mM) and **1**+ KMnO_4 (5 mg of **1** in 0.1 mM KMnO_4 solution)

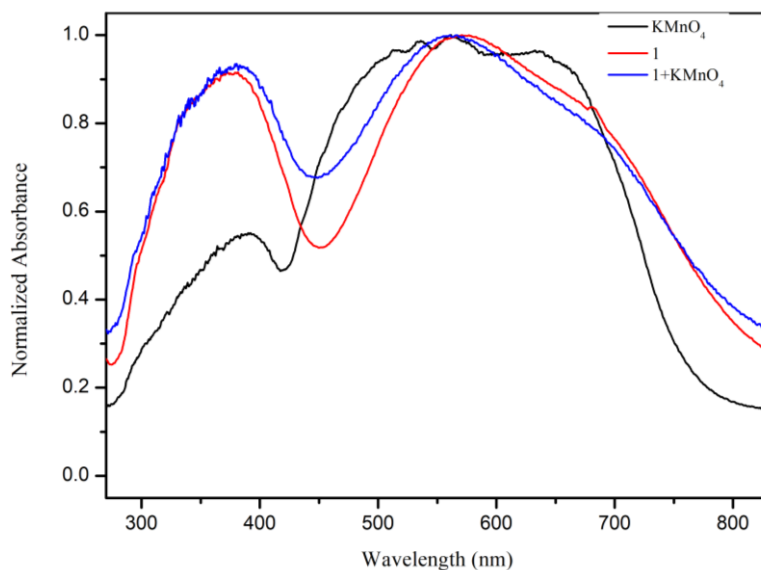


Fig.II.3.1-5. UV-Vis spectra on solid samples of KMnO_4 (black), **1** (red), and **1**+ KMnO_4 (blue)

In the UV-Vis spectrum on solid samples of **1** immersed in KMnO_4 (Figure II.3.1-5, blue line) can be observed that the spectrum has slightly narrowed, with a bathochromic shift from 372 nm to 380 nm and a hypsochromic shift from 570 nm to 560 nm compared to the initial **1** compound (Figure II.3.1-5, red line). The KMnO_4 spectrum is the black line, therefore, these two shifts can be assigned to a chemical modification of **1** due to the influence of the MnO_4^- on the system.

Variation of permanganate concentration

The influence of the permanganate anion was investigated using a series of 5 solutions with concentrations in the 0.1–10 mM range, prepared according to Table II.3.1-1. To these solutions, 5 mg of **1** were added and left for 24h.

Table II.3.1-1. Concentrations and volumes used for preparation of KMnO_4 solutions

No.	$V_{\text{KMnO}_4}(\mu\text{L})^*$	$V_{\text{H}_2\text{O}}(\mu\text{L})$	$C_{\text{KMnO}_4}(\text{mM})$
1	50	9950	0.1
2	250	9750	0.5
3	500	9500	1.0
4	2500	7500	5.0
5	5000	5000	10.0

* $[\text{KMnO}_4] = 20 \text{ mM}$

After 24h, the initial series changed the colours from shades of pink-purple to a palette of yellow to red to purple, depending on the concentration of the solutions (Figure II.3.1-6). Significant changes can be observed from 0.1 mM to 5 mM but not in the case of the 10 mM probe because of the intense colour of the solution.

The probes were analyzed using the UV-Vis on solution and the results are presented in Figure II.3.1-7. It can be observed that the same pattern is followed, with the decrease in intensity of the band in the visible region and increase of the band in the ultraviolet region. The 5 mM and 10 mM solutions were too concentrated to measure, but a similar behaviour was noticed from diluted samples of these solutions. This means that the oxidation of the ligand occurs in the same manner as in the case of the 0.1 mM and the colour variation is given from the different ratios of colloidal Mn(IV) and Mn(VII) ions present in solutions.

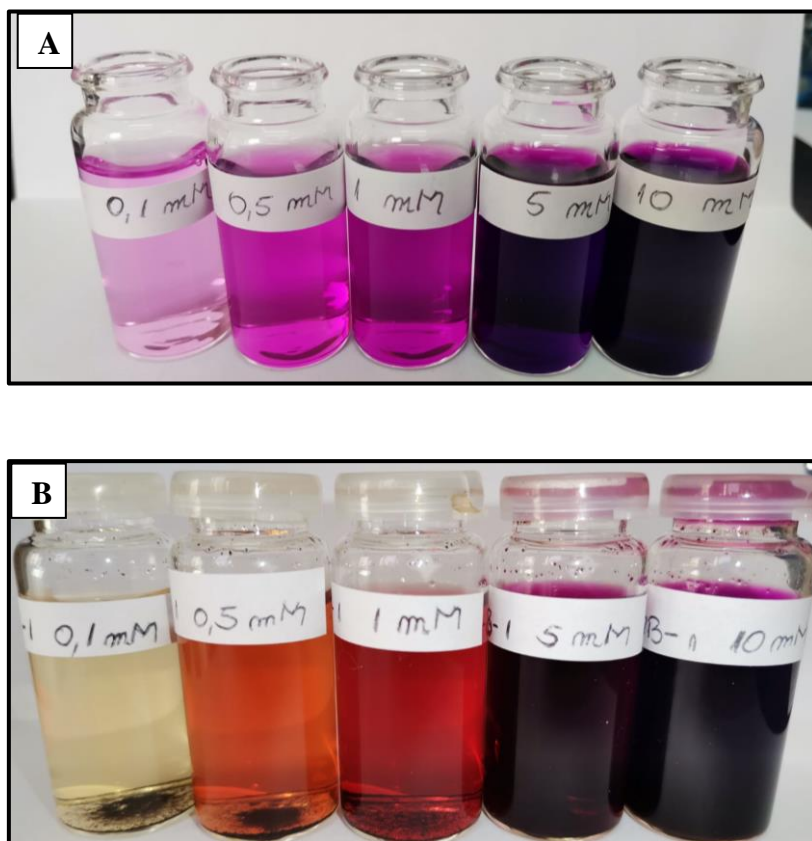


Fig.II.3.1-6. Photographs of initial series of KMnO₄ solutions at different concentration (A) and after 24h of contact with **1** (B)

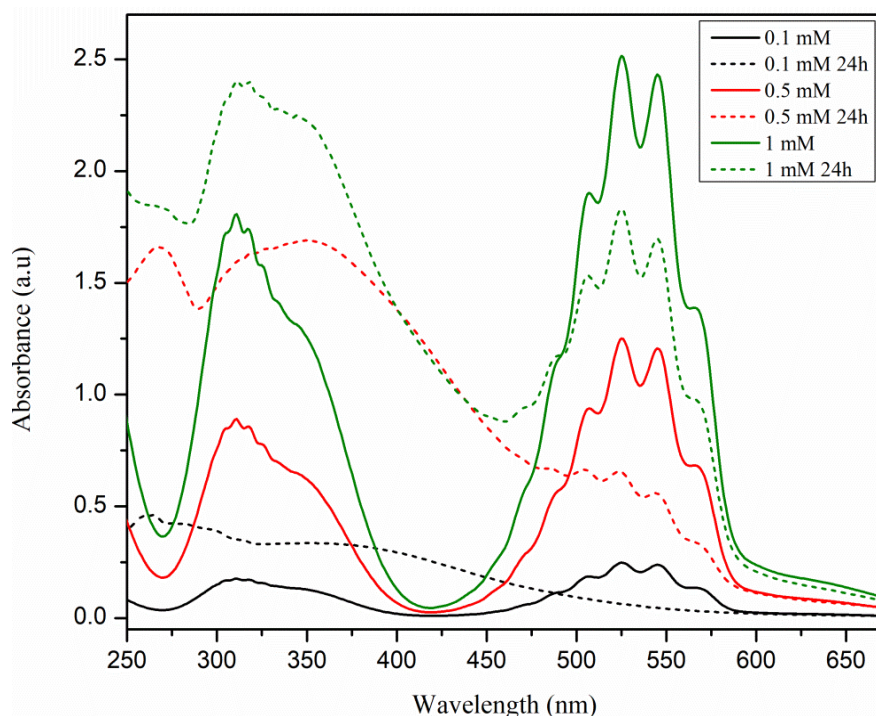


Fig.II.3.1-7. Initial series of KMnO_4 solutions (straight lines) and after 24h of contact with **1** (dotted lines)

High concentration of anions

To investigate the behaviour of the 3D systems in the presence of high concentration of anions, the experimental part was adapted from [33], using a molar ratio of MOF to the salt containing the exchange anions of 1:15. A 1 mL suspension containing 20 mg of microcrystalline MOF (**1** or **2**, respectively) was added to 4 mL solutions of different salts, namely: NH_4PF_6 , KNO_3 , KMnO_4 , K_2CrO_4 , and KClO_4 . The final solutions were then left for 10 days at room temperature and without any stirring, after which were analyzed by FTIR spectroscopy. The corresponding concentration of salt solution for this ratio is 58 mM.

The comparative FTIR spectra of **1** and **2** immersed in different anions solutions are presented in Figures II.3.1-8 and II.3.1-9, respectively. As it can be observed, no significant changes are present in the spectra, except in the case of MnO_4^- . For this solution the spectra is slightly modified which may be caused by a mild oxidation of the ligand to a vicinal diol.

This concludes that for the given conditions: room temperature, atmospheric pressure, no stirring and a high concentration of anions, no exchange occurred in these Cu-based coordination polymers when NO_3^- , PF_6^- , CrO_4^{2-} , or ClO_4^- were investigated for anion-exchange, while in the presence of MnO_4^- a chemical modification occurred.

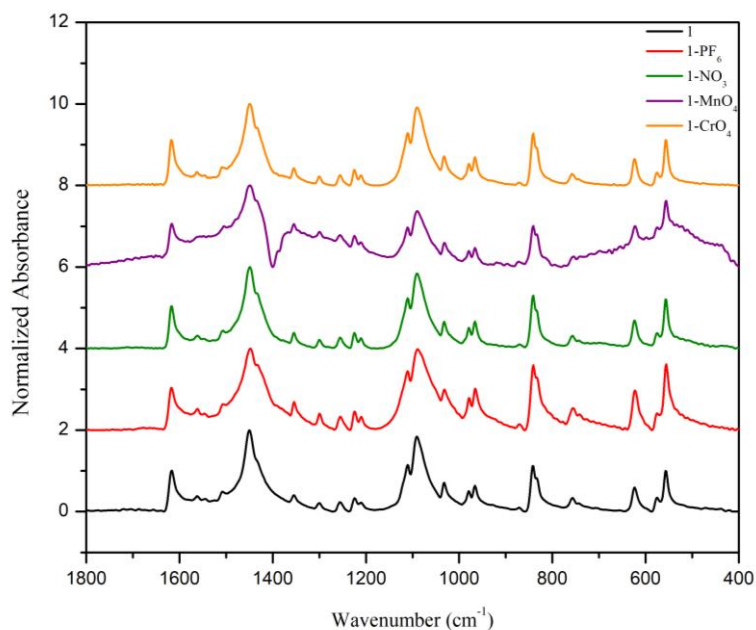


Fig.II.3.1-8. FTIR spectra of **1** immersed in solutions of different anions

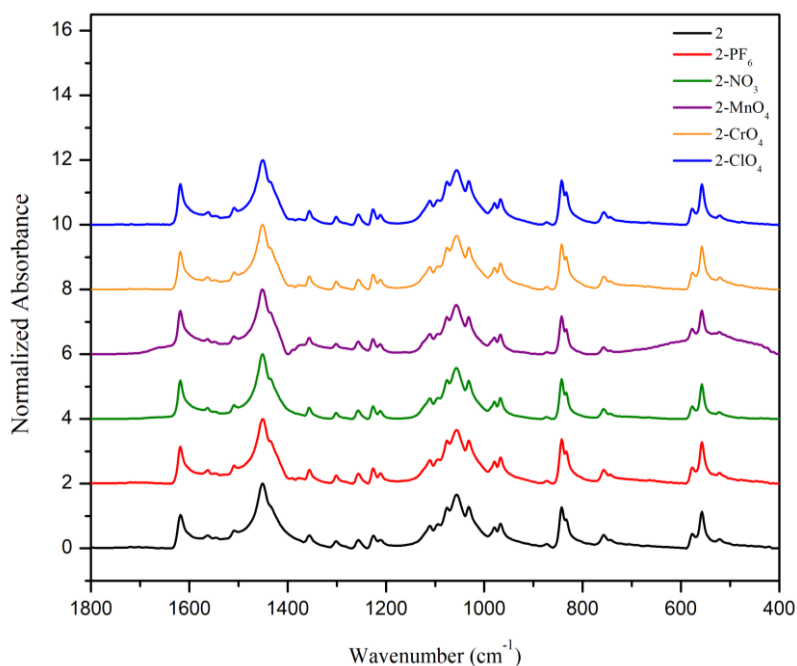


Fig.II.3.19. FTIR spectra of **2** immersed in solutions of different anions

II.3.2. Adsorption properties

The adsorption properties of the compounds were evaluated based on the nitrogen adsorption-desorption measurements performed at 77 K and a partial pressure (p/p_0) range of 10^{-3} – 1 bar. Samples of each compound were degassed under vacuum ($< 10^{-2}$ mbar) at 150 °C for 3 – 18h prior to measurement in order to free the pores of any guest molecules.

In Figure II.3.2-1 are presented the N₂ adsorption-desorption isotherms on the obtained compounds. It can be observed that for compounds **1-4** the adsorbed volumes are in the range of 9 – 25 cm³/g while for **5** and **6** the adsorbed volumes are 400 cm³/g and 150 cm³/g, respectively. It had been noticed that higher uptakes are achieved in the case of the compounds containing the perchlorate anions.

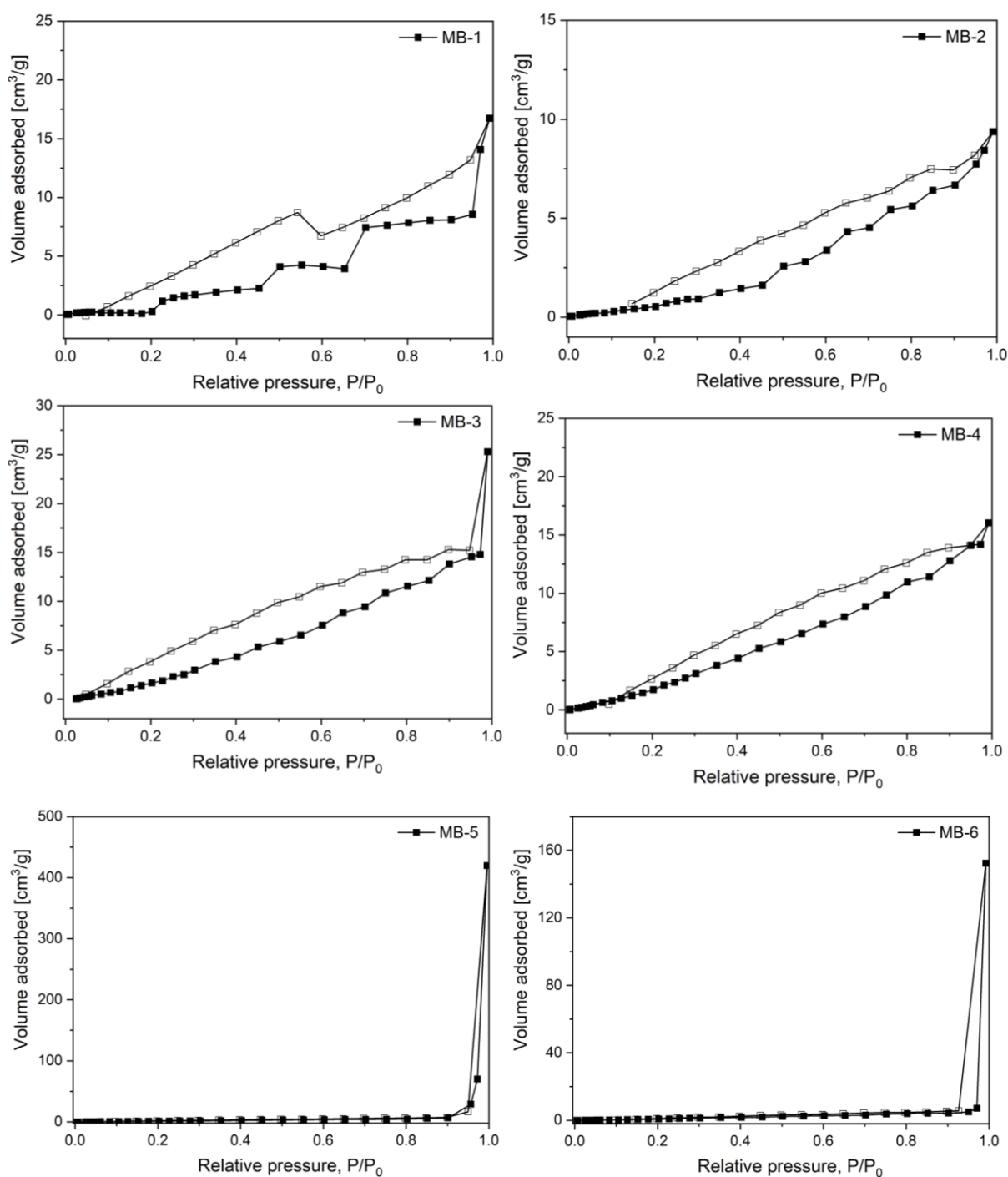


Fig.II.3.2-1. N₂ adsorption-desorption isotherms on compounds **1-6**

The adsorption isotherms of **1** and **2** are similar to a type VI isotherm combined with a H3 hysteresis loop. Usually, this type of isotherm describes a multilayer adsorption, but taking into account the structure of the synthesized compounds it would rather suggest a “breathing mechanism” with the steps associated to an expansion movement which allows a higher uptake as the relative pressure increases [40]. Compounds **3** and **4** exhibit a type III isotherm combined with a H3 hysteresis loop, which indicates a small adsorbed amount at low pressures, probably due to relatively weak interactions between the adsorbate and the adsorbent [41]. The higher adsorbed volume in the case of compounds **5** and **6** may be explained by an aggregation of the microcrystallites at high relative pressures ($p/p_0 = 0.9$) which provide a high surface area.

The N₂ adsorption measurements revealed that these compounds does not exhibit a high porosity, which is expected for MOFs, but at the same time confirm the existence of void space along the hexagonal channels. Powder X-ray diffractograms recorded before and after N₂ adsorption revealed that the crystallinity of the probes remain intact when exposed to pressure differences and are presented in Appendix (section D, Figures D.1 – D.6).

Conclusions

In the present dissertation thesis we have proposed the synthesis of Cu-based metal-organic frameworks capable of chemically fixing the atmospheric CO₂ into their structure and which, subsequently, will be able to allow its further capture by adsorption into the pores. The obtained compounds were characterized in solid state through single crystal and powder X-ray diffraction, along with spectroscopic techniques (FT-IR and UV-Vis), thermogravimetric analysis, and elemental analysis.

The single crystal XRD revealed the formation of 2D Cu(CO₃) layers with a Kagomé arrangement, through direct fixation of atmospheric CO₂, which are further link via bipyridine-based ligands yielding to a 3D cationic framework with hybrid structure. All six compounds are isostructural and have the general formula $\{[\text{Cu}_3(\text{CO}_3)_2(\text{L})_3](\text{Y})_2\}_n$, where L = organic ligand and Y = ClO₄⁻ or BF₄⁻ anions. The influence of the organic linker on the interlayer distance is directly proportional to the length of the linker. The purity of the compounds was assessed based on the powder X-ray diffraction, which shown only one crystalline phase. The thermogravimetric analysis revealed a relatively high thermal stability for this class of compounds, approximately 300 °C, generated by the arrangement of the building blocks as well as the non-covalent interactions established across the entire structure: hydrogen bonds, electrostatic, and CH- π interactions.

Anion-exchange and adsorption properties of the obtained MOFs were investigated. Different salts were employed for the anion-exchange, and the process was monitored with spectroscopic techniques. The result concluded that no anion-exchange occurred at room temperature and atmospheric pressure, regardless of concentration of the anion solutions used. This may be explained by the fact that the anions are rather trapped within the structure and does not allow any exchange. When MnO₄⁻ anion was employed, with compounds **1** and **2**, a post-synthetic chemical transformation on the surface of the crystals was most probable taking place, namely a Bayer oxidation of the ethylene double bond.

Regarding the adsorption properties, the compounds do not exhibit a high porosity, as most of the space is occupied by the counter anions. However, the compounds maintain their structure at pressure variations. A higher uptake could be achieved by utilizing longer ligands and/or metals salts with smaller anions (CuCl₂, Cu(NO₃)₂, Cu(CN)₂) or by recrystallizing the compounds from a salt solution that has smaller anions.

In the future, we aim to fully investigate the adsorption capacity of the synthesized compounds for water vapors, carbon dioxide and volatile organic compounds.

Acknowledgements

We would like to thank Prof. Dr. Christoph Janiak and Dr. Yangyang Sun from Heinrich-Heine-Universität, Düsseldorf, Germany for the adsorption measurements and to Assoc. Prof. Dr. Augustin M. Mădălan from Faculty of Chemistry, University of Bucharest for the single crystal X-ray diffraction measurements.

The present MSc. Thesis was carried out as part of the Cooperative and Partnership project GREENCAM, in the framework of Romania-Norway institutional collaboration, The Education, Scholarship, Apprenticeships and Youth Entrepreneurship Programmer—EEA Grants 2014-2021, Project No. 18-Cop-0041.

Materials and Instrumentation

Reagents and solvents

The reagents used in this study were: 1,2-bis(4-pyridyl)ethane (bpe), 1,2-bis(4-pyridyl)ethylene (bpy), 4,4'-azopyridine (azopy), Copper(II) tetrafluoroborate hexahydrate ($\text{Cu}(\text{BF}_4)_2 \cdot 6\text{H}_2\text{O}$), Copper(II) perchlorate hexahydrate ($\text{Cu}(\text{ClO}_4)_2 \cdot 6\text{H}_2\text{O}$), and aqueous ammonia (NH_4OH , 25%), ammonium hexafluorophosphate (NH_4PF_6), potassium nitrate (KNO_3), potassium permanganate (KMnO_4), potassium chromate (K_2CrO_4), and potassium perchlorate (KClO_4). All reagents were procured from Sigma-Aldrich and used without any further purification. The solvents used were methanol (CH_3OH) and distilled water (obtained in the laboratory).

Instrumentation

Weighing: Reagents and synthesized compounds were weighed on the analytical balance *Mettler Toledo XS204/M* with 5 decimal places.

Spectral determinations:

The infrared spectra were recorded in the $4000 - 400 \text{ cm}^{-1}$ range by the Fourier Transformer *Tensor 27* Spectrometer (FT-IR) using OPUS software. The processing of the samples consisted in preparation of pellets from a pre-ground mixture of sample with KBr using *Grasebz Spec 15011* press. The graphical representations were realized with Origin 8.5 software.

The UV-Vis spectra were recorded on solid and on solution in the 200 – 850 nm range with the help of a *JASCO V-670* spectrophotometer and with the use of *Spectra Manager* software. The graphical representations were prepared with *Origin 8.5* software.

X-ray diffraction:

Single crystal X-ray diffraction measurements were carried out using a *Rigaku XtaLAB Synergy-S* diffractometer operating with Mo-K α ($\lambda = 0.71073 \text{ \AA}$) micro-focus sealed X-ray tube. Calculations were performed using *ShelX* crystallographic software and the representations were achieved with the help of the *Diamond 3.2*.

The X-ray powder diffraction measurements (PXRD) were carried out on a *Proto AXRD Benchtop* using the Cu-K α radiation with a wavelength of 1.54059 \AA in the $5 - 35^\circ$ range of 2θ . The graphical representations were performed with *Origin 8.5* software.

PXRD data before and after the nitrogen physisorption isotherms were collected at room temperature on *Rigaku Miniflex 600* powder diffractometer (Germany) using Cu-K α radiation ($\lambda = 1.5418 \text{ \AA}$) between $2^\circ < 2\theta < 50^\circ$ with a scanning rate of 1.5 deg/min (600 W , 40 kV , 15 mA). Analyses of the diffractograms were carried out with *Origin 8.5* software.

Elemental analysis:

The elemental analysis was performed on a *Euro EA Elemental Analyzer* and the collected data were integrated with *Callidus 4.1* software.

TGA:

Thermogravimetric analysis (TGA) was performed on a *Netzsch TG209 F3 Tarsus* (*Netzsch, Selb, Germany*) device under nitrogen conditions, ramping with 10 K/min from $30 \text{ }^\circ\text{C}$ to $600 \text{ }^\circ\text{C}$.

N₂ physisorption:

The nitrogen (purity 99.9990%) physisorption isotherms were carried out at 77 K using a *Quantachrome Autosorb 6* instrument within a partial pressure range of $p/p_0 = 10^{-3}$ – 1 bar. Each sample of ca. 30 mg was degassed under vacuum ($< 10^{-2} \text{ mbar}$) at $150 \text{ }^\circ\text{C}$ for $3 - 18 \text{ h}$ prior to measurement.

References

1. United States Environmental Protection Agency (EPA), website: <https://www.epa.gov/ghgemissions/global-greenhouse-gas-emissions-data>
2. Friedlingstein, P., O'Sullivan, M., Jones, M.W., Andrew, R.M., Hauck, J., Olsen, A., Peters, G.P., Peters, W., Pongratz, J., Sitch, S., Le Quéré, C., Canadell, J.G., Ciais, P., Jackson, R.B., Alin, S., Aragão, L.E.O.C., Arneeth, A., Arora, V., Bates, N.R., Becker, M., Benoit-Cattin, A., Bittig, H.C., Bopp, L., Bultan, S., Chandra, N., Chevallier, F., Chini, L.P., Evans, W., Florentie, L., Forster, P.M., Gasser, T., Gehlen, M., Gilfillan, D., Gkritzalis, T., Gregor, L., Gruber, N., Harris, I., Hartung, K., Haverd, V., Houghton, R.A., Ilyina, T., Jain, A.K., Joetzjer, E., Kadono, K., Kato, E., Kitidis, V., Korsbakken, J.I., Landschützer, P., Lefèvre, N., Lenton, A., Lienert, S., Liu, Z., Lombardozzi, D., Marland, G., Metzl, N., Munro, D.R., Nabel, J.E.M.S., Nakaoka, S.-I., Niwa, Y., O'Brien, K., Ono, T., Palmer, P.I., Pierrot, D., Poulter, B., Resplandy, L., Robertson, E., Rödenbeck, C., Schwinger, J., Séférian, R., Skjelvan, I., Smith, A.J.P., Sutton, A.J., Tanhua, T., Tans, P.P., Tian, H., Tilbrook, B., van der Werf, G., Vuichard, N., Walker, A.P., Wanninkhof, R., Watson, A.J., Willis, D., Wiltshire, A.J., Yuan, W., Yue, X., Zaehle, S., Global Carbon Budget 2020, *Earth Syst. Sci. Data*, 12 (4) (2020), 3269:3340.
3. Oelkers, E.H., Cole, D.R., Carbon Dioxide Sequestration A Solution to a Global Problem. *Elements*, 4(5) (2008), 305:310.
4. Tamilselvi Dananjayan, R.R., Kandasamy, P., Andimuthu, R., Direct mineral carbonation of coal fly ash for CO₂ sequestration. *J. Clean. Prod.*, 112 (2016), 4173:4182.
5. Verma, R., Srivastava, A., Carbon dioxide sequestration and its enhanced utilization by photoautotroph microalgae. *Environ. Dev.*, 27 (2018), 95:106.
6. Keene, T.D., Murphy, M.J., Price, J.R., Sciortino, N.F., Southon, P.D., Kepert, C.J., Multifunctional MOFs through CO₂ fixation: a metamagnetic kagome lattice with uniaxial zero thermal expansion and reversible guest sorption. *Dalton Trans.*, 43(39) (2014), 14766:14771.
7. Zhou, H.-C., Long, J.R., Yaghi, O.M., Introduction to Metal–Organic Frameworks. *Chem. Rev.*, 112(2) (2012), 673:674.
8. Bu, F.-X., Hu, M., Xu, L., Meng, Q., Mao, G.-Y., Jiang, D.-M., Jiang, J.-S., Coordination polymers for catalysis: enhancement of catalytic activity through hierarchical structuring. *Chem. Commun.*, 50(62) (2014), 8543:8546.

9. Bon, V., Senkovska, I., Kaskel, S., Nanoporous Materials for Gas Storage, Green Energy and Technology, Ed. Springer, Singapore, 2019, Chapter 6: Metal-Organic Frameworks, pgs. 137-172.
10. Janiak, C., Vieth, J.K., MOFs, MILs and more: concepts, properties and applications for porous coordination networks (PCNs). *New J. Chem.*, 34(11) (2010), 2366-2388.
11. Mashhadzadeh, A.H., Taghizadeh, A., Taghizadeh, M., Munir, M.T., Habibzadeh, S., Salmankhani, A., Stadler, F.J., Saeb, M.R., Metal-Organic Framework (MOF) through the Lens of Molecular Dynamics Simulation: Current Status and Future Perspective. *J. Compos. Sci.*, 4(2) (2020), 75:88.
12. Seo, J., Sakamoto, H., Matsuda, R., Kitagawa, S., Chemistry of Porous Coordination Polymers Having Multimodal Nanospace and Their Multimodal Functionality. *J. Nanosci. Nanotechnol.*, 10(1) (2010), 3:20.
13. Sánchez-Serratos, M., Álvarez, J.R., González-Zamora, E., Ibarra, I.A., Porous Coordination Polymers (PCPs): New Platforms for Gas Storage. *J. Mex. Chem. Soc.*, 60(2) (2016), 43:57.
14. Robin, A.Y., Fromm, K.M., Coordination polymer networks with O- and N-donors: What they are, why and how they are made. *Coord. Chem. Rev.*, 250(15-16) (2006), 2127:2157.
15. Khandar, A.A., Afkhami, F.A., Hosseini-Yazdi, S.A., White, J.M., Kassel, S., Dougherty, W.G., Lipkowski, J., Van Derveer, D., Giester, G., Costantino, F., Anion influence in the structural diversity of cadmium coordination polymers constructed from a pyridine based Schiff base ligand. *Inorg. Chim. Acta*, 427 (2015), 87:96.
16. Liu, J.-J., Xia, S.-B., Duan, Y.-L., Liu, T., Cheng, F.-X., Sun, C.-K., Anion-Controlled Architecture and Photochromism of Naphthalene Diimide-Based Coordination Polymers. *Polymers*, 10(2) (2018), 165:176.
17. Ghosh, A., Hazra, A., Mondal, A., Banerjee, P., Weak interactions: the architect behind the structural diversity of coordination polymer. *Inorg. Chim. Acta*, 488 (2019), 86:119.
18. Hönicke, I., Senkovska, I., Bon, V., Baburin, I., Boenisch, N., Raschke, S., Kaskel, S., Balancing Mechanical Stability and Ultrahigh Porosity in Crystalline Framework Materials, *Angew. Chem. Int. Ed.*, 57(42) (2018), 13780:13783
19. Bureekaew, S., Shimomura, S., Kitagawa, S., Chemistry and application of flexible porous coordination polymers, *Sci. Technol. Adv. Mater.*, 9(1) (2008), 014108:014119.
20. Hasegawa, S., Horike, S., Matsuda, R., Furukawa, S., Mochizuki, K., Kinoshita, Y., Kitagawa, S., Three-Dimensional Porous Coordination Polymer Functionalized with

- Amide Groups Based on Tridentate Ligand: Selective Sorption and Catalysis. *J. Am. Chem. Soc.*, 129(9) (2007), 2607:2614.
21. El-Shall, M.S., Abdelsayed, V., Khder, A.E.R.S., Hassan, H.M.A., El-Kaderi, H.M., Reich, T.E., Metallic and bimetallic nanocatalysts incorporated into highly porous coordination polymer MIL-101. *J. Mater. Chem.*, 19(41) (2009), 7625:7631.
22. Kong, X., Deng, H., Yan, F., Kim, J., Swisher, J.A., Smit, B., Yaghi, O.M., Reimer, J.A., Mapping of Functional Groups in Metal-Organic Frameworks. *Science*, 341(6148) (2013), 882:885.
23. Chen, D., Liang, F., Feng, D., Xian, M., Zhang, H., Liu, H., Du, F., An efficient route from reproducible glucose to 5-hydroxymethylfurfural catalyzed by porous coordination polymer heterogeneous catalysts. *Chem. Eng. J.*, 300 (2016), 177:184.
24. Peedikakkal A.M.P., Adarsh N.N., Porous Coordination Polymers in Jafar Mazumder M., Sheardown H., Al-Ahmed A. (eds) *Functional Polymers. Polymers and Polymeric Composites: A Reference Series*. Springer, Cham (2019).
25. Li, H., Wang, K., Sun, Y., Lollar, C.T., Li, J., Zhou, H.-C., Recent advances in gas storage and separation using metal–organic frameworks. *Mater. Today*, 21(2) (2018), 108:121.
26. De, D., Pal, T.K., Neogi, S., Senthilkumar, S., Das, D., Gupta, S.S., Bharadwaj, P.K., A Versatile Cu^{II} Metal-Organic Framework Exhibiting High Gas Storage Capacity with Selectivity for CO₂: Conversion of CO₂ to Cyclic Carbonate and Other Catalytic Abilities. *Chem.: Eur. J.*, 22(10) (2016), 3387:3396.
27. Saha, D., Deng, S., Hydrogen adsorption on metal-organic framework MOF-177. *Tsinghua Sci. Technol.*, 15(4) (2010), 363:376.
28. He, Y., Chen, F., Li, B., Qian, G., Zhou, W., Chen, B., Porous metal–organic frameworks for fuel storage. *Coord. Chem. Rev.*, 373 (2018), 167:198.
29. Jiang, J., Furukawa, H., Zhang, Y.-B., Yaghi, O.M., High Methane Storage Working Capacity in Metal–Organic Frameworks with Acrylate Links. *J. Am. Chem. Soc.*, 138(32) (2016), 10244:10251.
30. Leroux, M., Mercier, N., Allain, M., Dul, M.-C., Dittmer, J., Kassiba, A.H., Bezverkhyy, I., Porous Coordination Polymer Based on Bipyridinium Carboxylate Linkers with High and Reversible Ammonia Uptake. *Inorg. Chem.*, 55(17) (2016), 8587:8594.
31. Belmabkhout, Y., Pillai, R.S., Alezi, D., Shekhah, O., Bhatt, P.M., Chen, Z., Eddaoudi, M., Metal–organic frameworks to satisfy gas upgrading demands: fine-tuning the soc-

- MOF platform for the operative removal of H₂S. *J. Mater. Chem. A*, 5(7) (2017), 3293:3303.
32. Kumar, P., Pournara, A., Kim, K.-H., Bansal, V., Rapti, S., Manos, M.J., Metal-organic frameworks: Challenges and opportunities for ion-exchange/sorption applications. *Prog. Mater. Sci.*, 86 (2017), 25:74.
33. Phuengphai, P., Massera, C., Reedijk, J., Youngme, S., Gamez, P., Anion Exchange in Coordination-Network Materials. *Eur. J. Inorg. Chem.*, 2013(27) (2013), 4812:4822.
34. Noori, Y., Akhbari, K., Post-synthetic ion-exchange process in nanoporous metal-organic frameworks; an effective way for modulating their structures and properties. *RSC Adv.*, 7(4) (2017), 1782:1808.
35. Nakamoto, K., *Infrared and Raman Spectra of Inorganic and Coordination Compounds*; John Wiley and Sons: New Jersey, USA, (2009).
36. Asadi, H.; Golchoubian, H., Synthesis, structural and solvent influence studies on solvatochromic of acetylacetonatocopper(II) with N,N' -dibenzyl or thiophene derivatives of ethylenediamine complexes. *J. Mol. Struct.*, 779 (2005), 30:37.
37. Lever, A.B.P., *Inorganic Electronic Spectroscopy* (2nd Edition), Elsevier, 1984.
38. Hoskins, B.F., Robson, R., Design and construction of a new class of scaffolding-like materials comprising infinite polymeric frameworks of 3D-linked molecular rods. A reappraisal of the zinc cyanide and cadmium cyanide structures and the synthesis and structure of the diamond-related frameworks [N(CH₃)₄][Cu^IZn^{II}(CN)₄] and Cu^I[4,4',4'',4'''-tetracyanotetraphenylmethane]BF₄·xC₆H₅NO₂. *J. Am. Chem. Soc.*, 112(4) (1990) 1546:1554.
39. Fernando, M.-P., Perez-Benito, J.F., Identification of the product from the reduction of permanganate ion by trimethylamine in aqueous phosphate buffers. *Can. J. Chem.*, 63(4) (1985), 988:992.
40. Bourrelly, S., Llewellyn, P.L., Serre, C., Millange, F., Loiseau, T., Férey, G., Different Adsorption Behaviors of Methane and Carbon Dioxide in the Isotypic Nanoporous Metal Terephthalates MIL-53 and MIL-47. *J. Am. Chem. Soc.*, 127(39) (2005), 13519:13521.
41. Cychosz, K.A., Guillet-Nicolas, R., García-Martínez, J., Thommes, M., Recent advances in the textural characterization of hierarchically structured nanoporous materials. *Chem. Soc. Rev.*, 46 (2016), 389:414.

Appendix

A. Powder X-ray diffractograms of compounds 1, 3-6

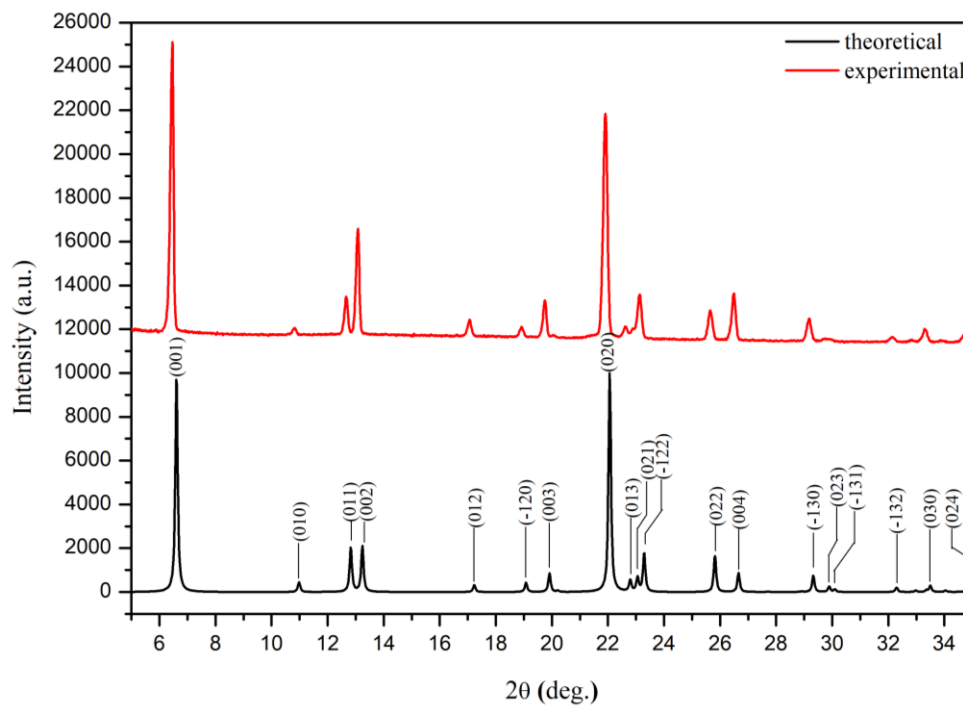


Fig.A1. Powder XRD pattern of compound 1

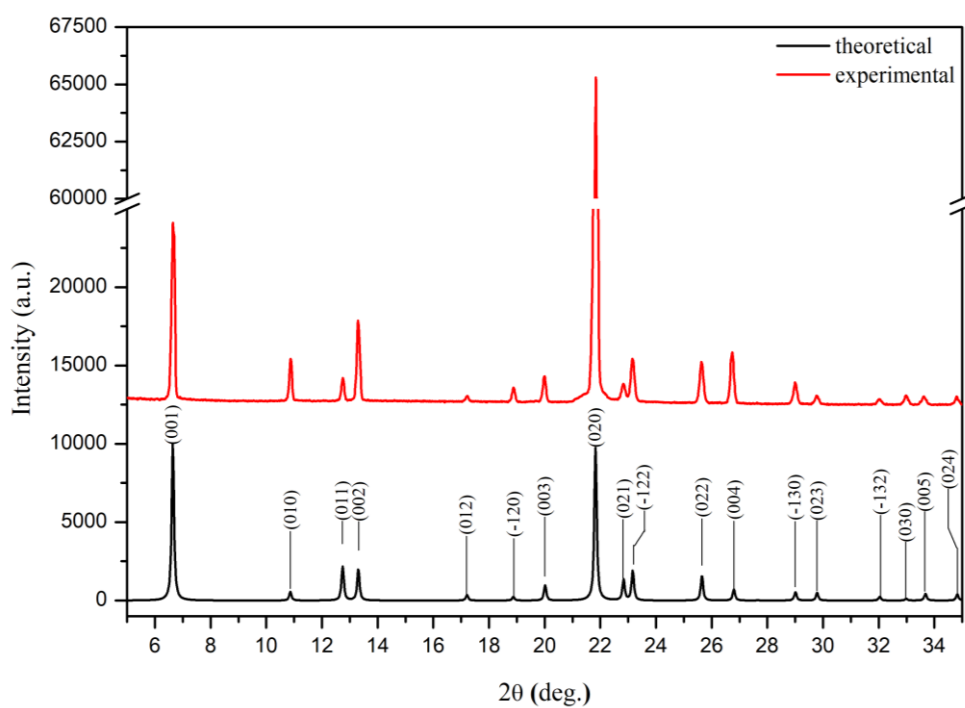


Fig.A2. Powder XRD pattern of compound 3

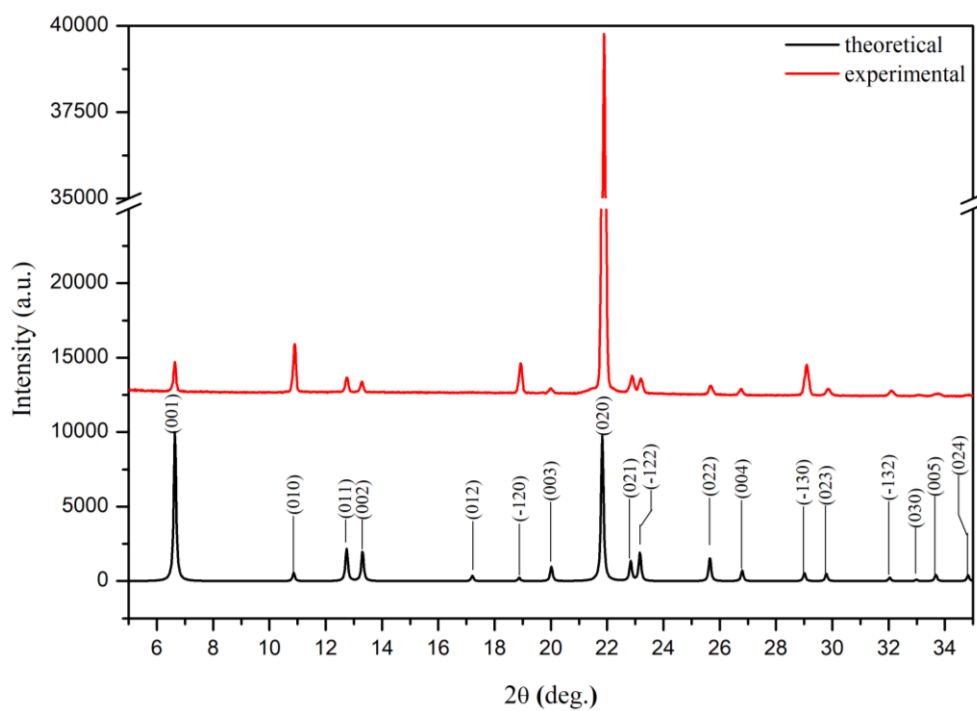


Fig.A3. Powder XRD pattern of compound 4

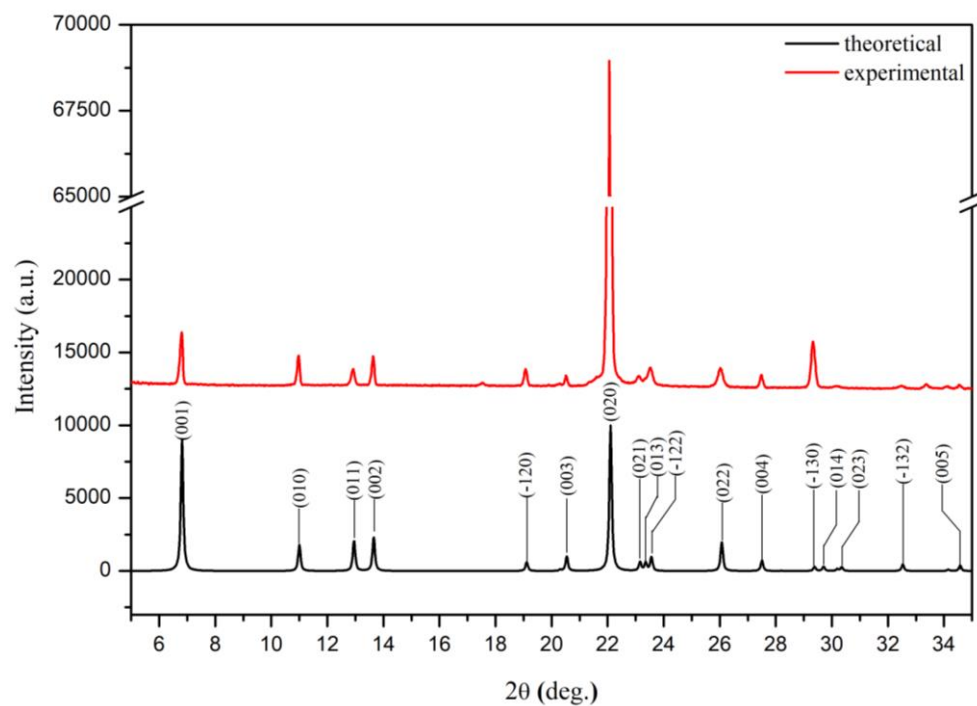


Fig.A4. Powder XRD pattern of compound 5

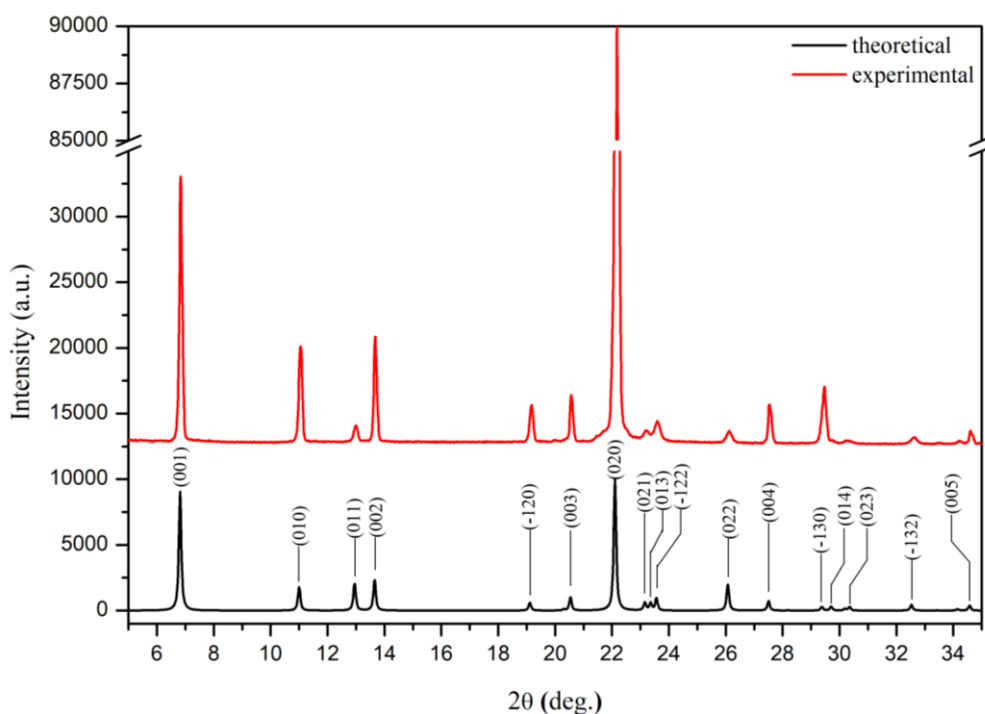


Fig.A5. Powder XRD pattern of compound **6**

B. Elemental analysis

Compound		% C	% N	% H
1	calculated	43.21	7.95	2.86
	found	42.41	7.87	2.79
2	calculated	44.27	8.15	2.93
	found	44.08	8.44	2.58
3	calculated	42.96	7.91	3.41
	found	42.40	7.99	3.40
4	calculated	44.01	8.10	3.50
	found	45.27	8.37	3.39
5	calculated	36.18	15.82	2.27
	found	36.26	15.66	2.21
6	calculated	37.06	16.21	2.33
	found	37.76	15.91	2.27

C. FTIR spectra of compounds 1-6

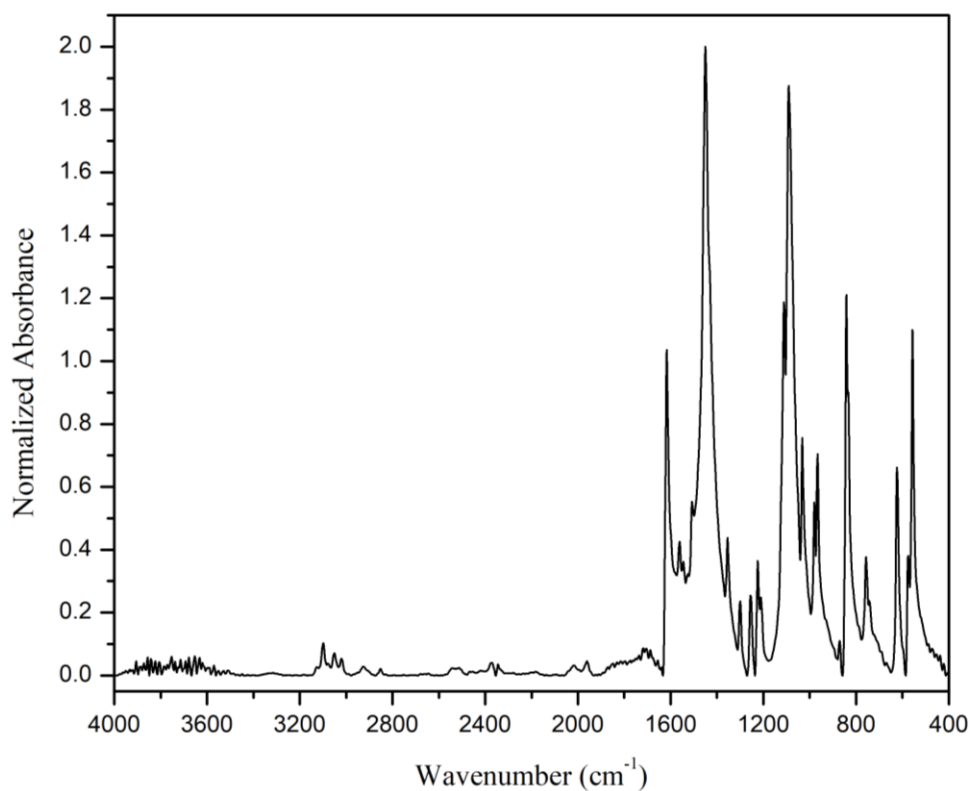


Fig.C1. FTIR spectrum of compound 1

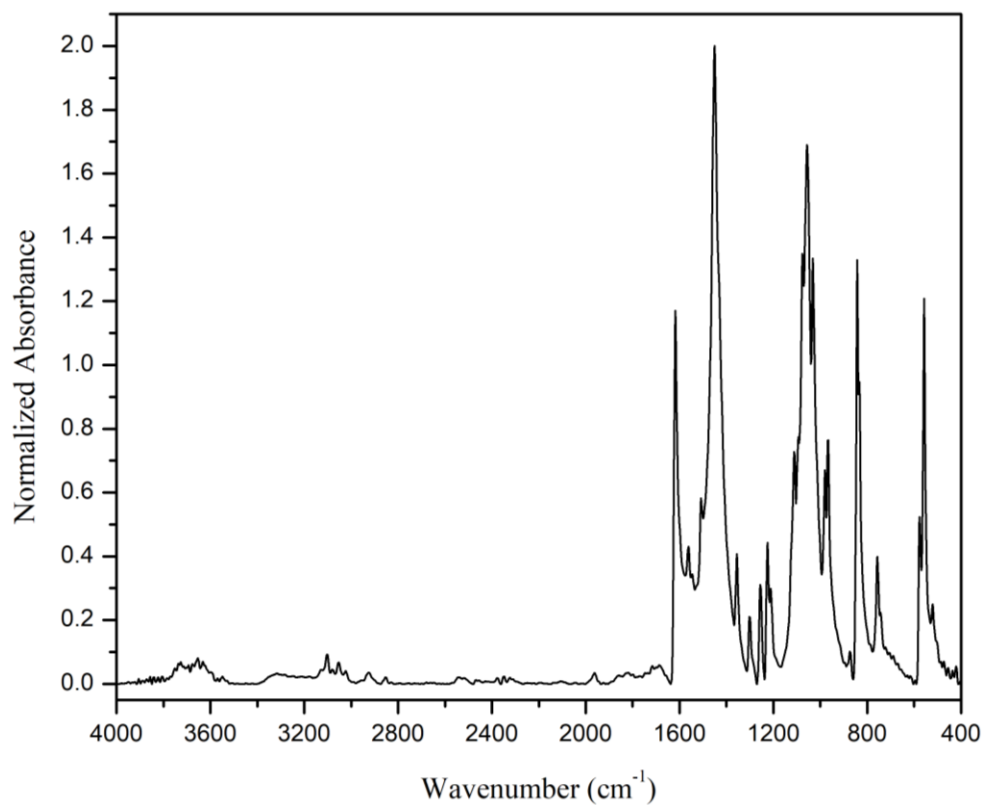


Fig.C2. FTIR spectrum of compound 2

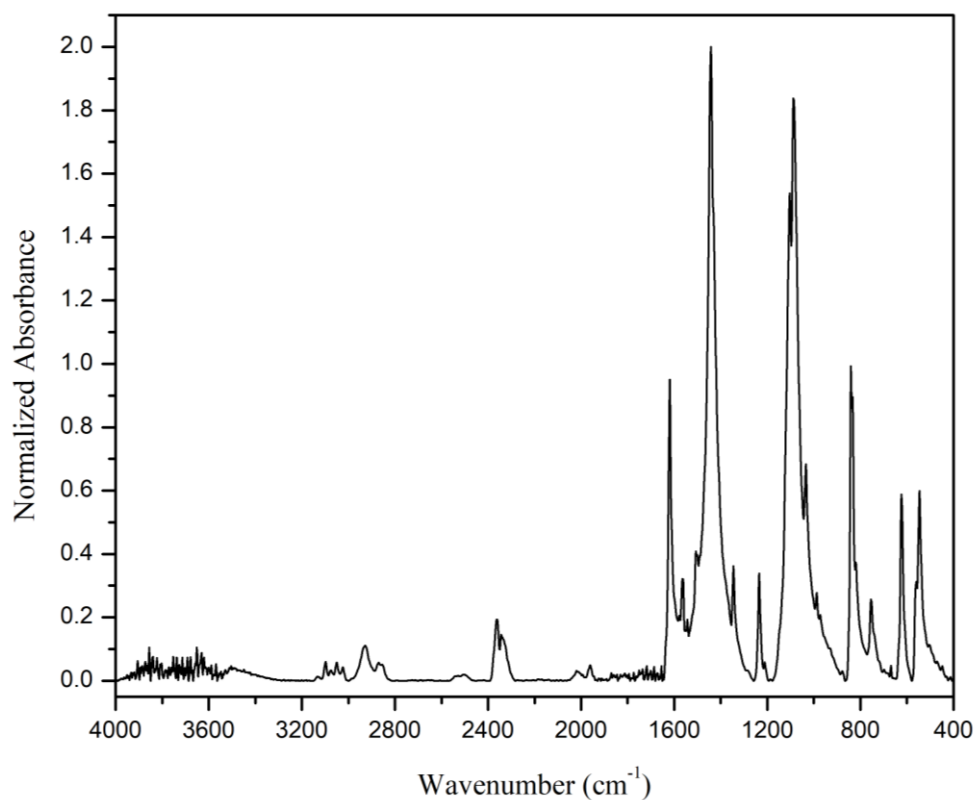


Fig.C3. FTIR spectrum of compound 3

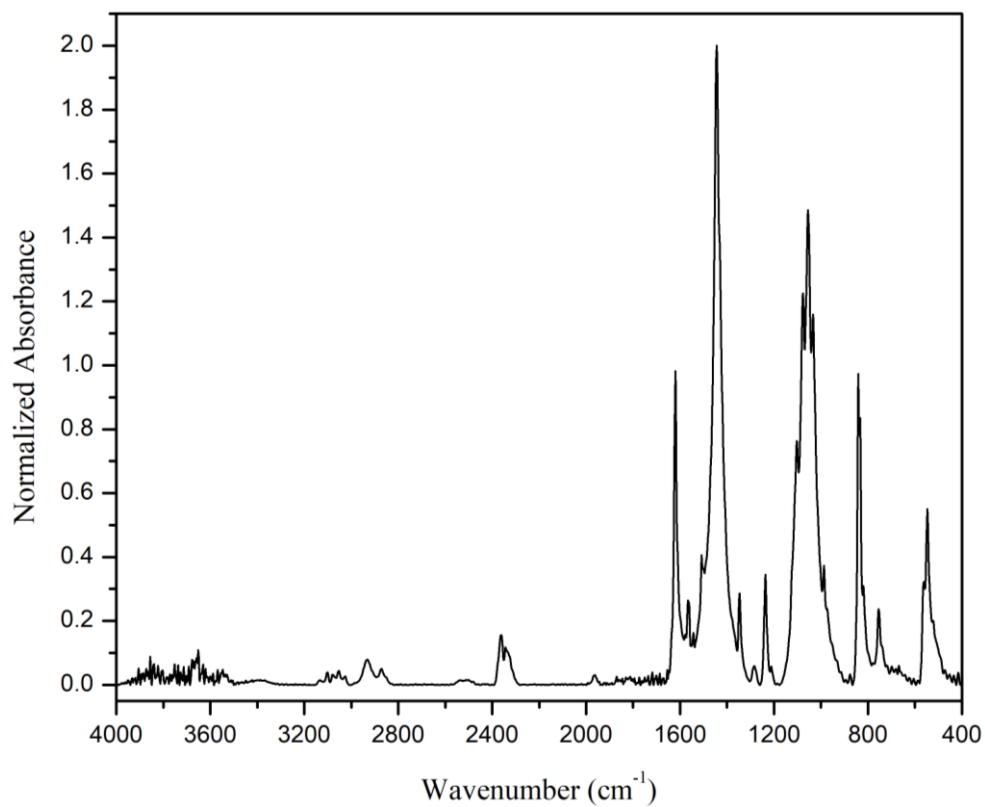


Fig.C4. FTIR spectrum of compound 4

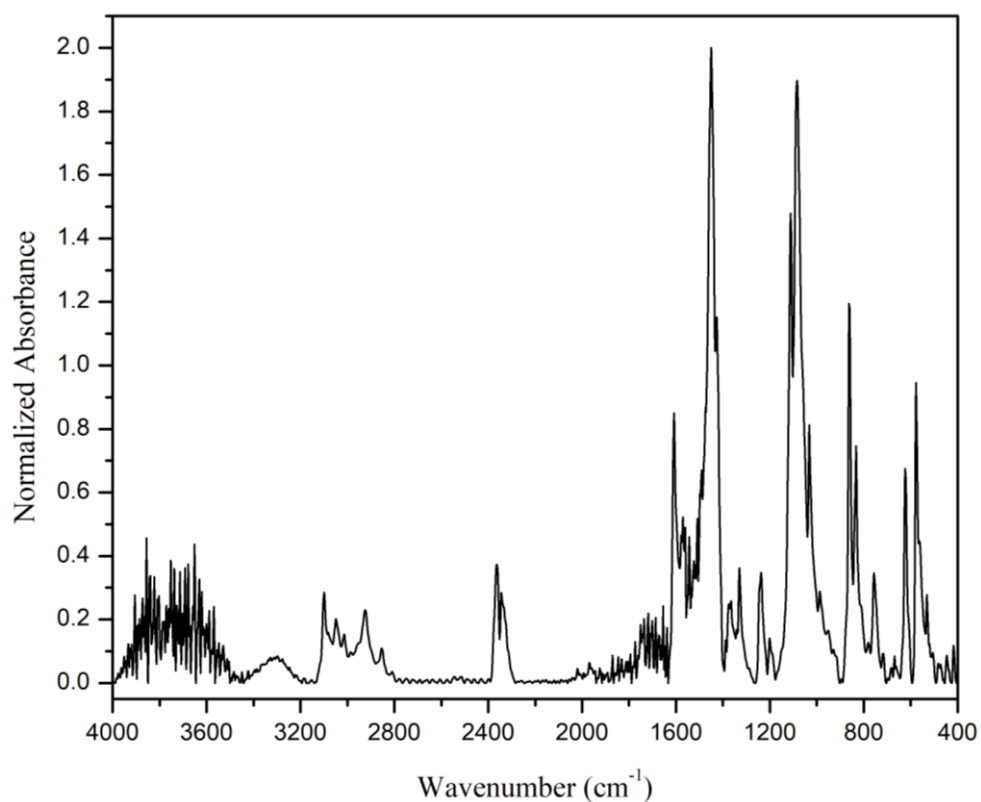


Fig.C5. FTIR spectrum of compound 5

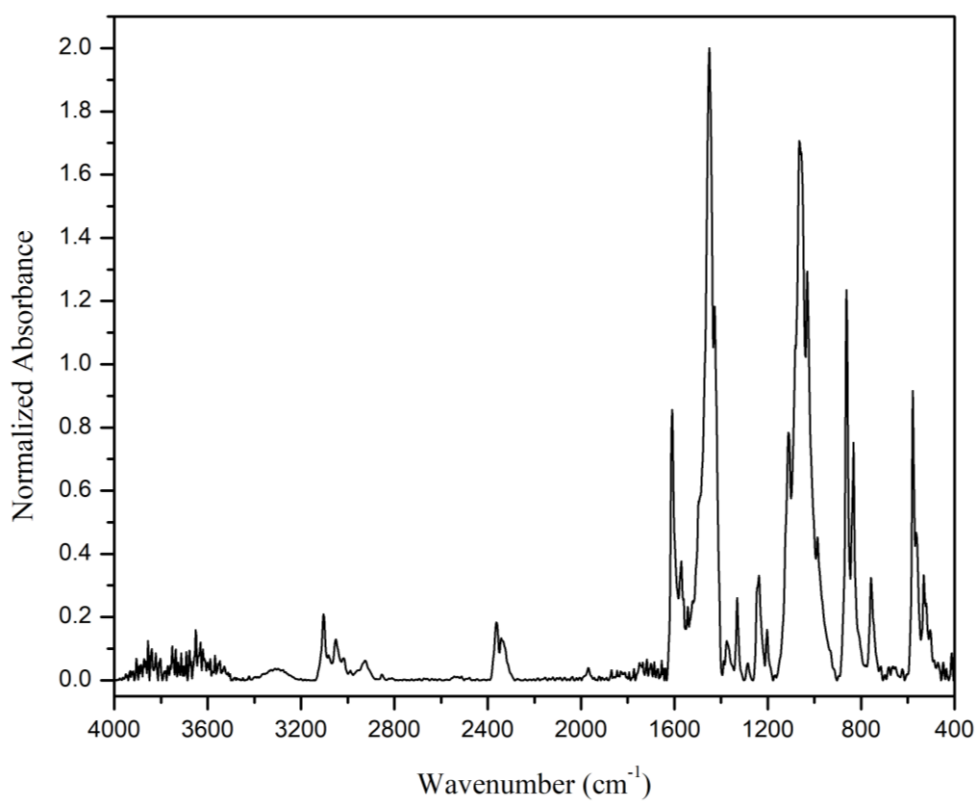
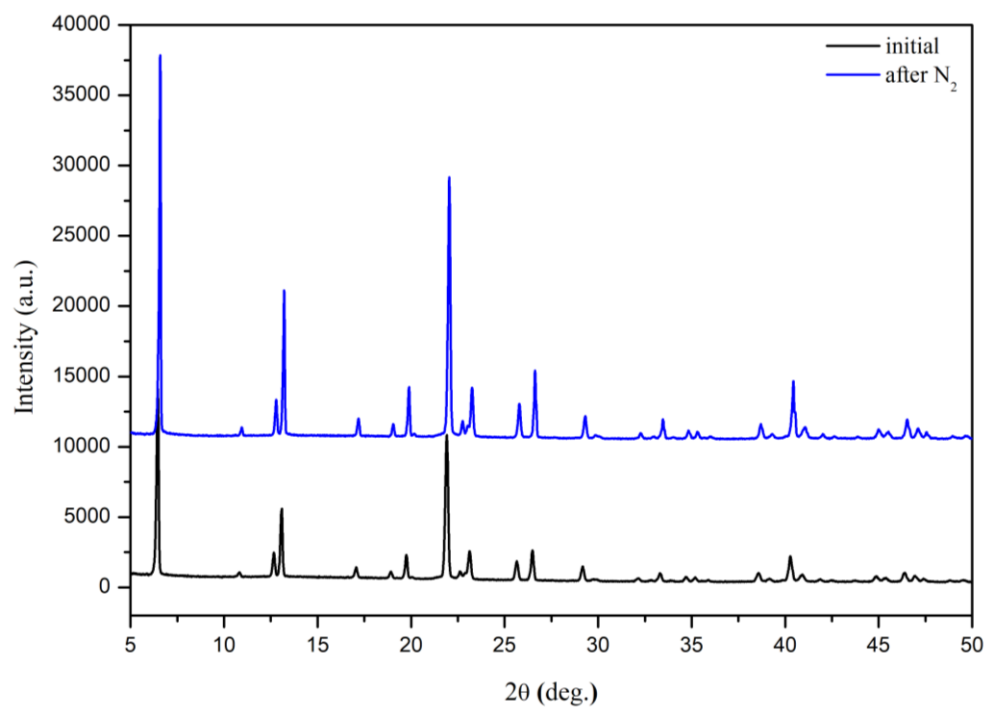
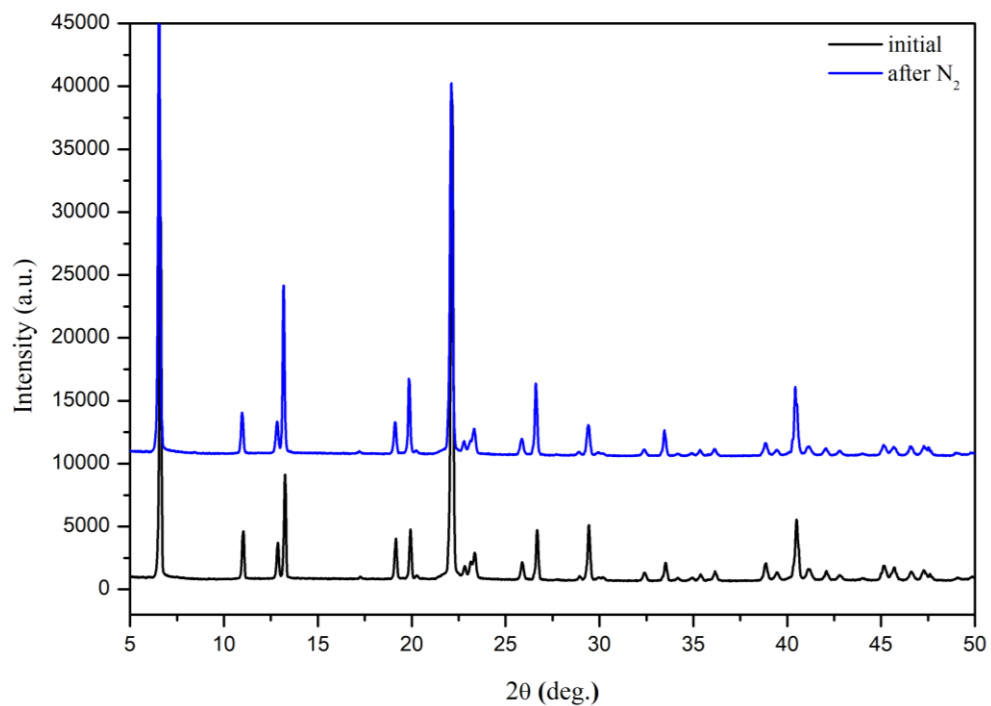


Fig.C6. FTIR spectrum of compound 6

D. Powder X-ray diffractograms after N₂ sorption**Fig.D1.** Powder XRD pattern of compound **1** before (black line) and after (blue line) N₂ sorption**Fig.D2.** Powder XRD pattern of compound **2** before (black line) and after (blue line) N₂ sorption

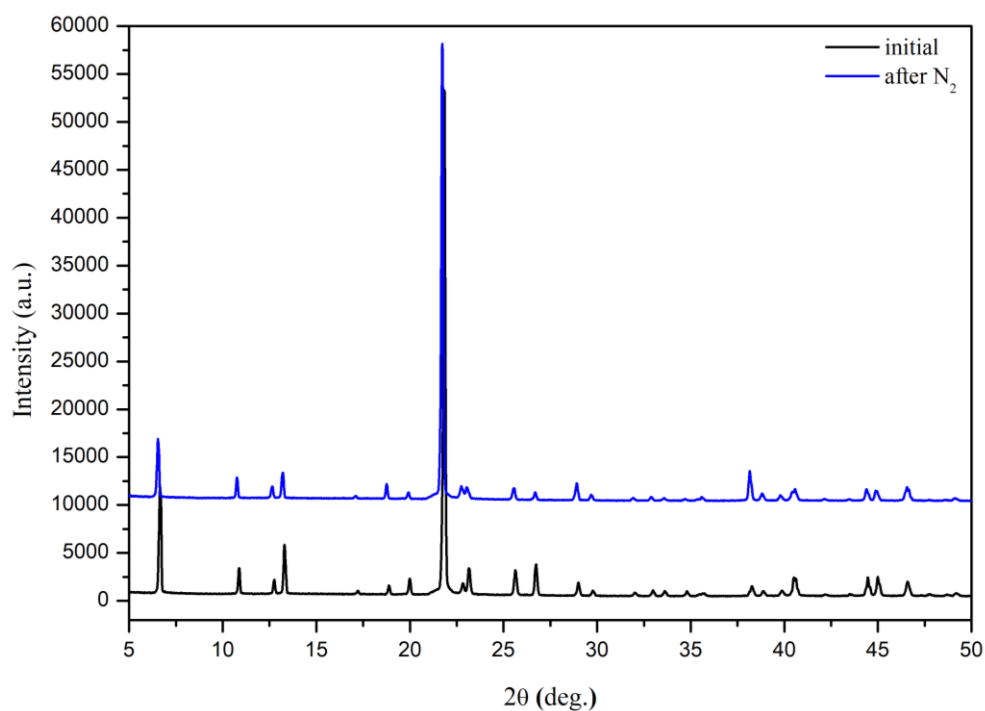


Fig.D3. Powder XRD pattern of compound **3** before (black line) and after (blue line) N₂ sorption

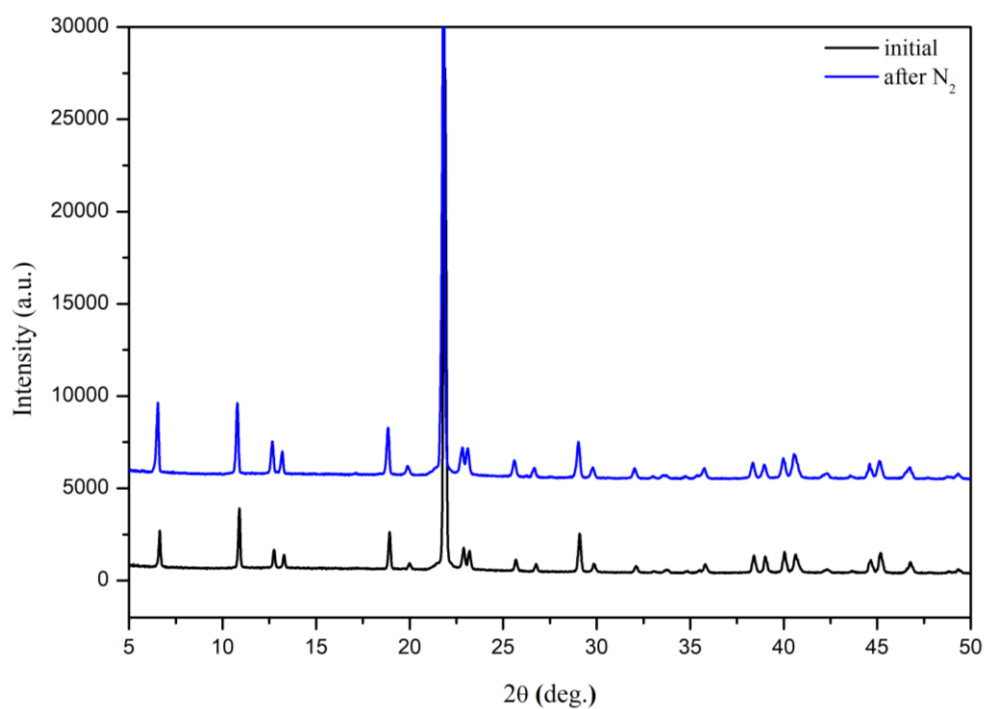


Fig.D4. Powder XRD pattern of compound **4** before (black line) and after (blue line) N₂ sorption

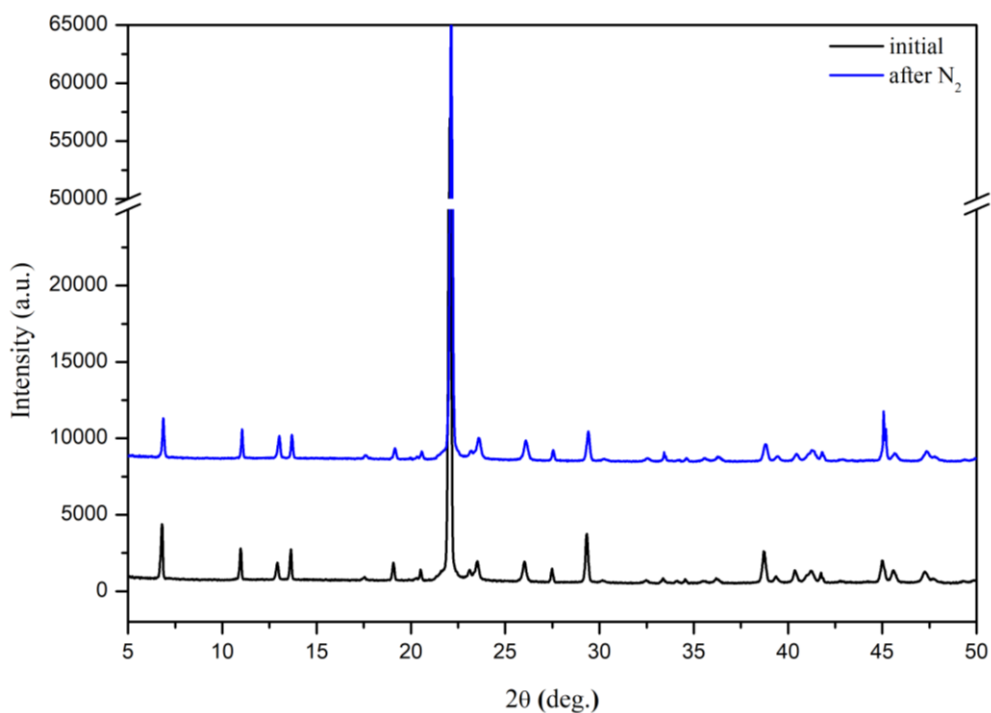


Fig.D5. Powder XRD pattern of compound **5** before (black line) and after (blue line) N₂ sorption

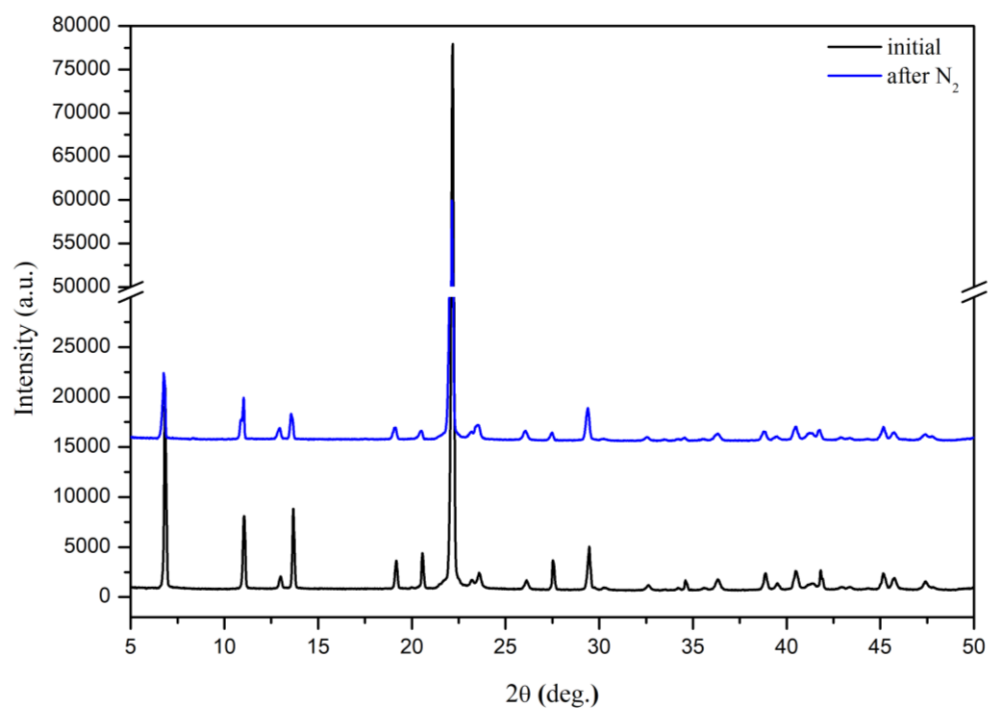


Fig.D6. Powder XRD pattern of compound **6** before (black line) and after (blue line) N₂ sorption



UNIVERSITY OF
BUCHAREST

VIRTUTE ET SAPIENTIA

FACULTY OF CHEMISTRY

MSc. Thesis

Master student: GUZO NICOLAE-CRISTIAN

Thesis Advisor:

Prof. SIMONA MARGARETA COMAN, PhD

2021



UNIVERSITY OF
BUCHAREST
VIRTUTE ET SAPIENTIA

FACULTY OF CHEMISTRY

**DEPARTAMENT OF ORGANIC CHEMISTRY,
BIOCHEMISTRY AND CATALYSIS**

MSc. Thesis

From humin wastes to Carbon Quantum Dots (CQDs) photocatalytic nanocomposites

Master: Chemistry of Advanced Materials

Master student: GUZO NICOLAE-CRISTIAN

Thesis Advisor:

Prof. SIMONA MARGARETA COMAN, PhD

June – July, 2021

CONTENT

INTRODUCTION	1
1. LITERATURE SURVEY	2
1.1. Biomass and its composition	2
1.2. The biorefinery and biomass valorization	3
1.3. Platform molecules and added-value products	5
1.4. Humins: structure and applications	6
1.5. Carbon Quantum Dots (CQDs)	7
1.6 TiO ₂ and photocatalysis	9
Objectives	11
2. EXPERIMENTAL SECTION	11
2.1 CQDS preparation	11
2.1.1 Humins synthesis	11
2.1.2 CQDs synthesis by hydrothermal treatment	12
2.2 CQDs@TiO ₂ nanocomposite synthesis	12
2.3 Characterization techniques	13
2.4 Catalytic tests	15
3. RESULTS AND DISSCUTIONS	16
3.1 Characterization of CQDs	16
3.2 Characterization of CQDs@TiO ₂ nanocomposites	23
4. Catalytic tests	38
5. Conclusions	42
Acknowledgements	43
Dissemination	43
References	44

INTRODUCTION

Last decades confirmed catalysis as a strategic field of science representing the new way to meet the challenges of sustainability. In this context, one of the big challenges is the development of cleaner catalytic processes to convert biomass to multiple platform molecules as strategic precursors for valuable products. At the same time, the production of chemicals should be made in an economical, ethical and environmentally friendly way and this requires complete and efficient valorization of non-edible feedstock. As an example, during the acid-catalyzed dehydration of carbohydrates for the production of renewable bulk chemicals large amounts of so-called humins, which are carbonaceous, insoluble by-products, are typically formed. The commercial processes for the acid-catalyzed conversion are, therefore, seriously hampered by the extensive formation of humins by-products that leads to great losses of the feed (around 10-50% carbon loss) and, in this way, to great efficiency losses in biorefinery operations. In order to improve the efficiency of acid-catalyzed conversions of sugars and, in this way, to improve the economically value of the process, humins should be recovered and valorized.

Photocatalysis is based on the use of photons to drive chemical reactions, thus enabling to obtain several benefits simultaneously, such as: (1) the reactions can be carried out at lower temperatures; (2) toxic substances can be easily degraded; (3) processes can be achieved in a sustainable and environmentally friendly way. Among different UV-active materials titanium dioxide (TiO_2) is the benchmark photocatalyst, due to its strong oxidizing capacity, long-term photostability, commercial availability and low cost. However, the large band gap (3.20 eV) makes TiO_2 inactive under visible light irradiation which largely restricts its practical applications. Therefore, the development of visible light active photocatalysts and techniques to shift the range of light absorption of UV active compounds towards the visible light range has gained increasing importance in the photocatalytic research. In view of their attractive optical properties and up-conversion in particular, a nanocomposite of carbon quantum dots (CQDs) and TiO_2 is expected to realize the efficient usage of the full spectrum of sunlight. However, even though the combination of CQDs with metal oxides can give a significant increase in the photocatalytic activity comparing to the metal-oxides alone, there is still a lot of work to be done in order to increase the lifespan of the as prepared catalysts and maintain their catalytic activity throughout the time.

1. LITERATURE SURVEY

1.1 Biomass and its composition

Biomass (i.e., any renewable organic matter including agricultural food and feed crop residues, energy crops and trees, wood and wood residues, aquatic plants and animal wastes) is a very valuable feedstock, both for the production of chemicals and of novel fuels, which in the future could replace crude oil and gas as the current major raw materials [1]. For such processes a controlled de-functionalization is necessary rather than the functionalization used in the chemical industry. Unfortunately, this means that most of the developed processes in petrochemical and chemical industry are not suitable for converting biomass and alternative pathways for the production of fuels and chemicals should be developed. Moreover, from sustainable development and environment protection reasons, an efficient biorefinery unit should provide a complete valorization of the biomass source by performing the overall processes with a minimum loss of energy and mass and should maximize the overall value of the production chain with the minimum formation of wastes. For the efficient utilization of biomass, it will be crucial to create a similar comprehensive network of process chains.

Lignocellulose is the most abundant biomass feedstock, with an annual growth of 170 billion tons and it does not directly compete with food supplies because of its non-edible nature. [2] Lignocellulose is mainly composed of three biopolymers: cellulose (28–50%, polymer of glucose), hemicellulose (20–35%, polymer of C5 and C6 carbohydrates), and lignin (15–28%, aromatic polymer), along with smaller amounts of pectin (generic term for a polymer comprising galacturonic acid units of at least 65%), protein, extractives (triglycerides, terpenes, pigments, waxes, etc.) and ash (Figure 1).

From the chemically point of view, *cellulose* is a non-branched long chain water-insoluble polysaccharide consisting of several hundred up to tens of thousands of D-glucose units linked to each other by β -(1,4)-glycosidic bonds. These long-chain cellulose polymers are linked together by physical (i.e., hydrogen and van der Waals) bonds, which cause the cellulose to be packed into microfibrils [3]. Unlike cellulose, *hemicellulose* has easily hydrolysable branches with short lateral chains consisting of C6-sugars (glucose, mannose and galactose), C5-sugars (mainly arabinose and xylose) and uronic acids (e.g., 4-*o*-methylglucuronic, D-glucuronic, and D-galactouronic acids), linked each other by β -(1,4)-glycosidic bonds (predominantly) and by α -(1,3)-glycosidic bonds (occasionally) [3]. The

fourth component, which is present in a quite considerable amount and it is called *lignin*. Lignin is acting as glue, holding together the cellulose microfibrils and hemicellulose fibers, imparting structural support, impermeability, and resistance against microbial attack. It comprises 15–28% of lignocellulosic biomass and is the only scalable renewable resource, consisting of abundant aromatic chemicals derived from p-coumaryl, coniferyl, and sinapyl alcohols. [3]

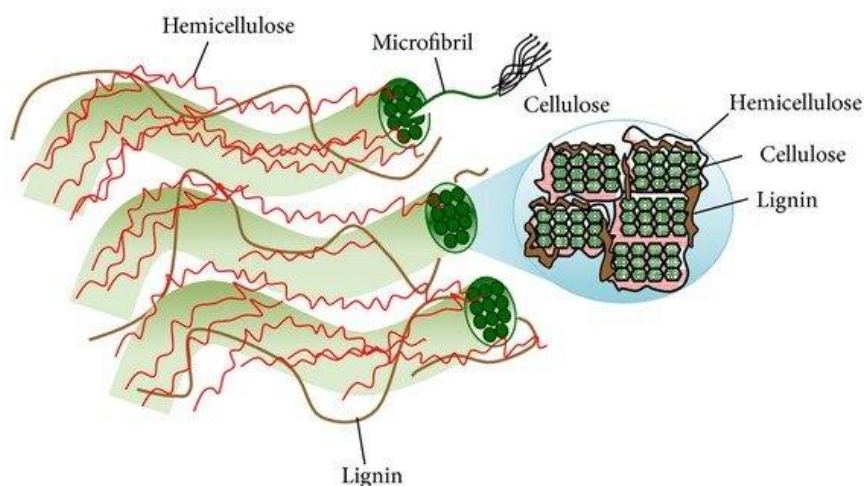


Figure 1. Composition of lignocellulose [3]

Hence, the efficient fractionation of lignocellulose into separated streams of these three polymers is often the entry point for a fruitful bio-refinery as it opens the possibility of subsequent transformations to high-value chemicals and fuels. In this context, reductive catalytic fractionation (RCF) of lignocellulose has received tremendous attention, providing stable lignin oil containing high-value phenolic mono-, di- and oligomers as well as a vaporizable solid carbohydrate pulp that can be used for the production of paper, fine chemicals, or biofuels. [4]

1.2 The biorefinery and biomass valorization

Due to the increasing pressure on the industries to step back from the fossil fuel based processes, they needed a green alternative. What is required is a source of carbon analogous to petrol, where a complex mixture of chemicals can be converted in several high-value molecules, through the development of efficient refinement procedure including cracking, chemical modification and separation in the so-called *bio-refineries* defined as “a facility or a

network of facilities that converts biomass including waste into a variety of chemicals, biomaterials and energy, maximizing the value of the biomass and minimizing waste” (National Renewable Energy Laboratory (NREL)). Advanced biorefineries are analogous in many ways to today’s petrorefineries [5]. A comparison between these 2 types of refineries is presented in the Figure 2:

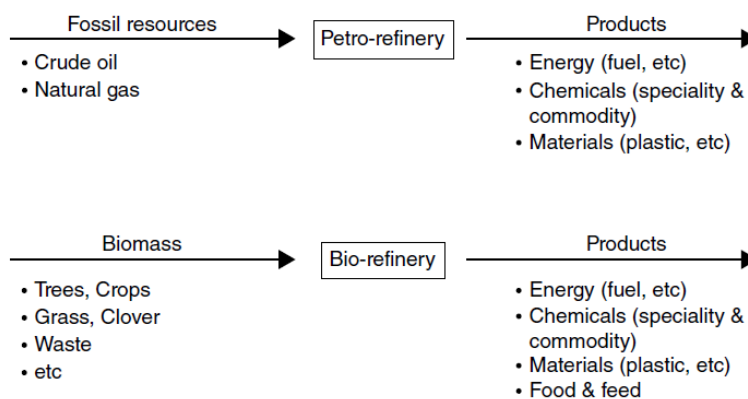


Figure 2. Comparison between petrorefinery and biorefinery [5]

Similarly to oil-based refineries, where many energy and chemical products are produced from crude oil, biorefineries produce many different industrial products from biomass. These include low-value high-volume products such as transportation fuels (e.g. biodiesel, bioethanol), commodity chemicals and materials and high-value low-volume products or specialty chemicals such as cosmetics or nutraceuticals (i.e., food containing health - giving additives and having medicinal benefit).

The obvious alternative to fossils is biological material (biomass) from living or recently living organisms, not metabolized for thousands of years into petrol and coal, thus not concurring to CO₂ emissions. In principle, the biorefining concept has similar objectives as today’s petroleum refineries, but the feedstocks are totally different. In chemical and pharmaceutical industry are required molecules that serve as a source of carbon atoms. This is necessary in order to be able to shape the compounds already existent, into the ones are needed. Driven by this, multiple paths in order to provide the industry with the necessary materials and molecules were taken, but the one more interested is the biomass valorization.

From other perspective, people realized that it is no easy job not only in finding renewable sources of carbon for the chemical and pharmaceutical industries but also in getting rid of the wastes generated by different industries. On one hand, the chemical industry does not produce that much of carbon dioxide, but on the other hand, these industrial processes produce a lot of other wastes, and in order to get rid of them, we have to use many different

procedures that sometimes can be even more expensive than the production process itself. This fact, has led to an interest in other ways of getting rid of the wastes created by mankind, and one of the most promising ones is the waste valorization. This procedure implies transforming by-products of industrial processes into compounds that can serve as raw materials or starting points for other transformations based on the molecules that we obtain.

1.3 Platform molecules and added-value products

A prime objective in the catalytic conversion of lignocellulosic feedstocks is the improving of the catalyst's efficiency and selectivity towards value-added products. However, the incorporation of compatible catalytic processes in the actual infrastructure of petrochemical industry plants requires as biomass feedstocks to be converted to building block chemicals with fewer oxygenated groups. These building block chemicals (also known as "platform molecules") are molecules with multiple functional groups that possess the potential to be transformed into new families of useful chemicals. The most important 15 platform molecules that can be produced from sugars via biological or chemical conversions and can be subsequently converted to a number of high-value bio-based chemicals or materials are given in Table 1.

Table 1. Building blocks obtained from biomass [6]

Building Blocks
1,4 succinic, fumaric and malic acids
2,5 furan dicarboxylic acid
3 hydroxy propionic acid
aspartic acid
glucaric acid
glutamic acid
itaconic acid
levulinic acid
3-hydroxybutyrolactone
glycerol
sorbitol
xylitol/arabinitol

Some of building blocks were the subject of intense research and development during the past few years (such as 5-hydroxymethylfurfural, furfural, levulinic, lactic and succinic acids, as

well as new industrial derivatives from sorbitol) while there was a comparatively modest interest for organic acids (such as aspartic, malic, fumaric, glutamic and itaconic acids).

1.4 Humins: structure and applications

The synthesis of 5-hydroxymethylfurfural (HMF), 5-alkoxymethylfurfural and levulinic acid (LA) by acid catalyzed fructose dehydration, is complemented with the formation of substantial quantities of a black tarry by-product, a complex polyfuranic polymer, called humins [7]. Humins are heterogeneous amorphous biomacromolecules, considered to have the idealized morphology of spherical core-shell architecture [8]. The chemical structure of humins consists of furfural and hydroxymethylfurfural moieties also with carbohydrate, levulinate and alkoxymethylfurfural chains linked together into macromolecules by ether, acetal bonds or aliphatic linkages. The nature of terminal groups could be of carboxylic, ketone, aldehyde and/or hydroxyl nature. Also, the presence of certain solvents such as acids or alcohols during the carbohydrate dehydration reactions could lead to the appearance of other functional groups such as alkoxy and ester groups [9].

The mechanism of the humins formation is supposed to be an acid catalyzed condensation between its formed intermediates but it is also possibly to be formed directly from the starting carbohydrate during their transformation to HMF/MMF/LA, leading to a network of furan rings [10] (Figure 3). The yield of humins is influenced by process parameters such as the type of substrate, time, temperature, and type of acid catalyst. For example, in the case of cellulose conversion to LA, humins yields range from 25–45 wt.%. In the case of HMF production, 10–50 wt. % of sugar substrates are converted into humins. Humins are thus a major waste fraction during sugar conversion [11]. However, despite intensive investigation on the various conversion routes of polysaccharides, understanding of the pathway of humins formation is poor. Furthermore, a clear description of the nature of humins itself is lacking. Generally, humins consists of carbon-rich agglomerate particles. It is composed of approximately 50–66 wt. % C, 25–46% wt.% O, and the remainder is H. [11]

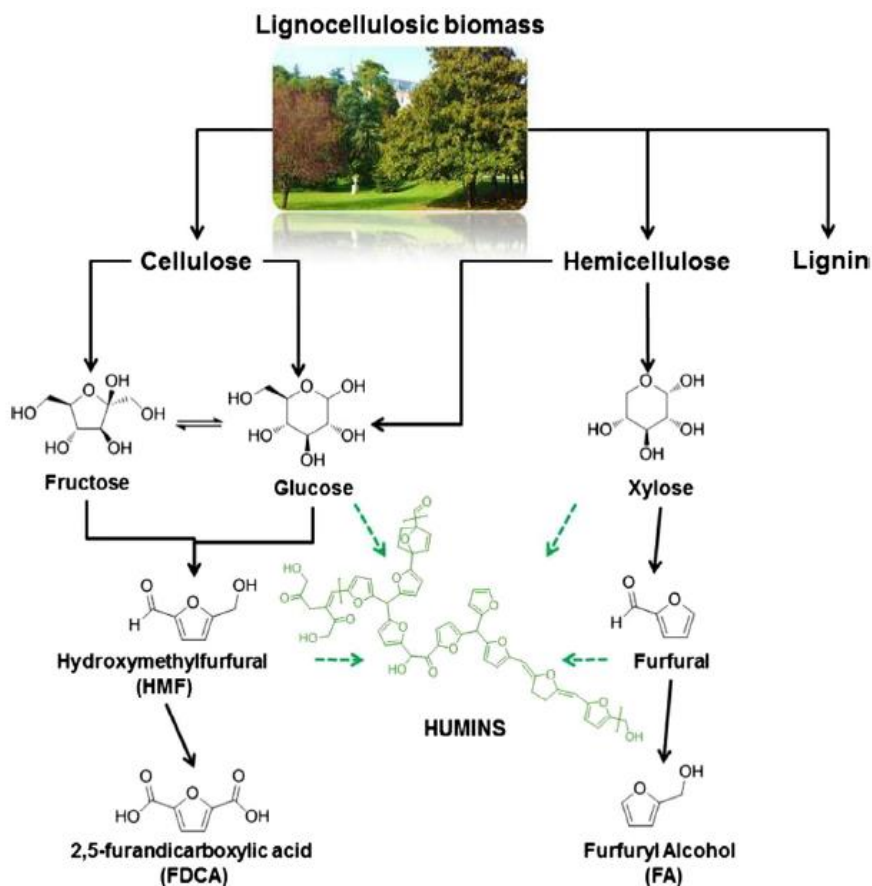


Figure 3. Mechanism of formation of humins [7]

Efforts have been made to suppress the formation of humins, for example, by co-feeding alcohol to stabilize HMF by esterification and thus prevent its further conversion to humins. However, the yield of humins is still 14–22 wt. %. Its main application is still limited to energy and heat applications such as burning and gasification but its valorization into higher added-value applications will be the key for making biomass conversion processes economically feasible. [7]

1.5 Carbon Quantum Dots (CQDs)

Quantum dots are particles of size smaller than Bohr exciton radius (≤ 10 nm), usually made from semi-conductors. Carbon-based quantum dots consisting of graphene quantum dots (QGDs) and carbon quantum dots (CQDs, C-dots or CDs) are a new class of carbon nanomaterials with sizes below 10 nm. They were first obtained during the purification of single-walled carbon nanotubes through preparative electrophoresis in 2004 [12] and then via laser ablation of graphite powder and cement in 2006 [13]. While carbon is a black material, with a low solubility in water and weak fluorescence, carbon-based quantum dots possess a

good solubility and strong luminescence, for which they are referred to as carbon nanolights [14].

Moreover, compared to traditional semiconductor quantum dots and organic dyes, photo luminescent carbon-based quantum dots are superior in terms of high (aqueous) solubility, robust chemical inertness, facile modification and high resistance to photo bleaching. On one hand the superior biological properties of carbon-based quantum dots, such as low toxicity and good biocompatibility, entrust them with potential applications in bioimaging, biosensor and drug delivery. On the other hand, the outstanding electronic properties of carbon-based quantum dots as electron donors and acceptors, causing chemiluminescence and electrochemical luminescence, endow them with wide potentials in optronics, catalysis and sensors. [15]

Since their discovery, Carbon Quantum Dots (Carbon QDs or CQDs) were heavily studied in order to find the optimal method for their synthesis and viable methods for their functionalization. Roughly, the methods of synthesis can be divided in two main groups – the first one being the so called “bottom-up” and the other one being “top-down” [16]. Using both of the methods, the nano-particles that are obtained can be modified either during the synthesis itself or after the synthesis is done.

Table 2. Methods of synthesis for Carbon QDs with their advantages and disadvantages. [16]

	Methods	Merits	Demerits
Top-down	Laser ablation	Controllable morphology and size	Complicated operation, high cost
	Electrochemical oxidation	High purity, high yield, controllable size, good reproducibility	Complicated operation
	Chemical oxidation	Easy operation, large scale production, no elaborate equipment	Non-uniform size distribution
	Ultrasonic treatment	Easy operation	Instrumental wastage, high energy cost
Bottom-up	Microwave synthesis	Short reaction time, uniform size distribution, easy size control	High energy cost
	Thermal decomposition	Easy operation, solvent-free, low cost, large scale production	Non-uniform size distribution
	Hydrothermal treatment	High quantum efficiency, low cost, non-toxicity	Low yield

Nevertheless, there are also some issues that need to be considered prior the synthesis: (I) carbonaceous aggregation during carbonization, which can be avoided by using electrochemical synthesis, confined pyrolysis or solution chemistry methods, (II) size control and uniformity, which is important for uniform properties and mechanistic study, and can be optimized via post-treatment, such as gel electrophoresis, centrifugation, and dialysis and (III) surface properties that are critical for solubility and selected applications, which can be tuned

during preparation or post-treatment. [15] In the Table 2 there are summarized the advantages and disadvantages of several methods for obtaining Carbon QDs.

As in the cases of many other new materials to the world, CQDs are heavily studied in order to figure out all the suitable applications for them. This part of their research is very important due to the fact that without important application, CQDs will remain just a demonstration of skill in the synthesis of advanced materials.

The most interesting application for us is the photocatalysis. The interest in photocatalysis has been motivated in part by the realization that sunlight is effectively an inexhaustible energy source. However, the high energy of UV and short wavelength visible light may adversely damage organic compounds. The demonstrated capability of harnessing long wavelength light and energy exchange with solution species of CQDs offers an excellent opportunity for their use as photocatalysts in organic synthesis. Indeed, a recent study has indicated that smaller CQDs (1–4 nm) are effective NIR light-driven photocatalysts for selective oxidation of benzyl alcohol to benzaldehydes with good conversion efficiency (92%) and selectivity (100%), due to their excellent catalytic activity for H₂O₂ decomposition and NIR light driven electron transfer property [17]. Further studies suggested that the photocatalytic activity of CQDs can be effectively modulated by doping and by tailoring the surface groups. On the other hand, larger CQDs (5–10 nm) synthesized by electro-chemical ablation of graphite showed light-induced proton properties in solution, which can be used as acid catalysts to catalyze a series of organic transformations in aqueous media under visible light. [18]

1.6 TiO₂ and photocatalysis

Photocatalytic reactions driven by sunlight represent a promising way to address the increasing environmental and energy concerns. Therefore, developing and optimizing highly efficient photocatalysts under visible light has attracted worldwide attention.

To date, various photocatalytic semiconductors were used, but undoubtedly, titanium dioxide (TiO₂) is one of the most widely studied photocatalysts due to its abundance, low cost, low toxicity, superior photostability, and high intrinsic catalytic activity under UV illumination [18]. Among different TiO₂ powders, as called TiO₂ P-25 Degussa, with a relatively large surface area and an anatase to rutile phases ratio of about 3 to 1 is the standard material for photocatalytic reactions. However, in spite of all these advantages, the poor

responses to visible light caused by its wide band gap (3.0–3.2 eV), and the fast recombination of photogenerated electron-hole pairs had significantly hindered the application of TiO₂ in photocatalysis [19].

The photocatalytic properties of TiO₂ depend on its intrinsic properties, such as specific surface area, crystal phase and crystallinity [20]. Generally, large surface area resulted from porous structure is favorable to improve photocatalytic activity, as demonstrated for mesoporous TiO₂ [21]. However, large surface areas, which often result not only from porous structure but also from small particle size, usually correspond to the low anatase phase crystallinity. Unfortunately, the high degree of defects in this phase further promotes the recombination of photogenerated electrons and holes [22]. Thus, a preferred way to enhance the photocatalytic activity is the synthesis of TiO₂ materials with simultaneously increased anatase crystallinity and large surface area. Examples of such materials were reported in literature and two of them refer to nanocrystalline TiO₂ photocatalysts synthesized by co-modifying TiO₂ with ammonia and cetyltrimethylammonium bromide [22] or by modifying it with mesoporous SiO₂ [23]. Several other modifications have been made, such as carbon modified TiO₂ [24] and hydrothermal treatment at 400 °C in air [25].

In particular, modification of TiO₂ with carbon nanomaterials, such as carbon nanotubes, fullerenes and graphene, have been used to produce TiO₂/carbon composites with promising photocatalytic activities in the visible region [26]. However, both carbon nanotubes and graphene aggregate easily and are difficult to disperse in conventional solvents, which limit their applications [27]. In connection with this, recently have been shown that the conjugated structure of CQDs leads to the excellent electron transfer/reservoir properties, which is the key factor in enhancing the semiconductors photocatalytic activity [28].

CQDs have the great advantage of having a band gap that can be adjusted by simply changing the size of the nanoparticles. This allows them to easily absorb radiation from different areas of the solar spectrum. Therefore, by introducing CQDs as electron transfer/reservoir materials on the surface of TiO₂, the recombination rates of photogenerated carriers can be modified, allowing the improvement of photocatalytic performance and increasing photocatalytic activity in visible light. In this way, CQD@TiO₂ nanocomposites possess much improved photocatalytic activity, as Gray and co-workers [29] demonstrated. In addition, problems induced by carbon and graphene nanotubes are avoided.

OBJECTIVES

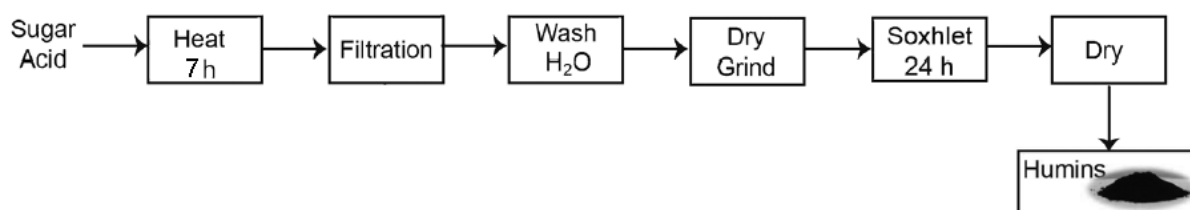
The main scope of the dissertation thesis was to extend the potential of humins valorization to the synthesis of CQDs. To reach this scope worthless humins by-product, generated in the glucose acid-dehydration, has been subjected to an environmentally friendly low-temperature hydrothermal process. The synthesized CQDs with optimized size, brightest blue fluorescence and highest QYs were then used as sensitizers in producing CQD@TiO₂ heterostructured nanocomposites. The photocatalytic activity of the as prepared CQDs@TiO₂ samples was evaluated in methylene blue (MB) dye degradation under the visible light irradiation.

2. Experimental Section

2.1 CQDs preparation

2.1.1 Humins synthesis

Since the glucose conversion is one of the most studied routes for making HMF, due to its commercial significance, in this study humins obtained from glucose dehydration were chose for the CQDs design. Humins were prepared in agree with a recently reported hydrothermal methodology applied in our laboratory [30] as follow: an aqueous solution containing D-glucose (36.0 g D-glucose in 200 ml water, 1.0M) and H₂SO₄ (1.078 g, 5.5 mM) were added into an autoclave and heated at 180 °C, for 7 h. Obtained humins were isolated by filtration, washed with water (300 mL), dried for 12 h at 80 °C, grounded and purified by Soxhlet extraction (Scheme 1).



Scheme 1. Preparation and purification of humins

2.1.2 CQDs synthesis by hydrothermal treatment

CQDs were synthesized by applying the following hydrothermal treatment methodology: 20 mg of humins were dispersed in 20 mL of water in an autoclave. To this suspension 0.1 mL of glacial CH_3COOH was added and the obtained mixture was vigorously stirred at temperatures of 160-200 $^\circ\text{C}$, for 4-12 h. After reaction, the obtained mixture was centrifuged at 8000 rpm for 40 min and the liquid phase was filtered through a Stericup Durapore filter with the pores of 0.22 μm on a polyvinylidene difluoride (PVDF) membrane. The obtained CQDs were denoted: $\text{CQD}_{\text{T-h}}$, where T – represent the synthesis temperature and h - represent the synthesis time.

For the $\text{CQD}_{180-12\text{S}}$ synthesis a separation protocol similar to that described in [31] was applied, as following: the obtained brown solution after the hydrothermal treatment of humins at 180 $^\circ\text{C}$ and 12 h was washed with dichloromethane to remove the adsorbed organic moieties (i.e., acetic acid and other small organic moieties from humins) and the aqueous solution phase was centrifuged at 8000 rpm for 40 min, filtered through a Stericup Durapore filter and concentrated under vacuum at 80 $^\circ\text{C}$ for 2 h.

2.2 CQDs@TiO₂ nanocomposites synthesis

For the synthesis of CQDs@TiO₂ nanocomposites, two kinds of TiO₂ materials were used: a commercial TiO₂ P-25 Degussa powder (consisting of ca. 85% anatase and 15% rutile in crystalline phase) and a modified TiO₂ synthesized from P25 powder by its treatment with NaOH. The two samples are denoted P-TiO₂ and M-TiO₂.

For the synthesis of M-TiO₂ sample 0.3 g P-TiO₂ powder was added to an aqueous solution of 30 mL NaOH (10 mol/L) and stirring for 1 h, at room temperature. Then, the mixture was slowly added into 40 ml autoclave and heated at 120 $^\circ\text{C}$ for 24 h under stirring. After cooling to the room temperature, the aqueous solution was separated by centrifugation and the sediment was washed with HCl solution (1 mol/L) until pH = 1, and subsequently washed with distilled water until pH = 7. After drying for 4 h, the sample was calcined for 2 h, at 450 $^\circ\text{C}$.

CQDs@TiO₂ composites were obtained by a hydrothermal method, following a reported methodology by Zhang and co-workers [32]. Typically, 20 mL distilled water and 6 mL ethanol were mixed together, and then 0.4 g TiO₂ (P-TiO₂ or M-TiO₂) powder and 2 mL of aqueous solution of CQDs (CQD_{180-4} , CQD_{200-4} , CQD_{180-12} , $\text{CQD}_{180-12\text{S}}$) was added. The mixture was kept stirring for 4 h at room temperature to obtain a homogeneous suspension.

After that, the suspension was transferred into an autoclave with glass inner and maintained at 140 °C for 4 h. Resulted CQDs@TiO₂ composites were washed three times with water and collected by centrifugation at 6100 rpm, for 15 minutes. Finally, the separated solid was dried under vacuum at 60 °C for 6 h.

Eight samples were obtained and denoted as CQD₁₈₀₋₄@P-TiO₂, CQD₂₀₀₋₄@P-TiO₂, CQD₁₈₀₋₁₂@P-TiO₂, CQD_{180-12S}@P-TiO₂, CQD₁₈₀₋₄@M-TiO₂, CQD₂₀₀₋₄@M-TiO₂, CQD₁₈₀₋₁₂@M-TiO₂ and CQD_{180-12S}@M-TiO₂, where the subscript numbers represent the hydrothermal parameters, i.e., temperature and time, respectively, used for the CQDs synthesis from humins.

2.3 Characterization techniques

The prepared CQDs and CQD@TiO₂ materials were exhaustively characterized by techniques as: X-ray diffraction (XRD), ATR- and DRIFT-IR spectroscopy, UV-Vis spectroscopy, photoluminescence spectroscopy (PL), adsorption-desorption isotherms of liquid nitrogen at 77K, elemental analysis, thermogravimetric-differential thermal analysis (TG-DTA), transmission electron microscopy (TEM) and energy dispersive X-ray spectroscopy in scanning transmission electron microscopy (STEM-EDS).

Powder X-ray Diffraction patterns were collected at room temperature using a Shimadzu XRD-7000 apparatus with the Cu K α monochromatic radiation of 1.5406 Å, 40 kV, 40 mA at a scanning rate of 0.1 2 θ min⁻¹, in the 2 θ range of 5^o–80^o.

ATR-FTIR spectra were recorded and collected by a Bruker Tensor-II FTIR spectrometer at room temperature at a 4 cm⁻¹ resolution in the range of 400–4000 cm⁻¹ and the final spectrum was obtained averaging 32 scans.

DRIFT spectra were recorded with a Thermo spectrometer 4700 (400 scans with a resolution of 4 cm⁻¹) in the range of 600–4000 cm⁻¹.

UV-Vis spectra were recorded and collected by a JASCO V-350 spectrophotometer equipped with tungsten and deuterium lamps for visible and UV light analysis, respectively.

Photoluminescence (PL) spectra were measured with a JASCO FP-8200 fluorescence spectrometer equipped with of 150 W xenon lamp as the excitation source.

The relative quantum yields (QYs) of the CQDs were calculated according to a literature method [33]. As reference standard fluorescein (1 x 10⁻⁷ M in 0.1 M aqueous NaOH (pH 9.6)) was chosen. Fluorescein has a QY of approximately 86% at $\lambda = 366$ nm and $\lambda =$

313 nm. The UV absorbance of the samples was adjusted to be below 0.02 to minimize the inner filter effect.

The QY was calculated by the following equation:

$$QY_s = Q_r \left(\frac{A_r}{A_s} \right) \left(\frac{E_s}{E_r} \right) \left(\frac{\eta_s}{\eta_r} \right)^2$$

Where subscribers “r” and “s” refer to the fluorescein (reference) and evaluated sample, respectively. “QYs” stands for the quantum yield of the sample, “E” stands for the integrated PL intensity, “A” stands for the absorbance, and “ η ” stands for the refractive index of the solvent. Fluorescein (quantum yield: 86%) was dissolved in 0.1 M NaOH (refractive index: 1.33) and the C-dots were dissolved in water (refractive index: 1.33). The QY was measured at an excitation wavelength of 366 nm.

Textural characteristics (surface area, pore volume and pore diameter) were determined from the adsorption-desorption isotherms of nitrogen at -196 °C using a Micromeritics ASAP 2020 Surface Area and Porosity Analyzer.

Elemental analysis was made with an elemental analyzer EUROVECTOR EuroEA 3000.

TG-DTA analyses were recorded using a Shimadzu apparatus in a Pt crucible. The heating rate was of 10°C min⁻¹, respectively, starting from room temperature till 850 °C under a nitrogen flow of 50 mL min⁻¹.

Transmission electron microscopy (TEM) was performed on an electron microscope, Titan G2 60-300 kV FEI Company, equipped with field emission gun (FEG), monochromator, three condenser lenses system, the objective lens system, image correction (Cs - corrector), HAADF detector. The EDS spectrometer (Energy Dispersive X-Ray Spectroscopy) EDAX Company with Si (Li) detector was used to display the prepared samples. Microscopic studies of the samples were carried out at an accelerating voltage of the electron beam equal to 300 kV.

The mapping was carried out in the STEM mode by collecting point by point EDS spectrum of each of the corresponding pixels in the map. The collected maps were presented in the form of a matrix of pixels with the color mapped significant for element and the intensity corresponding to the percentage of the element.

2.4 Catalytic tests

The photocatalytic efficiency of the prepared CQD@TiO₂ samples was evaluated in methylene blue (MB) dye adsorption and degradation under visible light irradiation. Photocatalytic activity tests were performed in a cylindrical quartz photoreactors and blue LED lamps (112W), emitting at 445-465 nm, were used as light source.

In a typical experiment, 7.5-15 mg of photocatalyst was added to 10 ml of MB aqueous solution (30 mg/L). Before the photocatalytic degradation, the suspension was magnetically stirred in the dark, for 15 min, to establish the adsorption–desorption equilibrium of MB. Subsequently, the solution was irradiated with blue or red LED lamp and aliquots of 2.5 mL were collected from suspension at certain time intervals (10 min) and filtered using a 0.22 μm filter membrane. The concentration of MB after illumination was determined by a UV-vis spectrometer (SPECORD 250 - 222P108). The intensity of the main absorption peak (666 nm) of the MB dye was referred to as a measure of the residual MB dye concentration. Control experiments with pristine P-TiO₂ and M-TiO₂ were also performed.

For calibration curve stock solution of 500 mL with a concentration of 30 mg/L was prepared (15 mg MB dissolved in distilled water in a volumetric flask). The stock solution was used to prepare other five different MB concentrations as: 5, 10, 15, 20 and 25 mg/L. For each concentration the UV-vis spectra was registered (Figure 4A) and the corresponding absorbance value for the 666 nm band was used to build the calibration curve (Figure 4B). The calibration curve presents a linear relation and relationship coefficient was 0.9515 (Figure 4B).

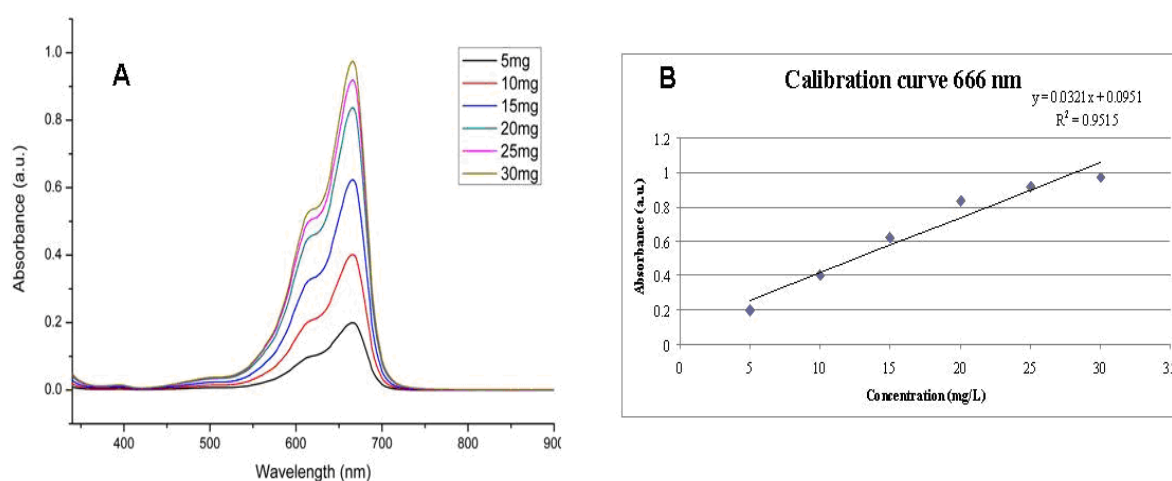


Figure 4. UV-vis band (665 nm) of MB at different concentrations (A) and calibration curve (B)

The MB conversion was defined as follows:

$$\text{Conversion (\%)} = \frac{C_0 - C}{C_0} \times 100$$

where C_0 is the initial concentration of MB and C is the concentration of the MB at a certain reaction time, respectively.

Chapter 3. RESULTS AND DISSCUTION

3.1 Characterization of CQDs

The reaction time and temperature are the key factors in the hydrothermal approach preparation of CQDs. To probe the chemical composition of CQDs, prepared at different reaction times and different reaction temperatures, ATR-IR measurements were performed.

As Figures 5 A, B and C show the chemical composition differs only slightly from sample to sample. Therefore, for the as-prepared CQDs, the main bands identified in IR spectra can be associated to C=O stretching (1730 cm^{-1}) indicating the presence of acid, aldehyde, and ketone groups in their composition. The absorption band at 1370 cm^{-1} is attributed to the O-H in-plane deformation vibration or CH_x ($x = 2, 3$) bending vibration. The peaks at 2837 and 2939 cm^{-1} are assigned to the CH_x ($x = 2, 3$) stretching vibrations. The absorption bands at 1230 and 1100 cm^{-1} are ascribed to the C-O-C stretching of the furan ring deformation. The wide strong absorption bands centered at 1640 , 2062 , and 3300 cm^{-1} are mainly attributed to the water molecules. However, the 1640 cm^{-1} peak may also be partially contributed by the C=C stretching vibration of numerous sp^2 structures that enriched the aromatic structure, in agree with Weckhuysen and co-workers [10].

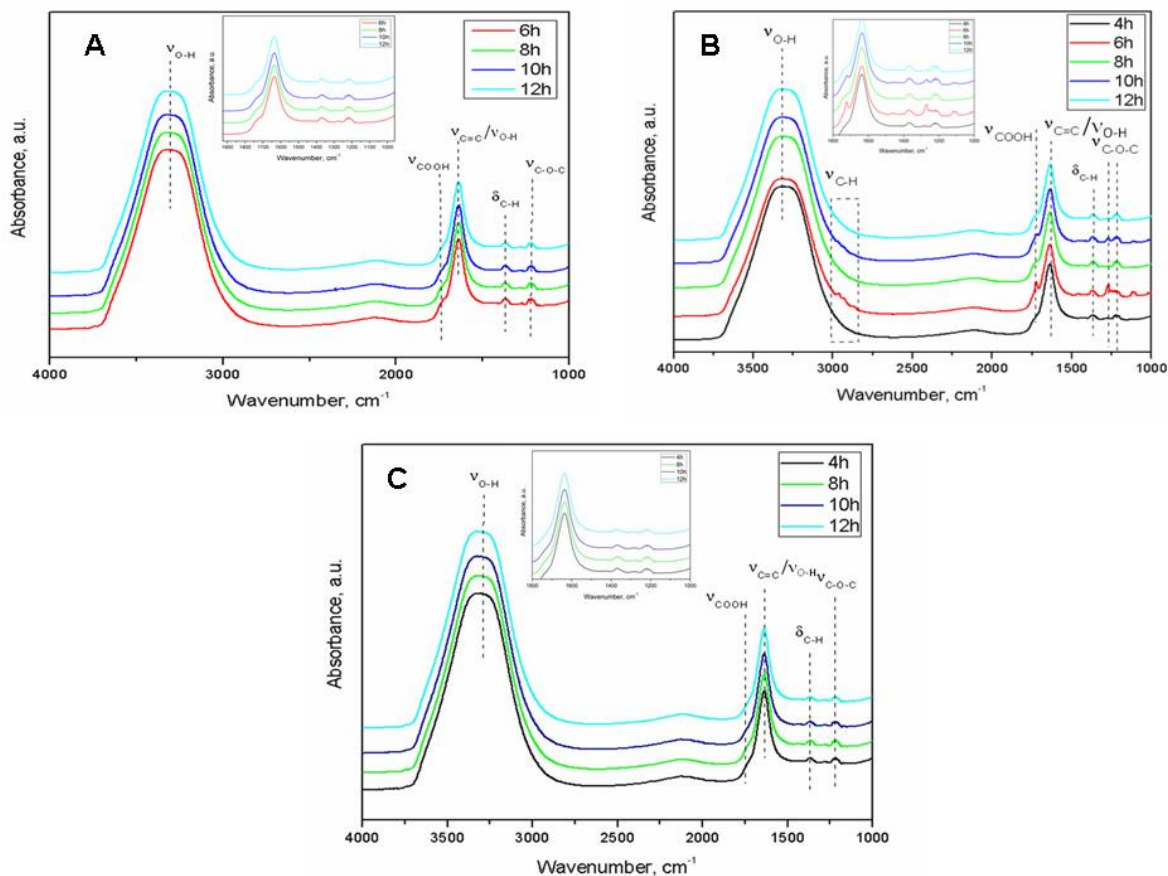


Figure 5. IR spectra on 1000-4000 cm^{-1} range of the CQDs synthesized at 160°C (A), 180°C (B) and 200°C (C) at different reaction times (insets: IR spectra on 1000-1800 cm^{-1} range)

The infrared spectrum of the CQDs shows similar features, except that the C=O absorption at 1730 cm^{-1} diminishes substantially when the hydrothermal temperature increased at 200°C. Such a variation supports the aforementioned speculation of the suppression of the C=O bonds with the hydrothermal parameters or their post-treatment [34]. Nevertheless, all synthesized CQDs are well dispersed and stable in water for a long period of time (several months) indicating the existence of a high concentration of the hydroxyl groups on their surface, irrespective of the synthesis conditions, in agree with literature reports [34; 35].

In the XRD pattern of CQD₂₀₀₋₄ (Figure 6) two diffraction lines centered at 22° and 42° are evidenced, indicating that a graphite-like structure existed in their carbon core. However, CQD₁₈₀₋₁₂ displays a broad line centered at 24° that is attributed to highly disordered graphitic carbons (JCPDS 26-1076) [35]. Moreover, the lower line intensity along with a relatively higher full width half maximum, indicate a smaller size of the CQD₁₈₀₋₁₂ sample [34].

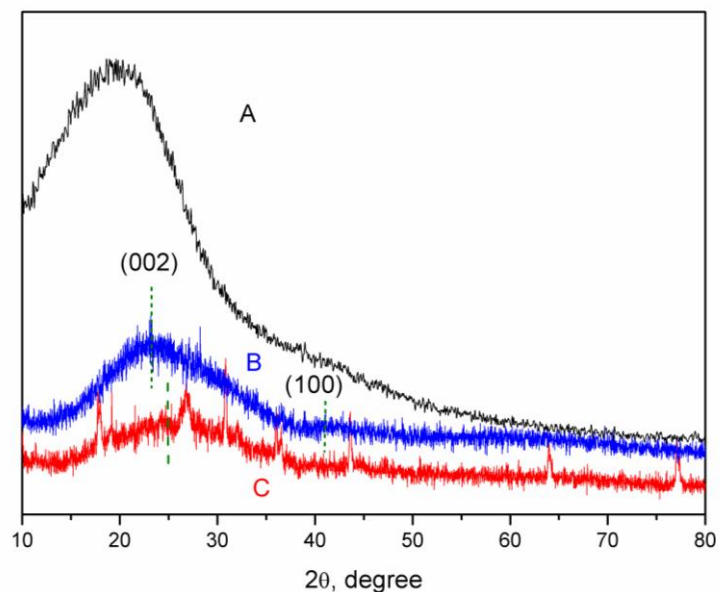


Figure 6. XRD pattern of the humins (A), CQD₂₀₀₋₄ (B) and CQD₁₈₀₋₁₂ (C)

In quest of exploring the spectral properties of the as-prepared CQDs, the UV-Vis absorption and PL spectra were acquired. Figures 7-9 shows the PL spectra of as-prepared CQDs aqueous solutions, excited at various λ_{ex} .

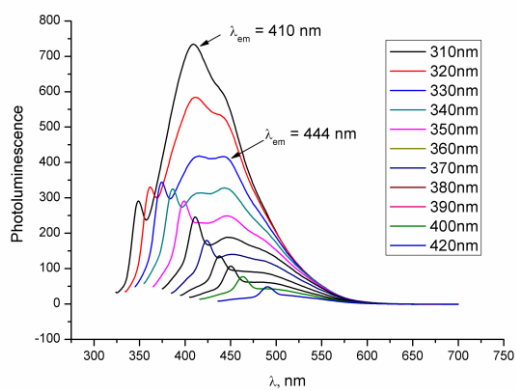


Figure 7. PL spectra of CQD₁₈₀₋₄ with λ_{ex} of 310-420 nm

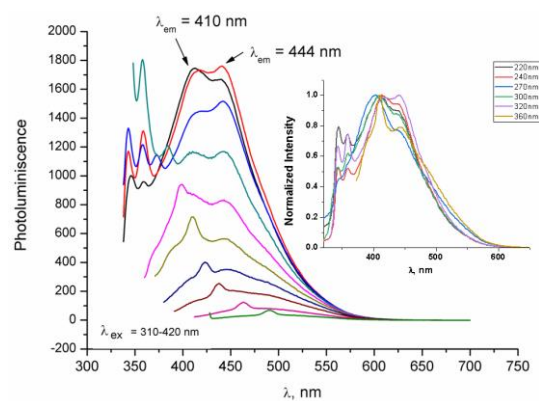


Figure 8. PL spectra of CQD₁₈₀₋₁₂ with λ_{ex} of 310-420 nm (inset: PL spectra with normalized intensity, λ_{ex} of 220-360 nm)

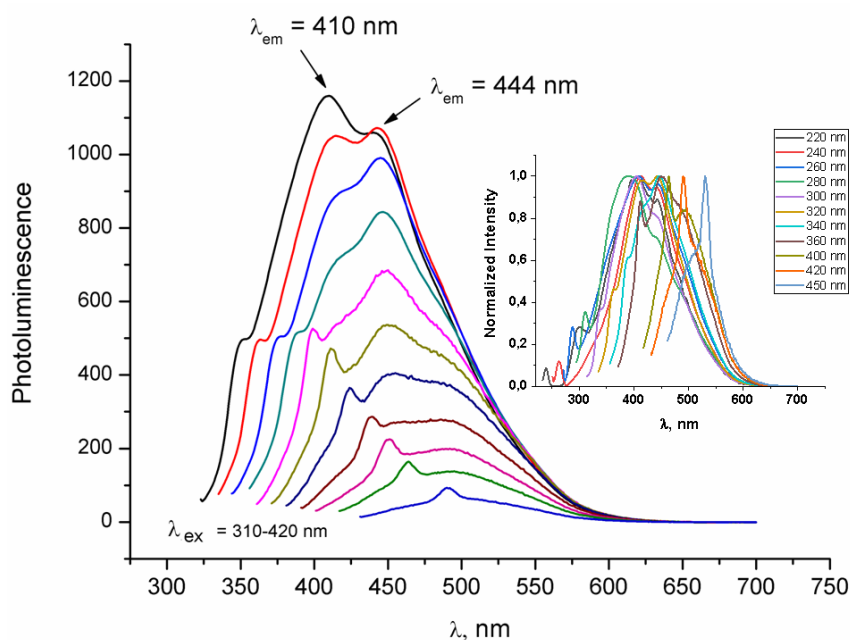


Figure 9. PL spectra of CQD₂₀₀₋₄ with λ_{ex} of 310-420 nm (inset: PL spectra with normalized intensity, λ_{ex} of 220-450 nm)

The broad and irregular emission peaks suggest that the fluorescence of CQDs derived from different surface functional groups or/and carbon core structure. The typical PL spectra comprise two fluorescence emission centers: one indigo-blue centered at around 410 and another blue peak centered at 444 nm. Also, some sharp violet peaks centered at below 400 nm are observed. The relative intensity of the indigo-blue emission (410 nm) decreases while that of the blue emission (444 nm) increases with increasing excitation wavelength. These contrary variation trends also suggest their different origins. However, both fluorescence emission centers are located at 410 and 444 nm without any perceptible excitation dependence when the λ_{ex} was less than 360 nm (inset Figures 7 and 9). When λ_{ex} moves from 360 to 450 nm a distinct red-shift in the emission wavelength of the CQD₂₀₀₋₄, from 445 nm to 530 nm, was observed (Figure 9). The same shifts were also observed in the case of CQD₁₈₀₋₁₂ sample (not shown in Figure 8).

The excitation-dependent PL behavior is usually attributed to the various size distributions (quantum effect) [36] that make the difference in optical selection, and to the presence of the oxygen-containing functional groups, which affected the band gap of CQDs [37]. On the other hand, the excitation-independent PL behavior derived from the homogeneous particle size, in agree with literature reports [38], but the high polarity of nanosized cluster and the sp^2 -carbon networks is claimed as being responsible for excitation-dependent PL behavior [39].

Taking into account this information and on the base of the obtained results, we can assume the formation of CQDs with preponderantly homogeneous particle with small size, for which the emission is due to the intrinsic luminescence of the sp^2 -carbon networks which is responsible for the shorter wavelength part of emission (excitation-independent; $\lambda_{ex} = 250-340$ nm, $\lambda_{em} = 445$ nm). However, the excitation-dependent behavior of the longer wavelength part ($\lambda_{ex} = 340 - 450$ nm, $\lambda_{em} = 445-530$ nm) indicate the formation of some nanoclusters with bigger size with a similar behavior as those formed by the aggregation of single CDs in high concentrated solution, claimed by Yang et al. [40]. In both cases it results a larger number of $-CO$ and $-OH$ get together, which leads to the higher polarity on the surfaces of nanoclusters. This high polarity leads to electron rapid relaxation from excited states to substates, which corresponds to longer wavelength. Then, the substates contribute to photo emission, which eventually gives rise to longer wavelength emission [41].

The irregular shape of the PL spectra of the CQD_{180-12} sample may indicate either the existence of different fluorophore or/and the presence of impurity states. In order to check the origin of these emissions part of CQD_s sample were washed with dichloromethane and the PL spectra of the obtained sample ($CQD_{180-12S}$) were again analyzed (Figure 10).

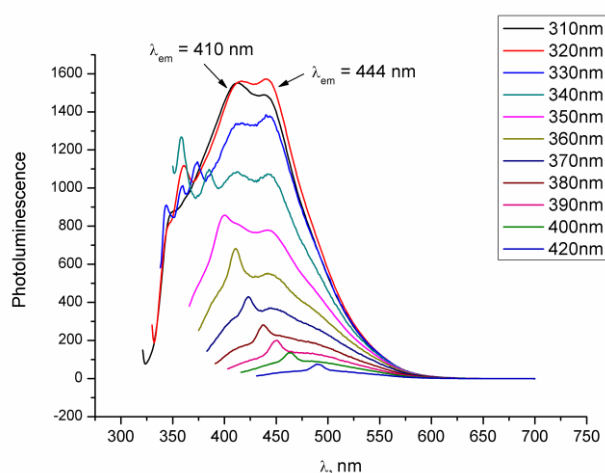


Figure 10. PL spectra of the $CQD_{180-12S}$ sample with λ_{ex} of 310-420 nm

Comparing the PL spectra of CQD_{180-12} (Figure 8) and $CQD_{180-12S}$ (Figure 10), some of sharp violet peaks centered at below 400 nm vanished after washing with dichloromethane. Remained peaks are similar with those observed in the other samples but with a higher intensity indicating the presence of fluorophore oxygen-containing functional groups in a higher amount on this sample, in agree with IR results.

The highest fluorescence emission is obtained at around 444 nm for an excitation at 320 nm (Figures 7-9). Therefore, in order to display the effect of hydrothermal parameters on the fluorescence characteristics of CQDs, their emission spectra ($\lambda_{\text{ex}} = 320$ nm), at hydrothermal temperatures of 180-200°C and 4-12h, were compared (Figure 11).

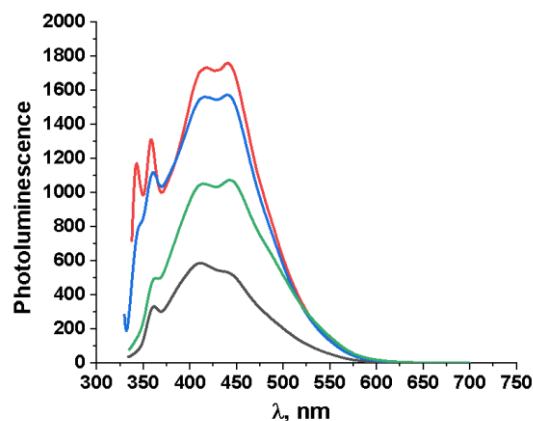


Figure 11. The PL spectra comparison for CQD₁₈₀₋₄ (black), CQD₂₀₀₋₄ (green), CQD_{180-12S} (blue) and CQD₁₈₀₋₁₂ (red) samples ($\lambda_{\text{ex}} = 320$ nm).

As Figure 11 shows both synthesis parameters affect the formation progress of quantum dots and their fluorescence properties. The highest PL intensities are displayed for CQD₁₈₀₋₁₂ followed by CQD_{180-12S}, CQD₂₀₀₋₄ and CQD₁₈₀₋₄ sample.

Clearly enough, the fluorescence intensity is highly dependent by the reaction time (Figure 11, CQD₁₈₀₋₄ (black) and CQD₁₈₀₋₁₂ (red)). This dependence suggests an increase in the carbon dot concentration with reaction time. However, CQD₂₀₀₋₄ displays an increased luminescence intensity than CQD₁₈₀₋₄ but longer reaction time (i.e., in excess of 4 h) causes a decrease in the luminescence intensity (not showed in Figure 11). This signifies that a long reaction time for high temperatures result in the formation of carbon particles with larger size due to the aggregation, which do not exhibit fluorescence.

On the other hand, it was shown that the surface status of CQDs markedly affects their PL properties [42]. For amorphous CQDs, the surface status is mainly affected by the number and type of the functional groups on the surface [43]. Hence, the PL properties of the amorphous CQD₁₈₀₋₁₂ were mainly determined by their surface groups. Indeed, IR results indicated that the CQD₁₈₀₋₁₂ contained more carboxyl acids and hydroxyl groups, which could act as radiative recombination centers and introduce more defects at their surface, leading to stronger fluorescence emission. In comparison, the CQD₂₀₀₋₄ had more epoxy and ether

groups, which acted as non-radiative recombination centers and resulted in the weaker fluorescence emission.

Additionally, when λ_{ex} was 366 nm, the calculated QYs of these samples varies from 8% (CQD₁₈₀₋₄) to 15% (CQD₂₀₀₋₄) to 21% (CQD₁₈₀₋₁₂), respectively. The QY of the CQD_{180-12S} slightly decreases to 20% by comparing with the CQD₁₈₀₋₁₂. Zhu and co-workers [51] showed not long ago that CQDs exhibit a higher PL intensity after surface reduction but no obvious emission shift, which shows that the QY of CQDs is controlled by the surface chemistry. Obtained values are in line with those reported in literature [38].

C-dots prepared by typical methods usually show strong ultraviolet (UV) absorption, but the positions of UV absorption peaks of C-dots prepared by different methods are quite different [44]. The UV-Vis absorption features of the CQDs produced in this work were examined and the detailed results are given in Figure 12. The inset in Figure 12 shows the images of the CQD₂₀₀₋₄ solutions taken under visible and ultraviolet light of 365 nm wavelength, which demonstrate a faint yellow color under visible light and emit a distinct blue light under UV light.

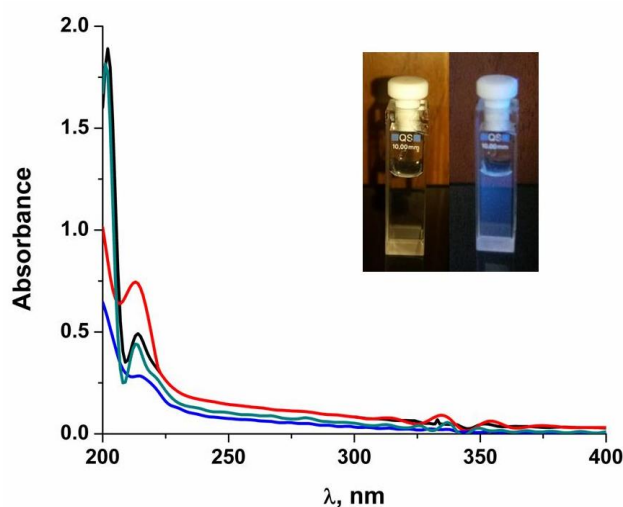
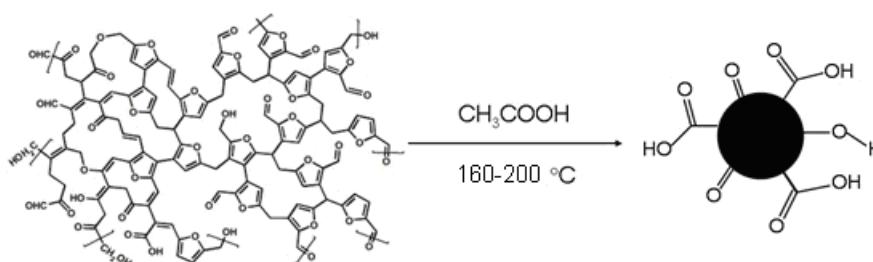


Figure 12. The UV-Vis absorption spectra for CQD_{180-12S} (black), CQD₁₈₀₋₁₂ (green), CQD₁₈₀₋₄ (blue), and CQD₂₀₀₋₄ (red) samples

Similar to the previous studies in CQDs and GQDs [48-56], the absorption peaks in shorter wavelength can be ascribed to $\pi-\pi^*$ transition of aromatic C=C bonds in sp^2 hybrid domains while and the shoulders at longer wavelength are attributed to $n-\pi^*$ transition of C=O or C-OH bond in the sp^3 hybrid region. However, it is clearly the nature of C=C bonds are different in CQD₁₈₀₋₁₂ and CQD₂₀₀₋₄ samples with a more disordered structure in the CQD₁₈₀₋₁₂ sample. When samples are illuminated by 365 nm light, the CQDs solutions emit

an intense blue color which indicates that the PL emission wavelength (λ_{em}) was red-shifted (the inset in Figure 12).

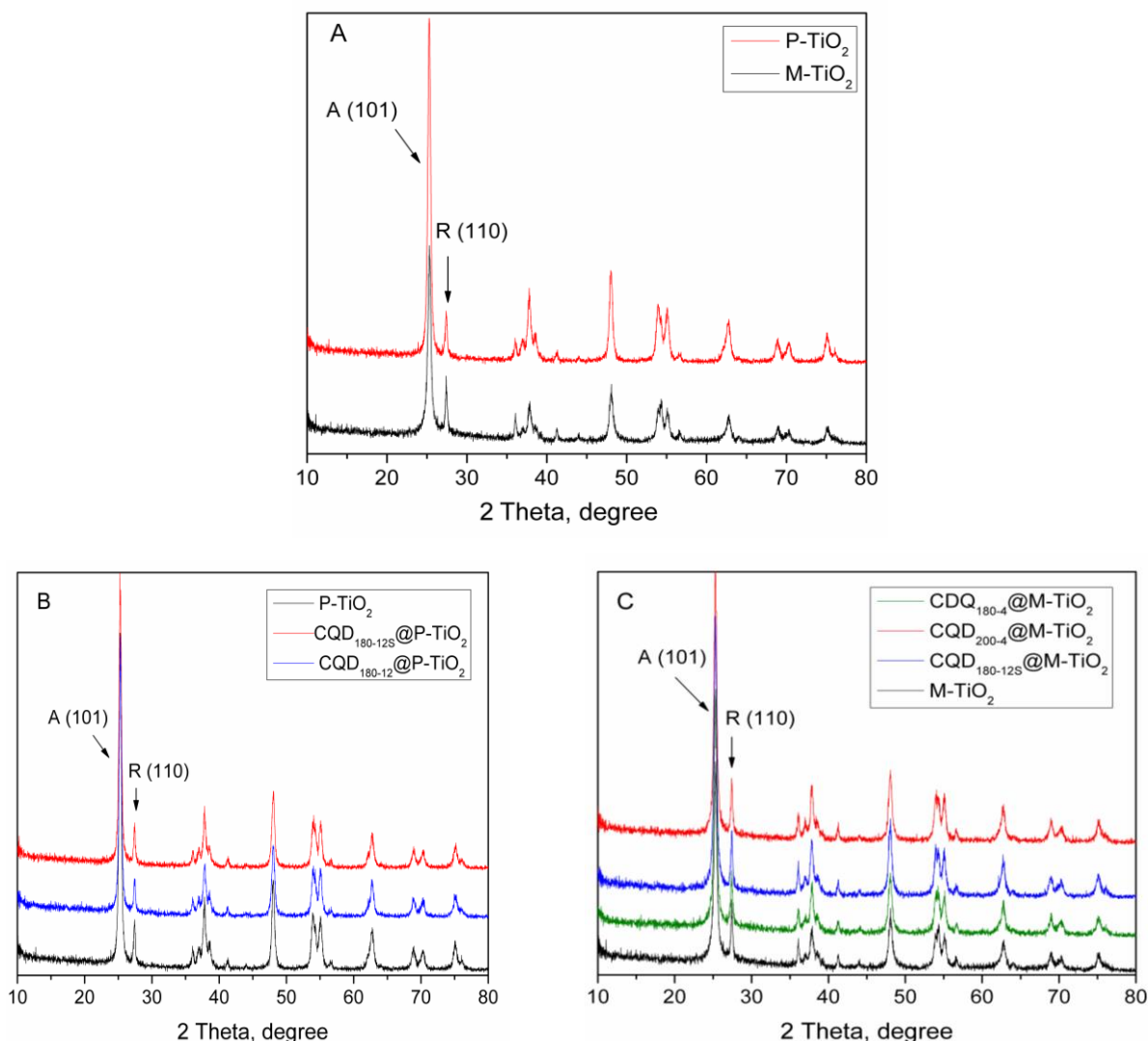
Based on the above results it can be stated that the CQDs structure retains the spherical core-shell morphology of the humins raw materials. However, both the core and shell have different structures as a function of the hydrothermal reaction conditions. Therefore, for a high temperature and a short reaction time CQDs with a graphite-like structure of the core and a shell which had more epoxy and ether groups along hydroxyl groups (CQD₂₀₀₋₄) are obtained while for lower temperature and a longer reaction time CQDs with an amorphous structure of the core and a shell which contained more carboxyl acids along hydroxyl groups (CQD₁₈₀₋₁₂). However, the difference in the core size is not high enough both kinds of CQDs emitting in blue light. A general schematic illustration of the spherical core-shell morphology of CQDs obtained in this work is given in Scheme 2.



Scheme 2. Schematic illustration of the spherical core-shell morphology of CQDs obtained by hydrothermal treatment of humins

3.2 Characterization of CQD@TiO₂ nanocomposites

The XRD patterns of P-TiO₂, M-TiO₂ and CQDs@TiO₂ are given in Figures 13A, B and C. The lines at 25.3°, 37.8°, 48.1°, 54.0°, and 62.7° are attributed to (101), (004), (200), (105), and (204) crystal planes of anatase TiO₂ (JCPDS card 21-1272) [46], while the lines at 27.4°, 35.9, 54.9 and 68.8° are attributed to (110), (101), (211) and (301) reflection of rutile TiO₂, respectively (Figure 13A) [47]. No diffraction lines at 29.8 and 44.4°, corresponding to those of brookite TiO₂ phase (JCPDS 74-1940) were identified [48].



Figures 13. XRD patterns of P-TiO₂ and M-TiO₂ carriers (A), CQD@P-TiO₂ (B) and CQD@M-TiO₂ (C) samples

Lines at $2\theta = 25.30^\circ$ and 27.40° (indicated with arrows in Figures 13A-C) are often taken as the characteristic lines of anatase (101) and rutile (110) crystal phase, respectively [49]. The mass percentage of anatase and rutile phases in the TiO₂-based materials is estimated from the respective integrated characteristic XRD lines intensities [50]:

$$Anatase (\%) = \frac{100}{1 + 1.265 \frac{I_R}{I_A}} \quad Rutile (\%) = 100 - Anatase (\%)$$

where I_R and I_A represent the lines intensities of (101) and (110) reflections for anatase and rutile, respectively; 1.265 represent the quality factor ratio of anatase to rutile.

The average size of crystallites was determined from using the reflection (101) of anatase and the Debye-Scherrer equation [49]:

$$d = \frac{k\lambda}{\beta \cos \theta}$$

where d is the crystallite size in nm; $k = 0.94$; λ is the wavelength of the X-ray (1.54178 Å); θ is the half-diffraction angle and β is the full width at half-maximum (FWHM) in radians for the 2θ value (25.3°).

As Figure 13A shows, the rutile content in the M-TiO₂ increased at the cost of anatase phase. Therefore, if P-TiO₂ sample is composed of 84.5% anatase TiO₂ and 15.5% rutile TiO₂, the M-TiO₂ is composed of 72% anatase and 28% rutile TiO₂.

However, the CQDs@TiO₂ samples exhibit identical patterns with the corresponding TiO₂ carrier (i.e., P-TiO₂ or M-TiO₂) without diffraction lines shifting. This demonstrates that the crystal structure of TiO₂ was not modified by the CQDs (Figures 13B and 13C). In other words, the CQDs were just well deposited on the surface of the TiO₂ and not incorporated into its lattice [50]. Moreover, the XRD patterns of the CQD@TiO₂ samples (Figures 13B and C) did not evidence diffraction lines characteristic to CQDs, indicating their small loading weight, poor crystallinity, small size and/or their high dispersion in the CQD@TiO₂ composites [51]. The average crystallite sizes, calculated with Debye-Scherrer equation, slightly vary in the range of 18.3 (M-TiO₂) - 20.0 (P-TiO₂) nm with CQD@TiO₂ inside these limits, indicating that such composites powders are made up of nanocrystalline particles.

The presence of CQDs in the CQD@TiO₂ nanocomposites was confirmed by the elemental analysis (Table 3) and TG-DTA analysis (Figure 14).

As Table 3 shows, the contents of C and H, derived from CQDs, varies in ranges of 1.1-4.2% and 0.3-1.3%, respectively, indicating different weight loadings of CQDs on the titania carrier.

Table 3. The C and H content in CQD@TiO₂ determined by elemental analysis

Sample	CQD ₁₈₀₋₄ @M-TiO ₂	CQD _{180-12S} @M-TiO ₂	CQD ₂₀₀₋₄ @M-TiO ₂	CQD _{180-12S} @P-TiO ₂	CQD ₁₈₀₋₁₂ @P-TiO ₂
C (%)	4.162	2.564	2.111	2.188	1.065
H (%)	1.329	0.878	1.127	0.638	0.334

The thermogravimetric/differential thermic analysis (TG/DTA) also confirms the successful deposition of the CQDs. In Figure 14 the TG/DTA profiles for CQD₁₈₀₋₄@M-TiO₂

and CQD₂₀₀₋₄@M-TiO₂ sample are given for exemplification, together with the TG/DTA profiles of M-TiO₂ and humins, for comparison

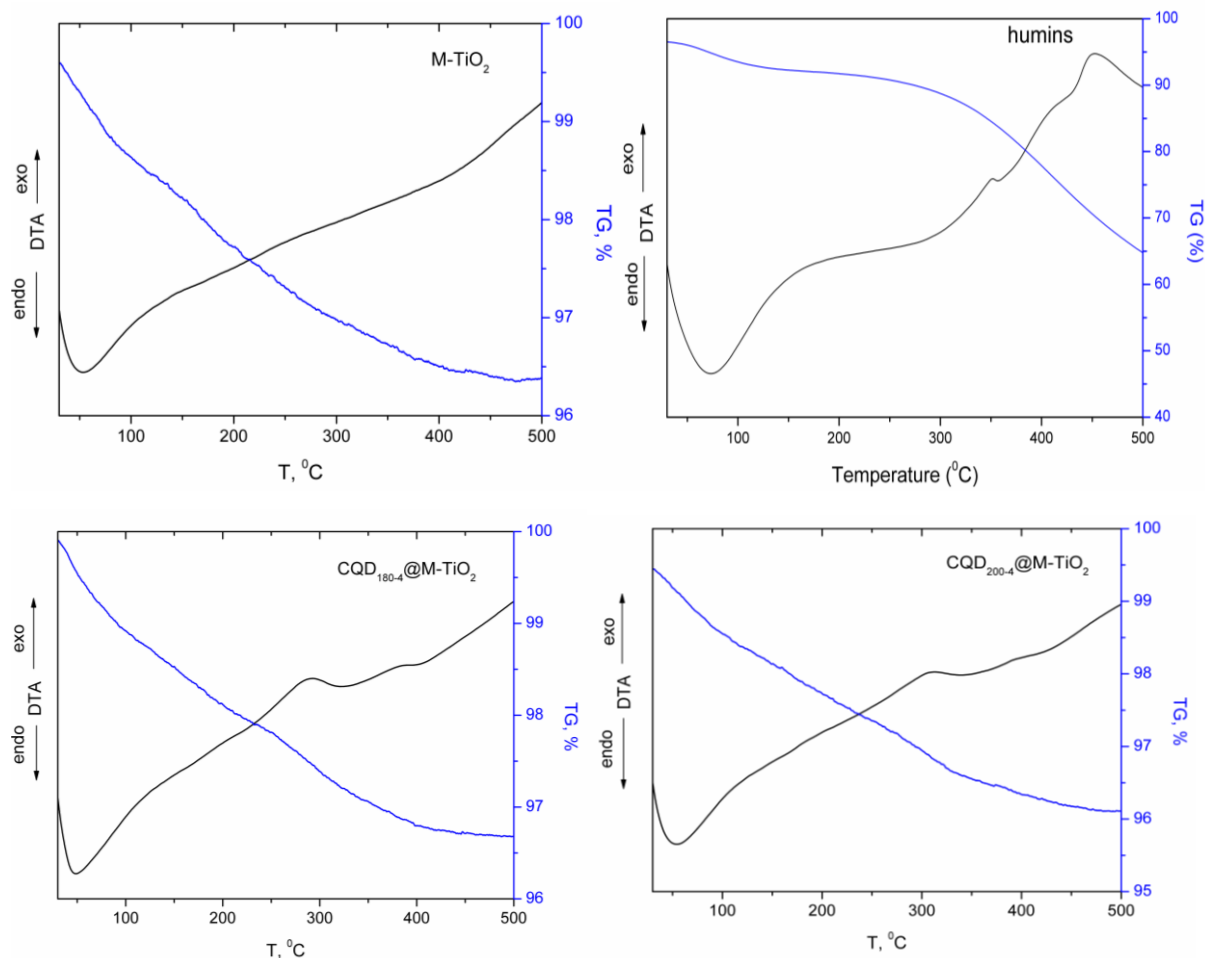


Figure 14. TG-DTA profiles of M-TiO₂, humins, CQD₁₈₀₋₄@M-TiO₂ and CQD₂₀₀₋₄@M-TiO₂ samples

As Figure 14 shows the DTA profile of all samples showed an endothermic effect at around 50-60°C, that is associated to a weight loss assigned to physically adsorbing water. However, in the case of CQD@TiO₂ samples other two exothermic effects, with maxima at 300 and 385°C, respectively (CQD₁₈₀₋₄@M-TiO₂ sample) and at 310 and 400°C, respectively (CQD₂₀₀₋₄@M-TiO₂ sample) are observed. Even if the loss weight cannot be quantitatively appreciated, the presence of these effects can be attributed to different decomposition processes which take place at high temperature, such as dehydroxylation, decarboxylation, and decarbonylation, indicating the presence of CQDs in CQD@M-TiO₂ samples. Such processes lead to the formation of a relative stable polycyclic aromatic structure, in accordance to previous literature reports [30].

The structural modifications in the M-TiO₂ sample were evidenced by TEM analysis (Figure 16). For comparison, the TEM images for the P-TiO₂ sample, with a similar magnification, are also presented in Figure 15.

TEM images of the P-TiO₂ powder (Figure 15) reveals lattice fringes of anatase and rutile stacked in the direction (101) and (110), respectively, indicating that the anatase and rutile particles exist separately, but in close proximity, by forming their agglomerates [25]. Also, the coexistence of (101) plane of anatase and (110) plane of rutile indicates the formation of mixed-phase TiO₂-based junctions. The combination of the anatase and rutile phases of P-TiO₂ exhibits higher photocatalytic performance in the decomposition of various organic pollutants than that of pure anatase or rutile phase due to the transfer of electrons from rutile to anatase TiO₂ across the junction interface, which inhibits the charge recombination of anatase, leading to more efficient separation of the photogenerated electron–hole pairs and greater photocatalytic activity [52]. However, photocatalytic activity of P-TiO₂ is still restricted by the small specific surface area and limited surface reaction sites [25].

When P-TiO₂ was hydrothermal treated with concentrated aqueous NaOH solution, followed by washing with HCl and subsequent calcination at 450°C, unexpected nanoparticle/nanotube hybrid nanostructures were obtained, as TEM image shows (Figure 16). During the hydrothermal treatment of the P-TiO₂ sample with aqueous NaOH solution some Ti-O bonds of the TiO₂ precursor are broken, leading to the formation of lamellar fragments, with a two-dimensional layered structure, that are the intermediate phase in the formation process of the nanotube material [31; 32]. However, while some studies showed that the condition of the post-treatment washing affected the formation, crystalline structure, or even chemical composition of the final products [53], some other studies claimed that nanotubes were formed during the NaOH treatment, and that the acidic post-treatment was not essential in their synthesis [54]. Moreover, a comparison of the microstructures between the products with and without a post-treatment with HCl indicated that the acidic treatment did not enhance the formation of the nanotubes, but introduced many defects on the nanotubes instead [55].

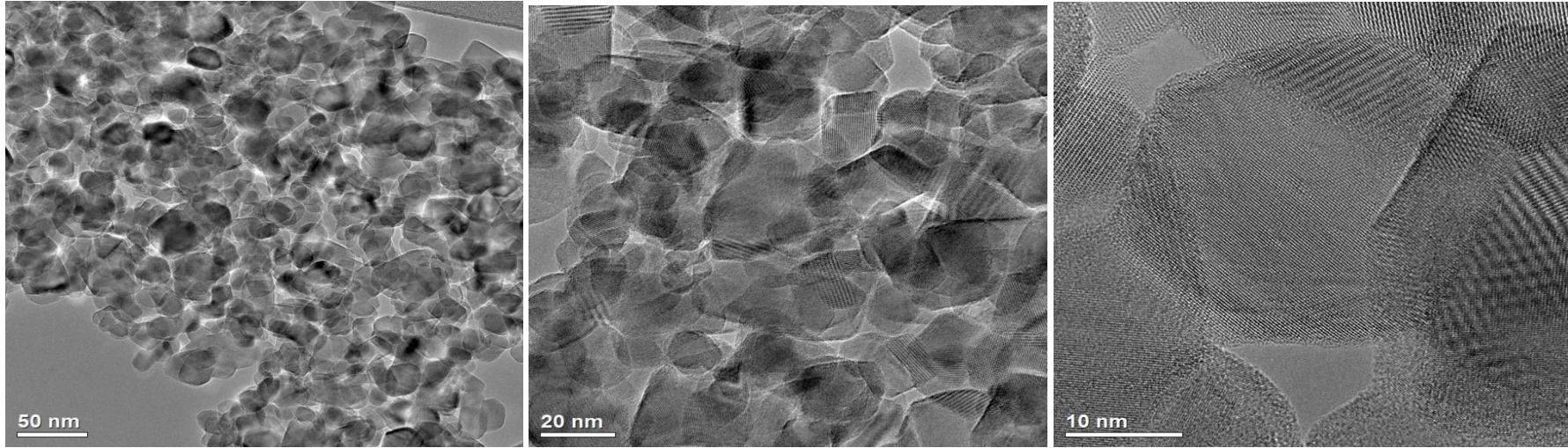


Figure 15. TEM images of P-TiO₂ sample

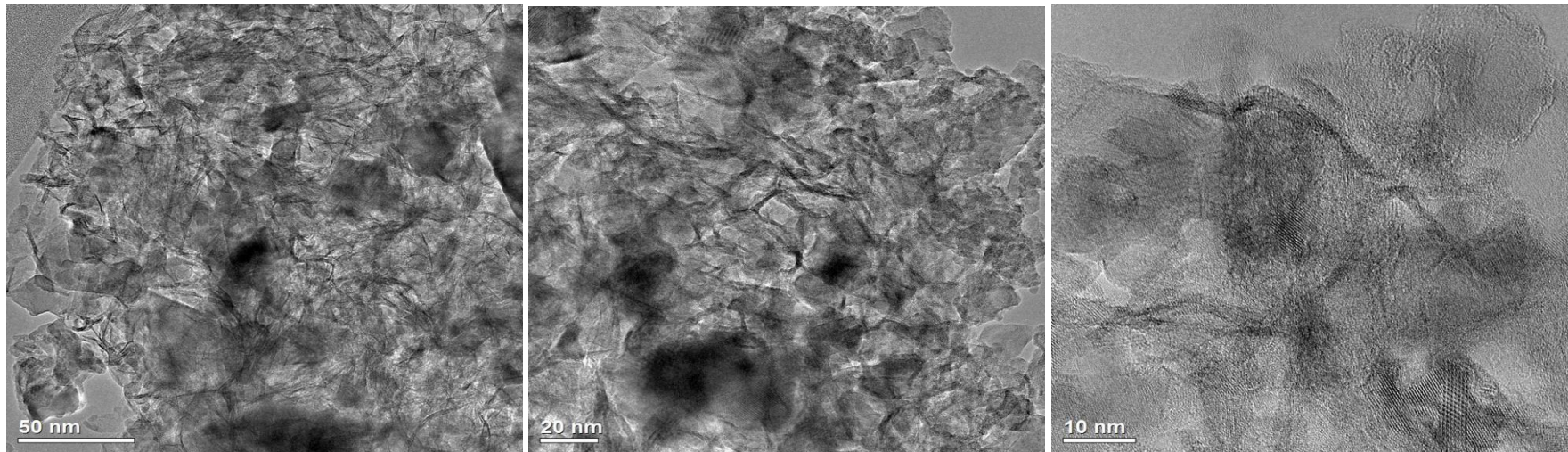


Figure 16. TEM images of M-TiO₂ sample

Considering the crystalline characteristics of anatase ($a = b \cong 3.78 \text{ \AA}$; $c \cong 9.52 \text{ \AA}$) and rutile ($a = b \cong 4.59 \text{ \AA}$; $c \cong 2:95 \text{ \AA}$) phase, Seok et al [56] deduced that anatase (with longer c axis) rather than rutile one is preferred to form the nanotube. Also, theoretical studies [57] suggested that the surface energy of anatase TiO_2 macroscopic crystal is smaller than that of rutile phase. This can also explain the fact that TiO_2 nanotubes are preferred to have the anatase structure. These findings are consistent with the increased diffraction line intensity of rutile TiO_2 in the XRD measurements (Figure 13A). Also, according with the TEM image of M- TiO_2 (Figure 16), TiO_2 -based heterophase junction, with three mixed phases of anatase and rutile nanoparticles but also anatase nanotubes has been successfully prepared. The existence of these phases and their intimate contact is considered to facilitate interfacial charge transfer in a higher degree than P- TiO_2 . Moreover, the acidic post-treatment and the subsequent heat-treatment procedure will generate oxygen vacancies in the mixed-phase junctions enhancing the adsorption and uniform dispersion of the reactant in photocatalytic degradation of dyes. Due to the enhanced charge separation around heterophase interfaces and the decreased charge transfer resistance, as-synthesized oxygen-deficient heterophase junctions should also exhibit significantly improved activity for photocatalytic degradations.

The morphology of different samples was studied by STEM-EDS analysis. As shown in Figures 15 and 16, in P- TiO_2 (Figure 15) a large number of nanoparticles with the diameter in a range of 27-30 nm are observed, while M- TiO_2 (Figure 16) are composed of 1-D nanostructures, which are further self-assembled into a 3D fibrous network with adhered nanoparticles to the surface. Moreover, individual CQDs, with spherical-like shape nanoparticles and the diameter of 2-8 nm, can be observed on the surface of TiO_2 . Obtained results confirm the different CQDs sizes as a function of the hydrothermal parameters (i.e., temperature and reaction time). Therefore, CQDs synthesized at 180°C and 12 h, possess a mainly size of 2 nm (Figure 17), while CQDs synthesized at 200°C and 4 h possess a main size of around 8 nm (Figure 18). Also, very important, their size is mainly homogenous, in agree with the PL results.

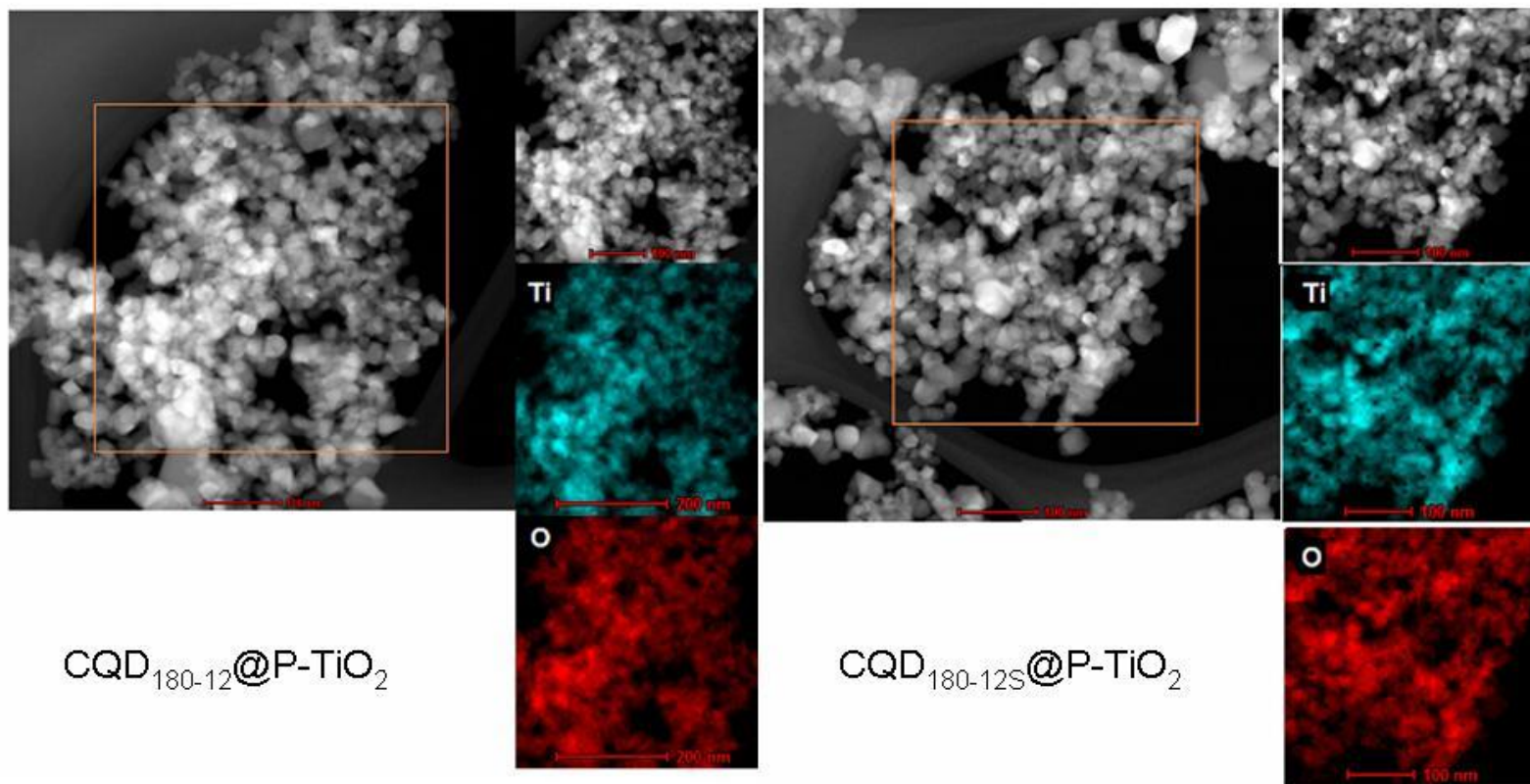


Figure 17. STEM images of CQD@P-TiO₂ samples

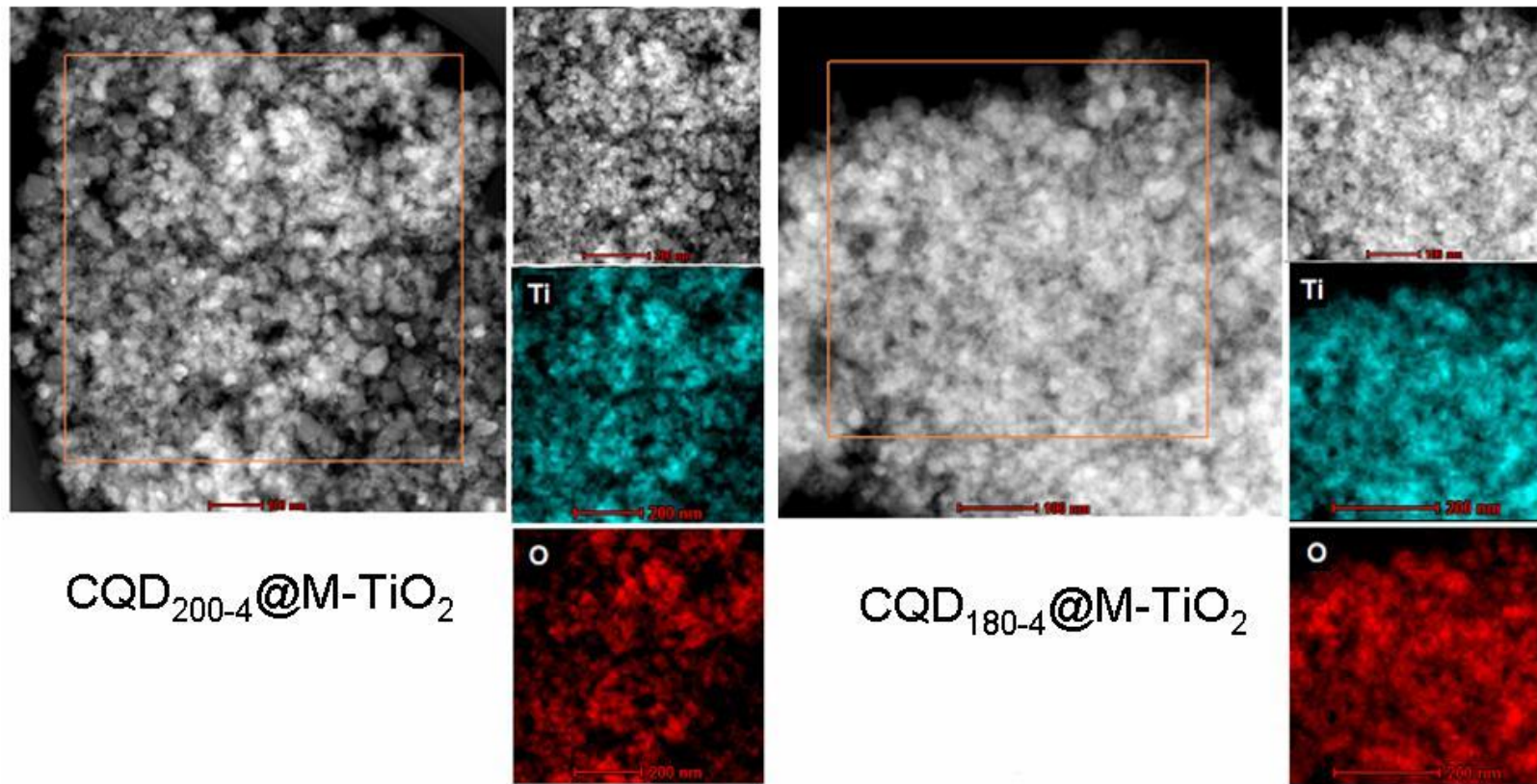


Figure 18. STEM images of CQD@M-TiO₂ sample

To discuss the chemical nature of the interaction between CQDs and titania carriers, CQDs@TiO₂ samples were further investigated by IR spectroscopy and obtained spectra were compared with titania carrier spectrum (Figure 19).

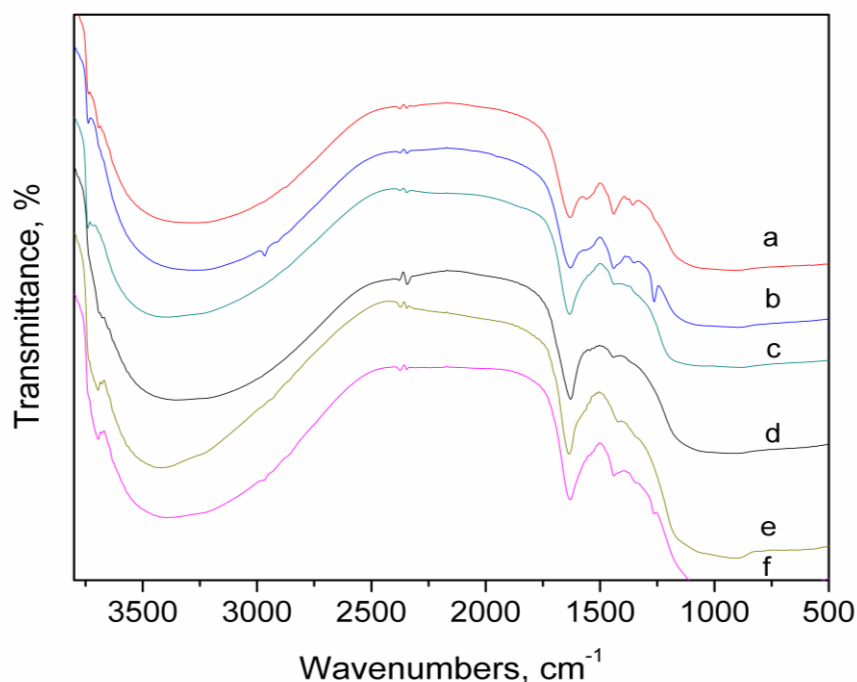
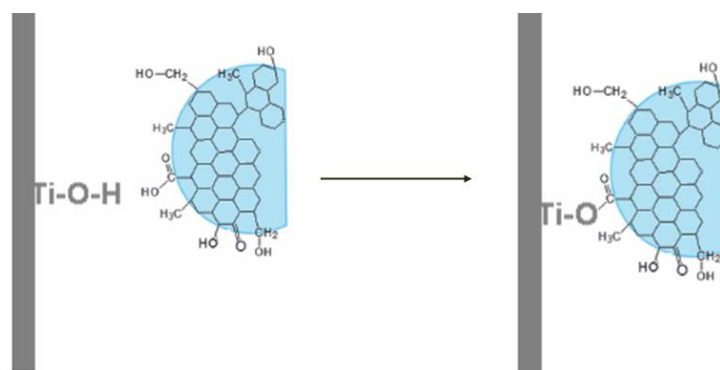


Figure 19. FT-IR spectra of the M-TiO₂ and CQD@TiO₂ nanocomposites: a. CQD_{180-12S}@M-TiO₂; b. CQD₂₀₀₋₄@M-TiO₂; c. CQD₁₈₀₋₄@M-TiO₂; d. M-TiO₂; e. CQD₁₈₀₋₁₂@P-TiO₂; f. CQD_{180-12S}@P-TiO₂

The absorption bands at 3380 cm⁻¹ are ascribed to the stretching vibration of the Ti-OH groups on the out-surface of the TiO₂ [58] which can capture the photoexcited electrons and holes to produce the reactive oxygen species in the photocatalytic process [59]. However, new distinct peaks at 3690 and 3740 cm⁻¹ are evidenced after the decoration of TiO₂ with CQDs, which most probably belongs to CQDs.

The peak at 1620 cm⁻¹ is corresponding to the surface adsorbed water molecules [60]. After surface modification with CQDs, the obvious change on the functional groups of TiO₂ was the appearance of two peaks at around 1380 cm⁻¹ and 1270 cm⁻¹. These peaks were conjectured to be -COOTi- group, which originated from the esterification between the carboxyl groups from CQDs and the hydroxyls groups from TiO₂ (Scheme 3) [61]. In addition, strong hydrogen bonds could form between the hydroxyl groups from the surface of CQDs and TiO₂. All these results confirm that the CQDs and TiO₂ have a good chemical connection, forming a heteroconjunction system which enables photoexcited charge carriers to transfer through the contact interface.



Scheme 3. Schematic representation of the esterification reaction between the carboxyl groups from CQDs and the hydroxyls groups from TiO_2

The Brunauer-Emmett-Teller (BET) surface area, pore volume, and pore size of the CQD@TiO_2 nanocomposites were determined by N_2 adsorption-desorption experiments. The isotherms are shown in Figure 20, while the insets show the Barrett-Joyner-Halenda (BJH) pore distribution.

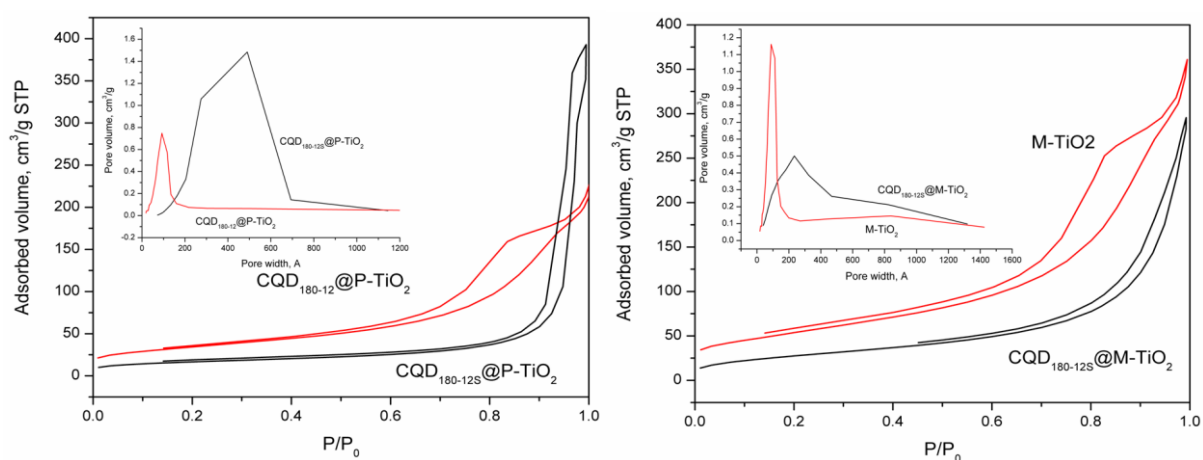


Figure 20. N_2 adsorption-desorption isotherms at 77 K for CQD@P-TiO_2 and CQD@ M-TiO_2 nanocomposites

The isotherm curves characteristic to samples presented in Figure 20 exhibit a distinct uptake of N_2 as a result of capillary condensation in a wide relative pressure (P/P_0) range of 0.5–1.0 (H3 type hysteresis loop), which suggested the existence of a mesoporous structure (2-50 nm). However, the high-pressure hysteresis loop ($0.8 < P/P_0 < 1.0$) characteristic for $\text{CQD}_{180-12\text{S}}@P\text{-TiO}_2$ is associated with the larger pores formed between secondary particles [42]. In the case of $\text{CQD}_{180-12\text{S}}@P\text{-TiO}_2$ there is also a bimodal pore size distribution

consisting of intra-aggregated pores with a maximum pore diameter of 27.1 nm and larger inter-aggregated pores with a maximum pore diameter of 49 nm (Table 4). According to Kumar et al. [62], the bimodal pore size distribution arose from the hard aggregated in the powders. In addition, there were two types of pores on the bimodal pore size distribution. One is the intra-aggregated pore (represented by the hysteresis loop in the lower P/P_0 range) and the other is the larger inter-aggregated pore (hysteresis loop in the higher P/P_0 range). For M-TiO₂ based samples (Figure 20, Table 4), the maximum pore sizes of the intra-aggregated pores shifted into larger mesopores regions (ca. 9.1 and 23.3 nm, respectively), indicating the growth of pores.

Table 4. BET surface areas, pore volumes and pore sizes of the CQD@TiO₂ nanocomposites

Entry	Sample	S_{BET} , m ² /g	V_p , cm ³ /g	D_p , nm
1	P-TiO ₂	54	0.31	19.7
2	CQD ₁₈₀₋₁₂ @P-TiO ₂	123	0.33	8.7
3	CQD _{180-12S} @P-TiO ₂	59	0.54	27.1 and 49.0
4	M-TiO ₂	194	0.56	9.1
5	CQD _{180-12S} @M-TiO ₂	203	0.45	23.3

As seen from Table 4 the BET surface areas of CQDs@P-TiO₂ (59 and 123 m²/g) are larger than that of pure P-TiO₂ (54 m²/g). The applied modification strategy of P-TiO₂ material also leads to an increased BET surface area of the obtained M-TiO₂ sample (194 m²/g) which further increased to 203 m²/g, as a result of the CQDs insertion (Table 4, entry 5, CQD_{180-12S}@M-TiO₂ sample). These modifications are obviously due to both the structural modifications of M-TiO₂ and the presence of CQDs. The nanoparticles/nanotubes heterophase junction obviously results in an increased surface area. Moreover, when coupling CQDs with TiO₂ nanospheres/nanotubes, the CQDs anchored on the surface of TiO₂ increases its surface roughness, resulting in the formation of a second interface between CQDs and TiO₂.

The wide application of titanate nanosheets [44] or titanate nanotubes [45] as photocatalysts is limited by the fact that their band gaps are wider (3.87 eV for titanate nanotubes and 3.84 eV for titanate nanosheets) than that of TiO₂ particles (3.2 eV). The high increase is attributed to the quantization of electronic states in these materials and the reduction of dimensionality from 3-D to 2D and/or 1D [45]. However, as we already showed, in this work generated high surface and defects (oxygen vacancy) in synthesized M-TiO₂ may play an important role in enhancing the photoactivity of heterophase conjunctions. Oxygen

vacancy can act as electron donor to improve the electron transfer in the heterostructured photocatalysts.

The photo-response ability of the of pristine P-TiO₂, M-TiO₂ and CQD@TiO₂ samples was measured by using UV-Vis spectrum. For the calculation of the band gap (E_g) values two different methods can be used: the method based on Tauc graphs (conversion of spectra into Kubelka Munk absorbance units) and the first order derivative method, applied to UV-VIS spectra, recorded in reflectance mode.

Tauc plots are obtained by representing the function:

$$f(h\nu) = (\alpha \cdot h\nu)^{1/n}$$

where: α - absorption coefficient; h - Planck' constant; ν - the inverse of the λ wavelength, and n - the coefficient corresponding to the transition mode (direct transition allowed $n = 1/2$; indirect transition allowed $n = 2$)

$$h\nu = \frac{1240}{\lambda}$$

The Kubelka-Munk transformation is applied by converting the reflectance into an absorption coefficient, according to the equation:

$$\alpha = \frac{(1 - R)^2}{2R}$$

From the linear extrapolation of the Tauc graphs, followed by the determination of the intersection points with the abscissa, the energy values of the band gap (E_g) are obtained [46].

It is well known that in the case of rutile, both direct ($n = 1/2$) and indirect ($n = 2$) transitions take place (E_g = 3.02 - 3.24 eV), while for anatase the electron transitions are indirect ($n = 2$) (E_g = 2.3 - 3.59 eV) [63] (Figure 22).

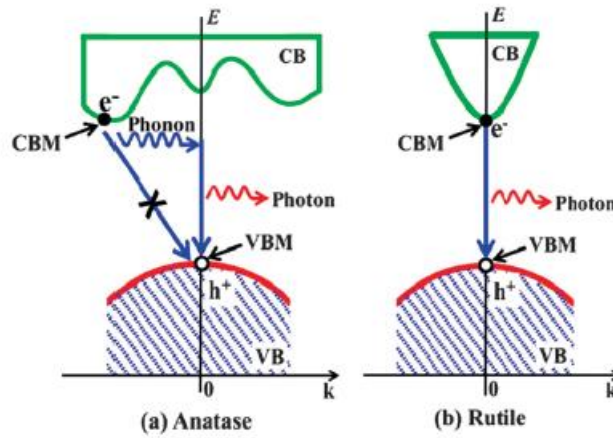


Figure 22. Comparison of recombination processes of photogenerated electrons and holes within indirect gap anatase (a) and direct gap rutile (b) (VBM - valence band maximum, CBM - conduction band minimum) [63]

The interpretation of Tauc plots becomes problematic in the case of photocatalysts consisting of several phases, such as P-TiO₂ and M-TiO₂. However, since TiO₂ is considered an indirect band gap semiconductor ($n = 2$), the E_g was estimated by the x-intercept of linear portion of Tauc's plot ($(\alpha h\nu)^{1/2}$ versus $h\nu$, at $\alpha = 0$). (Figures 23 and 24).

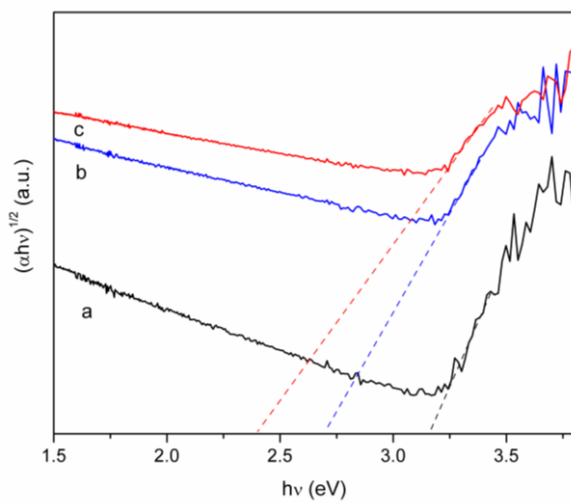


Figure 23. Plots of $(\alpha h\nu)^{1/2}$ vs. $h\nu$ for the P-TiO₂ (a), CQD₁₈₀₋₁₂@P-TiO₂ (b) and CQD_{180-12S}@P-TiO₂ (c) samples

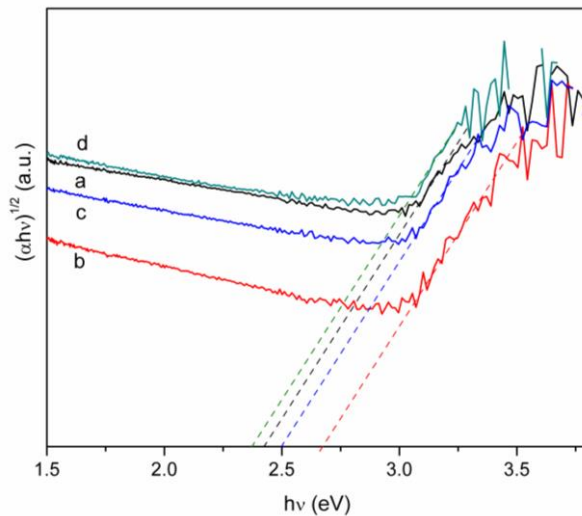


Figure 24. Plots of $(\alpha h\nu)^{1/2}$ vs. $h\nu$ for the M-TiO₂ (a), CQD₁₈₀₋₄@M-TiO₂ (b), CQD₂₀₀₋₄@M-TiO₂ (c) and CQD_{180-12S}@M-TiO₂ (d) samples

As Figures 23, 24 and Table 5 show that all determined band gap energies are smaller than that found for the original P-TiO₂ sample (3.15 eV).

Table 5. The E_g values obtained from Tauc plots

Sample	$E_g \pm 0.03$, eV
P-TiO₂	3.15
CQD₁₈₀₋₁₂@P-TiO₂	2.70
CQD_{180-12S}@P-TiO₂	2.40
M-TiO₂	2.42
CQD₁₈₀₋₄@M-TiO₂	2.68
CQD₂₀₀₋₄@M-TiO₂	2.50
CQD_{180-12S}@M-TiO₂	2.38

In the visible light range of 400 to 800 nm, anatase TiO₂ with a band gap of 3.2 eV shows no absorption, but the P-TiO₂ is a mixture of anatase TiO₂ which accounts for 84.5% and the rutile TiO₂ which accounts for 15.5% (according to the XRD analysis), thus the absorption edge expands from 387 nm to about 394 nm, with a band gap of 3.15 eV.

The M-TiO₂ sample shows a strong adsorption in the UV region with the adsorption edge at about 447 nm. Due to the high surface area and the formation of oxygen-deficient structure, bandgap energy of heterophase junction highly decreases from 3.15 (Figure 23) to 2.42 eV (Figure 24).

The band gaps of Titania materials also varied due to the CQDs presence. Therefore, in the series of P-TiO₂ based samples, the band gap decreases from 3.15 eV (P-TiO₂) to 2.70 eV (CQD₁₈₀₋₁₂@P-TiO₂) to 2.40 eV (CQD_{180-12S}@P-TiO₂), respectively (Figure 23, Table 5). Interesting enough, in the case of M-TiO₂ based samples, a comparison of the band gaps sizes clearly shows that except the CQD_{180-12S}@M-TiO₂ sample, which possess a lower band gap (2.38 eV), the CQD₁₈₀₋₄@M-TiO₂ and CQD₂₀₀₋₄@M-TiO₂ samples possess higher band gaps, i.e., 2.68 eV and 2.50 eV, respectively (Figure 25, Table 5). However, the differences are low. A schematically representation of these variations together with the % Carbon determined from elemental analysis is given in Figure 25.

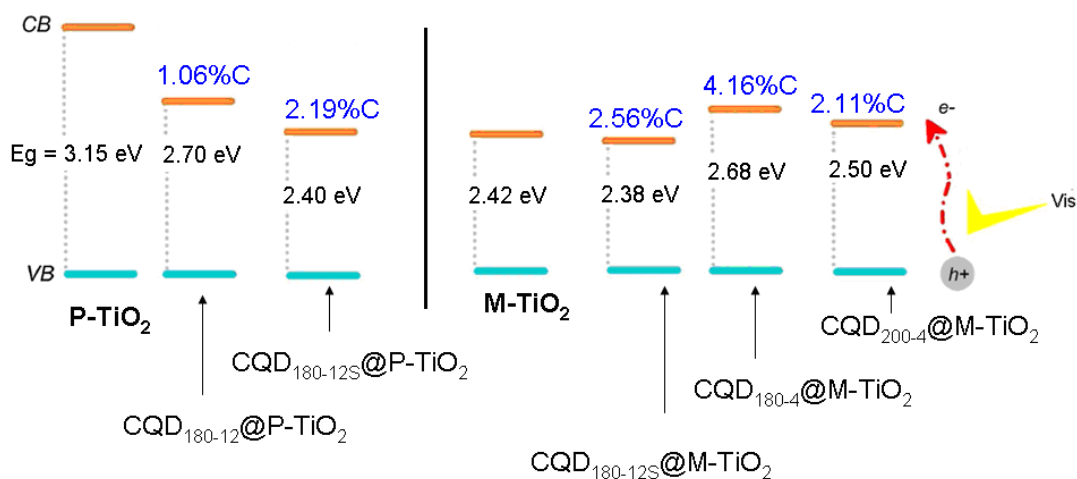


Figure 25. Schematic band diagram of the synthesized CQD@TiO₂ nanocomposites. Values in blue represent the % Carbon measured in elemental analysis.

In the case of the P-TiO₂ based samples there is a direct correlation between the CQDs content and the corresponding band gap size (Figure 25). Therefore, as the CQD content increased, the corresponding band gap decreased, which is expected to generate more photoelectron-hole pairs in the visible light region.

However, for M-TiO₂ based samples, there are only slightly modifications in the band gap size of the pristine M-TiO₂ and CQDs-based nanocomposites. For the moment we have any explanation for the increased E_g of CQD₁₈₀₋₄@M-TiO₂ sample.

4. Catalytic tests

Figure 26 shows the chemical structure of methylene blue and the photocatalytic reaction pathway. N-dealkylation of dyes containing auxochromic alkylamine groups plays an important role in photocatalytic degradation. The color of methylene blue solutions becomes weaker when part of the methyl groups degrade, and hypochromic shift occurs. Hence, N-demethylation (N(CH₃)₂, 666 nm) of MB occurs as described in the pathway at first, and finally phenothiazine ring (292 nm) degraded into H₂O, CO₂, and other inorganic molecules [64].

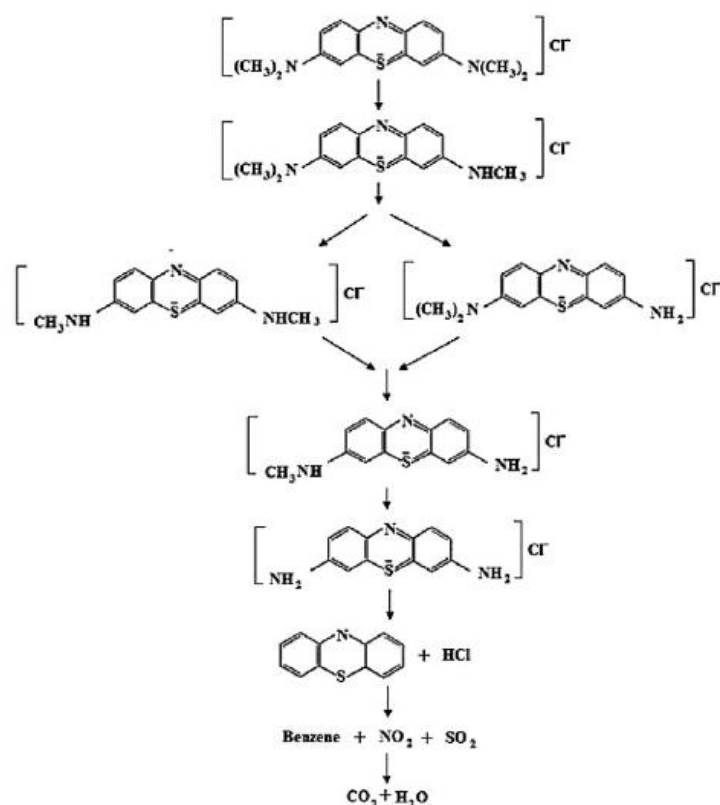


Figure 26. Chemical structure of MB and the photocatalytic reaction pathway [64]

For preliminary tests in the MB adsorption and photocatalytic degradation we have chosen two synthesized CQD-based materials with similar Carbon content and close E_g but different titania phase (P-TiO₂ and M-TiO₂), i.e. CQD_{180-12S}@P-TiO₂ and CQD₂₀₀₋₄@M-TiO₂. Obtained UV-vis spectra are shown in Figures 27-28.

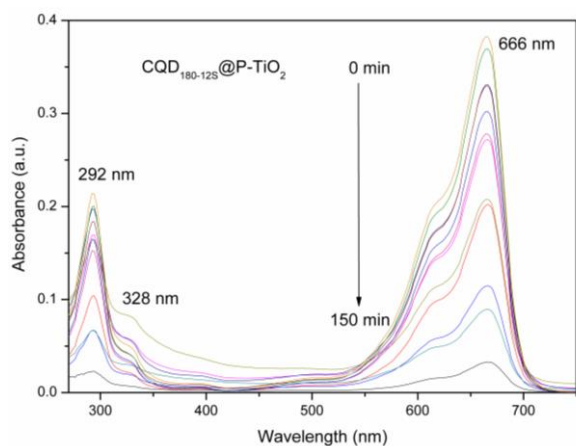


Figure 27. UV-Vis spectra of MB degradation versus reaction time in the presence of CQD_{180-12S}@P-TiO₂ (7.5 mg cat)

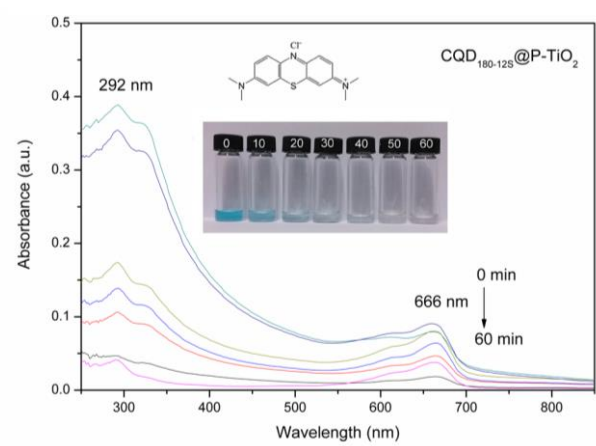


Figure 28. UV-Vis spectra of MB degradation versus reaction time in the presence of CQD_{180-12S}@P-TiO₂ (15 mg cat)

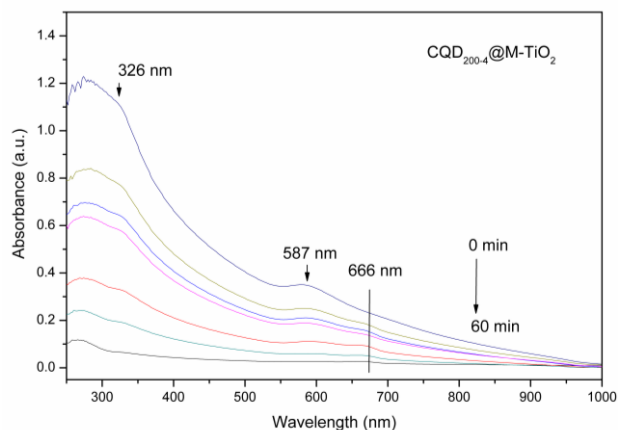


Figure 29. UV-Vis spectra of MB degradation versus reaction time in the presence of $CQD_{200-4}@M-TiO_2$ (15 mg cat)

As UV-vis spectra shows, the dimethylated groups (666 nm) are faster decomposed by comparing with phenothiazine ring (292 nm). Moreover, in the presence of the $CQD_{200-4}@M-TiO_2$ sample a new absorption peak appeared at 587 nm, which highly decreases in time.

The adsorption capacity of the P-TiO₂ sample is low but the presence of the CQDs highly improved it. Therefore, in the presence of the $CQD_{180-12S}@P-TiO_2$ sample the MB adsorption was 60.7%, which increased to 74.95% on doubled amount of catalyst (Figure 30). In the presence of the $CQD_{200-4}@M-TiO_2$ (15 mg) the MB adsorption value was 90.65%.

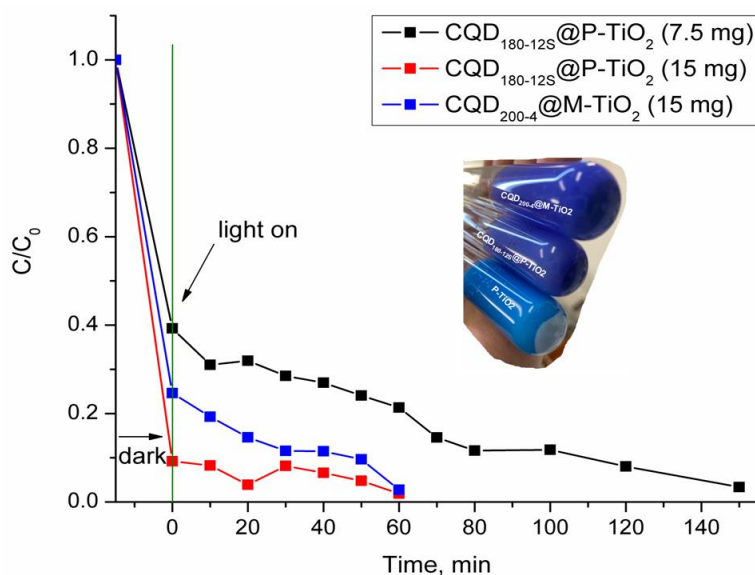


Figure 30. UV-Vis spectra of MB degradation (666 nm band) versus reaction time

High adsorption capacity of the samples can be associated with the presence of the acidic groups on the CQDs surface, making it easier to chemisorb the basic groups of MB.

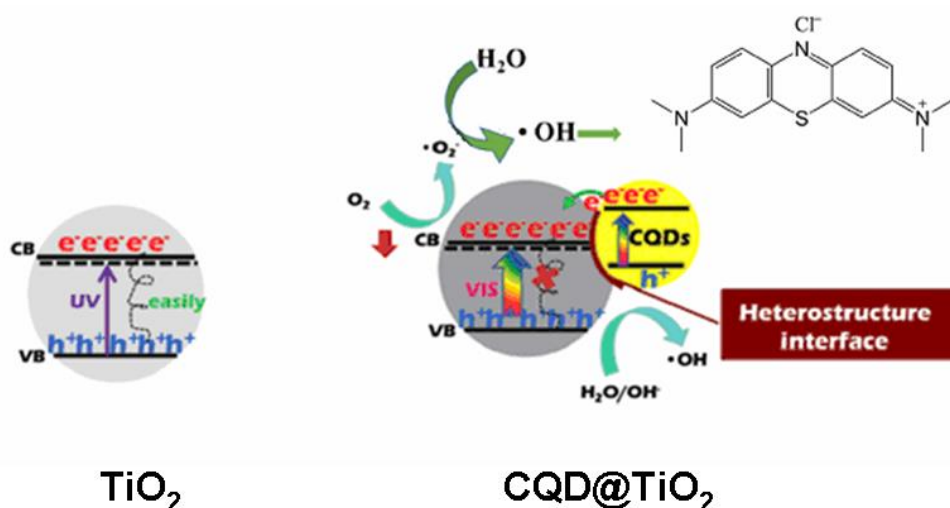
Furthermore, the absorbance of MB at 666 nm [$C_{Ar} = N(CH_3)_2$] and 292 nm (phenothiazine ring) change as the reaction progress, indicating a gradually degradation of MB, in agree with [65]. However, the level of the two entities degradation is slightly different, as a function of the reaction condition (i.e., catalyst amount, reaction time) as Table 6 shows.

Table 6. The decomposition level of the $N(CH_3)_2$ and phenothiazine ring moieties as a function of the catalyst nature, catalyst amount and illumination time

Catalyst	$N(CH_3)_2$ decomposition, %	Phenothiazine ring decomposition, %
CQD _{180-12S} @P-TiO ₂ (7.5 mg, 150 min)	96.7	97.0
CQD _{180-12S} @P-TiO ₂ (15 mg, 60 min)	97.3	93.4
CQD ₂₀₀₋₄ @M-TiO ₂ (15 mg, 60 min)	98.1	95.3

Clearly enough the photocatalytic conditions should be improved for a total mineralization of MB, more reaction conditions being necessary to be check. For the moment, we can only admit the high adsorption capacity of the generated CQD@TiO₂ heterostructures and the discoloration of MB.

In agree with literature [65] a possible mechanism for the photocatalytic degradation of MB in the CQD@TiO₂ system can be illustrated as in Scheme 4, which includes the following three features: i) the CQDs act as a photosensitizer to enlarge the absorption range of TiO₂ into the visible light region through electronic coupling between π states of CQDs and conduction band (CB) states of TiO₂, leading to transfer of excited electrons from CQDs to the CB of TiO₂; ii) the electrons in the CB of TiO₂ react with O₂ to form $\cdot O_2^-$ and H₂O/OH is oxidized by holes at the surface of TiO₂ to produce $\cdot OH$ radicals. Meanwhile, the CQDs act as an electron reservoir to trap photogenerated electrons from TiO₂ and promote separation of photogenerated electron-hole pairs; iii) the $\cdot OH$ radicals react with MB and degrade it to phenothiazine rings by demethylation. The phenothiazine rings are broken down to aniline, phenol, and other intermediate aromatic ring species, which are further degraded into H₂O, CO₂, NH₄⁺, HCOO⁻, and SO₄²⁺ as the final products.



Scheme 4. Proposed mechanism in the CQDs/TiO₂ heterostructure nanocomposites by adapted illustration from [65].

5. Conclusions

A facile method for the preparation of photo-luminescent CQDs based on a hydrothermal carbonization process is presented in this work using humins as the carbon precursor. The method has the advantage of being considerably cheaper than conventional methods and absolutely “green”.

The as-prepared CQDs possess different structures and size of the carbon core, but also different composition in the shell, as a function of the hydrothermal synthesis parameters. The best CQDs in view of their size, PL properties and QY were obtained at 180C and 12h (CQD₁₈₀₋₁₂) or at 200C and 4h (CQD₂₀₀₋₄). Also important, the produced CQDs were readily soluble in water to form a stable, yellowish, and transparent aqueous solution without precipitation for months.

When coupling CQDs with TiO₂, the CQDs anchored on the surface of TiO₂ increases its surface roughness, resulting in the formation of a heterointerface between CQDs and TiO₂ carrier. The CQDs play an important role in the visible light photocatalytic process, as preliminary results obtained in the methylene blue degradation shows. First of all, the electrons photogenerated from the TiO₂ can be trapped by the CQDs and retard the recombination of photoexcited electron-hole pairs. What’s more, these heterostructure formed between the CQDs and the TiO₂ can greatly prolong the life of the photoexcited electron and hole pairs.

So, this work is of great interest to introduce a new and high efficiency way to fabricate visible-light heterophases photocatalysts by using cheap inorganic oxide materials and useless humins waste generated in saccharides dehydration.

Acknowledgements

This work was financially supported by The Education, Scholarship, Apprenticeships and Youth Entrepreneurship Programmer—EEA Grants 2014-2021, Project No. 18-Cop-0041.

Authors are grateful to Prof. Joanna Gościańska from Department of Chemical Technology, Faculty of Chemistry, Adam Mickiewicz University, in Poznań, Poland for performing TEM and STEM measurements.

DISEMINATION

Experimental data obtained in this work are the subject of an abstract with the title "From humins wastes to carbon quantum dots (CQDs) based photocatalytic nanocomposites", authors: Nicolae Cristian Guzo, Magdi El Fergani, Bogdan Cojocar, Joanna Gościańska, Vasile I. Parvulescu, Simona M. Coman, submitted to the International Workshop "Contemporary solutions for advanced materials with high impact on society (CoSoIMat)", 11-15 October 2021, Bucharest, Romania

References

- [1] Coman, S. M., Tudorache, M., Parvulescu, V. I., Chapter 4: Green catalysis methods - Catalysis for lignocellulosic biomass capitalization into chemicals, In: „An introduction to green chemistry methods’, R. Luque, J. C. Colmenares (Eds.), Future Science Ltd, London, UK, 2013, pp. 54-68.
- [2] Sudarsanam, P., Zhong, R., Van den Bosch, S., Coman, S. M., Parvulescu, V. I., Sels B. F., Functionalised heterogeneous catalysts for sustainable biomass valorisation. *Chem. Soc. Rev.*, 47, (2018), 8349:8e402.
- [3] Saratale, G. D., Oh, S. E., Lignocellulosics to ethanol: The future of the chemical and energy industry. *Afr. J. Of Biotechnol.*, 11, (2012), 1002:1013.
- [4] Rinaldi, R., Jastrzebski, R., Clough, M. T., Ralph, J., Kennema, M., Bruijninx P. C. A., Weckhuysen. B. M., Paving the way for lignin valorisation: recent advances in bioengineering, biorefining and catalysis. *Angew. Chem., Int. Ed.*, 55, (2016), 8164:8215.
- [5] Clark, J., Deswarte, F., Introduction to chemicals for biomass. Second edition, John Wiley & Sons Ltd., 2015, Chapter 1. The biorefinery concept: An integrated approach, pgs. 1-31.
- [6] Serrano-Ruiz, J. C., Luque, R., Sepúlveda-Escribano, A., Transformations of biomass-derived platform molecules: from high added-value chemicals to fuels via aqueous-phase processing. *Soc. Rev.*, 40, (2011), 5266:5281.
- [7] Mija, A., van der Waal, J. C., Pin, J.-M., Guigo, N., de Jong, E., Humins as promising materials for producing sustainable carbohydrate-derived building materials. *Construction and Building Materials*, 139, (2017), 594:601.
- [8] Sevilla, M.; Fuertes, A.B., The production of carbon materials by hydrothermal carbonization of cellulose *Carbon*, 47, (2009), 2281:2289.
- [9] Mija, A., van der Waal, J. C., Pin, J.-M., Guigo, N., de Jong, E., Humins as promising material for producing sustainable polysaccharide-derived building materials., *Proceedings of the First International Conference on Bio-based Building Materials*, 22-24/06/2015 Clermont-Ferrand, France, 1:6.
- [10] van Zandvoort, I., Wang, Y., Rasrendra C.B., van Eck, E.R.H., Bruijninx, P.C.A., Heeres, H.J., Weckhuysen., B.M., Formation, Molecular Structure, and Morphology of Humins in Biomass Conversion: Influence of Feedstock and Processing Conditions. *ChemSusChem*, 6, (2013), 1745:1758.

- [11] Hoang, T.M.C., Lefferts, L., Seshan, K., Valorization of Humic-Based Byproducts from Biomass Processing – A Route to Sustainable Hydrogen. *ChemSusChem*, 6, (2013), 1651:1658.
- [12] Xu, X., Ray, R., Gu, Y., Ploehn, H. J., Gearheart, L., Raker, K., Scrivens, W. A., Electrophoretic Analysis and Purification of Fluorescent Single-Walled Carbon Nanotube Fragments. *J. Am. Chem. Soc.*, 126, (2004), 12736:12737.
- [13] Sun, Y.-P., Zhou, B., Lin, Y., Wang, W., Fernando, K. S., Pathak, P., Mezziani, M. J., Harruff, B. A., Wang, X., Wang, H., Quantum-sized carbon dots for bright and colorful photoluminescence. *J. Am. Chem. Soc.*, 128, (2006), 7756:7757.
- [14] Baker, S. N., Baker, G. A., Luminescent Carbon Nanodots: Emergent Nanolights. *Angew. Chem., Int. Ed.*, 49, (2010), 6726:6744.
- [15] Wang, Y., Hu, A., Carbon quantum dots: synthesis, properties and applications. *J. Mater. Chem. C*, 2, (2014), 6921:6939.
- [16] Wang, R., Lu, K.-Q., Tang, Z.-R., Xu, Y.-J., Recent progress in carbon quantum dots: synthesis, properties and applications in photocatalysis. *J. Mater. Chem. A*, 5, (2017), 3717:3734.
- [17] Li, H. T., Liu, R. H., Lian, S. Y., Liu, Y., Huang, H., Kang, Z.H., Near-infrared light controlled photocatalytic activity of carbon quantum dots for highly selective oxidation reaction *Nanoscale*, 5, (2013), 3239:3257.
- [18] Liu, J., Zhu, W., Yu, S., Yan, X., Three dimensional carbogenic dots/TiO₂ nanoheterojunctions with enhanced visible light-driven photocatalytic activity. *Carbon*, 79, (2014) 369:379.
- [19] Ohno, T., Sarukawa, K., Tokieda, K., Matsumura, M., Morphology of a TiO₂ Photocatalyst (Degussa, P-25) Consisting of Anatase and Rutile Crystalline Phases. *J Catal.*, 203, (2001), 82:86.
- [20] Hoffmann, M.R., Martin, S.T., Choi, W., Bahnemann, D.W., Environmental Applications of Semiconductor Photocatalysis. *Chem. Rev.* 95, (1995), 69:96.
- [21] Alvaro, M., Aprile, C., Benitez, M., Carbonell, E., Garcia, H., Photocatalytic Activity of Structured Mesoporous TiO₂ Materials. *J. Phys. Chem. B* 110, (2006), 6661:6665.
- [22] Tian, G.H., Fu, H.G., Jing, L.Q., Xin, B.F., Pan, K., Preparation and Characterization of Stable Biphasic TiO₂ Photocatalyst with High Crystallinity, Large Surface Area, Enhanced Photoactivity. *J. Phys. Chem. C* 112, (2008), 3083:3089.

- [23] Kang, C.H., Jing, L.Q., Guo, T., Cui, H.C., Zhou, J., Fu, H.G., Mesoporous SiO₂-Modified Nanocrystalline TiO₂ with High Anatase Thermal Stability and Large Surface Area as Efficient Photocatalyst. *J. Phys. Chem. C* 113, (2009), 1006:1013.
- [24] Janus, M., Morawski, A.W., New method of improving photocatalytic activity of commercial Degussa P25 for azo dyes decomposition. *Appl. Catal. B* 75, (2007), 118:123.
- [25] Yu, J.C., Lin, J., Lo, D., Lam, S.K., Influence of Thermal Treatment on the Adsorption of Oxygen and Photocatalytic Activity of TiO₂. *Langmuir* 16, (2000), 7304:7308.
- [26] Murgolo, S., Petronella, F., Ciannarella, R., Comparelli, R., Agostiano, A., Curri, M.L., Mascolo, G., UV and solar-based photocatalytic degradation of organic pollutants by nano-sized TiO₂ grown on carbon nanotubes. *Catal. Today*, 240, (2015), 114:124.
- [27] Zhang, Z. P., Zhang, J., Chen, N., Qu, L. T., Graphenequantum dots: an emerging material for energy-related applications and beyond. *Energy and Environ. Sci.*, 5, (2012), 8869:8890.
- [28] Wang, X., Cao, L., Lu, F. S., Mezziani, M. J., Li, H. T., Qi, G., Zhou, B., Harruff, B. A., Kermarrec, F., Sun, Y. P., Photoinduced electron transfers with carbon dots. *Chem. Commun.*, 2009, 3774:3776.
- [29] Yao, Y., Li, G. H., Ciston, S., Lueptow, R. M., Gray, K. A., Photoreactive TiO₂/carbon nanotube composites: synthesis and reactivity. *Environ. Sci. Technol.*, 42, (2008), 4952:4957.
- [30] El Fergani, M., Candu, N., Tudorache, M., Bucur, C., Djelal, N., Granger, P., Coman, S. M., From useless humins by-product to Nb@ graphite-like carbon catalysts highly efficient in HMF synthesis. *Appl. Catal. A: General*, 618, (2021) 118:130.
- [31] Prasannan, A. Imae, T., One-Pot Synthesis of Fluorescent Carbon Dots from Orange Waste Peels. *Ind. Eng. Chem. Res.*, 52, (2013), 15673:15678.
- [32] Yu, H., Zhao, Y., Zhou, C., Shang, L., Peng, Y., Cao, Y., Wu, L.-Z., Tunga, C.-H., Zhang, T., Carbon quantum dots/TiO₂ composites for efficient photocatalytic hydrogen evolution. *J. Mater. Chem. A*, 2, (2014), 3344:3351.
- [33] Galanin, M. D., Kut'enkov, A. A., Smorchkov, V. N., Timofeev, Y. P., Chizhikov, Z. A., *Opt. Spektrosk.* 53, (1982), 683:690.
- [34] Chen X., Zhang W., Wang Q., Fan J., C₈-structured carbon quantum dots: Synthesis, blue and green double luminescence, and origins of surface defects. *Carbon*, 79, (2014), 165:173.
- [35] Peng, H., Sejdic, J. T., Simple Aqueous Solution Route to Luminescent Carbogenic Dots from Carbohydrates. *Chem. Mater.*, 21, (2009), 5563:5565.
- [36] Loh, K.P., Bao, Q., Eda, G., Chhowalla, M., Graphene oxide as a chemically tunable platform for optical applications. *Nat. Chem.* 2, (2010), 1015:1024.

- [37] Wang, C., Xu, Z., Cheng, H., Lin, H., Humphrey, M. G., Zhang, C., A hydrothermal route to water-stable luminescent carbon dots as nanosensors for pH and temperature. *Carbon*, 82, (2015), 87:95.
- [38] Peng, W., Xueyun, W., Wei, L., Yushan, L., Zhijun, C., Shouxin, L., Ultra-small amorphous carbon dots: preparation, photoluminescence properties, and their application as TiO₂ photosensitizers. *J. Mater. Sci.*, 54, (2019), 5280:5293.
- [39] H. Liu, X. Zhao, F. Wang, Y. Wang, L. Guo, J. Mei, C. Tian, X. Yang, D. Zhao, High-Efficient Excitation-Independent Blue Luminescent Carbon Dots. *Nanoscale Research Letters* 12, (2017), 1:7.
- [40] Song, Y., Zhu, S., Xiang, S., Zhao, X., Zhang, J., Zhang, H., Fu, Y., Yang, B., Investigation into the fluorescence quenching behaviors and applications of carbon dots. *Nanoscale*, 6, (2014), 4676:4682.
- [41] Khan, S., Gupta, A., Verma, N., Nandi, C., Time-Resolved Emission Reveals Ensemble of Emissive States as the Origin of Multicolor Fluorescence in Carbon Dots. *Nano Lett*, 15, (2015), 8300:8305.
- [42] Han, L., Liu, S.G., Dong, J.X., Liang, J.Y., Li, L.J., Li, N.B., Luo, H.Q., Facile synthesis of multicolor photoluminescent polymer carbon dots with surface-state energy gap-controlled emission. *J. Mater. Chem.* 5, (2017), 10785:10793.
- [43] Zhu, S, Song, Y, Wang, J, Wan, H, Zhang, Y, Ning, Y, Yang, B., Photoluminescence in graphene quantum dots. *Nano Today*, 13, (2017), 10:14.
- [44] Li, H., He, X., Liu, Y., Yu, H., Kang, Z., & Lee, S-T., Synthesis of fluorescent carbon nanoparticles directly from active carbon via a one-step ultrasonic treatment. *Materials Research Bulletin*, 46, (2011), 147:151.
- [45] X. Wen, P. Yu, Y.-R. Toh, X. Ma, J. Tang, On the upconversion fluorescence in carbon nanodots and graphene quantum dots. *Chem. Commun.*, 50, (2014), 4703:4706.
- [46] Zhang, Y., Tang, Z.R., Fu, X., Xu, Y.J., TiO₂-Graphene Nanocomposites for Gas-Phase Photocatalytic Degradation of Volatile Aromatic Pollutant: Is TiO₂-Graphene Truly Different from Other TiO₂-Carbon Composite Materials. *ACS Nano*, 4, (2010), 7303:7314.
- [47] Tang, H., Chang, S. F., Jiang, L. Y., Tang, G. G., Liang, W., Novel spindle-shaped nanoporous TiO₂ coupled graphitic g-C₃N₄ nanosheets with enhanced visible-light photocatalytic activity. *Ceram. Int.*, 42, (2016) 18443:18452.
- [48] Yang D., Zhao J., Liu H., Zheng Z., Adebajo M., Wang H., Liu X., Zhang H., Zhao J., Bell J., Zhu H., Enhancing photoactivity of TiO₂(B)/anatase core-shell nanofibers by selectively doping cerium ions into the TiO₂ (B) core. *Chem. Eur. J.*, 19, (2013), 5113:5119.

- [49] Zhang, Q.H., Gao, L., Guo, J.K., Effects of calcination on the photocatalytic properties of nanosized TiO₂ powders prepared by TiCl₄ hydrolysis. *Appl. Catal. B*, 26, (2000), 207:215.
- [50] Spurr, R. A., Myers, H., Quantitative Analysis of Anatase-Rutile Mixtures with an X-Ray Diffractometer. *Anal Chem*, 29, (1957), 760:762.
- [51] Wu, P., Wu, X., Li, W., Liu, Y., Chen, Z., Liu, S., Ultra-small amorphous carbon dots: preparation, photoluminescence properties, and their application as TiO₂ photosensitizers. *J. Mater. Sci.* 54, (2019), 5280:5293.
- [52] He, J., Du, Y.-en, Bai, Y., An, J., Cai, X., Chen, Y., Wang, P., Yang, X., Feng, Q., Facile Formation of Anatase/Rutile TiO₂ Nanocomposites with Enhanced Photocatalytic Activity. *Molecules* 24, (2019), 2996:3010.
- [53] Tsai, C. C., Teng, H., Regulation of the Physical Characteristics of Titania Nanotube Aggregates Synthesized from Hydrothermal Treatment. *Chem. Mater.* 16, (2004), 4352:4358.
- [54] Chen, Q., Zhou, W. Z., Du, G. H., Peng, L. M., Trititanate Nanotubes Made via a Single Alkali Treatment. *Adv. Mater.* 14, (2002), 1208:1211.
- [55] Du, G. H., Chen, Q., Che, R. C., Yuan, Z. Y., Peng, L. M. Preparation and structure analysis of titanium oxide nanotubes. *Appl. Phys. Lett.*, 22, (2001), 3702:3704.
- [56] Dong-Seok, S., Jong Kook, L., Hwang, K., Preparation of nanotube-shaped powder TiO₂. *J. Crystal Growth*, 229, (2001), 428:432.
- [57] Lazzeri, M., Vittadini, A., Selloni, A., Structure and energetics of stoichiometric TiO₂ anatase surfaces. *Phys. Rev. B*, 63, (2001), 155409:155421.
- [58] Liu, R., Duan, L., Shen, H., Zhang, Y., Zhao, X., In situ synthesis and enhanced visible light photocatalytic activity of C-TiO₂ microspheres/carbon quantum dots. *Ceram. Int.*, 43, (2017), 8648:8654.
- [59] Hassan, M.E., Cong, L., Liu, G., Zhu, D., Cai, J., Synthesis and characterization of C-doped TiO₂ thin films for visible-light-induced photocatalytic degradation of methyl orange. *Appl. Surf. Sci.*, 294, (2014), 89:94.
- [60] Miao, R., Luo, Z., Zhong, W., Chen, S.-Y., Jiang, T., Dutta, B., Nasr, Y., Zhang, Y., Suib, S.L., Mesoporous TiO₂ modified with carbon quantum dots as a high-performance visible light photocatalyst. *Appl. Catal. B Environ.*, 189, (2016), 26:38.
- [61] Yu, B.Y., Kwak, S.Y., Carbon quantum dots embedded with mesoporous hematite nanospheres as efficient visible light-active photocatalysts. *J. Adv. Ceram.*, 22, (2012), 8345:8353.

- [62] K.N.P. Kumar, J. Kumar, K. Keizer, Effect of peptization on densification and phase transformation behaviour of sol-gel-derived nanostructured titania. *J. Am. Ceram. Soc.*, 77, (1994), 1396:1400.
- [63] Zhang, J., Zhou, P., Liu, J., Yu, J., New understanding of the difference of photocatalytic activity among anatase, rutile and brookite TiO₂. *Phys. Chem. Chem. Phys.*, 16, (2014), 20382:20386.
- [64] Zhang, T.Y., Oyama, T., Aoshima, A., Hidaka, H., Zhao, J.C., Serpone, N., Kinetics of Photocatalytic Degradation of Methylene Blue in Aqueous Dispersions of TiO₂ Nanoparticles under UV-LED Irradiation. *J. Photochem. Photobiol. A*, 140, (2001), 163:172.
- [65] Wu, P., Wu, X., Li, W., Liu, Y., Chen, Z., Liu, S., Ultra-robust carbon fibers for multi-media purification via solar-evaporation. *J Mater Sci.*, 54, (2019), 5280:5293.



Prof. UAM Dr. Habil. Joanna Gościańska

Poznań, 19.06.2021 r.

Department of Chemical Technology

tel. (61) 829-16-07

e-mail: asiagosc@amu.edu.pl

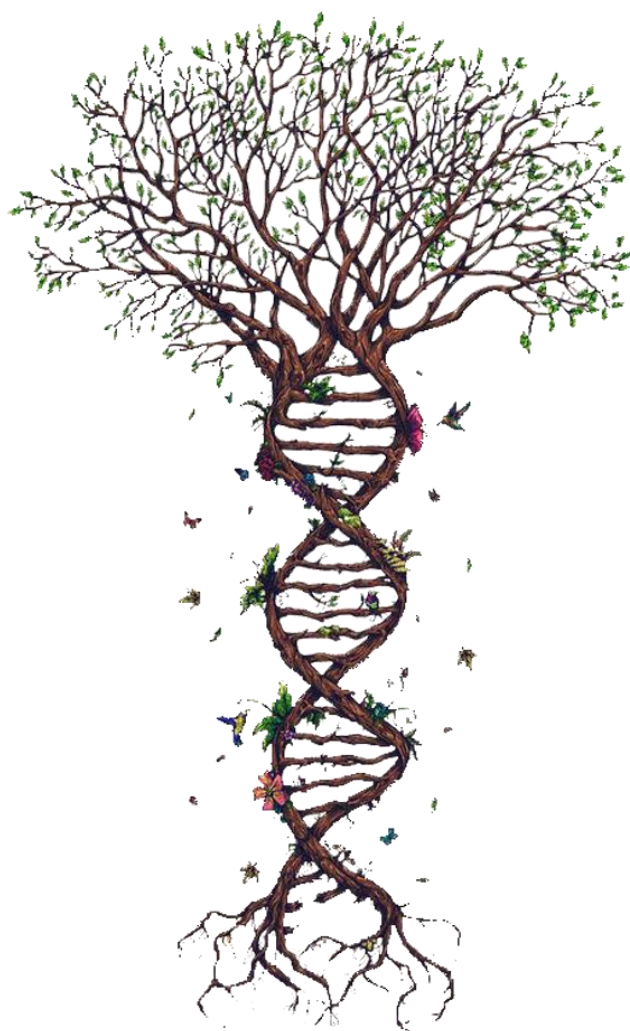
I, undersigned Joanna Gościańska, professor at Department of Chemical Technology, Faculty of Chemistry, Adam Mickiewicz University in Poznań, Poland, declare that I agree that the student Nicolae-Cristian Guzo can use the data obtained from the TEM and STEM measurements on CQD@TiO₂ samples, in the dissertation thesis that he will defend in the July 2021 session, at the Faculty of Chemistry, University of Bucharest.

These measurements were performed in the laboratories of the above-mentioned faculty, in a frame of a scientific collaboration between me and Prof. Simona Coman, regarding the synthesis and characterization of photocatalytic nanocomposites, in which the student Nicolae-Cristian Guzo was also involved.

Joanna Gościańska

Our cells engage in protein production, and many of those proteins
are enzymes responsible for the chemistry of life.

~Randy Schekman



CONTENT

INTRODUCTION	4
GRAPHICAL ABSTRACT	5
THEORETICAL OVERVIEW	6
I. Silymarin and its constituents	6
I.1. Silybin and flavonolignan relatives	6
I.2. Medicinal benefits of silymarin	8
I.3. Silymarin extraction from natural sources	10
I.4. Improvement of silymarin properties	11
II. The cold-active enzymes	13
II.1. Concept	13
II.2. Diversity of cold-active enzymes	14
II.3. Gene cloning and protein engineering	16
II.4. Applications of cold-active enzymes	17
II.5. Lipases vs. Cold-active lipase	19
III. Cold-active enzyme-based esterification of silybin with fatty acids	23
III.1. Esterification mediated by cold-active lipases	23
III.2. Design of the biocatalyst	26
MATERIALS AND METHODS	28
I. Structural analysis tools	28
I.1. Primary structure analysis	28
I.2. Homology and alignment of protein sequence	28
I.3. Secondary and tertiary structure analyses	29
II. Bacterial strain culturing	29
III. Biochemical methods	30
III.1. Plate screening assays	30
III.2. Extraction of the protein content	31
III.3. Determination of enzyme concentration	31
III.4. Determination of enzyme activity	31
IV. Chemical methods	32
IV.1. Enzyme immobilization	32
IV.2. Characterization of biocatalyst	33
IV.3. Biocatalytic system	33
RESULTS AND DISCUSSIONS	35
I. Structural analysis	35

I.1. Primary structure analysis	35
I.2. Conservation and alignment of cold-active lipase sequences	39
I.3. Secondary structure analysis	44
I.4. Tertiary structure analysis	45
II. Lipolytic activity. Plate screening assays	46
II. 1. Lipolytic activity on tributyrin	46
II. 2. Lipolytic activity on Tween 80	46
II.3. Lipolytic activity on vegetal oils	47
III. Biocatalyst preparation	49
III.1. Biocatalyst precipitation	49
III.2. Covalent immobilization	50
IV. Biocatalyst characterization	52
IV.1. FT-IR analysis	52
IV.2. SEM analysis	55
IV.3. Enzyme activity	58
V. Biocatalyst performance	59
V.1. Design of the biocatalytic system	59
V.2. Optimization of system parameters	60
V.3. Evaluation of the biocatalysts	62
CONCLUSIONS	64
REFERENCES	65

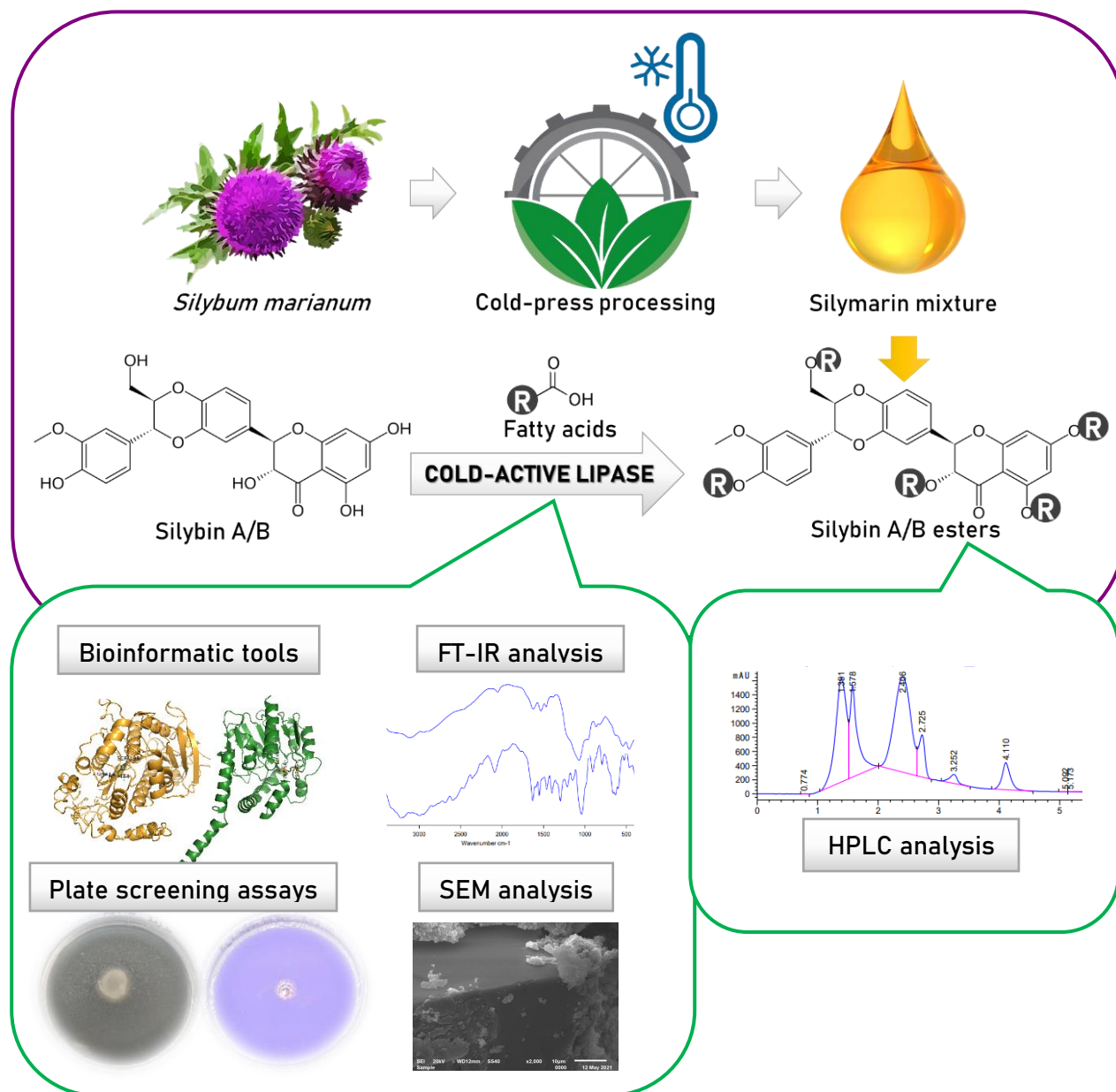
INTRODUCTION

The miraculous properties of the milk thistle have been made popular by the herbalist Discorides since the time of ancient Greece. He wrote that the tea of milk thistle seeds could annihilate the poison from the venomous snake bite. Pliny The Elder promoted that a mixture of plant juice and honey helps the gallbladder. It was in 1534 that the milk thistle began to be given as treatment for liver disease by Otto Brunfels. In the late sixteenth century, Culpepper claimed that the plant infusions are excellent for obstructions of the liver and the spleen and also curative for jaundice and for breaking and expelling stones. Rademacher popularized the ethanol extract from the seeds for hepatosplenic disorders [1].

Over the past 25 years, the herbal industry of the U.S. exploded due to the increased interest of the population for herbal products and remedies. In 1994, the Congress of the Dietary Supplement Health and Education Act classified vitamins, minerals and herbs as dietary supplements rather than drugs thus leaving the Food and Drug Administration without too much power over their manufacturing protocols. Since then, the natural remedies market has registered huge profits [1].

Silymarin is a natural supplement and besides this, it has extraordinary medicinal properties, whereas it is included in many phytochemical products. Its functionalization with hydrocarbon radicals in the active hydroxyl positions could give compounds with much higher affinity for lipophilic media. On one hand, these compounds introduced into creams or cosmetics products may overcome the skin's barrier and may exhibit preventive effects on tissue degeneration. On the other hand, they may be included in capsules and pills intended for oral administration, in order to metabolize and to reach the affected target much more easily. The study of the following pages engaged silybin, the main component of silymarin, and various fatty acids into a desired esterification process mediated by cold-active lipases as enzyme biocatalysts. As the extension to uses is traced down above, the novelty element stays beyond the biocatalyst material produced strating from a particular cold-adapted bacterial strain and adjusted up to immobilized protein networks.

GRAPHICAL ABSTRACT



THEORETICAL OVERVIEW

I. Silymarin and its constituents

I.1. Silybin and flavonolignan relatives

Silybum marianum is a very effective natural remedy which has been used since the ancient times, known in the popular consciousness as the milk thistle. It originates from Southern and Southeastern Europe, but due to the multiple colonization of the past, the milk thistle was also spread in the warm areas of America, Asia and Australia along with its medicinal benefits and applications. *Thistle* is the common name of a group of flowering plants characterized by spiked leaves with white veins from which the milk is extracted. *Silybum marianum* belongs to the aster family, *Asteraceae* or *Compositae*, as it could be found in daisies, artichokes and thistles. Reaching the maturity, the thistle plant blooms with a large, purple flower, while its spikes extend to the stem. In a heraldic direction, it is interesting to mention that the crowned thistle is the national emblem as well as a high chivalric order of Scotland since 1249 and also, the official symbol of the city of Nancy, the former capital of the Duchy of Lorraine [1].

From the biochemical point of view, *Silybum marianum* consists of a group of flavonolignans collectively known as the silymarin mixture. Highest concentrations of silymarin are found in the fruit, pericarp, seeds and leaves of the thistle plant with a range of 1.5%-3.5% flavonolignans in relation to the fruit weight [2].

In other words, silymarin comprises silydianin, silychristine and silybin, being noticed that the last compound shows more active biological properties. They fairly act as free radical scavengers and stabilizers of plasma membranes. Silymarin preparations for clinical use became officially adopted in 1969 [1], which has so far triggered an avalanche of studies on its flavonolignan components that induce hepatoprotective effects, as well as antioxidative, antiinflammatory, hypolipidemic and neuroprotective effects [2].

Nowadays, the term silymarin refers to the extract of *S. marianum* from milk thistle which is rich in flavonolignan compounds. European Pharmacopeia claims that milk thistle extract contains 30% to 65% silymarin corresponding to 20-45% silydianin, 40-65% silybin A and B, 10-20% isosilybin A and B. From a chemical point of view, flavonolignans are natural polyphenols, biogenetically related to lignans due to their similar synthetic pathways [3]. They consist of two phenylpropanoid units linked to another complex structural part that ensures the binding of the C₆C₃ ring with that of the flavonoid nucleus in different positions. Due to their extended and complicated structure, these compounds show multiple chirality which leads to the existence in nature of several

stereoisomers. The first known source of flavonolignans was isolated 2000 years ago from milk thistle and as a consequence of multiple chirality, *S.marianum* contains 23 natural related components [4].

As previously noticed, silymarin is mainly composed of individual flavonolignans and the flavonoid taxifolin. The chemical composition analyzed by HPLC-MS [5] could be studied from the following table (Table 1).

Silybin is the main component of silymarin and hence the most biologically active. Structurally, the chromone ring is responsible for the weak acidic properties and the antioxidant response is given by the phenolic hydroxyls from 3,4- and 4,5- suitable positions for the formation of complexes with various metal ions. Very low water solubility (430 mg/L) restricts its therapeutic efficacy even if it is clinically safe at high doses (>1500 mg/day for humans) [6]. Silybin exists in two stereoisomeric forms A (2R, 3R, 10R, 11R) and B (2R, 3R, 10S, 11S) having reduced solubility both in water and in lipid medium [7]. All silymarin components' structures are outlined in the figure below (Figure 1).

Table 1. Characterization of silymarin mixture by HPLC-MS [5].

Compound	Retention Time (min)	Content (%)
SB A	6,41	16,34+/-1,60
SB B	6,99	21,64+/-1,53
ISB A	8,15	5,73+/-1,16
ISB B	8,44	2,90+/-0,65
SC A	3,1	13,73+/-1,20
SC B	3,82	1,83+/-0,15
SD	3,68	4,55+/-0,62
DHSB	12,47	0,33+/-0,07
DHSC	8,02	0,56+/-0,09
TA	1,99	2,09+/-0,41

In this direction there are many semisynthetic modifications to increase the bioavailability while retaining its biological activity. It is the case of Legalon®, a common drug intended for liver therapy, which contains bis-hemisuccinate derivated silybin with high affinity for aqueous environment. There are also other modifications in order to increase the solubility in water, such as phosphodiesterification and glyco-conjugation. At the opposite pole, silybin derived at 7-OH group with palmitate or at 23-OH with acyl residues tends towards hydrophobic media [7]. Otherwise the structural modifications are imperious because silybin undergoes intensive Phase II metabolism and is rapidly excreted in bile and urine, leading to low therapeutic efficacy. By all means, oral administration of the drug is preferred, although in the case of silymarin extracts only 9 ng/mL concentrations are absorbed into plasma. When an active agent is orally delivered, it must first

dissolve in gastric and/or intestinal fluids in order to permeate the membranes of the gastrointestinal tract to reach systemic circulation [8].

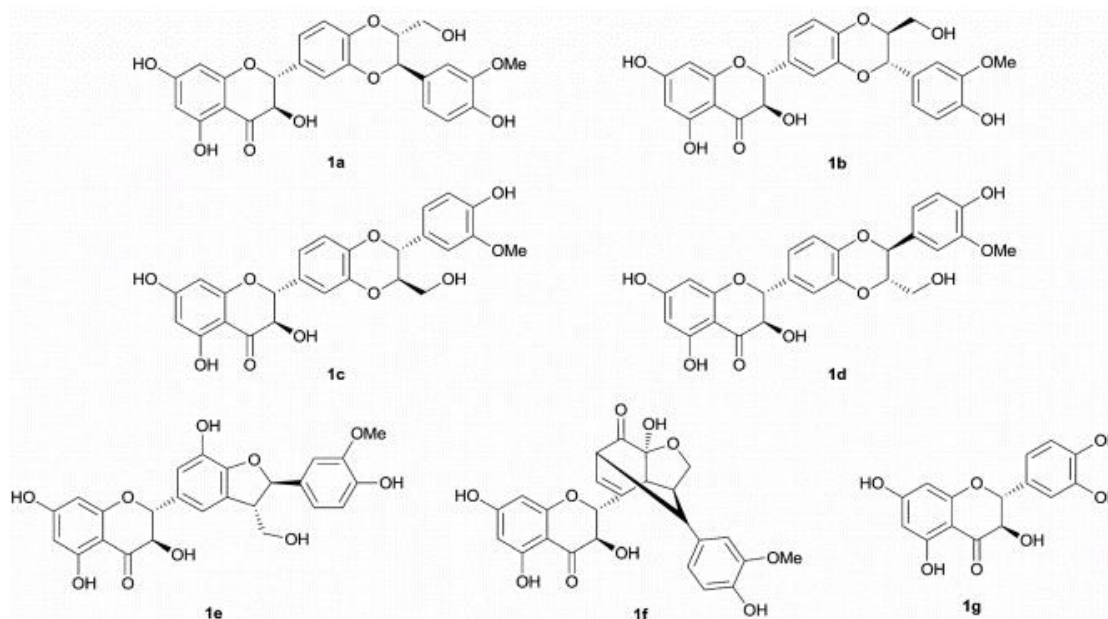


Figure 1. Structures of silymarin components: (1a)-silybin A, (1b)-silybin B, (1c)-isosilybin A, (1d)-isosilybin B, (1e)-silychristin A, (1f)-silydianin, (1g)-taxifolin.

I.2. Medicinal benefits of silymarin

In the last decades, many hypotheses and studies on the miraculous properties of silybin and silymarin have been stated. Silybin functions primarily as an antioxidant therefore this term must be correctly understood. Generally, antioxidants exert protective effects on the biomolecules and biocomponents which are subjected to oxidative stress. In the living organisms antioxidants associate themselves in complex biological systems, often as redox tandems in order to prevent and repair proteins, lipids and nucleotides from damage caused by reactive oxygen species (ROS, e.g., $\text{OH}\cdot$, $\text{O}_3\cdot$, NO , $\text{ROO}\cdot$, H_2O_2 , $^1\text{O}_2$, HClO , etc). Being inductive of oxidative stress, ROS are a cause of autoimmune diseases through the interaction between the intact and the damaged proteins, involving the so-called cross-immune reactivity [9]. It has to be mentioned that at larger concentrations, antioxidants could also become harmful oxidative stressors. The most important antioxidants are undoubtedly the vitamins (ascorbate, retinol and tocopherol), carotenoids and flavonoids. Recent studies revealed that antioxidants could also play the role of mediators for some nuclear receptors engaged in the production of intracellular enzymatic antioxidant systems. The combination of various antioxidants results in the formation of hybrids with a pronounced antioxidant effect. There are useful examples described in the literature: tocopherol and procaine, flavonolignans and fatty acids, improved ascorbic acid, iron chelator deferiprone [10].

In the recent past, silymarin started to be introduced in dermatological and cosmetic preparations for its antioxidant effect and its capacity to withstand the UVB- and chemically- induced damages. There are various factors, both intrinsic (genetic) and extrinsic (environmental), leading to a perpetual process of functional and structural modifications in skin tissue. Solar radiation caused by UV (295-400 nm) wavelengths reaches the earth surface and initiates skin reactions that result in reactive oxygen species formation (ROS). These free radicals drive to carbonylated proteins, peroxidated lipids and enzyme activation, thus causing the remodeling of the extracellular matrix. It is the first signal of collagen and elastan fibers destruction, of lowering the skin hydration and increasing the inflammatory susceptibility. Collagenase and elastase hydrolyze the support and integration networks of skin tissue, breaking down collagen and elastic fibers. Moreover, hyaluronidases section the hyaluronic acid into smaller fragments, influencing the hydration capacity of the skin [5].

As a consequence of the antioxidative effect proposed by silybin, a number of other properties related to the antioxidative ones could be formulated. Reported activities include inhibition of lipid peroxidation of hepatocyte, microsomal and erythrocyte membranes in rats, and protection against genomic damages by suppression of hydrogen peroxide and super oxide anions and of lipoxygenase. It is considered that silybin also influences hepatocyte synthesis by stimulating the activity of ribosomal RNA polymerase, as well as protecting against radiation-induced suppression of hepatic and splenic DNA and RNA synthesis [1]. Silymarin with anti-oxidative, anti-fibrotic, antiinflammatory, membrane stabilizing, immunomodulatory and liver regenerating properties plays an important role in experimental liver diseases. There are also significant responses of flavonolignans to mushroom (*Amanita sp.*) poisoning, hepatitis, cirrhosis and liver fibrosis [3]. Moreover, silymarin increases the activity of anti-oxidant enzymes like superoxide dismutase, catalase, glutathione peroxidase, glutathione reductase and glutathione-S transferase. The molecular mechanism of the antioxidant activity is based on the functions of each hydroxyl groups, these offering the suitable positions for silybin derivatization without losing the biological activity of the resulting conjugates [8].

Silymarin inhibits all stages of carcinogenesis, acting as a prophylactic and therapeutic agent in the treatment of more advanced and aggressive forms of cancer. It is highly recommended for effective control of chemotherapy and radiotherapy-induced toxicity by inhibiting the expression and the secretion of the growth factors that cause the formation of the tumor cell lines [8].

1.3. Silymarin extraction from natural sources

Freudenberg was the first who built the hypothesis of naturally biosynthetic processes in formation of flavonolignans in *S. marianum* (purple flowering plant): starting from (+)-taxifolin and coniferyl alcohol in an oxidative environment provided for peroxidase enzyme catalytic activity. Firstly, there are formed neutral phenoxy and quinone methide radicals, followed by O-coupling. Finally, a thermodynamically controlled nucleophilic attack of the hydroxyl group on the quinone methide system through an intermediate affords the 2,3-trans-substituted 1,4-benzodioxane skeleton. The production of flavonolignans in the white-flowered variant is different, whereas instead of taxifolin, the 3-deoxy derivative eriodictyol may be involved in the biosynthesis [3].

Synthetically, silymarin is extracted from *S. marianum* fruits with amphipolar solvents methanol, 80% methanol, ethanol and ethyl acetate by percolation or with the use of Soxhlet apparatus. The fatty materials from the fruit extract are removed by extraction with n-hexane or petroleum ether, being obtained flavonolignan-containing extracts. Typically, the seeds of *S. marianum* are partially defatted by pressing, which lowers the fat content from approximately 25 to 8%. Then the seeds are extracted with acetone (alternatively ethanol, methanol or ethyl acetate). Acetone extract is partially evaporated and the remaining fat is removed by hexane extraction. Crude silymarin (complex) precipitates after further evaporation. Pure silybin is prepared by dissolving silymarin in absolute ethanol followed by addition of about 10% water. Crude silybin, which precipitates could be further purified by recrystallization from ethanol [8].

At industrial level, the extraction of silymarin is performed with ethyl acetate and acetone. Further, silymarin components are separated by solvent-solvent partition and different chromatographic techniques such as OCC, TLC, LPLC, RP- and NP-MPLC, RP- and NP-HPLC. The separation of diastereoisomers of silybin, isosilybin and silychristin and regioisomers (–)-silandrin and (–)-isosilandrin was accomplished in the 2000s by RP-HPLC, MPLC and HPLC. Moreover, the isolation process of the extracted fractions was monitored by analytical TLC or HPLC [3].

A greener method of extracting the silymarin mixture from the milk thistle proposes the use of water that solubilizes natural compounds at high temperature and elevated pressure. Given the physical parameters: dielectric constant, surface tension and viscosity of the water, which all are absolutely dependent on the temperature, adjusting the temperature and the pressure could bring the water in a strong solvent stage with similar properties to organic solvents. Unlike organic solvents, which require defatting of the milk thistle prior to extraction, water extraction did not require defatting. This procedure assumes that 0.5 g of milk thistle seeds are milled to an average diameter of 0.4 mm and then introduced into the extraction cell along with 2 g of washed sea sand. The cell is installed in the GC oven and the water starts pumping into the cell with a constant flow. The pressure

is maintained above the water pressure at the desired temperature of 140°C. After collecting the fractions at well-defined time intervals, 1 mL of each sample is subjected to compressed nitrogen drying, then redissolved in methanol, filtered and analyzed by HPLC. The results could be observed in the next table (Tabel 2) [11].

Tabel 2. The efficiency of flavonolignan extraction by hot water procedure [11].

Temperature(°C)	Maximum yield (mg / g seed)			
	Taxifolin	Silychristin	Silybinin A	Silybinin B
100	0,6	2,3	1	1,6
120	0,7	2,5	1,2	2,2
140	0,5	2,4	1,2	2

Cold press method is proposed by Derya Duran et al. as being a more economical technique compared to solvent extraction and hot press along with its simplicity and energy efficiency. It has been reported to be the best way to produce high-quality oil. The popularity of the method increased since no heat or chemical treatment is used during the cold press process and all beneficial nutritional properties of the raw material are transmitted to the oils. These oils consist of natural phytochemicals as tocopherols, fatty acids, sterols and antioxidant phenolic compounds. However, after the cold press method two fractions are obtained: the oil and the waste and silymarin is completely passed into the residue, so the problem arises in the light of the valorization of biomass waste [2].

I.4. Improvement of silymarin properties

It is undeniable that nowadays silymarin is a popular medicine due to its hepatoprotective, antioxidant, antiviral and antitumoral properties, but there are also some drawbacks concerning its water solubility, poor intestinal absorption as well as an elevated metabolism for each of its flavonolignan components [12]. In this direction studies have been carried out in order to increase the bioavailability of silymarin by developing new drug designs. These include drug modifications such as salts, esters and complexes with hydrophilic excipients, complexation reactions with cyclodextrines and phospholipid, formation of biocompatible polymer dispersions, lipid-based delivery systems, nanoemulsions and encapsulation in biodegradable nanomaterials [6].

In the main area of pharmacological interest stays the self-emulsifying drug delivery technique through which amphiphilic particles are formed, with the drug inside a surfactant molecules coat. The gastrointestinal absorption is greatly facilitated due to the surface interactions of these amphiphilic systems. The supersaturation of these systems could drive a faster absorption but thermodynamically, it is an unstable state that tends to return to the equilibrium by drug precipitation. This inconvenient

can be overcome by precipitation inhibitors such as amorphous solid dispersions with PVP and PVA polymers [12]. The following figure outlines several methods by which the higher bioavailability of silymarin could be obtained (Figure 2).

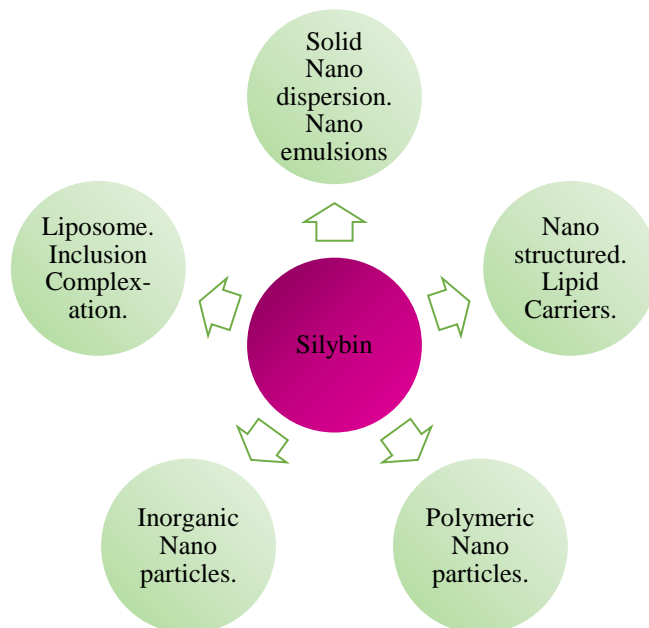


Figure 2. Silybin modification methods.

A demonstrative study of the bioavailability improvement is given to the scientific community by S. Drouet et al. which achieved a selective acylation of silybin in 3-OH position to give 3-O-palmitoyl-silybin in the presence of Lewis acid $\text{CeCl}_3 \cdot 7\text{H}_2\text{O}$ as it could be observed in the Figure 3. The yield reached was around 60%, with 85% of palmitate linked in position 3-OH and 15% in position 5-OH but with no negative change in antioxidant capacity of the derivative [7].

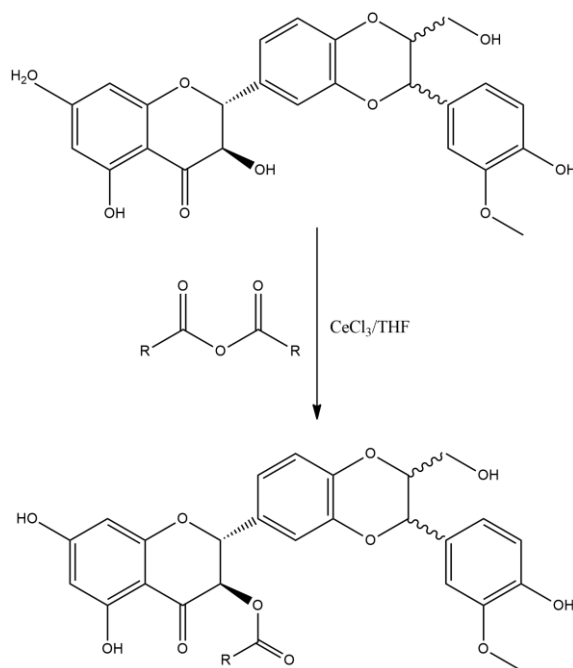


Figure 3. 3-O-palmitoyl-silybin synthesis

Two methods of radical scavenging were performed to demonstrate this: ferric reducing antioxidant power (FRAP) used for hydrophilic antioxidants, and copper reducing antioxidant capacity (CUPRAC) used for lipophilic and hydrophilic antioxidants. With FRAP assay the radical scavenging of silybin was 1.74 times more effective than give 3-O-palmitoyl-silybin while the derivative was 1.55 times more effective than silybin with the CUPRAC assay [7].

Besides the chemical modification methods, there are encapsulation variants of the compound of interest in matrices much better accepted by the organism. In the following are outlined some models. Silymarin could be included in natural β -cyclodextrines forming complexes often used because of their solubilization potential in the body barriers and of their preventive effect on metabolic degradation [6]. Other types of molecular complexes capable to enhance the bioavailability of the active constituents of silymarin are represented by phytophospholipid complexes known as phytosomes. The phytosome unit is a molecular complex between phospholipids and standardized polyphenolic constituents in a 1:1 or 2:1 molar ratios. The literature promotes the silybin-phytosome system as having a more intense therapeutic activity compared to that of the unmodified compound [12]. Further, liposomes are hollow spherical nanoparticles with a closed shell of a lipid membrane (mono- or multi-layer), inside of which an aqueous solution can be encapsulated. These supramolecular aggregates owe their success as carriers of therapeutic drugs for many advantages including the capability to encapsulate both hydrophilic and lipophilic drugs, having targeting and controlled release properties, cell affinity, tissue compatibility, reduced drug toxicity and improved drug stability. Moreover, liposomal systems are known to find an immediate access to the reticulo-endothelial system (RES) rich sites like liver and spleen, and this self-targeted nature of liposomal carriers can be exploited well for drug distribution to hepatic site. Thus being said, flavonolignan components of silymarin could be integrated into liposomal systems in order to increase their properties [6].

II. The cold-active enzymes

II.1. Concept

The biotechnology is highly promoted because it is environmentally friendly and has a valuable potential to take the place of the chemical industry based on the petrochemical refineries, which use harsh reaction conditions. With the interest of the scientific world focused on renewable resources and Green Chemistry, the bio-catalytic approach becomes highly appreciated in the new generation of synthetic processes, where chemicals of industrial value are obtained under mild conditions from renewable sources of biomass, in most cases [13]. Chemical syntheses based on

enzymes used as biocatalysts are topical because of the reduction of the number of synthesis stages, high efficiency of atoms, by avoiding the protection steps [14], to a good regio- / enantio-type selectivity, which could be achieved under mild process conditions, in other words, green conditions. New bio-catalytic concepts have been launched using enzymes, either solubilized in the reaction medium (homogeneous bio-catalysis) or immobilized (heterogeneous bio-catalysis) [15].

This study brings in the spotlight the enzymes from organisms that live in extremely harsh environmental conditions, which to some extent simulate the conditions available in industrial processes. Extremophile microorganisms that live in cold environments represent a particularly interesting source of living material adapted to abnormal conditions or considered extreme in comparison to those comfortable for human beings [16]. In contrast, organisms that live in moderate environmental conditions may be termed mesophiles or neutrophiles. As previously mentioned, microorganisms that adapted and colonized cold places on Earth may be divided into psychrophilic or psychrotolerant depending on the optimal temperature of development. Psychrophilic organisms grow onto significant low temperature range between -20 and 10°C being although unable to develop at temperatures higher than 15°C. Meanwhile, psychrotolerants optimally grow between 20 – 25°C and even register high metabolic activity at values below 0°C. This behavior could be explained by the fact that psychrophiles are usually found in marine ecosystems while psychrotolerants thrive in terrestrial cold environments. These cold-adapted microorganisms mostly include bacteria, yeasts, fungi and algae. Cold and frozen areas of the terrestrial biosphere include polar circles (Arctic and Antarctic), deep water and frozen altitudes of mountains along with glaciers, ice sheets and permafrost [17]. As a general information, the temperature recorded annually at the poles is always below zero degrees, and during the winter, the thermometers reach -80°C [16]. The polar regions represent 15% and the permafrost 20% of the total surface of the Earth, while the microorganisms able to maintain their life throughout the geological evolution of these platforms are of psychrotolerant type. The aquatic surface of the Earth represents 75% with an average temperature of 3°C, but it is extraordinary to be notified that at the bottom of the seas and oceans the microorganisms of psychrophilic type coexist and develop in the absence of light, at high pressures and without valid food. At the level of glaciers, they develop in the wires and films of liquid that spread over the mineral grains to ensure their nutrient needs [16].

II.2. Diversity of cold-active enzymes

Microorganisms inhabiting low-temperature environments have been adapted in order to survive by the production of cold-active enzymes to ensure the minimum rate of chemical and metabolic reactions and of ice-binding proteins, designed to control the growth of ice crystals thus

combating frost and membrane rigidity. Usually, the optimum temperatures for the activity of the cold-adapted enzymes are in the range of 20 – 30°C, which can be considered close to that of the thermophiles. The ability of these enzymes to incorporate a significant fraction of their activity at low temperatures is based on their structural flexibility. It is worth mentioning that an increase in the flexibility of the enzyme is not necessarily proportional to the decrease in their thermo-stability. There are two strengths related to the active enzymes operating, one of them is for the manipulation of thermo-labile and sensitive substrates at low temperatures and the other facilitates the inactivation of the enzyme as the temperature increases [17].

One aspect that may be less well known is that microorganisms that live in very cold areas, somehow avoid frost, rather than fight it. This contribution is due exclusively to proteins that mediate the binding capacity of ice crystals. The ice-binding proteins are adsorbed on the ice surface leading simultaneously to the decrease of the freezing point and to the slight increase of the melting point of water. This dependence could be clearly observed following the analysis of thermal hysteresis, whose width correlates with the concentration and functions of the protein [18].

Moreover, the adsorption of proteins on the ice crystals leads to their stabilization and inhibition of the recrystallization process. Indeed, ice recrystallization inhibition is of utmost relevance in all freezing processes involving living cells and food products, since large ice crystals damage cell membranes and impair cell viability and food quality [18].

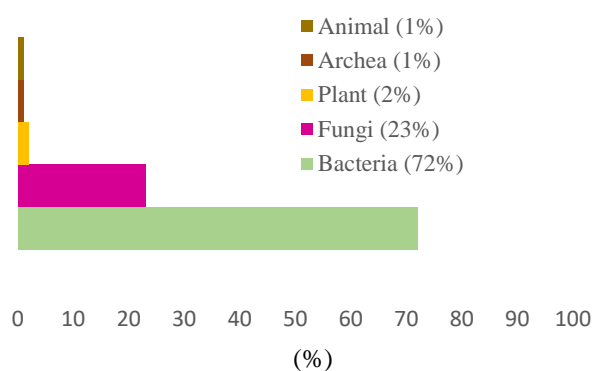


Figure 4. Organism sources of cold-active lipases

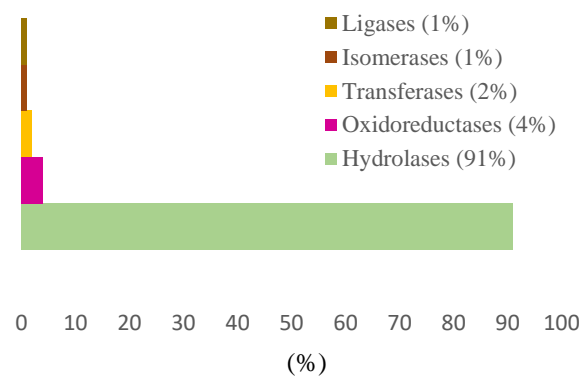


Figure 5. Distribution of cold-active enzymes based on enzyme classes

The majority of cold-adapted enzymes have been expressed in heterologous hosts being obtained from psychrophilic and psychrotolerant microorganisms, bacteria or fungi as it could be observed in Figure 4. Distribution of cold-active enzymes based on enzyme classes could be analyzed in Figure 5. To perform catalysis at low temperature demands high flexibility for proteins that adversely alters the stability of the enzyme. However, there are very interesting examples of enzymes

with high thermostability, as is the case of the superoxide dismutase, DaSOD, isolated from a psychrophilic organism, *Deschampsia antarctica*, whose optimum temperature is 20°C but it records a catalytic response even at -20°C. At 0 degrees it retains up to 80% of its catalytic activity [16].

Most of the time, the catalytic properties of mesophilic organisms at reduced temperatures are unusual, as is the case of *Candida albicans* lipase, with an optimal temperature of 15°C or *Arabidopsi* β -amylase 3 with great residual activity at low temperatures. More surprising is to discover a thermophilic enzyme with high activity at low temperatures. For instance, β -galactosidase isolated from *Pyrococcus furiosus* has optimal activity at 90°C, but retaining 8% of its activity at 0 degrees. Comparatively, the lactase activity of *P. furiosus* at 0°C was still 40% of the optimal activity from the main β -galactosidase use in the food industry (28 U/mg at 50°C and pH 7.0) from *K. marxianus*. In addition, the lactase activity of *P. furiosus* at 0°C was 31% of the optimal activity of a cold-active β -galactosidase from *Arthrobacter psychrolactophilus* strain F2 (33 U/mg at 10°C and pH 8.0) [16].

II.3. Gene cloning and protein engineering

The most convenient method to discover, even create new enzymes refers to the expression of protein chains in different cell and microbial cultures. Many studies have revealed the heterologous hosts used for the expression of cold-active enzymes as it could be observed in Figure 6. From the existence of microbial diversity, only a minor fraction can be reproduced through laboratory experiments in human handling conditions. Extremophile microorganisms depend upon drastic conditions to grow and reproduce, nonetheless, cloning techniques suppress the obstacle by various methods [17]. Metagenomics is the main culture-independent approach involving DNA extraction from the environmental sample, isolation of targeted genes and cloning the material further to create a genomic library. Novel enzymes could also be assembled by computational genomics using available information in genome databases without the need of a natural sample. The discovery of novel cold-adapted enzymes is a real challenge, because only a few genomes of psychrophiles have been deposited in public databases [19].

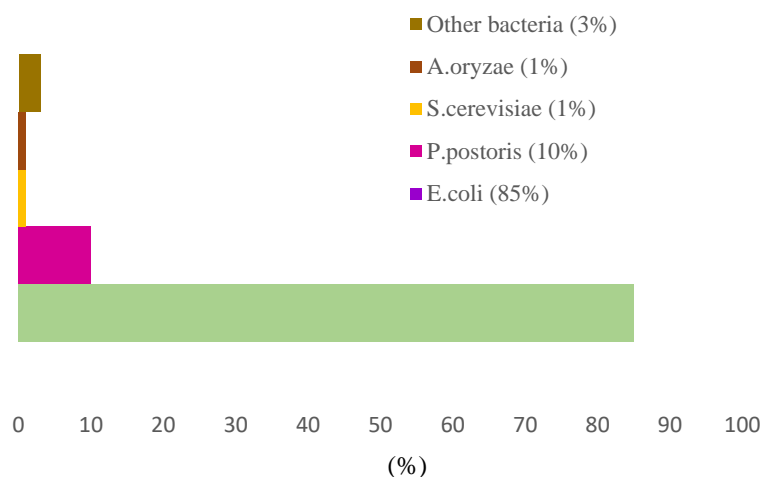


Figure 6. Distribution of heterologous hosts used in the expression of cold-active enzymes

The first step is the isolation of the adapted microorganism, which stands out with good enzymatic activity. The main cloning method is based on the creation of specific primers for gene amplification that uses a DNA strand as a template [19]. This method is possible if the genome of the species is completely sequenced and stored in the gene bank, so the microorganism can be cultivated. There are several valid hosts for gene expression, but *E. coli* is the most popular in this case. Various genotypes have been used but the preferred strain is BL21. Nevertheless, other expression hosts have been researched, such as *Halobacterium* sp. for the expression of a cold-adapted hydrolase, and *Pichia pastoris*, used as the expression host for 9 proteins including various fungal enzymes. Half of the adapted genes were cloned into pET vectors and only 5 were integrated into pCold plasmids. The enzyme purification process often calls for His tag fusion while optimal temperature is an important parameter of enzyme characterization as a result of their complete or partial adaptation to cold [16]. By far the most preferred cold-active enzymes are from the hydrolase class, more specifically lipases and esterases. This concentrates all the research efforts on solving their three-dimensional protein structure. Several strategies have been suggested to promote proper expression and folding of cold-active enzymes expressed in heterologous host, increasing their solubility, activity, and yield [19].

II.4. Applications of cold-active enzymes

Introduction of cold-adapted enzymes to traditional production schemes actually diminishes the panorama of the energy consumed at each step of the process, which is explainable because no thermal energy is needed, the reaction yields are appreciable, the enzymes retain their stereospecificity at low temperatures, which excludes secondary reactions. Moreover, their thermal lability at higher values rapidly leads to the inactivation of enzymes, hanging up the process [20].

The ability to heat-inactivate cold-active enzymes has particular relevance to the food industry where it is important to prevent any modification of the original heat-sensitive substrates and products. This is also of benefit in sequential processes (e.g. molecular biology) where the action of an enzyme needs to be terminated before the next process is undertaken, easily by heat-inactivation [20]. Examples of biotechnological applications of enzymes are provided further and the application classes are listed in Figure 7.

Nonetheless, the industrial applications of cold-active enzymes are still in the early stages. As far as concerns the food sector, cold-active amylases (EC 3.2.1.1) are of great interest for baking and brewing products, since they could be easily inactivated during cooking. A patent developed from *Bacillus licheniformis* with Novozymes improved the catalytic activity in a decreased temperature range from 10 to 60°C. Another patent developed with ColdZYMES ApS was used to heterologously express *Clostridium* α -amylase at lower temperatures than 10°C. The cold-active variants are frequently exploited for milk processing or refrigerated storage as is the case of β -D-Galactosidase usage. Among proteases (EC 3.4.) from psychrophilic sources, that from *Pseudoalteromonas* strain SM9913 might be used in tenderizing collagen-rich meat, while that from *Flavobacterium balustinum* promises wider applications, due to its optimal temperature of 40°C and high thermolability (full inactivation at 50 °C in ca. 10 min) [18].

Cold-active enzymes could be used in chemical manufacturing for organic compounds that are highly volatile and can only be modified at low temperature. In other cases, low temperature may make separations of the product easier and less expensive. Cold-active enzymes could be added to detergents for low-temperature washes or to other solutions for cleaners. Some enzymes might replace chemical preservatives in foods by depleting metabolites required by other organisms, disrupting microbial cells, or degrading other enzymes. Psychrophilic microorganisms and their enzymes are already crucial to nutrient cycling and biomass degradation and production. We can take advantage of the natural role of psychrophiles and use ones producing useful enzymes in waste-water treatment, biopulping and bioremediation in cold climates. Psychrophilic methanogens would be useful in anaerobic digestors to increase methane production in Northern regions. In research, reactions could be performed at low temperature and then the mixture heated to readily inactivate the enzyme before proceeding to the next step. Other cold-active enzymes could substitute for currently used enzymes that require higher temperatures than the cells or substrates require [17].

In the field of molecular biology, the enzymes are the main actors. Several *in vitro* reactions necessitate low temperature, a condition that could be fulfilled and enhanced by the cold-active enzymes. Ligases (EC 6.5.1.1) catalyse the formation of phosphodiester bonds, joining DNA fragments with protruding or blunt ends. For DNA with protruding ends, the optimal ligation temperature is a compromise between the ligase T_{opt} and the optimal temperature for annealing short

DNA protruding ends, usually very low. For this reason, the reaction efficiency can be increased by low temperatures (4 – 8°C) and by extending the incubation time over several hours. Proteases (EC 3.4.) are used to remove protein contaminants from nucleic acid preparations. The most popular is Proteinase K, which retains relatively high activity at 20°C and is stable up to 95°C [18].

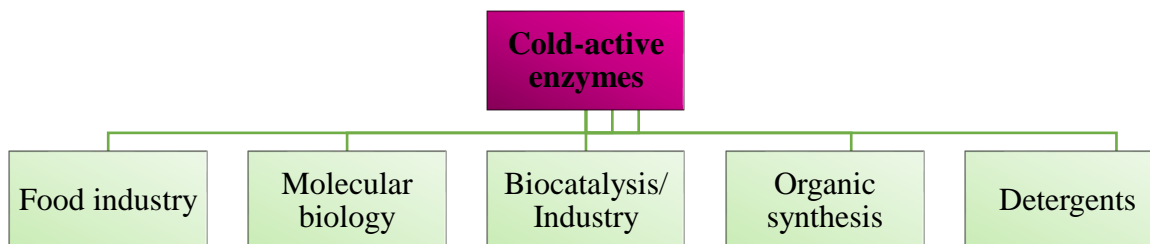


Figure 7. Application classes of cold-active enzymes.

II.5. Lipases vs. Cold-active lipase

Carboxylesterases (EC 3.1.1.1) and true lipases (EC 3.1.1.3) are altogether called lipolytic enzymes. Carboxylesterases (in the following text called esterases) usually act on water-soluble esters, while true lipases (in the following document called lipases) can hydrolyze water-insoluble substrates, too. The longer fatty acid chain in lipid is the less water-soluble it is; therefore, enzymes that hydrolyze olive oil (triglyceride ester with long-chain (C16, C18) fatty acids) are called lipases and those that hydrolyze tributyrin (triglyceride ester with short-chain (C4) fatty acids) are called esterases [21]. Essential characteristics of lipases must to be inserted, for the sake of structural complexity these present [21]

- The active site clefts of these lipases are covered with a flexible and amphiphilic α -helix, which functions as a “lid.” Upon binding to the surface of substrate micelles, the lid undergoes structural changes resulting in the displacement of the α -helical lid from the active site cleft. In this so-called “open” conformation, the hydrophobic surface area surrounding the catalytic site increases allowing the four substrates to diffuse into the active site freely. However, interfacial activation cannot be the property distinguishing between esterases and lipases as some lipases do not follow interfacial activation kinetics.
- Despite low amino acid sequence similarity among lipolytic enzymes, being very often even below 20%, most of them share a conserved α/β -hydrolase fold and a canonical GX SXG-pentapeptide around the catalytic serine. Later, a second sizeable structural family of lipolytic enzymes with a GD SL catalytic site consensus motif and an $\alpha/\beta/\alpha$ -fold was discovered. Presently, only a few lipolytic enzymes with a β -lactamase like fold structurally unrelated to α/β - and $\alpha/\beta/\alpha$ -hydrolases were found.

- The canonical α/β -hydrolase fold is characterized by a central hydrophobic sheet composed of eight β -strands with the second one mostly antiparallel. The strands β 3 to β 8 are connected by α -helical-loop structures organized at both sides of the sheet. This stable globular scaffold is characterized by extraordinary plasticity as different structural elements and even whole domains, e.g., the above mentioned “lid” or “cap” described for many lipases, can be inserted into these loops connecting β -strands and α -helices without disturbing the fold itself.
- The active sites of lipolytic enzymes contain a catalytic triad consisting of a strictly conserved nucleophilic serine and histidine and an aspartate or glutamate as acidic residues. The catalytic serine is usually embedded within the conserved motif Sm-X-Ser-X-Sm, where “X” and “Sm” denote any amino acid and small amino acid, respectively. For most lipolytic enzymes, a GX SXG-consensus motif located in the middle of the sequence was reported. Glycine residues of the GX SXG-pentapeptide account for the localization of the catalytic serine on the top of a sharp turn preceded by an α -helix and followed by a β -strand. This structural motif, named “nucleophilic elbow,” seems to be a steric prerequisite for substrate hydrolysis and represents one of the best conserved structural motifs among α/β -hydrolases.
- The catalytic cycle of serine hydrolases involves deprotonation of the side chain hydroxyl group of serine by a catalytic triad histidine, which is deprotonated by the acidic residue. The deprotonated serine initiates the hydrolysis of an ester bond by a nucleophilic attack on the carbonyl carbon atom of the ester substrate. After the corresponding alcohol is released, a lipase–acyl complex is formed, which is subsequently hydrolyzed by water releasing the free fatty acid and the enzyme. During the hydrolysis, the negatively charged intermediates with the tetrahedral configuration at the oxygen atom of the ester bond are stabilized by the so-called oxyanion hole (mostly formed by asparagine and glycine) varying in type but structurally strictly conserved among α/β -hydrolases.
- The canonical $\alpha/\beta/\alpha$ -hydrolase fold of the GDSL family of lipolytic enzymes is characterized by a conserved hydrophobic core consisting of five β -strands and at least four α -helices. The additional secondary structural elements and differences in the substrate-binding loops inserted in the canonical $\alpha/\beta/\alpha$ -fold are the cause of functional diversity among GDSL hydrolases. This is reflected by the broad spectrum of substrates hydrolyzed by these enzymes, including glycol esters, aryl esters, wax-like lipids, phospholipids, lysophospholipids, acyl-CoA thioesters, peptides, and triacylglycerols.
- The GDSL-motif containing the active-site serine residue is part of a consensus sequence designated as block I, which is positioned close to the N-terminus of the enzyme. The catalytic triad residues, namely aspartate and histidine, were identified in blocks III and V, respectively. The glycine belonging to the oxyanion hole is a strongly conserved residue of block II. This

observation led to the proposal of the new name SGNH-hydrolase family that is now used as a synonym to the GDSL-hydrolase family. Different from α/β -hydrolases, the catalytic histidine and aspartate are part of a DXXH-motif. Furthermore, the nucleophilic elbow strongly conserved among α/β -hydrolases is absent in GDSL-hydrolases. Despite notable differences, the GDSL-hydrolase catalytic mechanism is similar to the general mechanism of α/β -hydrolases, which all have a Ser-His-Asp catalytic triad.

Up to date, lipolytic enzymes are classified into nineteen families based on phylogenetic criteria, conserved sequence motifs, and biological functions. For this particular study, there have been identified two lipases out of the proteome of *Psychrobacter* sp. of Scarisoara Ice Cave (Romania), as belonging to the fourth and fifth family of lipases.

Family IV of lipases constitutes several esterases from distantly related prokaryotes, including psychrophilic, mesophilic, and thermophilic bacteria. The enzymes show a remarkable similarity to the family of mammalian hormone-sensitive lipases (HSL). Here, three sequence blocks with conserved motifs were identified, with blocks II and III containing the catalytic triad residues. Block I contain a conserved HGGG consensus sequence that is involved in hydrogen bonding interactions, which stabilize the oxyanion hole and promote catalysis as deduced from the crystal structure of *Brefeldin A* esterase from *Bacillus subtilis* [21].

Despite their homology to HSL, the substrate spectra of the enzymes of the bacterial HSL-family differ significantly. While human HSL has a broad substrate specificity and hydrolyzes short-chain esters as well as water-insoluble substrates like triolein, vinyl laurate, and olive oil, the bacterial HSL-family esterases show activity only towards short fatty acid chains length substrates like tributyrin and vinyl propionate. Moreover, esterase enzyme kinetics was observed, while HSL reactions show typical lipase kinetics.

Several family IV esterase structures, among them, thermostable esterase from *Alicyclobacillus acidocaldarius* (AaEst), were solved, which showed a unique structural feature: a “cap” which differs from the lid found in true lipases is formed by two separate helical regions and covers the active site. More recently, an oxadiazole inhibitor was identified, which covalently binds to the catalytically active serine. Interestingly, inhibition was specific in that the activity of other carboxylesterases was not affected, providing a promising option for quick discrimination among esterases.

From *Family V of lipases* [22], esterases originate from different bacterial genera representing mesophilic, cold-, or heat-adapted organisms as *Pseudomonas*, *Haemophilus*, and *Moraxella*. These enzymes share significant homology with other bacterial proteins like epoxide hydrolases, dehalogenases, and haloperoxidases that also possess the typical α/β -hydrolase fold.

Conserved amino acids are located in three blocks with the catalytic triad residues Ser located in block II, Asp, and His in block III. The esterases Est2 of *Acetobacter pasteurianus* and EstV of *Helicobacter pylori* are the only enzymes of this family that has been cloned and characterized yet. Both proteins revealed typical characteristics of carboxylesterases with EstV of *H. pylori* showing a preference for short fatty acid chain lengths, p-nitrophenyl esters (C2–C6), and triglycerides (C4) and typical Michaelis-Menten kinetics instead of interfacial activation. In the case of *A. pasteurianus* Est2, triglyceride substrates with even shorter fatty acid chain lengths like triacetin and tripropionin were hydrolyzed, preferably.

Starring cold-active lipases, extreme organisms develop in a reduced temperature range of 25 and 45°C, due to their adaptation to the inhabiting environment by producing enzymes, along with other biomolecules, which possess specific bio-catalytic activity at low temperatures [23].

Their cold adaptation provides such flexibility around the active sites, along with low enthalpy and affinity towards substrates, but high specific activity at low temperatures. Most of lipases investigated so far have been isolated from psychrophilic and psychrotolerant microorganisms of polar areas, deep water, or chilled food samples. However, these enzymes are slightly thermostable because they have developed in the context of very low temperatures, so the improvement of their thermal stability is obtained by immobilization, directed evolution, protein engineering, chemical treatments. An extremely interesting observation is that the cold-resistant lipases extracted from organisms of tropical areas show very good thermo-stability compared to the analogues of the alpine areas [23].

Like all other lipases, the cold-resistant possess the canonical α/β hydrolase fold (central, hydrophobic β -sheet that is covered by α -helices from both sides); the active site contains the catalytic triad, Ser105(nucleophile)-His224(basic residue)-Asp/Glu187(acidic residue) and an oxyanion hole. In most cases, the active site is covered by a lid which opens in the presence of an interface to facilitate contact with the substrate [24].

Naturally, the conformational structure of the lipases is adapted to accommodate the substrate at low temperatures. Their behavior is compared with those of mesophilic and thermophilic enzymes by crystallographic studies or site-directed mutagenesis [23]. For instance is the case of *Pseudomonas immobilis* and *Pseudomonas fragi* IFO 3458 lipases which compared with their counterparts reveals that they have a very low content of arginine residues in comparison with the lysine residues, weak hydrophobic core, very few salt bridges and few aromatic-aromatic interactions. In addition, the arginine residues are distributed differently from mesophilic enzymes. Some of them are at the level of salt bridges, but most cover the surface in the idea of increasing the conformational flexibility. The high content and aggregation of glycine residues depict local mobility. Another feature is associated with the production of trehalose and exopolysaccharides, acting like

cryoprotectants for protein precipitation and denaturation. If glycine is substituted by proline, the shift in the acyl chain length enhances the thermo-stability of the enzyme [23].

Cold-active enzymes, in general, inherit heat instability, which undergoes rapid inactivation of the enzymes at moderate temperatures. For industrial applications, the needs of thermostability are crucial. The psychrophilic yeast, *Candida antarctica* expresses two lipases, namely *C. antarctica* lipase A and *C. antarctica* lipase B, with different physicochemical behavior. CAL-A is considered to be the most thermostable enzyme (>90°C), while CAL-B is smaller in size and less thermostable. The factors commonly considered to increase thermal stability are the hydrophobicity, number of hydrogen bonds, amino acid composition, amino acid distribution and interactions in the protein. Directed evolution with random mutagenesis based on error-prone PCR (epPCR) and iterative saturation mutagenesis guided by rational design are more frequently employed nowadays to combat the thermolability of these enzymes [25].

Lipase A from *Bacillus subtilis* after ep-PCR shows an increase of 15°C of the melting point and of 20°C at optimal temperature, comparing with wild-type lipase. From *P. fragi*, a variant is obtained after two rounds of evolution which displays a shift of 10 degrees in the optimal temperature. The protein engineering strategy was adapted to enhance the thermostability where the disulphide and other bonds are modified to decrease the entropy of the unfolded form of proteins or to decrease the unfolding rate of irreversibly denatured proteins. CAL-B and *Geobacillus zalihae* T1 lipase were successfully engineered by mutating five amino acid pairs to cysteine and by introducing an ion-pair in the inter-loop [23].

As stated, lipases are structurally modified to accommodate the substrate at reduced temperatures. The greatest advantage of cold-active enzymes is the consumption of a small amount of energy associated with the high flexibility of their activity under low water conditions. They are cost-advantageous, of wide variety, stable to organic solvents and specific in mild reaction conditions [23].

III. Cold-active enzyme-based esterification of silybin with fatty acids

III.1. Esterification mediated by cold-active lipases

The lipase-mediated esterification reaction has come to prominence in recent decades, due to the interest in organic esters for biotechnology and the chemical industry. The main difference between lipases and esterases consists of the occurrence of non-polar residues clustered around the active site at high accessibility values [26].

The mechanism of the lipase esterification reaction is like the one proposed for the serine-based protease-mediated reaction, involving two tetrahedral intermediates. The serine residue in the triad attacks as the nucleophile of the reaction the acid, losing a water molecule. An acyl-enzyme complex is formed. The alcohol molecule interacts through nucleophilic attack with the first tetrahedral complex to form the second intermediate. Thus, finally the enzyme releases the ester and regains its native form. The mechanism of the reaction could be analyzed in Figure 8. In nature, lipases are found to be active at oil-water interface. In vitro, they are found to be active in aqueous as well as anhydrous organic solvents. The interfacial activation was hypothesized to be due to a conformational change resulting from the adsorption of the lipases onto a hydrophobic interface, where a significant role is also held by the lid [24].

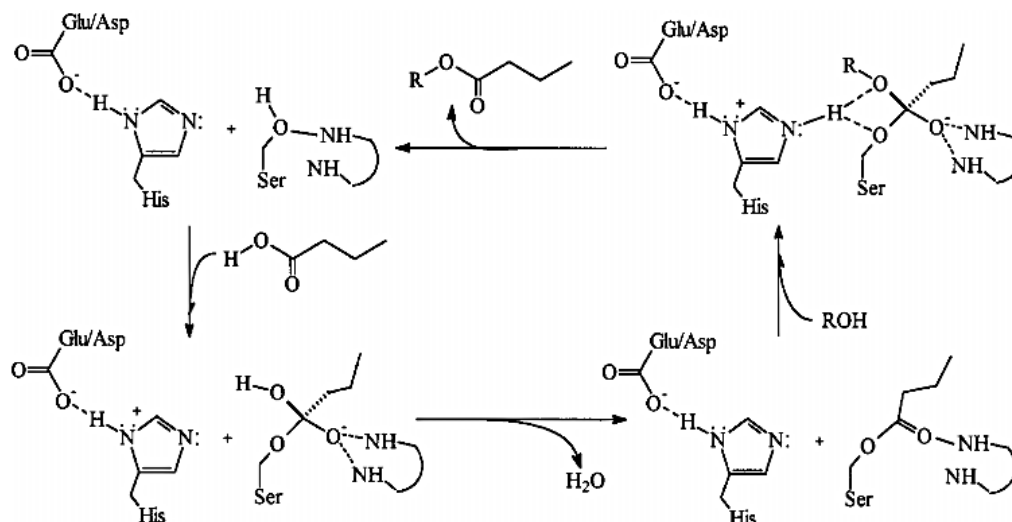


Figure 8. Mechanism of esterification by lipase catalyst.

During the esterification reaction, lipase could be deactivated due to several factors regarding temperature, exposure to interfaces, chemical denaturants, shear stress. The esterification reaction is always performed in non-aqueous solvents, in which the stability of the enzyme depends on the properties of the solvent. As Nakano et al have argued, lipase stability in organic solvent could be enhanced by random mutagenesis. Thermal deactivation of enzymes is greatly reduced by immobilization. Arroyo et al. and Moreno et al. have promulgated studies on the temperature deactivation of immobilized enzymes, having as reference lipase B from *Candida antarctica* and lipase from *Candida rugosa*. The deactivation in the case of the immobilized enzyme was much slower. Studies on deactivation of lipids in *Aspergillus oryzae* and *Candida cylindracea* under shear stress have shown that deactivation occurs due to energy consumption per unit volume and gas hold-up [24].

Saturated fatty acids are mainly involved in the production and storage of energy, being the first line of bio-components that by consuming 1 gram of lipids generates 9.3 kcal. Saturated fatty acids are also engaged in lipid transport and phospholipid and sphingolipid synthesis ensuring the

structural integrity of cellular membranes [27]. Stearic acid, the 18-carbon chain, is the most popular saturated fatty acid found in foods, but palmitic acid, the 16-carbon saturated chain, is the most prevalent in most nutrients, as well as in the body [28].

Monounsaturated fatty acids are key components due to their unsaturation, which confers a slight fluidity in the membrane lipid bilayer. Thus, they accompany monounsaturated fatty acids, displaying more structural properties [27]. Oleic acid is a major monounsaturated fatty acid, with the Cis configuration of the double bond. It is normally found in olive oil, palm oil and canola, which are promoted as monounsaturated oils. As mentioned earlier, polyunsaturated fatty acids contain two or more double bonds. Because of the cis configuration, the hydrocarbons chain aims a slightly bending, property with a special meaning in the physiological responses of fatty acids. The cis unsaturated fatty acids with their bent chains would behave in a more disorderly fashion, while the saturated and trans unsaturated fatty acids could stack together tightly exposing structural rigidity [28].

The term 'essential' for saturated and monounsaturated fatty acids are not commonly exploited, as this term is intended for polyunsaturated bio-components introduced through food intake that fulfill particular physiological functions [27].

Essential fatty acids are important constituents of cell membranes because the multitude of double bonds ensuring fluidity and affinity at the binding sites of enzymes and membrane receptors. They cannot be synthesized by the human or animal body, for which they are purchased from the diet. There are a series of essential fatty acids omega-6 derived from cis-linoleic acid and omega-3 derived from α -linolenic acid. For instance, the linoleic acid is polyunsaturated, having two double bonds, which extends the tendency to bend the chain. The common linoleic acid is an omega-6 mostly encountered in vegetable oils. There is also α -linoleic acid, a less widespread omega-3, found in flaxseed oil, canola, soy and wheat germ oil. All the omega-3 polyunsaturated fatty acids are generally considered to be essential [28]. The omega-9 series derived from oleic acid is considered not to be part of the essential fatty acids' category. However, all these series of polyunsaturated acids are metabolized similarly due to the large hydrocarbon chains, which are degraded by the same enzymes. These long-chain metabolites are of particular physiological importance in the brain, retina, liver, kidneys, gonads, adrenal glands [29].

Further it will be presented some aspects concerning the applications and implications of polyunsaturated fatty acids in the human body. The fluidity of the cell membrane is characterized by the composition of constituent lipids. Incorporation of saturated acids and cholesterol molecules increases rigidity. On the contrary, an advanced intake of unsaturated acids contributes to the formation of the fluid mosaic of the membrane, as well as to the improved response of the receptors to analogous hormones, growth factors or membrane proteins. A valuable example is insulin resistance due to the rigid membrane unable to bind insulin receptors. Thus, the therapeutic

implication of the lipid composition of the cell membranes on diabetes mellitus is outlined. Polyunsaturated fatty acids are shown to inactivate encapsulated viruses. Since neutrophils, macrophages and T cells stimulate the release of unsaturated fatty acids, it could be concluded that they are involved in the body mechanism of defense. Furthermore, their beneficial actions also sum up anti-fungal, anti-inflammatory, anti-viral and anti-bacterial responses. Studies have shown that acids have a guaranteed impact on atherosclerosis by modulating the expression of uncoupled proteins in vascular tissue [29].

III.2. Design of the biocatalyst

The immobilization technology was born in the 60s, aiming to improve the stability, reusability, activity, specificity, and manipulation of the catalyst. Conventionally, there are 4 major immobilization techniques: adsorption, covalent binding, cross-linking and entrapment, for each one knowing both the advantages and the disadvantages [30]. In Figure 9, there are outlined the immobilization possibilities, excepting the physical adhesion.

By adsorption on a solid support, a physical process itself, the enzyme retains its catalytic activity unchanged, but weak interactions between the enzyme and support can easily lead to the release of the biocatalyst. However, this method of adsorption immobilization is the most preferred [31]. A relatively small number of cold-adapted enzymes have been immobilized on solid supports such as diethyl-amino-ethyl-Sepharose or agarose-coated polyethylene-imine. For instance, cold-adapted

β -galactosidase from *Pseudoalteromonas sp.* is responsible for lactose degradation during storage of milk at low temperatures, was immobilized on DEAE-Sepharose. In this situation, the storage stability at 4°C lasted one week, but no extensive measurements have been made at higher temperatures [30].

A more modern approach refers to enzyme immobilization via covalent attachment to stimulus-responsive or smart polymer and magnetic particles. The enzyme could be easily removed from the reaction mix by applying a magnetic field for decantation or magnetically stabilized fluidized bed reactors [31]. The disadvantage in this case is that the nanoparticles oxidize in air [30]. The case of lipase immobilization on magnetic nanoparticles, initially follows an activation step with carbodiimide, the resulting suspension being sonicated and held at 4°C [32].

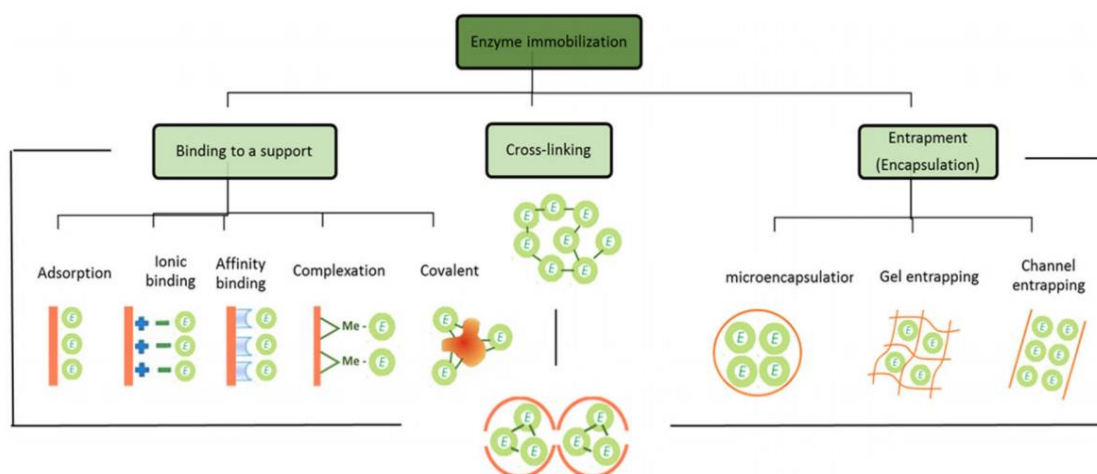


Figure 9. Enzyme immobilization techniques.

Cold-active enzymes have been covalently immobilized on several carriers, including agarose, chitosan, Sepharose, silica and graphene oxide. By covalent modifications generally the catalytic activity is diminished. Immobilization leads to the improvement of the thermal stability of the enzymes, which are markedly adapted to the temperatures considered critical, at which the enzymes begin to disorganize and destabilize. A psychrophilic pullulanase (*Exiguobacterium* sp.) starts losing its activity from 50°C, pointing no activity at 60°C. The immobilized enzymed on epoxy-functionalized silica maintains its thermal stability up to 90°C for one hour of incubation [30, 31].

Cross-linking technique aims to covalently link the enzymes together by creating aggregates. Firtly the enzymes are precipitated, then cross-linked using agents such as glutaraldehyde or aldehyde dextran.. Enzymes could also be encapsulated into a polymeric matrix. Nonetheless, few attempts have been published on this topic. For instance, a cold-adapted cellulase from *Pseudoalteromonas* sp. was covalently immobilized in sodium alginate gel beads for the ethanol fermentation of kelp cellulose. After 7 cycles, the enzymes still show 58% activity [30, 31].

Another topic of particular importance is the use of organic solvent in enzymatic environment. This intention is industrially supported for the ease of solubilization of water-insoluble substrates, but the enzyme can be negatively denatured. Cold-adapted enzymes are more sensitive to changes in temperature, outside the optimum range, and solvent. After the first identification of organic solvent-tolerant lipase Lip9 from *Pseudomonas aeruginosa* LST-03 with increased activity in n-decane, n-octane and DMSO, many enzymes were cloned, and the enzyme tolerance to an organic solvent was improved by directed evolution. Recently, the polar organic solvents, methanol and DMSO were shown to increase the conformational flexibility of the cold-adapted and organic solvent-tolerant lipases PML (*Proteus mirabilis*) and LipS (*P. mandelii*). The armistice path for best results could treat enzymes with organic solvent if they are properly immobilized on a solid support, to maintain both their structure conformation and thermo-stability [30].

MATERIALS AND METHODS

I. Structural analysis tools

The bioinformatics tools were used for the prediction of the secondary and tertiary (modeling) structures of the putative enzymes and the analysis of their molecular weight, amino acid composition, isoelectric point, hydrophobicity, etc., based on their primary structure.

Identification of genes coding for lipases/esterases in the genome of *Psychrobacter sp.* from Scarisoara Ice Cave, and primary, secondary, and tertiary structure analyses of the putative encoded enzymes were performed as preliminary investigations. To identify the putative lipases/esterases encoding genes, screening of the genome sequence of *Psychrobacter sp.* from Scarisoara Ice Cave using BLAST program of the NCBI web site (<http://www.ncbi.nlm.nih.gov/>) was carried out using previously reported bacterial lipases/esterases protein sequences as a template.

I.1. Primary structure analysis

The primary structure analysis of lipases was carried out using ExPASy proteomics tools (<https://www.expasy.org/>) [33]. ProtParam software was used for determining the amino acid composition, atomic composition, and the total number of positively/negatively charged residues, the molecular weight (Mw), and isoelectric point (pI).

I.2. Homology and alignment of protein sequence

With the obtained putative lipases enzymes, it was performed a BLAST screening to search for primary sequence homologs. As it comes to a newly identified species from the glacier of Scarisoara Ice Cave, the need to examine the constitutive proteins properly is without a doubt.

The amino acid composition and sequence identity and similarity scores (%) between lipases' primary structure of the target bacterium and other mesophilic, hyper-thermophilic, and psychrophilic bacteria were calculated using Emboss needle online tool (http://www.ebi.ac.uk/Tools/psa/emboss_needle/) [34].

To unravel the structural adaptation characteristics alongside the primary structure and to evaluate modification in the conserved regions, primary structure alignment of various lipases sequences was carried out using the CLUSTAL OMEGA EMBL-EBI multiple sequence alignment software (<http://www.ebi.ac.uk/Tools/msa/clustalo/>) [35].

I.3. Secondary and tertiary structure analyses

Predicted secondary structure of lipases/esterases was obtained using the online CFSSP (Chou & Fasman Secondary Structure Prediction Server) tool (<http://www.biogem.org/tool/chou-fasman/>) [36].

The theoretical model of lipases 3D structure was obtained using the I-TASSER (Iterative Threading ASSEmblY Refinement) server [37]. Model visualization was performed using the Pymol software (PyMOL Molecular Graphics System, Version 1.2r3pre, Schrödinger, LLC).

II. Bacterial strain culturing

Psychrobacters usually grow well on standard complex media such as infusion agar, tryptone-yeast extract agar, or trypticase soy agar. These organisms may be found growing slowly as contaminants on plates are stored at 4°C [38].

The bacterial strain used in this study belongs to *Psychrobacter SC65A.3* isolated from Scarisoara Ice Cave (Romania), which was extracted and completely analyzed in terms of taxonomic affiliation and microbiological characteristics by V. Paun (manuscript in preparation).

The bacterial strain cultivation was properly performed at 15°C in Trypticase soy (Scharlau Microbiology) (Table 3) and Reasoner's 2 (Melford Biolaboratories Ltd.) (Table 4) culture media (broth and agar).

Table 3. Composition of the Trypticase soy culture medium.

	Composition	Chemical ole
Tryptic soy broth	Casein peptone 17g/l	Assortment of peptides assuring the amino acids and nitrogenous substances as a nutritious content
	Soy peptone 3g/l	Nutritious content of amino acids for bacterial growing
	Sodium chloride 5g/l	Maintain the osmotic equilibrium
	Dipotassium phosphate 2.5 g/l	Maintain pH
	Dextrose 2.5g/l	Source of energy through carbohydrates cycle

The pH of the medium was adjusted to 7.3 at 25°C and further sterilized in the autoclave at 121°C for 15 minutes. For the corresponding solid medium, a suitable amount of agar was added to accomplish a final concentration of 15 g/L.

Table 4. Composition of Resoner's culture medium.

	Composition	Chemical role
Resoner's	Proteose peptone 0.5g/l	Assortment of peptides assuring the amino acids and nitrogenous substances as a nutritious content
	Magnesium sulphate 0.1g/l	
	Sodium pyruvate 0.3g/l	
	Casein acid hydrolysate 0.5 g/l	Amino acid source
	Dipotassium phosphate 0.3g/l	Maintain pH
	Yeast starch 0.5g/l	
	Soble starch 0.5g/l	Glucose polymer as an energy source
	Glucose 0.5g/l	Carbon energy source

For Resoner medium preparation, 3.2 g of the standard mixture will be dissolved into 1 liter of distilled water and sterilized in the autoclave for 15 minutes and the agar medium containing 1.5% agar as a final concentration.

III. Biochemical methods

III.1. Plate screening assays

For measuring the extracellular lipolytic activity of the *Psychrobacter SC65A.3* strain, the assays implied using different substrates such as: tributyrin 1%, Tween 80, Rhodamine B and, calcium chloride (Sigma Aldrich, Germany), and olive and sun-flower vegetal oils for commercial use.

The ability of *Psychrobacter sp.* strain to synthesize lipases was evidenced by cultivation on TSA and R2A culture media supplemented with 1% olive oil and 0.001% rhodamine B. Rhodamine solution was previously sterilized by filtration through a Millipore membrane of 0.22 μm . Volumes of 150 μL of the bacterial culture in the logarithmic growth phase were plated on Petri dishes containing solid media and incubated at 15°C for 96h. Lipase activity was detected by irradiating the Petri dishes with ultraviolet light at a wavelength of 350 nm leading to the appearance of a red-orange fluorescent halo, around the growth area of the bacterial strain [39]. The tests were performed in duplicate. The oils were added to the culture media after the media sterilization [40].

The culture media containing 1% tributyrin was sterilized for 20 minutes at 121°C and distributed in Petri dishes. The inoculation was performed as a spot on the surface of the culture media. Petri dishes were incubated for 7 days at 15°C, and the positive reaction was indicated by the appearance of a transparent halo around the bacterial culture. Similar manipulation applied for 1% Tween 80 assay, where the culture medium supplementary contains 0.01% $\text{CaCl}_2 \cdot 2\text{H}_2\text{O}$. The lipase

reaction was positive as off-white calcium oleate microcrystals were formed as a response to the biocatalytic hydrolysis around the reaction zone.

Direct quantitation of lipase activity is difficult, presumably because of the low amounts of lipase molecules released by a single colony. Quantification could be done, however, by filling culture supernatants into holes punched into the agar. The logarithm of lipase activity is linearly related to the zone diameter [39].

III.2. Extraction of the protein content

Psychrobacter cells cultured in Reasoner's medium were centrifuged at 4800 rpm for 20 minutes at 4°C to separate the culture supernatant containing extracellular proteins, including the two previously characterized lipases, from the cell debris. The culture medium was supplemented with 1% olive oil to increase extracellular lipase production as the literature specifies that the preferred carbon source for extracellular lipolytic protein production comes from oils and not from sugars/carbohydrates as usually expected for general microorganism culture [41]. The purification was performed by extraction with organic solvent. It was used 80% acetone to precipitate extracellular protein content from culture media using a 2/1 volumetric ratio. Adding drop by drop the solvent solution, the protein precipitate was obtained on ice and left overnight to completely settle [42]. The precipitate was then centrifuged at 10 000 rpm for 10 minutes and collected in Eppendorf tubes left unlocked to assure acetone evaporation. In this way, the newly formed protein extract was resuspended in 100 mM TRIS-HCl pH 7.5.

III.3. Determination of enzyme concentration

Aliquots of known concentrations, prepared from bovine serum albumin (Sigma Aldrich-Merck) in distilled water were used to achieve the standard curve within 0.1-0.9 mg/mL linearity range at 280 nm. The precipitate concentration was evaluated by interpolation within the standard curve.

III.4. Determination of enzyme activity

The following materials were used for the enzymatic activity: p-nitrophenyl butyrate/palmitate, Triton100, TRIS-HCl buffer, sodium carbonate, all being purchased from Sigma Aldrich-Merck, except for Triton100 which was kindly offered by Institute of Chemistry-Physics, Bucharest. The standard method for determining lipase activity involves changing to yellow the color of the newly formed phenol product and reading its absorbance at 347 and 410 nm, respectively as

agreed in the protocol. UV-VIS analysis was performed on a standard spectrophotometer (Specord 250, Analytik Jena), using 1 cm path length cuvettes.

Stock solution of 1 M TRIS-HCl (tris(hydroxymethyl)aminomethane hydrochloride) buffer was prepared by dissolving 6 g of TRIS base in 50 mL distilled water, while adjusting the pH value to 7 with concentrated hydrochloric acid. Proper dilution was then achieved in distilled water for 100 mM TRIS-HCl buffer. All the reagents involved in buffer preparation were supplied by Sigma Aldrich-Merck.

The reaction mixture was set as follows 0.25 mL protein extract, 0.65 mL 0.1 M TRIS-HCL pH 7, 0.1 mL 0.025 M substrate (p-nitrophenyl butyrate and p-nitrophenyl palmitate) dissolved in ethanol, and incubated for 30 minute at 25°C and 37°C. A blocking solution of 0.1 M Na₂CO₃ was used to stop the reaction after 30 minutes. Meanwhile, the reaction mixtures were centrifuge at 8000 rpm for 2 minutes in order to allow the immobilized extract to settle. The absorbance values were read at 347 nm, while plotted against the calibration curve realized on p-nitrophenol substrate of known concentrations dilluted in ethanol solvent.

IV. Chemical methods

IV.1. Enzyme immobilization

Two methods of immobilization were approached. Covalent immobilization via glutaraldehyde (Sigma Aldrich-Merck) linker was performed on amino-C₂-methacrylate type resin, using two buffers to mediate the reaction: PBS (phosphate buffered saline) and MES (2-(N-morpholino) ethanesulfonic acid) buffer. The support, kindly offered by the Purolite Life Sciences Company, is in the form of spherical beads (150–300 µm of diameter) originally functionalized with -NH₂ groups using methacrylate crosslinker polymer. 0.1 g amino-C₂-methacrylate support reacted with 0.1% glutaraldehyde and 100 µL protein extract in MES (pH 4.7) or PBS (pH 7.4) buffers for 2 hours under stirring [43]. The reaction mixture was centrifuged at 2000rpm for 10 minutes and the supernatant containing the unattached protein extract was separated from the resin beads with the immobilized proteins. Washing step and resuspension of resin beads was done in PBS pH 7.4 buffer 3 times.

MES buffer (pH = 4.7) used for modification of resin surface was prepared by dissolving MES solid in distilled water to a final concentration of 10 mM, followed by the addition of NaOH for adjusting the pH value of the solution to 4.7. Ten milli molar of PBS solution (pH = 7.4) was used as aqueous buffer solution. Its composition consisted of: 8 g NaCl, 0.2 g KCl, 1.43 g Na₂HPO₄ ×

2H₂O and 0.34 g KH₂PO₄ in 1 L distilled water. All of the reagents used for the preparation of MES and PBS buffers were purchased from Merck and Sigma-Aldrich, respectively.

Covalent immobilization on the functionalized surface of magnetite particles was experimented on Chemicell beads. The carbodiimide method involved the use of EDC, PBS / MES wash buffers and blocking and storage solution prepared in PBS with 0.1% bovine serum albumin and 0.05% sodium azide, all purchased from Sigma Aldrich-Merck.

1 mL of commercial suspension of Si-MAG-amine, Si-MAG-carboxyl and Fmp-carboxyl magnetic particles was washed and resuspended in MES buffer pH 6, proceeding further the same protocol of immobilization on both supports through carbodiimide method. The magnetic beads were gathered with a magnetic separator and foremost mixed with 0.25 M EDC in MES buffer. The immobilization reaction happened for 2 hours at room temperature and gently shaking after the addition of 200 µL of 6.6 mg/mL protein extract

Prior to the immobilization on Si-MAG-Hydrazine particles, 500 µL protein extract was incubated with 5mg NaIO₄ in the dark at room temperature for 30 minutes. Then, the magnetic beads were placed to react with 0.25mL of newly oxidized protein extract for 6 hours at room temperature (Figure 6.). The blocking and storage solution in all assays was PBS buffer pH 7 containing 0.1% BSA and 0.05% NaN₃. Gentle oxidation of the glycosidic groups within the protein extract was accomplished with sodium periodate (Sigma Aldrich-Merck).

IV.2. Characterization of biocatalyst

FTIR spectra of bio-composites and simple/functionalized supports were recorded using Vertex 70 (Bruker, Ettlingen, Germany) spectrophotometer equipped with the Diffuse Reflectance Infrared Fourier Transform cell. Sixty four scans were collected with a resolution of 4 cm⁻¹ in the wavenumber range of 400–4000 cm⁻¹.

IV.3. Biocatalytic system

1 mg of silybin was weighted and dissolved in 1 mL THF solvent, while adding 10 µL of fatty acid/ester. After thoroughly mixing the substrates, 100 µL of protein specimens, either free or immobilized, were added to reaction, while incubating at 25°C for 24 h at 1000 rpm. The reaction mixtures were then centrifuged for 15 minutes at 1500 rpm, allowing the enzyme extract or the immobilized to settle, while collecting the supernatant. Reaction mixtures were passed through 0.22 µm milipore filters into HPLC vials and left in the oven at 70°C for complete evaporation of the solvent. Final preparative step resumes at total solvation of the unreacted substrates and transformed products into mobile phase of the chromatographic analysis.

The catalytic performances of the above-mentioned system were analyzed by the HPLC-DAD method using a 1260 Infinity HPLC modular system from Agilent Technologies equipped with a Poroshell 120 EC-C18 column and a diode array-type detector (DAD). The experimental parameters of the analysis were as follows: acetonitrile and water (41/59, v/v) mixture as mobile phase, 1 mL/min flow rate and 25 μ L injection volume, while the chromatogram was recorded for 30 minutes.

RESULTS AND DISCUSSIONS

I. Structural analysis

I.1. Primary structure analysis

Sequence homology

A BLAST screening of the genome of *Psychrobacter SC65A.3* isolated from the perennial ice block of Scarisoare Ice Cave led to the identification of multiple genes encoding for lipases and esterases. Among these, the deduced amino acid sequence of the putative Lipase 2_65A.3 and Lipase 3_65A.3 (Table 5) was selected for evaluating the structural elements related to a cold-adaptation mechanism that necessities to be adequately elucidated.

Table 5. Protein sequences of the two lipases selected from *Psychrobacter SC65A.3* proteome.

	Protein sequence
Lipase 2_65A.3	MSNSTVLSVNTLLNKAVKTLNLMSFGQDKNPKSTDINLSDEIIDIEESALQDSREDKGLSIKEKILEHHLMTNYQP HLLHYAIKSFGLPTPILESLIKCLDGPTSKQYLHVD AHLRLILAVNSKLTPLQLIEMSELKRKFATDAVAMQAP KVWQQASDNLLSNLQFHKKGDS AISWQDRITNADDGDMTIRCYQNETSDNGFGFKKEQTSNPDET VLLFFH GGGFCIGDLNTHHEFCHAICEQTGWPVISVDYRLAPEHPAPAAVRDCISAYAWLAEHCEEFGALPSRIVLAGDS AGGGLSTLMAQQIITPNKEAWLDLGDGQKTFDILQGLPHPMAMPYLPVTDIETDYPWELYGEGLLLDHAD VAIFDAAACLENSPLPRQHILTSPMLGDNRQVCPSYVVAEELDVLRDEAFAYANQLKSFGLAVQTHTVL GAPHGF IHFMSVHQRLGQETQHIITGFANFVREIHKTRALLSA
Lipase 3_65A.3	MLLKRLGLATLLSFSVVGCTTAPNTLAINTTQKIIQYERSKSDLTTQSFTLSSGDKIVYAENGNVAGEPLLLI HGF GGNKDNFTRIA RQLENYNLIIPDLLGFGDSSKPMADYRSEAQATRLHELLQAKGLASNIHVGGNSMGG AISV AYAAKYPKEVKSLWLIDSAGFW SVGVPKSLESATLENNPLLVDKKEFDYAMYDFVMSKPPYIPKSVKAVFAQE RIANKAVESKILAQIVEDNVEQRAKVIAEYNIPTLVVWGEEKVIKPETVTLIKEIIPQSQVITMPKIGHVPMIEAV KDTANDYKAFREGLKN

Pair alignment of deduced amino acid sequences using Emboss needle software provides the identity and similarity scores of the two lipases from *Psychrobacter SC65A.3* with homologs from psychrophilic *Psychrobacter* sp. *G*, *Glaciibacter superstes*, and *Moritella* sp. *PE36*, mesophiles *Escherichia coli* and, *Pseudomonas aeruginosa* and, hyperthermophile *Strenothopomonas maltophilia* (Table 6). An alternating debate over their structure, composition, and the tendency will be further taken. Reference codes for every bacterial strain above-mentioned will be found in the ANNEX 1.

Both Lipase 2_SC65A.3 and Lipase 3_SC65A.3 showed the highest identity score (99%) with one psychrophilic species, while much more reduced (28%) with the other two psychrophilic strains. Interestingly, the identity and similarity scores of the two SIC originating lipases were somewhat higher with the homologs from both mesophilic bacteria (29-33% / 43-48% and 26-37% / 43-58%, respectively) and hyperthermophile (30% / 41% and 35 / 57%, respectively), suggesting a more complex thermal-adaptation mechanism related to structural composition.

Table 6. Identity and similarity scores for the two lipases of *Psychrobacter sp. SC65A.3* with homologous enzymes from psychrophilic, mesophilic, and thermophilic microorganisms.

	Lipase homologs	Lipase 2_65A.3		Lipase 3_65A.3	
		Identity (%)	Similarity (%)	Identity (%)	Similarity (%)
Psychrophiles	<i>Psychrobacter sp. G</i>	98.96	99.37	99.68	99.68
	<i>Glaciibacter superstes</i>	28.88	43.10	27.75	43.54
	<i>Moritella sp. PE36</i>	28.24	43.92	27.67	42.76
Mesophiles	<i>Pseudomonas aeruginosa</i>	32.78	48.96	36.92	58.06
	<i>Escherichia coli</i>	29.08	43.32	26.33	43.41
Hyperthermophile	<i>Stenotrophomonas maltoflia</i>	30.43	41.47	35.11	57.44

The highest identity score (98.96%) of Lipase 2_65A.3 was achieved with the α/β -hydrolase from *Psychrobacter sp. G* (WP_020444543.1, identified in the literature as Lip-1452 [44]), along with a considerable homology of 98.55% with *Psychrobacter cryohalolentis K5* [45] (ABE76235.1) (not shown in the table). While for Lipase 3_65A.3, the highest homology (99.68%) was achieved with the α/β -hydrolase from *Psychrobacter sp. G* (WP_020442424.1, identified in literature as Lip-948 [44]). By comparison with *Psychrobacter cryohalolentis K5* proteome [45], it also reveals a high homology of 98.10% (ABE73807.1) (not shown in the table).

Thus, a clear identity between lipases from *Psychrobacter sp.* of SIC and *Psychrobacter sp. G* should be firstly stated, as the protein enzymes are established to be charged with the same functionality in the cell.

Interestingly, the homology scores with the two cold-active lipases from *Glaciibacter* and *Moritella sp.* were very different, showing the lowest identity and similarity and suggesting that enzymes could have evolved a series of analogous cold modifications. Still, the habitat, nutrient supplies, or other physicochemical parameters are the drivers of crucial structural thermal adaptation. Even with the mesophilic *P. aeruginosa*, the scores are particularly low, but still the highest by comparison with the overall homologous values, as the explanation sustaining that the species belong to the same Pseudomonadaceae family.

Protein size and pI

Analysis of protein sequences of the two lipases using ProtParam software indicated that Lipase 2_65A.3 encounters a total number of 483 amino acids, a molecular weight of 53626.97 Da and the theoretical pI of 5.33 (Table 7/a), while Lipase 3_65A.3 comprises a total number of 315 amino acids corresponding to a molecular weight of 34606.86 Da and with a theoretical pI of 6.93 (Table 7/b). In comparison, the total number of negatively charged residues of Lipase 3_65A is 60, while the total number of positively charged residues is 38, and for Lipase 2_65A3 an equal number (35) of both positively and negatively charged residues, indicating a distinct overall charge of the two lipases.

Table 3. Dimension, molecular weight and theoretical isoelectric point (pI) of homologous lipases from psychrophilic, mesophilic and, hyperthermophilic strains.

a) Homologous lipases	No. of amino acids	Molecular weight (Da)	Theoretical pI
<i>Psychrobacter sp.</i> SC65A.3	483	53626.97	5.33
<i>Lipase 2_65A.3</i>			
<i>Psychrobacter sp. G</i>	483	53527.84	5.33
<i>Glaciibacter superstes</i>	321	33908.18	4.75
<i>Moritella sp. PE36</i>	305	34088.98	6.13
<i>Pseudomonas aeruginosa</i>	321	34743.32	4.72
<i>Escherichia coli</i>	322	35255.95	5.19
<i>Stenotrophomonas maltoflia</i>	308	32737.20	4.78
b) Homologous lipases	No. of amino acids	Molecular weight (Da)	Theoretical pI
<i>Psychrobacter sp.</i> SC65A.3	315	34606.86	6.93
<i>Lipase 3_65A.3</i>			
<i>Psychrobacter sp. G</i>	315	34650.96	7.72
<i>Glaciibacter superstes</i>	209	21844.94	4.74
<i>Moritella sp. PE36</i>	334	36512.78	4.96
<i>Pseudomonas aeruginosa</i>	315	34820.18	6.09
<i>Escherichia coli</i>	301	34348.64	8.54
<i>Stenotrophomonas maltoflia</i>	311	34898.25	6.00

The size of the psychrophilic enzymes corresponds to a larger protein chain as compared to that of the mesophilic (*E. coli* or *P. aeruginosa*) and hyperthermophilic (*Stenotrophomonas maltoflia*) homologous enzymes, with the general assumption of shortening the enzyme sequence at increasing environmental temperatures. The largest protein chains were found for the cold-adapted enzymes, while with the tendency of increasing heat, lower chains are expected for the hyperthermophilic species (Table 7).

On the values of the theoretical pI, it could not be assumed a particular tendency according to data from the tables. Generally speaking, a more acidic pI suggests structural mechanisms for low-temperature adaptation of the surface of the enzyme in psychrophilic bacteria. Lipase 2_65A.3, along with its cold-active homologs, are represented by an acid pI, but no specific changes are observed for the other enzymes [46]. While for Lipase 3_65A.3 and its cold-active series, a slight difference might be agreed to the mesophilic counterparts.

It could be considered that for a protein with the same functionality, the molecular weight would be oriented around equal value. A particularly exciting aspect stays at the level of the molecular weight of Lipase 2_65A.3 as being a doubled value comparing to the other enzymes. The first supposition is that this enzyme might be a homo-dimer and later on, the study will be sustained.

Amino acid composition

The values for the amino acid composition on each participant are listed in tables found in the ANNEX 2 at the end of the thesis.

In the first instance, Lipase 2_65A.3 from *Psychrobacter SC65A.3* is represented by a lowered amount of bulky aromatic residues as many flexible nonpolar amino acids are responsible for the structural flexibility of the enzyme in cold environments (Phe + Tyr + Trp = 7.4 % < Gly + Ala + Val + Leu + Ile + Met + Pro = 44.2%) [46].

Cysteine units cause the formation of interchain disulfide bonds intended for lower protein flexibility providing higher stability [47]. Interestingly, cysteines are present in the structure of the cold-active enzyme of *Psychrobacter SC65A.3*. In comparison with its counterparts, the considerable high value of His and Met residues are established for structure stability at low temperatures; a slight decrease of Glu content along with Asp proved the reduction of ionic interactions. Decreasing the number of Gln residues along with a higher number of Lys residues and lower Pro content stand for the overall thermal lability of the enzyme, which was also proved by the computed value of the instability index: 44.26; this classifies the protein as unstable.

On behalf of Lipase 3_65A.3 from *Psychrobacter* sp. of SIC, flexible nonpolar amino acids are widely spread along the protein chain, comparing with the aromatic ones (Phe + Tyr + Trp = 7.7 % < Gly + Ala + Val + Leu + Ile + Met + Pro = 47.2%). An alternating discussion over amino acid composition in all homologous enzymes reveals that the Cys content is comparable, while that of Met is higher in Lipase 3_65A.3, and His and Pro contents are reduced. The number of Glu residues is higher in comparison with the cold-active homologs but slightly small by evaluation with mesophilic *Pseudomonas aeruginosa*. This concludes a reduced number of ionic interactions over the whole protein. Considering the instability value for this lipase (35.91), it could be easily assumed that it is more stable than Lipase 2_65A.3.

Salt bridges

The (Arg / Arg + Lys) reports were calculated for each homolog (Table 8) to evaluate the salt bridges' impact on protein structure [48].

A typical cold-adaptation mechanism that supposes high-value reports in analogy with a reduced formation of salt bridges is observed just in the case of homologous enzymes from *Glaciibacter superstes* [47]. It was expected increased flexibility for the cold-active proteins [48], but for lipases of *Psychrobacter* sp. *SC65A.3* and *Moritella* sp., a rigid packing of the chains, stabilized by a high number of salt bridges, probably prevents cold protein denaturation.

Unexpectedly large values for mesophilic and hyperthermophilic enzymes revealed that the small number of salt bridges is not the main responsible for the lipase stability.

Table 8. Ratio of Arg and Lys residues to evaluate the presence of salt bridges.

Homologs	Arg / (Arg + Lys)	Homologs	Arg / (Arg + Lys)
<i>Psychrobacter SC65A.3</i> <i>Lipase 2</i>	0.39	<i>Psychrobacter SC65A.3</i> <i>Lipase 3</i>	0.26
<i>Glaciibacter superstes</i>	0.82	<i>Glaciibacter superstes</i>	0.86
<i>Moritella sp. PE36</i>	0.47	<i>Moritella sp. PE36</i>	0.43
<i>Escherichia coli</i>	0.89	<i>Escherichia coli</i>	0.81
<i>Pseudomonas aeruginosa</i>	0.88	<i>Pseudomonas aeruginosa</i>	0.72
<i>Stenotrophomonas maltophilia</i>	1	<i>Stenotrophomonas maltophilia</i>	0.84

I.2. Conservation and alignment of cold-active lipase sequences

Pair alignment of the cold-active lipases *SC65A.3* with those of the *Psychrobacter* sp. *G* homologs (Figure 10), indicated high conservation of their primary sequences with just one replacement of conserved and one partially conserved residues.

Lipase 2_65A.3

The intensive study of the literature was based on the high homology between Lipase 2_65A.3 from *Psychrobacter* sp. *SC65A.3* and Lip-1452 from *Psychrobacter* sp. *G* (Figure 11) [44], through CLUSTAL OMEGA pair alignment, to determine the conserved characteristics of the Lip-1452 as being overexpressed in Lipase 2_65A.3. Based on the conserved catalytic triad and overall identity of the amino acid sequences, Lip-1452 was identified as a member of the hormone-sensitive lipase (HSL) group, namely family IV of the bacterial lipases. Lip-1452 had the catalytic triad (Ser-His-Asp) and contained an oxyanion hole to stabilize the tetrahedral intermediate.

The two conserved motifs, HGGGF and GDSAG of lipases, could be identified in the amino acid sequences of Lip-1452 and Lipase 2_65A.3. The pentapeptide GDSAG contained Gly297 and Ser299 of the SIC enzymes. Perhaps Asp414 and His444 were the second and third members of the triad, respectively. The conserved Asp414 in a consensus sequence LDXL and the His constituting the triad was preceded by a Pro and followed by a Gly. All these characters indicated that Lip-1452 was a member of the HSL motif of bacterial lipases. These structural items are found in Lipase 2_65A.3 indicating that this enzyme belongs to Family IV of lipases.

Lipase 3_65A.3

Considerable sequence homology was also found between Lipase 3_65A.3 from *Psychrobacter* sp. from Scarisoara Ice Cave and Lip-948 from *Psychrobacter* sp. G (Figure 12) [44].

In Lip-948, the two conserved motifs, HGFGG and GNSMG, were identified. Lip-948 belongs to family V, based on sequence alignment, especially for the two conserved regions HGFGG and GNSMG. Moreover, Ser142, Asp264, and His292 composed the catalytic triad. It probably contained a signal peptide (Met1-Ala27), which indicated that Lip-948 might be a secreted protein. Lipase enzyme from *Psychrobacter* sp. SC65A.3 fulfills all the structural requests above by overexpressing the same conserved motifs of Lip-948. It could be concluded that Lipase 3_65A.3 belongs to the Family V of lipases.

CLUSTAL O(1.2.4) multiple sequence alignment			CLUSTAL O(1.2.4) multiple sequence alignment		
LIP2_65A.3 WP_020444543.1	MSNSTVLSVNTLLNKAVKTLNLMFSGQDKNPKSTDINLSDEIIDIEESALQDSREDKGLS MSNSTVLSVNTLLNKAVKTLNLMFSGQDKNPKSTDINLSAEIIDIEESALQDSREDKGLS *****.*	60 60	LIP3_65A.3 WP_020442424.1	MLLKRLGLATLLSFSVVGCTTAPNTLAINTTQKIIQYERSKSDLTTQSFTLSSGDKIVYA MLLKRLSLATLLSFSVVGCTTAPNTLAINTTQKIIQYERSKSDLTTQSFTLSSGDKIVYA *****	60 60
LIP2_65A.3 WP_020444543.1	IKEKILEHHLMTNYQPHLLHYAIKSFGLPTPILESLIKCLDGPSTSKQYLHVD AHLRLIL IKEKILEHHLMTNYQPHLLHYAIKSFGLPTPILESITCLDGPSTSKQYLHVD AHLRLIL *****.*	120 120	LIP3_65A.3 WP_020442424.1	ENGNVAGEPLLLIHGFGGNKDNFTRIA RQLENYNIIPDLLGFGDSSKPM AADYRSEAQA ENGNVAGEPLLLIHGFGGNKDNFTRIA RQLENYNIIPDLLGFGDSSKPM AADYRSEAQA *****	120 120
LIP2_65A.3 WP_020444543.1	AVNSKLLKTPQLIEMSELKRKFATDAVAMQAPKVVQQASDNLLSNLKQFHKKGDS AISWQ AVNSKLLKTPQLIEMSELKRKFATDAVAMQAPKVVQQASDNLLSNLKQFHKKGDS AISWQ *****	180 180	LIP3_65A.3 WP_020442424.1	TRLHELLQAKGLASNIHVGGNSMGG AISVAYA AKYPKEVKS LWLIDSAGFWSVGP KSL E TRLHELLQAKGLASNIHVGGNSMGG AISVAYA AKYPKEVKS LWLIDSAGFWSVGP KSL E *****	180 180
LIP2_65A.3 WP_020444543.1	DRTITNADDGDMTIRCYQNETSDNGFGFKKEQTSNPDETVLLFFHGGGFCIGDLNTHHEF DRTIANADDGDMTIRCYQNETSDNGFGFKKEQTSNPDETVLLFFHGGGFCIGDLNTHHEF *****.	240 240	LIP3_65A.3 WP_020442424.1	SATLENNPLLVDKKEDFYAMYDFVMSKPPYIPKSVKAVFAQERIANKAVESKILAQIVED SATLENNPLLVDKKEDFYAMYDFVMSKPPYIPKSVKAVFAQERIANKAVESKILAQIVED *****	240 240
LIP2_65A.3 WP_020444543.1	CHAICEQTGNPVISVDYRLAEPHPAAVRDCISAYAWLAEHCEEF GALPSRIVLAGDSA CHAICEQTGNPVISVDYRLAEPHPAAVRDCISAYAWLAEHCEEF GALPSRIVLAGDSA *****	300 300	LIP3_65A.3 WP_020442424.1	NVEQRAKVIAEYNIPTLVVWGEEDKVIK PETVTLIKEIIPQSQVITMPKIGHVPMIEAVK NVEQRAKVIAEYNIPTLVVWGEEDKVIK PETVTLIKEIIPQSQVITMPKIGHVPMIEAVK *****	300 300
LIP2_65A.3 WP_020444543.1	GGGLSTLMAQIITPNKEAWLDLGDEGQKTFDILQGLPHPMQMPLYPVTDIETDYP SWE GGGLSTLMAQIITPNKEAWLDLGDEGQKTFDILQGLPHPMQMPLYPVTDIETDYP SWE *****	360 360	LIP3_65A.3 WP_020442424.1	DTANDYKAFREGLKN 315 DTANDYKAFREGLKK 315 *****.	
LIP2_65A.3 WP_020444543.1	LYGEGLLLDHADVAIFDAACLENSPLRQHILTSPLMGNRQVCP SYVVAE L DVL RDEA LYGEGLLLDHADVAIFDAACLENSPLRQHILTSPLMGNRQVCP SYVVAE L DVL RDEA *****	420 420			
LIP2_65A.3 WP_020444543.1	FAYANQLKSGIAVQTHTVLGAPHGFIHFMSVHQR LGQETQHIITGFANFVREI I KTRAL FAYANQLKSYGIAVQTHTVLGAPHGFIHFMSVHQR LGQETQHIITGFANFVREI I KTRAL *****.	480 480			
LIP2_65A.3 WP_020444543.1	LSA 483 LSA 483 ***				

Figure 10. CLUSTAL multiple sequence alignment of Lipase 2_65A.3 and Lipase 3_65A.3 from *Psychrobacter* sp. of SIC and Lip-1452 and Lip-948, respectively, from *Psychrobacter* G. Legend:(*) identical residues; (:) conserved residues; (.) partially conserved residues.

LIP2	MSNSTVL SVNTLLNKAVKTLNLMSFGQDKNPKSTDINLSDEIIDIEESALQDSREDKGLS	60
P.sp.G	MSNSTVL SVNTLLNKAVKTLNLMSFGQDKNPKSTDINLSAEIIDIEESALQDSREDKGLS	60
Moritella	-----	0
G.superstes	-----	0
S.maltophilia	-----	0
P.aeruginosa	-----	0
E.coli	-----	0
LIP2	IKEKILEHHLMTNYQPHELLHYAIKSFGLPTPILES LIKCLDGPSTSKQYLHVD AHLRLIL	120
P.sp.G	IKEKILEHHLMTNYQPHELLHYAIKSFGLPTPILES LITCLDGPSTSKQYLHVD AHLRLIL	120
Moritella	-----ML-----N-----	3
G.superstes	-----MSHTPA-KP-----	8
S.maltophilia	-----MQ-----	2
P.aeruginosa	-----MA-----	2
E.coli	-----MA-----	2
LIP2	AVNSKLLK TPLQLIEMSELRKR FATDAVAMQAPKV-----WQQASDNLLSNLKQFHKKGD	174
P.sp.G	AVNSKLLK TPLQLIEMSELRKR FATDAVAMQAPKV-----WQQASDNLLSNLKQFHKKGD	174
Moritella	QIELGIR---ELVEGFVE---AGCPCPSKQ-SVIQRREGYIDSV-----VL-----AG	44
G.superstes	PYPDEL TASLAAM--GDL---AYISVTLE TLPAARA---SRPTQSVDELL-----AG	52
S.maltophilia	-LEPALQQFVDAVAHPL---PEELRELRA-----ISESALPQLQGA-----PQ	42
P.aeruginosa	-LNPDIAAYLELVGNRS---SGKSLPMHQLTVQQAREQFDQSSALMDPGL-----DE	51
E.coli	-LHPDLAAFL ELVEFGRL---TGRSLPMHAMDV AQARAEFEGSSQVLDPSP-----PG	51
LIP2	SAISWQDRTITNADDG-DMTIRCYQNETSDNGFGFKKEQTSNPDET VLLFFHGGGFCIGD	233
P.sp.G	SAISWQDRTIANADDG-DMTIRCYQNETSDNGFGFKKEQTSNPDET VLLFFHGGGFCIGD	233
Moritella	PSPKMHEE FEDEFD---GIRIKIFKPTS-----E---KLLPLTIYFHGGCFVSGG	88
G.superstes	RAVDHVEHTVPGQGGEPDVLSVFTPRG-----LAA--PVPVYHAHGGGMIMGD	100
S.maltophilia	PVAHVIEHTVIARDGQ-ALDVRLYTPEG-----LPDGP-APALLFAHGGGWFQCS	90
P.aeruginosa	PLARVETLFVPARDGT-SL PARLYSPQG-----LSASPSLPGVLYLHGGGYVVG	100
E.coli	NVT-ASELQITARDGT-RLAARLYRQG-----DAGAALQPVILY LHGGGYVVG	98
	. : : .	. *** .
LIP2	LNTHEFCHAICEQTGWPI SVDYRLAPEHPAPA AAVRDCISAYAWLAEHCEEF GALPSRI	293
P.sp.G	LNTHEFCHAICEQTGWPI SVDYRLAPEHPAPA AAVRDCISAYAWLAEHCEEF GALPSRI	293
Moritella	FATHEQMRQLAKLSNTIVVCIRYRLAPEYHYPA AHDDVYKASIHIDHGYEYGGDKPRI	148
G.superstes	RFANIGRVL DWENLGIVAVSVEYRLAPEAPYPA AAVEDCYAGLLWTV EHAADLGIDPERV	160
S.maltophilia	LAVYDGP CRALANASGCVI VAVGYRLAPEHPFPVPL HDVADAWSWLQDNAERLGLDPQRL	150
P.aeruginosa	LDSHDAL CASLAERAGCVVLS LAYRLAPEWRFP TAAEDAEDAWCWLAAEAERL GIDPQRL	160
E.coli	LDSHDSVCCRRLAALGEFAVLAADYRLAPEQQFPKAL HDVLDAA NWLAEQAASLGLDNRRV	158
	. : .	. * * * .
LIP2	VLAGDSAGGGLSTLMAQQIITPNKEAWLDL GDEGQKTFDILQGLPHPMAQMPLYPVTDIE	353
P.sp.G	VLAGDSAGGGLSTLMAQQIITPNKEAWLDL GDEGQKTFDILQGLPHPMAQMPLYPVTDIE	353
Moritella	SFVGDSAG AHLALV TSLRLK-----AKSNWLP RKQVLIY PMLDPQ	188
G.superstes	IIGGSSGGGITAGLALLR-----DRGGPKVAGQWLS SPMLDDR	200
S.maltophilia	ATGGDSAGGNLAAACLLLR-----DLGLPQPCHQLLLYPALDAG	190
P.aeruginosa	AVAGDSVGGSLCAVLSRQLALR-----GDASQRLQVLIY PVTDAS	201
E.coli	VLAGDSV GASLA AVL AITSVQQ-----PEALAFKPLAQLL FYPVTDIS	201
	. * * * . : .	. * * *
LIP2	TDYPSWEL YGEGLLDHADVAIFDAACLENSPLP-RQHILTS PMLGDN-RQVCPSYVVA	411
P.sp.G	TDYPSWEL YGEGLLDHADVAIFDAACLENSPLP-RQHILTS PMLGDN-RQVCPSYVVA	411
Moritella	GKSDSYQNGKDF IITGGMLLSGFEMYLEG SNV-SNKHPEIS LLLRNDFSGLPPTYIVTA	247
G.superstes	DVTVSSKQYVDGAIWSGRSDNTAWRALLGDDFQTENVS IYAAPARATDLSNLPPAFIDVG	260
S.maltophilia	MGSDSYRDYATGYLSAELMQRQWQAYLGNLDQPS---SLASPAQATDLQGLAPASVLS	247
P.aeruginosa	RTRQSIERYAVGHLLLEKDSLEW FYQHYQRS PEDRQ---DPRFSP LLGAVPAELAP TLLVLA	259
E.coli	CQRESHREHAEGYLL ETPTLEW FYQHYAPQREQL--DWRVSP LLSTLRQPLPPAYLSVA	259
	* . : : * : :	
LIP2	ELDVLRDEAFAYANQLKSGI AVQTHTVL GAPHGFIHFMSVHQRLGQETQHIIITGFANFV	471
P.sp.G	ELDVLRDEAFAYANQLKSGI AVQTHTVL GAPHGFIHFMSVHQRLGQETQHIIITGFANFV	471
Moritella	ELDPLRDEGEELYKLLSSGVDAYCDRYLGV I HGFQLSAVKS AVRCIE---NVARQI	303

Figure 11. Amino acid sequence alignment of Lipase 2_65A.3 with the homologous enzymes by framing the common catalytic pocket and conserved motifs.

I.3. Secondary structure analysis

Secondary structure alignment of psychrophilic, mesophilic and hyperthermophilic homologous chains (Table 9) indicated a variable distribution of helices and turns, with a relatively high content of random coils in the amino acid sequence of the psychrophilic enzymes. The temperature-dependent secondary structure appeared to be related to a decreased content of turns for lipases 2_65A.3 and 3_65A.3 from *Psychrobacter* SC65A.3 compared to the *P. aeruginosa* homolog.

Table 9. Analysis of the secondary structure composition.

Homologous proteins	Secondary structure composition (%)			
	Helix	Sheet	Coil	Turn
<i>Psychrobacter sp. SIC Lipase 2</i>	50.1	31.9	11.4	6.6
<i>Glaciibacter superstes</i>	51.4	28.7	13.4	6.5
<i>Moritella sp. PE36</i>	40	37.4	15.7	6.8
<i>P. aeruginosa</i>	46.7	31.8	14.3	7.2
<i>Escherichia coli</i>	51.2	35.4	7.8	5.6
<i>Stenotrophomonas maltophilia</i>	47.1	34.4	12	6.5

Homologous proteins	Secondary structure composition (%)			
	Helix	Sheet	Coil	Turn
<i>Psychrobacter sp. SIC Lipase 3</i>	57.8	25.4	10.1	6.7
<i>Glaciibacter superstes</i>	34.5	37.3	19.1	9.1
<i>Moritella sp. PE36</i>	39.5	45.2	10.2	5.1
<i>P. aeruginosa</i>	64.8	21	7.9	6.3
<i>Escherichia coli</i>	39.5	37.2	17.3	6
<i>Stenotrophomonas maltophilia</i>	49.8	28.6	14.5	7.1

Interestingly, the coil content of Lipases 2_65A.3 is significantly higher than that in the mesophilic *E. coli*, while for Lipase 3_65A.3 this particular assumption could be made with the *P.aeruginosa* representative, suggesting that their position in the amino acid sequence could play a critical role in the protein folding and flexibility to adapt the catalytic process to extremely low

temperatures. A lower sheet content was also observed in lipases from *Psychrobacter* sp., confirming the reduced ionic interactions [47] in comparison with the mesophilic and hyper thermophilic enzymes, as described above. No major differences were observed in the case of helix structures that are almost equally represented.

Meanwhile, the cold-active lipases preserved independent behaviors. Lipases from *Psychrobacter* SC65A.3 showed high secondary structure conservation with the mesophilic enzyme.

I.4. Tertiary structure analysis

The 3D model of Lipase 2_65A.3 from *Psychrobacter* sp. SIC was calculated using metagenome-derived esterase Est8 as a template (PDB: 4YPV.A). The sequence identity is low (30%) because of the homo-dimer structure prediction.

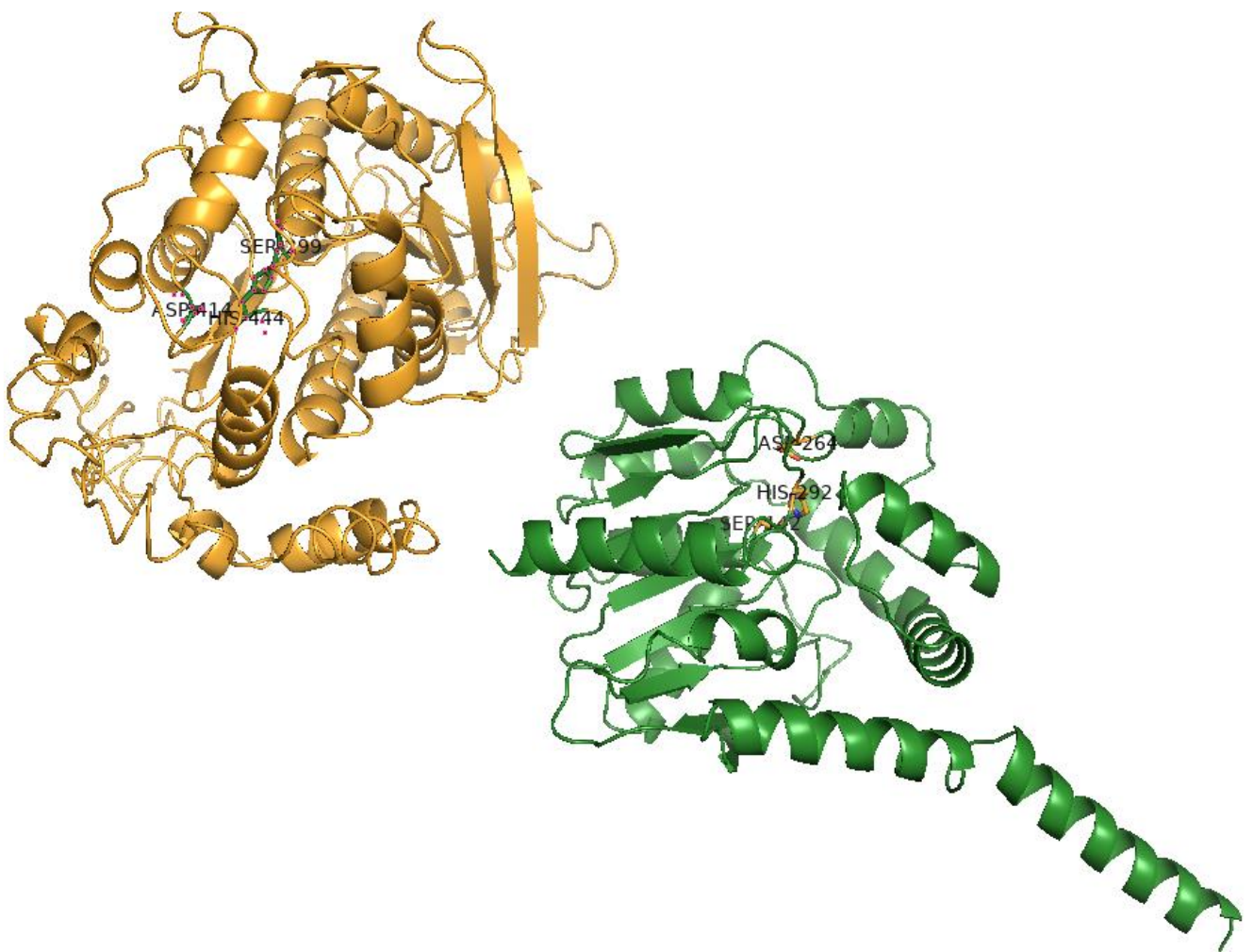


Figure 13. Tertiary structure of Lipase 2_65A.3 (yellow) and Lipase 3_65A.3 (green) predicted by 3D modeling.

In the case of Lipase 3_65A.3 3D modeling, the closest tertiary structure was superimposed with that of a cold-active esterase from *Psychrobacter cryohalolentis* K5T (PDB: 4NS4.A) used as the template. The sequence identity emerged with 98.1% coverage and the oligo-state prediction reveals a monomer.

II. Lipolytic activity. Plate screening assays.

II. 1. Lipolytic activity on tributyrin

The inoculation was performed as a spot on the surface of the culture media. Petri dishes were incubated for 7 days at 15°C, and the positive reaction was indicated by the appearance of a transparent halo around the bacterial culture. The diameter of the hydrolysis zone represents the intensity of the enzymatic activity so that the larger hydrolysis zones, the more intense activity [16 40].

No activity was recorded in the presence of tributyrin (Figure 14). Although the bacterial strain used the culture media to grow, being more visible in the case of TSA media.

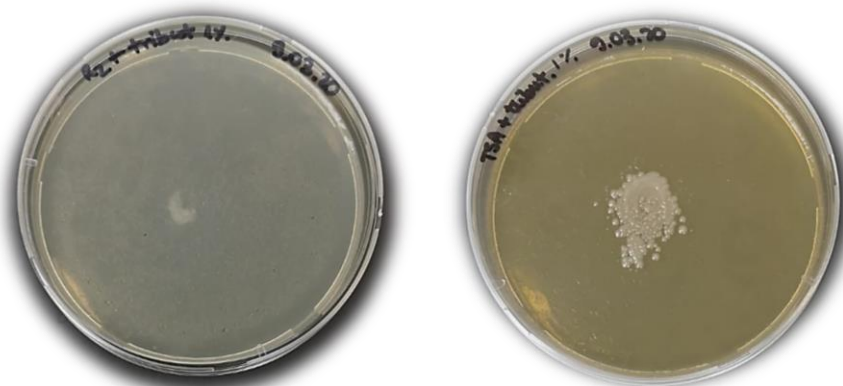


Figure 14. Petri dishes with 1% tributyrin assay.

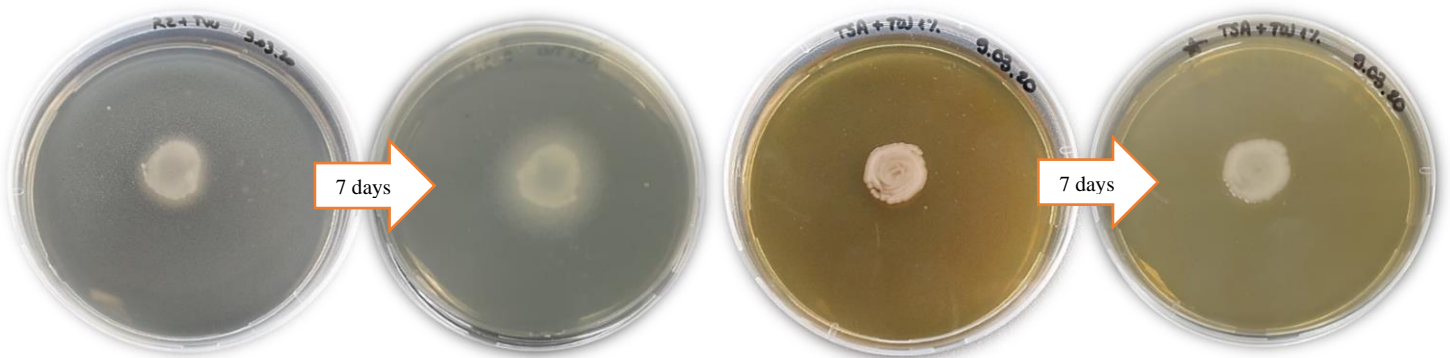
II. 2. Lipolytic activity on Tween 80

The lipase reaction was positive as off-white calcium crystals were formed and visible on the hydrolysis zones (Figure 15). After seven days of incubation at 15°C, the hydrolysis area was clearly expanded nearby the reaction spot.

Qualitative reactions in the presence of tributyrin and Tween 80 as substrates (Table 10) revealed that the R2A medium is more suitable for the hydrolysis catalytic reaction of the extracellular lipases secreted by *Psychrobacter* sp. strain.

Table 10. Time dependent hydrolysis diameter

Culture media	The diameter of the hydrolysis zone (cm)	
	3 days of incubation	7 days of incubation
TSA + Tween 1%	0	0,2 (Replicate ¹) 0,2 (Replicate ²)
TSA+ Tributyrin 1%	0	0
R2+Tween 1%	0,2 (Replicate ¹) 0,2 (Replicate ²)	0,7 (Replicate ¹) 0,6 (Replicate ²)
R2+Tributyrin 1%	0	0

**Figure 15.** Petri dishes with Tween 80, bacterial strain, on R2A, respectively, TSA culture media.

II.3. Lipolytic activity on vegetal oils

Olive and sunflower oils, in concentrations of 0.5%, 1%, and 1.5% were added to the growth media as a lipase substrate to determine the optimal conditions for extracellular lipase activity. The oils were added to the culture media after the media sterilization. Lipase activity was detected according to the described protocol as red-orange fluorescent halo occurrence due to Rhodamine B input [40].

When using R2A culture media, the highest lipolytic activity of the bacterial strain was observed for a concentration of 1% sunflower oil. However, in the case of TSA medium, a significantly improved activity occurred in the presence of 1.5% sunflower oil (Figure 16), suggesting that this cold-active bacterial strain has a higher lipase activity when using 1.5% sunflower oil concentration. The same high lipolytic activity was appreciated for the highest concentration of the olive oil (1.5%), with a considerable extension around the hydrolysis zone, regardless of the culture media used (Figure 17).

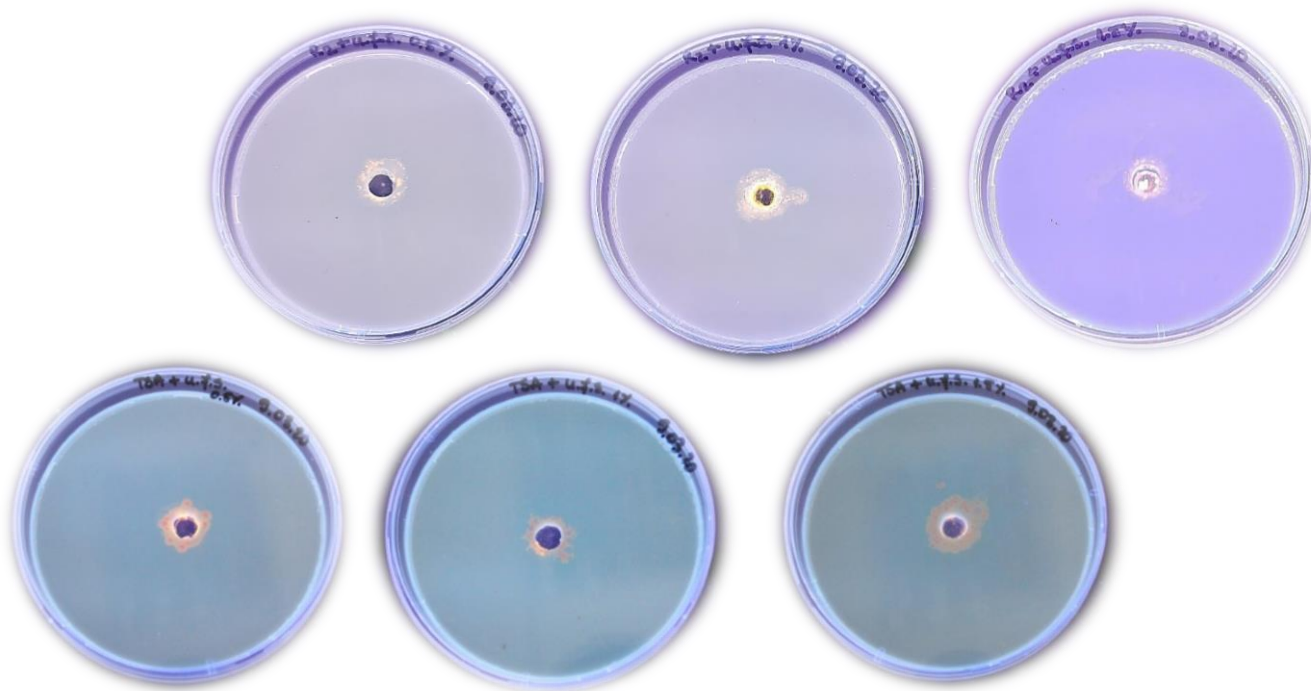


Figure 16. Bacterial growth on R2A (upward), and TSA (downward) media respectively, supplemented with sunflower oil (0.5%, 1%, 1.5%).

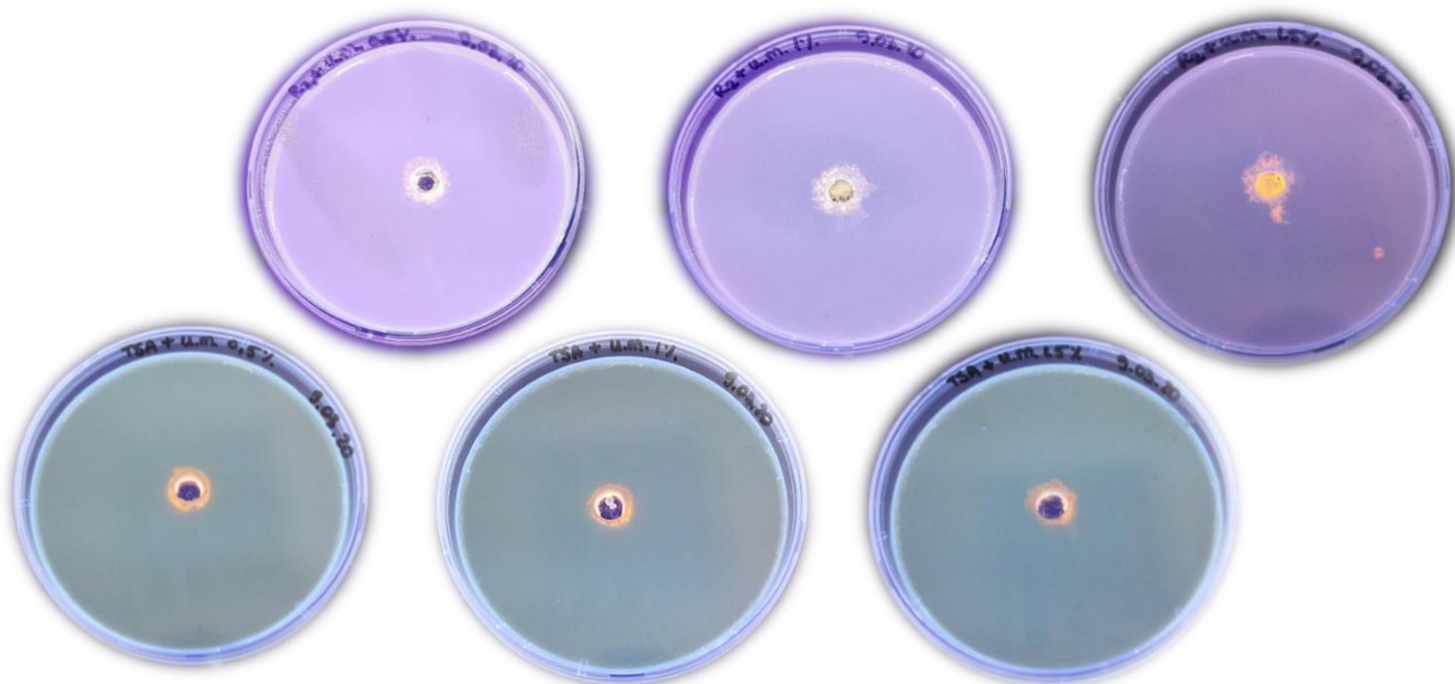


Figure 17. Bacterial growth on R2A (upper) and TSA (lower) culture media supplemented with olive oil (0.5%, 1%, 1.5%)

III. Biocatalyst preparation

III.1. Biocatalyst precipitation

Systematically, the *Psychrobacter* sp. strain was incubated for 3 days at 15°C and fully grown cell colonies are able to produce and extracellularly release proteins into the culture media. As for that, to favour the production of lipases the culture media was initially supplemented with 1% olive oil, as this provides the preferred carbon source for lipolytic hydrolysis.

The culture media is now enriched, assuming the feasible production of extracellular proteins together with lipases of interest. Further, to exclude the intereferents of the media (e.g. nutrients, salts), the total protein was precipitated with 80% acetone, that competes with water molecules linked to the biomolecules, and triggered the precipitation stage. The total protein is obtained as a white powder (Figure 18) and suspended in 100mM TRIS-HCl buffer pH 8.

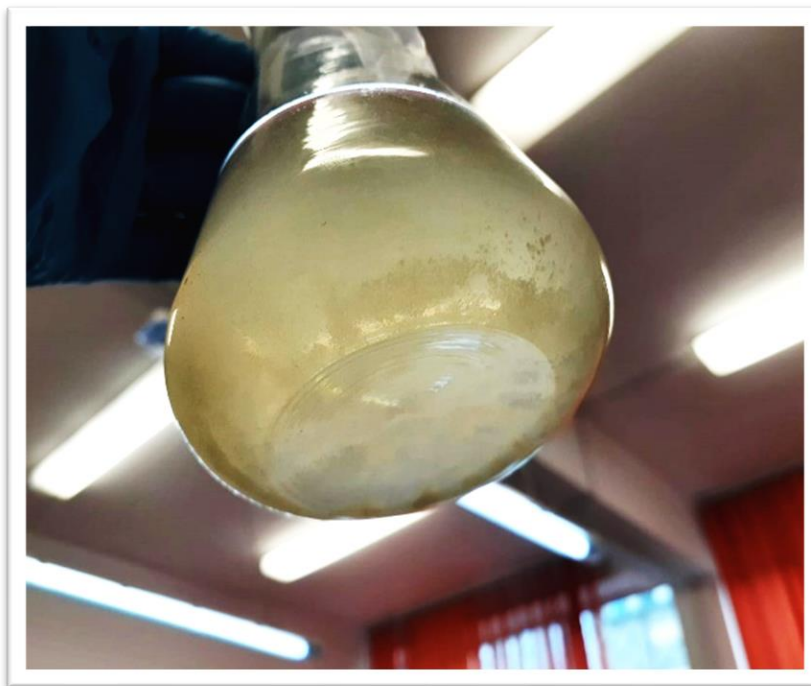


Figure 18. Precipitation of extracellular protein content of *Psychrobacter* sp. culture medium

For the validation of partially purified protein content obtained after extraction with organic solvent, the extract was measured at 280 nm, and the absorbance value was extrapolated on the calibration curve with bovine serum albumin standards, to estimate the concentration (Figure 19). Sample series of protein precipitate were obtained in the range of 5 – 8 mg/mL.

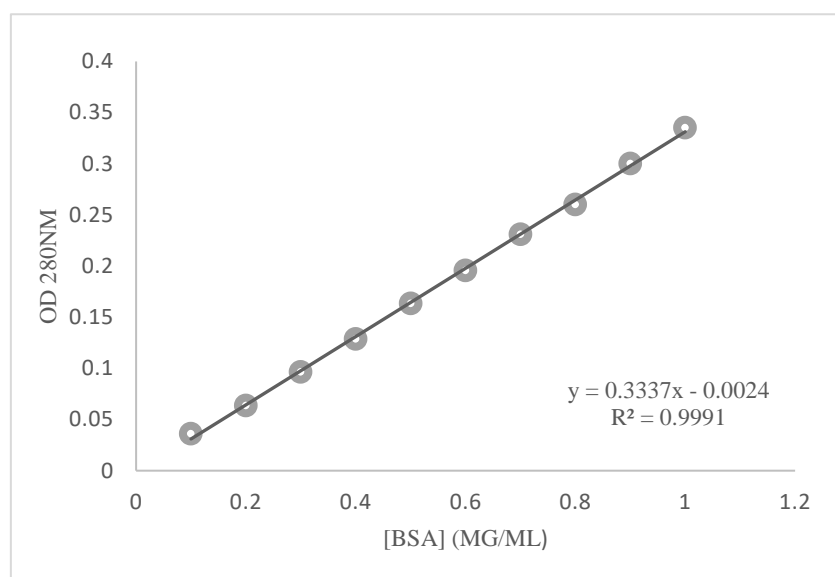


Figure 19. Calibration curve on 0.1 – 1 mg/mL bovin serum albumin (BSA) standards in distilled water.

III.2. Covalent immobilization

III.2.1. Immobilization on modified resin

Covalent immobilization of the enzyme on amino-C₂-methacrylate with glutaraldehyde spacer was firstly performed. The enzyme provides lateral amino groups for linking via -CHO groups, which simultaneously captured the amino groups of the support. After the immobilization procedure, the amount of protein extract left unattached to the support is discriminated by measuring the absorbance of the reaction supernatant, which obviously contains the remained soluble protein fraction. The following performances in Table 11. were obtained after the immobilization procedure:

Table 11. Immobilization capacity of protein extract on amino-C₂-methacrylate.

Starting concentration	Immobilized	Protein loading	Protein recovery
4.96 mg/mL	4.382 mg/mL	41.73 mg protein/g support	88.35%
	4.47 mg/mL	42.33 mg protein/g support	90.12%

As the immobilization results revealed, the reaction in MES buffer was achieved with 90% succes, while for PBS buffered reaction, with 88%. Therefore, good attachment of protein extract on resin beads is accomplished through the above-mentioned protocol (Figure 20.).

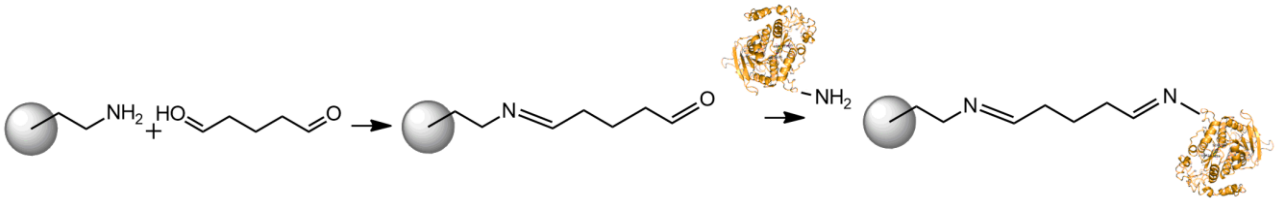


Figure 20. Mechanism of immobilization on amino-C2-metacrylate polymeric beads

III.2.2. Immobilization on magnetic particles

Coated magnetic particles that provide different functional groups on the outer face were tested as supports for the immobilization of the protein extract obtained out of the bacterial culture. There were performed different approaches in the case of the carbodiimide method (Figure 21), the nanosized and microsized magnetic particles with lateral carboxyl groups were diectly treated with EDC activator. A one pot immobilization reaction was also achieved by capturing enzyme carboxyl groups via EDC and linking them further with microsized magnetic beads with lateral amino supply.

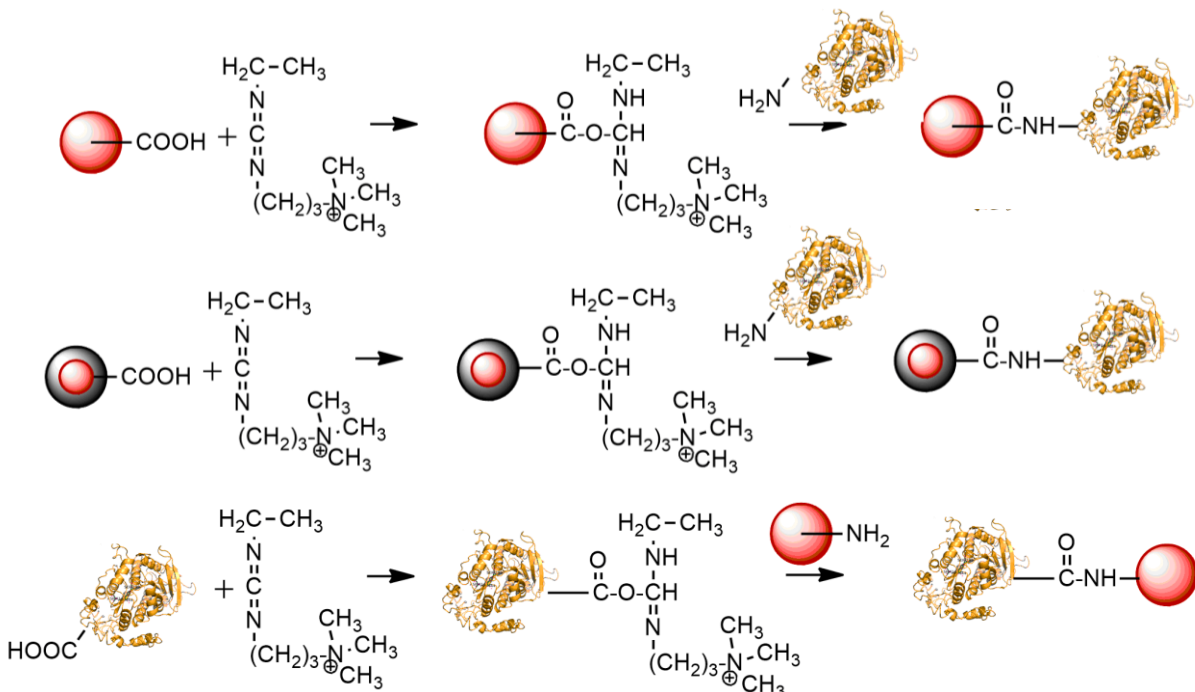


Figure 21. Mechanism of immobilization via carbodiimide methods.

Because the structural analysis agreed to the existence of glycosidic groups for bacterial lipases of classes IV and V, an oxidizing step was introduced prior to immobilization. Sodium periodate targeted the glycosidic groups from lipases and added a plus reactivity by opening the cycle (Figure 22). Magnetic particles providing hydrazine groups ended the immobilization reaction through imine bonds.

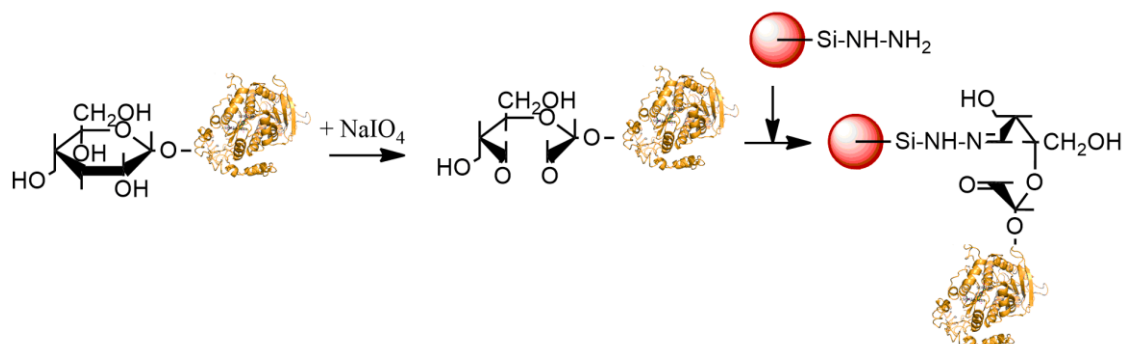


Figure 22. Mechanism of immobilization on Si-MAG-Hydrazine magnetic beads.

The immobilization performance was estimated using UV-analysis at 280 nm against the calibration curve, while the values are listed in Table 12:

Tabel 12. Immobilization capacity of protein extract on different coated magnetic beads.

Starting concentration	Immobilized on			
	Si-MAG-Amine	Si-MAG-Carboxyl	Si-MAG-Hydrazine	Fluid-MAG-ARA
6.6 mg/mL	6.55 mg/mL	6.545 mg/mL	6.53 mg/mL	6.33 mg/mL

The performance of the immobilization is similar regardless of the working protocol chosen or the particle matrix. It could be noted that on micro-sized particles the immobilization went with a few percentages better.

IV. Biocatalyst characterization

IV.1. FT-IR analysis

Diffuse Reflectance Infrared Fourier Transform (DRIFT) spectra were measured for free and immobilized support beads. A minimum amount of sample was diluted with potassium bromide matrix. Amide I band, corresponding to (CO) carbonyl stretching mode of the peptide is present in the region of 1700–1600 cm^{-1} . This band consists of a group of overlapped signals, which contain

information on secondary protein structure of the enzyme. Bands centered at around 1550 cm^{-1} are assignable to the amide II band, which is a out-of-phase combination mode of the NH in plane bend and the CN stretching vibration with smaller contributions from the CO in plane bend and the CC and NC stretching vibrations. Additionally, the peak at 1600 cm^{-1} can be assigned to the asymmetric stretching. Finally, a set of bands can be distinguished in the region of $1400 - 1200\text{ cm}^{-1}$ due to amide III mode. This mode is assigned to the in-phase combination of the NH deformation vibration with CN, with a minor contribution of CO and CC stretching. These polypeptide bands are complex and do not allow a direct correlation with the protein structure mode of carboxylic groups, (COO), of aspartic acid (Asp A.) and/or glutamic acid (Glu A.) in side chain. α -Helices show a strong and characteristic absorption band centered at 1660 cm^{-1} . Additionally, it is also possible to identify a band at 1645 cm^{-1} , which can be assigned to random structures, such as turns and coil specific for cold-active proteins. β -Sheets have two signals at ~ 1635 (intense) and $\sim 1683\text{ cm}^{-1}$ (weak), but not distinguishable in this case. The splitting of the amide I mode in β -sheets structures is a consequence of differences in hydrogen-bridged bonds and the dipole transition coupling. The band at 1683 cm^{-1} may also contain overlapping contributions (i.e. that could not be resolved in our spectra) due to turn structures [49, 50].

It is clear that the immobilization was successfully achieved via covalent linking of the biomaterial to amino- C_2 -metacrylate support given the interferogram (Figure 23). For the immobilized specimen, the specific bands of amide I and II around $1600 - 1700\text{ cm}^{-1}$ are well distinguished, as coming from the peptide bonds provided by the protein. The support, as being a crosslinking metacrylate polymer with amino- disposable groups, has a specific band at 1730 cm^{-1} as C=O stretching carboxyl for methacrylate, as well as 2 peaks between 3300 and 3500 cm^{-1} signing for primary amino groups projecting out by the outer face of the polymer.

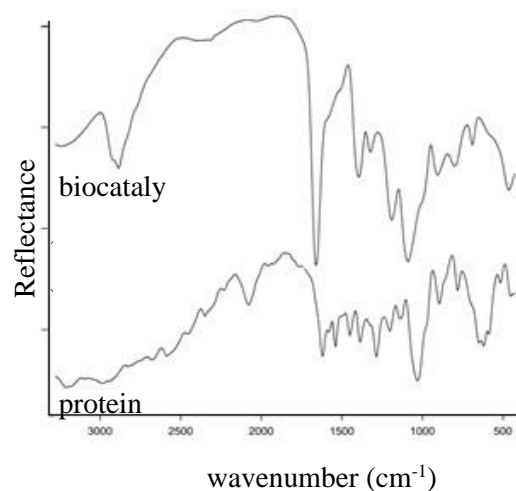


Figure 23. DRIFT spectra of protein and MTC-NH₂ biocatalyst.

FTIR spectra of magnetite exhibit two strong infrared absorption bands at 570 and 390 cm^{-1} . According to Ishii and Nakahira, these bands can be assigned to the Fe–O stretching mode of the tetrahedral and octahedral sites (the band at 570 cm^{-1}) and to the Fe–O stretching mode of the octahedral sites (the band at 390 cm^{-1}). Maghemite, a defective form of magnetite, has absorption bands at 630, 590 and 430 cm^{-1} [51]. The strong asymmetrical band at 578 cm^{-1} characteristic to Fe–O stretching vibrations includes also the Fe–OH vibration band located at 630 cm^{-1} and possible Fe–O vibration bands of maghemite (635 cm^{-1}) [51].

Important to be considered is that for the immobilization performance, the bands for amide I, II and III are evidenced, while specific sharp peaks are located in the low wavenumber region for the support evidence (Figure 24 – 27). In biological materials and protein spectra, large bands in the region of large wavenumbers are clearly related to OH stretching groups, as the water traces could not be overcome.

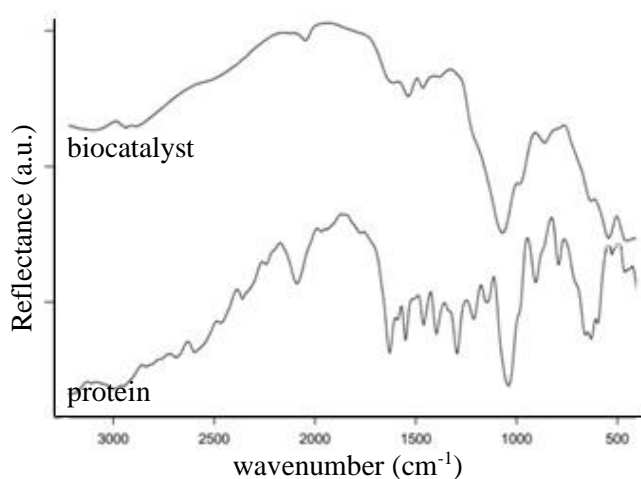


Figure 24. DRIFT spectra of protein and sMP-NH-NH₂ bc.

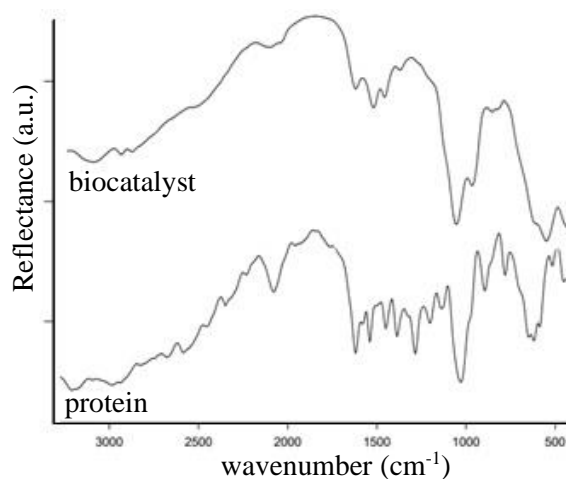


Figure 25. DRIFT spectra of protein and sMP-NH₂ bc.

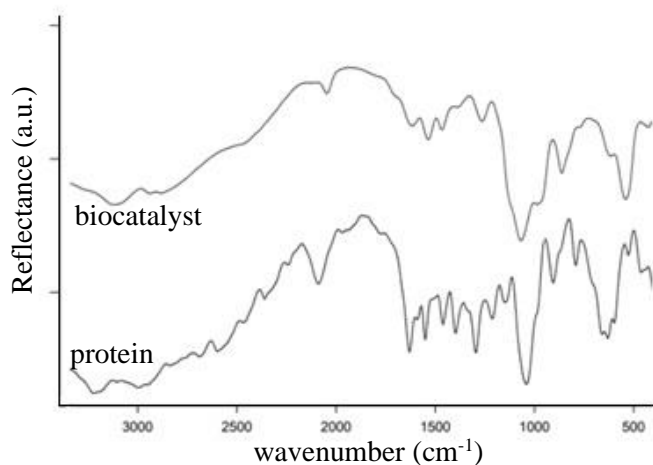


Figure 26. DRIFT spectra of protein and fMP-COOH bc.

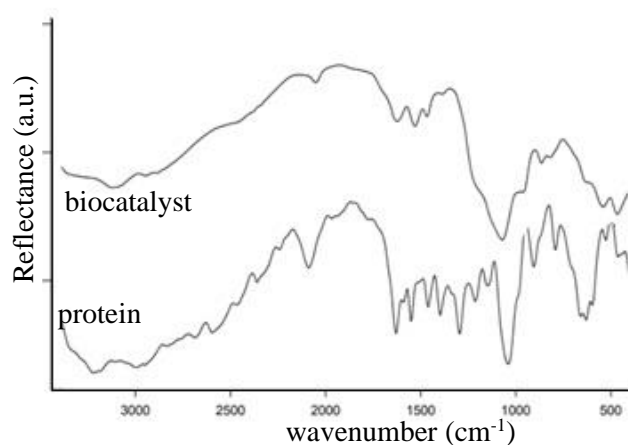


Figure 27. DRIFT spectra of protein and sMP-COOH bc.

IV.2. SEM analysis

The following micrographs were performed by Surface Electron Microscopy on biocatalyst specimens to highlight the immobilization of the protein content on the functionalized surface of the support particles. The appearance of magnetic particles is defined and characteristically crystallized for magnetite and maghemite. In the case of the free support based on methacrylate polymer, the beads have a clear, smooth aspect. The analysis of the immobilized specimen intervenes with the change in the morphology of the magnetic crystals or in the smoothness of the resin beads. A lighter contrast highlights the protein deposits that adhere covalently to the support surface. The analysis involved *a priori* metallization with gold (Figure 28 – 32).

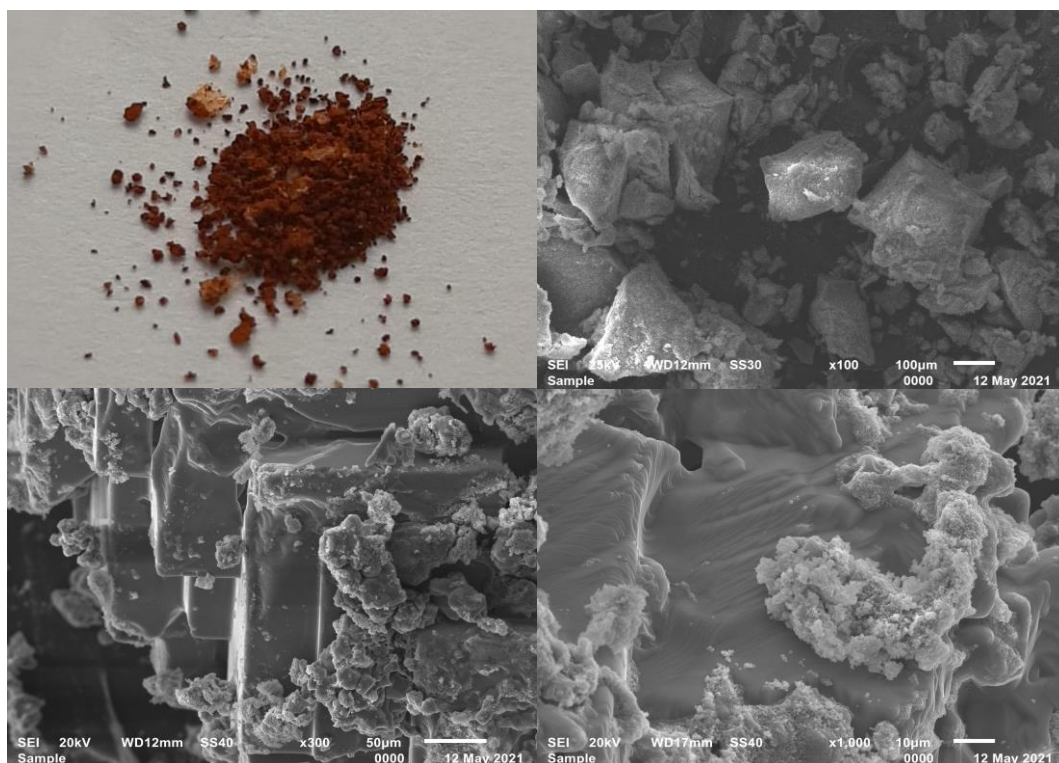


Figure 28. A. Real evidence of SMP-COOH material. SEM micrographs: B. Free support, C. Immobilized-protein support (50 μm), D. Immobilized-protein support (10 μm).

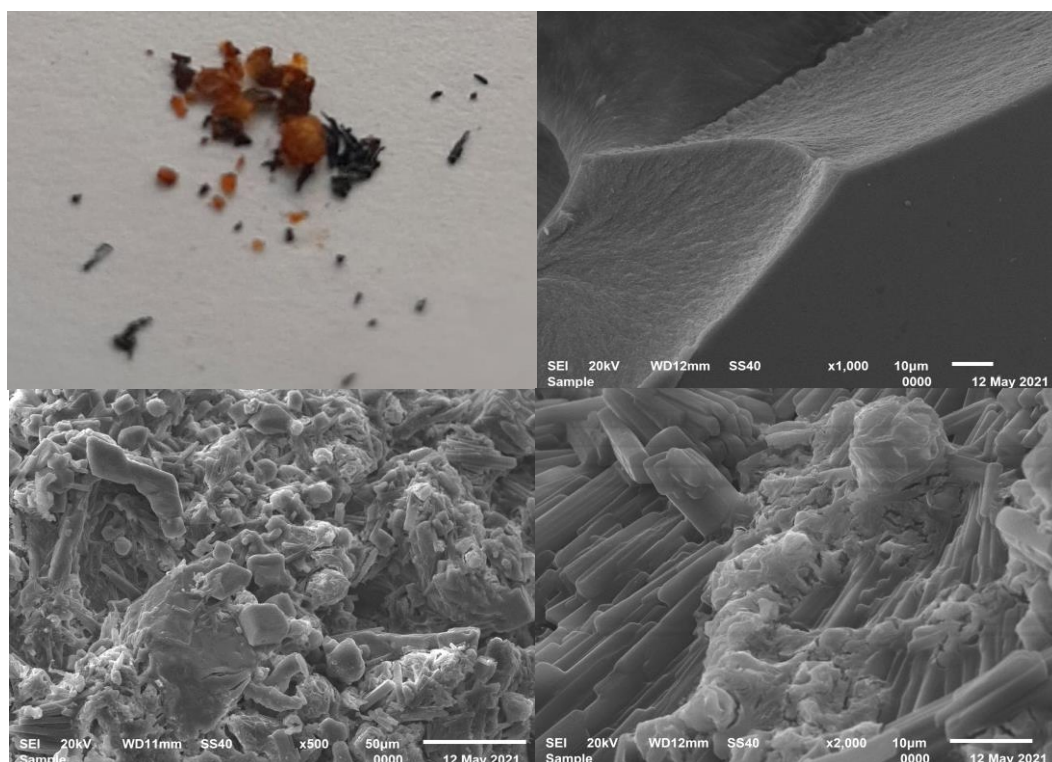


Figure 29. A. Real evidence of fMP-COOH material. SEM micrographs: B. Free support, C. Immobilized-protein support (50 μm), D. Immobilized-protein support (10 μm).

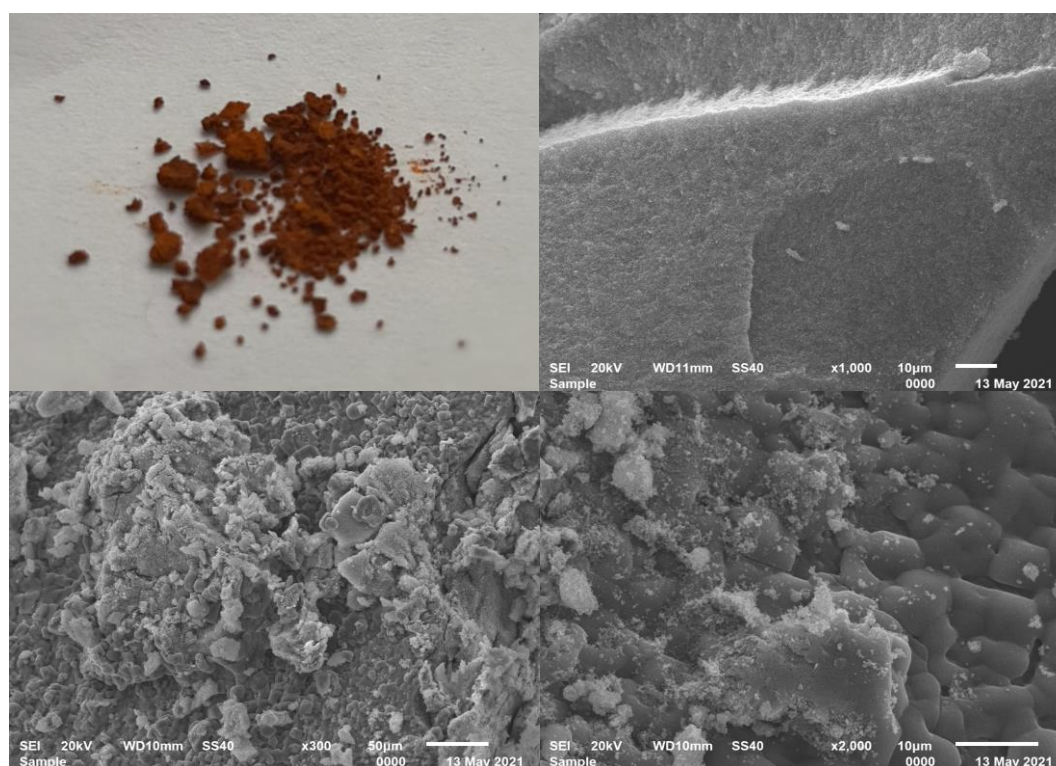


Figure 30. A. Real evidence of sMP-NH₂ material. SEM micrographs: B. Free support, C. Immobilized-protein support (50 μm), D. Immobilized-protein support (10 μm)

C.

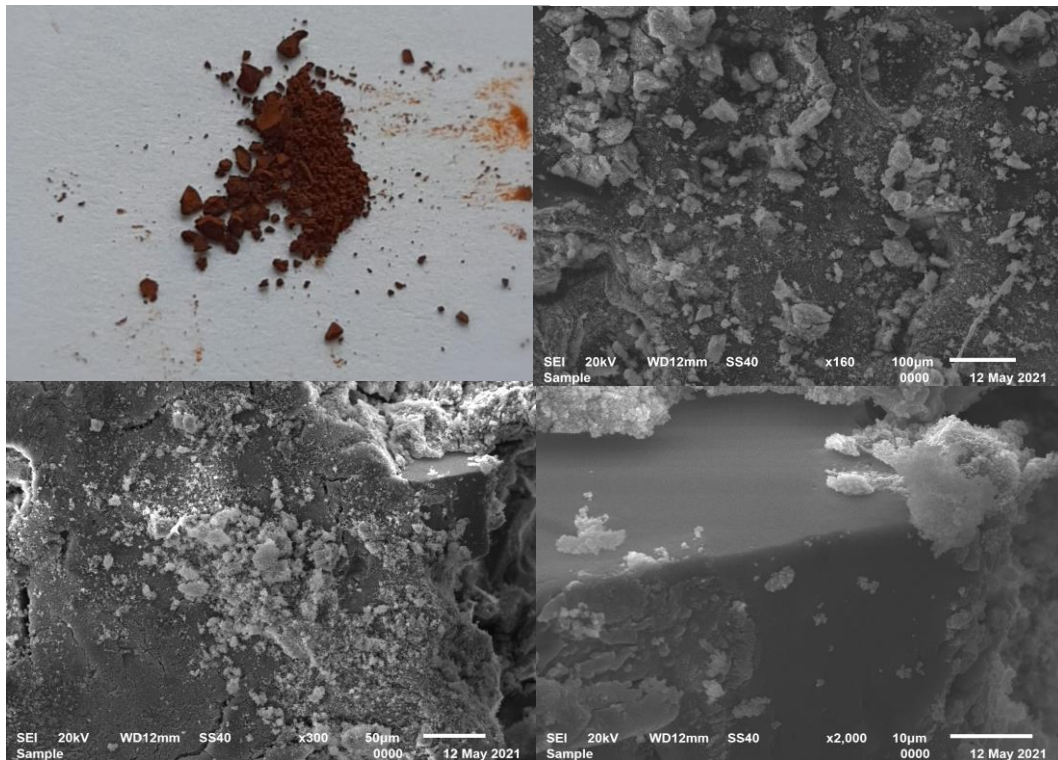


Figure 31. A. Real evidence of sMP-NH- NH₂ material. SEM micrographs: B. Free support, C. Immobilized-protein support (50 μm), D. Immobilized-protein support (10 μm)

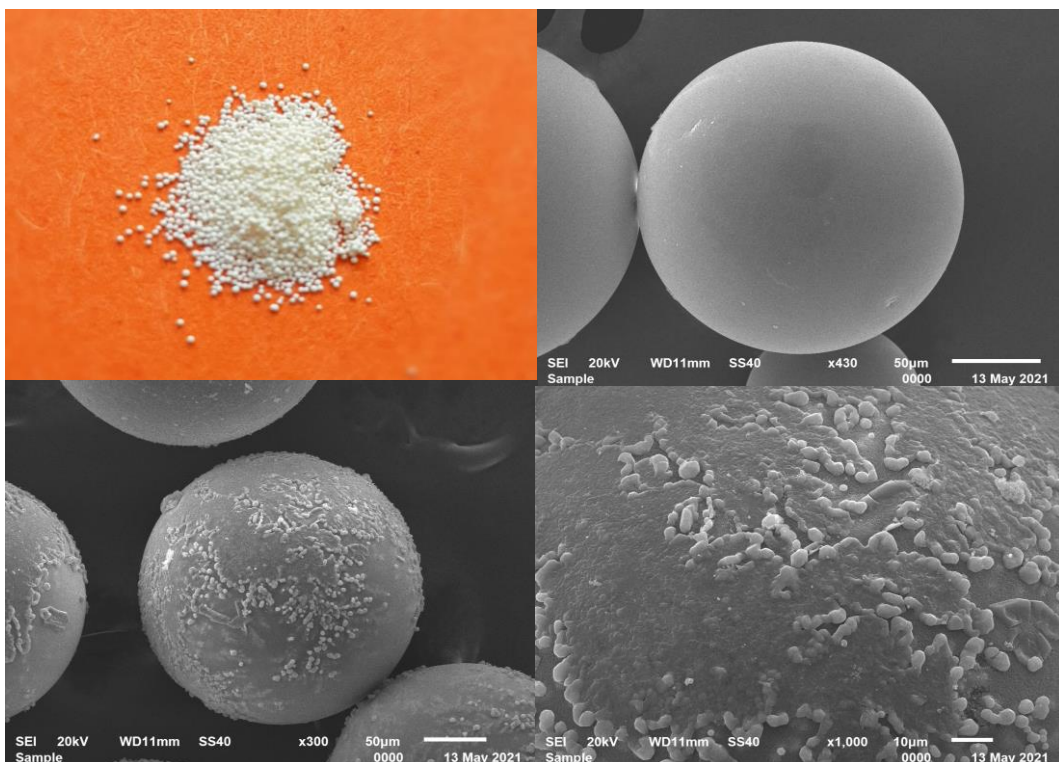


Figure 32. A. Real evidence of MTC- NH₂ material. SEM micrographs: B. Free support, C. Immobilized-protein support (50 μm), D. Immobilized-protein support (10 μm)

IV.3. Enzyme activity

The system for lipase activity implies the formation of fatty acids in an aqueous solution, as in other terms a not clear, but a dispersed solution is continuously formed during the enzymatic reaction. For this reason, a discontinuous kinetics is approved in the literature for measuring the lipase activity, as the formation of acid product is measured after 30 minutes, and activity is reported in terms of concentration per min against the calibration curve obtained with different known substrate concentrations (Figure 33). Moreover, the classical pathway for hydrolysis happened at 37°C, while in this study the reaction at 25°C was introduced to evaluate the cold-active character of lipases.

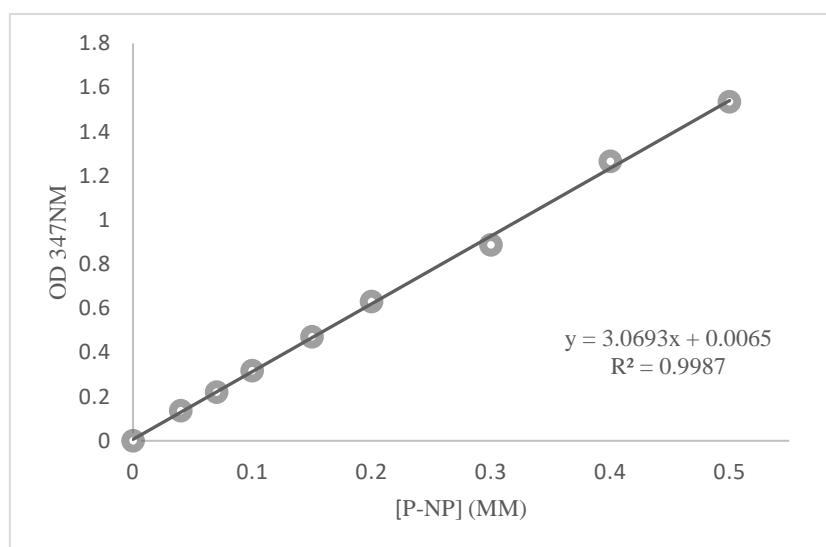


Figure 33. Calibration curve on 0 – 0.5 mM p-nitrophenol standards in ethanol.

On the p-nitrophenol butyrate substrate of different concentrations, activity measurements were performed according to the protocol. By plotting Lineweaver-Burk were calculated the kinetic constants K_m and V_{max} , and particularly k_{cat} , for two reaction temperatures (Figure 34). According to the K_m values, the cold-active character of the lipases is maintained with the increase of the temperature by up to 15 degrees in addition, compared to the optimum T estimated at 25°C, without substantial changes of the characteristic lipolytic activity. In the case of the catalytic constant, similar values are recorded for both temperatures.

Catalytic efficiency was calculated as the ratio between k_{cat} / K_m . The close values of the ratio for both temperatures support the structural and functional stability of the proteinaceous material. An at least interesting observation is in the case of the specimen immobilized on magnetic nanoparticles, where the catalytic efficiency proves to be the most promising.



Figure 34. Lipolytic activity for all biocatalysts on p-nitrophenyl butyrate substrate.

V. Biocatalyst performance

V.1. Design of the biocatalytic system

The biocatalytic system was composed based on the main idea on which the thesis is founded, namely, the valorization of silymarin. Starting from one of the most biologically active compounds of silymarin, e.g., silybin, esterification reactions were directed to its hydroxyl groups of aromatic and alcoholic origin. Experiments were performed both with fatty acids (octanoic acid, oleic acid) for esterification reaction, but also with fatty acid esters (methyl decanoate, methyl laurate, methyl myristate, methyl palmitate) via transesterification. A useful comparison could be outlined by using the free and immobilized protein material involved in catalyzing the reaction. Given the origin of the protein extract from the extremophilic strain of *Psychrobacter* sp., the reaction temperature was set to 25°C.

Given the HPLC-DAD analysis, unreacted substrates were constantly identified against standards as having the following retention times: silybin at 2.4 minutes, octanoic acid at 2.9 minutes, oleic acid at 3.7 minutes, methyl decanoate at 3.1, methyl laurate at 3.3, methyl myristate at 3.7,

methyl palmitate at 4.1 minutes, respectively. The process performance was related to each calculated value obtained in terms of substrate conversion for every synthesis, by using the well-know formula:

$$C(\%) = \frac{\text{mass of converted silybin}}{\text{initial mass of silybin}} \cdot 100$$

V.2. Optimization of system parameters

Raw culture media vs. Protein precipitate

The culture medium contains multiple interferences that imprint nonspecific peaks on the control chromatograms for the reaction of interest. At the same time, the culture medium was supplemented with 1% olive oil to increase the extracellular lipase production, and this may work towards side reaction of hydrolysis or synthesis from the oil supplement. The protein precipitate rises to the desired performance, with a good differentiation of the product peaks and unreacted substrate.

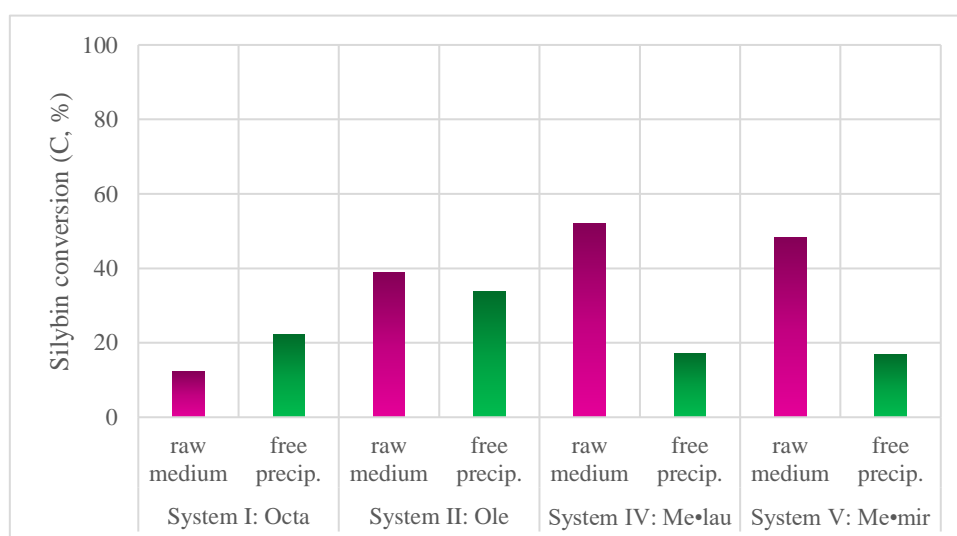


Figure 35. System performance in terms of silybin conversion by using raw culture media vs. protein precipitate.

Free biocatalyst performance at 25°C or 40°C

Knowing that the biocatalyst is cold-active, its catalytic potential is expected to be at low temperatures. However, the results in terms of substrate conversion involve higher values at 40°C. One possible explanation is that the lipase biocatalyst is stable even with increasing temperature, having considerable residual catalytic activity. At the same time, the esterification reaction may be stimulated by the increase of temperature and esters could be formed uncatalyzed. For this reason and for the evaluation of the biocatalyst at its potential, the system temperature remains settled at 25°C.

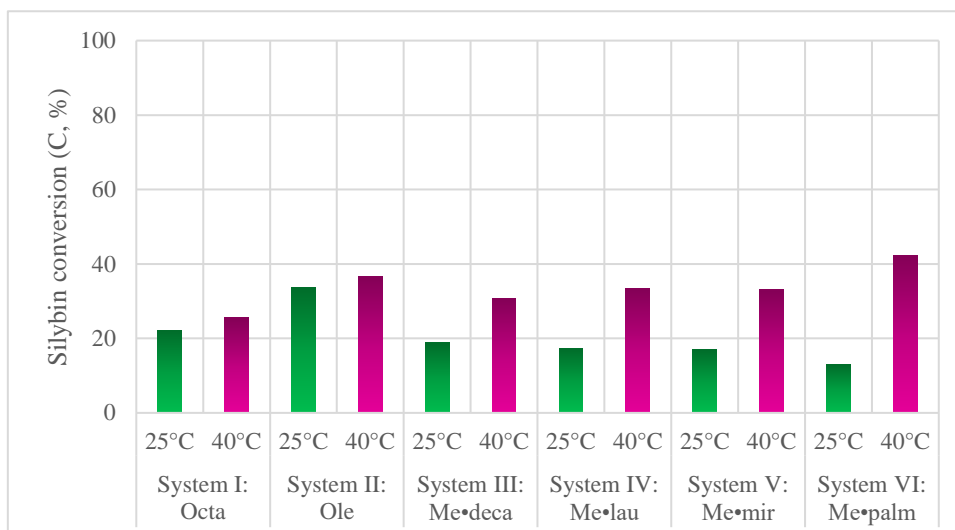


Figure 36. System performance in terms of silybin conversion by using different temperature with free biocatalyst

Immobilized biocatalyst at 25°C or 40°C

An increased performance of the biocatalytic system is desired to support the esterification of silybin and to contribute to the improvement of the liposolubility properties of silymarin. Preliminary testing of the immobilized biocatalytic material involved the use of the support based on polymer resin at 2 temperatures. It is observed that the cold-active potential of the proteinaceous material is supported by its immobilization, as lipases tend towards an increased catalytic activity when adhere between two heterogeneous media, in this case the support and the liquid medium of the reaction. At the same time, for the temperature of 25°C, the best conversion values are obtained, another evidence of the cold-active catalytic character storage.

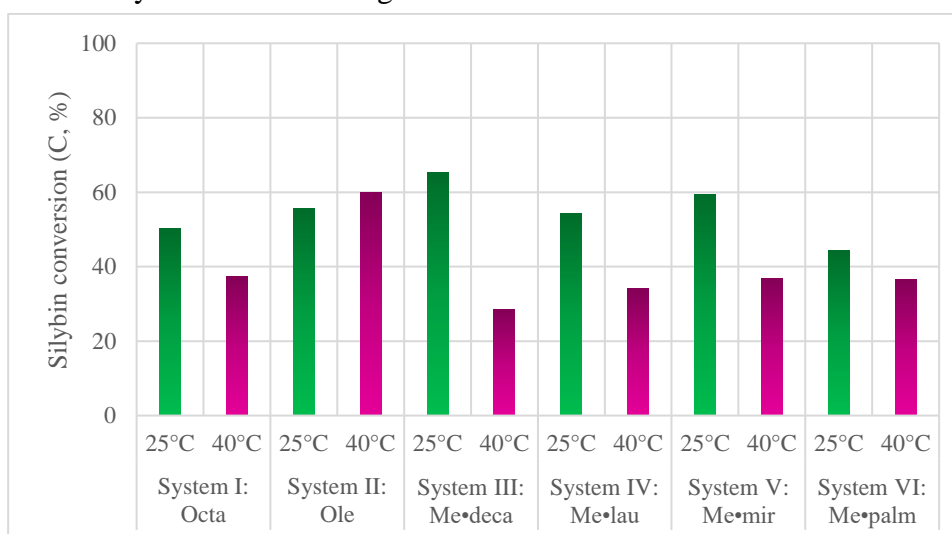


Figure 36. System performance in terms of silybin conversion by using different temperature with MTC-NH₂ immobilized biocatalyst.

V.3. Evaluation of the biocatalysts

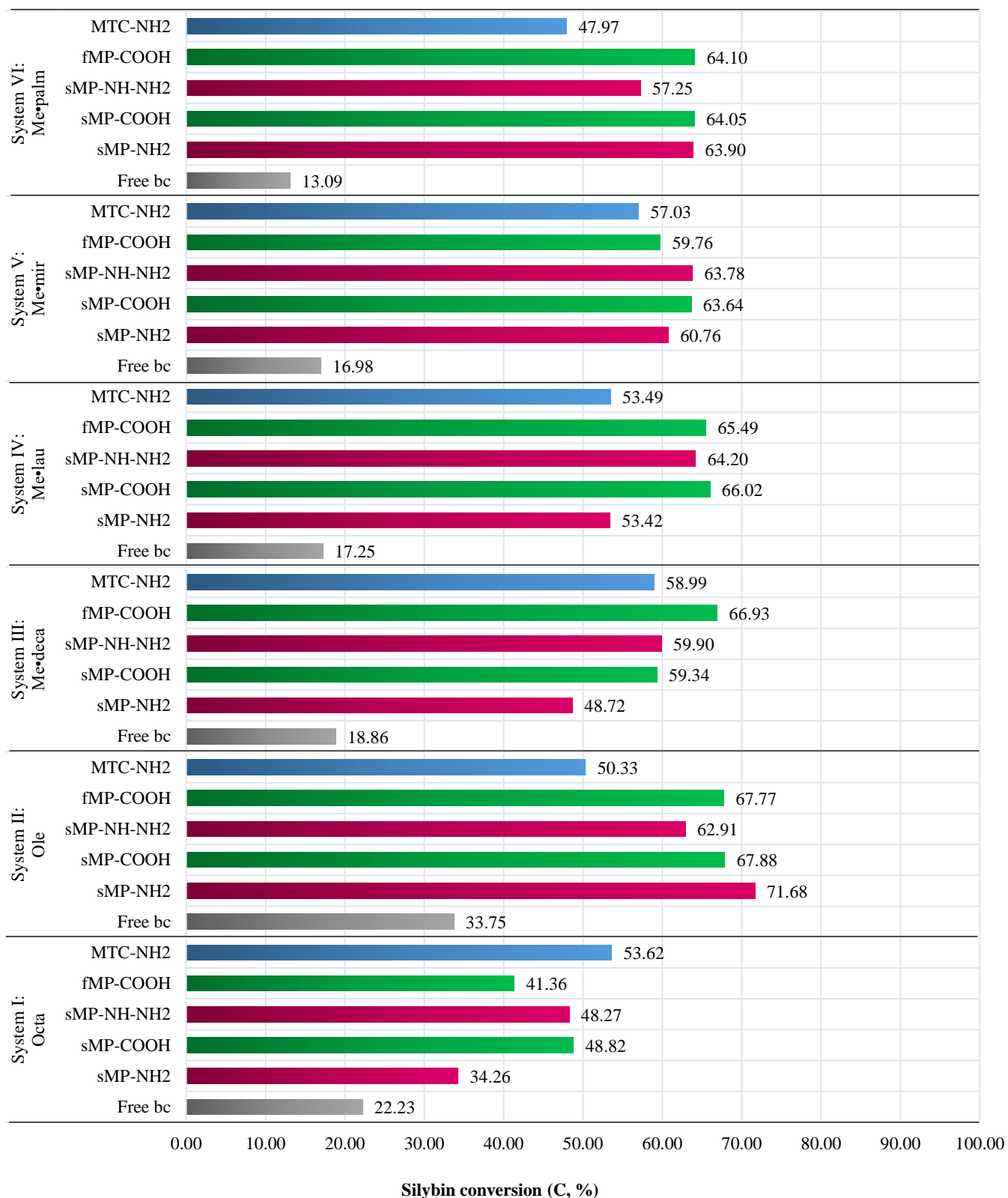


Figure 37. System performance in terms of silybin conversion for every biocatalyst specimen

Following the screening performed on the biocatalytic systems proposed for the esterification of silybin with different fatty acids, 3 questions arise:

- a) Why does the free biocatalyst have a lower performance than the immobilized biocatalyst?
- b) Why after immobilization the lipases adhering to the support show an improved catalytic activity?
- c) What is the most promising immobilized biocatalyst for the esterification process?

With these nuances in mind, one could evade very useful observations and information.

In the case of the free biocatalyst, the performance range in terms of substrate conversion varies between 13 and 34%. The conversion values decrease in the case of the free biocatalyst, with the increase of the hydrocarbon chain of the acylating agent: 34% for the oleic acid system, 13% for the methyl palmitate system. It is true that being a total protein content embedded generically in the free biocatalyst, steric hindrances are a risky factor in achieving the synthesis, the lipase catalytic lid being restricted by the neighboring interactions.

In the case of the immobilized biocatalyst, the performance range varies between 41 and 66%. There is no decisive trend for the behavior of immobilized biocatalysts, but a first important observation is based on a catalytic activity improved by several tens of percent compared to the free biocatalyst. Thus, by immobilization even though covalent, protein stability is sustained. It is approved in the scientific community that lipases have an unusual behavior, but very beneficial when they are found at the interface between two different environments. Most studies are based on interfacial activation between organic and aqueous medium. In the present case, the heterogeneity of the system is given by the immobilized form and the liquid reaction medium.

A second observation correlated with the immobilized biocatalyst is given by the increased biocatalytic potential in a constant trend with the increase of the hydrocarbon chain coming from the acylating agent. Basically, the protein conformation sustained by immobilization allows the facial reception of the substrate at the catalytic site.

It is easy to notice that the immobilized catalysts have similar performance values, considering the functionality of each support and the immobilization method used, for each individual biocatalytic system. Thus, there is no major difference that can serve as a conclusion for a particular biocatalyst. However, globalizing this study, values of 65% (excluding the octanoic acid system) were obtained with the biocatalyst based on nanoparticle support.

CONCLUSIONS

REFERENCES

- [1]. Flora, K., Hahn, M., Rosen, H., Benner, K., *Milk Thistle (Silybum marianum) for the Therapy of Liver Disease*. AJG, 93 (1998), 139-143.
- [2]. Duran, D., Otles, S., Karasulu, E., *Determination Amount of Silymarin and Pharmaceutical Products from Milk Thistle Waste Obtained from Cold Press*. Acta Pharmaceutica Scientia, 57 (2019), 85-101.
- [3]. Begum, S. A., Sahai, M., Ray, A. B., *Non-conventional Lignans: Coumarinolignans, Flavonolignans, and Stilbenolignans*, Springer-Verlag/Wien, 2010, Chapter 3. Flavonolignans, pg. 29-48.
- [4]. Csupor, D., Csorba, A., Hohmann, J., *Recent advances in the analysis of flavonolignans of Silybum marianum*. Journal of Pharmaceutical and Biomedical Analysis, 130 (2016), 301-317.
- [5]. Vastalova, J., Tinkova, E., Biedermann, D., Kosina, P., Ulrichova, J, Svobodova, A.R., *Skin Protective Activity of Silymarin and its Flavonolignans*. MDPI Journal- Molecules, 24 (2019), 1022.
- [6]. Di Costanzo, A., Angelico, R., *Formulation Strategies for Enhancing the Bioavailability of Silymarin: The State of the Art*. MDPI Journal-Molecules, 24 (2019), 2155.
- [7]. Drouet, S., Doussot, J., Garros, I., Mathiron, D., Bassard, S., Favre-Reguillon, A., Molinie, R., Laine, E., Hano, C., *Selective Synthesis of 3-O-Palmitoyl-Silybin, a New-to-Nature Flavonolignan with Increased Protective Action against Oxidative Damages in Lipophilic Media*. MDPI Journal-Molecules, 23 (2019), 2594.
- [8]. Theodosiou, E., Purchartova, K., Stamatis, H., Kolisis, F., Kren, V., *Bioavailability of silymarin flavonolignans: drug formulations and biotransformation*. Phytochem Rev, (2013).
- [9]. Fidrus, E., Ujhelyi, Z., Feher, P., Hegedus, C., Janka, E. A., Paragh, G., Vasa, G., Bacskay, I., Remenyik, E., *Silymarin: Friend or Foe of UV Exposed Keratinocytes?*, MDPI-Molecules, 24 (2019), 1652.
- [10]. Chambers, C.S., Biedermann, D., Valentova, K., Petraskova, L., Viktorova, J., Kuzma, M., Kren, V., *Preparation of Retinoyl-Flavonolignan Hybrids and Their Antioxidant Properties*. MDPI Journal-Antioxidants, 8 (2019), 236.
- [11]. Duan, L., Carrier, D.J., Clausen, E.C., *Silymarin Extraction from Milk Thistle Using Hot Water*. Applied Biochemistry and Biotechnology, 113-116 (2004)

- [12]. Bijak, M., *Silybin, a Major Bioactive Component of Milk Thistle (Silybum marianum L. Gaernt.)-Chemistry, Bioavailability, and Metabolism*, MDPI-Molecules, 22 (2017), 1942.
- [13]. Tufvesson, P., Fu, W., Jensen, J. S., Woodley, J. M., *Process considerations for the scaleup and implementation of biocatalysis*, Food and Bioproducts Processing, 88 (2010) 3-11.
- [14]. Tufvesson, P., Lima-Ramos, J., Nordblad, M., Woodley, J. M., *Guidelines and Cost Analysis for Catalyst Production in Biocatalytic Processes*, Organic Process Research & Development, 15 (2011) 266-274.
- [15]. Santacoloma, P. A., Sin, G., Gernacy, K., V., Woodley, J. M., *Multienzyme-Catalyzed Processes: Next-Generation Biocatalysis*, Organic Process Research & Development, 15 (2011) 203-212.
- [16]. Santiago, M., Ramirez-Sarmiento, C.A., Zamora, R.A., Parra, L.P., *Discovery, Molecular Mechanisms and Industrial Applications of Cold-Active Enzymes*. Frontiers in Microbiology, 7 (2016), 1408.
- [17]. Brenchley, JE, *Psychrophilic microorganisms and their cold-active enzymes*, Journal of Industrial Microbiology, 17 (1996), 432-437.
- [18]. Mangiagalli, M., Brocca, S., Orlando, M., Lotti, M., *The cold revolution. Present and future applications of cold-active enzymes and ice-binding proteins*. New Biotechnology, 55 (2020), 5-11.
- [19]. Hackett, E. S., Twedt, D.C., Gustafson, D.L., *Milk Thistle and Its Derivative Compounds: A review of opportunities for Treatment of Liver Disease*, J Vet Intern. Med., 27 (2013), 10-16.
- [20]. Cavicchioli, R., Siddiqui, K., Andrews, D., Sowers, K. R., *Low-temperature extremophiles and their applications*, Current Opinion in Biotechnology, 13 (2002), 253-261.
- [21]. Kovacic, F., Babic, N., Krauss, U., Jaeger, K.E., *Classification of Lipolytic Enzymes from Bacteria*. Research Gate, (2019).
- [22]. Konwar, B.K., Sagar, K., *Lipase. An Industrial Enzyme Through Metagenomics*, Apple Academic Press, NJ, 2018, Chapter 1.6. Classification of Bacterial Lipolytic Enzymes, pgs. 16-20.
- [23]. Kavitha, M., *Cold active lipases-an update*, Frontiers in Life Science, 2016.
- [24]. Gandhi, N. N., Patil, N., Sawant, S. B., Joshi, J. B., Wangikar, P. P., Mukesh, D., *Lipase-Catalyzed Esterification*, Catal. Rev.- Sci. Eng., 42 (2000), 439-480.

- [25]. De Maria, P., D., Carboni-Oerlemans, C., Tuin, B., Bargeman, G., van der Meer, A., van Gemert, R., *Biotechnological applications of Candida antarctica lipase A: State-of-the-art*, Journal of Molecular Catalysis B: Enzymatic, 37 (2005), 36-46.
- [26]. Stergiou, P.-Y., Foukis, A., Filippou, M., Koukouritaki, M., Parapouli, M., Theodorou, L. G., Hatziloukas, E., Afendra, A., Pandey, A., Papamichael, E. M., *Advances in lipase-catalyzed esterification reactions*, Biotechnology Advances (2013).
- [27]. Spector, A. A., *Essentiality of Fatty Acids*, Lipids, 34 (1999), 51-53.
- [28]. Lawrence, G. D., *The Fats of Life. Essential Fatty Acids in Health and Disease*, Rutgers University Press, 2010, Chapter 2, 15-20.
- [29]. Das, U. N., *Essential fatty acids: biochemistry, physiology and pathology*, Biotechnol. J., 1 (2006), 420-439.
- [30]. Lee, C.W., Jang, S.H., Chung, H.S., *Improving the Stability of a Cold-Adapted Enzymes by Immobilization*. MDPI Journal-Catalysts, 7 (2017), 112.
- [31]. Vaghari, H., Jafarizadeh-Malmiri, H., Mohammadlou, M., Berenjian, A., Anarjan, N., Jafari, N., Nasiri, S., *Application of magnetic nanoparticles in smart enzyme immobilization*, Biotechnol. Lett., 38 (2016), 223-233.
- [32]. Xie, W., Ma, N., *Enzymatic transesterification of soybean oil by using immobilized lipase on magnetic nano-particles*, Biomass and Bioenergy, 34 (2010), 890-896.
- [33]. Gasteiger, E., Hoogland, C., Gattiker, A., Duvaud, S., Wilkins, M.R., Appel, R.D., Bairoch, A., *The Proteomics Protocols Handbook*, Humana Press Inc., Totowa, NJ, 2005, Chapter 52. Protein Identification and Analysis Tools on the ExPASy Server, pgs. 571-607.
- [34]. Needleman, S.B., Wunsch, C.D., *A general method applicable to the search for similarities in the amino acid sequence of two proteins*, J. Mol. Biol. (1970), 48(3):443-53.
- [35]. Sievers, F., Wilm, A., Dineen, D., Gibson, T.J., Karplus, K., Li, W., Lopez, R., McWilliam, H., Remmert, M., Söding, J., Thompson, J.D., Higgins D.G., *Fast, scalable generation of high-quality protein multiple sequence alignments using Clustal Omega*, Mol. Syst. Biol. (2011), 7:539.
- [36]. Ashok Kumar, T., *CFSSP: Chou and Fasman Secondary Structure Prediction server*, Wide Spectrum: Research Journal (2013), 1(9):15-19.
- [37]. Yang, J., Yan, R., Roy, A., Xu, D., Poisson, J., Zhang, Y., *The I-TASSER Suite: Protein structure and function prediction*. Nature Methods (2015), 12(1):7-18.
- [38]. Juni, E., *The Prokaryotes*, Springer Science+Business Media, New York, 1992, Chapter 174. The Genus Psychrobacter, pgs. 3242-3246.

- [39]. Kouker, G., Jaeger, K.E., *Specific and Sensitive Plate Assay for Bacterial Lipases*, Applied and Environmental Microbiology (1987), 53: 211-213.
- [40]. Ramnath, L., Sithole, B., Goviden, R., *Identification of lipolytic enzymes isolated from bacteria indigenous to Eucalyptus wood species for application in the pulping industry*. Biotechnology Reports (2017), 15:114-124.
- [41]. Illanes, A., *Enzyme Biocatalysis*, Springer, 2008, Cap. 6.3. Chimioselektive Esterifikation of Wood Sterols with Lipases, pg. 292-308.
- [42]. Neagu, S., Preda, S., Anastasescu, C., Zaharescu, M., Enache, M., Cojoc, R., *The functionalization of silica and titanate nanostructures with halotolerant proteases*, Rev. Roum. Chim., 59 (2014), 97-103.
- [43]. Lite, C., Ion, S., Tudorache, M., Zgura, I., Galca, A., C., Enache, M., Maria, G., M., Parvulescu, V.I., *Alternative lognopolymer-based composites useful as enhanced functionalized support for enzymes immobilization*, Catalysis Today, In press (2020).
- [44]. Xuezheng, L., Shuoshuo, C., Guoying, X., Shuai, W., Ning, D., Jihong, S., *Cloning and heterologous expression of two cold-active lipases from the Antarctic bacterium Psychrobacter sp.* G. Polar Research (2010), 29:421-429.
- [45]. Novototskaya-Vlasova, K., Petrovskaya, L., Yakimov, S., Gilichinsky, D., *Cloning, purification and characterization of a cold-adapted esterase produced by Psychrobacter cryohalolentis K5T from Siberian cryopeg*. FEMS Microbiol Ecol (2012), 2:1-9.
- [46]. Santiago, M., Ramirez-Sarmiento, C.A., Zamora, R.A., Parra, L.P., *Discovery, Molecular Mechanisms and Industrial Applications of Cold-Active Enzymes*. Frontiers in Microbiology, 7 (2016), 1408.
- [47]. Mondini, A., Necula-Petrareanu, G., Pauna, V.I., Iancu, L., Purcarea, C., *Cold adaptation mechanisms of Aspartate Transcarbamoylase from Glaciibacter superstes, an arctic psychrophilic bacterium*. Rom. J. Biol.-Plant Biol. (2019), 64: 19-30.
- [48]. Bosshard, H.R., Marti, D.N., Jelesarov, I., *Protein stabilization by salt bridges: concepts, experimental approaches and clarification of some misunderstandings*, J. Mol. Recognit. (2004), 17: 1-16.
- [49]. Collins, S., E., Lasalle, V., Ferreira, M., L., *FTIR-ATR characterization of free Rhizomucor meihei lipase (RML), Lipozyme RM IM and chitosan-immobilized RML*, Journal of Molecular Catalysis B: Enzymatic, 72 (2011), 220-228.
- [50]. Barth, A., *Infrared spectroscopy of proteins*, Biochimica et Biophysica Acta, 1767 (2007), 1073-1101.
- [51]. Stoia, M., Istrate, R., Pacurariu, C., *Investigation of magnetite nanoparticles stability in air by thermal analysis and FTIR spectroscopy*, J Therm Anal Calorim, 125 (2016), 1185-1198.

ANNEX 1

The taxonomic codes corresponding to each protein sequence in each homologous microorganism, according to GenBank.

Homologs	Lipase 2_65A.3 taxid	Lipase 3_65A.3 taxid
<i>Psychrobacter sp. G</i>	WP_020444543.1	WP_020442424.1
<i>Glaciibacter superstes</i>	WP_026851928.1	WP_022887568.1
<i>Moritella sp. PE36</i>	WP_043994174.1	WP_006031208.1
<i>Escherichia coli</i>	WP_153671715.1	WP_153670496.1
<i>Pseudomonas aeruginosa</i>	WP_003148542.1	WP_070333250.1
<i>Stenotrophomonas maltophilia</i>	WP_043400862.1	KAF1051810.1

ANNEX 2

The proportion of amino acids for each protein sequence corresponding to each microorganism homologous to the sequence of Lipase 2 from *Psychrobacter SC65A.3*.

Amino acid (%)	<i>Psychrobacter SC65A.3. Lipase 2</i>	<i>Glaciibacter superstes</i>	<i>Moritella sp. PE36</i>	<i>Escherichia coli</i>	<i>Pseudomonas aeruginosa</i>	<i>Stenotrophomonas maltophilia</i>
Ala (A)	8.3	15.0	5.6	12.7	13.4	15.6
Arg (R)	3.1	5.6	4.9	7.1	6.9	4.9
Asn (N)	4.1	1.9	3.0	0.9	0.6	1.3
Asp (D)	6.6	6.9	5.2	5.9	7.2	5.8
Cys (C)	2.1	0.3	2.0	0.6	1.9	3.2
Gln (Q)	5.2	2.2	3.6	5.6	5.0	7.5
Glu (E)	5.8	5.3	6.9	6.2	6.5	4.9
Gly (G)	6.0	9.7	8.5	8.1	7.5	8.4
His (H)	4.3	2.5	3.6	3.1	2.5	3.6
Ile (I)	6.4	3.7	6.9	1.9	2.2	2.6
Leu (L)	11.6	9.3	10.2	13.7	14.0	14.9
Lys (K)	4.8	1.2	5.6	0.9	0.9	0
Met (M)	2.3	1.9	2.0	1.6	1.9	1.3
Phe (F)	3.9	2.2	4.3	3.1	1.9	1.3
Pro (P)	5.0	6.2	5.2	5.6	6.5	7.8
Ser (S)	6.6	6.9	8.2	5.9	7.2	4.9
Thr (T)	5.8	4.7	2.6	3.7	2.5	1.9
Trp (W)	1.2	2.5	0.3	1.6	1.2	1.3
Tyr (Y)	2.3	2.8	4.9	3.7	3.4	3.2
Val (V)	4.6	9.3	6.6	8.1	6.9	5.5

The proportion of amino acids for each protein sequence corresponding to each microorganism homologous to the sequence of Lipase 2 from *Psychrobacter SC65A.3*.

Amino acid (%)	<i>Psychrobacter SC65A.3. Lipase 3</i>	<i>Glaciibacter superstes</i>	<i>Moritella sp. PE36</i>	<i>Escherichia coli</i>	<i>Pseudomonas aeruginosa</i>	<i>Stenotrophomonas maltophilia</i>
Ala (A)	9.2	10.5	9.6	7.0	11.1	9.3
Arg (R)	2.9	6.2	2.7	8.3	7.6	8.4
Asn (N)	5.4	1.4	4.8	1.3	3.2	1.6
Asp (D)	4.4	5.7	5.7	4.3	4.4	6.4
Cys (C)	0.3	0.0	0.3	2.0	0.3	0.6
Gln (Q)	3.5	0.5	3.9	6.6	4.4	4.5
Glu (E)	6.7	5.7	4.5	5.0	7.3	5.1
Gly (G)	6.3	11.0	7.2	7.6	7.0	6.1
His (H)	1.3	1.4	2.4	4.3	2.5	2.9
Ile (I)	7.6	4.3	7.8	3.3	3.5	3.5
Leu (L)	9.5	10.0	10.8	13.3	14.0	15.8
Lys (K)	8.3	1.0	3.6	2.0	2.9	1.6
Met (M)	2.2	1.9	3.6	2.7	1.9	1.6
Phe (F)	3.2	1.9	3.6	4.0	4.1	5.1
Pro (P)	4.8	8.6	7.2	5.6	7.0	7.7
Ser (S)	7.0	7.7	7.8	6.6	4.4	4.8
Thr (T)	5.4	4.8	5.1	2.3	2.2	4.2
Trp (W)	1.0	1.0	2.1	3.0	0.6	1.0
Tyr (Y)	3.5	3.3	3.0	3.0	2.5	2.9
Val (V)	7.6	12.9	4.5	7.6	8.9	6.8



UNIVERSITATEA DIN
BUCUREȘTI
VIRTUTE ET SAPIENTIA

FACULTY OF CHEMISTRY

DISSERTATION THESIS

Student: MARIA CRISTINA GHEȚU

Coordinator: Assoc Prof. dr. MĂDĂLINA TUDORACHE

2021



UNIVERSITATEA DIN
BUCUREȘTI
VIRTUTE ET SAPIENTIA

FACULTATY OF CHEMISTRY

**DEPARTAMENT OF ORGANIC
CHEMISTRY, BIOCHEMISTRY AND
CATALYSIS**

DISSERTATION THESIS

**DESIGNING BIOCATALYSTS BASED ON
THE MODEL OF ENZYMES CO-
IMMOBILIZATION WITH APPLICATION
FOR CASCADE BIOCATALYSIS**

MASTER: CHEMISTRY OF ADVANCED MATERIALS

Student: MARIA CRISTINA GHEȚU

Coordinator: Assoc Prof. dr. MĂDĂLINA TUDORACHE

July 2021

Table of contents

INTRODUCTION.....	3
CHAPTER I: GENERAL NOTIONS.....	4
1.1. Enzymes in biocatalysts.....	4
1.1.1. Lipases	5
1.1.2. Epoxide hydrolases	6
1.2. Enzyme immobilization.....	6
1.2.1. Immobilization on support surface	7
1.2.2. Immobilization into a matrix	8
1.3. Multi-enzymatic reactions	8
1.3.1. Cascade processes in biocatalysis.....	9
1.3.2. Simultaneous biocatalytic reactions.....	10
1.4. Monoterpenes.....	10
1.5.1. Limonene	11
1.5.1. α -Phellandrene	12
1.5. Aim of this thesis.....	13
CHAPTER II: EXPERIMENTAL.....	14
2.1. Substances and solutions.....	14
2.1.1. Sample preparation and pre-treatment.....	15
2.1.2. Enzyme co-immobilization-based biocatalyst preparation.....	15
2.2. Methods of analysis	16
2.2.1. Identification/ quantification of substrate/products	16
2.2.2. Characterization of the biocatalyst	18
2.2.3. Determination of enzyme loading.....	18
2.2.4. Determination of enzymatic activity.....	18
CHAPTER III: RESULTS AND DISCUSSIONS	20

3.1. Mono-enzymatic system	20
3.1.1. Comparison between free enzyme and immobilized enzyme	20
3.1.2. Variation of reaction temperature	23
3.1.3. Testing acid-trapping reagents	28
3.2. Bienzymatic system	30
3.2.1. Enzyme screening	30
3.2.2. Development of enzyme co-immobilization-based composite.....	34
3.2.3. Testing of enzyme co-immobilization-based composite	36
3.3. Correlation between biocatalyst behavior and characteristics	40
3.3.1. FTIR analysis	40
3.3.2. Deconvolution of FTIR data	42
3.3.3. Enzyme loading	44
3.3.4. Enzymatic activity	44
CONCLUSIONS	48
ACKNOWLEDGMENTS	48
BIBLIOGRAPHY	49
SUPPLEMENTARY INFORMATION	52

Introduction

Multi-enzymatic reactions are processes composed of minimum two reactions steps catalyzed by enzymes. There are some inherited advantages of such systems arising from the environmentally friendly nature of biocatalysts, along with their high substrate specificity, high product chemo-, stereo-, and enantioselectivity. Design of such eco-friendly systems proposes great advantages over typical industrial processes.

Cascade reactions represent a minimum of two consecutive processes occurring in the presence of enzymes. Commonly known as one pot processes, they provide an alternative for synthesizes of various compounds that would be obtained in a series of different steps, because there is no need for intermediate isolation and purification between each step. Therefore, making the cascade processes advantageous for a facile way of producing various substances with higher yields.

Lipases are enzymes which catalyzes the reaction on ester bonds. These enzymes have a high preference for water-insoluble substrates, and their most attractive feature is their inherit ability for interfacial catalysis. One of the most studied is lipase B from *Candida antarctica*.

Epoxide hydrolases are another class of enzymes which directs the hydrolytic ring opening of epoxides, resulting in the corresponding vicinal diols.

Enzyme co-immobilization is a process in which different enzymes are attached on a support, matrix, or form a network. This approach in enzymatic catalysis provides better catalytic activity, enhanced stability, and the possibility of reusing the biocatalyst over various reaction cycles, thus overcoming the disadvantages imposed by free enzyme catalysis.

Monoterpenes are natural compounds widely occurring in plants. These compounds have a typical hydrocarbon structure, however, their oxygenated derivates, known as monoterpenoids have a wide range of applications for flavor and fragrance products, being employed as such from centuries. There are various processes which are based on terpenes to terpenoid valorization, however, the majority employs the use of whole cell biocatalyst, which attracts some disadvantages that would be overcome by pure enzyme catalysis.

In this paper, we detail the steps performed to design a biocatalyst based on lipase and epoxide hydrolase co-immobilization with applications for monoterpenes valorization to flavor and fragrance products.

CHAPTER I: General notions

1.1. Enzymes in biocatalysts

Biocatalysis represents a chemical transformation which occurs inside or outside of the cell catalyzed by biological components, such as enzymes or antibodies. High catalytic efficiency, substrate selectivity and reaction specificity are some of the properties that make biocatalysis an attractive field. Those proprieties may be translated into the biocatalyst recognizing the substrate and obtaining the desired product with little to no side reactions. Biocatalysis is considered a part of green chemistry because of its eco-friendly nature [1].

Enzymes are biocatalysts that catalyze reactions in a living organism. They are proteins, meaning that enzymes are composed of one or more polypeptide chains. The sequence of the composing aminoacids is determined during the protein synthesis inside the living organism. As a protein, the enzyme is composed of a primary structure – the sequence of the composing aminoacids –, the secondary structure – the conformation of the aminoacid chain –, tertiary structure – the over-all 3D structure of the polypeptide chain –, and sometimes the quaternary structure – made by multiple proteins subunits [2].

Enzymes are molecules with complex proprieties, however, there are some misconceptions about them. Some of those misconceptions arise from their complicated structure and mechanism of action, and enzymes might be considered too sensitive, too expensive, or to be catalytically active only with their natural substrates or only in their natural environment [3].

Overall, enzymes are very efficient catalysts and have some major advantages. A typical reaction rate of enzyme-mediated processes is faster by a factor of 10^8 – 10^{10} the noncatalyzed reactions and are far above the values achieved by chemical catalysts. For example, chemical catalysts are generally employed in concentrations of a mole percentage of 0.1–1%, whereas most enzymatic reactions can be performed at reasonable rates with a mole percentage of 10^{-3} – 10^{-4} % of catalyst, which clearly makes them more effective by some orders of magnitude. The high catalytic efficiency for enzymatic reactions is explained by the close contact between the enzyme and substrate because the substrate is located inside the protein structure, exactly on the catalytic site during the bioconversion [4].

A general example of biocatalysis mediated by enzymes is the yeast-mediated transformation of sugars into alcohol, commonly known as fermentation. Due to the protein nature of the enzymes, they are very sensible to changes in the reaction medium, because it may conduct to changes in their

structure that could result in a modification of the active site and, therefore, the enzyme can lose its catalytic activity [5].

Another downside of employing enzymes as biocatalysts is that for them to be used for a specific substrate, the enzyme needs to be purified, which is a time-consuming and highly costly process. An alternative would be the use of whole cells which represent a convenient strategy because in this case the enzyme acts in its natural cellular environment, which provides protection against destabilization and degradation [5]. However, the employment of whole cell catalysis is not without disadvantages [6].

Some downsides of using whole cells to mediate transformations would be the restriction of accessibility for the substrate to the catalytic site, which would result in low conversion degrees, and interaction with other enzymes, which would result in possible side reactions. To overcome such restrictions, surface displayed enzymes are usually used in whole cells reactions. Therefore, both whole cell and pure enzyme catalysis have advantages and disadvantages, however, by making a compromise between the two, enzyme catalysis is still the highly useful, especially in scientific research field, providing promising possibilities for industrial applications [6].

Today, over 3700 enzymes have been recognized by the International Union of Biochemistry and Molecular Biology. For identification purposes, every enzyme has a four-digit number in the general form 'EC a.b.c.d', where EC stands for 'Enzyme Commission', and 'a' denotes the main type of reaction, 'b' indicates the substrate class or the type of transferred molecule, 'c' shows the nature of the co-substrate, and 'd' is the individual enzyme number. Enzymes have been classified into six categories according to the catalyzed type of reaction in the following order: oxidoreductases, transferases, hydrolases, lyases, isomerases, and ligases [3].

1.1.1. Lipases

Lipases are triacylglycerol acylhydrolases, with the code E.C. 3.1.1.3, and are catalyze reactions on ester bonds with preference on water-insoluble substrates, such as monoterpenoids. They are produced by microorganisms either alone or together with other hydrolases. Fungi microorganisms are preferred as a source of lipase because they generally produce extracellular enzymes, facilitating the enzyme recovery from fermentation broth [7].

Lipases have the ability of interfacial catalysis, meaning that the biocatalyst becomes more active in presence of a substrate partially soluble in aqueous environment. They possess a wide range of catalytic properties and are frequently used as a crude extract for synthesis of chiral building blocks and enantiomeric compounds [7].

Lipase B from *Candida antarctica* (CALB) is one of the most studied biocatalysts due to high selectivity and catalytic activity. CALB is highly enantioselective and efficient in various organic reactions in a wide range of reaction environments, such as solventless or organic media. Its activity is higher in water environment than in organic media, but in immobilized form, CALB shows improved catalytic activity than the free enzyme, being able to withstand higher reaction temperatures. CALB can be immobilized both by physical and chemical means. An example of immobilized CALB is the commercially available Novozym® 435 [8].

1.1.2. Epoxide hydrolases

Epoxide hydrolases, abbreviated as EHs, having the code EC 3.3.2.9, are enzymes that catalyze the hydrolytic opening of epoxide rings resulting in the corresponding vicinal diols. EHs have been largely studied as biocatalysts for production of enantiopure epoxides and diols, two classes of chiral building blocks useful in the pharmaceutical industry. Specifically, the applications of EHs are usually favored because they possess the ability to transform a relatively large substrate spectrum with excellent stereo-, regio-, and chemoselectivity without the presence of a cofactors. These enzymes are very under operative conditions [9].

There is a family of atypical EHs named limonene-1,2-epoxide hydrolases (LEHs, EC 3.3.2.8) according to the natural substrate of the first isolated member, limonene oxide. LEHs were discovered after an interesting enzymatic activity from the bacteria *Rhodococcus erythropolis* DCL14 strain was discovered. This particularly strain was able to grow in the presence of both (+)- and (-)-limonene as the sole carbon and energy source [9].

Metagenomic investigations showed the existence of new thermophilic strains, such as CH55-LEH, which shows increased optimal temperature and melting point compared to previously known Re-LEH. Apart from the higher thermal stability, CH55-LEH maintained high substrate specificity on a boarder pH range, achieving a maximum around the value of 8. CH55-LEH shows high affinity for substrates related to limonene-1,2-epoxide resulting in enantio-conversion to corresponding vicinal diols. This biocatalyst promises great results for hydrolytic ring opening applications due to its increased stability [10].

1.2. Enzyme immobilization

Some of the drawbacks of enzymatic catalysis are overcame, such as the expensive process of purifying and isolating the enzymes being replaced by recombinant DNA techniques able to produce most enzymes for a reasonable price. Advances in protein engineering made possible to tailor enzymatic characteristics, such as substrate specificity, activity, selectivity, stability, or optimum pH

values, making enzymes more available than ever for potential applications. However, when it comes to possible industrial uses of enzymes as catalysts, it is clear that their lack of long-term operational stability and the difficulty of their separation from the reaction environment and reuse, makes them unfit [11].

Enzymatic immobilization is a technique that consists of confinement of protein molecules onto a support or matrix by chemical or physical means, leading to enhanced stability of enzymes, easier recovery from the reaction environment, improved catalytic performance and the possibility of reuse of the biocatalyst. Therefore, by immobilization approach, the drawbacks of pure enzyme catalysis compared to whole cell one are overcome, making enzymes suitable catalysts [11].

Enzyme immobilization is an important aspect of the biocatalytic process especially for industrial biotechnology. Immobilized enzymes offer many advantages, as previously mentioned, and, sometimes, as in the case of lipases, the enzyme is apparently activated after this immobilization step [12]. Depending on the immobilization technique employed, the properties of the biocatalyst, such as stability, selectivity, rate constant value, optimum pH or temperature, might be altered. The immobilization approaches developed comprises different strategies: adsorption, covalent attachment, cross-linking, entrapment, and encapsulation [13].

1.2.1. Immobilization on support surface

Support binding can be achieved both by physical and chemical means. The physical attachment can be achieved by hydrophobic and van der Waals interactions. Immobilization on a support can be done by ionic or covalent interactions, as well. Physical interactions between enzymes and support are usually very weak and leaching of the biological material may occur, but this method is highly cost effective. However, even though the ionic and covalent interactions employ stronger forces and prevent leaching, they can lead to the enzyme deactivation due to conformational changes of the recognition site, preventing the interaction between the active site and substrate. The support material can be synthetic resins, biopolymers, or inorganic polymers [11].

The easiest, cheapest, and oldest method employed is the adsorption onto a water-insoluble macroscopic carrier. It may be equally well applied to isolated enzymes as well as to whole cells [14].

The downside of this method is that forces employed in the support attachment are relatively weak, such as London forces, ionic interactions, hydrogen bonding. As a result of the weak binding forces, loss of catalytic activity is relatively low, but desorption from the carrier might occur. Also, minor changes in the reaction parameters, such as a variation of substrate concentration, solvent changes, temperature, or pH variations, could cause the leaching of the biological material [14].

However, the most appealing feature of this type of immobilization is the simplicity of the procedure, and various supports might be used, such as activated charcoal, alumina, silica, cellulose, controlled-pore glass, and synthetic resins [14].

1.2.2. Immobilization into a matrix

Some other immobilization approach for enzymes is entrapment, which refers to the inclusion of the biomolecule in a gel-like polymeric matrix. The polymers used for this method are usually organic polymers or silica sol-gel [11]. Encapsulation refers to the inclusion of an enzyme within a semi-permeable membrane, such as lipid vesicles. These are by far the best approaches which avoid any negative influence of the protein structure of the biocatalysts and prevent their aggregation and denaturation [13]. However, physical restrains of an enzyme might be too weak and lead to leaching of the biomolecules, therefore, the addition of covalent attachment might be necessary [11].

Cross-linking of the enzyme aggregates or crystals using a bifunctional reagent that result in carrier less macroparticles. This method is worth mentioning, because the presence of a carrier leads to a ‘dilution’ of catalytic activity due to the introduction of a large non-catalytic ballast [11]. The disadvantage of cross-linked enzyme crystals is that enzyme crystallization is an extremely laborious process and expensive. The other possible approach is cross-linked enzyme aggregates, which refers to the precipitation of physical protein aggregates [13]. The most used linker is glutaraldehyde, and the immobilization is based on the reaction between protein surface and amino group of the linker [15].

Overall, every immobilization method has its own downsides, meaning that there is not a standard method suitable for every process. Depending on the structure of the enzyme and the applications the biocatalyst is designed for, an immobilization method is chosen [13].

1.3. Multi-enzymatic reactions

Multi-enzymatic reactions represent a combination of several enzymatic transformations in a continuous process. They offer considerable advantages, such as less time demand, costs and chemicals for product recovery may be reduced, reversible reactions can be driven to completion and the concentration of harmful or unstable compounds can be kept to a minimum. A particular case of multi-enzymatic reactions is the bienzymatic ones, which refer to a series of reactions which use two different enzymes with specificity for different substrates [16].

Multi-enzymatic reactions are of great importance for technology to succeed in industrial process development, such as synthesis of pharmaceutical, cosmetic, and nutritional compounds. Different strategies to construct multienzyme structures have been widely reported. Enzymes complexes are designed by three types of routes: fusion proteins, enzyme scaffolds, or immobilization.

As a result, enzyme complexes can enhance cascade enzymatic activity through substrate channeling [17].

Biocatalysis has made tremendous advances in the field of synthesis of industrially important products and intermediates, especially by employing immobilized enzymes. By immobilization, the biocatalysts show improved operational temperature, improved convenience in separation from the reaction mixture, reducing costs. Therefore, immobilized multi-enzymatic biocatalysts gain an increased interest for potential industrial applications due to economic and environmental considerations [17].

1.3.1. Cascade processes in biocatalysis

Cascade reactions represent a chemical process that comprises at least two consecutive reactions coupled in such a way that each subsequent reaction occurs only in virtue of the chemical functionality formed in the previous step. It has the great advantage that the isolation of intermediates is not required because each reaction composing the sequence occurs spontaneously. Another advantage of cascade processes over others are that the reaction conditions do not change among the consecutive steps of a cascade and no new reagents are added after the initial step. Cascade processes are also known as one-pot procedures because the lastly mentioned similarly allow at least two reactions to be carried out consecutively without any isolation of intermediates, but do not preclude the addition of new reagents or the change of conditions after the first reaction. Although often composed solely of intramolecular transformations, cascade reactions can also occur intermolecularly [18].

The concept of performing multi-step syntheses in one-pot has gained some attention in the past period because from an environmental point of view, cascades represent a very promising approach. There are, however, some technological and scientific challenges to be overcome to reach industrial scale implementation of cascades. One of the most common challenges for the practicability of a cascade reaction is the combination of biocatalysts from different sources, which often have different optimal reaction conditions and show undesired side reactions [18].

Overall, multi-enzymatic cascade reactions offer considerable advantages: the demand of time, costs and chemicals for product recovery may be reduced, reversible reactions can be driven to completion and the concentration of harmful or unstable compounds can be kept to a minimum. They can be employed for the asymmetric synthesis of chiral alcohols, amines and amino acids, as well as for C-C bond formation [19]. As for example, the stereoselective three-enzyme cascade synthesis of diastereomerically pure γ -oxyfunctionalized α -amino acids [18].

1.3.2. Simultaneous biocatalytic reactions

On the other hand, a simultaneous reaction consists of any of two or more chemical reactions occurring at the same time in the same system, independently of each other. These types of processes are usually employed in industrial reactions, and are usually used in adjustment of the enzyme feed rate which helps to maximize the value of the product less the cost of the enzymes [20].

In a multi-enzymatic system, simultaneous reactions are not preferred. This reasoning is due to some factors intervening during the reaction. For example, competition of different substrates for the same active site, a product of a reaction might act as an inhibitor for another enzyme present in the system, or the presence of competitive inhibition phenomenon are just some aspects worth considering if one is to develop a multi-enzymatic simultaneous process [20].

An example of a simultaneous multi-enzymatic reaction which overcomes the mentioned drawbacks is the simultaneous multi-enzymatic hydrolysis and lactic fermentation, which would result in low lactose yogurt. This is a single stage process, which couples the fermentation process with the addition of β -galactosidase which would convert the lactose while it is produced [21].

1.4. Monoterpenes

Every year, large amounts of carbon dioxide are assimilated by plants, and part of this amount is converted and released back into the environment. A significant part of those substances released are volatile organic compounds, which include monoterpenes and sesquiterpenes [22].

Monoterpenes have the general formula $C_{10}H_{16}$ and are composed of two linked C_5H_8 isoprene units, therefore, represent a class of hydrocarbons [22]. They are known to act mainly as deterrent agents against herbivores, as well as antifungal defenders and to attract pollinators. Higher terpenes are present in mammals as well, and act as stabilizers of cell membranes, metabolic pathways, or regulators of enzymatic reactions [23].

Two of the most encountered monoterpenes are pinene, present in the wood plants as a constituent of their resin, and limonene, present in citrus plants. The term ‘terpene’ refers only to hydrocarbons, whereas ‘terpenoids’ is the term which refers to the oxygenated derivatives of terpenes, and are mainly produced by flowers, and are used as flavor and fragrance products [22].

Released monoterpenes are transformed in the atmosphere within hours in reactions with molecular oxygen, ozone, hydroxyl radicals, nitrogen oxides, chlorine atoms by photolysis or chemical reactions. The products resulting from these transformations constitute secondary aerosols that are transported to the soil by rain. Therefore, it would represent a great advantage to be able to develop a

method in which the widely occurring monoterpenes could be safely converted in flavor and fragrances [22].

Due to their wide impact on the global market, terpenes valorization is an important topic. Accounting for the need for a natural and sustainable approach for industrial processes, the bioconversion of such compounds might have an added value. Therefore, biocatalytic approach in monoterpenes conversion is an important aspect worth considering when developing a process. However, any strategy which proposes the valorization of this class of compounds has some challenges arising from the fact that this class of compounds is highly chemical instable, has low water solubility, high volatility, high toxicity of both substrates and products, relatively low yields, and high fermentation cost [24].

Most bioconversion processes of monoterpenes reported in the last years employed the use of whole cell biocatalysts due to the use of microbial cell conversions is easier to apply than to use purified enzymes. This might be advantageous in some cases due to low yield reported in enzyme catalyzed processes due to enzyme high substrate specificity. However, the high toxicity of both terpenes and terpenoids possess a high risk in affecting the cell catalytic activity [25]. Therefore, it would be of great interest to develop a biocatalyst based on enzyme immobilization able to convert monoterpenes into flavor and fragrance products, thus minimizing the disadvantages of using whole cell catalysts, and maximizing the possibility of obtaining enantiopure products.

1.5.1. Limonene

Limonene is the most abundant monocyclic monoterpene and second most abundant volatile organic compound indoors. It is the main component of citrus essential oil [22]. It has a precursory role for some other monocyclic monoterpenes, such as carveol, carvone, α -terpineol, pulegone, or 1,8-cineole [26].

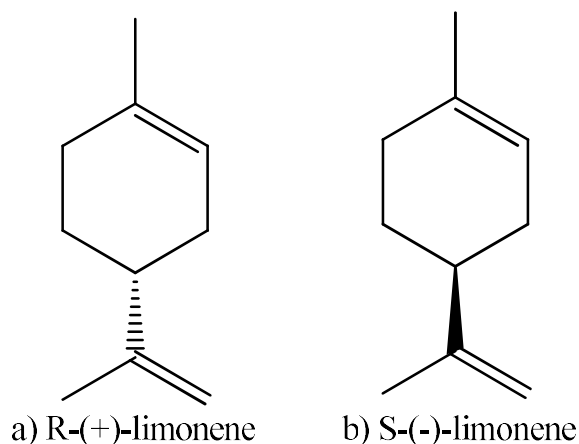


Image 1. Structure of a) R-(+)-limonene and b) S-(-)-limonene.

Limonene is an optically active compound. It exists in two enantiomeric forms: S and R, presented in image 1. The R-(+)-limonene isomer is known as d-limonene and it is the main component in essential oils from citrus peels. The l-limonene is mainly found in essential oils from pine needles and spearmint [26].

This monoterpene is widely used as flavor and fragrance additive in many products, such as perfumes, beverages, detergents, soap, or other house cleaning products. In addition to its additive use, limonene is also important as a starting material for the synthesis of other natural compounds, such as p-cymene. This wide range of application combined with vulnerability to ozone aided oxidation make limonene a highly commercially important molecule [26].

1.5.1. α -Phellandrene

α -Phellandrene is the main constituent of evergreen trees essential oils, but it might be also found in other essential oils from eucalypt, menthe, citrus, pine needles in lower amounts. This compound is often used in fragrances. α -Phellandrene is described as having a very distinctive citrus, green, black pepper-like scent [27].

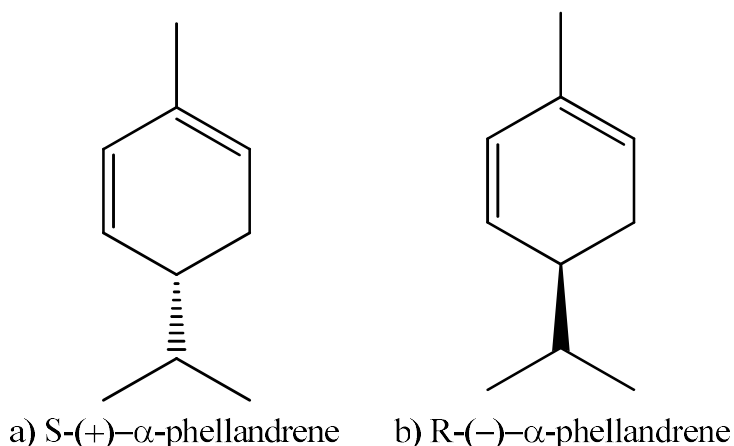


Image 2. Structure of a) S-(+)- α -phellandrene and b) R(-)- α -phellandrene.

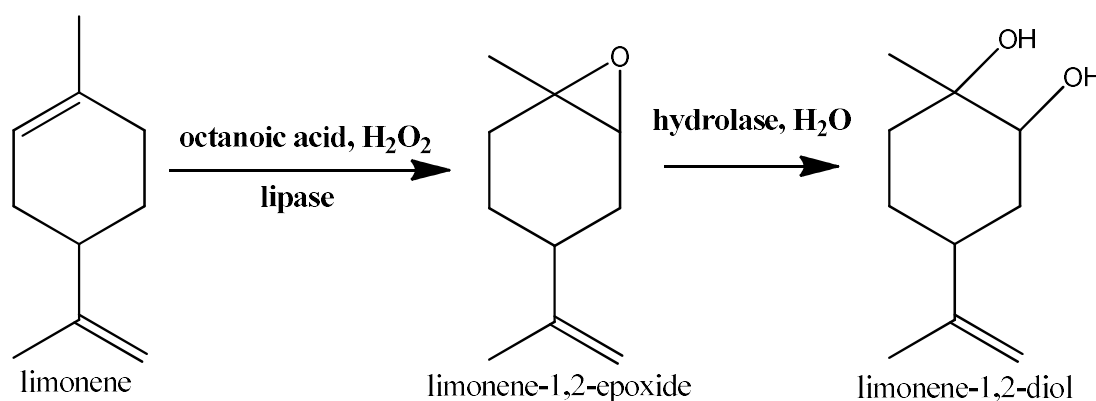
This monoterpene exist is the form of two enantiomers presented in image 2, the enantiomers have different physicochemical and olfactive properties. Biological activity of α -phellandrene was studies and it was reported to be inactive as an antimicrobial agent [27].

Chiral monoterpenes usually occur in nature as a single enantiomer, but the isomers possess different olfactory properties. Therefore, a stereo- and enantioselective approach in their valorization is of high interest for pharmaceutical and chemical industries large scale applications [27].

1.5. Aim of this thesis

Due to the wide occurrence of monoterpenes, the chiral nature of these molecules and the most used approach in their valorization being whole cell catalysis, we propose a bienzymatic biocomposite designed by co-immobilization for cascade conversion of R-(+)-limonene to flavor and fragrance products.

We based our study on literature reports of lipase-mediated epoxidation on limonene to limonene oxide using fatty acids [28] using a cheap oxidizing agent, hydrogen peroxide [29], cupelled with a thermophilic epoxide hydrolase able to withstand higher reaction temperatures [10]. Therefore, we developed a biocomposite able to convert monoterpenes into monoterpenoids with potential applications for industrial processes, being able to overcome potential drawbacks of using whole cell catalysts, such as loss of catalytic activity due to high toxicity of substrates and products in large amounts, or the presence of secondary mediated by other biocatalysts present in the system. The reaction scheme is presented in scheme 1.



Scheme 1. Proposed scheme for limonene bioconversion.

Our process is composed of a two-step cascade bienzymatic conversion of our substrate. In the first step, uses an indirect lipase-mediated conversion of monoterpenes [28], meaning that the lipase oxidized a fatty acid present in the system, which in our case is octanoic acid, to its corresponding peracid by means of hydrogen peroxide as an oxidizing agent. The then formed octanoic peracid converts the R-(+)-limonene substrate into limonene oxide. In the second step of our process, the hydrolase directs the hydrolytic ring opening of the epoxide intermediate toward the formation of an enantiopure vicinal diol, more exactly (1S,2S,4R)-limonene-1,2-diol.

The biocatalyst is based on the adsorption of CH55-LEH hydrolase on the surface on commercially available lipase B from *Candida antarctica* immobilized on the surface of a hydrophobic acrylic resin in the form of Novozym® 435. Therefore, in our study we optimized the biocatalytic process, characterized the obtained material, and propose possible applications for our biocatalyst.

CHAPTER II: Experimental

2.1. Substances and solutions

For our study various substances and solutions were used. It is worth mentioning that the vast majority of the substances used were provided by Sigma Aldrich, meaning octanoic acid, R-(+)-limonene, α -phellandrene, limonene oxide, (1S, 2S, 4R)-(+)-limonene-1,2-diol, hydrogen peroxide 30%, ethyl acetate, pyridine, p-nitrophenyl palmitate, p-nitrophenol, the acid-trapping salts, as well as the three lyophilized lipase A and B from *Candida antarctica*, and lipase from *Aspergillus niger*, and two immobilized lipases from *Candida cylindracea* and *Pseudomonas cepacia*, both immobilized in a sol-gel matrix. The few differently sourced substances and solutions are mentioned further.

The phosphate-buffered saline (PBS) with a pH around 8 contains sodium chloride (NaCl), potassium chloride (KCl), disodium phosphonate (Na_2HPO_3), dipotassium phosphonate (K_2HPO_3) in water, and the pH is adjusted using sodium hydroxide (NaOH).

The tris-HCl buffer used as the environment of choice for some of our studies due to its relatively neutral pH. This buffer was prepared by mixing 0.1 M of tris(hydroxymethyl)aminomethane with a concentration of 12.1 g/L with 44.2 mL of 0.1 M hydrochloric acid to obtain a pH of 7.2.

Some commercially available immobilized lipases were studied. Six different immobilized enzymes provided by Strem Chemicals in collaboration with Novozymes®. From their range we studied the behavior of Lipozyme® TL IM – lipase from *Thermomyces lanuginosus* immobilized on a non-compressible silica gel carrier -, Novozym® 435 – lipase B from *Candida antarctica* immobilized in hydrophobic acrylic resin -, Transenzyme – lipase from *Geobacillus stearothermophilus* immobilized in acrylic resin -, Lipozyme® RM IM – lipase from *Rhizmucor miehei* which is immobilized on an anionic exchange resin carrier. The immobilized lipases were all stored in the fridge.

The hydrolases studied are not commercially available. These enzymes were provided by Dr. Daniela Monti from Chemical Institute of Molecular Recognition, C. N. R., Milan, Italy, and her team. The hydrolases were provided in the form of enzymatic solutions. For our studies we used Re-LEH, which has the optimum temperature around room temperature, and Tomsk-LEH and CH55-LEH, both thermophilic enzymes [10]. The solutions provided to us have the following concentrations: 1.81 mg/mL CH55-LEH, 1.27 mg/mL Tomsk-LEH, and 2.63 mg/mL Re-LEH. The hydrolase samples were stored at -40 °C and defrost only when preparing samples.

2.1.1. Sample preparation and pre-treatment

A sample contain the following components in order:

1. Octanoic acid – in a concentration of 1.6 M;
2. Substrate – with concentration of 1.59 M;
3. Phosphate-buffered saline (PBS) with the pH of 8.00 and concentration of 0.04 M – it is used to maintain a constant volume among all samples;
4. Lipase – 43.89 µg/mL is the concentration of the free lipases, and 9.66 mg/mL is the concentration of immobilized lipases;
5. Hydrolase – with a concentration of 2.81% v/v in the final solution;
6. Hydrogen peroxide (H₂O₂) 30% - its concentration of 0.44 mM;
7. Acid-trapping reagent – 0.3 milimols of acid-trapping salt.

For the lyophilized lipases, an enzyme solution with a concentration of 1 mg/mL was prepared beforehand by solubilizing the enzyme powder in PBS with pH 8.

The experimental procedure consists of sample reaction for 24 hours at temperatures between 25 °C and 50 °C, 1000 rotations per minute in a thermoshaker. The extraction step is 1:1 volume ratio of sample and ethyl acetate, followed by 30 minutes of agitation at room temperature at 1500 rotation per minute. Depending on our study goal, here might be an additional derivatization step consisting of 100 µL of sample previously extracted and agitated mixed with 150 µL pyridine, and 66 µL acetic anhydride, 24 hours at 25 °C at 1000 rotations per minute in a thermoshaker reaction. The derivatization step is usually employed for the bienzymatic system to increase the resolution of diol detection.

The final solution is analyzed using gas chromatography. We developed a series of methods of analysis using different chromatographic columns to better tailor the methods to our system.

2.1.2. Enzyme co-immobilization-based biocatalyst preparation

The immobilization procedure is based on the adsorption of the hydrolase on the surface of a support already containing a lipase. Our biocomposite candidates were CH55-LEH hydrolase and Novozym® 435, and Re-LEH and Lipozyme® RM IM.

For both materials, the same procedure was followed. 32 µL of hydrolase solution with a concentration of 2.63 mg/mL Re-LEH, or 1.81 mg/mL CH55-LEH were added on 11 mg of immobilized lipase. The samples were prepared in a 2 mL Eppendorf. The vials were left open in the fridge for 4 to 5 days to dry. After completely drying the biocomposite was washed with 1 mL PBS pH 8. This step was repeated three times.

2.2. Methods of analysis

2.2.1. Identification/ quantification of substrate/products

Gas chromatography (GC) was the method of choice for the sample analysis, giving their volatile nature. We used different chromatographic columns for a proper detection, more exactly GC with a polar chiral column and a flame ionization detector (GC*-FID) which provide a better detection for the limonene-1,2-diol products. This method is used for the bienzymatic acetylated sample. The other chromatographic methods use another GC with flame ionization detector (GC-FID) having a different column than the previous, and GC with mass spectrometer detection (GC-MS). Both GCs use the same non-polar separation column.

The GC*-FID analysis uses hydrogen as a carrier gas. The injector has a temperature of 230 °C. Injection mode is split. Flow control mode is pressure. The carrier gas has the following parameters: pressure of 0.74 bar, total flow 23.9 mL/min, column flow 1.90 mL/min, linear velocity 50.2 cm/sec, purge flow 3.0 mL/min, split ratio 10. The temperature regime of the column starts from 50 °C with a holding time of 20 minutes. The temperature increases with 10 °/min till 150 °C. The holding time at this temperature is 10 minutes. The analysis time for a sample is 40 minutes. The column stationary phase is a β -cyclodextrin modified with S-hydroxypropyl.

The GC-FID analysis also uses hydrogen as a carrier gas. The injector has a temperature of 230 °C. Injection mode is split. Flow control mode is linear velocity. The carrier gas has the following parameters: pressure of 1.82 bar, total flow 20.5 mL/min, column flow 1.59 mL/min, linear velocity 45.0 cm/sec, purge flow 3.0 mL/min, split ratio 10. The temperature regime of the column starts from 50 °C without holding time. The temperature increases with 7 °/min till 250 °C. The holding time at this temperature is 5 minutes. The analysis time for a sample is 34.57 minutes. The column stationary phase is a (5%-phenyl)-methylpolysiloxane.

The GC-MS analysis uses helium carrier gas. The injector has a temperature of 230 °C. Injection mode is split. The carrier gas has the following parameters: flow mode constant flow with vacuum compensation, gas saver flow 10 mL/min, gas saver time 2 minutes, split flow 30 mL/min, split ratio 30. MS transfer line has a temperature of 250 °C. The temperature regime of the column starts from 50 °C with a holding time of 3 minutes. The temperature increases with 5 °/min till 230 °C. The holding time at this temperature is 1 minutes. The analysis time for a sample is 40 minutes. The column stationary phase is a (5%-phenyl)-methylpolysiloxane.

The GC*-FID method is used to quantify the ratio between the S and R isomers of the limonene-1,2-diol. For sample analysis the sample is acetylated, this step increasing the resolution for

the enantiomer separation, but might derivatize some unreacted substrate as well. Therefore, this method cannot be reliably used to calculate the substrate conversion, but it is useful to determine the yield of limonene-1,2-diol, and enantiomeric excess (ee%).

The other two methods of analysis are exclusively for extracted samples. Therefore, the substrate can be properly quantified. GC-MS is used to identify the products of the enzymatic system. Once the structures are attributed, the method of choice for analysis is GC-FID. Both methods use the same stationary phase, meaning that the resulting chromatograms are relatively similar.

To properly calculate the conversion of limonene and the products yield, calibration curves were constructed. For R-(+)-limonene quantification, eight solutions were prepared in ethyl acetate. The concentration varied between 3.32 M and 0 M. The samples were homogenized by agitation at room temperature in a vortex for 30 minutes at 1500 rotations per minute. The same procedure was followed for limonene oxide, with a concentration range between 3.26 M to 0 M.

The procedure for the limonene-1,2-diols is the same for the most part, the concentration range being between 3.32 M and 0 M. Homogenization done as well at room temperature in a vortex for 30 minutes at 1500 rotations per minute. The difference was that 100 μ L of sample were derivatized with 150 μ L pyridine, and 66 μ L acetic anhydride, and reacted for 24 hours at 25 $^{\circ}$ C at 1000 rotations per minute in a thermoshaker. The solutions were analyzed using the GC*-FID.

It is worth mentioning that the curve for (1S, 2S, 4R)-(+)-limonene-1,2-diol has a correction factor equal to 0.30, because the calibration curve was obtained using a previously employed GC*-FID method with a higher split ratio. Another calibration curve could not be prepared due to commercial unavailability of (1S, 2S, 4R)-(+)-limonene-1,2-diol.

All mentioned calibration curves are presented in the supplementary information (figures A to C), and have a correlation coefficient close to 1, therefore, they all present good linearity.

For the sample analysis, the formulas 1 to 4 were used to calculate the conversion degree of R-(+)-limonene, the yield of limonene oxide intermediate, or limonene-1,2-diol products, and the enantiomeric excess of (1S, 2S, 4R)-(+)-limonene-1,2-diol.

$$1) C\% = \frac{\text{initial concentration of limonene} - \text{concentration of limonene from figures 1 or 3}}{\text{initial concentration of limonene}} * 100$$

$$2) \text{ epoxide yield}\% = \frac{\text{concentration of epoxide from figures 2 or 4}}{\text{initial concentration of limonene}} * 100$$

$$3) \text{ diol yield}\% = \frac{\text{concentration of diol from figure 5} * \text{correction factor}}{\text{initial concentration of limonene}} * 100$$

$$4) \text{ enantiomeric excess}\% = \frac{\text{peak area S-pe} \quad \text{are R}}{\text{peak area S+pe} \quad \text{are R}} * 100$$

2.2.2. Characterization of the biocatalyst

Fourier-transform infrared (FTIR) spectroscopy was used to characterize the prepared biocomposites. FTIR spectra of the materials were recorded using Bruker Tensio-II FTIR spectrometer with Diffuse Reflectance “Smart Accessory”. The absorption spectra were collected between 400 and 4000 cm^{-1} , at room temperature. The registered spectra have an average of 64 scans with a resolution of 16 cm^{-1} . The samples were not pre-treated before analysis.

The spectra were collected from solid samples by mixing a small amount with potassium bromide (KBr). Besides the biocomposites, the hydrolase solutions, Novozym® 435 and Lipozyme® RM IM beads, and lyophilized lipase B from *Candida antarctica* were analyzed as well.

2.2.3. Determination of enzyme loading

The loading of CH55-LEH hydrolase on the surface of the acrylic beads of Novozym® 435 was determined employing a calibration curve for BSA. The curve was constructed by solubilizing the protein in tris-HCl buffer, varying the protein concentration between 0.1 to 1 mg/mL. The liquid samples were analyzed using UV-VIS spectrophotometer Specord 250, Analytik Jena, and the absorbance was registered at 280 nm. The calibration curve is presented in the supplementary information (figure G).

For the quantification of the amount of CH55-LEH hydrolase adsorbed on the Novozym® 435 beads, the absorbance of an initial enzymatic solution of CH55-LEH with a concentration of 1.81 mg/mL, as well as the absorbance of the washing solution after immobilization. This last solution is composed of all three washing solutions mixed and homogenized before analysis. Both absorption values were recorded at 280 nm.

2.2.4. Determination of enzymatic activity

The washing solution of the biocomposite and an enzymatic solution of 2.63 mg/mL Re-LEH were analyzed using a UV-VIS spectrophotometer Specord 250, Analytik Jena between 214 and 400 nm. For a better comparison, 11 mg of Novozym® 435 and other 11 mg of Lipozyme® RM IM were washed three times with 1 mL of PBS pH 8 following the same procedure as for the biocomposite. This washing solution was analyzed as well between 200 and 400 nm.

The determination of the enzymatic activity is based on the conversion of p-nitrophenyl palmitate catalyzed by the lipase to p-nitrophenol, which has an absorption peak in the near-UV region.

A calibration curve was prepared for the quantification of p-nitrophenol. The curve was prepared by varying the amount of p-nitrophenol between 0.5 and 0 mM in ethanol. The absorption was registered at 347 nm using a UV-VIS spectrophotometer Specord 250, Analytik Jena.

The procedure employed to determine the enzymatic activity of immobilized lipases consists on the construction of two calibration curves of the amount of formed p-nitrophenol by different amounts of both Novozym® 435 and Lipozyme® RM IM. The amount of immobilized lipase was varied between 1 and 11 mg. The enzymes were mixed with 900 μL of tris-HCl buffer 0.05 M with a pH of 7.2, and 100 μL of p-nitrophenol palmitate 0.025 M in ethanol. Then, were incubated for 30 minutes at 37 °C. After, the reaction was ceased by the addition of 250 μL of a solution of 0.1 M Na_2CO_3 . The samples were then centrifugated at 12000 rpm for 2 minutes. The analysis was done on the liquid sample at 410 nm using a UV-VIS spectrophotometer Specord 250, Analytik Jena.

All calibration curves are presented in the supplementary information (figures D to F).

For the determination of the enzymatic activity of our samples, the same procedure was followed as for bare Novozym® 435 and Lipozyme® RM IM. The immobilized lipases were analyzed before the immobilization of the hydrolase, as well as after. The activity of the resulting biocomposite was determined before the washing procedure, as well as after each washing step, and after up to 3 reaction cycles.

The washing solution was analyzed as well, each washing solution separately, to determine if the lipase might be lost during the procedure. The protocol is the similar, only the amounts are slightly changed, 250 μL of washing solution is mixed with 650 μL of tris-HCl buffer 0.05 M with a pH of 7.2, and 100 μL of p-nitrophenol palmitate 0.025 M in ethanol. Followed by incubation, reaction cessation, centrifugation, and UV-VIS analysis.

The enzymatic activity of the CH55-LEH hydrolase was determine before and after the co-immobilization. The determination was realized by preparing a sample containing 1.6 M limonene-1,2-epoxide, 1.6 M octanoic acid, 0.04 M PBS pH 8, and 2.81% v/v hydrolase solution. The enzymatic activity value before co-immobilization was determined using the calibration curve for limonene-1,2-epoxide constructed using GC-FID method, presented in the supplementary information (figure B). The value after the co-immobilization was determined from the percentage of hydrolase loading on the Novozym® 435 surface.

CHAPTER III: Results and discussions

3.1. Mono-enzymatic system

3.1.1. Comparison between free enzyme and immobilized enzyme

The behavior of lyophilized enzymes was compared with the one of immobilized enzymes. This study focuses on how the system components influence parameters, such as limonene conversion and epoxide yield, depending on lipase source and state (free or immobilized), and the effect of immobilization on enzymatic activity.

For the study of lipases available in lyophilized form, solutions with the concentration of 1 mg/mL lipase in PBS pH 8 were prepared prior. We tested lipase from *Aspergillus niger*, and lipase A and B, both from *Candida antarctica*.

The samples were prepared, pre-treated, and analyzed using the GC-FID method. The conversions and epoxide yields were obtained using the calibration curves are presented in figures 1 and 2.

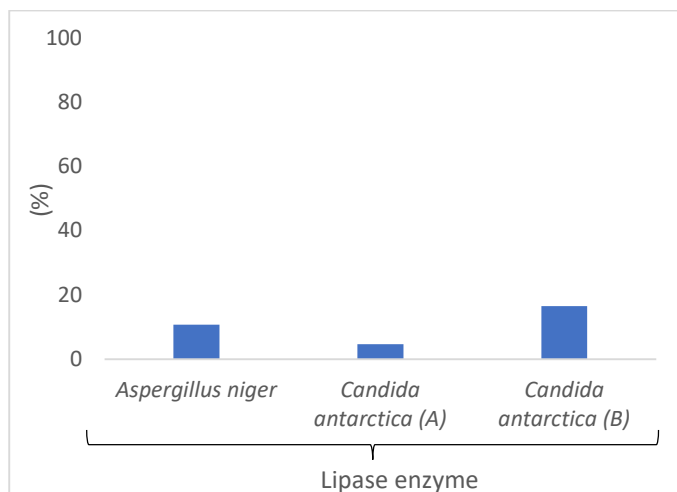


Figure 1. Conversion of R-(+)-limonene obtained with lyophilized lipases.

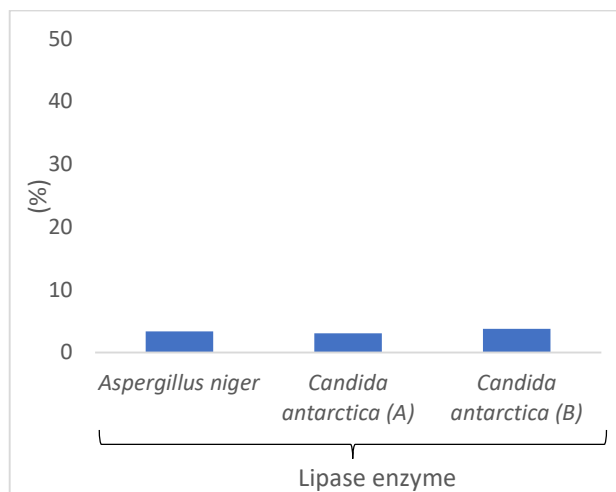


Figure 2. Yield of limonene oxide obtained with lyophilized lipases.

(1.6 M R-(+)-limonene, PBS pH 8 0.04 M, 1.60 M octanoic acid, 0.44 mM hydrogen peroxide, and 43.89 $\mu\text{g/mL}$ lipase. Reaction: 24 h, 25 $^{\circ}\text{C}$, 1000 rpm. Liquid-liquid extraction - 1:1 = sample : ethyl acetate (v/v) \rightarrow 30 min stirring at room temperature)

In figure 1 are presented the values for limonene conversion obtained using different lyophilized enzymes. The conversion increases in the following order: lipase A from *Candida antarctica*, lipase from *Aspergillus niger*, and the highest value is obtained for lipase B from *Candida antarctica*. The lowest value for conversion is 5% in the case of lipase A, and the maximum one is 16% for lipase B. The conversion percent obtained for lipase from *Aspergillus niger* is 11%. Therefore, there is only a 5% difference between the lipase from *Aspergillus niger* and lipase B from *Candida antarctica*.

In figure 2, there are represented the yield values for limonene oxide, the product of the enzymatic transformation of limonene. The yield values are not as different as in the case of the conversion. The values are contained between 3 to 4%. The lowest value is again obtained when lipase A is used, and the highest in the presence of lipase B. The value for the yield obtained when lipase from *Aspergillus niger* is employed is only 0.4% smaller than the maximum value obtained for lipase B.

The highest values for conversion and yield were obtained for lipase B from *Candida antarctica*. However, considering that we previously worked with liquid lipase from *Aspergillus niger*, in our succeeding studies we chose to work with lyophilized lipase from *Aspergillus niger*, that would provide a better understanding of the variation of efficiency of our system when other factors are varied.

For the study of lipases available in immobilized form, we tested six different immobilized lipases commercially available. We tested Lipozyme® TL IM which contains lipase from *Thermomyces lanuginosus* immobilized on a non-compressible silica gel carrier, Novozym® 435 which is lipase B from *Candida antarctica* immobilized in hydrophobic acrylic resin, Transenzyme which is lipase from *Geobacillus stearothermophilus* immobilized in acrylic resin, and Lipozyme® RM IM which is lipase from *Rhizomucor miehei* immobilized on an anionic exchange resin carrier.

The sample preparation and pre-treatment before analysis, as well as analysis method employed are the same as previously mentioned. The conversions and epoxide yields were obtained from the corresponding calibration curves are presented in figures 3 and 4.

In figure 3, it can be observed how the conversion varies when different immobilized enzymes are used. The lowest limonene conversions were obtained in when the sol-gel immobilized lipases were employed. The conversion value obtained for Lipozyme® TL IM is also in the lower end. This is to be expected because the lipase from *Thermomyces lanuginosus* is thermophilic, and its optimum temperature is higher than our reaction temperature. From information available on Strem Chemicals, the temperature range for this immobilized lipase is between 50 and 75 °C. We chose to use this lipase in our succeeding studies because its optimum range is at very increased temperatures. This proposes two problems. First, the hydrolase can become denatured at such increased temperatures, and second, the remaining three immobilized lipases can convert higher amounts of limonene at lower temperatures, therefore, there would not be a need to input higher energy in our system.

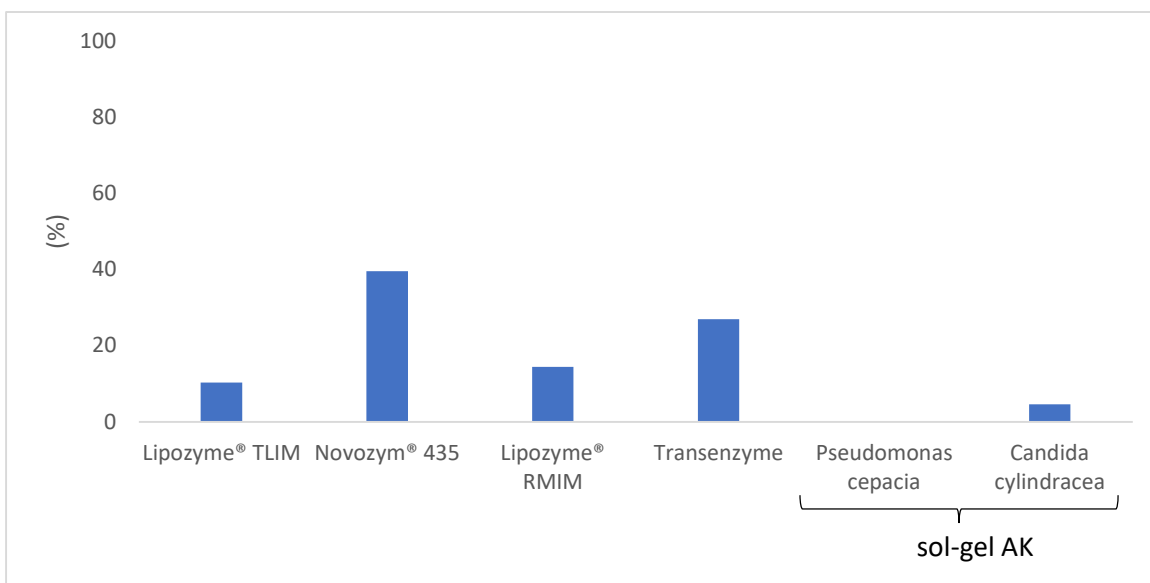


Figure 3. Conversion of R-(+)-limonene obtained with immobilized lipases. (1.6 M R-(+)-limonene, PBS pH 8 0.04 M, 1.60 M octanoic acid, 0.44 mM hydrogen peroxide, and 9.66 mg/mL immobilized lipase. Reaction: 24 h, 25 °C, 1000 rpm. Liquid-liquid extraction - 1:1 = sample : ethyl acetate (v/v) → 30 min stirring at room temperature)

From the remaining three immobilized lipases we chose Novozym® 435 and Lipozyme® RM IM because they provided high conversions of limonene at room temperature. Even thou Transenzyme performed compared to Lipozyme® RM IM, we choose to go further with our tests with two lipases immobilized on different supports for a proper comparison.

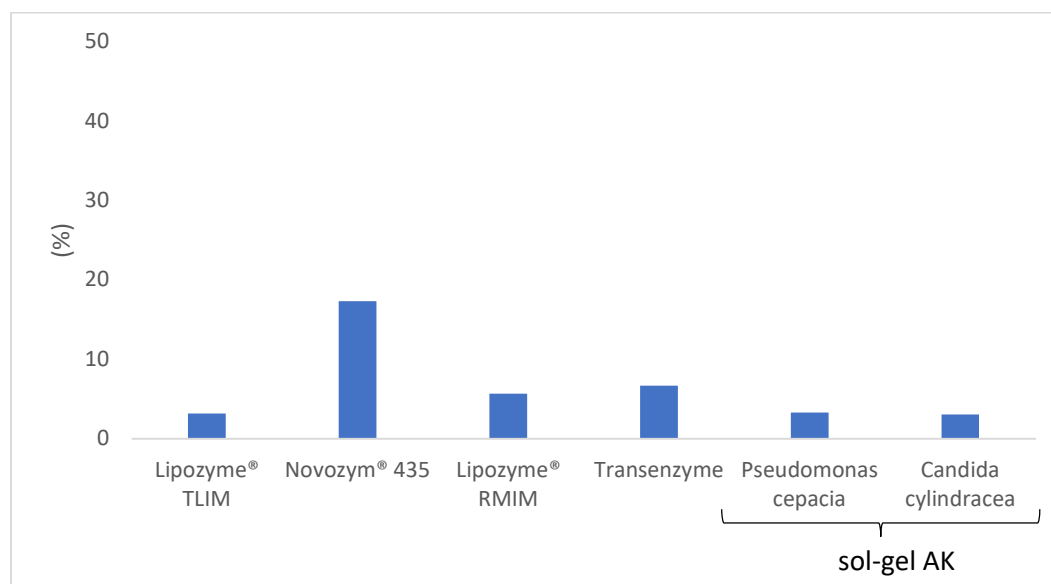


Figure 4. Yield of limonene oxide obtained with immobilized lipases. (1.6 M R-(+)-limonene, PBS pH 8 0.04 M, 1.60 M octanoic acid, 0.44 mM hydrogen peroxide, and 9.66 mg/mL immobilized lipase. Reaction: 24 h, 25 °C, 1000 rpm. Liquid-liquid extraction - 1:1 = sample : ethyl acetate (v/v) → 30 min stirring at room temperature)

The yield values from figure 4 follow the same trend as the values for limonene conversion from figure 3. This supports our choice to continue our studies using Novozym® 435 and Lipozyme® RM IM.

As shown in figures 3 and 4, Novozym® 435 provided the most efficient in converting limonene to limonene oxide. The conversion was 40% and the yield is around 17%. We previously shown in figures 8 and 9 that lipase B from *Candida antarctica* performs better to indirectly convert limonene, it was to be expected that its immobilized form in Novozym® 435 would provide higher efficiency.

Therefore, we proposed for our next study to test the behavior of lipase from *Aspergillus niger*, Novozym® 435 and Lipozyme® RM IM, along systems without hydrogen peroxide and without biocatalysts, when the reaction temperature is varied between 25 and 50 °C.

3.1.2. Variation of reaction temperature

For the study of the influence of reaction temperature on R-(+)-limonene conversion in the presence of the lipase as the only biocatalysts we varied the reaction temperature between 25 and 50 °C. This range of reaction temperatures would show best the influence it has on the process.

From the tested immobilized lipases, we chose Novozym® 435 and Lipozyme® RM IM, because these two performed the best in the given conditions, and characteristic information about these products is available on Strem Chemicals website.

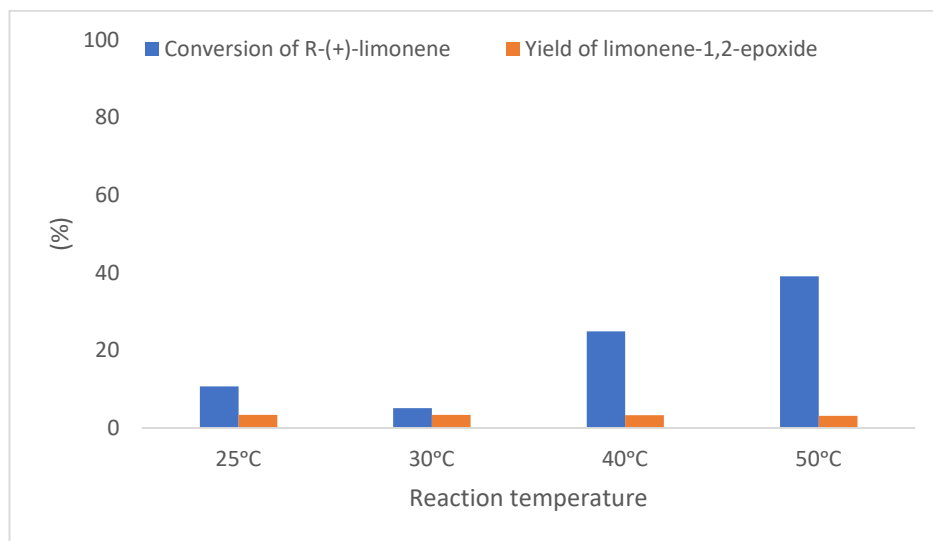


Figure 5. Influence of reaction temperature on samples containing lyophilized lipase from *Aspergillus niger*. (1.6 M R-(+)-limonene, PBS pH 8 0.04 M, 1.60 M octanoic acid, 0.44 mM hydrogen peroxide, and 43.89 µg/mL free lipase. Reaction: 24 h, 25-50 °C, 1000 rpm. Liquid-liquid extraction - 1:1 = sample : ethyl acetate (v/v) → 30 min stirring at room temperature)

The samples were prepared, pre-treated, and analyzed using the GC-FID method. The conversions and epoxide yields were obtained using the calibration curves are presented in figures 5 to 9, each representing the influence of the reaction temperature on each type of sample.

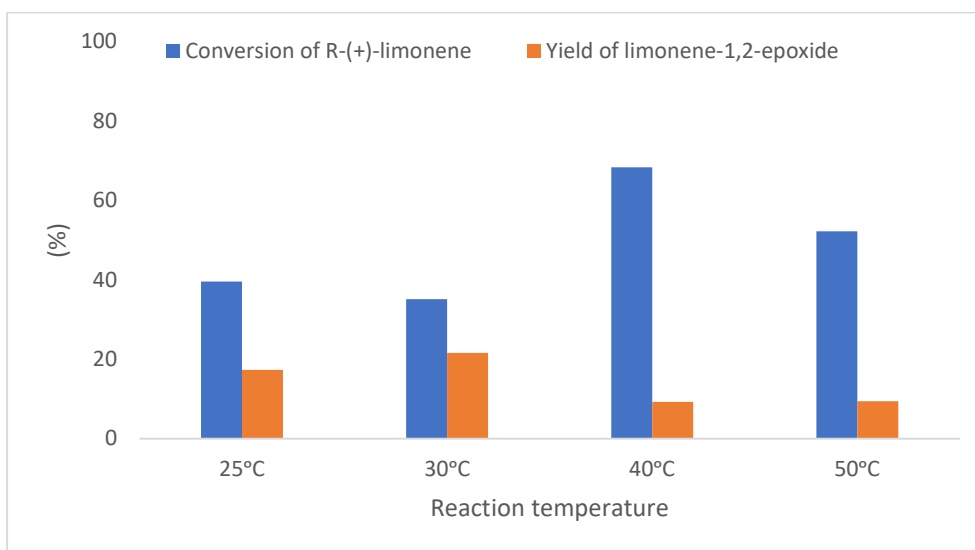


Figure 6. Influence of reaction temperature on samples containing Novozym® 435. (1.6 M R-(+)-limonene, PBS pH 8 0.04 M, 1.60 M octanoic acid, 0.44 mM hydrogen peroxide, and 9.66 mg/mL immobilized lipase. Reaction: 24 h, 25-50 °C, 1000 rpm. Liquid-liquid extraction - 1:1 = sample : ethyl acetate (v/v) → 30 min stirring at room temperature)

At room temperature, the sample containing Novozym® 435 had the most promising results, having a conversion of 40%, and a yield around 17%. The second performance is also for an immobilized lipase in the sample containing Lipozyme® RM IM. This result proves the better efficiency of immobilized enzymes over the lyophilized one. The other two samples had lower performances. The sample without a biocatalyst managed to produce a small amount of limonene oxide, but the sample without hydrogen peroxide did not. This is explained by the role of hydrogen peroxide in our system to oxidize limonene to its corresponding epoxide. Therefore, when no oxidizing agent is present, no epoxide was detected in our extracted sample.

For the next samples set, we modified the reaction temperature with +5 °C, meaning a reaction temperature of 30 °C. From the figures, it can be observed that the values for conversion of limonene and epoxide yield did not visibly increase in the mono-enzymatic samples. As for the previous samples, this set follows the same trend, meaning that the systems with immobilized lipases performed better than the one containing lyophilized lipase from *Aspergillus niger*. From figures 14 and 15, there can be observed that the behavior of the samples without biocatalyst and the one without hydrogen peroxide behave differently than the ones realized at a reaction temperature of 25 °C. In both cases, the conversion of limonene is increased visibly than in the previous set. The most interesting aspect is that the conversion when no oxidizing agent is present is drastically increased, however, the substrate is not

converted into limonene oxide. This means that by increasing the reaction temperature with as low as 5 °C, more R-(+)-limonene tends to transform, but taking into account that without hydrogen peroxide the lipase cannot epoxidize limonene, the reaction is not directed toward our desired product.

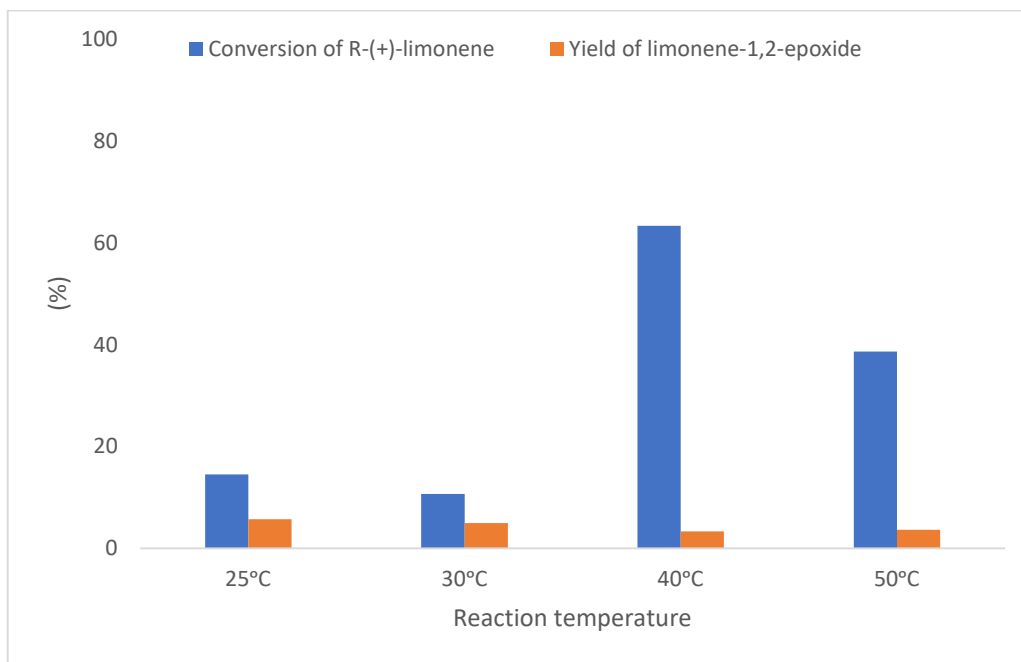


Figure 7. Influence of reaction temperature on samples containing Lipozyme® RM IM. (1.6 M R-(+)-limonene, PBS pH 8 0.04 M, 1.60 M octanoic acid, 0.44 mM hydrogen peroxide, and 9.66 mg/mL immobilized lipase. Reaction: 24 h, 25-50 °C, 1000 rpm. Liquid-liquid extraction - 1:1 = sample : ethyl acetate (v/v) → 30 min stirring at room temperature)

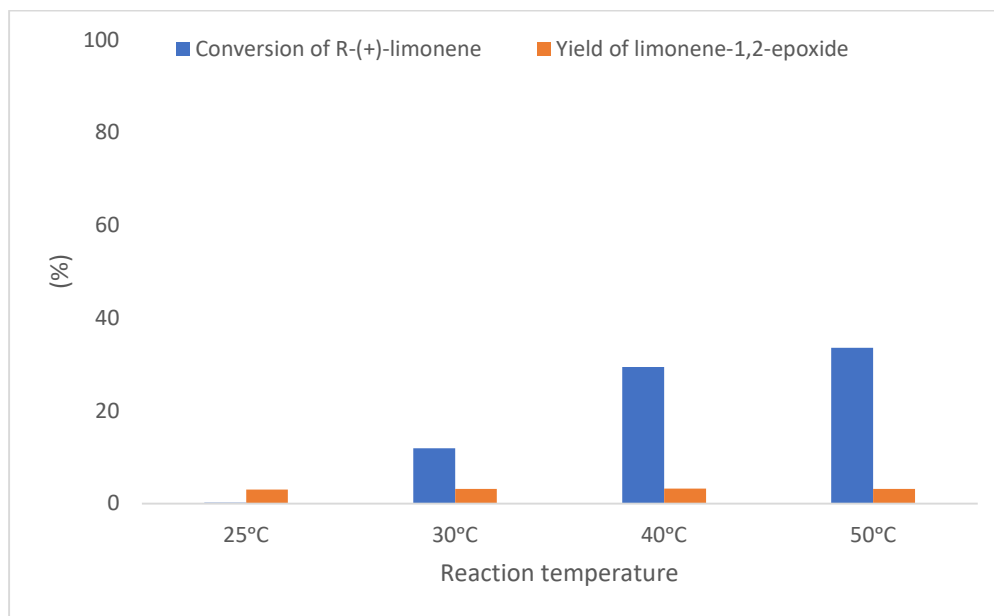


Figure 8. Influence of reaction temperature on samples without biocatalyst. (1.6 M R-(+)-limonene, PBS pH 8 0.04 M, 1.60 M octanoic acid, 0.44 mM hydrogen peroxide. Reaction: 24 h, 25-50 °C, 1000 rpm. Liquid-liquid extraction - 1:1 = sample : ethyl acetate (v/v) → 30 min stirring at room temperature)

For the next samples set, we modified the reaction temperature with +5 °C, meaning a reaction temperature of 30 °C. From the figures, it can be observed that the values for conversion of limonene and epoxide yield did not visibly increase in the mono-enzymatic samples. As for the previous samples, this set follows the same trend, meaning that the systems with immobilized lipases performed better than the one containing lyophilized lipase from *Aspergillus niger*. From figures 14 and 15, there can be observed that the behavior of the samples without biocatalyst and the one without hydrogen peroxide behave differently than the ones realized at a reaction temperature of 25 °C. In both cases, the conversion of limonene is increased visibly than in the previous set. The most interesting aspect is that the conversion when no oxidizing agent is present is drastically increased, however, the substrate is not converted into limonene oxide. This means that by increasing the reaction temperature with as low as 5 °C, more R-(+)-limonene tends to transform, but taking into account that without hydrogen peroxide the lipase cannot epoxidize limonene, the reaction is not directed toward our desired product.

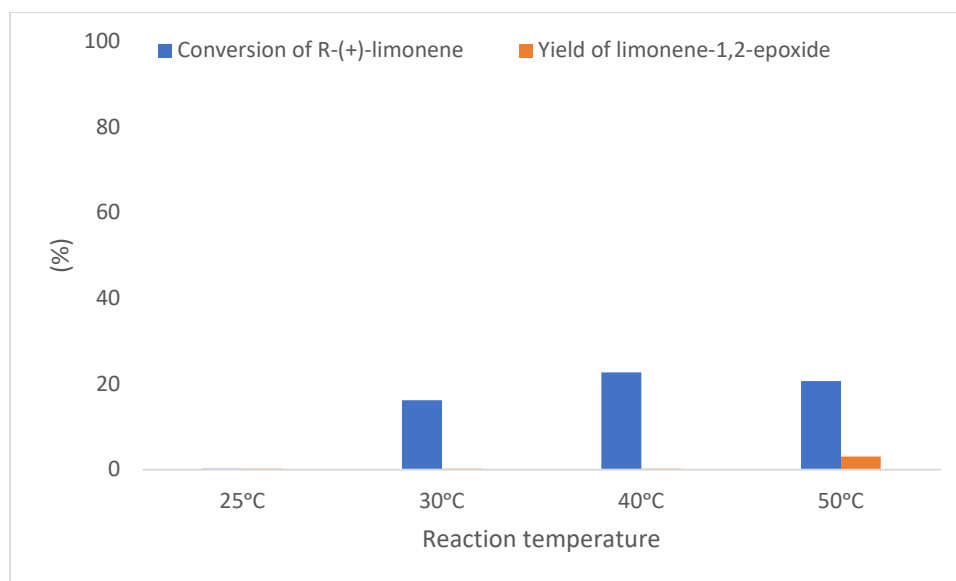


Figure 9. Influence of reaction temperature on samples containing lyophilized lipase from *Aspergillus niger* and no hydrogen peroxide. (1.6 M R-(+)-limonene, PBS pH 8 0.04 M, 1.60 M octanoic acid, and 43.89 µg/mL free lipase. Reaction: 24 h, 25-50 °C, 1000 rpm. Liquid-liquid extraction - 1:1 = sample : ethyl acetate (v/v) → 30 min stirring at room temperature)

The next samples were reacted at a temperature of 40 °C, meaning a modification from the initial temperature with +10 °C. from figures 5 to 9, it can be observed that the efficiency parameters are drastically increased compared to the ones corresponding to a reaction temperature of 25 °C. As for the previous sets, the trending is the same. The samples containing immobilized enzymes had the most promising results. The best conversion degree was obtained for the sample containing Novozym® 435 as biocatalyst and its value is 68%, which is higher than we expected giving the ratio between lipase and substrate, around 250 mg limonene to 11 mg immobilized lipase. This result may be due to a

combination of factors, such as the increased enzymatic activity of the lipase in immobilized form, which was proved by our previous study, and the higher energy input in the system. All the factors combined result in more than half of the substrate quantity being converted. It is observed that the highest amount of epoxide was also obtained in the presence of Novozym® 435. As expected, no limonene oxide was found present in the sample without hydrogen peroxide.

The last sample set was reacted at a temperature of 50 °C. As before, the highest conversion degree and the highest epoxide yield are registered for Novozym® 435. This establish Novozym® 435 as our preferred biocatalyst for the epoxidation of limonene. The sample containing lyophilized lipase from *Aspergillus niger* has a drastic increase in the conversion value. The same can be observed for the sample without biocatalyst and the one without hydrogen peroxide. In all these cases, the increase can be attributed to the high energy input in the samples. Our substrate for those studies, limonene, is not a very stable molecule and this combined with a high reaction temperature may explain the increase in conversion.

In this study, the efficiency of the mono-enzymatic system was registered at different reaction temperatures. Even thou when no enzyme is present there is some epoxide obtained due to the presence of hydrogen peroxide, this result in low limonene oxide obtained and low substrate conversion. When the enzyme is present, but there is no hydrogen peroxide, the biocatalytic process cannot take place.

In table 1 are presented the values obtained from the study on reaction temperature. From conversion values of samples containing lipase from *Aspergillus niger*, it can be observed that as the reaction temperature is increased also does the amount of substrate converted. This is explained by the higher energy input that converts more limonene, because from yield variation is clear that the amount of epoxide does not increase as well.

An interesting aspect is that the maximum conversion degree obtained for a reaction temperature of 50 °C is only 39% which is comparable to the values obtained for Novozym® 435 at lower temperatures of reaction, as it can be observed from table 1. This means that same amount of product can be obtained with a lower energy input.

Table 1 . Values of substrate conversion and epoxide yield from the data presented in figures 5 to 9. (1.6 M R-(+)-limonene, PBS pH 8 0.04 M, 1.60 M octanoic acid, 0.44 mM hydrogen peroxide, and 9.66 mg/mL immobilized lipase or 43.89 µg/mL free lipase. Reaction: 24 h, 25-50 °C, 1000 rpm. Liquid-liquid extraction - 1:1 = sample : ethyl acetate (v/v) → 30 min stirring at room temperature)

	Conversion of R-(+)-limonene (%)				Yield of limonene oxide (%)			
	25 °C	30 °C	40 °C	50 °C	25 °C	30 °C	40 °C	50 °C
<i>Lyophilised lipase from Aspergillus</i>	11	5	25	39	3	3	3	3

<i>niger</i>								
<i>Novozym® 435</i>	40	35	68	52	17	22	9	9
<i>Lipozyme® RM IM</i>	14	11	63	39	6	5	3	4

Form epoxide yields values of samples containing Novozym® 435, it can be observed that the highest amount of limonene oxide is obtained at a reaction temperature of 30 °C. If the temperature is increased further the amount of epoxide decreases. This is explained by the increase energy input which provides a higher probability of limonene oxide to convert in side-reactions.

The results obtained for the two immobilized lipases is also sustained by the information available on the website of Strem Chemicals. Novozym® 435 has its optimum temperature between 30 and 60 °C, and the pH range between 5 and 9. Lipozyme® RM IM has its optimum parameters between 30 – 50 °C, and pH between 7 and 10. This information supports the obtained results and explain why when the temperature of reaction is 50 °C, the conversion degree when Lipozyme® RM IM is used decreases more drastically than with Novozym® 435.

Overall, the drastic increase in R-(+)-limonene conversion at 40 °C reaction temperature compared to room temperature means that a higher energy input settles the advantages of increasing the reaction temperature. However, this increase comes with a downside, it also increases the possibility of losing limonene oxide in random side reactions. This could also affect the efficiency of the bienzymatic system. Therefore, for our next quest in the optimization of the mono-enzymatic system, we decided to manage a way of increasing the epoxide yield.

3.1.3. Testing acid-trapping reagents

The variation of reaction temperature showed that an increased energy input increases the conversion degree to as high as 68% for Novozym® 435 at 40 °C, which was the goal of that specific study. However, the limonene oxide yield registered for 40 °C is only 9%, which is not even comparable to the valued obtained at 30 °C of 22%. This drastic decrease in the intermediate yield was expected due to the relatively unstable nature of limonene oxide and the increased reaction temperature. It was inevitable that a higher reaction temperature would increase the probability of side reactions. Therefore, our new quest in optimizing our system was to increase the epoxide yield at 40 °C.

A possible solution to hopefully increase the yield toward the formation of the epoxide and ceasing the cause of the side reactions would be the use of acid-trapping reagents. These are salts of

weak acids which have a double role, to protect the lipase and to neuter the residual acid, in our case the octanoic acid, which might cause the ring-opening of limonene oxide [30].

A study on lipase-mediated epoxidation of α -pinene shows that the corresponding epoxide could be degraded by acidic conditions. The researching team tested the effect of some alkali compounds that would constrain the acidic protons and, therefore, would increase the epoxidation yield. They proposed different acid-trapping reagents, such as trisodium citrate ($\text{Na}_3\text{C}_6\text{H}_5\text{O}_7$), sodium bicarbonate (NaHCO_3), sodium carbonate (Na_2CO_3), disodium phosphate (Na_2HPO_4). Their reasoning was that trisodium citrate and disodium phosphate are usually components of pH buffers and, therefore, would not have a negative effect on the lipase activity. The other two salts would theoretically be converted in carbon dioxide and water by the acidic media [30].

The study also concluded that the best acid-trapping reagent is trisodium citrate. This one had the best compatibility with the lipase. The other reagents tested, especially the carbonates, proved to be highly alkaline and, therefore, would deactivate the lipase during the reaction resulting in a drastic decrease of the conversion degree [30].

We decided to test the effect of their proposed trapping reagents on our mono-enzymatic system. The samples were prepared, pre-treated, and analyzed using the GC-FID method. The results are presented in figure 10. We tested trisodium citrate ($\text{Na}_3\text{C}_6\text{H}_5\text{O}_7$), sodium bicarbonate (NaHCO_3), sodium carbonate (Na_2CO_3), and disodium phosphate (Na_2HPO_4).

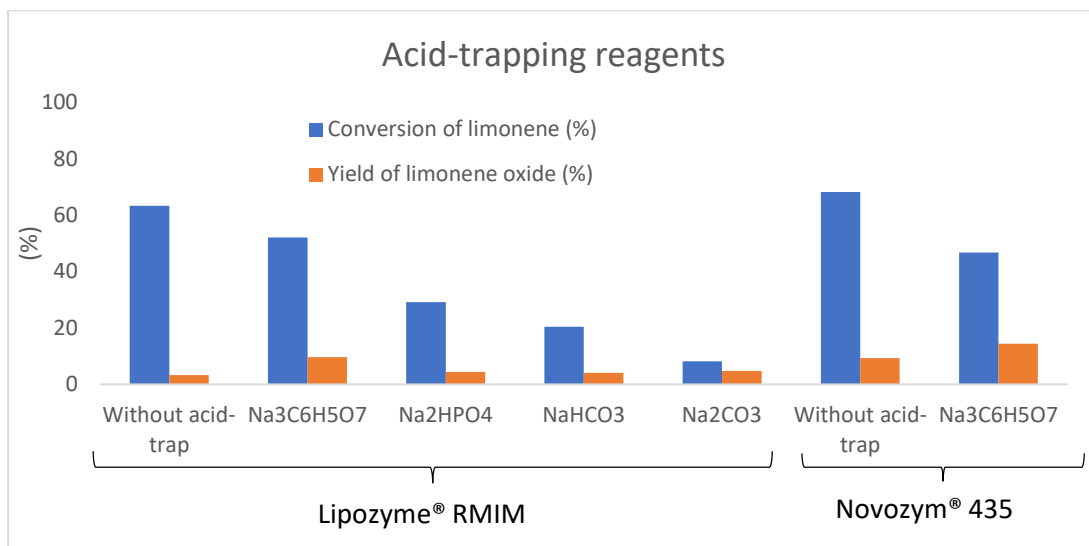


Figure 10. Efficiency parameters for different acid-trapping reagents at 40 °C. (1.6 M R-(+)-limonene, PBS pH 8 0.04 M, 1.60 M octanoic acid, 0.44 mM hydrogen peroxide, 9.66 mg/mL immobilized lipase, and 0.26 M acid-trapping reagent. Reaction: 24 h, 40 °C, 1000 rpm. Liquid-liquid extraction - 1:1 = sample : ethyl acetate (v/v) → 30 min stirring at room temperature)

Right off, it can be clearly observed that samples containing no acid-trap reagent registered the highest R-(+)-limonene conversion. However, the limonene oxide yield is low, as shown previously

when the influence of the reaction temperature was studied. This means that an increased energy input converts a more of the substrate but it also increases the epoxide degradation during the reaction which is undesirable.

In samples containing acid-trapping reagents, the highest conversions were registered for trisodium citrate followed by disodium phosphate which was to be expected due to literature reports on the good compatibility between it and lipases, especially Novozym® 435. The samples containing sodium carbonate registered a drastic decrease in R-(+)-limonene conversion which was caused by its high alkalinity which inactivates the lipase [30].

The epoxide yields registered clearly show that the trisodium citrate managed to preserve the epoxide only when coupled with Novozym® 435. The yield was slightly increased in this case. Trisodium citrate coupled with Lipozyme® RM IM did not affect the epoxide yield in a meaningful way. However, the carbonates and the phosphate not only drastically decreased the conversion, but also the limonene oxide yield, meaning that their action on the lipase activity is undesirable.

Overall, trisodium citrate had the best outcome of all trapping reagents employed in this study managing to preserve the epoxide, and affecting the R-(+)-limonene conversion the least, meaning it has a good compatibility with the lipase. Considering the effect of the on the enzyme activity and limonene oxide yield, we decided to include trisodium citrate in our samples.

3.2. Bienzymatic system

3.2.1. Enzyme screening

From the the previously obtained data, the best reaction temperature is 40 °C, but the temperature increase would also produce a decrease of limonene oxide yield which was managed to be solved by the addition of trisodium citrate acid-trapping reagent. Therefore, we started the optimization of the bienzymatic process by screening to find the best couple lipase-hydrolase for our system. However, the presence of a second enzyme can affect the behavior of the samples unexpectedly, therefore, samples containing lyophilized lipase from *Aspergillus niger* were prepared as a performance reference. We decided to perform the enzyme screening without the acid-trapping reagent present in the system to avoid any possible side effects of trisodium citrate on the enzymatic activity of the hydrolase.

From the three hydrolases tested, CH55-LEH and Tomsk-LEH are thermophilic. From the data provided by Ferrandi et al [1], the optimum temperature for Re-LEH is around 30 °C, for Tomsk-LEH is around 40 °C, and CH55-LEH goes for as far as 60 °C. We tested the two immobilized lipases with all three hydrolases, however, for lipase from *Aspergillus niger*, we chose only Re-LEH and CH55-

LEH. The reason for our choice was that the optimum temperature for Re-LEH is around room temperature, and we also wanted to compare the performance of CH55-LEH at room temperature, due to its high thermal stability.

The samples were prepared, pre-treated, and analyzed using both GC-FID, and GC*-FID methods. The efficiency parameters are presented in figures 11 and 12 and the efficiency values are in table 2.

In the figure 11 are presented the values for R-(+)-limonene conversion among all combinations between lipases and hydrolases. The samples containing lipases in immobilized form had a reaction temperature of 40 °C because in our previous study at this reaction temperature we recorded the best performance.

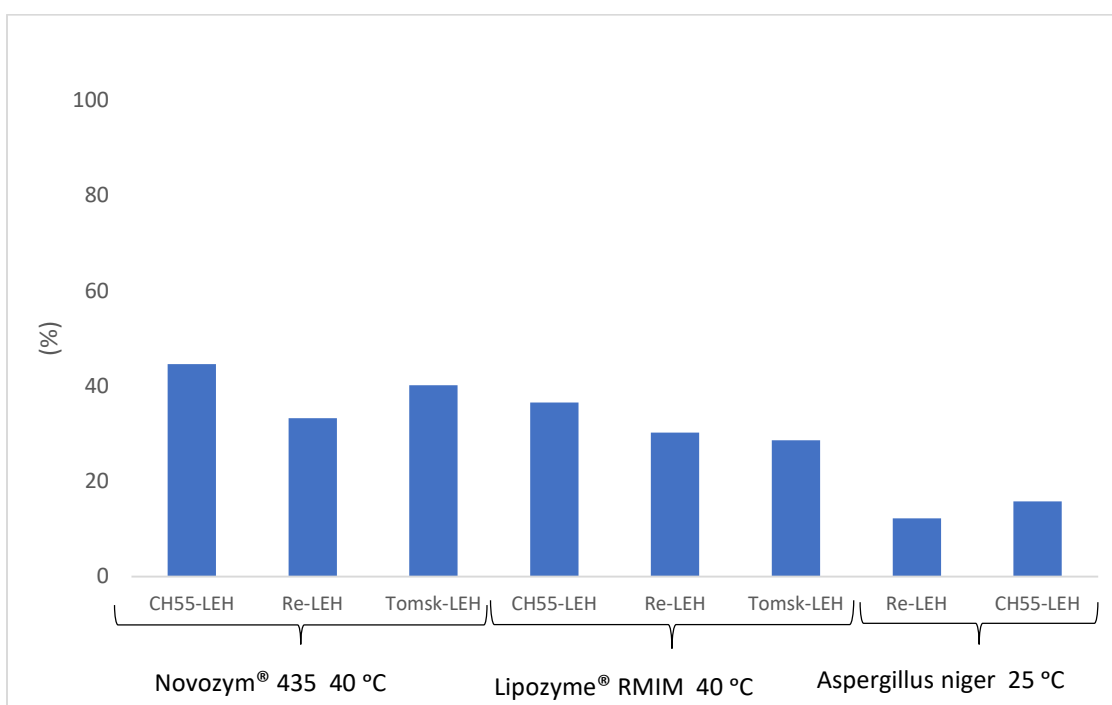


Figure 11. Conversion of R-(+)-limonene among different bienzymatic systems. (1.6 M R-(+)-limonene, PBS pH 8 0.04 M, 1.60 M octanoic acid, 0.44 mM hydrogen peroxide, 43.89 µg/mL free lipase or 9.66 mg/mL immobilized lipase, and 2.81 % v/v hydrolase. Reaction: 24 h, 25 or 40 °C, 1000 rpm. Liquid-liquid extraction - 1:1 = sample : ethyl acetate (v/v) → 30 min stirring at room temperature)

Among the samples containing lipase Novozym® 435, the highest values for substrate conversion were recorded for samples containing thermophilic hydrolases. This result was expected, because CH55-LEH and Tomsk-LEH have the optimum temperature range above room temperature. The difference between the two conversion is only 5%.

The samples containing Lipozyme® RM IM behaved quite different compared to the ones containing Novozym® 435. The conversion decreases from CH55-LEH to Tomsk-LEH, which means that the sample containing Re-LEH performed better than the one containing Tomsk-LEH. However,

the sample containing Re-LEH has a conversion degree only 1% higher than the one containing Tomsk-LEH.

Among samples prepared with lyophilized lipase from *Aspergillus niger*, the one containing CH55-LEH resulted in a higher conversion degree than the one containing Re-LEH. This means that hydrolase CH55-LEH is more active even at room temperature than Re-LEH.

By comparing the samples with the reference couple of lipase and hydrolase, more exactly, lipase from *Aspergillus niger* and hydrolase Re-LEH, every other combination converted more substrate than this initial mixture. The samples containing immobilized lipase is that they performed better in our previous studies. This combined with the increased reaction temperature used for this sample sets may explain the increased conversion degree.

The drastic decrease in the conversion degree of R-(+)-limonene might be attributed to the free hydrolase present in the system. This enzyme might adsorb randomly on the support of the immobilized lipases resulting in blocking the reagents access to the active sites of the lipase.

Overall, the samples containing immobilized enzymes registered a higher conversion degree than the ones containing free enzyme. Between the samples containing Novozym® 435 and the ones containing Lipozyme® RM IM, the first ones performed better. The highest efficiency was recorder in every set for samples containing hydrolase CH55-LEH.

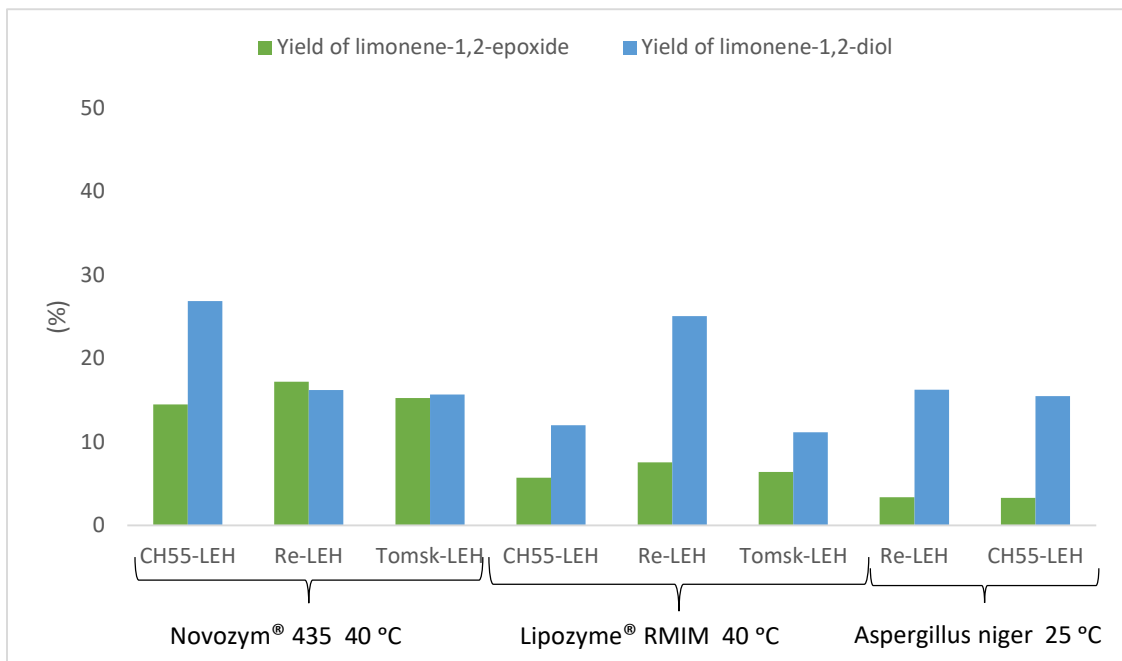


Figure 12. Yield values for limonene-1,2-epoxide and limonene-1,2-diol among different bienzymatic systems. (1.6 M R-(+)-limonene, PBS pH 8 0.04 M, 1.60 M octanoic acid, 0.44 mM hydrogen peroxide, 43.89 µg/mL free lipase or 9.66 mg/mL immobilized lipase, and 2.81 % v/v hydrolase. Reaction: 24 h, 25 or 40 °C, 1000 rpm. Liquid-liquid extraction - 1:1 = sample : ethyl acetate (v/v) → 30 min stirring at room temperature. Diol derivatization - 100 µL extract, 150 µL pyridine, 66 µL acetic anhydride → 24 h, 25 °C, 1000 rpm)

In the figure above are presented the results obtained for epoxide and diol yields. Our ideal bienzymatic system has high yield for limonene-1,2-diol, and small yield value for limonene oxide. However, this ideal case is highly unlikely, because it means that the hydrolase would convert most of the amount of epoxide present in the system in diols. The de-cyclization reaction of epoxide intermediate depends on more factors than the presence of hydrolase. Therefore, our goal for this study is to obtain a bienzymatic system which favors the formation of limonene-1,2-diol.

From figure 12 can be observed that the majority of the bienzymatic systems tested favor the formation of diol products over the formation of epoxide intermediates. In the samples containing lipase from *Aspergillus niger* limonene-1,2-diol is preferentially obtained in both cases. The yield for limonene oxide is as low as 3%, while the yield for diol is around 16%.

However, only the ratio between the two yields is favorable in the *Aspergillus niger* – hydrolase couple, because higher diol yields were obtained in the bienzymatic systems Lipozyme® - Re-LEH, and Novozym® - CH55-LEH. Both yields are around 30%, more exactly, 25% for Lipozyme® RM IM - Re-LEH, and 27% for Novozym® 435 - CH55-LEH. Between these two bienzymatic couples, the one that favors more the formation of limonene-1,2-diol over limonene oxide is Lipozyme® - Re-LEH, which has an epoxide yield of only 8%. The other sample, Novozym® - CH55-LEH has a yield value for epoxide of 14%, almost double.

The other samples containing the couple Novozym® 435 – hydrolase do not favor the formation of either limonene-1,2-diol, nor limonene oxide. Both products have similar values for yields. On the other hand, the other two samples containing Lipozyme® RM IM favor the formation of diol products, but the yield values are lower than in the case when lipase from *Aspergillus niger* was used.

One other factor to give consideration when choosing the best couple lipase – hydrolase is the value of enantiomeric excess. The obtained values are presented below in table 2.

Table 2. Values of enantiomeric excess of (1S, 2S, 4R)-(+)-limonene-1,2-diol of the samples presented in figures 11 and 12. (1.6 M R-(+)-limonene, PBS pH 8 0.04 M, 1.60 M octanoic acid, 0.44 mM hydrogen peroxide, 43.89 µg/mL free lipase or 9.66 mg/mL immobilized lipase, and 2.81 % v/v hydrolase. Reaction: 24 h, 25 or 40 °C, 1000 rpm. Liquid-liquid extraction - 1:1 = sample : ethyl acetate (v/v) → 30 min stirring at room temperature. Diol derivatization - 100 µL extract, 150 µL pyridine, 66 µL acetic anhydride → 24 h, 25 °C, 1000 rpm)

Reaction temperature (°C)	Lipase	Hydrolase	Enantiomeric excess of (1S, 2S, 4R)-(+)-limonene-1,2-diol (ee%)
40	Novozym® 435	CH55-LEH	96
		Tomsk-LEH	89
		Re-LEH	89
	Lipozyme® RM IM	CH55-LEH	88

		Tomsk-LEH	89
		Re-LEH	97
25	Lyophilized lipase from <i>Aspergillus niger</i>	CH55-LEH	89
		Re-LEH	91

The values of the enantiomeric excess obtained from our samples are in majority close to 90%, meaning that our systems favor the formation of the S isomer of limonene-1,2-diol. However, just two couples of lipases – hydrolases obtained values closer to 100%, meaning Lipozyme® RM IM - Re-LEH and Novozym® 435 - CH55-LEH, with the values of 97% and 96%, respectively. Besides these those two samples, the rest favors the S isomer as well, however, the combination of lipases with their respective hydrolases are not as close to produce an enantiopure limonene-1,2-diol.

Overall, the systems containing lyophilized lipase from *Aspergillus niger* coupled with either Re-LEH or CH55-LEH, had an enantiomeric excess around 90%, and favored the formation of limonene-1,2-diol over limonene oxide, however, the conversion of limonene substrate was low. From the samples containing immobilized lipases, only Lipozyme® RM IM - Re-LEH and Novozym® 435 - CH55-LEH stood out, because the enantiomeric excess was closer to 100%, and they both favored the formation of diol product while converting higher amounts of limonene.

3.2.2. Development of enzyme co-immobilization-based composite

After the optimization of the enzymatic cascade process for R-(+)-limonene valorization, we decided to test the biocomposite candidates which had the most promising results in our enzyme screening test in the presence of the acid-trapping reagent of choice. For a better comparison, we decided to prepare samples containing both enzymes immobilized, in the form of a biocomposite, and immobilized lipase coupled with free hydrolase. This would provide a better understanding of how the system efficiency is affected in different conditions.

The samples were prepared, pre-treated, and analyzed using both GC-FID, and GC*-FID methods. The analysis was done using GC-FID method for extracted samples, and GC*-FID for the derivatized samples. The efficiency parameters are presented in figure 13 and table 3.

The bienzymatic cascade system in which the immobilized lipases were coupled with free hydrolase registered low conversions degrees, even lower than the systems in which the immobilized lipases were used alone. This drastic decrease cannot be attributed to the presence of trisodium citrate acid-trap, because, as it can be observed in figure 13, the co-immobilized systems did not register a decrease of the conversion degree, but the opposite.

The Lipozyme® RM IM containing system appear to be more affected in both cases, converting drastically low amounts of R-(+)-limonene each time. This might be due to the support choose for the immobilization, because the anionic resin used for this biocatalyst has a tendency of aggregating in liquid medium and this would block some active sites. This effect would explain only the results for the free hydrolase system and its relatively high diol yield registered. For the Lipozyme® RM IM – Re-LEH biocomposite additional testing needs to be done, because there is a possibility that the lipase desorbs during the washing procedure, and therefore the conversion would be highly affected but not the limonene-1,2-diol yield, as it can be observed.

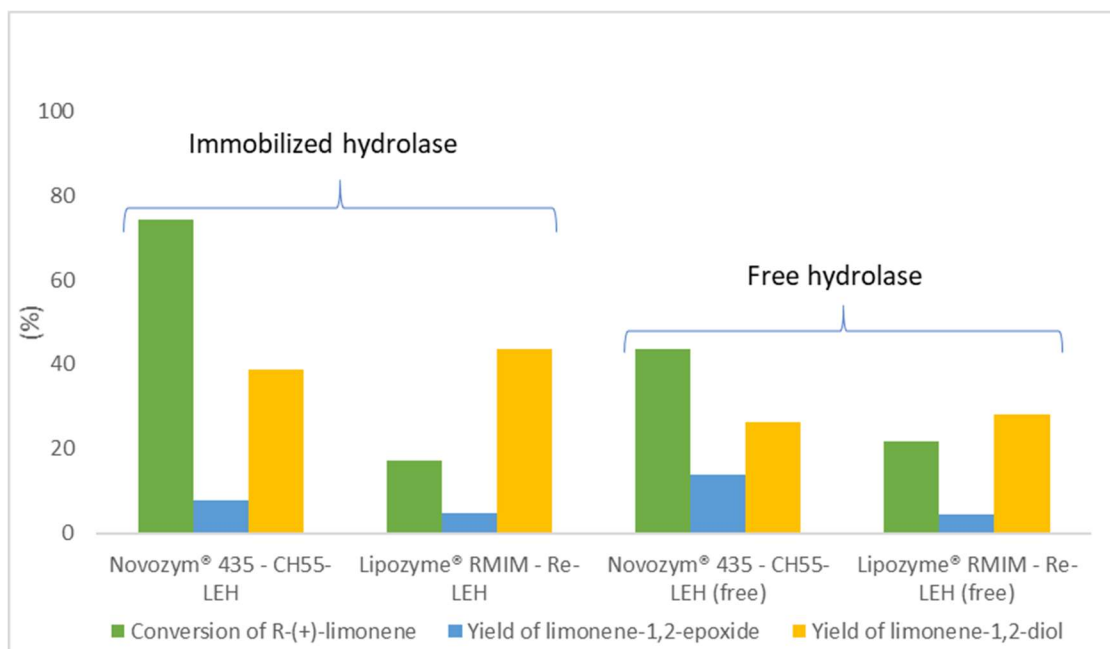


Figure 13. Efficiency parameters for different bienzymatic systems. (1.6 M R-(+)-limonene, PBS pH 8 0.04 M, 1.60 M octanoic acid, 0.44 mM hydrogen peroxide, 9.66 mg/mL immobilized lipase or bienzymatic biocatalyst, 2.81 % v/v hydrolase, and 0.26 M trisodium citrate. Reaction: 24 h, 40 °C, 1000 rpm. Liquid-liquid extraction - 1:1 = sample : ethyl acetate (v/v) → 30 min stirring at room temperature. Diol derivatization - 100 µL extract, 150 µL pyridine, 66 µL acetic anhydride → 24 h, 25 °C, 1000 rpm)

The Novozym® 435 coupled with free CH55-LEH registered low conversion degree and the highest limonene oxide yield among all samples. At first sight, one might be tempted to assume this might be due to the action of the trisodium citrate trapping salt. However, the other samples are not affected in the same way, meaning that there might be another explanation.

By comparing the Novozym® 435 containing samples, it is obvious that the co-immobilization-based composite performed the best. The only difference between the two samples is the state of the hydrolase, free or immobilized. Therefore, we concluded that the reason for the poor performance of the Novozym® 435 coupled with the free CH55-LEH hydrolase system is the tendency of the CH55-LEH to adsorb on the surface of the acrylic support during the reaction. This process taking place

during the reaction time resulted in the blocking of the active sites of both enzymes which explains the low conversion degree and high epoxide yield.

The hydrolase adsorption on support during reaction hypothesis might be applied for the Lipozyme® RM IM coupled with free Re-LEH system. However, if the adsorption would have such an important effect this would lead to an accumulation of epoxide during the reaction, because the hydrolase active site would be blocked by random interactions with the support, and this is not the case. The most affected parameter is the R-(+)-limonene conversion which sustains the aggregation hypothesis previously mentioned.

In table 3 are presented the enantiomeric excess values for all the samples. It can be observed that there is not a high difference between the values for the co-immobilized systems and immobilized lipase coupled with the free hydrolase samples. This means that the hydrolase ability to convert the epoxide to a preferential enantiomer of the limonene-1,2-diol is not affected.

Table 3. Enantiomeric excess of (1S, 2S, 4R)-(+)-limonene-1,2-diol values corresponding to the data from figure 13. (1.6 M R-(+)-limonene, PBS pH 8 0.04 M, 1.60 M octanoic acid, 0.44 mM hydrogen peroxide, 9.66 mg/mL immobilized lipase or bienzymatic biocatalyst, 2.81 % v/v hydrolase, and 0.26 M trisodium citrate. Reaction: 24 h, 40 °C, 1000 rpm. Liquid-liquid extraction - 1:1 = sample : ethyl acetate (v/v) → 30 min stirring at room temperature. Diol derivatization - 100 µL extract, 150 µL pyridine, 66 µL acetic anhydride → 24 h, 25 °C, 1000 rpm)

Biocatalyst	Enantiomeric excess (1S, 2S, 4R)-(+)-limonene-1,2-diol (ee%)
<i>Novozym® 435 – CH55-LEH composite</i>	91
<i>Lipozyme® RM IM – Re-LEH composite</i>	91
<i>Novozym® 435 and free CH55-LEH</i>	89
<i>Lipozyme® RM IM and free Re-LEH</i>	89

The most promising results were obtained from the Novozym® 435 – CH55-LEH biocomposite, which managed to convert around 70% of the R-(+)-limonene present in the initial system. Low amounts of epoxide were found during the analysis, meaning that most of it was converted into the corresponding diol. The limonene-1,2- diol yield was as high as almost 40%, from which 91% is the (1S, 2S, 4R)-limonene-1,2-diol isomer. Therefore, this biocomposite had the most promising results, and was choose for further testing.

3.2.3. Testing of enzyme co-immobilization-based composite

As previously shown, from the two biocomposites developed, meaning Novozym® 435 – CH55-LEH composite and Lipozyme® RM IM – Re-LEH composite, only the first registered promising results. Therefore, we chose to further test only the biocatalyst composed of Novozym® 435 and CH55-LEH co-immobilization for reusability in consecutive reaction cycles. Another possible

application for the developed biocatalyst is the bioconversion of α -phellandrene. For this study we tested both materials, for a better comparison.

The samples were prepared, pre-treated, and analyzed using both GC-FID, and GC*-FID methods. The analysis was done using GC-FID method for extracted samples, and GC*-FID for the derivatized samples. The efficiency parameters are presented in figure 14 and table 4.

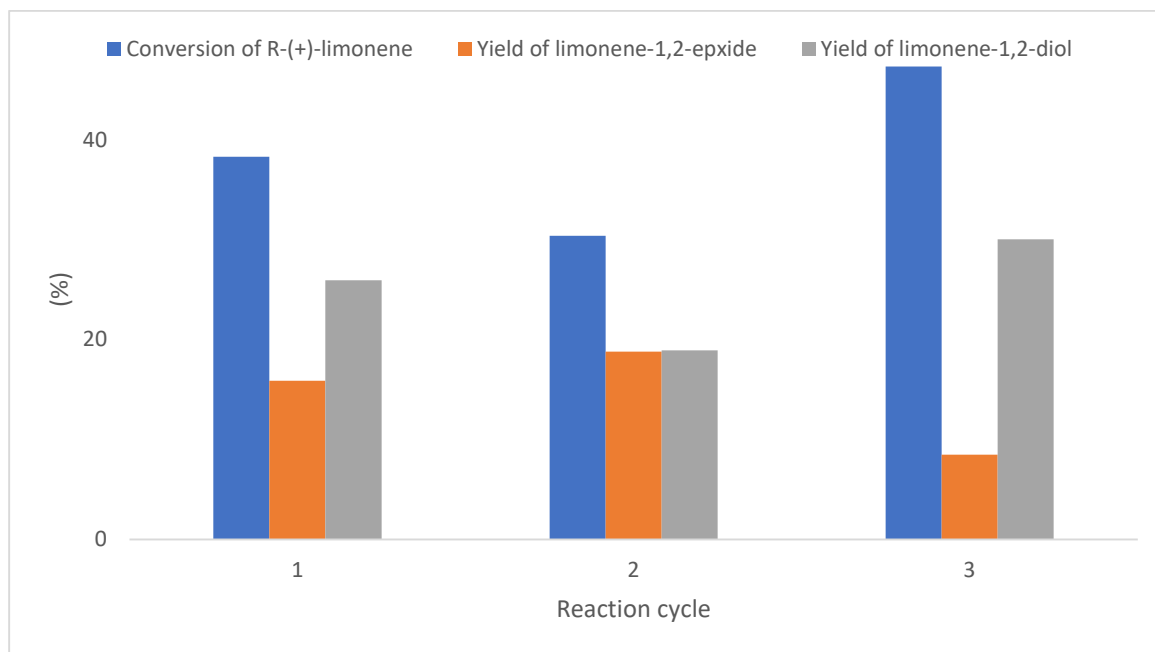


Figure 14. Efficiency parameters of Novozym® 435 – CH55-LEH biocomposite recycling. (1.6 M R-(+)-limonene, PBS pH 8 0.04 M, 1.60 M octanoic acid, 0.44 mM hydrogen peroxide, 9.66 mg/mL immobilized lipase or bienzymatic biocatalyst, and 0.26 M trisodium citrate. Reaction: 24 h, 40 °C, 1000 rpm. Liquid-liquid extraction - 1:1 = sample : ethyl acetate (v/v) → 30 min stirring at room temperature. Diol derivatization - 100 μ L extract, 150 μ L pyridine, 66 μ L acetic anhydride → 24 h, 25 °C, 1000 rpm)

In the figure 14 are presented the efficiency parameters of R-(+)-limonene conversion for the three reaction cycles. The conversion degree varies among the cycles. It registered a decrease of around 8% between the first and second cycle, but it increases with around 17% in the third one. This shows that our material conserved most of its activity among all reaction cycles. The average conversion degree of R-(+)-limonene among all consecutive transformations is 39% \pm 9, meaning that the biocomposite manages to convert most of the substrate in each process.

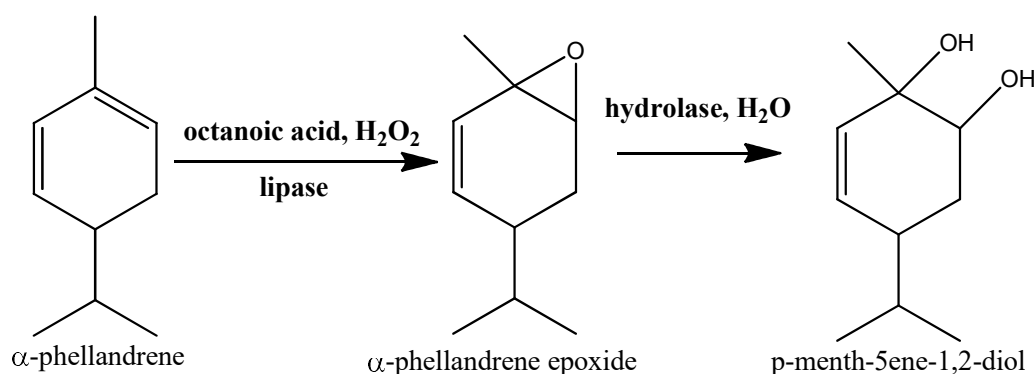
The formation of limonene-1,2-diol is favored over the one of limonene oxide. The diol yield increases in the third cycle compared to the first two. By comparison, the epoxide yield increases from the first cycle to the second, but drastically decreases in the third. However, after each process, the formation of (1S,2S,4R)-limonene-1,2-diol isomer is favored, as it can be observed from the enantiomeric excess of (1S, 2S, 4R)-(+)-limonene-1,2-diol values presented in table 4.

Table 4. Values of the efficiency parameters of Novozym® 435 – CH55-LEH biocomposite recycling presented in figure 14. (1.6 M R-(+)-limonene, PBS pH 8 0.04 M, 1.60 M octanoic acid, 0.44 mM hydrogen peroxide, 9.66 mg/mL bienzymatic biocatalyst, and 2.81 % v/v hydrolase. Reaction: 24 h, 40 °C, 1000 rpm. Liquid-liquid extraction - 1:1 = sample : ethyl acetate (v/v) → 30 min stirring at room temperature. Diol derivatization - 100 μL extract, 150 μL pyridine, 66 μL acetic anhydride → 24 h, 25 °C, 1000 rpm)

Reaction cycle	1 st cycle	2 nd cycle	3 rd cycle	Average ± confidence interval (%)
Conversion of R-(+)-limonene (%)	38	30	47	39±8
Yield of limonene-1,2-epoxide (%)	16	19	8	14±5
Yield of limonene-1,2-diol (%)	26	19	30	25±6
Enantiomeric excess of (1S, 2S, 4R)-(+)-limonene-1,2-diol (ee%)	93	96	95	95±2

The developed biocatalyst was tested for R-(+)-limonene conversion in up to three consecutive reaction cycles. Overall, the material managed to conserve most of its activity after each cycle, the formation of limonene-1,2-diol is favored over the limonene oxide, and the formation of (1S,2S,4R)-limonene-1,2-diol isomer is favored after each cycle.

For another possible application of our developed materials, we tested the bioconversion of α -phellandrene. The process is similarly to the one for R-(+)-limonene and it is presented in scheme 2. The two-step process is based on the epoxidation of one of the double bonds on α -phellandrene cycle with the formation of α -phellandrene epoxide indirectly catalyze by the lipase in the presence of hydrogen peroxide and octanoic acid, followed by the selective hydrolytic ring opening in the presence of the hydrolase.



Scheme 2. Scheme of the α -phellandrene biotransformation.

The sample contents is the same, as previously mentioned, with the only difference being that the R-(+)-limonene is replaced with the same amount of α -phellandrene. For this application we tested both biocomposites Novozym® 435 – CH55-LEH and Lipozyme® RM IM – Re-LEH. The samples were extracted and derivatized. The analysis was done using both GC-FID and GC*-FID methods for a proper quantification of all reaction products.

In table 5 are presented the registered efficiency parameter values for the substrate conversion, and in figure 15 is a graphic representation of the substrate conversion and product yields. It can be observed that both biocatalysts registered promising results in the valorization of a different monoterpene.

In both cases, similar values of the conversion degree of α -phellandrene, α -phellandrene epoxide and p-menth-5-ene-1,2-diol yields were registered, as well as similar enantiomeric excesses for the (1S,2S,4R)-p-menth-5-ene-1,2-diol isomer.

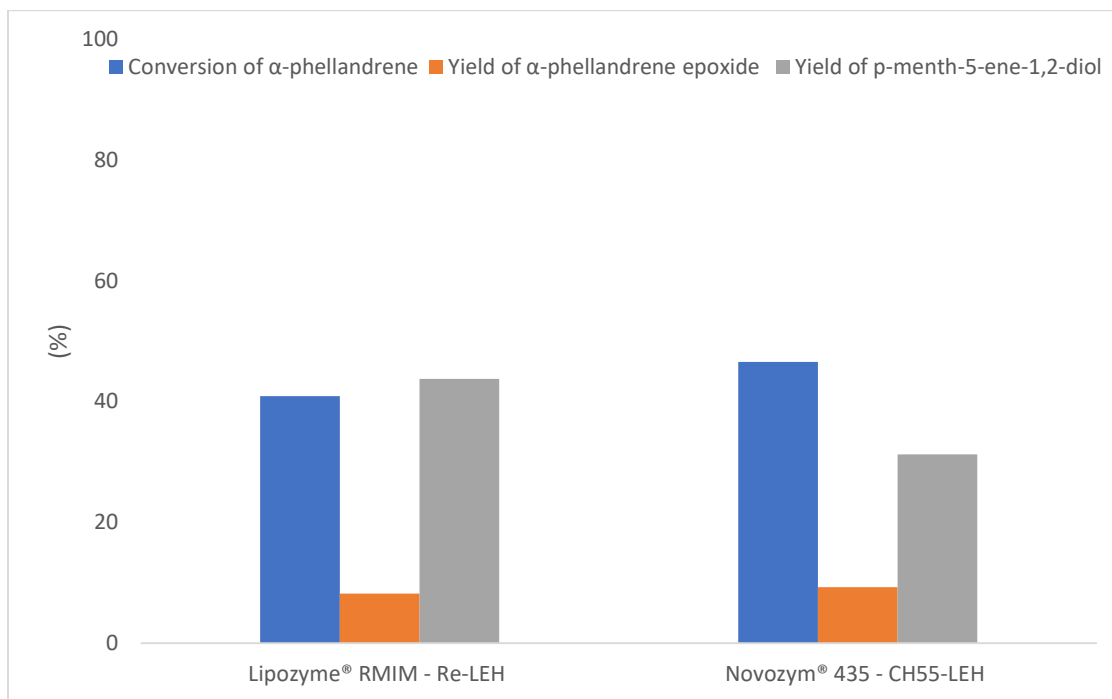


Figure 15. Efficiency parameters of α -phellandrene biotransformation. (1.6 M α -phellandrene, PBS pH 8 0.04 M, 1.60 M octanoic acid, 0.44 mM hydrogen peroxide, 9.66 mg/mL bienzymatic biocatalyst, 0.26 M trisodium citrate. Reaction: 24 h, 40 °C, 1000 rpm. Liquid-liquid extraction - 1:1 = sample : ethyl acetate (v/v) \rightarrow 30 min stirring at room temperature. Diol derivatization - 100 μ L extract, 150 μ L pyridine, 66 μ L acetic anhydride \rightarrow 24 h, 25 °C, 1000 rpm)

The formation of p-menth-5-ene-1,2-diol is favored over α -phellandrene epoxide, meaning that most of the converted substrate is then transformed in the desired diol product. It appears that the biocomposite containing Lipozyme® RM IM lipase managed to yield a higher diol amount compared to the Novozym® 435 containing one, with a difference of around 13%.

The conversion degree is again higher in the case of Lipozyme® RM IM – Re-LEH composite, having a value close to 50%, compared to close to 40% in the case of Novozym® 435 – CH55-LEH composite. However, the overall values presented in table 4 are close to each other, which offers promising perspectives for future applications for α -phellandrene valorization using a bienzymatic cascade process.

Table 5. Values of the efficiency parameters of α -phellandrene biotransformation from figure 15. (1.6 M α -phellandrene, PBS pH 8 0.04 M, 1.60 M octanoic acid, 0.44 mM hydrogen peroxide, 9.66 mg/mL bienzymatic biocatalyst, 0.26 M trisodium citrate. Reaction: 24 h, 40 °C, 1000 rpm. Liquid-liquid extraction - 1:1 = sample : ethyl acetate (v/v) \rightarrow 30 min stirring at room temperature. Diol derivatization - 100 μ L extract, 150 μ L pyridine, 66 μ L acetic anhydride \rightarrow 24 h, 25 °C, 1000 rpm)

Biocomposite	Novozym® 435 – CH55-LEH	Lipozyme® RM IM – Re-LEH
Conversion of <i>R</i> -(+)-limonene (%)	41	47
Yield of limonene-1,2-epoxide (%)	9	8
Yield of limonene-1,2-diol (%)	31	44
Enantiomeric excess of (1 <i>S</i> ,2 <i>S</i> ,4 <i>R</i>)- <i>p</i> -menth-5-ene-1,2-diol (<i>ee</i> %)	96	95

3.3. Correlation between biocatalyst behavior and characteristics

3.3.1. FTIR analysis

The developed materials were characterized using FTIR spectroscopy. The samples were analyzed between 400 and 4000 cm^{-1} and the resulted spectra are presented in figures 16 and 17.

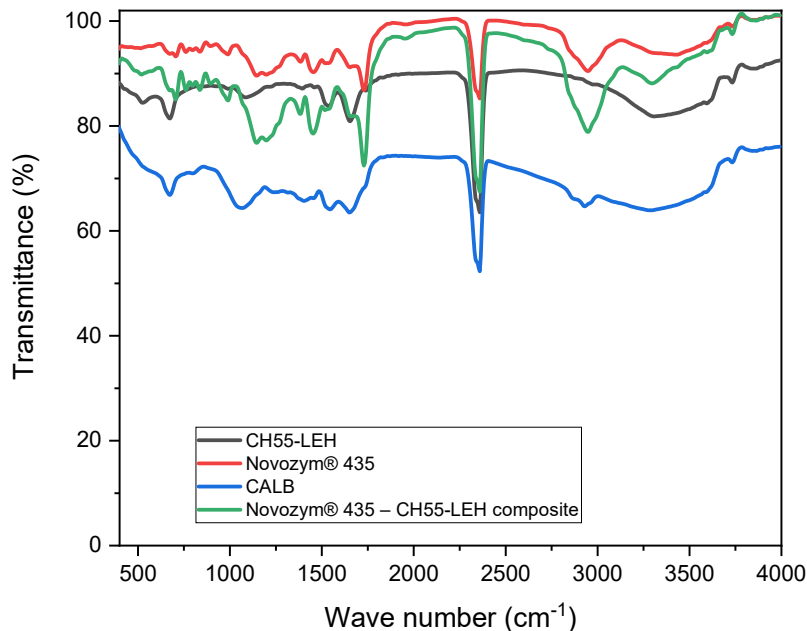


Figure 16. FTIR spectra of free and immobilized lipase and hydrolase components of Novozym® 435 – CH55-LEH composite.

A comparative FTIR analysis of the enzymes before and after immobilization provides significant information about the effect of the immobilization on the protein secondary structure. Due

to the polypeptide and protein repeating units which compose the backbone of enzymes, there are nine characteristic IR bands arising from this type of structure, meaning amide A and B and I to VII. From all these bands, only amide I and amide II have the most prominent vibrations. However, the most sensitive to the protein secondary structure changes is amide I between 1600 and 1700 cm^{-1} [31], and this would be our band of interest.

In figure 16 is presented the FTIR spectra of Novozym® 435 – CH55-LEH composite along with free CALB, bare Novozym® 435 and free CH55-LEH. Right off, the band registered between 2300 and 2400 cm^{-1} corresponds to the asymmetric stretching mode of CO_2 [32], meaning it is an interference and not a part of our materials. The same CO_2 characteristic vibration can be observed in the figure 17. However, due to the protein nature of our samples, we would be focusing only on the amide I region of our samples.

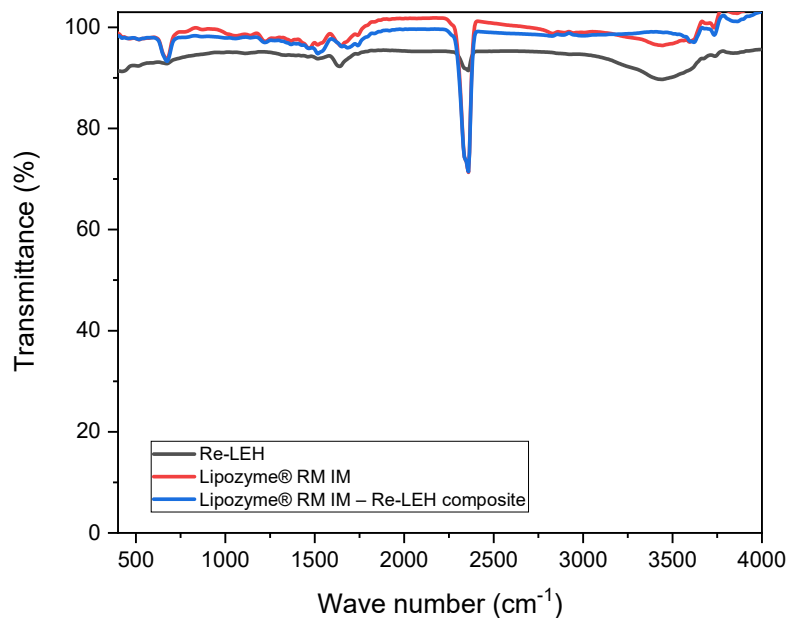


Figure 17. FTIR spectra of free and immobilized lipase and hydrolase components of Lipozyme® RM IM – Re-LEH composite.

By comparison between figure 16 and figure 17, it can be observed that the IR amide I bands of Lipozyme® RM IM – Re-LEH composite and its components is less intense than the ones of Novozym® 435 – CH55-LEH composite and its components. The spectra from figure 16 have bands intense enough that it can be observed the presence of one in the 1000-1200 cm^{-1} region, which corresponds to carbohydrate content and glycoform distribution of protein [33]. This band is visible for

free lipase B from *Candida antarctica*, bare Novozym® 435 and our biocatalyst, being more intense for the lipase than for the CH55-LEH hydrolase.

By comparison between figure 16 and figure 17, it can be observed that the IR amide I bands of Lipozyme® RM IM – Re-LEH composite and its components is less intense than the ones of Novozym® 435 – CH55-LEH composite and its components. The spectra from figure 16 have bands intense enough that it can be observed the presence of one in the 1000-1200 cm⁻¹ region, which corresponds to carbohydrate content and glycoform distribution of protein [33]. This band is visible for free lipase B from *Candida antarctica*, bare Novozym® 435 and our biocatalyst, being more intense for the lipase than for the CH55-LEH hydrolase.

Due to the more intense spectra and the fact that we managed to analyze both free lipase B from *Candida antarctica* and CH55-LEH hydrolase, we chose to focus on the characterization of the amide I region of the Novozym® 435 – CH55-LEH composite.

3.3.2. Deconvolution of FTIR data

Amide I band of the FTIR spectra of proteins is the most sensitive region to modifications in the secondary structure. This band is situated between 1600 and 1700 cm⁻¹. Its apparition is mostly caused by the stretching vibration of C=O of the peptide chain, in proportion of 80%. The rest of around 20% is due to the stretching of C-N bond. The exact position of this band is correlated to the backbone conformation of the enzyme and the pattern of hydrogen bonds [31].

The structural component of amide I band are scattered within its region. We choose the following spectral regions of the components from literature data, β-sheets between 1610-1640 cm⁻¹, α-helix between 1640-1660 cm⁻¹, turns between 1660-1690 cm⁻¹. The deconvolution of FTIR data results in a semi-quantitative analysis, giving the percentage of each component [33].

The deconvoluted bands of the graph from figure 16 are presented in the supplementary information in figures K to N. In table 6 are presented the wave numbers of the deconvoluted elements of the amide I region of each enzyme, whereas in table 7 are the percentages of each component.

Table 6. Wave numbers corresponding to the structural elements of amide I region of the developed biocatalyst.

	Wave number (cm ⁻¹)		
	β-sheet	α-helix	turns
<i>Free CH55-LEH</i>	1627	1650	1674
<i>Free CALB</i>	1616	1648	1681
<i>Novozym® 435</i>	1603	1649	1678

<i>Novozym® 435 – CH55-LEH biocomposite</i>	1603	1649	1678
---	------	------	------

From the component positions, it can be observed that the lipase B from *Candida antarctica* records a shift in the wave numbers of components bands after immobilization in the form of Novozym® 435. This means that the adsorption on the acrylic support caused small conformational changes in the secondary structure of the lipase.

The wave numbers of the components are the same in Novozym® 435 and our biocatalyst. Due to the small ratio between lipase and hydrolase used for our system, the CH55-LEH hydrolase might be present in such a small amount that the band positions are not visibly affected. However, the percentage of each component is changed in the final biocatalyst, as seen in table 7.

The free CH55-LEH hydrolase has a preponderant percentage of turns elements and a more of an α -helix structure than β -sheets, but the difference is around 8% between the last two. On the other hand, the free CALB has a higher preference toward the α -helix structure. In the bare Novozym® 435, CALB registers an increase of β -sheet conformation than in the free form, as well as a decrease in the turn elements.

By comparing bare Novozym® 435 with Novozym® 435 – CH55-LEH composite, our material registers a decrease in β -sheet and α -helix elements and an increase of the turn elements. This means that the adsorption of the CH55-LEH hydrolase on the surface of the acrylic support already containing the immobilized lipase determined a change in the conformational structure in the final material.

Table 7. Structural elements of amide I region of the developed biocatalyst.

	β-sheet (%)	α-helix (%)	turns (%)
<i>Spectral range (cm⁻¹)</i>	<i>1610-1640</i>	<i>1640-1660</i>	<i>1660-1690</i>
<i>Free CH55-LEH</i>	24	32	44
<i>Free CALB</i>	8	57	35
<i>Novozym® 435</i>	23	60	17
<i>Novozym® 435 – CH55-LEH biocomposite</i>	17	49	34

The Novozym® 435 – CH55-LEH composite maintained the preference for α -helix conformation of CALB due to its abundance in the final material, but also registered an increase in the proportion of turn elements from the adsorption of the hydrolase.

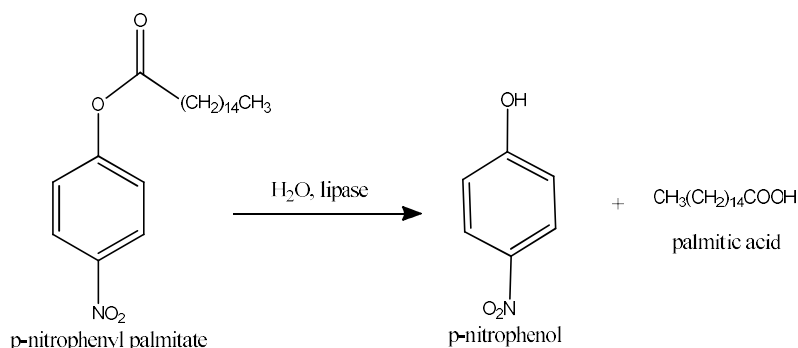
3.3.3. Enzyme loading

The enzyme loading was determined only for the Novozym® 435 – CH55-LEH composite, giving the confirmation of the hydrolase immobilization by the FTIR analysis. The percentage of loading was determined by UV-VIS measurement at 280 nm, because at this wavelength absorb two aromatic amino acids, tryptophan (Trp) and tyrosine (Tyr) and, to a small extent, cystine of the disulfide bonds of the protein tertiary structure [34].

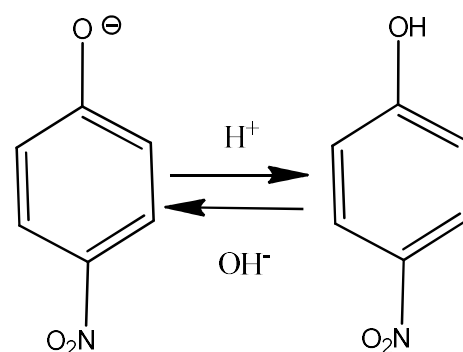
The loading percentage was determined by the protein ratio of an enzymatic solution before immobilization and the washing solutions collected after immobilization. The initial solution registered a concentration of 0.29 mg/mL, and 0.23 mg/mL is the protein concentration after immobilization. From this determination, it resulted that 21% of CH55-LEH hydrolase adsorbed on the surface of the Novozym® 435 beads.

3.3.4. Enzymatic activity

The determination of the enzymatic activity is based on the reaction between the lipase and p-nitrophenyl palmitate. The substrate is converted by the lipase in presence of water to form palmitic acid and p-nitrophenol. The reaction is presented in scheme 3.



Scheme 3. Reaction scheme for determination of lipase enzymatic activity.



Scheme 4. Ionized and non-ionized forms of p-nitrophenol [35].

For the determination of the enzymatic activity, the amount of p-nitrophenol is measured. The quantity of the product detected after the ceasing of the reaction is proportional with the activity of the enzyme. The enzymatic activity of Novozym® 435 – CH55-LEH composite was determined before washing, after each washing step, and after each one, two and three consecutive reaction cycles. The activity of Lipozyme® RM IM – Re-LEH composite was determine before washing, after each of the tree washing steps, as well as after one reaction cycle.

It is worth mentioning, that the calibration curve for p-nitrophenol was constructed at 347 nm where the non-ionized form is preponderant due to the acidic environment, whereas in our samples the

ionized form is in higher amounts due to the relatively neuter pH, and it has an adsorption peak at 410 nm [35]. The equilibrium between the ionized and non-ionized form is presented in scheme 5.

Before the determination of the enzymatic activity of our materials, UV-VIS absorption spectra were registered between 200 and 400 nm of an enzymatic solution of Re-LEH hydrolase. The resulted graph is presented in the supplementary information (figure H). The absorption spectra of the hydrolase has a peak at 280 nm, corresponding to aromatic aminoacids in its composition [34]. In figures 18 to 19 are presented the near-UV absorption spectra of the washing solutions of immobilized lipase, as well as the ones of the resulting biocomposite.

Both Novozym® 435 – CH55-LEH and Lipozyme® RM IM – Re-LEH composites washing solutions have a maximum absorption at 258 nm, which corresponds as well to aromatic aminoacids within the protein chain [36]. However, the absorption peak does not correspond to the one of the hydrolase enzymatic solution. Therefore, there might be a possibility of lipase desorption during the washing procedure.

In figures 18 and 19 are presented the near-UV absorption graphs of bare Novozym® 435 and Lipozyme® RM IM washing solutions. The procedure was the same as the one performed on the developed biocatalysts, the only difference being that this time it was performed on bare immobilized lipases. Because the immobilization approach used for the enzymes was based on adsorption on support, it was to be expected that some enzyme would desorb due to weak interaction between the protein and support material [11].

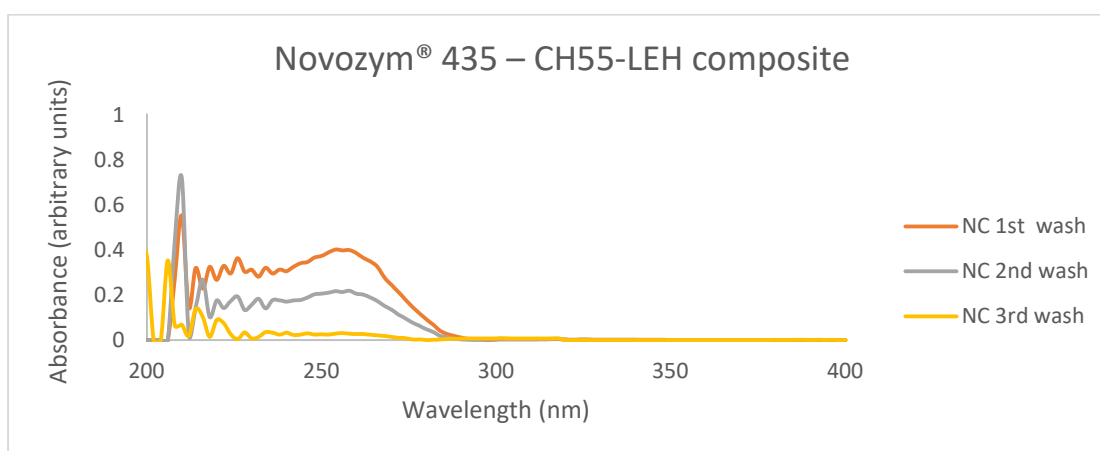


Figure 18. Near-UV absorption spectra of washing solutions of Novozym® 435 – CH55-LEH composite.

From the graph in figure 19 it is clear the peak detected at 258 nm corresponds to some lipase being desorbed during the washing step. It is worth mentioning that the highest amount of lipase CALB desorbs during the first washing step and around the third step the amount becomes negligible in both

cases. The same happens for the Lipozyme® RM IM – Re-LEH composite, the absorption decreases with each washing, but in the third washing solution there is still some non-negligible amount of lipase. The near-UV absorption spectra are in the supplementary information (figures I and J).

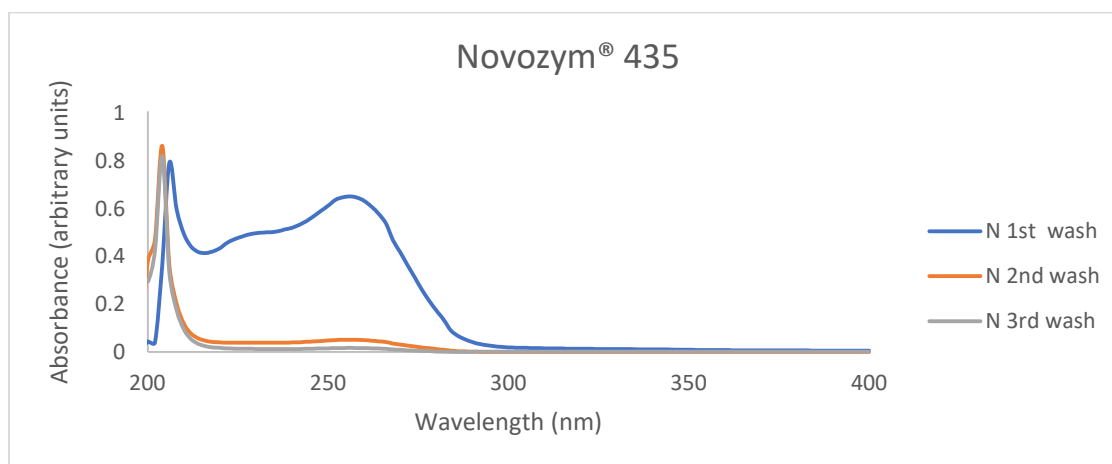


Figure 19. Near-UV absorption spectra of washing solutions of Novozym® 435.

Concluding that the peak detected corresponds to the lipase and not the hydrolase, the enzymatic activity was determined for the Novozym® 435 – CH55-LEH composite before washing, after each washing step, and after each of the three consecutive reaction cycles. The results for both composites are presented in table 8.

Table 8. Enzymatic activity values for the developed biocatalysts.

Novozym® 435 – CH55-LEH composite (washed with PBS pH8)	Enzymatic activity (µM p-NP/min/mg ptotein)	Lipozyme® RM IM – Re-LEH composites (washed with PBS pH 8)	Enzymatic activity (µM p-NP/min/mg ptotein)	Lipozyme® RM IM – Re-LEH composites (washed with PBS pH 6)	Enzymatic activity (µM p-NP/min/mg ptotein)
<i>Before washing</i>	0.8	<i>Before washing</i>	4.2	<i>Before washing</i>	9.8
<i>After 1st wash</i>	0.7	<i>After 1st wash</i>	6.4	<i>After 1st wash</i>	7.5
<i>After 2nd wash</i>	0.7	<i>After 2nd wash</i>	4.0	<i>After 2nd wash</i>	3.9
<i>After 3rd wash</i>	0.8	<i>After 3rd wash</i>	2.7	<i>After 3rd wash</i>	2.5
<i>After 1st cycle</i>	0.7	<i>1st washing solution</i>	12.0	<i>1st washing solution</i>	4.7
<i>After 2nd cycle</i>	0.8	<i>2nd washing solution</i>	6.6	<i>2nd washing solution</i>	1.6
<i>After 3rd cycle</i>	0.7	<i>3rd washing solution</i>	1.5	<i>3rd washing solution</i>	0.8
		<i>After 1st cycle</i>	1.5		

For the Novozym® 435 – CH55-LEH composite the activity is maintained constant even after three consecutive reaction cycle. The biocatalyst manages to conserve more than 90% of its initial

activity after each reaction cycle. The leaching of the lipase during the washing procedure is negligible, the activity of the biocatalyst is not significantly affected, and the enzymatic activity value detected for the washing solutions is below 0.003 arbitrary units. Therefore, the desorption of the lipase is not a problem for the Novozym® 435 containing composite.

Table 8 results clearly show that the lipase leaching is a major problem of the Lipozyme® RM IM – Re-LEH composite. The material was washed with PBS having a slightly basic or slightly acidic pH to determine if this would influence the amount of enzyme desorbed during the washing procedure. In both cases significant enzymatic activity is lost during the washing. Using a more acidic/ basic pH for the washing solution is not an option because it could lead to the hydrolase deactivation prior to reaction and would not prevent the lipase leaching in the reaction environment. After the first reaction cycle, the biocatalyst manages to conserve only 53% of the enzymatic activity at the end of the washing procedure.

The enzymatic activity of an enzymatic solution of CH55-LEH (1.81 mg/mL) before the immobilization is 11.14 IU. IU are expressed as μmol s of substrate per minute per mL of enzymatic solution. The value after immobilization is 53.06 IU. This increased value represents the enzymatic activity apparently induced by the presence of the lipase in the co-immobilized bienzymatic biocatalyst.

Conclusions

In conclusion, we developed a biocatalyst based on enzyme co-immobilization composed of the couple CH55-LEH hydrolase and Novozym® 435, which is commercially available lipase B from *Candida antarctica*. The immobilization approach is based on the adsorption of the hydrolase on the support surface of Novozym® 435 already containing the lipase in immobilized form.

Adsorption approach in immobilization, even if it is the cheapest and easiest method, comes with disadvantages, such as weak enzyme-support interaction which would result in the enzyme randomly desorbing from the surface. However, our enzymatic activity and near-UV absorption studies show a good stability of both CALB and CH55-LEH on the surface of the acrylic polymer beads.

The biocatalyst had a hydrolase loading of 21% and was characterized using FTIR analysis. The deconvoluted amide I region of the Novozym® 435 – CH55-LEH composite registered a change in the conformation of the secondary structure of the proteins which was different compared to bare Novozym® 435 beads. The absorption bands that the co-immobilization of the CH55-LEH hydrolase did not cause major conformational changes which might have resulted in the loss of enzymatic activity.

Our developed biocatalyst showed outstanding results in R-(+)-limonene conversion to (+)-limonene-1,2-diol, the system even favors the formation of the (1S, 2S, 4R)-(+)-limonene-1,2-diol isomer. Our Novozym® 435 – CH55-LEH composite managed to convert over 60% more substrate than Novozym® 435 alone or coupled with free CH55-LEH hydrolase.

The biocatalyst reusability was tested for up to three reaction cycles. After each cycle the material managed to conserve more than 90% of its initial activity. This proposes promising results for potential industrial uses of the enzyme co-immobilization-based composite.

As another possible application for the developed Novozym® 435 – CH55-LEH composite is the bioconversion of α -phellandrene to its corresponding vicinal diol. This opens the possibility of applications of our developed biocatalyst for valorization of various monoterpenes candidates.

The results obtained from our studies propose great future perspectives for developing enzyme co-immobilization-based biocatalysts for cascade valorization of monoterpenes to flavor and fragrance products with possible applications for industrial processes.

Acknowledgments

This work was financially supported by The Education, Scholarship, Apprenticeships and Youth Entrepreneurship Programmer—EEA Grants 2014-2021, Project No. 18-Cop-0041.

Bibliography

- [1] Sheldon, R.A, Woodley, J.M., Role of Biocatalysis in Sustainable Chemistry. *Chem. Rev.*, 118 (2018) 801:838.
- [2] Feher, J., *Quantitative Human Physiology*, Academic Press, 2017, Chapter 2. Protein Structure, pgs. 13:140.
- [3] Faber, K., *Biotransformations in Organic Chemistry. A Textbook*. Sixth revised and corrected edition, Springer, 2011, Chapter 1. Introduction and Background Information: Enzyme Properties and Nomenclature, pgs. 11: 27.
- [4] Chapman, J., Ismail, A.E., Dinu, C.Z., Industrial applications of enzymes: Recent advances, techniques, and outlooks. *Catalysts*, 8 (2018) 20:29.
- [5] Renge, V.C., Khedkar, S.V., Nandurkar, N. R., Enzyme Synthesis By Fermentation Method: a Review. *SRCC*, 2 (2012) 585:590.
- [6] Lin, B., Tao, Y., Whole-cell biocatalysts by design. *Microb. Cell Fact.*, 16 (2017) 1:12.
- [7] Pera, L.M., Romero, C.M., Baigori, M.D., Castro, G.R., Catalytic properties of lipase extracts from *Aspergillus niger*. *Food Technol. Biotechnol.*, 44 (2006) 247:252.
- [8] Kundys, A., Biańska-Florjańczyk, E., Fabiszewska, A., Małajowicz, J., *Candida antarctica* Lipase B as Catalyst for Cyclic Esters Synthesis, Their Polymerization and Degradation of Aliphatic Polyesters. *J. Polym. Environ.*, 26 (2018) 396:407.
- [9] Bassanini, I., Ferrandi, E.E., Monti, D., Riva, S., Studies on the Catalytic Promiscuity of Limonene Epoxide Hydrolases in the Non-hydrolytic Ring Opening of 1,2-Epoxides. *ChemBioChem*, 21 (2020) 1868:1874.
- [10] Ferrandi, E.E., Sayer, C., Isupov, M.N., Annovazzi, C., Marchesi, C., Iacobone, G., Peng, X., Bonch-Osmolovskaya, E., Wohlgemuth, R., Littlechild, J.A., Monti, D., Discovery and characterization of thermophilic limonene-1,2-epoxide hydrolases from hot spring metagenomic libraries. *FEBS J.*, 282 (2015) 2879:2894.
- [11] Sheldon, R.A., Enzyme immobilization: The quest for optimum performance. *Adv. Synth. Catal.*, 349 (2007) 1289:1307.
- [12] Fernandez-Lafuente, R., Armisen, P., Sabuquillo, P., Fernández-Lorente, G., Guisán, J. M., Immobilization of lipases by selective adsorption on hydrophobic supports. *Chem. Phys. Lipids*, 93 (1998) 185:197.
- [13] Homaei, A.A., Sariri, R., Vianello, F., Stevanato, R., Enzyme immobilization: An update. *J. Chem. Biol.*, 6 (2013) 185:205.

- [14] Jesionowski, T., Zdarta, J., Krajewska, B., Enzyme immobilization by adsorption: A review. *Adsorption*, 20 (2014) 801:821.
- [15] Sheldon, R.A., Cross-Linked Enzyme Aggregates as Industrial Biocatalysts. *Pharm. Process Chem.*, 213 (2010) 159:181.
- [16] Ricca, E., Brucher, B., Schrittwieser, J. H., Multi-enzymatic cascade reactions: Overview and perspectives. *Adv. Synth. Catal.*, 353 (2011) 2239:2262.
- [17] Hwang, E.T., Lee, S., Multienzymatic Cascade Reactions via Enzyme Complex by Immobilization. *ACS Catal.*, 9 (2019) 4402:4425.
- [18] Enoki, J., Meisborn, J., Müller, A.C., Kourist, R., A multi-enzymatic cascade reaction for the stereoselective production of γ -oxyfunctionalized amino acids. *Front. Microbiol.*, 7 (2016) 1:8.
- [19] Schrittwieser, J.H., Velikogne, S., Hall, M., Kroutil, W., Artificial Biocatalytic Linear Cascades for Preparation of Organic Molecules. *Chem. Rev.*, 118 (2018) 270:348.
- [20] Sisak, C., Nagy, E., Burfeind, J., Schügerl, K., Technical aspects of separation and simultaneous enzymatic reaction in multiphase enzyme membrane reactors. *Bioprocess Eng.*, 23 (2000) 503:512.
- [21] Martins, A.R., Monteiro, R.L., Fernandes de Medeiros Burkert, J., Burkert, A.V.C., Simultaneous enzymatic hydrolysis and lactic fermentation to obtain a yogurt with low lactose content. *Cienc. agrotec.*, 36 (2012) 551:559.
- [22] Marmulla, R., Harder, J., Microbial monoterpene transformations-a review. *Front. Microbiol.*, 5 (2014) 1:14.
- [23] De Carvalho, C.C.C., Da Fonseca, M.M.R., Biotransformation of terpenes. *Biotechnol. Adv.*, 24 (2006) 134:142.
- [24] Sales, A., Pastore, G.M., Bicas, J.L., Biotransformation of limonene to limonene-1,2-diol by two *Colletotrichum* species. *Process Biochem.*, 86 (2019) 25:31.
- [25] Çorbacı, C., Biotransformation of terpene and terpenoid derivatives by *Aspergillus niger* NRRL 326. *Biologia*, 75 (2020) 1473:1481.
- [26] Sales, A., Afonso, L.F., Americo, J.A., Rebelo, M.F., Pastore, G.M., Bicas, J.L., Monoterpene biotransformation by *Colletotrichum* species. 40 (2018) 561:567.
- [27] Işcan, G., Kirimer, N., Demirci, F., Demirci, B., Noma, Y., Başer, K.H.C., Biotransformation of (-)-(R)- α -phellandrene: Antimicrobial activity of its major metabolite. *Chem. Biodivers.*, 9 (2012) 1525:1532.
- [28] Wiemann, L.O., Faltl, C., Sieber, V., Lipase-mediated epoxidation of the cyclic monoterpene limonene to limonene oxide and limonene dioxide. *Z. Naturforsch.*, 67 (2012) 1056:1060.

- [29] Aouf, C., Durand, E., Lecomte, J., Figueroa-Espinoza, M.C., Dubreucq, E., Fulcrand, H., Villeneuve, P., The use of lipases as biocatalysts for the epoxidation of fatty acids and phenolic compounds. *Green Chem.*, 16 (2014) 1740:1754.
- [30] Su, W., Li, Q., Liu, Y., Qin, Y., Liu, H., Tang, A., Improved efficiency of lipase-mediated epoxidation of α -pinene using H₂O₂ in single- phase systems. *Molecular Catalysis*, 508 (2021) 579:585.
- [31] Kong, J., Yu, S., Fourier transform infrared spectroscopic analysis of protein secondary structures. *Acta Biochim. Biophys. Sin.*, 39 (2007) 549:559.
- [32] Kauffman, K.L., Culp, J.T., Goodman, A., Matranga, C., FT-IR study of CO₂ adsorption in a dynamic copper(II) benzoate-pyrazine host with CO₂-CO₂ interactions in the adsorbed state. *J. Phys. Chem. C*, 115 (2011) 1857:1866.
- [33] Tudorache, M., Gheorghe, A., Viana, A.S., Parvulescu, V.I., Biocatalytic epoxidation of α -pinene to oxy-derivatives over cross-linked lipase aggregates. *J. Mol. Catal. B Enzym.*, 134 (2016) 9:15.
- [34] Pathak, M., Mishra, R., Agarwala, P.K., Ojha, H., Singh, B., Singh, A., Kukreti, S., Binding of ethyl pyruvate to bovine serum albumin: Calorimetric, spectroscopic and molecular docking studies, *Thermochim. Acta*, 633 (2016) 140:148.
- [35] Peng, Y., Fu, S., Liu, H., Lucia, L.A, Determining esterase activity. *BioResources*, 11 (2016) 10099:10111.
- [36] Schmid, F.X., Biological Macromolecules: UV-visible Spectrophotometry. *Encycl. Life Sci.*, (2001) 1:4.

SUPPLEMENTARY INFORMATION

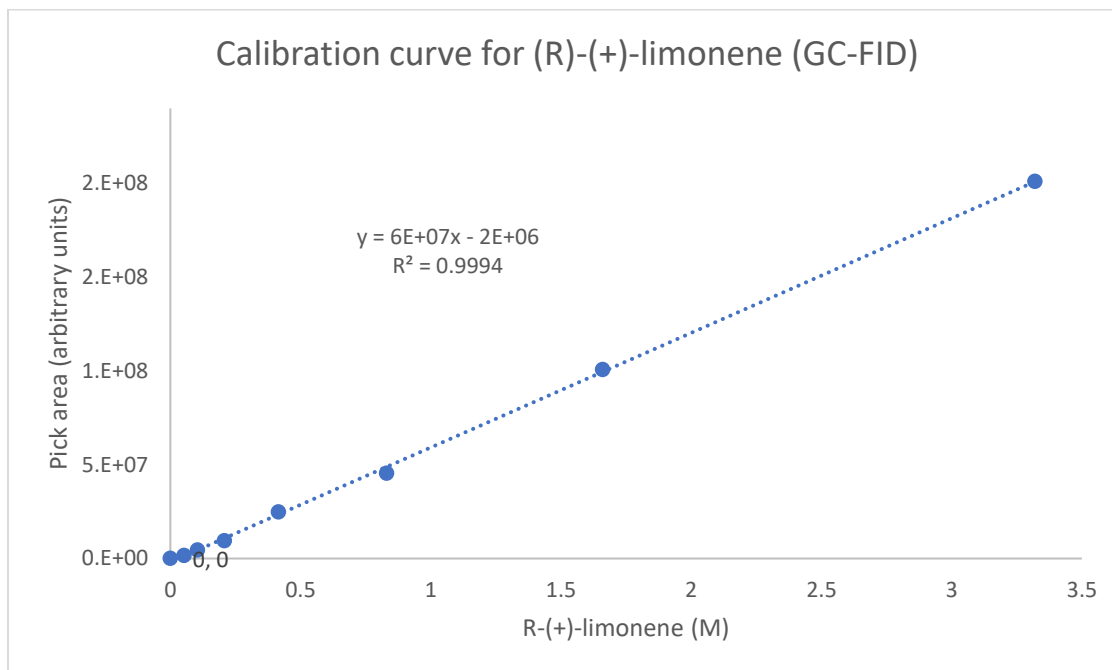


Figure A. Calibration curve for R-(+)-limonene in ethyl acetate analyzed using GC-FID.

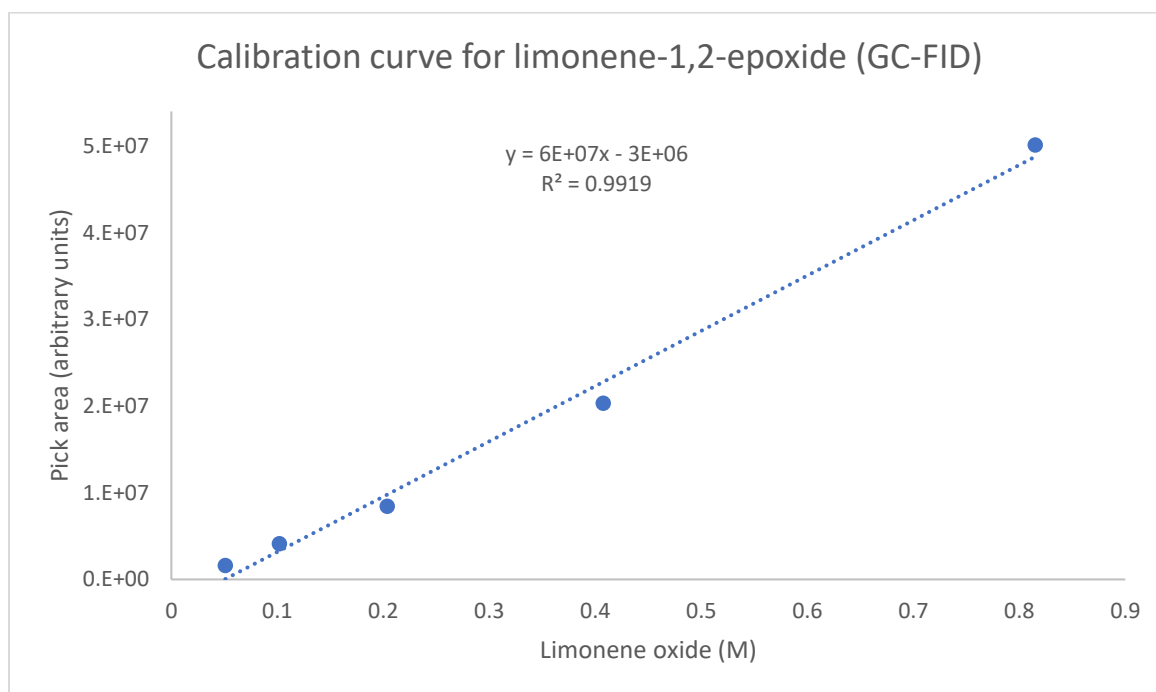


Figure B. Calibration curve for limonene oxide in ethyl acetate analyzed using GC-FID.

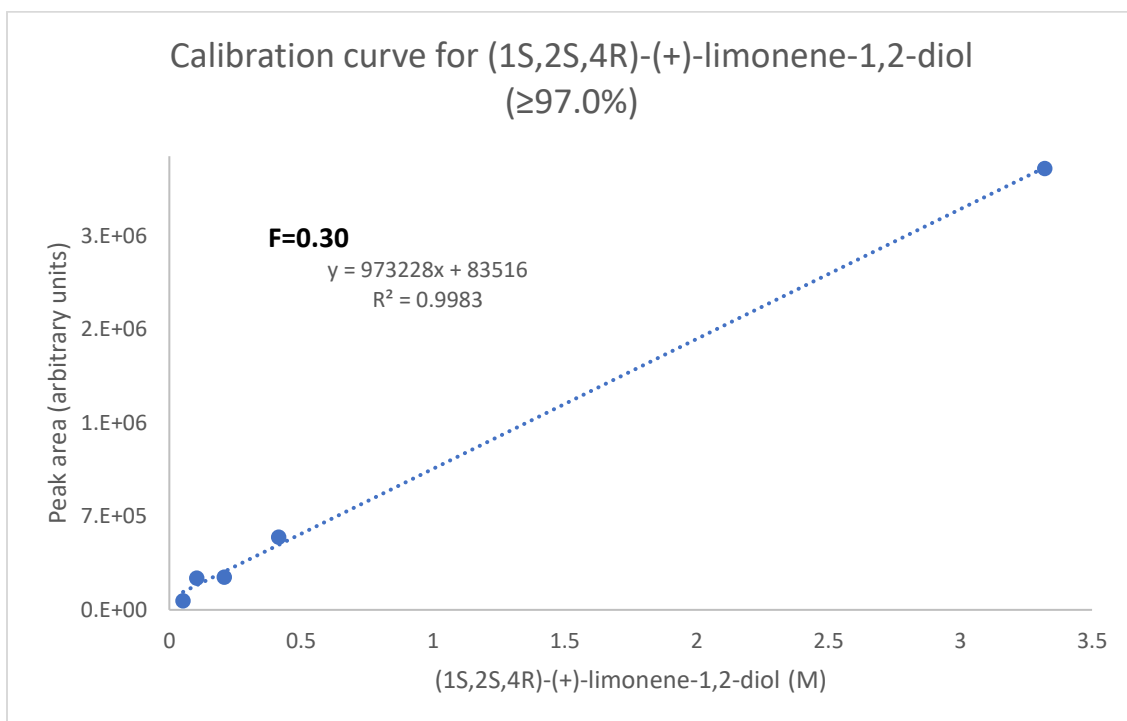


Figure C. Calibration curve for (1S,2S,4R)-(+)-limonene-1,2-diol in ethyl acetate analyzed using GC*-FID.

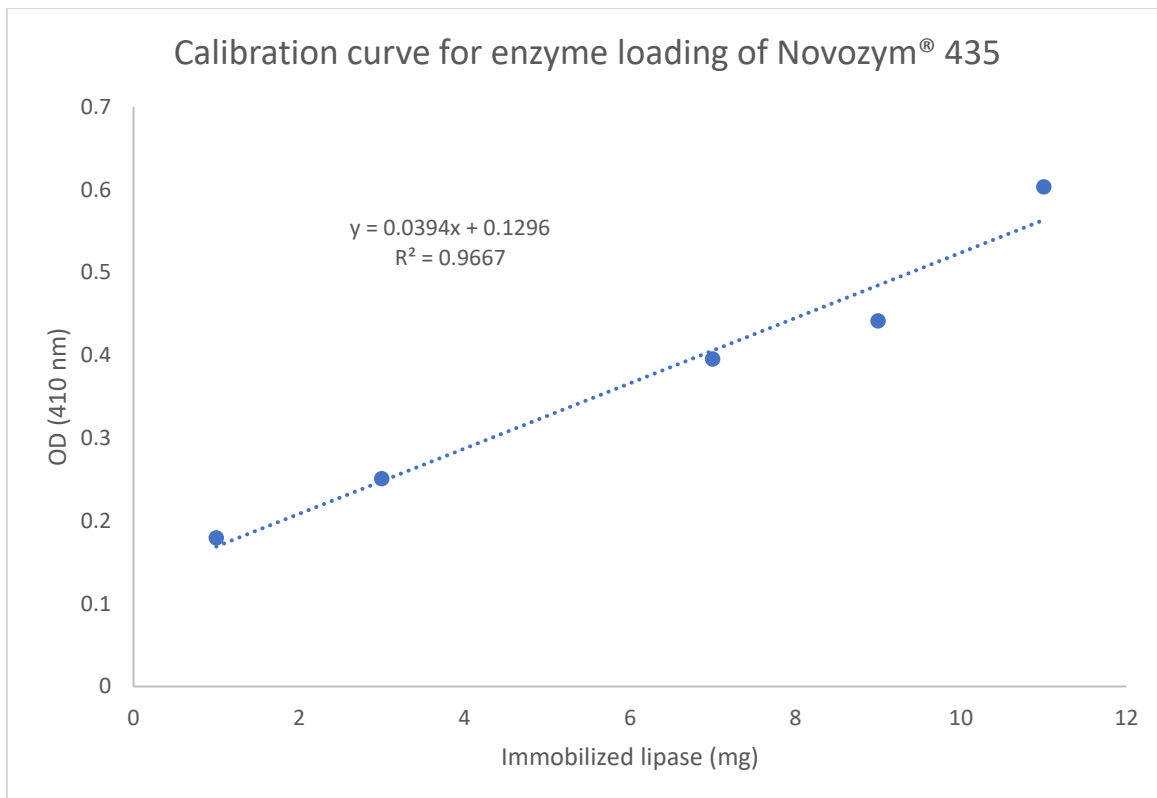


Figure D. Calibration curve of the enzymatic activity of Novozym® 435.

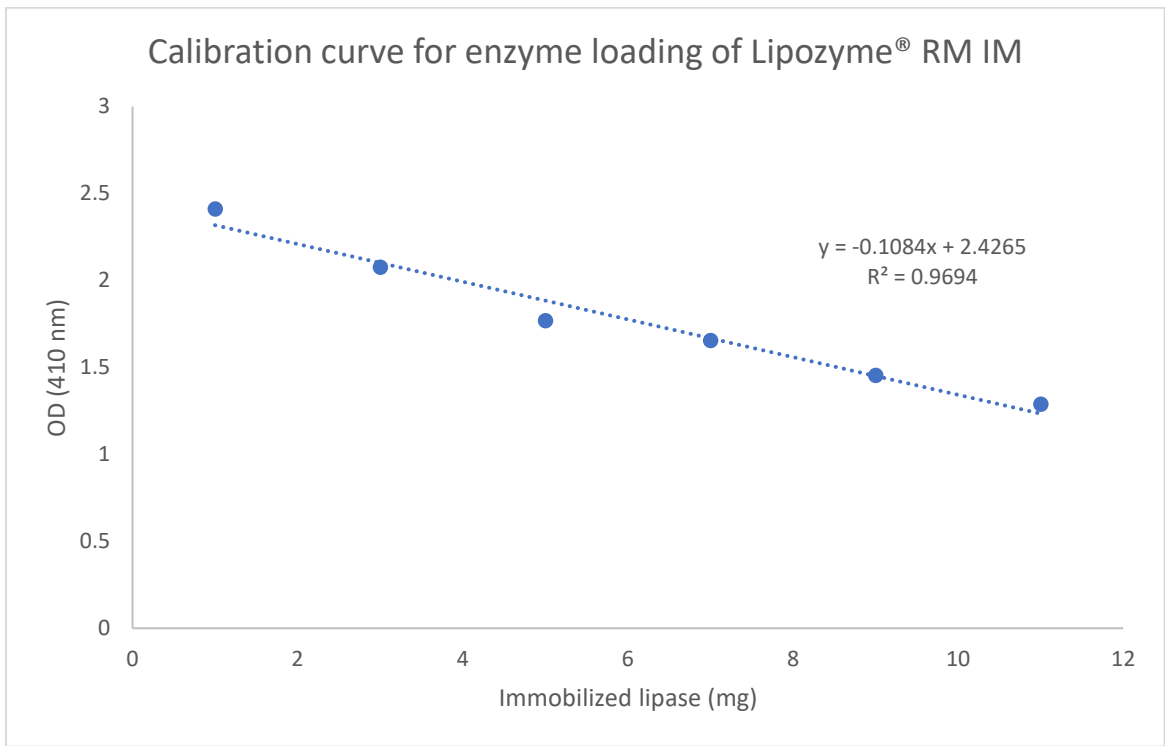


Figure E. Calibration curve of the enzymatic activity of Lipozyme® RM IM.

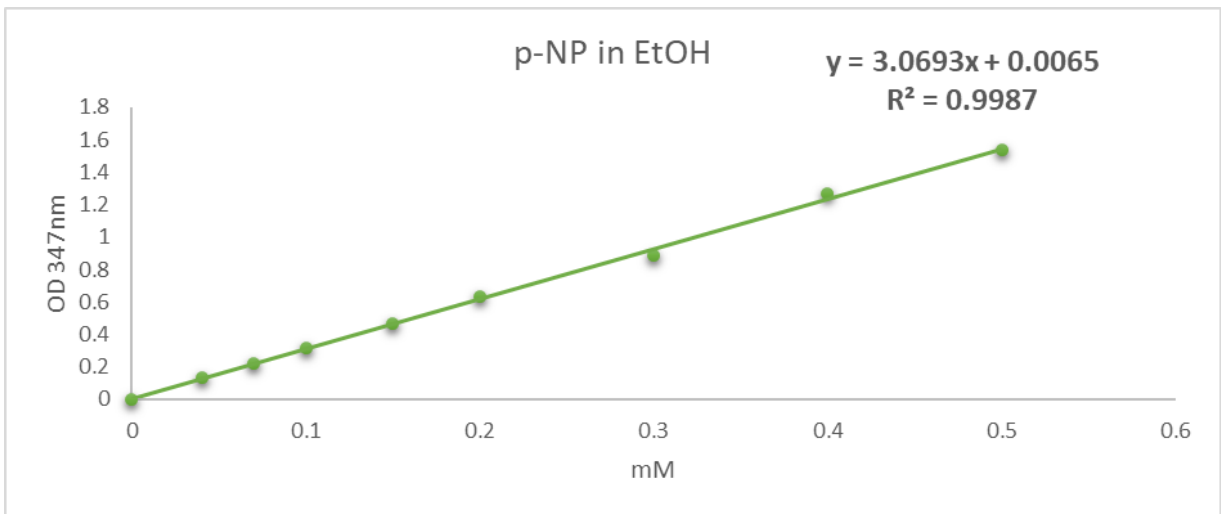


Figure F. Calibration curve of p-nitrophenol in ethanol.

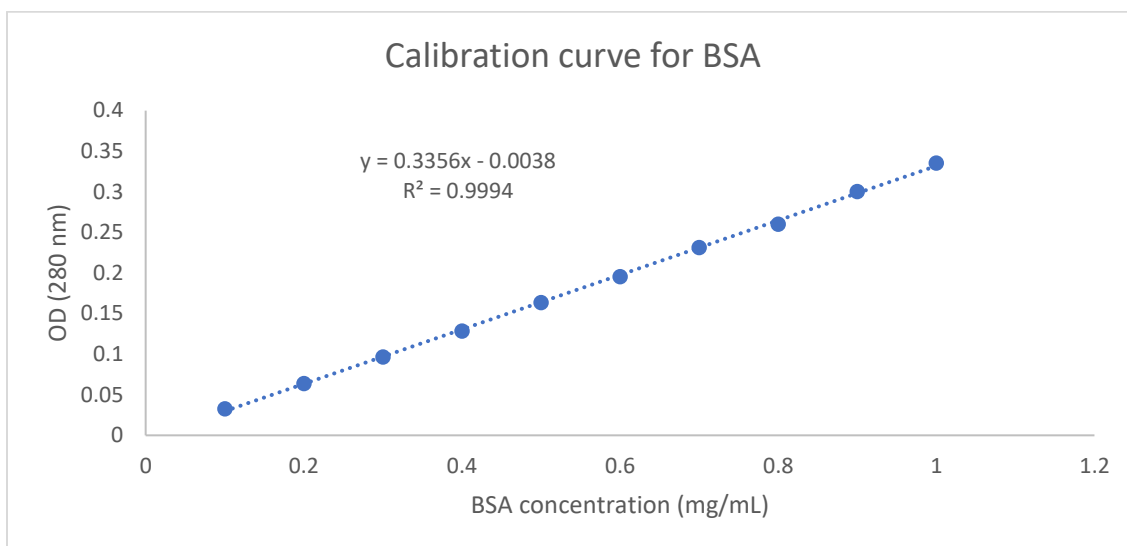


Figure G. Calibration curve of BSA in tris-HCl buffer.

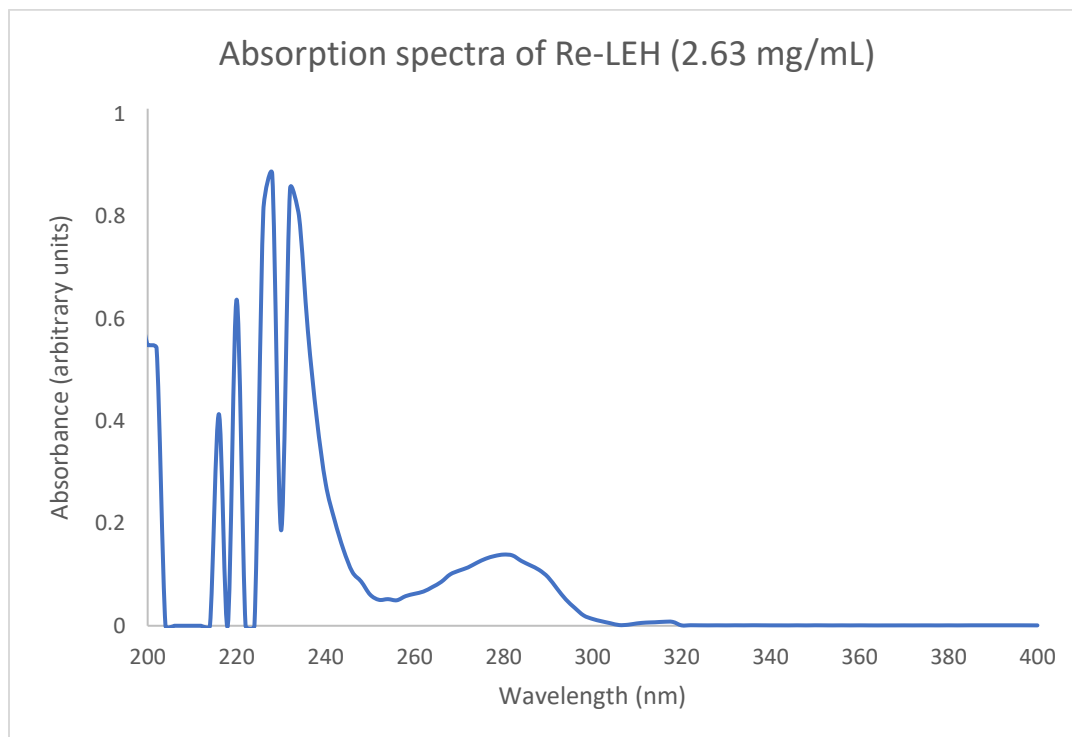


Figure H. Near-UV absorption spectra of an enzymatic solution of Re-LEH with a concentration of 2.63 mg/mL.

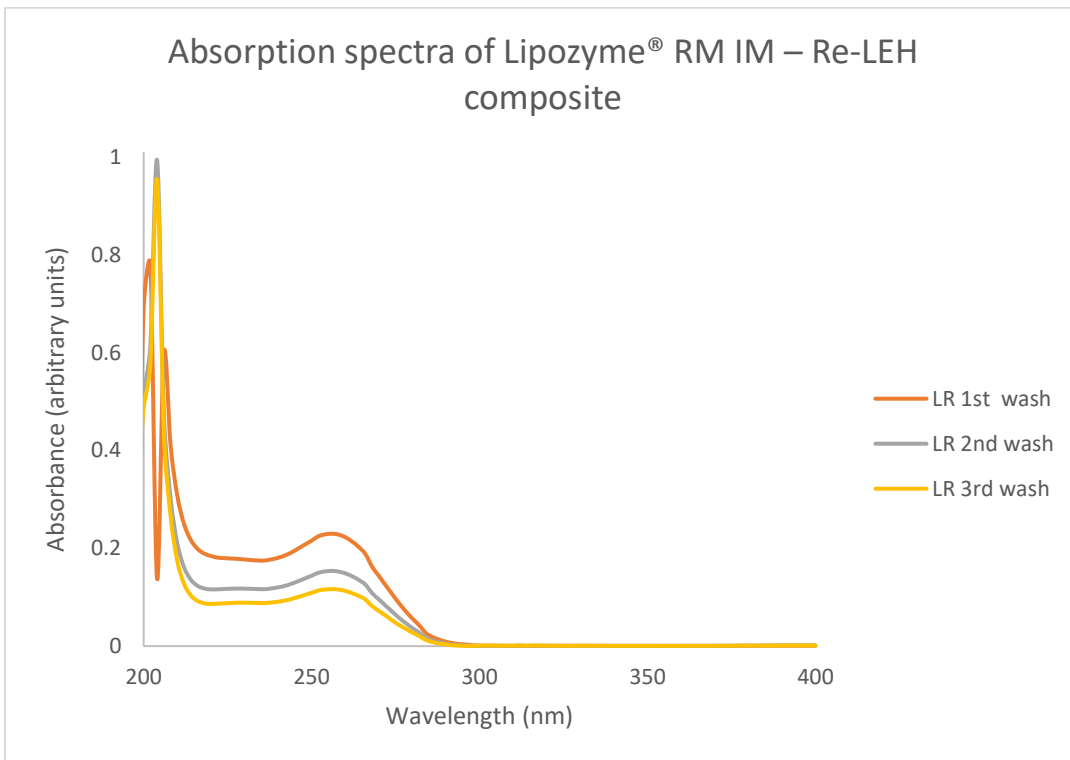


Figure I. Near-UV absorption spectra of washing solutions of Lipozyme® RM IM – Re-LEH composite.

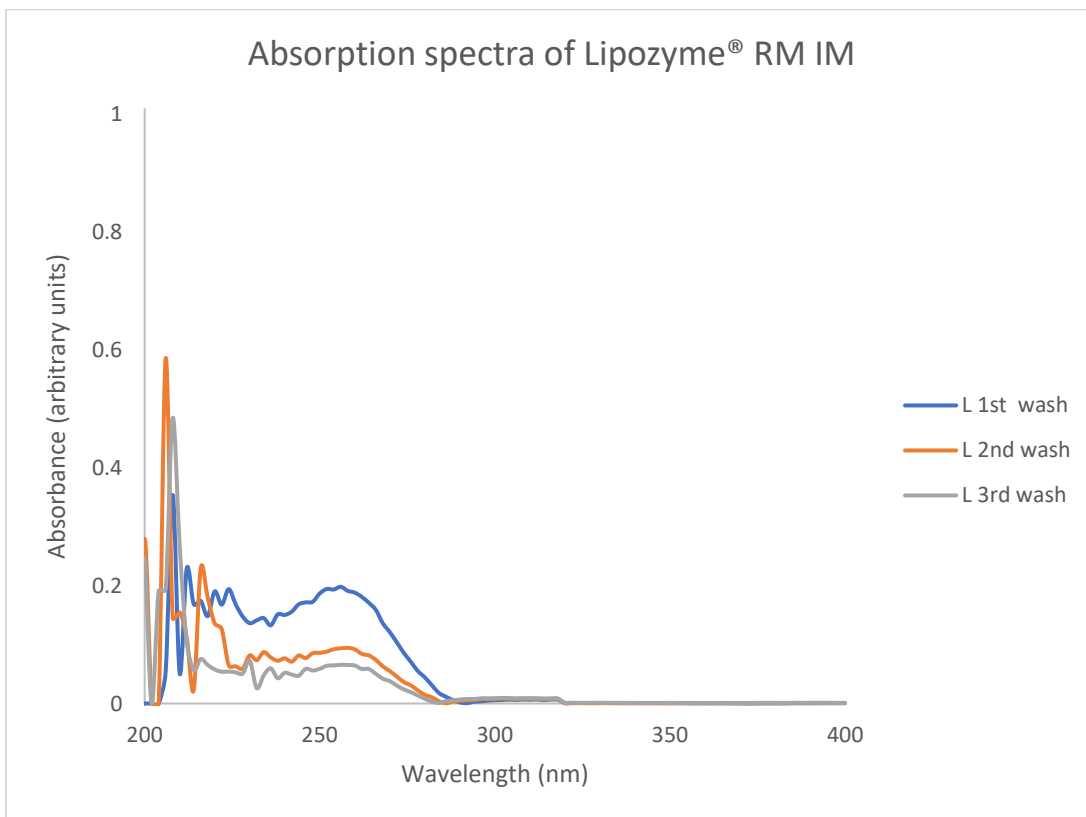


Figure J. Near-UV absorption spectra of washing solutions of Lipozyme® RM IM.

Peak Analysis

Data Set: % ([Book1]FitPeaks1,@WL,Input.IDTR1.IDTC2)

Date: 6/16/2021

Baseline: Line

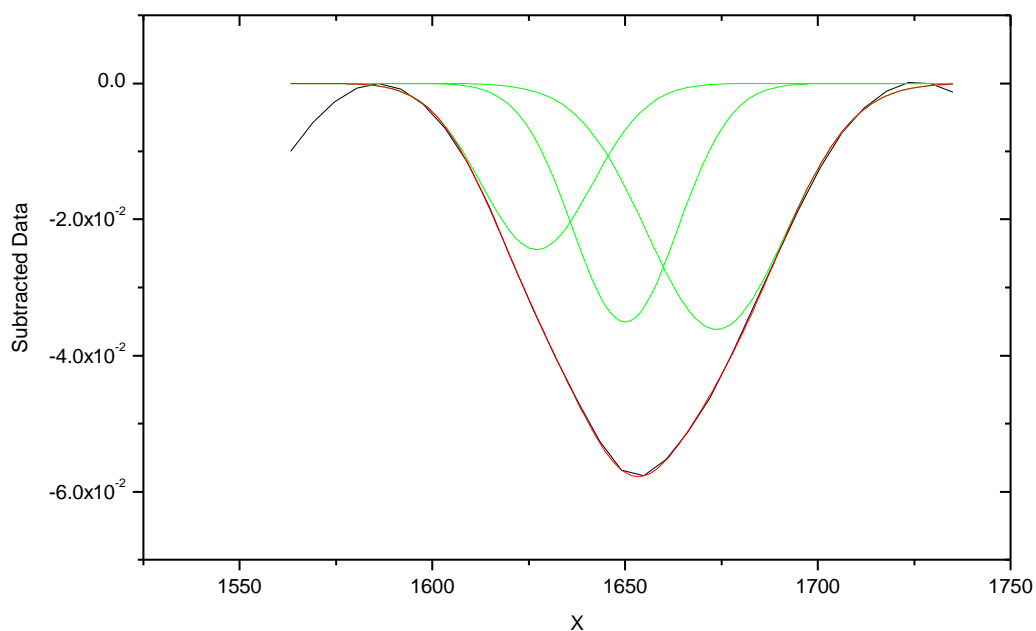
Chi^2=--

Adj. R-Square=--

of Data Points= % ([Book1]FitPeal

SS=--

Degree of Freedom= % ([Book1]FitPeaks1,@WL,RegStats.C1.DOF)



Fitting Results

Peak Index	Peak Type	Area Intg	FWHM	Max Height	Center Grvty	Area IntgP
1.	Gaussian	-0.88127	33.92317	-0.02441	1627.06395	-23.69462
2.	Gaussian	-1.20211	32.2342	-0.03503	1650.02108	-32.32089
3.	Gaussian	-1.63591	42.53986	-0.03614	1673.71108	-43.98449

Figure K. Deconvoluted amide I band of free CH55-LEH from figure 16.

Peak Analysis

Data Set: % ([Book1]FitPeaks2, @WL, Input.IDTR1.IDTC2)

Date: 6/16/2021

Baseline: Line

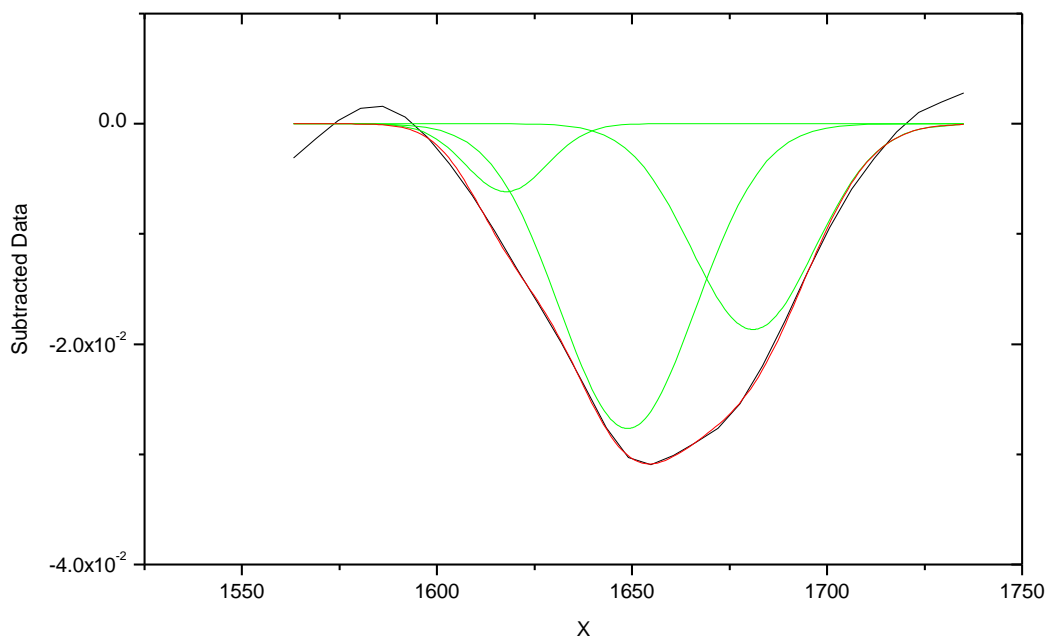
Chi^2=---

Adj. R-Square=---

of Data Points= % ([Book1]FitPeal

SS=---

Degree of Freedom= % ([Book1]FitPeaks2, @WL, RegStats.C1.DOF)



Fitting Results

Peak Index	Peak Type	Area Intg	FWHM	Max Height	Center Grvty	Area IntgP
1.	Gaussian	-0.15988	24.378	-0.00616	1617.7398	-7.57894
2.	Gaussian	-1.20758	41.02756	-0.02765	1648.88968	-57.2444
3.	Gaussian	-0.74206	37.3594	-0.01867	1681.04379	-35.17667

Figure L. Deconvoluted amide I band of free lipase B of *Candida antarctica* from figure 16.

Peak Analysis

Data Set: % ([Book1]FitPeaks3,@WL,Input.IDTR1.IDTC2)

Date: 6/16/2021

Baseline: Line

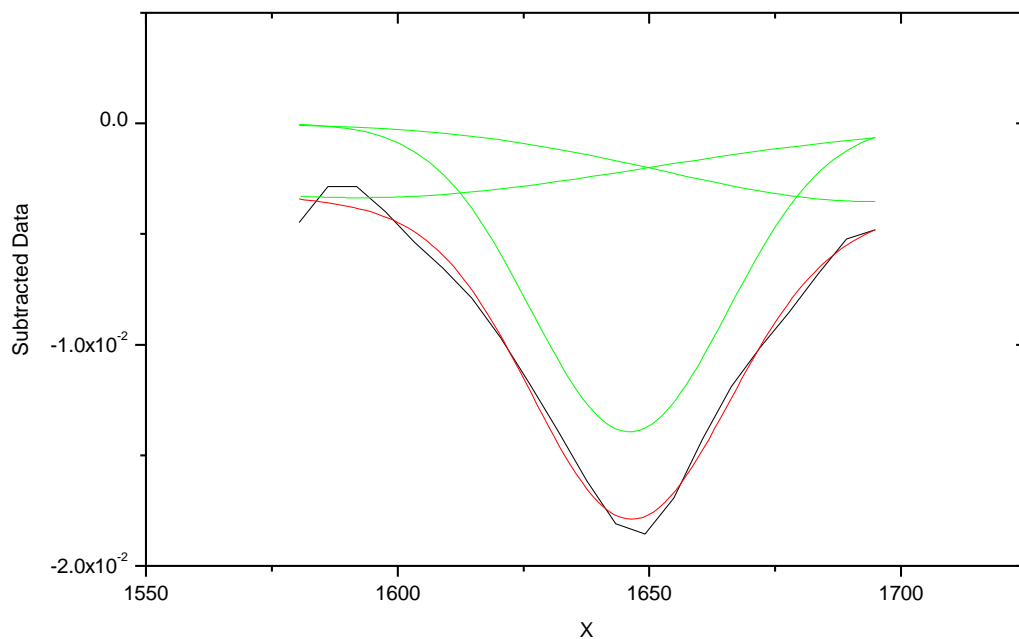
Chi^2=--

Adj. R-Square=--

of Data Points=% ([Book1]FitPeaks3,@WL,RegStats.C1.DOF)

SS=--

Degree of Freedom=% ([Book1]FitPeaks3,@WL,RegStats.C1.DOF)



Fitting Results

Peak Index	Peak Type	Area Intg	FWHM	Max Height	Center Grvty	Area IntgP
1.	Gaussian	-0.26096	133.54202	-0.00336	1592.1256	-23.18832
2.	Gaussian	-0.6782	46.02967	-0.01393	1646.09518	-60.2643
3.	Gaussian	-0.18622	99.11765	-0.00353	1694.59205	-16.54738

Figure M. Deconvoluted amide I band of bare Novozym® 435 from figure 16.

Peak Analysis

Data Set: % ([Book1]FitPeaks4, @WL, Input.IDTR1.IDTC2)

Date: 6/16/2021

Baseline: Line

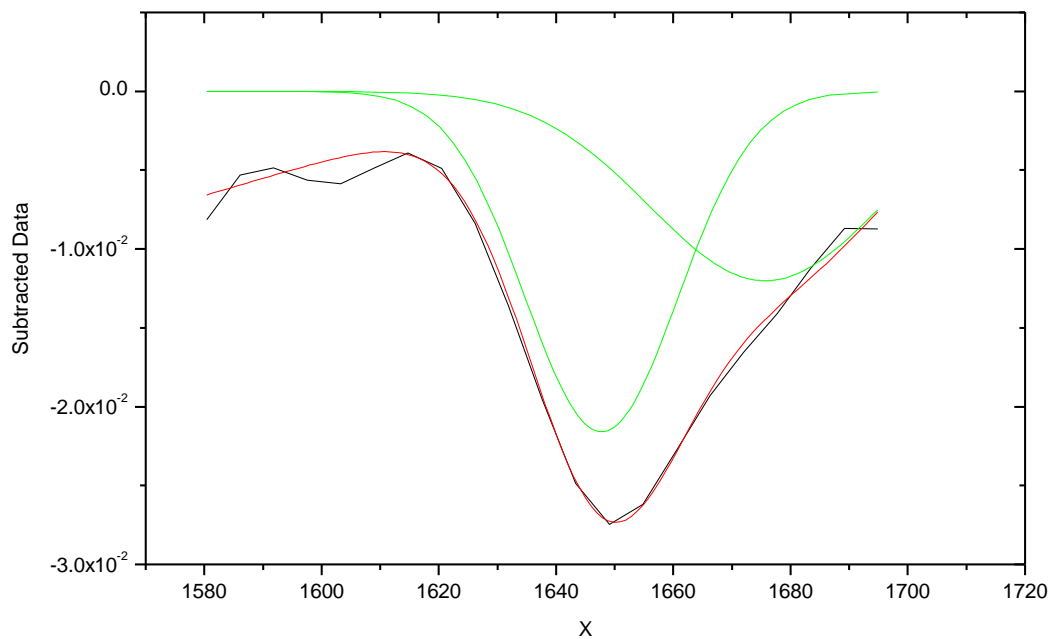
Chi²--

Adj. R-Square--

of Data Points= % ([Book1]FitPeaks4, @WL, RegStats.C1.DOF)

SS--

Degree of Freedom= % ([Book1]FitPeaks4, @WL, RegStats.C1.DOF)



Fitting Results

Peak Index	Peak Type	Area Intg	FWHM	Max Height	Center Grvty	Area IntgP
1.	Gaussian	-0.2446	126.7799	-0.00974	1532.57083	-16.92171
2.	Gaussian	-0.7044	30.6636	-0.02158	1647.77035	-48.73042
3.	Gaussian	-0.4965	46.57293	-0.01201	1675.72771	-34.34787

Figure N. Deconvoluted amide I band of Novozym® 435 – CH55-LEH composite from figure 16.



**UNIVERSITATEA
DIN BUCUREȘTI**

VIRTUTE ET SAPIENTIA

FACULTATEA DE CHIMIE

DISERTATION THESIS

Student: BADEA MARA-ALEXANDRA

**Supervisor: Prof. Dr. Habil. SIMONA MARGARETA
COMAN**

2022

Sesiunea IUNIE - IULIE 2022



FACULTATEA DE CHIMIE

DECLARAȚIE

Subsemnata Badea Mara-Alexandra, candidat la examenul de Disertație, la Facultatea de Chimie, specializarea Chimia Materialelor Avansate – cu predare în limba engleză declar pe proprie răspundere că lucrarea cu titlul Catalytic synthesis of alanine by lactic acid amination, având drept coordonator pe Prof. Dr. Habil. Simona-Margareta Coman depusă în vederea susținerii publice reprezintă rezultatul muncii mele, are la bază rezultate experimentale obținute de mine și informații obținute din surse care au fost citate și indicate, conform normelor etice în note de subsol și bibliografie. Declar că nu am folosit în mod tacit sau ilegal munca altora și nici o parte a lucrării nu încalcă drepturile de proprietate intelectuală ale altcuiva, persoană fizică sau juridică. Declar de asemenea că lucrarea nu a mai fost prezentată în această formă vreunei instituții de învățământ superior în vederea obținerii unui grad / titlul științific sau didactic.

Data: 27.06.2022

Semnătură candidat

M. Badea

Coordonator: Prof. Dr. Habil. Simona-Margareta Coman

Coman

Semnătură:

APROBAT

Director departament:

Conf. Dr. Habil. Ileana Fărcășanu

Ileana Farcasanu

CERERE pentru susținerea Lucrării de Disertație

„Catalytic Synthesis of Alanine by Lactic Acid Amination”

Subsemnata, Badea Mara-Alexandra, absolventă a Facultății de Chimie, la masterul „Chemistry of Advanced Materials”, vă rog să aprobați susținerea publică a lucrării mele de dizertație, cu titlul “Catalytic Synthesis of Alanine by Lactic Acid Amination”, în sesiunea Iunie-Iulie, 2022, coordonatorul lucrării fiind Prof. Dr. Habil. Simona-Margareta Coman.

Conținutul lucrării:

1. Partea de literatură (*tematica urmărită, obiectivele referatului de literatură*)

S-a realizat o cercetare exhaustivă a literaturii disponibile privind utilizarea biomasei pentru sinteze de chimicale fine sau molecule platformă care, mai departe, pot fi convertite în produse cu valoare adăugată pe piața de desfacere. Totodată, s-a realizat o amplă documentare pe problematica design-ului catalizatorilor utilizați în astfel de procese și pe sinteza de aminoacizi. Importanța aminoacizilor derivă din faptul ca sunt elementele de bază ale biosintezei proteinelor și sunt utilizați în nenumărate aplicații industriale, inclusiv în produsele alimentare umane, în hrana animalelor și ca precursori pentru materiale bio-plactice. Ca atare, dezvoltarea unor metode chimice eficiente de transformare a materiilor prime abundente și regenerabile în aminoacizi este extrem de importantă dar puținele încercări raportate în literatură arată insuccesul relativ al acestora. Ca alternativă, abordările chemo-catalitice pentru producerea de aminoacizi din materii prime regenerabile, cum ar fi zaharurile, ar putea oferi un mijloc rapid și potențial mai eficient de sinteză al acestora. Din păcate însă, o abordare durabilă și generalizabilă a utilizării NH₃ pentru sinteza directă a aminoacizilor din materii prime abundente și regenerabile rămâne o raritate. Una dintre cele mai studiate astfel de abordări este sinteza alaninei prin aminarea acidului lactic, în prezența catalizatorilor pe bază de ruteniu depus pe suporturi nanotuburi de carbon, nanotuburi de carbon dopate cu azot sau dioxid de titan. În ciuda acestor progrese însă, producția chimică de alanină din resurse regenerabile rămâne la început.

2. Partea originală (*contribuții metodice, didactice, utilizarea unor programe de calcul, realizarea unor noi programe de calcul, realizarea și testarea unei instalații noi, determinări experimentale proprii, dezvoltare/validare metode, modelarea unor procese fizico-chimice, prelucrarea și interpretarea rezultatelor, etc.*)

Partea experimentală a lucrării este structurată în doua capitole. Primul capitol conține descrierea metodologiilor de sinteză ale catalizatorilor, tehnicile de caracterizare utilizate, condițiile de testare ale acestora în aminarea acidului lactic și metoda de analiza a produșilor de reacție obținuți. În al doilea capitol sunt discutate pe larg rezultatele obținute încercându-se o corelare a proprietăților catalitice cu performanțele acestora în aplicația catalitică. Pentru catalizatorii studiați, pe bază de ruteniu, s-au utilizat trei tipuri diferite de suporturi: nanotuburi de carbon, nanotuburi de carbon

oxidate și particule magnetice acoperite cu silice și APTES. Prepararea celor trei catalizatori a presupus impregnarea acestora cu 1%, 3% și 5wt% ruteniu, urmată de calcinare și reducere. Catalizatorii au fost caracterizați utilizând tehnici precum difracție de raze X (XRD), adsorbție-desorbție de azot lichid la -196°C , desorbție la temperatură programată de H_2 și NH_3 (H_2 -TPD, NH_3 -TPD), spectroscopie Raman și IR, analiză termogravimetrică (TG) și microscopie electronică de scanning cuplată cu cea de transmisie (STEM). Prelucrarea datelor s-a realizat utilizând softul Origin. Testele catalitice au fost realizate în autoclavă, sub presiune de hidrogen. Amestecurile de reacție au fost apoi aduse la sec, silanizate și analizate cu ajutorul unui gas cromatograf cuplat cu spectrometrie de masă (GC-MS). Rezultatele catalitice au fost prelucrate utilizând softul Excel.

Aprecierea coordonatorului:

Activitatea pe care studenta Mara-Alexandra BADEA a depus-o a condus la o lucrare de disertație structurată în trei capitole (aspecte teoretice, metodologii experimentale și rezultate și discuții) la care se adaugă secțiunile de concluzii, diseminare și referințe bibliografice. În toată această perioadă Mara a dat dovadă de o dorință remarcabilă de progres științific reușind într-un timp relativ scurt să dobândească cunoștințe importante atât în sinteza de materiale catalitice cât și în utilizarea metodelor de investigație ale acestora. Deși munca susținută și relativ neîntreruptă nu a fost lipsită de anumite întârzieri obiective, tenacitatea și dorința de progres manifestată de Mara în această perioadă au asigurat încheierea cu succes a acestei etape profesionale.

Implicarea candidatei în realizarea studiului de literatură și a etapelor de cercetare experimentală au generat un volum extrem de mare de informații utile noi, care fac obiectul acestei Lucrări de Disertație. Ca atare, sunt extrem de mulțumită de tenacitatea și efortul susținut de studenta Mara-Alexandra BADEA în realizarea acestei teze de disertație. Apreciez, de asemenea, că Mara, datorită adaptabilității rapide la diferite situații particulare care solicită o implicare pe măsură, dispune de un potențial foarte mare în dezvoltarea unei activități de cercetare similare viitoare.

Rezultatele obținute în această Lucrare de Disertație fac obiectul unei comunicări științifice (Poster), cu titlul „Catalytic production of amino acids from biomass-derived intermediates”, autori: M.-A. Badea, B. Cojocaru, V. I. Parvulescu, S. M. Coman, prezentată de către candidată la Simpozionul „The 13th International Symposium of the Romanian Catalysis Society (RomCat2022), 22-24 Iunie 2022, Băile Govora, România, organizat de Societatea de Cataliză din România, în parteneriat cu Universitatea din București și Institutul Național de Cercetare și Dezvoltare pentru Tehnologii Criogenice și Izotopice (ICSI).

Acordul conducătorului pentru susținerea lucrării: Da

Coordonator: Prof. Dr. Habil. Simona-Margareta Coman



Semnătură:

Data completării cererii: 27.06.2022



UNIVERSITATEA DIN
BUCUREȘTI
VIRTUTE ET SAPIENTIA

**FACULTY OF CHEMISTRY
DEPARTMENT OF ORGANIC CHEMISTRY,
BIOCHEMISTRY AND CATALYSIS**

MSc Thesis

**Catalytic synthesis of alanine by lactic acid
amination**

MASTER: CHEMISTRY OF ADVANCED MATERIALS

STUDENT: MARA ALEXANDRA BADEA

SCIENTIFIC COORDINATOR:

Prof. Dr. Simona-Margareta Coman

July 1, 2022

CONTENT

Introduction	1
1. Theoretical aspects	2
2. Objectives	15
3. Experimental part	15
3.1. Materials preparation methodologies	16
3.1.1. Ru supported onto MWCNT (Ru/CNT).....	16
3.1.2. MWCNTs oxidation.....	16
3.1.3. Ruthenium based magnetic nanoparticles	17
3.2. Characterization techniques	18
3.3. Catalytic tests	19
4. Results and discussions	20
4.1. Ru/CNT samples characterization	20
4.2. Oxidation of CNTs: Purification and functionalisation.....	30
4.3. Ruthenium based magnetic nanoparticles carrier.....	39
4.4. Catalytic tests	42
Conclusions	47
Acknowledgements.....	48
Disemination.....	48
References	48

Introduction

Due to their versatility amino acids are valuable products for industry [1]. Amino acids are primarily manufactured *via* microbial cultivation processes, which are costly, time consuming, and require extensive separations processes. The development of efficient chemical methods to convert abundant and renewable feedstocks into amino acids is, therefore, highly attractive but it have been largely unsuccessful to date. As an alternative, chemocatalytic approaches could offer a rapid and potentially more efficient means of amino acid synthesis, but efforts to date have been limited by the development of facile chemistry and associated catalyst materials to selectively produce α -amino acids.

In our knowledge, only one recent report on the directly catalytic transformation of the lignocellulosic biomass-derived α -hydroxyl acids into α -amino acids, including alanine, leucine, valine, aspartic acid, and phenylalanine in high yields exist in literature [2]. The synthesis follows a dehydrogenation-reductive amination pathway, with dehydrogenation as the rate-determining step. Ruthenium nanoparticles supported on carbon nanotubes (Ru/CNT) exhibit exceptional catalytic efficiency due to the unique, reversible enhancement effect of NH_3 on Ru in dehydrogenation step.

The CNT application in heterogeneous catalysis is based on their specific important characteristics such as: (i) resistance to acid/basic media, (ii) possibility to control, up to certain limits, the porosity and surface chemistry and (iii) easy recovery of precious metals by support burning resulting in a low environmental impact [3]. The combination of these properties makes CNT attractive and competitive catalyst supports by comparison with activated carbons.

In the case of as-produced CNT's it has to be noticed that such materials do not possess a high amount of functional groups on their surface and mainly surface defects can be considered as anchoring sites for metals. In order to evaluate the role of surface defects on the final metal dispersion, the interaction between iron, cobalt or nickel and MWNT, SWNT, activated carbon or layered graphite has been studied [4]. On SWNT and layered graphite, no coating was observed due to the low density of surface defects. However, for MWNT and activated carbon, a better wetting has been achieved and, in the case of iron on MWNT, a particle size of 5–15 nm has been measured. Several other metals were deposited on MWNT by using the wetness impregnation technique. For instance, palladium, platinum, gold and silver particles obtained presented a mean size of 7, 8, 8 and 17 nm, respectively, and were mostly found on the outer surface of the CNT [5].

Like for classical carbon materials used in catalysis the possibility of chemical or thermal activation, in order to modify the nature and concentration of surface functional groups, has been studied in the case of CNT. Among the different techniques that have been applied for the more or less

pronounced surface oxidation, nitric acid treatments are the most common and it has been shown that surface oxygen functionalities like carboxylic groups can be introduced on the outer and possibly inner walls of the CNT [6]. In the case of MWNT the main significant structural modification occurs on the nanotubes tip and can result(s) in their opening. The formation of edges and steps on the graphene sheets is also possible [7]. Deposition of different metals (i.e., silver, cobalt, cerium) on nitric-acid treated MWNT showed the critical factor to well dispersed nanoparticles is the oxidation step [3].

On the other hand, magnetic nanoparticles (MNPs) have been gaining increasing interest in the last years due to their valuable properties such as high surface area, low toxicity and super-paramagnetic behavior [8]. This intrinsic property may allow an easier separation from reaction mixtures by the use of an external magnetic field. In addition, the presence of a large number of hydroxyl groups on the external surface affords both the deposition of inorganic shells containing different catalytic active phases and the direct immobilization of a variety of catalytic functionalities *via* covalent bonds [9]. In this context, not long ago an efficient Ru(4wt%)-MNP-SiO₂ catalyst for the oxidation of levulinic acid (LA) to succinic acid (SA) ($S_{SA} = 96-98\%$ for $X_{LA} = 59-79\%$) was reported [10].

1. Theoretical aspects

Due to the rapid population growth and vast economic developments nowadays there is an increase in global energy demand that is estimated to double between 2000 and 2035 [11]. Fossil fuel sources, such as crude oil, coal and natural gas currently hold the major share of energy supply. However, these sources are non-renewable and global petroleum production is predicted to peak by 2020 due to increasing demand for chemical industries, before decaying.

Another major concern of the 21st century is the increasing levels of greenhouse emissions (CO₂ in special) caused by the enormous consumption of fossil fuels. The global CO₂ emissions reached an all-time record of 41.5 ± 4.4 billion tonnes in 2017, contributing to an atmospheric CO₂ concentration of 408 ppm, the highest since the beginning of the industrial revolution. If this situation continues, global average temperatures are estimated to increase drastically in the range of 2.5 – 5.4 °C [11]. In the same manner, global warming is a major threat to humankind as well as to the biosphere if we think at the increased rate and intensity of many climate catastrophes from recent time. Due to this situation created worldwide the scientists from many countries try to find alternative pathways to replace the actual industry which is based almost in totally on petroleum with an industry based on clean, sustainable resources for the production of fuels and chemicals.

Various renewable resources are available for the production of energy and/or chemicals. Some of these resources are: wind, geothermal, solar, hydropower and biomass. Although renewable energy from wind and water holds considerable potential, it is insufficient and incapable to fill the entire global energy demand. For a short and medium term solution to the deficit of both sustainable energy and renewable carbon, most experts look to biomass as a most viable alternative source. As a highly abundant natural carbon source, biomass is considered a promising renewable alternative to fossil fuels that can be transformed into a wide range of value-added chemicals, clean solvents and biodiesel. Several biomass resources such as animal waste, agricultural crops, wood and aquatic plants are available for the production of sustainable chemicals. If we think at the fuels, which are of great necessity in our society, we realize that the humankind is on the verge of collapse. Bearing this in mind, we need to give it a chance to the biofuels with products derived from lignocellulosic biomass, because this is the future.

Lignocellulosic biomass is the most abundant and bio-renewable resource, with great potential for sustainable production of chemicals and fuels [12]. Lignocellulose functions as the most important structural component in a majority of plants, making it widely available in much larger quantities than starch, oils and fats, the source materials of first generation biofuels [13]. Any materials rich in cellulose, hemicellulose and lignin are commonly referred to as lignocellulosic biomass. For example, wood, bamboo, grass and their derived pulp and paper, and agricultural residues like corn cobs and sugarcane bagasse are typical sources of lignocellulosic biomass. Generally, most of the lignocellulosic biomass contains 35-50% cellulose, 20-35% hemicellulose and 10-25% lignin. Unfortunately, these components are indigestible by humans, but are readily available in several industrial waste streams, especially from the paper and agricultural industries. This severs to the direct competition between lignocellulose valorization and human food supply.

Since cellulose is the main component of lignocellulosic biomass it is imperative to know more about it. Cellulose is one of the most abundant compounds on earth because it is contained in almost all woody materials. It has the same molecular formula as amylose, one of the main components of starch ($C_6H_{10}O_5$), but between them is a fundamental difference: in amylose the glucose monomers are linked by α -1,4-glycosidic bonds whereas in cellulose the glucose monomers are linked by β -1,4-glycosidic bonds as shown in Figure 1. This seemingly trivial difference has important physico-chemical consequences.

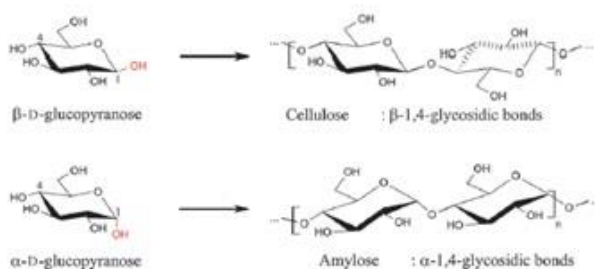


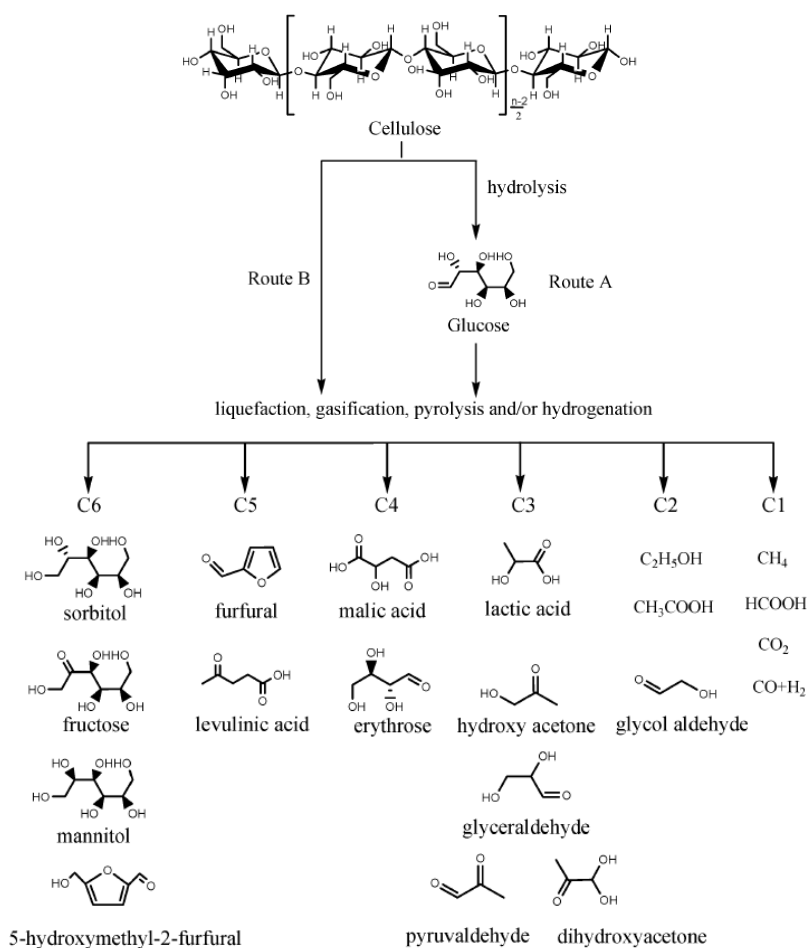
Figure 1. Structure of cellulose and amylose (starch) [13]

In cellulose, the glucose monomers are forced into a 4C_1 chair conformation, while successive monomers are rotated over 180° around the polymer axis, to satisfy the bond angle of the bridging oxygen. This forces the hydroxyl and hydroxymethyl groups in an equatorial position, stabilizing the chair conformation and decreasing the flexibility of the glycosidic bond. As a result, the cellulose chain is linear, forming a rigid polymer, whereas amylose chains show more flexibility. Two intramolecular hydrogen bonds per anhydroglucopyranose unit further increase its rigidity. Every cellulose crystal phase exhibits a O3-H-O5 \cdots bond. In addition, another crystal phase dependent hydrogen bond is formed. Finally, the β bond is intrinsically more stable than the α bond, presented in amylose.

The main utilization of cellulose in industry is currently limited to textiles and paper manufacturing. In some biological processes such as fermentation and enzymatic catalysis, peculiar enzymes, bacteria and other microorganisms are used to break down cellulose molecules and thus a few commodity chemicals can be obtained. Nevertheless, such biological processes generally suffer from unsolvable problems such as low efficiencies, narrow reaction conditions and limited scale of production. Chemo-catalytic conversion of cellulose [12] has been around for some time, but it only receives serious attention with the advent of a series of novel chemo-catalytic reaction routes since the fossil oil crisis in the 1970s. Nowadays, researchers in the entire world try to find ways to break down more easily cellulose and transform it in useful chemicals. Some typical chemicals and fuels which can be produced by chemo-catalytic conversion of cellulose by different chemical processes as presented in the Scheme 1.

Clearly, a variety of fuels, including ethanol, hydrogen, methane and chemicals such as glucose, fructose, sorbitol, levulinic acid and lactic acid can be obtained from catalytic conversion of lignocellulosic biomass. Lignocellulosic biomass can also be used to produce syngas ($\text{CO} + \text{H}_2$) which can then be transformed into fuels and myriad chemicals. In many instances, depolymerization and hydrolysis of cellulose to glucose monomer is regarded a necessary first step. Then glucose is further catalytically degraded into various intermediates, chemicals and fuels, following the A route.

Following the route B, it is desirable to obtain fine chemicals directly from cellulose, without having one more step implying the formation of glucose.



Scheme 1. Potential chemicals and fuels from the catalytic conversion of cellulose

Compared to cellulose, hemicellulose has a very diverse composition [13] containing several pentoses (mostly xylose and arabinose), hexoses (mostly galactose, glucose and manose) and nonsugar compounds as monomers. Furthermore, a typical hemicellulose chain is branched and shorter than that in cellulose, inhibiting crystal formation and making hemicellulose much easier to hydrolyse than cellulose. The utilization of the saccharides derived from hemicellulose is essential for its efficient transformation to biofuels (mainly ethanol) or other high value-added chemicals. These two alternative purposes for hemicellulose valorization can be attained by chemical or biological conversion of the hemicellulosic monomers. Hemicellulose can be depolymerized into monomeric and oligomeric components with high purity and yield by chemical, enzymatic or thermal processes [14].

Lignin is another major component of lignocellulose, mainly present in woody biomass. It is a heavily branched and interconnected hydrophobic polymer consisting of three typical aromatic monomers: p-coumaryl alcohol, coniferyl alcohol and sinapyl alcohol. These alcohols polymerize by random coupling reactions, forming a very complex structure. Lignin is extremely resistant to degradation. The reactivity of lignins is dominated by the substructures containing aryl esters, biaryls, phenols, benzyl and aliphatic alcohols.

Related to the activities connected to the biomass conversion, the biorefining concept was introduced not long ago and defined as a “facility that integrates biomass conversion processes and equipment to produce fuels, power and chemicals from biomass” [15]. In principle, the biorefining concept is similar with today’s petroleum refineries, the difference being the feedstocks. Regarding the polymeric components of lignocellulose, almost each carbon atom is connected to an oxygen atom. Because of this, in biorefineries, is necessary a controlled defunctionalization (e.g. reducing the oxygen content through efficient catalytic processes) rather than the functionalization used in the chemical industry so far. Unfortunately, this means that most of the developed processes in the petrochemical and chemical industry are not suitable for converting biomass, and alternative pathways for the production of fuels and chemicals should be developed. Moreover, for sustainable development and environmental protection reasons, an efficient biorefinery unit should provide a complete valorization of the biomass source, by performing the overall processes with a minimum loss of energy and mass, and should maximize the overall value of the production chain with the minimum formation of wastes.

Solid catalysts are in principle very suitable for the processing of biomass. However, the requirements for biomass conversion are rather different, compared to the processing of hydrocarbon feedstocks, which form the backbone of our current energy and raw materials supply. A large number of technologies based on biological, thermal, and chemical processes have been developed for biomass valorization. Among those, chemical processing of biomass is of paramount research interest as the resulting products can exhibit relatively equating characteristics to petro-based products [11]. Various kinds of chemical processes, such as fast pyrolysis, hydro-processing, oxidation, dehydration, hydrolysis, transesterification, isomerisation, and many others have been reported, in which the application of a catalyst is crucial to enhance reaction rates and to obtain high yields of desirable products in a short time period. Indeed, catalysis is a key technology in modern chemical industry and plays an essential role in the production of a vast majority of bulk and commodity chemicals. Catalysis greatly contributes to the development of new, greener, and potential chemical processes, offering

feasible alternatives to stoichiometric reactions, thus acting as a driving force towards a more sustainable chemical industry.

Homogeneous and heterogeneous catalysts are both used in petrochemical industry [11] as well as in biomass upgrading. Homogeneous catalysts, where the active sites are in the same phase as the reactants, can interact efficiently with the reaction substrates, typically resulting in higher turnover frequency (TOF) rates compared to heterogeneous catalysts. However, homogeneous catalysts are often associated with high toxicity, corrosivity, energy-intensive separation and purification procedures, and inefficient reusability. Stringent government regulations have therefore directed chemical industries to search for alternative catalytic materials. In this respect, heterogeneous catalysis, where the catalyst exists in a different phase (typically solids) as the reactants (mostly liquids or gasses), could offer tremendous potentials for several energy and environmental-related applications including biomass upgrading. Availability of facile preparation methods, low production costs, remarkable robustness, high resistance to common reaction conditions (moisture, air, pressure, and temperature) and durable lifetime are some of the primary advantages of solid catalysts. More importantly, solid catalysts can be efficiently recovered from reaction mixtures and can be readily reused in multiple catalytic cycles, making the process cost-effective and more sustainable. Separation processes represent more than half of the total investment in equipment for the chemical and fuel industries [16]. It is not overstatement that the separation costs are a decisive factor in the final analysis of a new process. So, the ease of separation of solid catalysts can be a crucial advantage. However, it is necessary that these catalysts have high selectivities in order to guarantee the cost-effectiveness of the process.

If we talk about the usage of solid catalysts (heterogeneous catalysis) we need to bear in mind that are quite a few challenges face ahead in the design of these. Some of these challenges are: the discovery of new reaction media, the optimum catalyst composition, the porosity of the catalyst and the active sites presented by last. Carbon materials have emerged as promising catalyst supports as well as metal-free active phase catalysts for various biomass transformation reactions [11]. They exhibit a broad spectrum of crucial catalytic properties such as large specific surface area, tailorable porous structures and surface chemistry, excellent chemical stability in acid or base media, remarkable hydrothermal stability, and efficient functionalisation. Many types of conventional carbon materials, such as activated carbon, carbon black, glassy carbon, pyrolytic carbon, and polymer-derived carbon have been employed for stabilizing catalytic active phases. Owing to high specific surface area and rich surface chemistry, these carbon materials allow the formation of highly dispersed metal particles (Pd,

Ru, Ni, Cu, Ag, Fe, etc.) throughout the catalyst matrix, resulting in enhanced resistance to sintering even at higher metal loadings and elevated temperature conditions. Moreover, advances in materials science and nanotechnology have provided several innovative strategies for the development of new carbon materials, such as carbon nanotubes (CNTs), graphene, and mesoporous carbons that can be used as catalyst supports or active catalysts.

Carbon nanotubes (CNTs) are characterized by a hexagonal arrangement of sp^2 carbons with well-controlled cavity geometries. CNTs can be classified as single-walled (SWCNTs) and multi-walled CNTs (MWCNTs) based on the number of carbon layers present in the tubular wall. SWCNTs are semiconductive with diameters of around 0.4–2 nm, whereas MWCNTs are metallic. Interestingly, the cavities of CNTs can prevent the aggregation of active metal nanoparticles (NPs) during catalyst synthesis or catalytic reactions. Defect sites and surface chemistry are the key parameters that determine the catalytic efficiency of carbon materials in biomass conversions. For example, defect sites incorporated into the sp^2 framework of CNTs, graphene or activated carbon can strongly influence surface properties and catalytic functionalities. Heteroatom doping is an appealing strategy, which exploits defect structures in carbon materials. Carbon nanotubes offer potential possibilities for stabilising metal NPs, metal oxides, acid–base functional molecules, and even complex hierarchical hybrids. CNTs exhibit defective sp^2 carbon surfaces and improved electron transport, which facilitates the interaction of active phases with the CNTs. In addition to preventing particle aggregation, the nanoscale confinement within CNTs can also control the diffusion of reactive species and their interactions with the active phases. These fascinating characteristics have been exploited in the field of biomass upgrading, in order to achieve improved conversion rates with high yields of desired products.

A prime objective in the catalytic conversion of lignocellulosic feedstocks is the improving of the catalysts efficiency and selectivity towards value-added products. However, the incorporation of compatible catalytic processes in the actual infrastructure of petrochemical industry plants requires biomass feedstocks to be converted into building block chemicals with fewer oxygenated groups. These building block chemicals, also known as “platform molecules”, are molecules with multiple functional groups that possess the potential to be transformed into new families of useful chemicals. The most important 12 platform molecules [17] that can be produced from sugars via biological or chemical conversions and can subsequently be converted to a number of high-value bio-based chemicals or materials are given in the Figure 2.

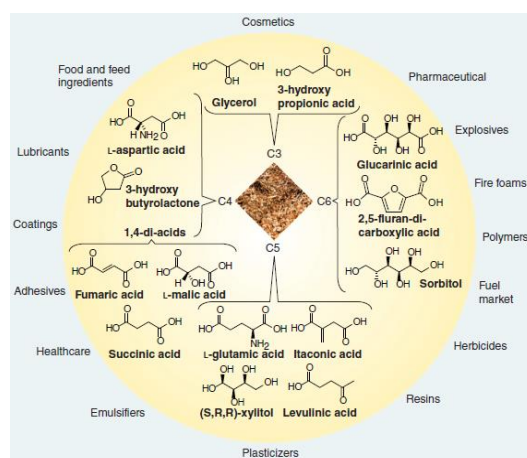
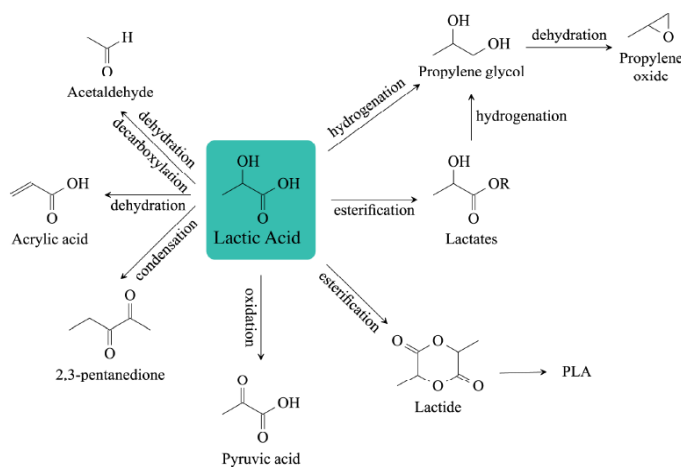


Figure 2. The 12 building blocks (platform molecules) identified in the biomass feedstock conversion [17]

Lactic acid (2-hydroxypropanoic acid, LA) is an encouraging renewable building block for the development of biodegradable plastics and to substitute current petrochemical-based materials [18] but it is also extensively employed in the food and pharmaceutical industries. New applications [19] have been recently intensified in the field of commodity chemicals such as propylene oxide and propanoic acid, liquid fuels and polymers. In Scheme 2 it can be seen some chemicals obtained starting from lactic acid as well as the specific routes [20].



Scheme 2. Lactic acid as a platform chemical [20]

LA and other hydroxy acids can also be used as raw materials in the catalytic synthesis of the amino acids, which are the building blocks of proteins and the primary source of nitrogen for tissues in the human body. Nowadays, amino acids are widely produced and used in many fields, their annual production reaching about 6.5 million tons in 2014 [1].

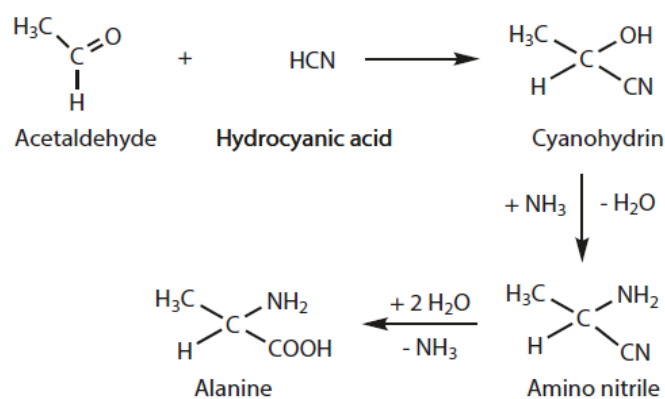
The literature for the use and transformation of amino acids is extremely diverse. In general, however, these focus on the use of amino acids in nutrition, medicine, impact on physiological function, along with their use as platform molecules. In particular, they promote health by several actions, including reduction of the adiposity, regulation of the muscle protein metabolism and the control of the growth and immunity of the organism. Also, it is well documented that amino acids deficiency causes serious diseases, both in humans and animals [21]. Therefore, the interest in investigating and developing new routes to produce them in a more cost-effective and sustainable way has significantly increased in the last years.

In present, amino acids are produced through three different routes: microbial processes (fermentation and enzymatic synthesis), chemical synthesis and extraction from protein-hydrolysates. However, most of the current industrial processes for amino acids production are based on fermentation route, under aerobic or anaerobic conditions, and several microorganism are used in order to convert the sugars present in a substrate into a broad spectrum of amino acids [22]. Generally, the fermentation takes place in an aqueous medium containing essential nutrients such as sources of carbon, nitrogen, phosphorus and sulphur, vitamins and minerals. Identifying a suitable carbon source is a major challenge of the process, because it should not only serve as an energy source for the microorganism, but also as a precursor for the structural skeleton of the amino acid metabolite [1].

The second biological process in the production of amino acids is the enzymatic one or the enzymatic conversion and is based on the action of an enzyme or a combination of enzymes to catalyze the production of the desired amino acids [21].

Historically, chemical synthesis has been the classical pathway to produce achiral amino acids like glycine or a racemic mixture of D,L-methionine or D,L-alanine [21]. In present, the chemical synthesis refers to the Strecker synthesis (production of methionine), the Gabriel malonic ester synthesis (when amino acids are obtained as secondary product) and the Miller synthesis (which aims to obtain amino acids by reproducing the primitive conditions when organic compounds were formed in an atmosphere rich in methane, ammonia, water and hydrogen) [23].

The Strecker synthesis was reported for the first time in 1850. According to this reaction the conversion of an aldehyde or ketone and amine or ammonia to α -amino acids can be achieved by means of an acid catalysts, metal cyanide and water, as shows in Scheme 3.

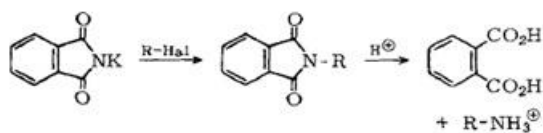


Scheme 3. Strecker synthesis of alanine [24]

The Strecker synthesis of amino acids has been considered as one of the modes of formation of amino acids in the primordial Earth [24]. In particular it consists in the reaction of an aldehyde with hydrogen cyanide and D- α -methylbenzylamine in methanol, followed by the hydrolysis of the resulting amino nitrile to yield the N- α -methylbenzyl amino acid. Finally, a catalytic hydrogenolysis is performed to remove the methylbenzyl group from the amino acid molecule [21]. The main drawbacks of the chemical synthesis are associated to the price of the catalyst as well as to the use of hazardous cyanide sources. To overcome these problems new methods were developed in 1963 by K. Harada [24], starting from the catalytic asymmetric Strecker-type reaction.

The most common industrial chemical process for the manufacture of racemic amino acids is the so-called Bucherer-Bergs method [25] which is a variant for the Strecker synthesis. This method proceeds via a hydantoin intermediate that is generated from an aldehyde, hydrogen cyanide and an ammonium salt. However, the approach is far less attractive than fermentation or enzymatic catalysis because an expensive optical resolution step is required to isolate the bio-active L-isomer from the amino acid racemate [1]. This approach is therefore involved only in the production of achiral glycine and D,L-methionine, since the adults and animals are able to convert D-methionine to the L-isomer by transamination. Although the Bucherer-Bergs approach is the most common because of its simplicity and effectiveness, the main drawbacks of this method are the long reaction time and the elevated temperature.

Another method of producing amino acids is the Gabriel malonic ester synthesis. The reaction takes place in two steps as shown in the Scheme 4.



Scheme 4. Gabriel's synthesis [26]

In the first step potassium phthalimide reacts with halogenoalkanes and with a variety of other alkylating agents and leads to the N-alkylphthalimide. Furthermore, the N-substituted phthalimides may be converted into the corresponding primary amine by hydrolysis or hydrazinolysis [26]. The importance of the Gabriel synthesis lies in the absence of secondary or tertiary amine contamination of the primary amine and the toleration of a very wide range of other functional groups in the molecule. In the same time, the mild conditions are now available for accomplishing both stages so there is hope.

The last production method of amino acids is the Miller's synthesis which is based on the idea that organic compounds that serve as the basis of life were formed when the earth had an atmosphere of methane, ammonia, water and hydrogen, instead of carbon dioxide, nitrogen, oxygen and water [23]. In order to test this Miller built an apparatus (Figure 3) which circulated CH_4 , NH_3 , H_2O and H_2 , past an electric charge. Electrical discharge, according to Miller, may have played a significant role in the formation of compounds in the primitive atmosphere.

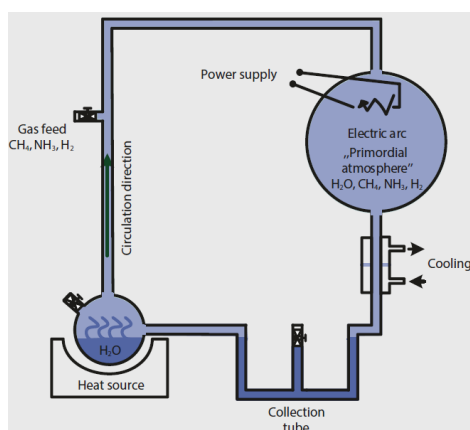
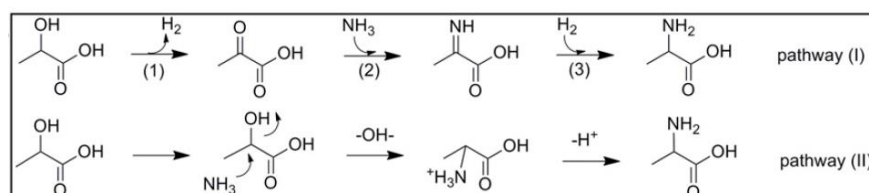


Figure 3. The apparatus used in Miller's synthesis [23]

Water is boiled in the flask and it is mixed with the gases in the 5 liters flask. Then, the water circulates past the electrodes, condenses and empties back into the boiling flask. The U-tube is used because it prevents circulation in the opposite direction. The acids and amino acids formed in the discharge, not being volatile, accumulate in the water phase. In the condensed water phase, various

organic molecules were detected at the end of the experiment, including larger amounts of the amino acids glycine and alanine. It is regarded to be certain that these were formed by Strecker synthesis with the intermediate products hydrocyanic acid, formaldehyde and acetaldehyde, respectively [27].

In present are many attempts to transform lignocellulose biomass-derived α -keto acids and α -hydroxy acids into α -amino acids. In this context W.Deng et al. [2] reported the catalytic synthesis of α -amino acids, including alanine, leucine, valine, aspartic acid and phenylalanine, in high yields, in the presence of ruthenium nanoparticles supported on carbon nanotubes (Ru/CNT). The reaction mechanism is presented in the Scheme 5.



Scheme 5. Two possible reaction pathways for amination of lactic acid to alanine [2]

The catalyst exhibits exceptional efficiency compared with catalysts based on other metals. This happens due to the unique, reversible enhancement effect of NH_3 on Ru in dehydrogenation step. Based on the catalytic system, a two-step chemical process was designed to convert glucose to alanine in 43% yield, comparable with the well-established microbial cultivation process presented above. The presented strategy enables a route for the production of amino acids from renewable feedstocks.

Another pathway of obtaining amino acids (in special alanine) was proposed by Y.Wang et al.[17]. The procedure involves a one-step conversion of the crude glycerol from the biodiesel industry into 43% yield alanine over a $\text{Ru}_1\text{Ni}_7/\text{MgO}$ catalyst. The multifunctional catalytic system promotes glycerol conversion into lactic acid, and then into alanine, as shown in Figure 4.

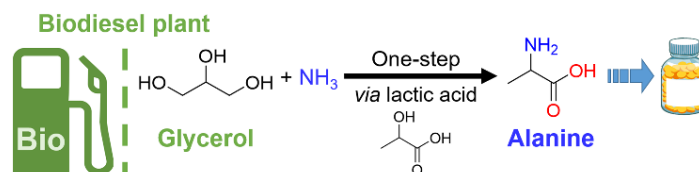


Figure 4. An illustration of one-step conversion of waste glycerol to alanine [16]

They concluded, after performing X-ray absorption spectroscopy and scanning transmission electron microscopy, that existent bimetallic RuNi species and Ni-doped Ru substantially decreases the

E_a of C-H bond dissociation of the lactate alkoxide to form pyruvate, which is the rate determining step. A plausible explanation for this behavior is that the unreacted glycerol inhibits lactic acid and amination reaction.

An attempt of converting biomass to amino acids was made in 2020 by S. Song et al. [28] by using CdS nanosheets, an efficient and stable catalyst which exhibits a higher activity in production of alanine from lactic acid, compared to commercial CdS as well as to CdS nanoobjects bearing other morphologies. The occurring reaction, presented in Figure 5 is a photocatalytic one, CdS representing the only material able to promote the desired transformation under visible light.

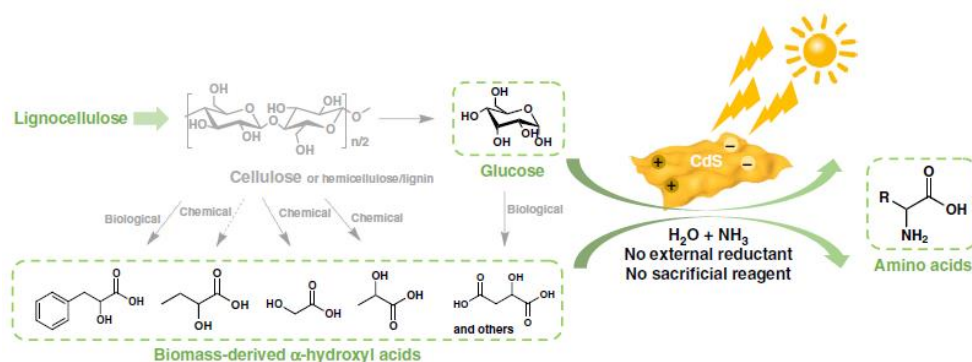


Figure 5. Photocatalytic amination of glucose or biomass-derived α -hydroxyl acids to amino acids [28]

The unique properties of CdS nanosheets are attributed mainly to the preferential formation of oxygen-centered radicals to promote α -hydroxyl acids conversion to α -keto acids and partially to the poor H_2 evolution which is an undesired reaction. Encouragingly, a number of amino acids were prepared using the proposed protocol, with high yields, and one-pot conversion of glucose to alanine was also achieved, under mild conditions.

T. Fukushima and M. Yamauchi [29] made another attempt to transform biomass into amino acids by electrochemical synthesis. They reported that seven amino acids were electrochemically synthesized from biomass-derivable α -keto acids and NH_2OH with faradaic efficiencies (FEs) of 77-99%, using an earth-abundant TiO_2 catalysts.

2. Objectives

The aim of this work was to develop efficient solid catalysts able to directly transform lignocellulosic biomass-derived lactic acid (LA) into alanine (AL) through a dehydrogenation-reductive amination pathway. For this a series of Ru-based catalysts with (1) as-received MWCNT, (2) oxidised MWCNT and (3) magnetic nanoparticles (MNPs) carriers and 1wt%, 3wt% and 5wt%Ru were prepared and characterised.

(1) As already specified, literature indicates that ruthenium nanoparticles supported on carbon nanotubes (Ru/CNT) exhibit exceptional efficiency compared with catalysts based on other metals, due to the unique, reversible enhancement effect of NH_3 on Ru in dehydrogenation step. However, the authors claim the use of a catalyst with only 3wt%Ru, prepared by impregnation on as-received CNT. Much more attention must be paid to the concentration of ruthenium which can lead to ruthenium particles with varying degrees of dispersion and oxidation, these characteristics being able to decisively influence the course of the reaction in which they are applied.

(2) Different oxidation processes were applied in the view of producing functionalized CNTs and their use as carrier for ruthenium deposition, in the next step of the research. By using such type of carriers (i.e., as-received CNT and oxidized CNT) Ru-based catalysts with different catalytic features related to the metal dispersion, location (ruthenium in- and out-tubes) and reduction degree, can be easily created.

(3) To overcome the catalysts separation issue, the use of magnetic nanoparticles emerge as a viable solution; their insoluble and paramagnetic nature enables their easy and efficient separation from the reaction mixture with an external magnet. That is why, a second kind of Ru-based catalysts used as carrier magnetic nanoparticles (MNP) for the synthesis of cationic Ru(III)/functionalized silica coated magnetite nanoparticles.

3. Experimental part

All the chemicals and reagents were of analytical purity grade, purchased from Sigma-Aldrich and used without further purification. Two kind of multi-walled carbon nanotubes (MWCNTs) were purchased with the following features: (1) preparation method Catalytic Chemical Vapor Deposition (CVD) (CoMoCAT®), over 95% carbon, O.D×L/6-9 nm × 5 μm and armchair configuration, and (2) preparation method Catalytic Chemical Vapor Deposition, over 90% carbon basis, D×L/110-170 nm ×

5-9 μm and armchair configuration. Hydrated ruthenium chloride ($\text{RuCl}_3 \cdot x\text{H}_2\text{O}$) had $\sim 37\%$ Ru basis. PTFE membrane filters with 0.45 μm pore size were purchased from Merck.

3.1. Materials preparation methodologies

3.1.1. Ru supported onto MWCNT (Ru/CNT)

The CNT-supported Ru nanoparticles were prepared by wet impregnation method. Typically, 0.5g CNT (CoMoCAT®) was added into the aqueous solution of RuCl_3 (200mg/10 mL H_2O) and then subjected to stirring for 1 h at room temperature. The solution was aged 2 h and after that the water was evaporated at 80°C. The catalyst was calcined at 350°C, in static atmosphere, for 4 h. The calcination temperature was established based on the TG analysis of CNT carrier (see Annex 1). The solid product was reduced in H_2 gas at 450°C for 2 h or using sodium borohydride (fresh aqueous solution) following a procedure from literature [30]. The metal loadings were ~ 1 wt %, ~ 3 wt % and ~ 5 wt % and the obtained samples were denoted 1%Ru/CNT, 3%Ru/CNT and 5%Ru/CNT.

3.1.2. MWCNTs oxidation

The oxidation of MWCNTs has the scop of the opening up of carbon nanotubes, their purification and fictionalization. Eight different oxidation procedures were performed in order to establish the optimum oxidation conditions in the view of the synthesis of an optimal functionalized CNTs structure. The prepared samples and the oxidation conditions are summarized in Table 1. For the first seven procedures CoMoCAT® MWCNT were used to produce the $\text{CNT}_{\text{ox}-1}$ - $\text{CNT}_{\text{ox}-7}$ samples while the $\text{CNT}_{\text{ox}-8}$ sample was produced from MWCNTs with 95% carbon, O.D \times L/6-9 nm \times 5 μm and armchair configuration. In order to minimize the tube damage, a low power sonicating bath and a relatively low acid exposure time were used. The oxidation processes were carried out either under reflux, by using a sonication bath or by refluxing followed by sonication. Nitric acid (65 wt%) or a mixture of HNO_3 and H_2SO_4 were used as oxidation reagents and the oxidation time was varied from 1h to 3h. Irrespective of the applied methodology the resulted solid was washed up to neutral pH and dried at 80°C for 24 h. All procedures methodologies are detailed in Annex 2.

Table 1. The oxidation conditions used for the synthesis of CNT_{ox} samples

Entry	Sample	m _{MWCNT} (g)	V _{HNO₃} (mL)	V _{H₂SO₄} (mL)	V _{H₂O₂} (mL)	Procedure		
						Ultrasoundication time (h)	Reflux	
							Time (h)	Temperature (°C)
1	CNT _{ox} -1	2	200	-	-	3	-	-
2	CNT _{ox} -2	1	200	-	-	3	2	80 (1h) 100 (1h)
3	CNT _{ox} -3	1	200	-	-	3	2	80
4 ^a	CNT _{ox} -4	0.3	14	42	-	2	15 min	60
5 ^b	CNT _{ox} -5	0.3	14	42	7.5	2	15 min	60
6	CNT _{ox} -6	0.1	7.5	-	7.5	3	15 min	60
7	CNT _{ox} -7	0.1	-	-	12.5	-	72	65
8 ^c	CNT _{ox} -8	0.1	10	-	-	3	24	r.t.

^a - 70 mL mixture of HNO₃ (65wt%) and H₂SO₄ (8M), mechanical stirring; ^b - 70 mL mixture of HNO₃ (65wt%) and H₂SO₄ (3M), mechanical stirring; ^c - distillation of CH₂Cl₂

3.1.3. Ruthenium based magnetic nanoparticles

The two steps preparation followed a literature reported procedure [31]: (a) the synthesis of the magnetic carrier that is comprised of spherically amino functionalized silica-coated Fe₃O₄ nanoparticles. In a typical procedure, 7 g of sodium dodecylbenzenesulfonate (technical grade, purchased from Acros Organics) was added in 60 mL dried xylene (purchased from Aldrich) and ultrasounded for 20 minutes, then stirred in an oil bath at room temperature. The air was removed from the reaction vessel by purging it with nitrogen. 3.23 g (8.0 mmoles) iron (III) nitrate nonahydrate and 0.8 g (0.4 mmoles) iron (II) chloride tetrahydrate were dissolved in 3.6 mL deionized water purged with nitrogen and added to the mixture of xylene and surfactant. The obtained mixture was stirred overnight under inert atmosphere at room temperature till homogenization. The emulsion was heated at 90°C, for 1 h, and then 4 mL of hydrazine 35% solution was added and stirred for 3 h, at 90°C and 1 h at 40°C, under inert atmosphere. Afterwards a mixture of 3 mL tetraethylortosilicate (TEOS, purchased from Aldrich) and 3 mL 3-aminopropyltriethoxysilane (purchased from Aldrich) was added and the

emulsion was stirred overnight in air atmosphere. The obtained black solution was transferred in a Berzelius flask and the obtained particles were separated with the aid of a Fe-Nd-B magnet. The separated particles were then washed five times with ethanol, recovered with a magnet, washed again with acetone and dried under vacuum. (b) the impregnation of the magnetic nanoparticles carrier with RuCl₃ solution in basic medium as follow: 2 g of Fe₃O₄-SiO₂/NH₂ were added to 200 mg RuCl₃ aqueous ruthenium (III) chloride (purchased from Aldrich) dissolved in 400 mL distilled water. The pH was adjusted at 13 with the aid of a NaOH aqueous solution (1M). The mixture was kept under stirring at 25 °C for 24 h. The solid was then magnetically collected from the solution, washed twice with distilled water and acetone and dried in vacuum.

3.2. Characterization techniques

Prepared samples were characterized by adsorption-desorption isotherms of liquid nitrogen at -196 °C, X-ray diffraction (XRD), temperature programmed desorption of H₂ and NH₃ (H₂-TPD and NH₃-TPD), IR diffuse reflectance with Fourier transform (DRIFT) and Raman spectroscopy, thermogravimetric-differential thermal analysis (TG-DTA) and scanning transmission electron microscopy (STEM).

Textural characteristics (surface area, pore volume and pore diameter) were determined from the adsorption-desorption isotherms of nitrogen at -196 °C using a Micromeritics ASAP 2020 Surface Area and Porosity Analyzer.

The morphology of the particles was analyzed using a scanning transmission electron microscopy (STEM) system. Bright field scanning transmission electron microscopy (BF-STEM) and dark field scanning transmission electron microscopy (DF-STEM) images were collected from Hitachi S-5500 operating at 30 kV accelerating voltage.

Powder X-ray Diffraction patterns were collected at room temperature using a Shimadzu XRD-7000 apparatus with the Cu K α monochromatic radiation of 1.5406 Å, 40 kV, 40 mA at a scanning rate of 1.0 2 θ min⁻¹, in the 2 θ range of 10°–90°.

Hydrogen and NH₃-temperature programmed desorption (H₂- and NH₃-TPD) were recorded using a Micromeritics apparatus – Autochem II (Chemisorption Analyzer). Approximately 20 mg freshly reduced Ru/CNT was heated at 650°C under N₂ for 0.5 h to remove the hydrogen adsorbed on Ru atoms. After that, the temperature was reduced to 150°C and waited until baseline became stable. Subsequently, successive doses of H₂ gas (H₂-TPD) or NH₃ gas (NH₃-TPD) were provided. The NH₃-TPD measurements for CNT_{ox} samples were performed in the same manner.

DRIFT spectra were recorded with a Thermo 4700 spectrometer (400 scans with a resolution of 4 cm^{-1}) in the range of $400\text{--}4000\text{ cm}^{-1}$.

Raman spectra were recorded using a microscope equipped triple monochromator. The spectra were acquired in the back-scattering geometry, while for excitation the 514.4 nm line of an Ar^+ laser was focused on the sample by means of a 50 objective, measured directly.

TG-DTA analyses were recorded using a Shimadzu apparatus in a Pt crucible. The heating rate was of $10^\circ\text{C min}^{-1}$, respectively, starting from room temperature till 850°C under a nitrogen flow of 50 mL min^{-1} .

3.3. Catalytic tests

The catalytic experiments were carried out in a stainless steel autoclave (15 mL, HEL Instruments). Briefly, to a solution of 25 mg lactic acid in 10 mL $\text{NH}_3\cdot\text{H}_2\text{O}$ (solution of 28 wt%), 5-50 mg of catalyst was added. The resulted mixture was stirred at $180\text{--}250^\circ\text{C}$, under 10 atm of H_2 and for 0.5-8h. After reaction the autoclave was quickly cooled at room temperature, the catalyst was recovered by centrifugation and the products were separated by solvent distillation under vacuum. Two blank reactions in which a solution of 25 mg of lactic acid in 2.5 mL $\text{NH}_3\cdot\text{H}_2\text{O}$ (solution of 28 wt%) was maintained at 200°C , in the presence (10 atm of H_2) or absence of hydrogen and for 2h were also performed. Also, two reactions in which 25 mg of lactic acid in water or in 2.5 mL $\text{NH}_3\cdot\text{H}_2\text{O}$ (solution of 28 wt%) was maintained under stirring, at 180°C for 2h.

The recovered products were silylated (200 μL of a derivatization agent (1% w/w of trimethylchlorosilane in N,O-Bis(trimethylsilyl)-trifluoroacetamide) and 200 μL of pyridine, 80°C for 4 hours), diluted with 1 mL of ethyl acetate and analyzed with a GC-MS Carlo Erba Instruments (Waltham, MA, USA) QMD 1000 equipped with a Factor Four VF-5HT column ($0.32\text{ mm} \times 0.1\text{ mm} \times 15\text{mm}$).

The lactic acid conversion (X) and selectivities (S_n) to reaction products n were calculated from the chromatographic analysis by using the follow equations:

$$X\% = \frac{n_i - n_t}{n_i} \times 100 \qquad S_n\% = \frac{\text{Yield}_n}{X} \times 100$$

Where: n_i – initial moles of lactic acid; n_t – moles of untransformed lactic acid at time “t”, determined from chromatographic analysis

4. Results and discussions

4.1. Ru/CNT samples characterisation

Liquid nitrogen adsorption-desorption isotherms at -196°C

Figures 6-8 show the nitrogen adsorption-desorption isotherms at -196°C and the corresponding pore size distribution obtained through the Barret–Joyner–Halenda (BJH) method for the 1%, 3% and 5% Ru/CNT samples.

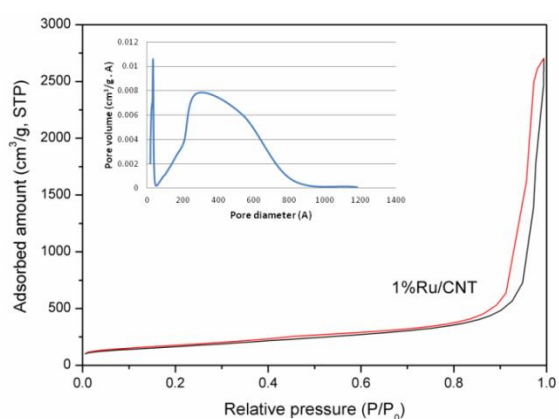


Figure 6. Nitrogen adsorption-desorption isotherm and pore size distributions (inset) for 1% Ru/CNT sample

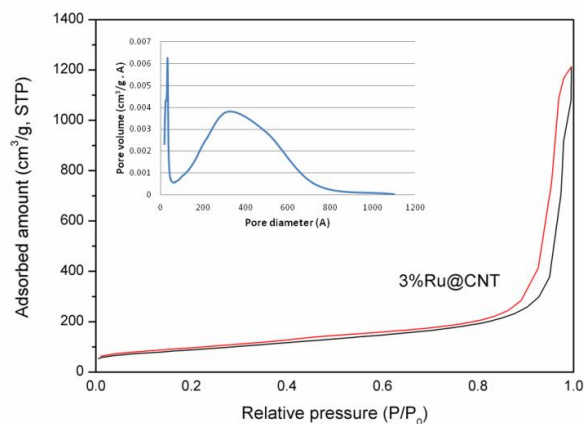


Figure 7. Nitrogen adsorption-desorption isotherm and pore size distributions (inset) for 3% Ru/CNT sample

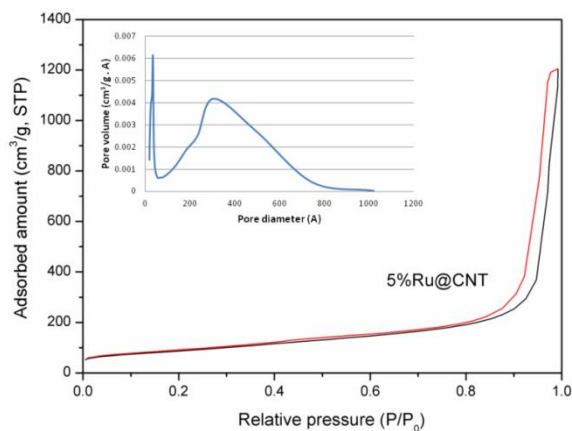


Figure 8. Nitrogen adsorption-desorption isotherm and pore size distributions (inset) for 5% Ru/CNT sample

The pore structure parameters of Ru/CNT sample determined by BET, t-plot and BJH methods are summarized in Table 2. The specific surface area (S_{BET}), the total pore volume (V_{p}) and the porosity of the samples are presented in Table 2. The specific surface area (S_{BET}) of the samples was calculated following the BET (Brunauer–Emmett–Teller) procedure with eight relative pressures (p/p_0) of nitrogen in the range of 0.07–0.2. The t-plot method was used to determine the micropore and external surface area and also the micropore volume. The Barret–Joyner–Halenda (BJH) method was used to determine pore size distribution, considering the desorption curves.

Table 2. The pore structure parameters of Ru/CNT sample determined by BET, t-plot and BJH methods

Entry	Sample	S_{BET} (m^2/g)	Micropore surface area (m^2/g)	External surface area (m^2/g)	Total pore volume (cm^3/g)	Micropore volume (cm^3/g)	Mezopores volume (cm^3/g)	Avarage pore size (BJH, nm)
1	1%Ru	584	56	527	3.82	0.02	3.80	3.3 and 27.7
2	3%Ru	315	22	293	1.67	0.01	1.66	3.3 and 31.9
3	5%Ru	310	20	291	1.88	0.01	1.87	3.3 and 30.5

All the nitrogen adsorption-desorption isotherms (Figures 6-8) can be divided in four parts as shown in Figure 9, indicating a multistage adsorption process.

In part I (around p/p_0 of 0.01), the isotherm is normally of type I characteristic indicated by the fact that the nitrogen adsorption amount increases at ultra-low pressure. Such a process occurs in pores with molecular size, suggesting that in the samples there are micropores contributed by the opened inner cavities in the CNT with very small diameter. Nitrogen molecules, whose diameter is about 0.364 nm, can fill in these pores under ultra-low adsorption pressure. However, as Figure 9 shows, in the case of our samples, there is only a very slightly increased amount of nitrogen adsorption in this portion of isotherms. Table 2 shows both very low micropores surface area and micropores volume. Part II of the isotherms ($p/p_0 = 0.01-0.4$) shows a slowly increases of the nitrogen adsorption amount with the formation of the surface monolayer.

A hysteresis loop is clearly visible in part III and IV of the isotherm, associated with the capillary condensation in mesopores [32]. These ranges show Type IV isotherm characteristics. Part III corresponds to capillary condensation occurring at medium relative pressure range ($p/p_0 = 0.4-0.85$) in

small mesopores with a size of 3.3 nm (Table 2, column 9), which is similar to the inner cavity diameter of the pristine opened CNT [33]. As Table 2 shows this size remains constant, irrespective of the ruthenium concentration, indicating a lack of ruthenium deposition during the impregnation process in the inner hollow cavity of the CNT.

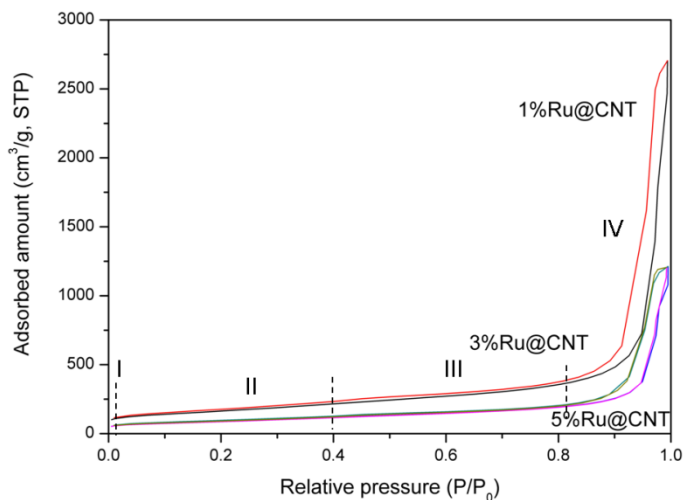


Figure 9. Nitrogen adsorption-desorption isotherms of Ru/CNT samples

When the pressure nears to the saturation pressure (part IV of the isotherm, $p/p_0 = 0.85-0.99$), the adsorption amount shows a great increase, indicating a strong capillarity in larger mesopores. In MWCNTs these hysteresis loop (H3 type) correspond to pore size of about 20-40 nm which is likely to be contributed by aggregated pores since there are not CNT with so large inner cavity diameter and, accordingly, to form so big inner porosity [33]. Therefore, the so-called aggregated pores are formed by the confined space among the isolated nanotubes of different orientation which interacts by intermolecular force creating a relatively stable aggregated structure (Figure 10).

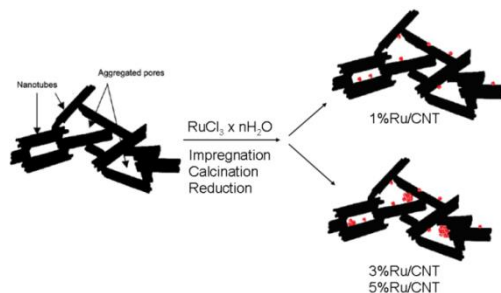


Figure 10. Schematic structural model for the aggregated pores in CNTs adapted from [13] and the structural models of the Ru/CNT samples

The corresponding pore sizes to aggregated pores in Ru/CNT samples slightly vary in a range of 27.7-31.9 nm (Table 2). This variation, along with the decreases of the external surface area clearly indicates the deposition of the ruthenium take place on the outer side of the CNT tubes. Moreover, the high difference between the S_{BET} of the 1%Ru/CNT sample (Table 2, entry 1) and the S_{BET} of the 3%Ru/CNT and 5%Ru/CNT (Table 2, entries 2 and 3), respectively, indicates a high uniform deposition, with a high dispersion degree, of the ruthenium particles for the 1%Ru/CNT sample and a high agglomeration of the ruthenium particles in the case of the last two samples (Figure 10). These results are in agree with Chu and co-workers which showed not long ago [34] that the main Ru particle size is smaller if ruthenium is deposited on the inner surface of the carbon nanotubes (denoted Ru-in-CNTs) than that of deposited ruthenium on the external surface of the nanotubes (denoted Ru-out-CNTs), indicating that particle sintering is prevented in Ru-in-CNTs under the reduction condition due to the spatial restriction of the CNT channels. The narrower size of the aggregated pores in the case of the 1%Ru/CNT sample also indicates a slightly denser packaging of the CNT network, again confirming the high uniform deposition of the ruthenium particles in the case of this sample. The agglomeration of the Ru particles on the outer walls of CNT for high concentrations of ruthenium (i.e., 3% and 5%, respectively) is also confirmed by XRD and STEM measurements.

X-Ray diffraction (XRD)

The X-ray diffraction (XRD) patterns of the as-synthesized Ru/CNT powders were recorded to examine their phase purity and crystallinity. As shown in Figure 11, CNT has two characteristic reflection lines at 26° and 43.9° , corresponding to the (002) and (100) facets, respectively, according with literature data [35, 36]. The line from 26° indicates that the spacing between the sp^2 -C layers in the multi-walls CNTs is 0.343 nm [35]. As the XRD pattern of the CNT carrier shows the impregnation of the CNTs with different quantities of ruthenium salts and the activation steps does not damaged the CNT structure.

In the case of 1%Ru/CNT sample no diffraction lines corresponding to ruthenium particles are evidenced suggesting the formation of nanoparticles with narrow size and high dispersion for this sample (Figure 11, spectrum in black). However, for the samples 3%Ru/CNT and 5%Ru/CNT, apart from the lines characteristic to the CNT carrier, some characteristic lines corresponding to the Ru (hexagonal phase; JCPDS Card No. 06-0663) at 38.3° , 42.8° , 58.4° , 69.6° and 78.7° , assigned to (100), (101), (102), (110) and (103) reflections of metallic Ru are evidenced [37]. This indicates an

agglomeration of the ruthenium species during the samples preparation with the formation of larger ruthenium particles.

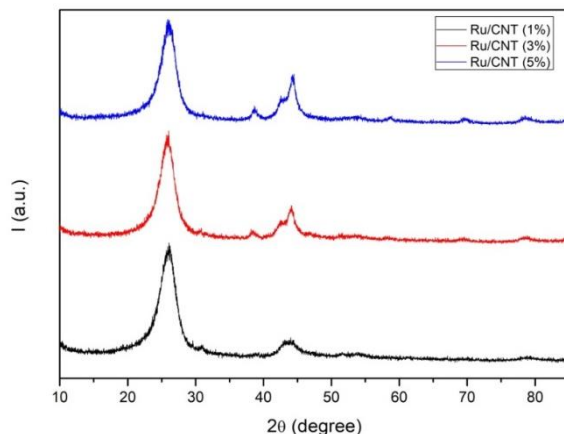


Figure 11. XRD patterns of different Ru-based CNTs catalysts

The average size of ruthenium crystallites was determined from the Debye-Scherrer equation taking the (100) reflection of ruthenium particles [38]:

$$d = \frac{k\lambda}{\beta \cos \theta}$$

Where: d is the crystallite size in nm; $k = 0.94$; λ is the wavelength of the X-ray (1.54178 \AA); θ is the half-diffraction angle and β is the full width at half-maximum (FWHM) in radians for the 2θ value (38.3°).

The ruthenium particles size diameter is 9.0 nm for the 3%Ru/CNT sample and 10.6 nm for the 5%Ru/CNT sample.

Scanning transmission electron microscopy (STEM)

Scanning transmission electron microscopy (STEM) was used in order to describe the morphology of the ruthenium nanoparticles. Bright field and dark field images were collected at different resolutions in order to see better the dispersion of metals onto the external surface of the carbon nanotubes. For each loading (1wt%, 3wt%, 5wt%) were selected three images. The average diameter of the particle was calculated using a graphical method, taking into account minimum 10 ruthenium nanoparticles.

For the sample 1%Ru/CNT, as it can be seen from Figure 12, we observe that the distribution of ruthenium nanoparticles is uniformly. The ruthenium particles, with an average size of 2.5 nm, are deposited on the external surface of the carbon nanotubes and no agglomeration is present.

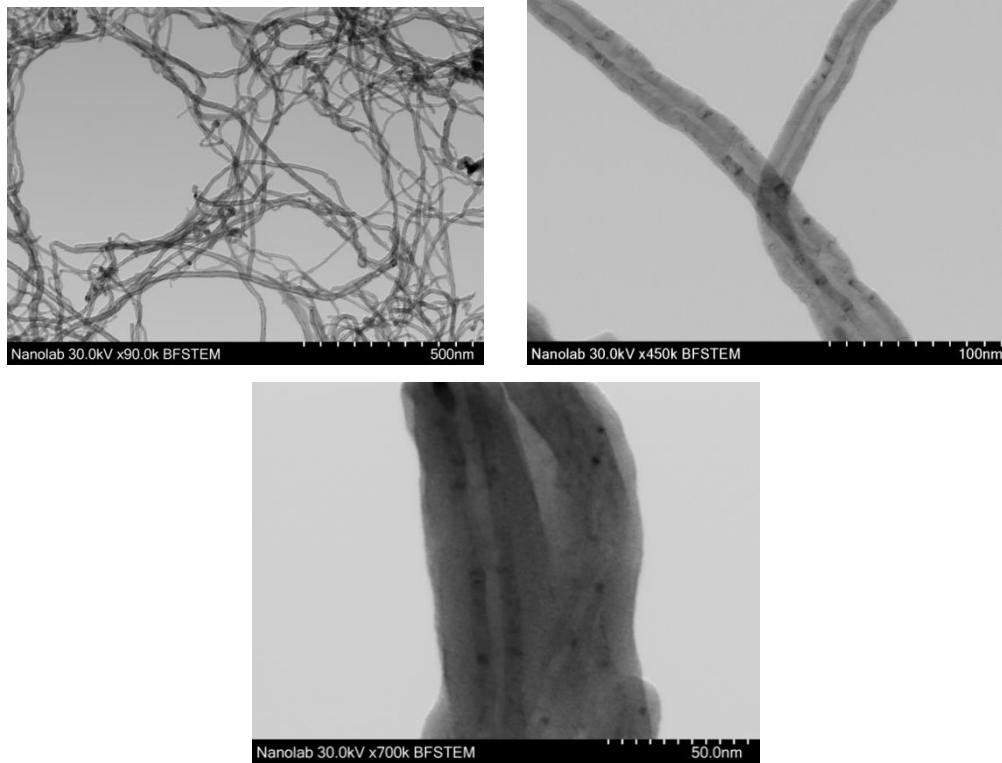


Figure 12. BF-STEM images for the 1%Ru/CNT sample

For the sample 3%Ru/CNT, as can be seen from Figure 13, the distribution of ruthenium nanoparticles is still uniform. The ruthenium particles are deposited on the external surface of the carbon nanotubes and a slightly agglomeration is present. The average particle size is 5.0 nm this being expected because it is well known that the particles aggregate as the metal loading increases.

For the sample 5%Ru/CNT, as can be seen from Figure 14, the distribution of ruthenium nanoparticles is uniform until some extent. A few particles agglomeration was observed but the deposition on the external surface of the carbon nanotubes is preserved. The average particle size is 7.0 nm.

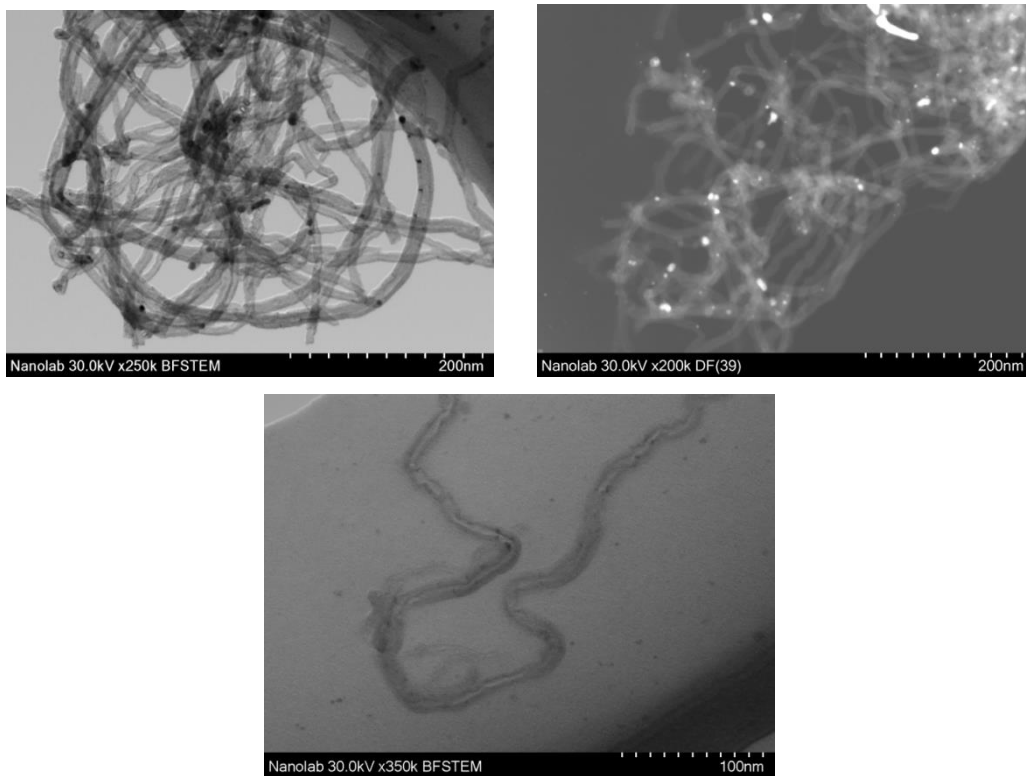


Figure 13. BF and DF-STEM images for the 3% Ru/CNT sample

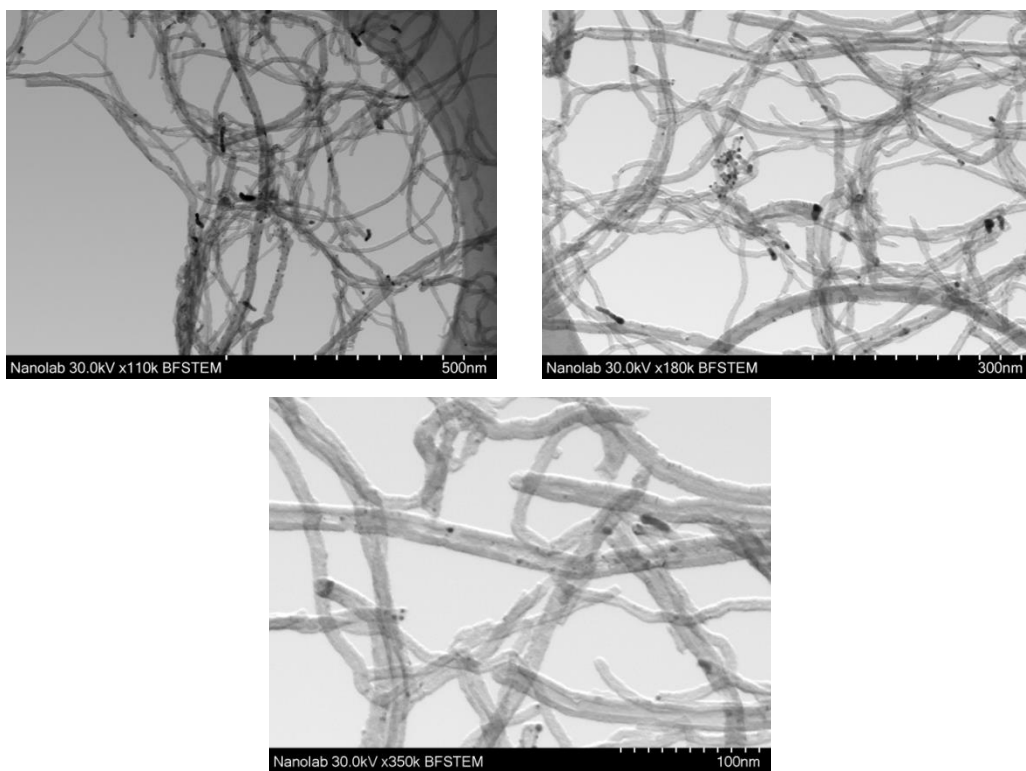


Figure 14. BF-STEM images for the 5% Ru/CNT sample

NH₃-TPD

Chen et al. [39] reported that the deviation of the CNT graphene layers from planarity causes p-electron density shifting from the concave inner surface to the convex outer surface, leading to an electron deficient internal surface and an electron-enriched external surface. This electron density loss is partially compensated through the interaction with the encapsulated metal [40] which would destabilize the metal nanoparticles and facilitate their reduction. In connection with this statement and with the findings from the previously results obtained from the characterization techniques applied for the elucidation of the structural and chemical characteristics of the Ru/CNT samples, temperature programmed desorption of ammonia (NH₃-TPD) was performed to assess the acid properties of the CNTs support and corresponding Ru-based catalysts. It is well known the oxide form of the noble metals display Lewis acid characteristics. The existence of the Brønsted acidity should also does not be excluded through the possibility of the -OH groups existence, anchored on the oxide particles.

The temperature of maximum desorption rate, i.e., the temperature of a TPD peak, is used as a measure of the acid strength of the sorption sites. The method has the limitation that it can distinguish sites by sorption strength but not Lewis (L) from Brønsted (B) type sites. However, for zeolites there are several literature reports which divide desorption regions in two, below and above 400°C, referring to low-temperature (LT) and high-temperature (HT) regions, respectively [41]. The peaks in the HT region are attributed to the desorption of NH₃ from strong B and L sites while the assignment of the LT peaks is still controversial [41]. The possibility that weak L acid sites were responsible for the LT peak was considered [42] but the release of NH₃ hydrogen-bound to NH₄⁺ cations were also not excluded [43]. The NH₃-TPD profiles of the CNT and Ru/CNT samples are given in Figure 15.

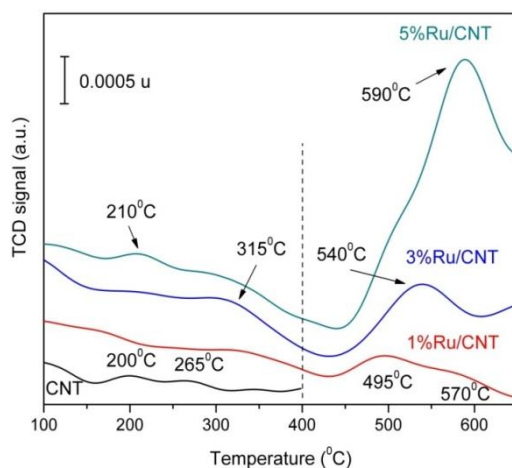


Figure 15. NH₃-TPD profiles for the Ru/CNT samples

As Figure 15 shows, the CNT carrier contains only an insignificant amount of acid sites, situated in the LT region. However, their impregnation with ruthenium salt followed by calcination and reduction leads to the appearance of acid sites, their highest concentration being in the HT region. Moreover, the higher the ruthenium concentration the higher the concentration of the L and B acid sites. Nevertheless, the level of the acid site concentration is very low and vary from around 0.4 $\mu\text{mol/g}$ (1%Ru/CNT) to 2.2 $\mu\text{mol/g}$ (5%Ru/CNT).

As previously shown, the obtained results from the nitrogen adsorption-desorption isotherms, XRD and STEM measurements clearly indicate that ruthenium particles are deposited on the external surface of the CNT tubes. However, if in the case of 1%Ru/CNT sample, small ruthenium particles with a high dispersion are formed, for samples with 3% and 5%Ru, the formation of larger particles with a low dispersion is also observed. In agree with Wang et al. [44] such large particles are hardly reduced. Therefore, the new peaks from the NH_3 -TPD profiles of Ru/CNT (Figure 15) could be assigned to a partial reduction of Ru^{3+} to Ru^0 species with the formation of some $\text{RuO}_x\text{-OH}$ species alongside the metallic particles.

H₂-TPD

The effect of reduction temperature on catalytic behavior has been the subject of many investigations. Many studies have shown both reduced catalytic activity and reduced hydrogen chemisorption capacity after reduction in hydrogen at high temperatures ($> 500^\circ\text{C}$) but a clear understanding of the phenomena involved is still lacking. Reduction at high temperatures may result in strongly chemisorbed hydrogen, may cause loss of spillover hydrogen altering the local charge transfer from the support to the metal at the particle boundary, may induce changes in morphology of the metal crystallite and may affect reduction of the support leading to the formation of an alloy with atoms from the support [45].

In this study the temperature-programmed desorption of hydrogen was performed in order to check the strength of metallic ruthenium interactions with hydrogen. Therefore, the H_2 -TPD spectra of previously reduced (450°C) Ru/CNT samples were measured. The maximum desorption temperatures and corresponding desorbed amount of hydrogen are given in Table 3.

The maximum of the hydrogen desorption peak found in this study for CNT carrier is lower than that for graphite (143°C versus 207°C) [46], suggesting a lower binding energy of the hydrogen

adsorption in the case of CNT. Many authors claim that hydrogen molecules mostly adsorb on the outer surfaces of CNT and the reduction in binding energy value is generally attributed to the surface curvature [47].

Table 3. H₂-TPD parameters for Ru/CNT samples and CNT carrier

Entry	Catalyst	H ₂ desorbed (mmol/g)	Peak temperature (°C)
1	CNT	1.18	143
2	1%Ru/CNT	0.010	328
		0.008	340
		0.008	370
	Total	0.026	
3	3%Ru/CNT	0.003	290
		0.005	310
		0.008	390
		0.004	520
	Total	0.020	
4	5%Ru/CNT	0.002	590

The hydrogen desorption begins at 200°C for all Ru-based catalysts. However, the maximum desorption peak depends on the ruthenium concentration. For catalysts with 1% and 3%Ru the H₂-TPD profiles comprise three or more peaks (the maximum temperature for these peaks are given in Table 3) owing to the formation of various active sites or to the effect of spillover hydrogen, while for 5%Ru/CNT sample, the only one maximum desorption peak was visible at 590°C. The peaks at the desorption temperature lower than 500°C (1% and 3%Ru) can be attributed to the dissociative adsorbed hydrogen and spillover hydrogen simultaneity, while the peak at above 500°C (3% and 5%Ru) can be associated to the spillover hydrogen stabilized by hydroxyl groups from the ruthenium oxides surface. A low temperature of the hydrogen desorption indicates, therefore, a weaker adsorption of H₂ and its greater mobility on the catalyst surface while a high temperature for the hydrogen desorption indicates a strongly chemisorbed hydrogen [48]. Based on H₂-TPD results, the mobility of hydrogen on the surface of catalysts can be ordered in the following sequence: 1%Ru/CNT > 3%Ru/CNT > 5%Ru/CNT. Moreover, the higher the ruthenium concentration the lower the hydrogen desorbed

amount. These data are also in agree with the NH_3 -TPD results according to which the higher the amount of ruthenium the lower the reduction degree of the agglomerated ruthenium particles.

DRIFT spectroscopy

It should be noted that the spectrum of the pristine CNT is quite similar to others presented in the literature [49]. Some claimed MWCNT-specific infrared (IR) spectral features include peaks associated with O–H vibrations (1600 and 3740 cm^{-1}), carboxylic groups (1740 cm^{-1}), $-\text{C}=\text{C}$ -stretching vibration (1523 cm^{-1}) and C–H stretching vibrations (close to 3000 cm^{-1}), even though they correspond to defects and impurities rather than the MWCNT structure itself (Figure 16). The most important use of infrared spectroscopy in MWCNT research is the characterization of surface functionalization [50] and this will be discussed in the next section.

The infrared spectra of the CNT and Ru/CNT samples are given in Figure 16. Similar peaks were identified for all samples. However, in the case of Ru/CNT samples a new peak at 3630 cm^{-1} was identified into the corresponding spectra, associated with possible O–H vibrations from $\text{RuO}_x\text{-OH}$ groups.

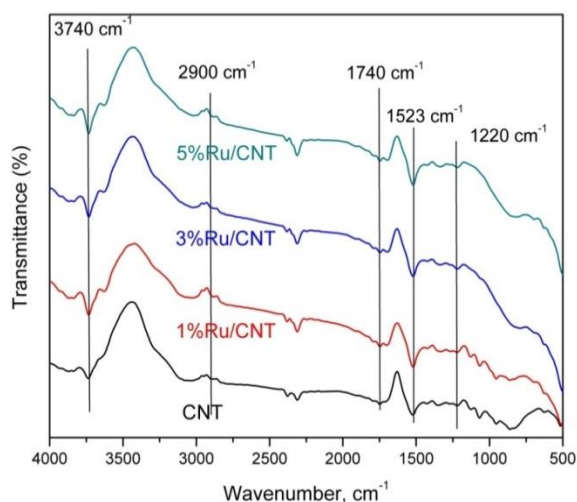


Figure 16. IR spectra of the CNT and Ru/CNT samples

4.2. Oxidation of CNTs: Opening up of carbon nanotubes, purification and functionalisation

As the nitrogen adsorption-desorption isotherms of the Ru/CNT samples showed, the capillarity mainly occurs in the small cylindrical mesopores (inner cavities) and the aggregated pores of CNT, the latter being associated with the larger portion of the total nitrogen adsorption amount. The small

fraction of the total nitrogen adsorption amount in the inner cavities (Figures 6-9) indicate that not all ends of nanotubes are opened [33]. However, to improve the adsorption and capillarity of CNTs both the opening-up of the nanotubes and the control of their aggregated pore texture is important.

The simplest method to open nanotubes is their oxidative treatment. It is well known that graphite oxidizes primarily at defects of the hexagonal lattice to create etch pits. When such defect sites are present in the wall of the nanotubes, they become the center of preferential etching. However, nanotubes have additional structural features such as high curvature and helicity, and may contain five- and seven-membered rings, which modify the initiation and also the propagation of oxidation. Particularly for MWCNTs, the oxidation tends to start near the tips, providing a mechanism for opening the tubes.

Oxidative treatment of nanotubes results not only in nanotubes open at their tips, but also nanotubes that are thinner in diameter [51]. The concentric layers of MWCNTs do not react at the same rate, since each shell has its own tip. It follows that the inner shells might persist longer than the outer ones. Therefore, different oxidation rates are assumed for oxidation of an open MWCNTs. The extent of the thinning depends on the duration of treatment.

A further consequence of oxidative treatment is the partial functionalization of the tubes, i. e., the nanotubes become covered with carboxyl or hydroxyl groups at their ends. These functional groups make the NTs partially soluble. The number or concentration of the inserted carboxyl groups can be estimated by acid–base titration or NH_3 -TPD. The concentration of the surface acid groups on nanotubes opened by various oxidants is in the range of 2×10^{20} – 10×10^{20} sites per gram of nanotube [52].

XRD

In case of carbon nanotubes, after some authors, the resolution of the XRD diffraction pattern is a complex matter because of the extremely large variation in their size, curvature and the disorder in the packing of the graphene sheets. [53] All these factors combined together affect the reflectance, as well as diffraction line positions and widths from one sample to another.

The X-ray pattern for the pristine CNTs (Figure 17, inset) presents a sharp well defined diffraction line at $2\theta = 25.8^\circ$ and one smaller line at 43° , corresponding with (002) and (101) planes. According to literature [55] the diffraction line from 25.8° correspond to the spacing between graphene sheets. Besides these out-of-plane ordering reflectance, CNTs also show two lines at 2θ values of 28°

and 52° respectively, corresponding with (100) and (102) planes. However, in this case, the XRD pattern does not present the out-of-plane reflectance and in-plane reflectance, thus implying the lack of in-plane ordering in these specific directions. Subsequent to acid treatment, the XRD spectra show a change in the magnitude and the 2θ shifting position of the reflectance lines (Figure 17).

In the case of CNT_{ox-1}, CNT_{ox-2} and CNT_{ox-3} samples the intensity of the line at $2\theta = 25.8^\circ$ is higher than that of the pristine CNT, this increases being attributed to an increase in the number of walls of the CNTs [56]. In the case of CNT_{ox-4}, CNT_{ox-7} and CNT_{ox-8} the intensity of the line at $2\theta = 25.8^\circ$ is lower than that of the pristine CNT, being attributed to a decrease in the number of walls of the CNTs. The lower intensity has also been related to a lower packing density or the presence of defects. Not less important, the decrease in the intensity of the (002) plane ($2\theta = 25.8^\circ$) is also attributed to the disordered structure of the nanotubes. This disorder is the effect of the attachment of functional groups at the surface and ends of the nanotubes, thus causing steric hinderance and impelling the individual nanotubes to misalign. The comparatively greater height of the (002) plane ($2\theta = 25.8^\circ$) in case of as-received CNTs has also been explained in terms of the greater graphitic character of the tubes [53]. This may only be true if there are a large number of equidistant tubes in the MWCNT so that their reflectances overlap to give a high intensity line.

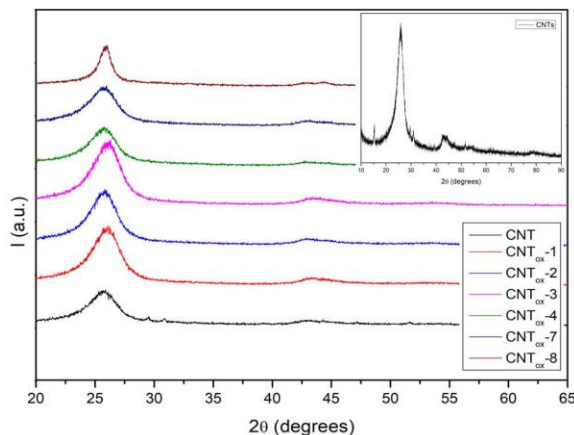


Figure 17. XRD pattern of as-received MWCNTs and oxidised CNTs

The shifting of the (002) plane ($2\theta = 25.8^\circ$) toward higher values of 2θ angle from as-received CNTs until CNT_{ox-8} is a result of an decrease in the intertubular spacing, which in turn indicates a loss in the ordered structure of the nanotubes.

The X-ray diffraction patterns of oxidized CNTs show a relatively greater broadness of the line at 43.3° indicating a lower crystallinity and a greater curvature in the nanotubes surface. According to

literature [54], the greater the diameter of CNTs the smaller is its curvature, thus resulting in a larger value of the d-spacing which, in this case, implies a smaller diameter of the tubes.

The broader distribution of lines in CNT_{ox-5} and CNT_{ox-6} as compared to the as-received CNTs reflects the turbostratic character of the nanotubes (Figure 18). This is because the debundling of CNTs decreases the crystalline domains size, resulting in the increased amorphous character of the nanotubes. It has also been reported that a broader distribution of d-spacing results in broader peaks [55] which is also a direct consequence of over-oxidation and loss of graphitic character.

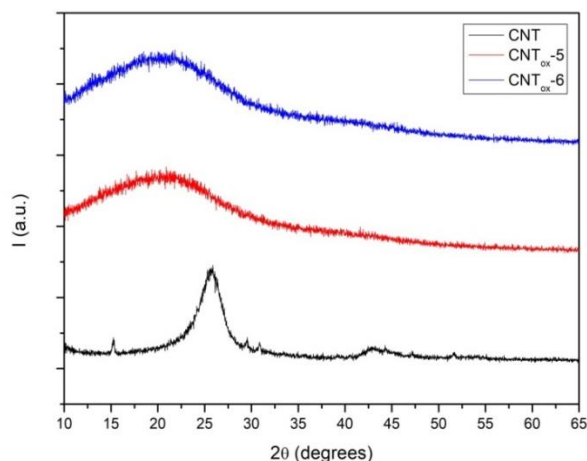


Figure 18. XRD patterns of oxidized (5-6) MWCNTs and as-received MWCNTs for comparison

NH₃-TPD

It is known that the amount and type of oxygen-containing functional groups strongly depends on the treatment methods and their process parameters. In case of nitric acid, the nitronium ion NO₂⁺ is believed to be able to attack the aromatic compounds, which is assumed to be the first step in the generation of oxygen-containing functional groups, followed by the formation of carbonyls and their conversion into carboxylic groups and carboxylic anhydrides [56]. In addition, nitrogen-containing groups can also be created by the nitric acid treatment.

Figure 19 shows the NH₃-TPD profiles for the CNT_{ox} samples obtained by HNO₃-treated nanotubes in different conditions (for oxidation conditions see Table 1).

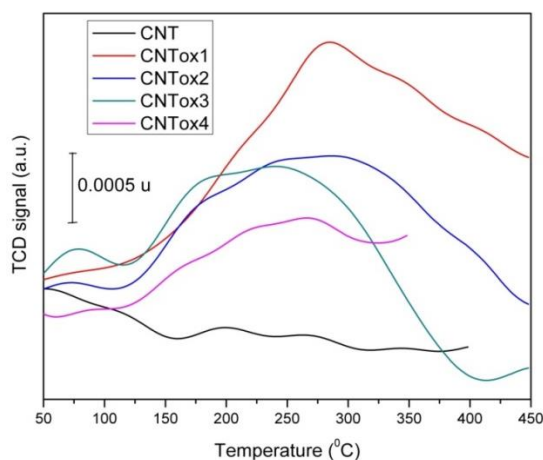


Figure 19. The NH₃-TPD profiles of the CNT_{ox} samples

The main ammonia TPD peak appeared at about 260-280 °C (Figure 19), indicating that most of the ammonia molecules are chemisorbed with a medium strength. The shoulder at high temperatures (cca 400°C, CNT_{ox}-1 and CNT_{ox}-2 samples) can be assigned to carboxylic structures, onto which ammonia chemisorbs strongly presumably *via* the formation of ammonium carboxylates. Most of the acidic groups act as primary adsorption centers, which bind additional ammonia molecules weakly through hydrogen bonds [57].

The total desorbed ammonia (mmol/g) varied in order: 0.073 (CNT_{ox}-2) > 0.053 (CNT_{ox}-1) ≥ 0.052 (CNT_{ox}-3) >> 0.004 (CNT_{ox}-4), which strongly depends on the oxidation procedure conditions.

IR spectroscopy

In Figure 20, IR spectra of the CNTs before and after the oxidation process (CNT_{ox}-1 - CNT_{ox}-4) are presented. The presence of typical C=O and O-H bonds are due to the formation of COOH groups on the nanotubes after acid treatment. This is evident in the IR spectrum shown in Figure 20. Different peaks at 3600-3900 cm⁻¹ are assigned to the O-H stretches of terminal carboxyl groups, the peaks at 2800-2944 cm⁻¹ can be assigned to the C-H stretch, and the peaks near 1742 cm⁻¹ correspond to the carboxylic C=O stretching vibrations. The peak at 1527 cm⁻¹ is attributed to the -C=C- stretching mode of the CNTs [58]. IR spectra also indicates the presence of the carbonyl (C=O) (1223 cm⁻¹) groups and the presence of the epoxide groups indicated by the presence of an absorption band in the 910-920 cm⁻¹ range, related to the contraction of the C-C bond and the stretching of C-O bonds of the epoxy ring [59].

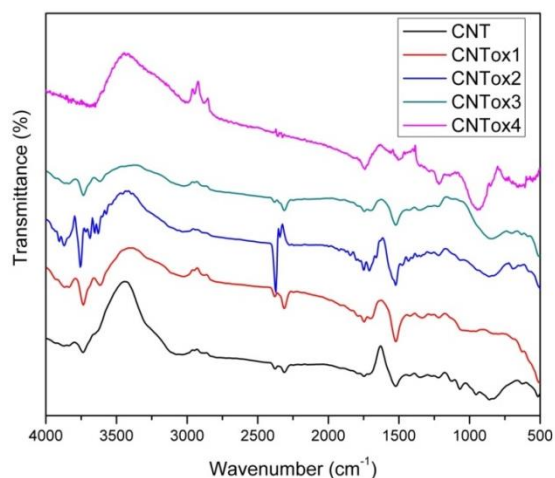


Figure 20. IR spectra of CNT and oxidised CNTs samples (see procedures 1-4 from Annex 2).

The highest amounts of -COOH and carbonyl groups were generated on CNT_{ox}5-7 (Figure 21). Unfortunately, a too advanced oxidation lead to a structure collapse as XRD analysis show for the CNT_{ox}-5 and CNT_{ox}-6 samples. Indeed, the IR spectra also shows a high increases of the bands intensity corresponding to the C-H stretch (2800-2944 cm⁻¹) and of those corresponding to the contraction of the C-C bond (910-920 cm⁻¹ range) in the detriment of the -C=C- stretching mode (1527 cm⁻¹).

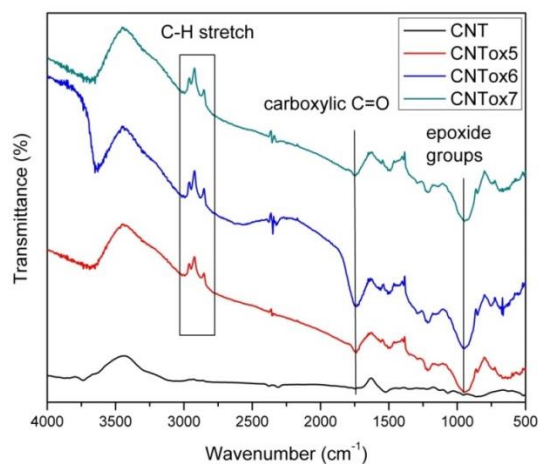


Figure 21. IR spectra of CNT and oxidised CNTs samples (see procedures 5-7 from Annex 2).

Raman spectroscopy

Raman spectroscopy is a very valuable tool for the characterization of carbon-based nanostructures. The Raman spectrum of as-received CNTs is shown in Figure 22.

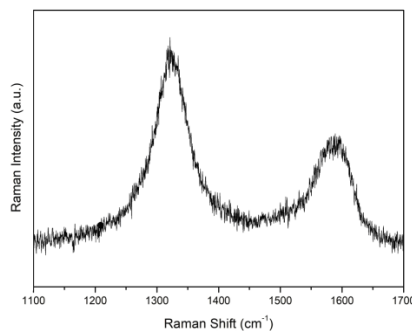


Figure 22. Raman spectra for as-received MWCNTs (i.e., CNT sample)

The Raman spectrum consists of three characteristic bands: D band, G band and D' band. In the as-received carbon nanotubes the D band appears at 1322 cm^{-1} , the G band appears at 1587 cm^{-1} and the D' band appears at 1606 cm^{-1} . The D-band is a disordered induced feature, arising from double resonance Raman scattering process from a non-zero centre phonon mode [60]. The D band is usually attributed to the presence of amorphous or disordered carbon in the CNT samples. The carbon structural disorder is due to the finite or nanosized graphitic planes and other forms of carbon such as rings along with defects on the nanotube walls. The G band originates from in-plane tangential stretching of the carbon-carbon bonds in graphene sheets [60]. The D' band, which appears as a weak shoulder in the G band at higher frequencies, is also a double resonance feature induced by disorder and defects. Also, it should be underlined that the radial breathing modes are too weak to be observed due to the large diameters of the tubes.

The Raman spectra obtained for some of oxidised CNT samples are shown in Figure 23. A slightly up-shift for the G band, indicating an increase of the number of sp^2 carbons, is observed from CNT_{ox-1} toward the CNT_{ox-7} sample. This effect usually indicates the strength of the oxidation process: the greater the displacement the stronger the oxidative process. Therefore, CNT_{ox-7} sample is stronger oxidised than the CNT_{ox-1} sample. This statement is in agreed with the results obtained from DRIFT measurements (Figures 20-21).

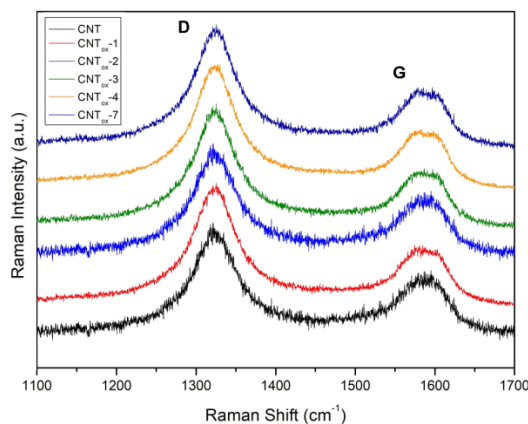


Figure 23. Raman spectra for as-received and oxidized MWCNTs from 1-4 and 7

The Raman spectra of the CNT_{ox}-5, CNT_{ox}-6 and CNT_{ox}-8 samples are presented in Figures 24 and 25. As Raman spectra of CNT_{ox}-5 and CNT_{ox}-6 samples (Figure 24) shows an up-shift of the D band and a slightly decrease in intensity for D and G bands takes place, most probably due to an over oxidation of the CNTs according to Chernyak S.A. and al. [61]. This over oxidation also lead to an increased amorphous character of the nanotubes, as corresponding XRD patterns showed (Figure 18).

In the Raman spectrum for CNT_{ox}-8 (Figure 25) a decrease in the wavenumber of the G band accompanied by an increase in the wavenumber of the D band is visible. Moreover, the D' band, corresponding to the defects in the CNT structure is more visible. These new features of the Raman spectra suggest a successful synthesis of an oxidized CNT with a concomitant increase in the number of defects compared to pristine CNT.

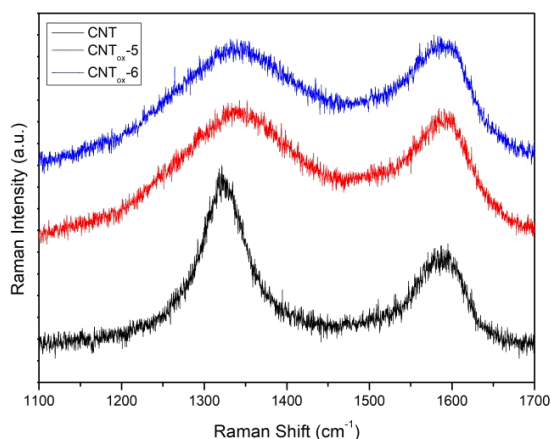


Figure 24. Raman spectra for as-received CNT and CNT_{ox}-5 and CNT_{ox}-6 samples

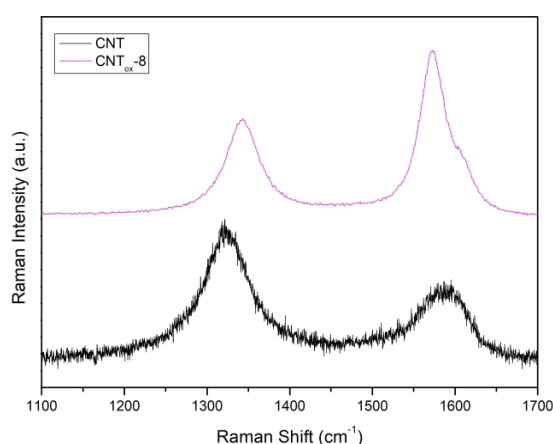


Figure 25. Raman spectra for as-received CNT and CNT_{ox}-8 sample

The intensity ratio of G to D band in the Raman spectra of oxidized samples is presented in the Table 4.

Table 4. I_G/I_D intensity ratios for the treated CNTs

Sample	Pristine	CNT _{ox-1}	CNT _{ox-2}	CNT _{ox-3}	CNT _{ox-4}	CNT _{ox-5}	CNT _{ox-6}	CNT _{ox-7}	CNT _{ox-8}
I_G/I_D	0.63	0.38	0.21	0.37	0.43	0.96	1.01	0.34	1.66

As Table 4 shows the intensity ratio G to D band (I_G/I_D) is almost the same indicating a similar defect population for the CNT_{ox-1}, CNT_{ox-3} and CNT_{ox-7} samples. However, compared to the as-received CNT, the I_G/I_D ratio of these samples is considerable lower, indicating a destruction of the graphitic integrity and the subsequent formation of small graphitic fragments. A I_G/I_D ratio of around 1.0 indicates a fully oxidation of the CNT_{ox-5} and CNT_{ox-6} samples, while the higher intensity ratio I_G/I_D for CNT_{ox-8} compared with the pristine CNT indicate the highly increased of the defects population.

TG-DTA

It is well known that different structural forms of carbon can exhibit different oxidation behaviour depending on the available reactive sites. For instance, disordered or amorphous carbons tend to be oxidised at around 500°C [53] because of their lower activation energies for oxidation or due to the presence of a large number of active sites. On the other hand, a well graphitized structure starts to oxidize at a relatively higher temperature, as a function of the type of CNTs.

The thermogravimetric measurements conducted on the as-received CNTs and on the oxidized samples CNT_{ox} 1-8 are presented in Figure 26. As expected, the thermal degradation of MWCNT is a multistage process. The first step, up to a temperature of 150°C, shows a weight loss of 1-5% for the highly hydrophilic nitric acid-treated CNTs samples and for the CNT_{ox-4} (nitric acid/sulphuric acid), which corresponds to the evaporation of the adsorbed water. The second step, from 150°C to 350°C is attributed to the decarboxylation of the carboxylic groups present on the CNTs walls. This second step appears in all the samples treated with nitric acid but do not appear in the samples treated with H₂O₂.

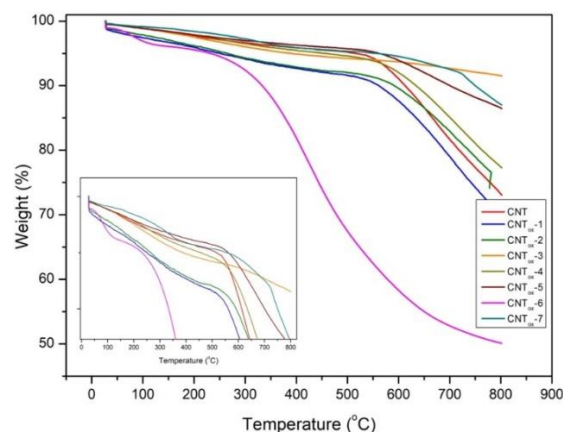


Figure 26. TGA profiles in N₂ atmosphere for CNT_{ox} 1-8 and as-received CNTs for comparison

Thermal degradation in the range of 350-500°C may be explained by the elimination of hydroxyl functionalities attached to the CNTs. This step is characteristic for the samples treated with nitric acid, and is more evident for the CNT_{ox}-6 sample, indicating the highest population of -OH groups. Finally, at a temperature higher than 500°C, the observed degradation corresponds to the thermal decomposition of the remained disordered carbon. From these results it can be concluded that the best procedure for the oxidation of multi-walled nanotubes implies nitric acid, in agree with literature reports.

4.3. Ruthenium based magnetic nanoparticles carrier

Magnetite nanoparticles are very sensitive to oxygen, and in the presence of air some might undergo oxidation to maghemite (γ -Fe₂O₃) phase. Since both magnetite (Fe₂O₃) and maghemite (γ -Fe₂O₃) have a spinel structure, their diffraction lines are close and it is difficult to distinguish them from one another by X-ray diffraction pattern. Moreover, depending on pH of the aqueous solution containing Fe³⁺ ions, it is also possible to form goethite, α -FeOOH by hydrolysis or by reaction with OH⁻ species [62]. The formation of hematite (α -Fe₂O₃) is more difficult than that of the maghemite phase, occurring only under thermal dehydration conditions.

To quantify the proportion of iron oxide, formed in a mixture iron oxide-silica, the XRD diffraction patterns were used. As visible in Figure 18, X-ray diffractogram (XRD) of the as synthesized samples showed a diffraction pattern characteristic of dominant magnetite (Fe₃O₄) phase. In particular, the peaks at 2 θ equal to 30.1°, 35.4°, 43.1°, 53.4°, 57.1°, and 62.6° can be indexed as

(220), (311), (400), (511), and (440) lattice planes of cubic magnetite, respectively (JCPDS 19-629). Nevertheless, the sharp diffraction lines indicate the presence of trace amounts of goethite phase probably formed as contaminants during the preparation processes. Finally, the broad diffraction line at around $2\theta = 20^\circ$ is due to the amorphous silica shell on the surface of the magnetite nanoparticles. Very important, no characteristic diffraction lines for ruthenium particles appeared after the magnetite impregnation, indicating a well dispersion of these particles on the surface (Figure 27, spectrum in red).

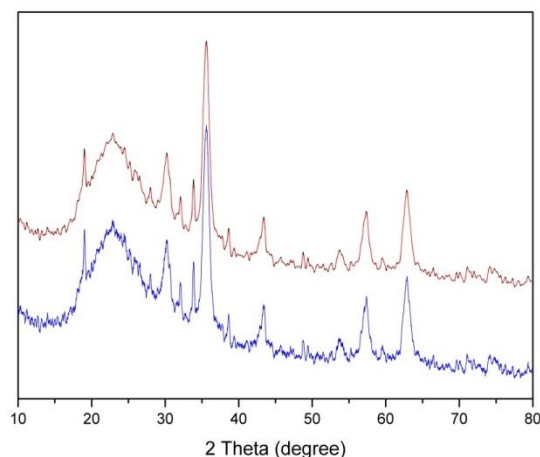


Figure 27. The XRD patterns of $\text{Fe}_3\text{O}_4\text{-SiO}_2/\text{NH}_2$ (blue) and $\text{Ru-Fe}_3\text{O}_4\text{-SiO}_2/\text{NH}_2$ (red) sample

In addition, the crystallite size was calculated through evaluation of the line broadening β and the corresponding Bragg angle θ , by using the Scherrer Equation ($D_{hkl} = 0.9\lambda/\beta\cos\theta$, in which β stands for the half-width of the XRD diffraction line, θ is the peak position in angles, and λ is the $\text{CuK}\alpha$ radiation wavelength, that is 1.54056 \AA [63]. The average Fe_3O_4 crystallite size, calculated by applying the Debye-Scherrer equation to the most intense reflection peak (311), was approximately of 18 nm.

The DRIFT spectrum (Figure 28) confirms the coating of the magnetite surface and the existence of amino groups ($-\text{NH}_2$ bending) on the surface of the particles. The presence of magnetite nanoparticles is signalled by the presence of two strong absorption bands at around 632 and 585 cm^{-1} , resulted from the split of ν_1 band at 570 cm^{-1} corresponding to the Fe-O bond of bulk magnetite (not shown in figure) [64]. The silica network is adsorbed on the magnetite surface by Fe-O-Si bonds which were confirmed by the band at around 584 cm^{-1} . Moreover, the SiO-H and Si-O-Si groups are present in the IR spectra with bands at 1113 , 1048 and 989 cm^{-1} . The absorption bands at 922 and 862 cm^{-1} revealed the presence of Si-O-H stretching and OH vibrations on the surface of magnetite, while the two broad bands at 3417 and 1625 cm^{-1} can be ascribed to the N-H stretching vibration and NH_2

bending mode of free NH_2 group, respectively [67]. The presence of the anchored propyl group was confirmed by C–H stretching vibrations that appeared at 2930 and 2862 cm^{-1} while the hydrogen-bonded silanols were confirmed by the bands at around 3200 and 3470 cm^{-1} [65].

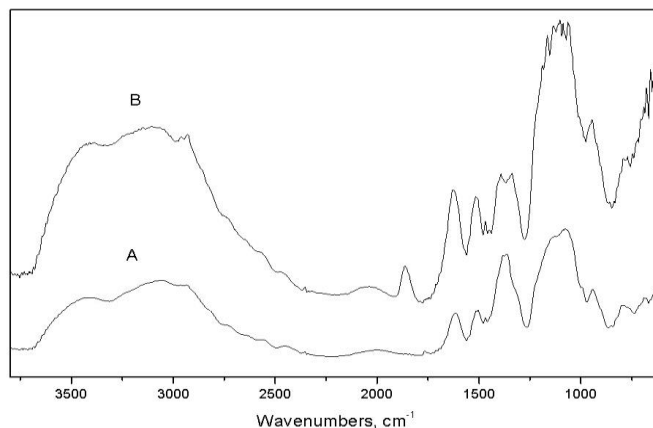


Figure 28. The DRIFT spectra of the $\text{Fe}_3\text{O}_4\text{-SiO}_2/\text{NH}_2$ (spectra A) and $\text{Ru-Fe}_3\text{O}_4\text{-SiO}_2/\text{NH}_2$ (spectra B) sample

The deposition of ruthenium species led to a reduction of the intensity bands of both 3417 and 1625 cm^{-1} bands, ascribed to the N–H stretching vibration and NH_2 bending mode of free NH_2 group, in the same time with the appearance of a new band at 1850 cm^{-1} assigned to hydrochloride $-\text{C-NH}_3^+\text{Cl}^-$ species (Figure 19, spectra B). This band confirms the docking of the $\text{Ru}(\text{OH})_x\text{Cl}_{3-x}$ ruthenium species onto the silica-coated magnetite nanoparticles.

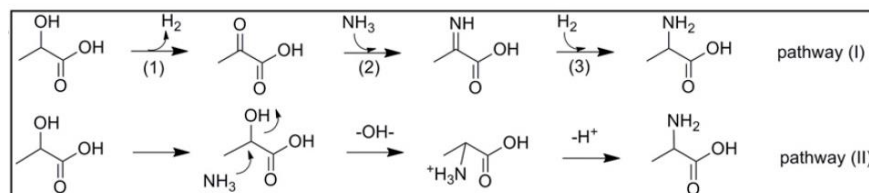
Not less important, the obtained catalyst still preserves its magnetic properties, the separation from the aqueous solution being easily done with the aid of an external magnet (Figure 29).



Figure 29. The separation of the $\text{Ru-Fe}_3\text{O}_4\text{-SiO}_2/\text{NH}_2$ sample

4.4. Catalytic tests

According to literature [2] the catalytic conversion of lactic acid to alanine takes place through two possible reaction pathways, an indirect (pathway I) and a direct (pathway II) one (Scheme 5, Literature survey). The indirect pathway (I) includes the dehydrogenation of lactic acid to pyruvic acid followed by its reaction with ammonia to afford the 2-iminopropionic acid, which next is hydrogenated to alanine. The direct pathway (II) involves a S_N2 substitution of the α -OH group with an $-NH_2$ group. In this route the catalyst is crucial in the dehydrogenation step.



On the other hand, some other authors claim the initial formation of the lactamide intermediate, under the temperature effect, which becomes the raw material for the alanine formation [66] in the presence of the catalyst. Not the last, the formation of the same amide is claimed by other authors [30]. However, in agree with these authors, the alanine is formed by the pathway (I) of dehydrogenation-amination-hydrogenation, paralleling the formation of the lactamide (Figure 30).

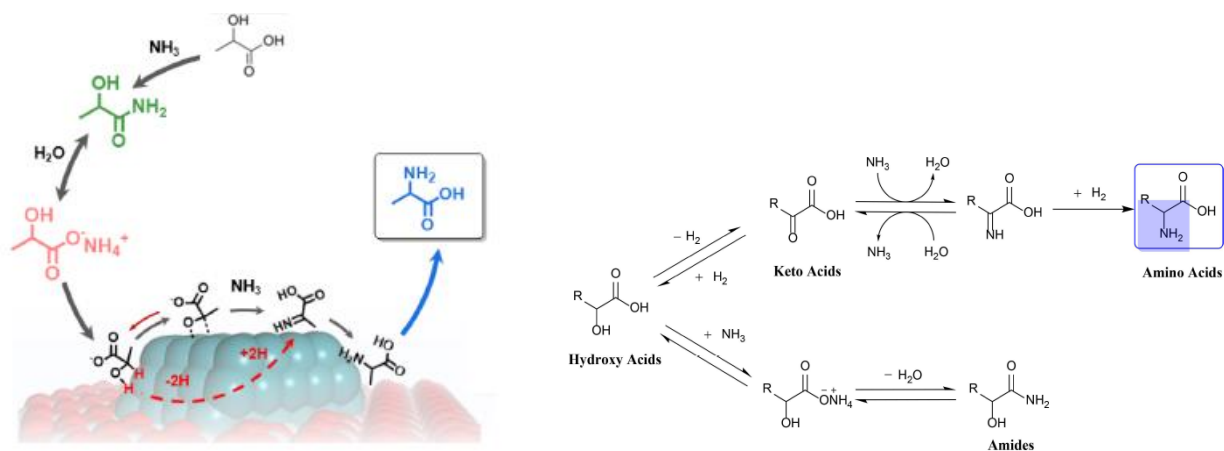


Figure 30. Pathways for the synthesis of alanine from hydroxiacids [30, 66]

In order to confirm the catalytic character of the alanine synthesis the present study started with blank experiments as described in “Experimental section, Catalytic tests”. Interesting enough, if in the absence of the ammonia solution lactic acid was not converted in the used reaction conditions, in the

presence of the ammonia solution lactic acid was converted to lactamide, irrespective of the presence or the absence of the hydrogen. The slightly increases of the temperature, from 180 to 200°C, lead to a slightly increases of the lactic acid conversion, from 10.2% to 12.6% with a total selectivity to the observed compound. In agree with Tian et al. [66], lactamide is derived from the neutralization reaction of the lactic acid with ammonia followed by its dehydration to amide under heating conditions. However, in the presence of the Ru-based catalyst, the reaction follows a dehydrogenation-reductive amination pathway. It worth mentioning here that ruthenium has superior catalytic performance over other group VIII metals in the direct amination of hydroxyl group [2, 67]. Moreover, as already stated in literature [30], ruthenium exhibit a high efficiency in the alcohol dehydrogenation which is claimed as the rate-determining step in the amination of lactic acid.

The catalytic system was optimized for the hydrogen pressure (Table 5), the reaction temperature (Table 6), the amount of the catalyst (Table 7) and the reaction time (Table 8) in the presence of 1%Ru/CNT catalyst.

Table 5. The influence of hydrogen pressure upon the lactic acid conversion and alanine selectivity

Entry	Hydrogen pressure (atm)	Conversion (%)	Selectivity (%)		
			Lactamide	Intermediate/by-product	Alanine
1	0	1.6	100	-	-
2	5	3.4	85.0	15.0	-
3	10	31.2	-	56.8	43.2
4	15	42.8	27.9	72.1	-
5	20	71.5	100	-	-

Reaction conditions: 25 mg Ru/CNT(1%), 2.5 mL NH₄OH, 25 μL lactic acid, 200°C, 2 h

As Table 5 shows the conversion of the lactic acid increased with the hydrogen pressure, while at lower hydrogen pressure (5 atm) lactamide was the only formed compound. As the hydrogen pressure is increased from 5 to 10 atm lactamide start to be converted to alanine. However, it is not clearly why a higher hydrogen pressure seems to inhibit the alanine formation. An optimum hydrogen pressure for the alanine synthesis can be explained if we assume the reaction mechanism involves the hydrogenation of an imine intermediate formed through the condensation of ketone with ammonia, in

agree with [30]. In this case a high hydrogen pressure may induce the reverse reaction of ketone hydrogenation, inhibiting the desired amino acid production.

Lactic acid conversion gradually increased when temperature elevated from 180°C to 220°C (Table 6). The catalytic selectivity to the reaction products also showed temperature dependence. Therefore, alanine selectivity initially increased and then, with a further increasing of the temperature, slightly decreased. In contrast, lactamide yield showed opposite trend. These results indicate that the reaction pathway for lactamide formation via neutralization and dehydration was able to happen under a lower temperature. These results also indicate that high reaction temperature may facilitate alcohol dehydrogenation and further transformation to amino acid, underlying the fact that the reaction pathway is the one which involves the imine intermediate. Too high temperature resulted in decreasing the desired product selectivity probably because of alanine decomposition. In conclusion, the optimal temperature choosed for further experiments was 200°C.

Table 6. The influence of reaction temperature upon the lactic acid conversion and alanine selectivity

Entry	Temperature (°C)	Conversion (%)	Selectivity (%)		
			Lactamide	Intermediate/by-product	Alanine
1	180	18.3	100	-	-
2	200	31.2	-	56.8	43.2
3	220	31.4	-	84.3	15.7

Reaction conditions: 25 mg Ru/CNT(1%), 2.5 mL NH₄OH, 25 μL lactic acid, 10 atm H₂, 2 h

When a low amount of catalyst (5 mg) was used, the lactamide amount was dominant in the reaction products (Table 7). With the increase of catalyst amount, the selectivity in alanine increased and selectivity in lactamide decreased substantially, indicating that the Ru-based catalyst promote the alanine formation. The optimal molar ratio between catalyst and substrate was found to be 100:1 (25 mg catalyst).

Table 7. The influence of amount of catalyst upon the lactic acid conversion and alanine selectivity

Entry	Catalyst (mg)	Conversion (%)	Selectivity (%)		
			Lactamide	Intermediate/by-product	Alanine
1	5	3.87	100	-	-
2	10	6.20	68.3	31.7	-
3	25	31.2	-	56.8	43.2
4	50	37.1	-	55.4	44.6

Reaction conditions: 2.5 mL NH_4OH , 25 μL lactic acid, 10 atm H_2 , 200°C, 2 h

Not the last, lactic acid conversion increased with elongated reaction time (Table 8). At the beginning of the reaction, lactamide was obtained as a main product, in line with the blank experiments, in the absence of the catalyst. These results show that lactamide formation is thermodynamically favored and only with the help of a catalyst alanine is formed. However, the alanine passes a maxim in selectivity. This behavior can be an indication of the formation of a by-product which is continuously accumulated alongside the alanine. In Figure 31 the GC analysis and the MS spectrum of alanine is presented.

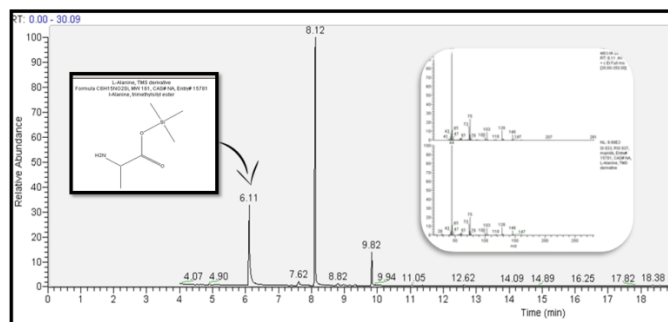


Figure 31. Identification of alanine by GC-MS

Table 8. The influence of reaction time upon the lactic acid conversion and alanine selectivity

Entry	Time (h)	Conversion (%)	Selectivity (%)		
			Lactamide	Intermediate/by-product	Alanine
1	0.5	1.6	100	-	-
2	1	3.19	100	-	-
3	2	31.2	-	56.8	43.2
4	4	42.8	-	85.2	14.8
5	6	71.5	-	88.4	11.6
6	8	72.6	-	100	-

Reaction conditions: 25 mg $Ru/CNT(1\%)$, 2.5 mL NH_4OH , 25 mg lactic acid, 10 atm H_2 , 200°C

In this stage of the research the pathway of the alanine formation is not very clearly, further experiments being needed to elucidate it. However, based on the obtained results it is possible the catalytic transformation to involves three steps: dehydrogenation of alcohol to ketone (starting from lactamide which loses the ammonia), condensation of the formed ketone with ammonia to imine, which acts like an intermediate and further hydrogenation to the desired product, in agree with the mechanism proposed by Tian et al. [66]. The overall process is represented in Figure 31. The first two steps are reversible reactions [68] and dehydrogenation is rate-determining step for the reported amination of lactic acid.

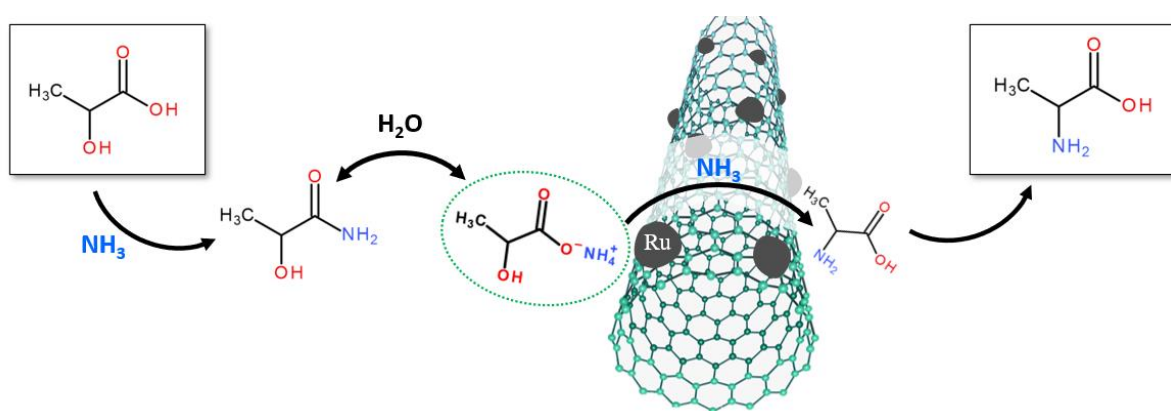


Figure 32. Proposed pathway for converting lactic acid to alanine by amination

The optimum reaction conditions established for the amination of lactic acid into alanine (i.e., 25 mg of catalyst, 10 atm H₂ pressure, 2.5 mL NH₄OH, 2.5 mL H₂O, 25 μL lactic acid, 200°C, 4 h) were used for performing the synthesis in the presence of 3% and 5% Ru/CNT, 1%, 3% and 5% Ru/CNT_{ox}-1 and 5% Ru/MNP-SiO₂-APTES. The obtained results are presented in the Table 9.

Table 9. The influence of the catalyst type on the lactic acid conversion and alanine selectivity

Entry	Catalyst	Conversion (%)	Selectivity (%)		
			Lactamide	Intermediate	Alanine
1	1%Ru/CNT	42.8	-	85.2	14.8
2	3%Ru/CNT	52.8	-	74.2	25.8
3	5%Ru/CNT	71.5	-	100	-
4	5%Ru/MNP-SiO ₂ -APTES	25.2	-	100	-

Reaction conditions: 25 mg catalyst, 10 atm H₂, 200°C, 2.5 mL NH₄OH, 2.5 mL H₂O 25 μ lactic acid, 4h

It worth noting that in the case of all catalysts the reaction mechanism remains unchanged due to the use of ruthenium which is the key factor in the amination of lactic acid. However, the best loading of ruthenium was 3wt%. Clearly enough the catalytic performance of Ru/CNT can be attributed to the high dispersion of Ru nanoparticles, which was confirmed by STEM measurement. However, it is also not excluded an influence of the reduction degree of the ruthenium nanoparticles.

Conclusions

In summary, we succeeded to synthesize four Ru-based catalysts with CNT and MNP particles as carriers. The characterization of the obtained samples indicate the formation of different kind of ruthenium active phase, as a function of the preparation method and the carrier nature. Therefore, in the case of CNT-based samples, catalysts with ruthenium nanoparticles of different size and oxidation degree were identified on the external side of the CNT tubes: the higher the ruthenium concentration, the larger the nanoparticles; the larger nanoparticles, the higher the proportion of RuO_x (the lower the reduction degree). On the other hand, the MNP-based sample strictly contains cationic ruthenium species with a high degree of dispersion.

CNT carrier was subjected to different oxidation procedures by using different oxidation agents. As characterization results showed, different kind of functional groups (i.e., carboxylic, hydroxyl and epoxy groups) were inserted on the external surface of the CNT, their nature and population highly depending on the applied oxidation procedure. It is not also excluded the formation of -NH₂ groups in the case of CNT oxidized with nitric acid. A too aggressive oxidation process, by using mixtures of nitric/sulphuric acids lead to a collapse of the CNT structure through its amorphization.

The preliminary results obtained from the catalytic synthesis of alanine from lactic acid showed that the optimum reaction conditions for the highest selectivity to alanine are: 25 mg catalyst, 2.5 mL NH₄OH, 2.5 mL H₂O, 10 atm H₂, 200°C, 4h. All the catalyst follows the same mechanism which involves three steps: dehydrogenation of alcohol to ketone, condensation of the formed ketone with ammonia to imine, which acts like an intermediate and further hydrogenation to the desired product. The best catalyst was found to be the one which has 3wt% loading of ruthenium.

Acknowledgements

This work was financially supported by The Education, Scholarship, Apprenticeships and Youth Entrepreneurship Programmer—EEA Grants 2014-2021, Project No. 18-Cop-0041.

M. Badea is grateful to Assoc. Prof. Elisabeth E. Jacobsen from Department of Chemistry, Norwegian University of Science and Technology, Trondheim, Norway, for performing STEM measurements. The analyses were performed during her Short Term Scientific Mission (STSM) stay at the above mentioned department, during September 1-30- 2021

Dissemination

Experimental data obtained in this work were the subject of a communication with the title "Catalytic production of amino acids from biomass-derived intermediates", authors: M. Badea, B. Cojocaru, E. Jacobsen, Vasile I. Parvulescu, Simona M. Coman, accepted to The 13th International Symposium of the Romanian Catalysis Society (RomCat Conference 2022), 22-24 June 2022, Baile Govora, Romania.

References

- [1] F.D. Schouwer, L. Claes, A. Vandekerckhove, J. Verduyck, D. E. De Vos, Protein-rich biomass waste as a resource for future bio-refineries: state of the art, challenges and opportunities, *ChemSusChem*, 12 (2019) 1272-1303
- [2] W. Deng, Y. Wang, S. Zhang, K. M. Gupta, M. J. Hulsey, H. Asakura, L. Liu, Y. Han, E. M. Karp, G. T. Beckham, P. J. Dyson, J. Jiang, T. Tanaka, Y. Wang, Catalytic amino acid production from biomass derived intermediates, *PNAS*, 115 (2018) 5093-5098
- [3] P. Serp, M. Corrias, P. Kalck, Carbon nanotubes and nanofibers in catalysis, *Appl. Catal. A: General*, 253 (2003) 337-358
- [4] Z. Zhong, B. Liu, L. Sun, J. Ding, J. Lin, K.L. Tan, Dispersing and coating of transition metals Co, Fe and Ni on carbon materials, *Chem. Phys. Lett.*, 362 (2002) 135-143
- [5] P. Chen, X. Wu, J. Lin, K.L. Tan, Synthesis of Cu Nanoparticles and Microsized Fibers by Using Carbon Nanotubes as a Template, *J. Phys. Chem*, 103, 22 (1999) 4559-4561

- [6] A. Kuznetsova, I. Popova, J.T. Yates, M.J. Bronikowski, C.B. Huffman, J. Liu, R.E. Smalley, H.H. Hwu, J.G. Chen, Oxygen-Containing Functional Groups on Single-Wall Carbon Nanotubes: NEXAFS and Vibrational Spectroscopic Studies, *J. Am. Chem. Soc.*, 123 (2001) 10699-10704
- [7] R. Giordano, P. Serp, P. Kalck, Y. Kihn, J. Schreiber, C. Marhic, J.L. Duvail, Preparation of Rhodium Catalysts Supported on Carbon Nanotubes by a Surface Mediated Organometallic Reaction, *Eur. J. Inorg. Chem.*, 2003, 610-617
- [8] S. Shylesh, V. Schunermann, W.R. Thiel, Magnetically Separable Nanocatalysts: Bridges between Homogeneous and Heterogeneous Catalysis, *Angew. Chem. Int. Ed.*, 49 (2010) 3428-3459
- [9] E. McCafferty, J.P. Wightman, Determination of the Concentration of Surface hydroxyl Groups on Metal Oxide Films by a Quantitative XPS Method, *Surf. Interface Anal.* 26 (1998) 549-564
- [10] I. Podolean, V. Kuncser, N. Gheorghe, D. Macovei, V.I. Parvulescu, S.M. Coman, Ru-based magnetic nanoparticles (MNP) for succinic acid synthesis from levulinic acid, *Green Chem.*, 15 (2013) 3077-3082
- [11] P. Sudarsanam, R. Zhong, S. Van den Bosch, S. M. Coman, V. I. Parvulescu, B. F. Sels, Functionalised heterogeneous catalysts for sustainable biomass valorisation, *Chem. Soc. Rev.*, 47 (2018) 8349-8402
- [12] C. H. Zhou, X. Xia, C. X. Lin, D. S. Tong, J. Beltramini, Catalytic conversion of lignocellulosic biomass to fine chemicals and fuels, *Chem. Soc. Rev.*, 40 (2011) 5588-5617
- [13] J. A. Geboers, S. Van de Vyver, R. Ooms, B. Op de Beeck, P. A. Jacobs, B. F. Sels, Chemocatalytic conversion of cellulose: opportunities, advances and pitfalls, *Catal. Sci. Technol.*, 1 (2011) 714-726
- [14] R. Abejón, A bibliometric Study of Scientific Publications regarding Hemicellulose Valorization during the 2000-2016 Period: Identification of Alternatives and Hot Topics, *Chem.Eng.*, 2 (2018) 1-31
- [15] S. M. Coman, M. Tudorache, V. I. Parvulescu, *An Introduction to Green Chemistry, Future Science*, 2013, Chapter 4: Green catalysis methods: catalysis for lignocellulosic biomass capitalization, 54-69
- [16] R. Rinaldi, F. Schüth, Design of solid catalysts for the conversion of biomass, *Energy. Environ. Sci.*, 2 (2009) 610-626
- [17] Y. Wang, S. Furukawa, S. Song, Q. He, H. Asakura, N. Yan, Catalytic production of alanine from waste glycerol, *Angew. Chem. Int. Ed.*, 59 (2020) 2289-2293

- [18] M. Dusselier, P. V. Wouwe, A. Dewaele, E. Makshina, B. F. Sels, Lactic acid as a platform chemical in the biobased economy: the role of chemocatalysis, *Energy Environ. Sci*, 6 (2013) 1415-1442
- [19] G. G. Millán, S. Hellsten, J. Llorca, R. Luque, H. Sixta, A. M. Balu, Recent Advances in the Catalytic Production of Platform Chemical from Holocellulosic Biomass, *ChemCatChem*, 11 (2019) 1-22
- [20] M. Janssen, Market potential of biorefinery products, *Publications. Lib. Chalmers. Se.*, 2012 , 1-10
- [21] M. D'Este, M. Alvarado-Morales, I. Angelidaki, Amino acids production focusing on fermentation technology – A review, *Biotechnol. Adv.*, 36 (2018) 14-25
- [22] E. Scott, F. Peter, J. Sanders, Biomass in the manufacture of industrial products – the use of proteins and amino acids, *Appl. Microbiol. Biotechnol.*, 75 (2007) 751-762
- [23] S. L. Miller, A Production of Amino Acids Under Possible Primitive Earth Conditions, *Science*, 117 (1953) 528-29
- [24] K. Harada, Asymmetric Synthesis of α -Amino-acids by the Strecker Synthesis, *Nature*, 4912 (1963) 1201
- [25] U. D. Wermuth, I. D. Jenkins, R. C. Bott, K. A. Byriel, G. Smith, Some Stereochemical Aspects of the Strecker Synthesis and the Bucherer-Bergs Reaction, *Aust. J. Chem.*, 57 (2004) 461-465
- [26] M. S. Gibson, R. W. Bradshaw, The Gabriel Synthesis of Primary Amines, *Angew. Chem.* 7 (1968) 919-929
- [27] A. Behr, T. Seidensticker, *Chemistry of Renewables : An introduction*, Springer, 2020, Chapter 14: Building Blocks of Life – Amino Acids, 251-263
- [28] S. Song, J. Qu, P. Han, M. J. Hulsey, G. Zhang, Y. Wang, S. Wang, D. Chen, J. Lu, N. Yan, Visible-light-driven amino acids production from biomass-based feedstocks over ultrathin CdS nanosheets, *Nat. Commun.*, 4899 (2020) 1-10
- [29] T. Fukushima, M. Yamauchi, Electrosynthesis of amino acids from biomass-derivable acids on titanium dioxide, *Chem. Comm.*, 55 (2019) 12721-12724
- [30] Z. Xie, B. Chen, F. Peng, M. Liu, H. Liu, G. Yang, B. Han, Highly Efficient Synthesis of Amino Acids by Amination of Bio-derived Hydroxy Acids with Ammonia over Ru Supported on N-doped Carbon Nanotube, *ChemSusChem*, 13 (2020) 5683-5689
- [31] A. Negoii, I.T. Trotus, O.M. Steiner, M. Tudorache, V. Kuncser, D. Macovei, V.I. Parvulescu, S.M. Coman, Direct Synthesis of Sorbitol and Glycerol from Cellulose over Ionic Ru/Magnetite Nanoparticles in the Absence of External Hydrogen, *ChemSusChem*, 6 (2013) 2090-2094

- [32] S.J. Greeg, K.S. Sing, Adsorption, Surface Area and Porosity, 1982, 957
- [33] Q.H. Yang, P.X. Hou, S. Bai, M.Z. Wang, H.M. Cheng, Adsorption and capillarity of nitrogen in aggregated multi-walled carbon nanotubes, Chem. Phys. Lett., 345 (2001) 18-24
- [34] M. Ran, Y. Liu, W. Chu, A. Borgna, Enhanced Conversion of Cellobiose to Sugar Alcohols by Controlled Dispersion of Ruthenium Nanoparticles Inside Carbon Nanotube Channels, Catal. Lett., 143 (2013) 1139-1144
- [35] J. Kang, W. Deng, Q. Zhang, Y. Wang, Ru particle size effect in Ru/CNT-catalyzed Fischer-Tropsch synthesis, J. Energy Chem., 22 (2013) 321-328
- [36] S. Thoka, C.M. Tsai, Z. Tong, A. Jena, F.M. Wang, C.C. Hsu, H. Chang, S.F. Hu, R.S. Liu, Comparative Study of Li-CO₂ and Na-CO₂ Batteries with Ru@CNT as a Cathode Catalyst, ACS Appl. Mater. Interfaces, 13 (2021) 480-490
- [37] F. Su, L. Lv, F.Y. Lee, T. Liu, A.I. Cooper, X.S. Zhao, Thermally Reduced Ruthenium Nanoparticles as a Highly Active Heterogeneous Catalyst for Hydrogenation of Monoaromatics, J. Am. Chem. Soc., 129 (2007) 14213-14223
- [38] Q. Zhang, L. Gao, J. Guo, Effects of calcination on the photocatalytic properties of nanosized TiO₂ powders prepared by TiCl₄ hydrolysis, Appl. Catal. B: Environ., 26 (2000) 207-215
- [39] W. Chen, Z. Fan, X. Pan, X. Bao, Effect of Confinement in Carbon Nanotubes on the Activity of Fischer-Tropsch Iron Catalyst, J. Am. Chem. Soc., 130 (2008) 9414-9419
- [40] R.M.M. Abbaslou, A. Tavassoli, J. Soltan, A.K. Dalai, Iron catalyst supported on carbon nanotubes for Fischer-Tropsch synthesis: Effect of catalytic site position, Appl. Catal. A: Gen., 367 (2009) 47-52
- [41] F. Lonyi, J. Valyon, On the interpretation of the NH₃-TPD patterns of H-ZSM-5 and H-mordenite, Micropor. Mesopor. Mat., 47 (2001) 293-301
- [42] N.R. Meshram, S.G. Hedge, S.B. Kulkarni, Active sites on ZSM-5 zeolites for toluene disproportionation, Zeolites, 6 (1986) 434-438
- [43] H. Igi, N. Katana, M. Niwa, in: M. M. J. Treacy, B. K. Marcus, M. E. Bisher, J. B. Higgins (Eds.), Proceedings of the 12th International Zeolite Conference, Materials Research Society, Warrendale, PA, 1999, 2643
- [44] C.F. Wang, X.L. Pan, X.H. Bao, Direct production of light olefins from syngas over a carbon nanotube confined iron catalyst, Chem. Phys. Lett., 55 (2010) 1117-1119

- [45] J.T. Miller, B.L. Meyers, F.S. Modica, G.S. Lane, M. Vaarkamp, D.C. Koningsberger, Hydrogen Temperature-Programmed Desorption (H_2 TPD) of Supported Platinum Catalysts, *J. Catal.*, 143 (1993) 395-408
- [46] G. Vidali, Potentials of physical adsorption, *Surf. Sci. Reports*, 12 (1991) 133-181
- [47] K. Masenelli-Varlot, E. McRae, N. Dupont-Pavlovsky, Comparative adsorption of simple molecules on carbon nanotubes. Dependence of the adsorption properties on the nanotube morphology, *Appl. Surf. Sci.*, 196 (2002) 209-215
- [48] T. Szilagyi, Fourier-Transform Infrared Study of Weak Adsorption of hydrogen on Pt/SiO₂, *J. Catal.*, 121 (1990) 223-227
- [49] J. Chen, M.A. Hamon, H. Hu, Y. Chen, A.M. Rao, P.C. Eklund, R.C. Haddon, Solution Properties of Single-Walled Carbon Nanotubes, *Science*, 282 (1998) 95-98
- [50] M.E. Lipinska, S.L.H. Rebelo, M.F.R. Pereira, J.A.N.F. Gomes, C. Freire, J.L. Figueiredo, New insights into the functionalization of multi-walled carbon nanotubes with aniline derivatives, *Carbon*, 50 (2012) 3280-3294
- [51] N. Yao, V. Lordi, S.X.C. Ma, Structure and oxidation patterns of carbon nanotubes, *J. Mater. Res.*, 13, 9 (1998) 2432-2437
- [52] B.C. Satishkumar, A. Govinndaraj, J. Mofokeng, G.N. Subbanna, C.N.R. Rao, Novel experiments with carbon nanotubes: opening, filling, closing and functionalizing nanotubes, *J. Phys. B: At. Mol. Opt. Phys.*, 29 (1996) 4925-4934
- [53] S. Aftab, S.T. Hussain, M. Siddique, H. Nawaz, Comprehensive study of trends in the functionalization of CNTs using same oxidizing acids in different conditions, *Der. Pharma. Chemica*, 2 (2010) 354-365
- [54] C.P. Poole, F.J. Owens, *Introduction in Nanotechnology*, Wiley, 2003, Chapter 5.4: Carbon Nanotubes, 114-124
- [55] G.W. Lee, J. Kim, J. Yoon, J.S. Bae, B.C. Shin, I.S. Kim, W. Oh, M. Ree, Structural characterization of carboxylated multi-walled carbon nanotubes, *Thin Solid Films*, 516 (2008) 5781-5784
- [56] M.L. Toebes, J.M.P. van Heeswijk, J.H. Bitter, A. Jos van Dillen, K.P. de Jong, The influence of oxidation on the texture and the number of oxygen-containing surface groups of carbon nanofibers, *Carbon*, 42 (2004) 307-315
- [57] G.S. Szymanski, T. Grzybek, H. Papp, Influence of nitrogen surface functionalities on the catalytic activity of activated carbon in low temperature SCR of NO_x with NH₃, *Catal.*, 90 (2004) 51-59

- [58] J. Zhang, H. Zou, Q. Qing, Y. Yang, Q. Li, Z. Liu, X. Guo, Z. Du, Effect of Chemical Oxidation on the Structure of Single-Walled Carbon Nanotubes, *J. Phys. Chem. B*, 107 (2003) 3712-3718
- [59] M.R. loos, L.A.F. Coelho, S.H. Pezzin, S.C. Amico, Effect of Carbon Nanotubes Addition on the Mechanical and Thermal Properties of Epoxy Matrices, *Mater. Res.*, 11 (2008) 347-352
- [60] V. Datsyuk, M. Kalyva, K. Papagelis, J. Pathenios, D. Tasis, A. Siokou, I. Kallitsis, C. Galiotis, Chemical oxidation of multiwalled carbon nanotubes, *Carbon*, 46 (2008) 833-840
- [61] S.A. Chernyak, A.S. Ivanov, K.I. Maslakov, A.V. Egorov, Z. Shen, S.S. Savilov, V.V. Lunin, Oxidation, defunctionalisation and catalyst life cycle of carbon nanotubes: a Raman spectroscopy view, *Phys. Chem. Chem. Phys.*, 19 (2017), 2276-2285
- [62] M. Yamaura, R.L. Camilo, L.C. Sampaio, M.A. Macedo, M. Nakamura, H.E. Toma, Preparation and characterization of (3-aminopropyl) triethoxysilane-coated magnetite nanoparticles, *J. Magn. Mater.*, 279 (2004) 210-217
- [63] M.P. Morales, S.V. Verdaguer, M.I. Montero, C.J. Serna, Surface and Internal Spin Canting in γ -Fe₂O₃ Nanoparticles, *Chem. Mater.*, 11 (1999) 3058-3064
- [64] M. Ma, Y. Zhang, W. Yu, H. Shen, H. Zhang, N. Gu, Preparation and characterization of magnetite nanoparticles coated by amino silane, *Colloids and Surfaces A: Physicochem. Eng. Aspects*, 212 (2003) 219-226
- [65] L.D. White, C.P. Tripp, Reaction of (3-aminopropyl)dimethylethoxyxilane with Amine Catalysts on Silica Surfaces, *J. Colloid Interface Sci.*, 232 (2000) 400-407
- [66] S. Tian, Y. Jiao, Z. Gao, Y. Xu, L. Fu, H. Fu, W. Zhou, C. Hu, G. Liu, M. Wang, D. Ma, Catalytic Amination of Polylactic acid to Alanine, *J. Am. Chem. Soc.*, 143 (2021) 16358-16363
- [67] D. Ruiz, A. Aho, T. Saloranta, K. Eranen, J. Warna, R. Leino, D. Y. Murzin, Direct amination of dodecanol with NH₃ over heterogeneous catalysts. Catalyst screening and kinetic modelling, *Chem. Eng. J.*, 307 (2017) 739-749
- [68] D. Pinggen, C. Muller, D. Vogt, Direct Amination of Secondary Alcohols Using Ammonia, *Angew. Chem. Int. Ed.*, 49 (2010) 8130-8133

Annex 1. Thermogravimetric analysis of CNT carrier

In order to establish the optimum temperature for the calcination of samples 1%Ru/CNT, 3%Ru/CNT and 5%Ru/CNT the TG analysis of CNT was previously performed. According to the TGA profile in the air atmosphere (Figure 1), the mass loss of the CNT starts slowly in the temperature range 440-460 °C. However, after 500°C the CNT begins to be fast oxidized (a process possible catalysed by the transition metals remained into the material from the synthesis of CNT) and the mass of the sample quickly declines with the increase of temperature. Bearing in mind this, the calcination step of the Ru-based catalysts was performed at 350°C in order to avoid the decomposition of the support.

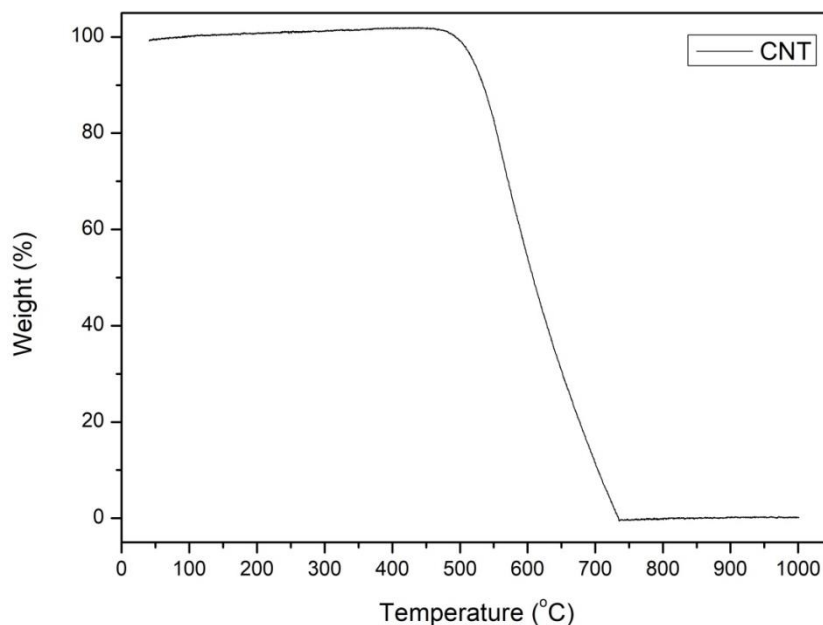


Figure 1. TGA profile in air atmosphere for as-received CNT

Annex 2. Detailed oxidation procedures for the synthesis of CNT_{ox} samples.

CNT_{ox}-1: 2 g of the agglomerated MWCNTSs were dispersed in 200 mL nitric acid (65 wt%) in a 500 mL round bottom flask. In order to minimize the tubes damage, a low power sonicating bath and a relatively low acid exposure time were used. Therefore, the mixture was sonicated in a conventional ultrasonic bath for 3 h, promoting CNT disentanglement within the acid solution. In order to neutralize the strong acidity NaOH solution was added in the slurry. Then, the slurry was filtered and thoroughly washed with distilled water, until a neutral pH. Finally, the slurry was filtered using PTFE membrane filter with 0.45 µm pore sized and then dried at 80°C for 24 h.

CNT_{ox}-2: 1 g of MWCNTs were dispersed in 200 mL nitric acid (65 wt%) in a 500 mL round bottom flask. The mixture was sonicated for 3 h, promoting carbon nanotubes disentanglement within the acid solution. Next, the reaction flask equipped with reflux condenser, magnetic stirred and thermometer was mounted in the preheated oil bath and the mixture was refluxed for 1 h at 80°C and another hour at 100°C. After cooling at r.t., to the resulted slurry water was added and then filtered. The resulted solid was washed up to neutral pH and dried at 80°C for 24 h.

CNT_{ox}-3: 1 g of MWCNTs were dispersed in 200 mL of fresh nitric acid (65 wt%) in a 500 mL round bottom flask. The mixture was sonicated for 3 h in order to promote the disentanglement of CNTs within the acid solution. Next, the round bottom flask equipped with reflux condenser, magnetic stirring and thermometer was mounted in the preheated oil bath. The mixture was refluxed for 2 h at 80°C. After cooling at r.t., to the resulted slurry water was added and then filtered. The resulted solid was washed up to neutral pH and dried at 80°C for 24 h.

CNT_{ox}-4: 0.3 g of the agglomerated MWCNTs were mixed with 70 mL mixture of HNO₃ (65 wt%) and H₂SO₄ 8M by mechanically stirring on a hot plate, for 15 min at 60°C and then sonicated for 2 h. Then, the slurry was filtered and thoroughly washed with distilled water, until a neutral pH. The resulted solid was dried at 80°C for 24 h.

CNT_{ox}-5: 0.3 g of the agglomerated MWCNTs were mixed with 70 mL mixture of HNO₃ (65 wt%) and H₂SO₄ 3M by mechanically stirring on a hot plate for 15 min at 60°C, and then sonicated for 2 h. The solid was separated, washed with distilled water, re-immersed in H₂O₂ (30% v/v) and the

procedure was identically repeated. Then, the slurry was thoroughly washed with distilled water, until a neutral pH and filtered. The resulted solid was dried at 80°C for 24 h.

CNT_{ox-6}: 0.3 g of the agglomerated MWCNTs were mixed with 7.5 mL mixture of HNO₃ (65 wt%) by mechanically stirring in a hot plate for 15 min at 60°C, and sonicated for 3 h. The solid was separated, washed with distilled water, re-immersed in H₂O₂ (30% v/v) and the procedure was identically repeated. The subsequent treatment with H₂O₂ was given in order to complete the oxidative process started by nitric acid, but in a gentler manner. Then, the slurry was thoroughly washed with distilled water, until a neutral pH and filtered. The resulted solid was dried at 80°C for 24 h.

CNT_{ox-7}: 0.1 g of the agglomerated CNTs were mixed with 5 mL hydrogen peroxide (30%) by mechanically stirring in a hot plate at 65°C for 72h. 2.5 mL of hydrogen peroxide was added at each 24h in order to keep a constant volume. After oxidizing the nanotubes the slurry was thoroughly washed with distilled water until a neutral pH and filtered. The resulting solid was dried at 80°C for 24 h.

CNT_{ox-8}: 0.1 g of the agglomerated CNTs were dispersed in 10 mL nitric acid (65 wt%) in a 50 mL round bottom flask. The mixture was sonicated for 3 h in a conventional ultrasonic bath Bandelin SONOREX™ SUPER with build-in heating, RK 103H, promoting CNT disentanglement within the acid solution. Then, the slurry was filtered and thoroughly washed with distilled water until a neutral pH. Recovered filter was immersed into distilled water and ultrasonated until the carbon nanotubes redispersion (2 min). The redispersed carbon nanotubes were then centrifuged for 5 min at 4000 rpm. Remained nanotubes into the liquid phase were collected by adding 100 mL dichloromethane (CH₂Cl₂) followed by filtration, washing with additional amounts of CH₂Cl₂ and ultrasonication for 3h. The obtained solution was the subject of a slow evaporation (r.t. for 24 h). Finally, the obtained solid was completely dried at 80°C for 24 h.

13TH INTERNATIONAL SYMPOSIUM
OF THE ROMANIAN CATALYSIS SOCIETY

THIS CERTIFIES THAT PHD Stud.


Maria Alexandra Badea

University of Bucharest

attended the RomCat2022 conference which was held in
Băile Govora, Romania on June 22-24, 2022

President of the Romanian Catalysis Society

Prof. Vasile Parvulescu


S SOCIETATEA
C DE CATALIZA
R DIN ROMANIA


22-24 June 2022
Baile Govora, Romania

Norwegian University of Science and Technology

N-7491 Trondheim, Norway

Telephone: +47 73596256

E-mail: Elisabeth.E.Jacobsen@ntnu.no

Department of Chemistry



Trondheim, June 12th 2022

To whom it may concern

I hereby confirm that master candidate Mara Badea, University of Bucharest, Romania, can use the analysis results of her Ruthenium Carbon Nanotube (RuCNT) catalyst samples performed by Scanning Transmission Electron Microscopy (STEM) at NTNU Nanolab.

The analyses were performed during her Short Term Scientific Mission stay at Department of Chemistry, Norwegian University of Science and Technology, under my supervision, during September 1-30- 2021.

The work was funded by The Education, Scholarship, Apprenticeships and Youth Entrepreneurship Programme -EEA Grants 2014-2021, Project No. 18-Cop-0041.

Best regards,

Elisabeth E. Jacobsen

Elisabeth E. Jacobsen

Associate professor, PhD



UNIVERSITATEA
DIN BUCUREȘTI
— VIRTUTE ET SAPIENTIA

FACULTY OF CHEMISTRY

DISSERTATION THESIS

Master: CHEMISTRY OF ADVANCED MATERIALS

Student: FTODIEV ANDREEA-IULIANA

Coordinator: Conf. Dr. MĂDĂLINA SĂNDULESCU



**UNIVERSITATEA
DIN BUCUREȘTI**
VIRTUTE ET SAPIENTIA

FACULTY OF CHEMISTRY

**DEPARTMENT OF ORGANIC CHEMISTRY, BIOCHEMISTRY
AND CATALYSIS**

Valorization of plastic polymers leading to value-added products

Master: CHEMISTRY OF ADVANCED MATERIALS

Student: FTODIEV ANDREEA-IULIANA

Coordinator: Conf. Dr. MĂDĂLINA SĂNDULESCU

Summary

Introduction.....	5
Theoretical part.....	6
1. Synthetic plastics – general consideration.....	6
2. Types of synthetic plastics.....	6
2.1 Polystyrene (PS).....	7
2.2 Polypropylene (PP).....	8
2.3 Polyethylene (PE).....	9
2.4 Polyurethane (PUR).....	10
2.5 Polyvinyl chloride (PVC).....	11
2.6 Polyethylene terephthalate (PET).....	11
3. Plastic waste.....	12
3.1 Methods of disposing plastic waste.....	12
3.2. Methods of disposing PET wastes.....	13
3.2.1 Mechanical recycling.....	13
3.2.2 Hydrolysis.....	14
3.2.3 Glycolysis.....	15
3.2.4 Pyrolysis.....	16
3.2.5 Alcoholysis.....	16
4. Additional steps for the PET degradation/decomposition.....	17
4.1 Pre-treatment and post-treatment of plastic waste.....	17
4.2 Analytical methods for monitorization of PET degradation.....	18
5. Derivatization of PET using biocatalytic methods.....	18
5.1 Surface modification of poly(ethylene terephthalate) (PET) fibers by a cutinase from <i>Fusarium oxysporum</i>	18
5.2 Production of heterologous cutinases by <i>E. coli</i> and improved enzyme formulation for application on plastic degradation.....	19
5.3 Rapid Hydrolyse of of Poly(ethylene terephthalate) using a hydrolase from <i>T. Fusca</i>	19

5.4 Degradation of Poly(ethylene terephthalate) Catalyzed by Metal-free 2 Choline-Based Ionic Liquids.....	20
6. The aim of this thesis.....	20
Experimental part.....	22
1. Substances and methods.....	22
1.1 Substances, reagents	22
1.2 Method for grinding/chopping PET.....	23
1.3 Methods of sample pre-treatment.....	23
1.4 Methods of sample preparation.....	24
1.4.1 Sample preparation for BHET hydrolysis.....	24
1.4.2 Sample preparation for PET degradation.....	24
1.5 Methods for modifying PET surface.....	24
1.5.1 Reaction of PET with DMC.....	24
1.5.2 Reaction of PET/ BHET with thiols.....	24
1.5.3 Reaction of PET/ BHET with aniline.....	24
1.6 Method of pre-treatment before analysis.....	25
1.7 Method of sample PET characterization.....	25
1.7.1 FT-IR.....	25
1.7.2 Dinamic light scattering.....	25
1.8 Method of sample analysis after reaction.....	25
1.9 Method for the preparation of the enzyme entrapment.....	26
2. Results and discussions.....	26
2.1 The PET degradation.....	26
2.2 BHET system.....	28
2.3 Choosing the pre-treatment approach.....	30
2.4 Reactions of BHET with thiols.....	31
2.5 Reaction of PET with thiols.....	33
2.6 Reaction of BHET with aniline.....	37
2.7 Reaction of PET with aniline.....	38
2.8 Reaction of PET with DMC.....	40
2.9 DLS.....	43

2.10 Enzyme entrapment.....	43
3.Conclusions.....	50
References.....	51

Introduction

The production of plastic dates back to 1950' and since then they have become one of vital materials used in everyday life applications. The variety of plastics available and the cheap production of those are the main reasons of the grow of plastic industry [1]. Although the plastic industry consumed 6% of world oil production in 2014, from the 26% used in packaging applications, only 5% was recycled causing a huge economic loss. By 2050 the plastic industry is estimated to consume 20% of the world oil production [1].

The plastic wastes accumulation has been growing in the recent years and it became one of the most severe environmental and social issue [2]. It is estimated that between 2010 and 2025 100 MT of plastic waste will enter in the ocean [1]. It is predicted that by 2025 for each three tons of fish, there will be one tone of plastic in the ocean [3]. This will cause widespread contamination of marine ecosystems since the microplastics (smaller fragments of plastics which was degraded) can be ingested by zooplankton and phytoplankton which will have a negative impact on their health. Since approximatevely 70% of the world's oxygen is produced from the photosynthesizing of marine plants, the plastic will have a huge impact in climate change and global warming [1].

Since the plastics with polymer structures are especially designed to mentain optimal material properties, most of the plastics can not be attacked by microorganisms. The evolution could not develop enzymes to degrade these man made materials and therefore usually the plastics do not rot in the biological environment [4].

With the discovery of Tokiwa and Suzuki in 1977 of some lipases that are able to attack the ester bonds in some aliphatic polyesters and can depolymerize such materials, more attempts were made to design similar enzymes [4]. Also with the increasing problem of plastic waste, the pursuing of making biodegradable plastics started [4].

Theoretical part

1. Synthetic plastics – general consideration

The term "plastics" generally refers to synthetic polymers that are omnipresent in modern society. Plastics are that common in our everyday life, that it is estimated each person consumes 50 kg per year in European Union and 68 kg per year in the United States [5].

Plastics find applications in a different domains such as packaging, biomedical devices, clothing and sport equipment, electronic components [5].

Unfortunately, the main problems of them are that they are obtained from the nonrenewable sources of petroleum/natural gas and the deposition rate accelerated past the rate of production [5][6].

The global production and consumption of plastics increased at an alarming rate over the last few decades accumulating persistent in the landfills and the environment, only 9% of plastic waste being successfully recycled in 2015 in the United States [5].

2. Types of synthetic plastics

Synthetic plastics like polystyrenes (PS), polyethylene (PE), polyurethane (PUR), polypropylene (PP), polyvinyl chloride (PVC) and polyethylene terephthalate (PET) have a very important role to almost every aspect of our lives [2].

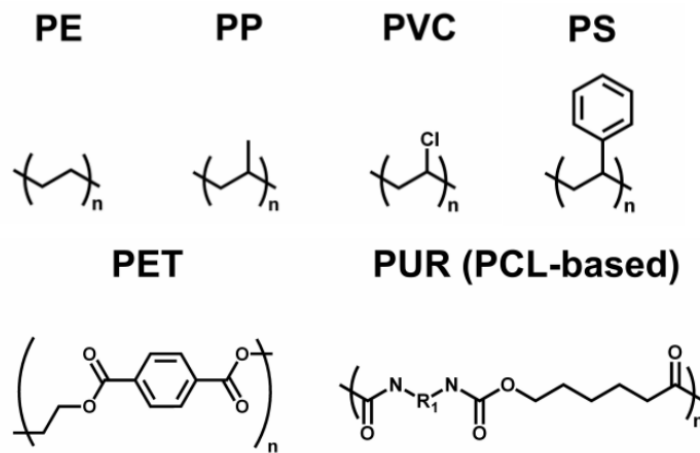


Figure 1. The main types of synthetic plastics [2]

2.1 Polystyrene (PS)

Polystyrene is the simplest aromatic hydrocarbon polymer based on the monomer styrene having a hard texture, high tensile strength and excellent transparency [7][8]. Since it can be monoextruded, coextruded with other types of plastics, injection molded or foamed, it can generate a large range of products [7]. Polystyrene is generally used in the food industry having applications like protective packaging (for eggs, meat, fish etc.) and disposable plastic silverware (lids, plates, bottles, cups etc.) [7][8]. It is one of the most widely used plastics, mostly because it is an inexpensive resin per unit weight [9].

PS is a clear, odorless, hard, tasteless, colorless material with outstanding properties including thermal stability, mechanical strength, relatively low density and low production cost. The particular reason for its highly stable structure and resistance to decomposition is its structure of phenyl groups and single C-C bonds [10].

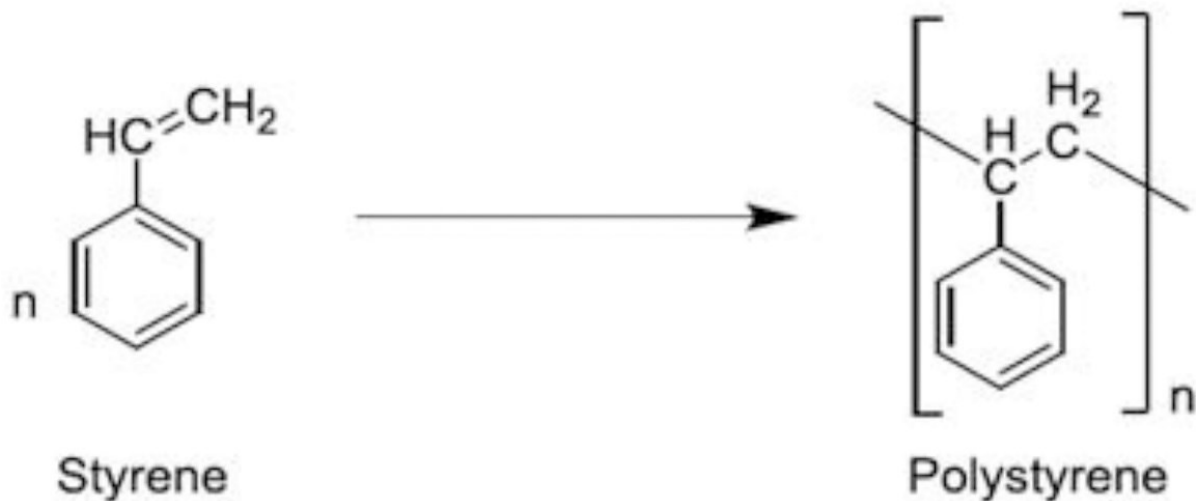


Figure 2. Polymerization of styrene to polystyrene [10]

Naturally polystyrene is transparent, but it can be coloured with different colourants. Being a thermoplastic polymer, polystyrene is in solid state at room temperature, but above 100°C it starts to flow [11].

Polystyrene is rather chemically inert being waterproof and resistant to many acids and bases, this being one of the reasons of its popularity in fabricating many objects of commerce. But it can be easily attacked by organic solvents like acetone, aromatic hydrocarbon solvents and chlorinated solvents [11].

Polystyrene can be used in either solid and expanded forms, both of which can be recycled. Solid PS such as coffee cups, trays etc. can be recycled and transformed into office equipments, videocassette cases etc [12].

PS is manufactured in three main commercial forms: expanded polystyrene (EPS), general purpose polystyrene (GPPS) and high-impact polystyrene (HIPS). There is a fourth type of fabricated PS with the name of syndiotactic polystyrene (SPS), but it has a relatively minor grade [10].

2.2 Polypropylene (PP)

Polypropylene is one of the most popular plastics because of its low density and excellent chemical resistance. It can be processed through many converting methods including injection molding and extrusion [13].

Polypropylene is an olefin polymer, thermoplastic with a low melting poing. PP fiber is the fourth largest volume artificial fiber, the 2014 worldwide production value being US\$56.73 million. PP's major use is in industrial applications like geotextiles, ropes, carpets, surgical sutures and sanitary products [14].

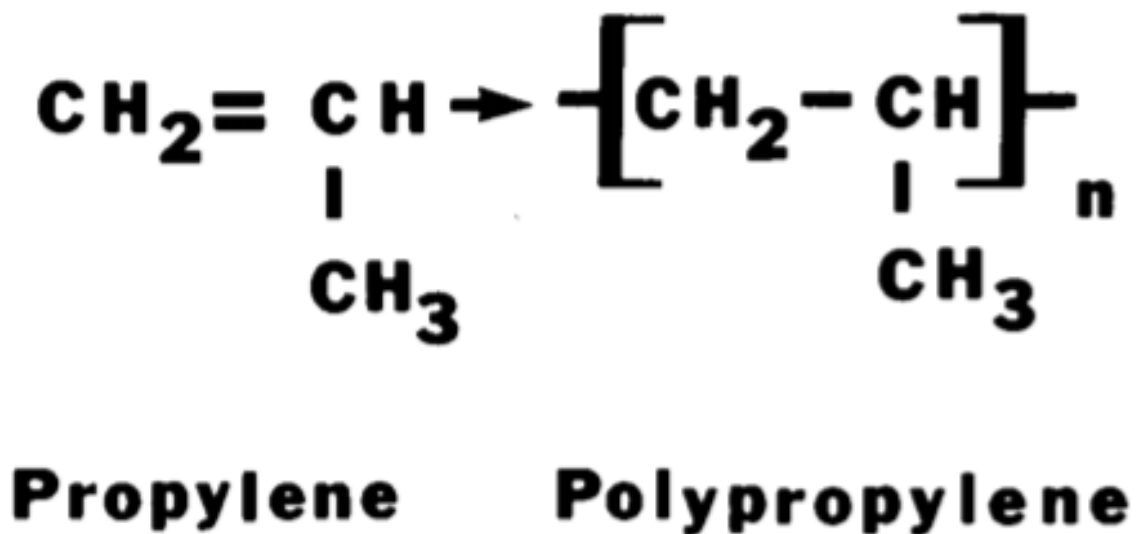


Figure 3. Polymerization of propylene to polypropylene [15]

Polypropylene is a transparent, free-color material and it is produced through a process of monomer connection called addition polymerization [13]. PS is formed from propylene, a liquefiable hydrocarbon gas [15].

Three stereoisomeric forms of PP exist: isotactic, syndiotactic and atactic. Isotactic PP has methyl groups on one side of the polymer chain, syndiotactic PP has methyl groups that alternate along the chain and atactic PP has methyl groups arranged randomly. Between all three types of PP, only the isotactic one has commercial importance [15].

Its high temperature resistance makes polypropylene suitable for items such as funnels, bottles, trays, pails and jars that have to be sterilized frequently [13]. The melting point of PP is around 165°C, but this can vary with the degree of chemical and steric purity [15].

2.3 Polyethylene (PE)

Polyethylene is the most common plastic in use today having the simplest molecular structure of any polymer [16][17]. It is primarily used for packaging and it is the largest tonnage plastic material [16][17]. Polyethylene represents 34% of the total plastic produced annually with over 100 million tonnes [16].

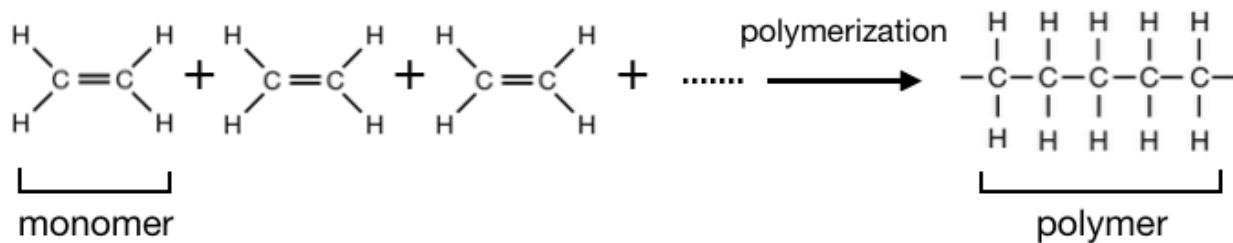


Figure 4. Polymerization of ethylene to polyethylene [17]

PE is an inert material and it is very difficult to degrade in the environment. In a study made with a polyethylene sheet, only after 12-32 years it showed partial degradation and negligible weight loss being kept in a moist soil. The particular reason for this circumstance is the water insolubility, the hydrophobicity due to high molecular weight, presence of linear backbone of carbon atoms and its degree of crystallinity [17].

PE is a mixture of similar polymers of ethylene. It can be low density or high density, depending on the pressure and temperature applied when manufactured: the low density PE (LDPE) is prepared at high pressure and high temperature and high density PE (HDPE) is prepared at low pressure and low temperature [16].

LDPE is inert at room temperature, but it can be attacked by strong oxidizing agents and some solvents. LDPE is characterized by tear strength, tensile strength, opacity, rigidity and

chemical resistance due to its degree of crystallinity within the range of 50-60%. It is generally used coating on paper, textiles, mulching agricultural fields and constructing polyhouse [17].

HDPE is produced during a catalytic process and has little branching. It provides stronger intermolecular forces and greater tensile strength than LDPE. It is widely used industrial and day-to-day applications like milk jugs, carry bags, margarine tubs, detergent bottles, water pipes etc. due to its opacity, hardness and durability at higher temperatures [17].

2.4 Polyurethane (PUR)

Polyurethane is a very versatile polymer having the structure property relationship of diisocyanates and polyols providing ample customization to the manufacture [18].

Polyurethane is formed by the reaction between di/poly isocyanate and a diol or polyol, creating repeated urethane linkage in the presence of chain extender and other additives [18].

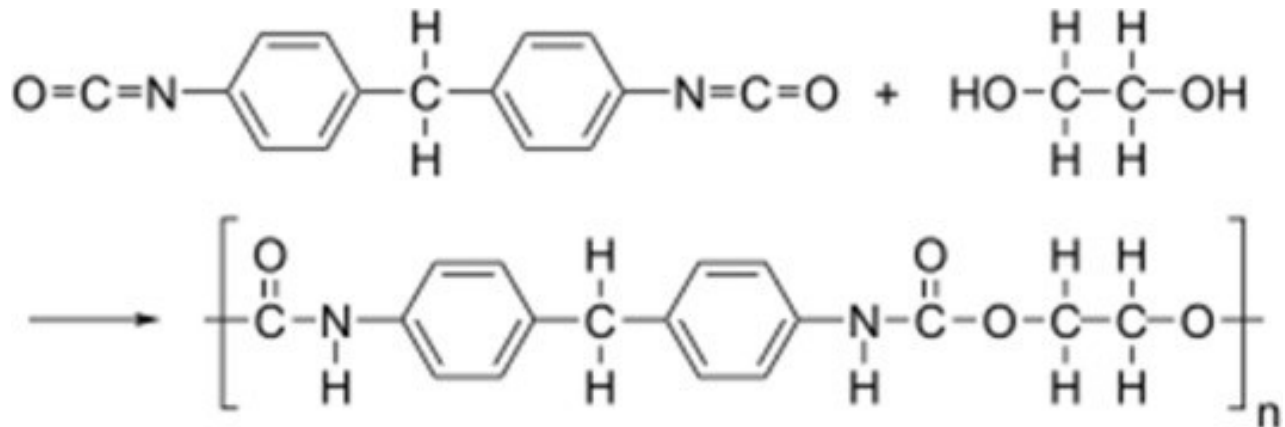


Figure 5. Polyurethane formation [18]

The properties of polyurethane are diverse, these can range from soft touch coatings to very hard rigid material used in construction. PUR has attracted not only the scientific community, but also the industries due to its properties and ease of tailoring [18].

PUR has many different applications in different domains. Due to the advances in different techniques of modern times, manufactures are able to produce this polymer in a wide range of polyurethane apparel. Some applications of PUR in this department are: manmade skin and leathers, sports clothes, and a variety of accessories [19].

PUR find other application in major appliances like rigid foams for refrigerator and freezer thermal insulation systems, in household materials such as flexible foam padding cushions, floors, in modern material science like composite woods [19].

2.5 Polyvinyl chloride (PVC)

Polyvinyl chloride is a widely used polymer and it is one of the most valuable products of the chemical industry. PVC is produced from its polymer, vinyl chloride, and is a hard plastic that it can be made softer with the help of plasticizers. Over 50% of PVC manufactured is used in construction being inexpensive, hard and easy to assemble [20].

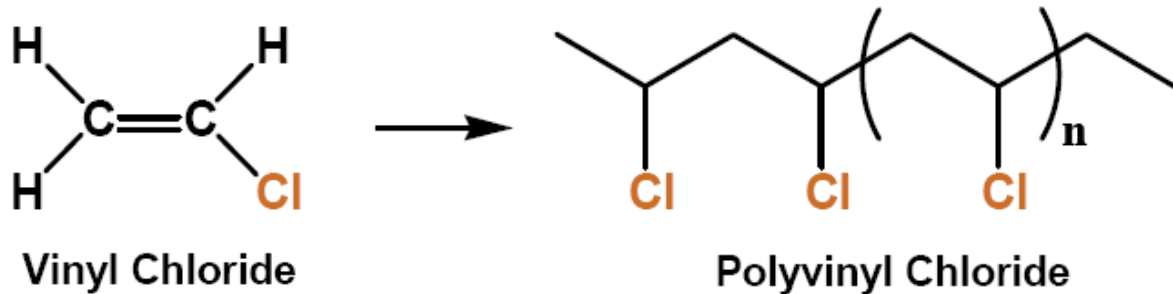


Figure 6. Polymerization of vinyl chloride to polyvinyl chloride [21]

PVC with 57% of mass by chlorine is an ‘infrastructure thermoplastic’ material. Being thermoplastic, PVC softens when heated and hardens when it cools. Because of this property, PVC can be subjected to different techniques: extrusion, calendaring, injection and blow molding [22].

Due to its low density, PVC provides low material cost on a volume basis [22]. Although appearing to be an ideal building material, replacing in recent years the traditional building materials as wood and concrete, concerns have been raised about the environmental and human health costs of PVC [20].

2.6 Polyethylene terephthalate (PET)

Polyethylene terephthalate, commonly referred as polyester or PET, is a semiaromatic polymer synthesized from ethylene glycol and terephthalic acid [23].

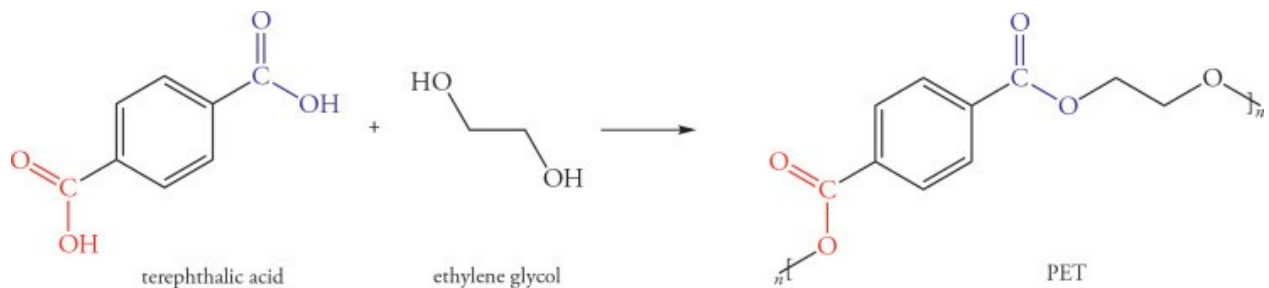


Figure 7. Polymerization of terephthalic acid and ethylene glycol to PET [24]

PET is used in industrial applications due to its excellent moisture and fair oxygen barrier characteristics having a glass transition temperature of around 67-81°C and a melting point of 260°C [23].

The half life of the polymer at 37°C in a normal saline environment is of 700 years [25]. Due to its very important property to be colourless and transparent (if amorphous) or translucent (if semi-crystalline), the consumers can see the content from the bottles [26].

PET is lightweight (compared to a 750 ml wine bottle, a 1L PET bottle weighs 335 less grams), thermoplastics, semi-rigid to rigid, robust and mechanically resistant to impact. It is extremely inert compared with other plastics and it does not contain plasticizers (in the case of PVC the use of plasticizers is essential), but it can be blended with other polymers to improve certain properties [26].

Because all of these properties, PET is the third most commonly used plastic in the packaging industry with a continuous growing demand [26].

3. Plastic waste

3.1 Methods of disposing plastic waste

The current methods for disposing of plastic wastes mainly include landfilling, producing the same or similar product (primary recycling), mechanical recycling (secondary recycling), chemical recycling (tertiary recycling) and incineration (quaternary recycling) [1][2]. Landfilling is the major method due to its low cost and operability, especially in the developing countries [2].

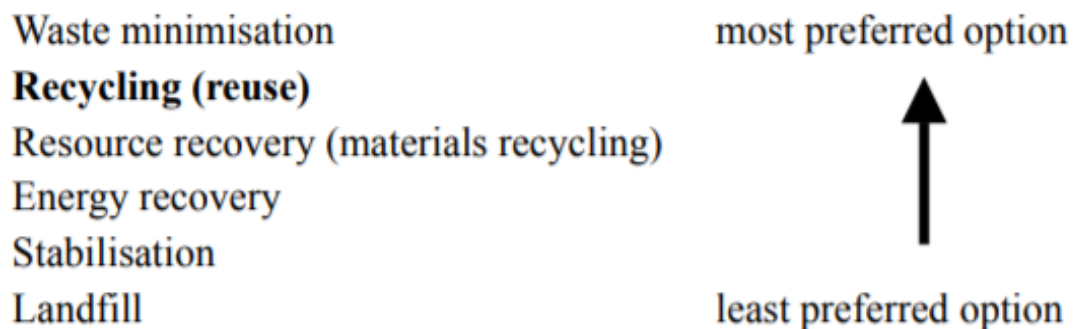


Figure 8. Generally accepted European Community Strategy for dealing with waste [27]

Primary recycling refers to either reusing the material or recycling the plastic to produce products with the original structure. It is a closed loop recycling method and can be only used on high quality plastic [1].

Secondary recycling indicates the conversion of waste plastic into a less demanding product via mechanical transformations. Mechanical recycling has various advantages over chemical recycling (tertiary recycling): lower global warming potential, less acidification and eutrophication, more renewable energy use and last, but not least, a lower processing cost [1].

Tertiary recycling describes the chemical reaction used to depolymerise and degrade plastic waste into monomers or into other useful materials. There are many chemical recycling methods and these depend on the polymer type and on techniques used, each of them having advantages and disadvantages. Although mechanical recycling presents some advantages over chemical recycling, the tertiary recycling has also some advantages over the secondary one: the potential of producing circular polymer since recovered monomers can be repolymerised and the opportunity to achieve new materials with added value [1].

Quaternary recycling indicates the energy that is recovered via incineration of low grade plastic waste. When plastics are burned, they result in heat energy that is used to generate steam and electricity. The quaternary recycling should only be used as a last solution since the imbedded energy of the polymers molecular structure is lost and harmful chemicals and dioxins are released into the atmosphere [1].

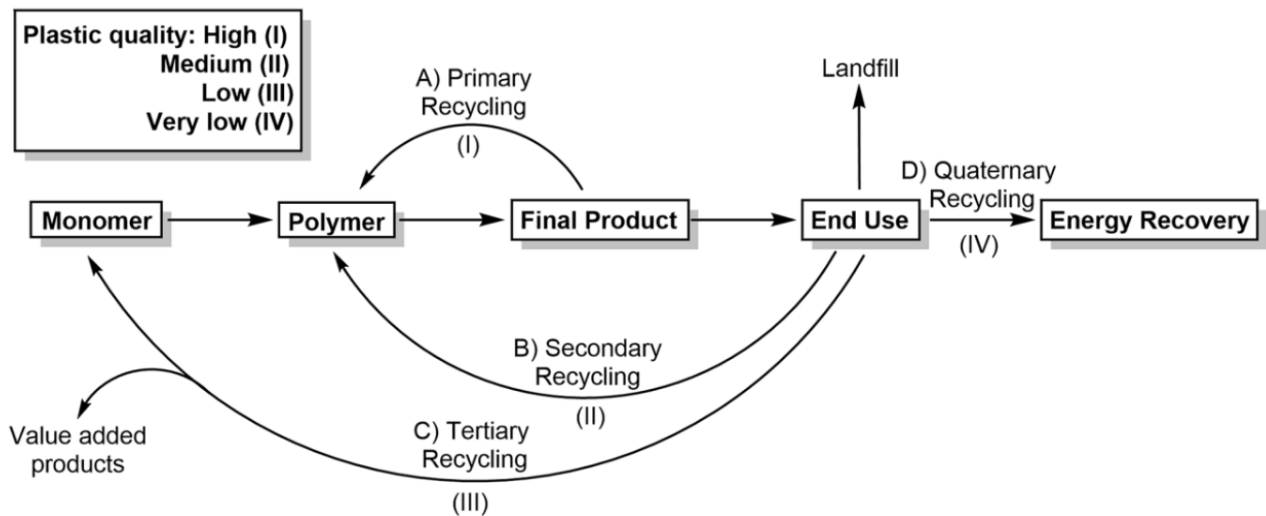


Figure 9. Different plastic waste treatment options and associated plastic quality [1]

3.2. Methods of disposing PET wastes

3.2.1 Mechanical recycling

Because of the large amount of PET circulating, its mechanical recycling is well established and the recycled PET has applications in a variety of domains. In the process of mechanical recycling, PET usually suffers the process of yellowing discoloration, a nontoxic procedure. Around 72% of recycled PET found its use in fibre applications. If the PET becomes so low grade that it can not be mechanically recycled anymore, then chemical recycling should be used to recover its monomers [1].

PET can be subjected to mechanical recycled via melt extrusion up to 40 cycles without a significant change to be observed in its mechanical properties. After this, the melting temperature is dropping due to recuded crystallinity of the polymer. PET is highly stable to any type of solvolysis [1].

3.2.2 Hydrolysis

PET can be hydrolysed into its monomers terephthalic acid (TA) and ethylene glycol (EG) and the conditions are either acidic, alkaline or neutral. Hydrolysis has some disadvantages like high temperature and pressure requirements in addition to long reaction times [1].

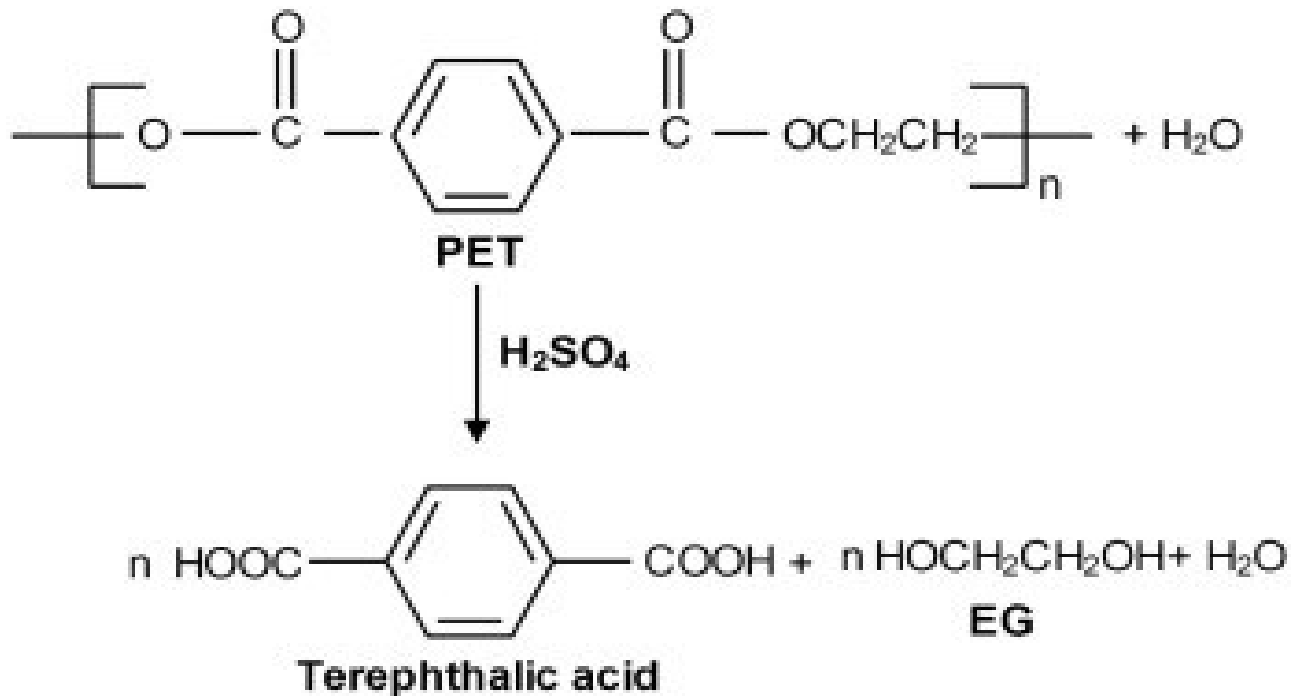


Figure 10. Hydrolysis of PET [28]

Acidic hydrolysis takes place using concentrated acids like phosphoric, nitric or sulfuric acid. The yields obtained from this methods are high, but the main disadvantage is that the

separation of EG from the highly acid solution is difficult. Additionally, the high amount of acid needed to industrialize this method poses economic and environmental problems [29].

Alkaline hydrolysis is typically carried out in aqueous solutions of 4–20 wt% NaOH. This process has relatively good yields, but the longer reaction times and high temperatures are some drawbacks of the method [29].

Neutral hydrolysis uses also high temperature and elevated pressures. Without the need for stoichiometric acid or base, this type of hydrolysis would be the ideal one, but this process usually produces low purity monomers and has a slow rate of reaction [29].

3.2.3 Glycolysis

Glycolysis is the most used chemical recycling method for PET and it consists in the insertion of a glycol into the PET chains. The glycol breaks the ester linkages and it replaces them with hydroxyl terminals for producing Bis 2-Hydroxyethyl Terephthalate (BHET), oligomers and dimers. For obtaining mostly BHET with a very little amount of oligomers the optimum parameters for glycolysis are: a pressure of 0.1–0.6 Mpa, a temperature range of 180–240 °C, a transesterification catalyst, between 0.5 and 8 h for completion and a high EG/PET ratio [1].

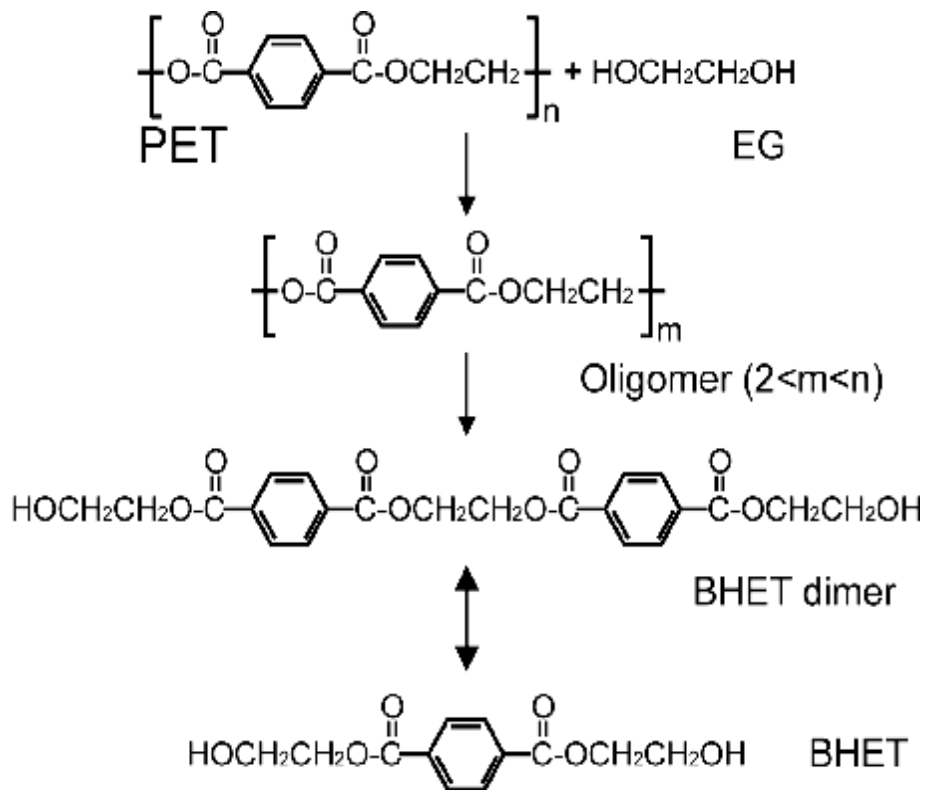


Figure 11. Glycolysis of PET [30]

Glycolysis takes place using a very large variety of glycols such as EG, diethylene glycol (DEG), propylene glycol (PG) and dipropylene glycol. Usually, the catalysts used are metal acetates. The zinc acetate is considered the best among them. Although, these catalysts are often used in industry, they have some disadvantages like: difficulty separating the catalyst from the products, side reactions and product impurities. For more recyclable and simpler purification, ionic liquid catalyst can replace the usual ones [1].

3.2.4 Pyrolysis

There are two major types of pyrolysis of PET: thermal pyrolysis and catalytic pyrolysis [29]. The thermal pyrolysis of PET takes place at high pressure and temperature leading to the formation of a solid char and a volatile fraction. Then, the fraction can also be separated into a condensable hydrocarbon oil and a noncondensable gas. The hydrocarbon oil is composed of a mixture of organic compounds like toluene, styrene, ethylbenzene etc [1].

Catalytic pyrolysis utilizes a catalyst for reducing the temperature and reaction time and thus improving the selectivity and economic viability [29]. Although catalytic pyrolysis has a narrower distribution of hydrocarbon products, it presents a higher market value. Catalysts like silica alumina, ZSM-5 and zeolites are usually used and it was proven that some of them achieved a higher conversion rate of valuable aromatic compounds in the oil compared with the thermal pyrolysis [1].

3.2.5 Alcoholysis

PET can be depolymerised via methanolysis resulting a stoichiometric mixture of its monomers N,N-Dimethyltryptamine (DMT) and ethylene glycol (EG). Methanolysis is carried out at high temperatures and pressures using divalent metal catalysts. The methanolysis also generates several byproducts like Bis(2-Hydroxyethyl) terephthalate (BHET), 2-hydroxyethyl methyl terephthalate (MHET), oligomers, and dimers of DMT and BHET [1].

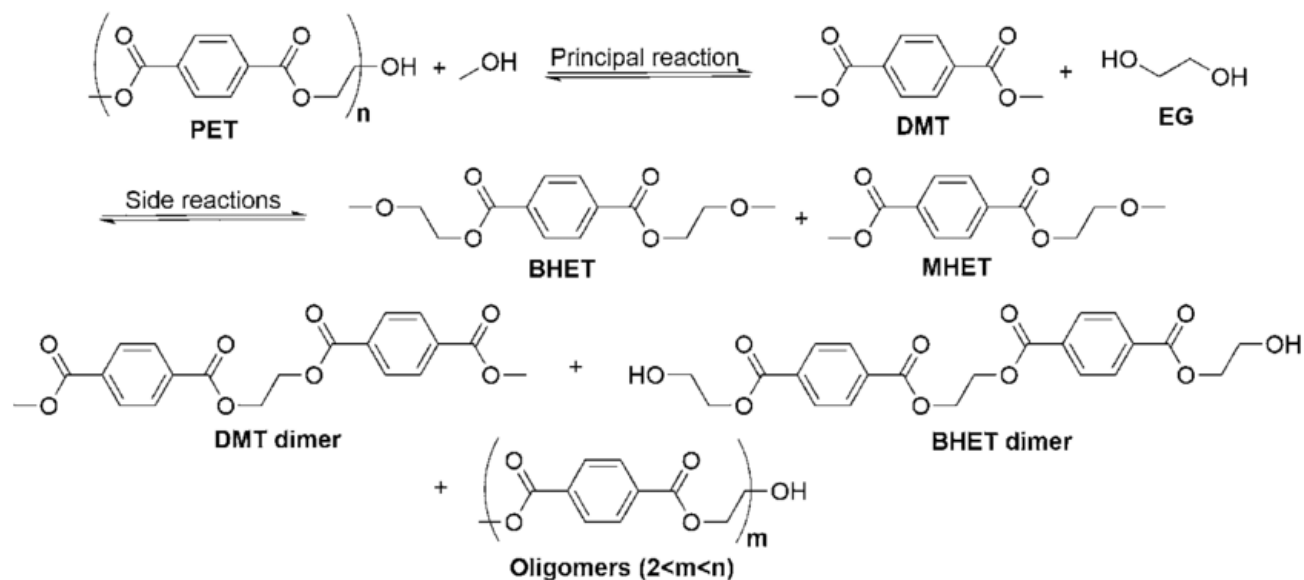


Figure 12. Overall reactions for PET alcoholysis using supercritical methanol [1]

Although in this process the products obtained have high value, it has some major problems. Firstly, it is a costly process because of the separation and refinement of the byproducts produced. Secondly, the major product of this process is DMT and nowadays the majority of PET is synthesis from terephthalic acid (TA). Therefore, an additional conversation of DMT to TA is needed in order to complete the cycle [1].

4. Additional steps for the PET degradation/decomposition

4.1 Pre-treatment and post-treatment of plastic waste

In order to improve the process performance for PET recycling (degradation/fragmentation/ decomposition), PET samples are often pre-treated in different ways. PET fabrics were cut into pieces of 0.5 - 1 g and only after that were incubated in glass vessels. [31, 32]. Another method involved to cut into pieces smaller than 20 x 20 mm. Then, the samples were subjected of a solution of Tween-80 at 2% v/v at 50°C for 1 hr. The last step of the pre-treatment consisted in washing of the samples with distilled water for 1 h and drying in an oven at 40°C for 24 h [33].

The PET can be designed as a film of size 1.0 / 0.5 cm which was washed with an aqueous Na_2CO_3 solution (2g l^{-1}) at 37°C for 0.5 h followed by washing twice with distilled water [34]. Also, the PET films were prepared by melting in a heated hydraulic press. Then, each film was washed with ethanol and placed in a 10 ml glass vial. The glass vials contained 5 ml of phosphate

buffer ($\text{Na}_2\text{HPO}_4/\text{KH}_2\text{PO}_4$, 100×10^{-3} M, pH 7) [4]. There was another alternative for which a circular film (Ø 64 mm) was punched out of the polyester films. It was cleaned with ethanol and placed in a 300 ml glass beaker. Then 10 ml of 25 mM $\text{NaH}_2\text{PO}_4 \cdot \text{H}_2\text{O}$ buffer was added [35].

After degradation process, the plastic samples were often treated before analysis. So that, they were simple washed with water and dried in air [32], or washed with 2g L^{-1} Na_2CO_3 at 60°C for 1 h. Finally, these were double-washed with deionized water for 1 h [31]. Sometimes, the samples were washed in a solution of 2g/L of Na_2CO_3 for 2 h in order to stop the enzymatic reaction. At the end, the polymers were washed firstly in 10g/L Tween-80 at 25°C for 1 h and then in distilled water [33].

Other alternatives could be washing with water and ethanol and dried overnight at 50°C [4] or only the adjustment of the solution pH to 5-6 with a small amount of 1 M HCl.

After the enzymatic treatment, until the HPLC analysis, the solution was stored at 4°C [35].

Another type of treatment is the UV pre-treatment before enzymatic degradation. In this case, amorphous PET films had a thickness of 250 μm . Then, UV irradiation of PET samples was carried out over 14 days using a 1-kW xenon arc lamp. A water filter was applied to filter the IR radiation and a water bath was used for further cooling during irradiation [36].

4.2 Analytical methods for monitorization of PET degradation (decomposition)

The samples after degradation process could be considered the pieces of PET and also the solution resulted after degradation process. The solid samples were analysis in order to identify any modifications of the surface morphology. In this case, the characterization techniques for solid surface were useful (FTIR, AFM, XRD, SEM/TEM, TSC-TGA, XPS) [31]. The second direction of analysis was focused on the solution. In this case, HPLC and GC coupled with MS for identification and DAD/RID for quantification were performed [34, 35].

5. Derivatization of PET using biocatalytic methods

5.1 Surface modification of poly(ethylene terephthalate) (PET) fibers by a cutinase from *Fusarium oxysporum*

Cutinases are serine esterases that have the role of hydrolysis of ester bonds in cutin and belong to the hydrolase fold family. They have the capacity to hydrolyze the ester bonds of synthetic polyesters and this makes them proper for the surface modification of PET [31].

The polyester fabrics were cut in pieces and incubated in glass vessels. It was applied the enzymatic treatment and then the fabrics were washed with Na_2CO_3 for an hour. At the end, it was double-washed with deionized water [31].

The whole enzymatic process was proved to be environmentally friendly and without affecting the thermal and mechanical properties of the PET fabric. The changes were confirmed by DSC-TGA analyses, tensile tests, FT-IR ATR analysis, XPS and SEM. The free hydroxyl and carboxyl groups were detected with the help of FT-IR ATR and XPS analyses [31].

It was concluded that the enzyme *F. oxysporum* cutinase is capable of derivatization of PET without compromising the polymer structure and properties [31].

5.2 Production of heterologous cutinases by *E. coli* and improved enzyme formulation for application on plastic degradation

The aim of this work was to optimize the process of degradation of polyethylene terephthalate using an enzyme from *E. Coli*. The hydrolytic action of the enzyme was applied to the degradation of the plastic [33].

The enzyme used was cutinase. Two types of cutinase were prepared for this experiment: one wild type form from *Fusarium solani* pisi and its C-terminal fusion to cellulose binding domain N1 from *Cellulomonas fimi*. The cultures used were *E. Coli* CUT for the first type and *E. Coli* CUT-N1 for the second type [33].

Both cutinases were treated first with ampicillin and isopropyl β -D-1-thiogalactopyranoside. The optimum pH of both cutinases was around 7.0 and they were stable between 30 and 50°C. By addition of glycerol, PEG-200 and $(\text{NH}_4)_2\text{SO}_4$ to the metabolic liquid, followed by ultra filtration, the mixture became stable during 60 days at 28°C. Treating the PET with the help of cutinase led to a weight loss of 0.90% [33].

In conclusion, recombinant microbial cutinases have advantages in the treatment of PET using enzymatic treatments [33].

5.3 Rapid Hydrolyse of Poly(ethylene terephthalate) using a hydrolase from *T. Fusca*

Due to the increasing problem of plastic waste at the end of 1980, there were attempts to design biodegradable plastics. But most of the biodegradable plastics are based on aliphatic polyesters which exhibit limited useful properties. Aromatic polyesters such as PET or poly(butylene terephthalate) (PBT) which provide excellent properties can not be attacked by hydrolytic enzymes and can not serve as biodegradable source of plastic [4].

But the reason of missing biodegradability of aromatic polyesters was found by Marten et al.; the mobility of the polymer chains in the crystalline part controls the biodegradability. This can be correlated with the temperature difference between the melting point and the temperature at which degradation takes place [4].

This work presents the ability of a hydrolase isolated from the actinomycete *Thermobifida fusca* to depolymerize the aromatic polyester PET at a higher rate than other hydrolases such as lipases [4].

The experiment started with the characterization of the samples of PET. For the degradation process, the materials were melted using a heated hydraulic press. The samples were washed with ethanol and placed in a glass vial containing phosphate buffer. Degradation was started by adding the enzyme solution. At the end, the vials were placed in a rotational shaker and thermostated [4].

The results of the experiment demonstrated that commercial PET can be hydrolyzed by an enzyme. Within 8 weeks, microbial action resulted in an approx. 15% weight loss of the PET fibers [4].

5.4 Degradation of Poly(ethylene terephthalate) Catalyzed by Metal-free 2 Choline-Based Ionic Liquids

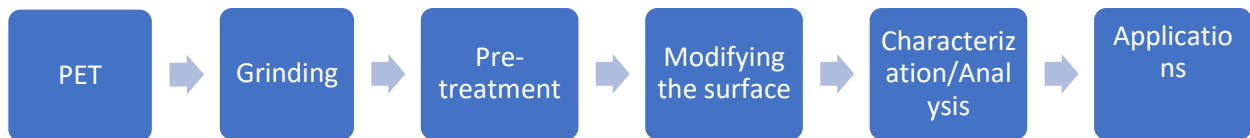
The glycolysis of PET is an expected way for degradation of PET to its monomer bis(hydroxyethyl) terephthalate (BHET) since BHET can be polymerized again to form new PET materials and provides possibilities for a permanent loop recycling. However, most of the used glycolysis catalysts are metal-based which have a high cost and present a negative environmental impact [37].

This study aims to develop a series of choline-based ionic liquids with a role in the glycolysis of PET without using any metals [37].

The catalyst used was Choline acetate [Ch][OAc], a cheaper, more biologically compatible and environmentally friendly substitute of the conventional imidazolium metal-based ionic liquids. It was found that under the optimum conditions (PET (5.0 g), ethylene glycol (EG) (20 g), [Ch][OAc] (5 wt %), 180 °C, 4 h, atmospheric pressure), the choline acetate can achieve even better performance than the initial metal based catalyst, the yield of BHET reaching up to 85.2 % [37].

6. The aim of the thesis

We proposed a detailed study for developing a technology for PET recycling. So that, our study will be directed to set up and optimise an enzyme biocatalysis for PET degradation/ fragmentation/ decomposition. Screening of enzymes will allow to decide and choose the best biocatalyst for process performance. Detailed optimization of the biocatalytic method will be considered. The system performance will be monitored directed the analysis to the characterization of the plastic surface and also looking for the composition of the process environment after incubation time. For the determination of any modifications of the surface morphology, the techniques such as FTIR, XPS, DSC-TGA, AFM, SEM/Tem will be used. HPLC-DAD/RID and/or GC-MS/FID will be performed for the evaluation of the reaction phase containt after incubation time.



Experimental part

1.1 Substances and reagents

Commercial Bis(2-hydroxyethyl) terephthalate (BHET) was purchased from Sigma-Aldrich and needed for optimizing the system for future use in PET degradation.

An attempt was made to build reaction systems based on different types of DES. Six types of DES were created starting from the solubility of BHET in different solvents: DES 1 (one part acetic acid, three parts ethylene glycol), DES 2 (one part acetic acid, three parts glycerol), DES 3 (one part oleic acid, three parts ethylene glycerol), DES 4 (one part oleic acid, three parts glycerol), DES 5 (one part octanoic acid, three parts ethylene glycol) and DES 6 (one part octanoic acid, three parts glycerol).

The system of BHET and DES was completed by adding free (lipase from *Aspergillus niger*) and immobilized enzymes (Lipozyme RMIM, Lipozyme TLIM, Novozyme 425 and Transenzyme) as catalysts. Lipozyme® TL IM –*Thermomyces lanuginosus* in silica gel, Novozym® 435 – lipase B from *Candida antarctica* in PMMA, Transenzyme – lipase in PMMA (no additional information found), Lipozyme® RM IM –*Rhizomucor miehei* in anionic exchange resin.

PET from four different sources and with different purity was used in the experimental processes and was noted with initials according to their origin: ST (PET from a bottle of juice), TA (PET from a packing tray), CU (PET from an ice cream box) and CF (PET from a bottle of Cif). The PET was cut into pieces of around 0.5 cm x 0.5 cm.

PET was subjected to the reaction with dimethyl carbonate (DMC) which was anhydrous, $\geq 99\%$, of HPLC purity and purchased from Sigma-Aldrich.

The catalyst used in the degradation of PET was the enzyme *Aspergillus niger*.

PET was subjected to the reaction with dimethyl carbonate, thiols and aniline.

Dimethyl carbonate (DMC) was anhydrous, $\geq 99\%$, of HPLC purity and purchased from Sigma-Aldrich. Aniline was also purchased from Sigma-Aldrich.

The reaction medium was the buffer Tris hydrochloride with the concentration of 10 mM and a pH of 8.3.

The catalyst used in the reaction with DMC and thiols was an immobilized enzyme Novozyme 425

1.2 Method for grinding/chopping PET

PET was subjected to grinding firstly using a Ultra centrifugal mill ZM 200 from Retsch. The mill has been set at 400 rot/min and the PET was introduced multiple times until tiny pieces resulted. For a better performance and for obtaining a powder texture, the PET was then introduced in a Ball mill PM 100 from Retsch and was let for half an hour at 400 rot/min.

1.3 Methods of sample pre-treatment

Both PET pieces and PET powder were pre-treated using five different methods.

Table 1. Pre-treatment of PET samples

Method 1	Method 2	Method 3	Method 4	Method 5		
Immersion in aqueous solution 2g/L Na ₂ CO ₃ at 37°C (over the weekend)	Immersion in 2% Tween 80 solution at 50°C, for 1 hour	Immersion in 2% Tween 80 solution at 50°C, for 1 hour	Immersion in 20% ethanol aqueous solution for 1 hour	Simple	In distilled water (AD)	In hydrogen peroxide (AO)
Washing with distilled water	Immersion in distilled water for 1 hour under stirring at room temperature	Repeated washing with distilled water	Washing with distilled water		Exposure to UV lamp for several days	
Dry in the oven at 40°C	Dry in the oven at 40°C	Immersion in aqueous solution 2g/L Na ₂ CO ₃ at 37°C for 1 hour	Dry in the oven at 40°C	Dry in the oven at 40°C		
		Washing with distilled water				
		Dry in the oven at 40°C				

Samples were washed with Na₂CO₃ and distilled water in order to clean and remove finishing agents.

1.4 Methods of sample preparation

1.4.1 Sample preparation for BHET hydrolysis

The experiment involved the hydrolysis of 0.001 g BHET with 1 mL of different types of DES and 0.001 g of each type of enzyme mentioned above. The reaction was left in a thermoshaker for 24 hours under agitation at 60°C.

1.4.2 Sample preparation for PET degradation

The PET was pretreated using five different methods. After the pre-treatment, the PET pieces were put in vials with 500 µL DMC, 500 µL Tris hydrochloride and 2 mg of the *Aspergillus niger* enzyme. The vials were put in a thermoshaker at 60°C for three days.

1.5 Methods for modifying PET surface

1.5.1 Reaction of PET with DMC

PET was put in reaction with 500 µL DMC, 500 µL Tris hydrochloride and 1 mg of enzyme Novozyme 425. The vials were left in a thermoshaker for different periods of time at 60° C.

1.5.2 Reaction of PET/ BHET with thiols

PET and BHET were put in reactions with thiols. The thiols used were 2-mercaptoethanol, 2-aminothiophenol and 4-acetamidothiophenol.

Firstly, 0.001 g of BHET (5 mM) reacted with 25 mM of each thiol, 1000 µL Tris hydrochloride and 1 mg of enzyme Novozyme 425. The reaction was left in a thermoshaker at 60° C for one day.

For PET reaction, 0.01 g of PET (45 mM) with 90 mM of thiols, 1000 µL Tris hydrochloride and 1 mg of Novozyme 425 were put in vials. These were put in a thermoshaker at 60° C for 3 days.

1.5.3 Reaction of PET/ BHET with aniline

For the BHET reaction, all the peroxidases described at 2.1 Substances and reagents were used. For each peroxidase, 100 µL were put in reaction with 894 µL Tris hydrochloride, 5 µL H₂O₂, 1 µL aniline and 0.001 g BHET for 1 day at 40° C.

After the liquid phase from BHET reactions was analysed using HPLC and the results were examined, the peroxidases with the best results were chosen: Lacase M120, Peroxidase EP010 and Versatile peroxidase 2-1B Variant 12,97 ABTS. These were put again in the reaction in the same amount, but with 0.01 g PET (45 mM), 5 μL H_2O_2 , 9 μL anilina and 886 μL Tris hydrochloride for 3 days at 40° C.

1.6 Method of pre-treatment before analysis

Sample was mixed with an equal volume of the mobile phase for removing the enzyme and the salt content (provided by the buffer solution), and also for adjusting the polarity of the sample comparing to the mobile phase. The resulted mixture was centrifugated and the supernatant was collected and acidified with 1 μL HCl for neutralizing the potential acidic products from the sample.

1.7 Method of sample PET characterization

1.7.1 FT-IR

FTIR spectra were recorded using a Spectrum Two FTIR spectrometer (Perkin Elmer, Hamburg, Germany) equipped with a total attenuated reflectance cell in the range of 8300-350 cm^{-1} .

1.7.2 Dinamic light scattering

The particle size was determined by the DLS method using a Mastersizer 2000 device with Hydra 2000S accessory, equipped with two light sources: HeNe red laser (632 nm) and blue LED (455 nm). Water was used as a dispersion medium.

1.8 Method of sample analysis after reaction

Monitorization of the content of the reaction phase was performed based on HPLC-DAD analysis using a modular system (Agilent 1260) equipped with a C18 column (Poroshell 20) and DAD detector. The HPLC-DAD system was set up for injecting 10 μL sample and the analysis was performed at 25 °C with a flow rate of 1 $\mu\text{L}/\text{min}$ mobile phase (20 % acetonitrile and 20 % H_2SO_4 (10 mM) dispersed in distilled water). The detection was performed at 241 nm, ie the

specific wavelength for TPA and its derivatives. Retention time of the substrate and the products are: 1 min for TA, 1.14 for MHET and 1.31 min for BHET.

1.9 Method for the preparation of the enzyme entrapment

Carbohydrate biopolymers using Na-alginate and K-carrageenan were created for entrapment of enzyme. A 4% Na-alginate solution of 3 mL was dropped with disposable pipette in a 5% CaCl₂ solution. For the K-carrageenan beads, a 1.4 wt% solution was made and dropped in a 0.5 M KCl solution [9].

In some beads, PET was added to test if it influences the specific activity of the enzyme.

2. Results and discussions

2.1 The PET degradation

The degradation of PET was carried out in two steps: the first one being the pretreatment of the PET surface and the second one the degradation reaction itself.

Five different methods of pre-treatment listed at 2.3 were used.

For each sample, the specific chromatograms have been recorded. It is not possible to identify all the peaks from the chromatograms since most of them are small polymeric fragments (oligomers) from PET structure. So that, the quantification of the system performance involved the total sum of the peak area from the chromatograms which were not present in the initial phase of the reaction. Relative area of these sum for each type of PET and each pre-treatment method were calculated. The results for all the methods were plotted as in the graphic below:

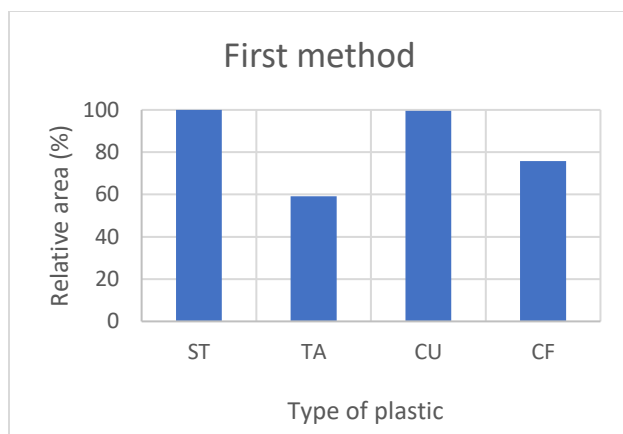


Figure 13. Relative area calculated for each type of plastic that was pretreated with the first method

Table 2. Sums of the relative areas

Sum of the relative areas	
First method	334
Second method	251
Third method	346
Fourth method	265
Fifth method	214
Fifth method (AD)	236
Fifth method (AO)	239

It can be observed that first and third method have the biggest sums of relative areas, so the degradation went better in these conditions. Although the second method had an error (the liquid phase of the CF reaction evaporated), it can be considered a valid method.

The PET samples were weighed before the reaction and after. The masses were listed in the tables below.

Table 3. The masses of PET samples before and after reactions

	Method 1				Method 2				Method 3				Method 4			
	ST	TA	CU	CF	ST	TA	CU	CF	ST	TA	CU	CF	ST	TA	CU	CF
Before reaction (mg)	0,0122	0,0159	0,0197	0,0420	0,0220	0,0216	0,0276	0,0326	0,0106	0,0163	0,0197	0,0321	0,0218	0,0197	0,0284	0,0369

After reaction (mg)	0,0130	0,0163	0,0194	0,0418	0,0240	0,0216	0,0272	0,0328	0,0112	0,0170	0,0194	0,0320	0,0220	0,0201	0,0283	0,0373
Difference (mg)	+0.8	+0.4	-0.3	-0.2	+2	0	-0.4	+0.2	+0.6	+0.7	-0.3	-0.1	+0.2	+0.4	-0.1	+0.4

Method 5											
Simple				Distilled water				Hydrogen peroxide			
ST	TA	CU	CF	ST	TA	CU	CF	ST	TA	CU	CF
0,0186	0,0193	0,0256	0,0429	0,0286	0,0148	0,0262	0,0553	0,0259	0,0213	0,0260	0,0553
0,0196	0,0193	0,0255	0,0430	0,0305	0,0159	0,0260	0,0555	0,0275	0,0216	0,0260	0,0555
+1	0	-0.1	+0.1	+1.9	+1.1	-0.2	0	+1.6	+0.3	0	0

With red were listed the samples which had a mass increase after reaction, with green the samples that had a mass decrease. after reaction and with grey the ones that had no mass change. It can be observed that the samples which had a higher durability, CU and CF, were the only ones with a decrease of the mass.

Pretreatment method 1,2 and 3 allowed to achieve the most degraded PET surface. Positive difference between masses could be the effect of DMC attached on the PET surface (carboxy methylation).

2.2 BHET system

BHET is one of the most useful substrate which can mime very well the PET behavior. So that, BHET was mixed with free/immobilized lipase enzyme in DES environment. DES composition of two substances (one as H donor and the other as H acceptor) was prepared and used as the reaction environment. The components were organic acids and alcohol (see table 4). Both of them can interact with the products of BHET hydrolysis. In this way, the equilibrium of hydrolysis could be shefted to the more products and finally the total conversion of the process could be improved. BHET hydrolysis takes place according to the following scheme.

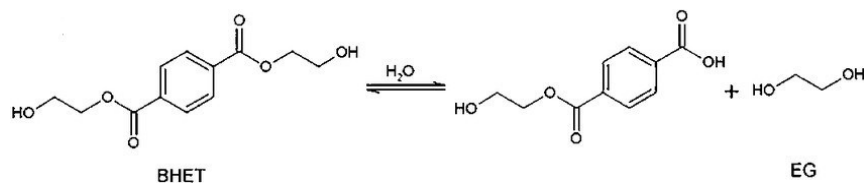


Figure 14. BHET hydrolysis

Table 4. The compositions of DES

DES COMPOSITION											
1		2		3		4		5		6	
25%	75%	25%	75%	25%	75%	25%	75%	25%	75%	25%	75%
acetic acid	ethylene glycol	acetic acid	glycerol	oleic acid	ethylene glycol	oleic acid	glycerol	octanoic acid	ethylene glycol	octanoic acid	glycerol

After the HPLC analysis, the conversion for each type of DES and each type of enzyme was calculated. Graphics were made to see which type of DES is the best system for each enzyme.

In figure 10, experimental results for BHET system using free lipase from *Aspergillus niger* are presented. DES5 and 6 exhibited maximum conversion of 17.7% and 16.6%. Low conversion was noticed for DES3.

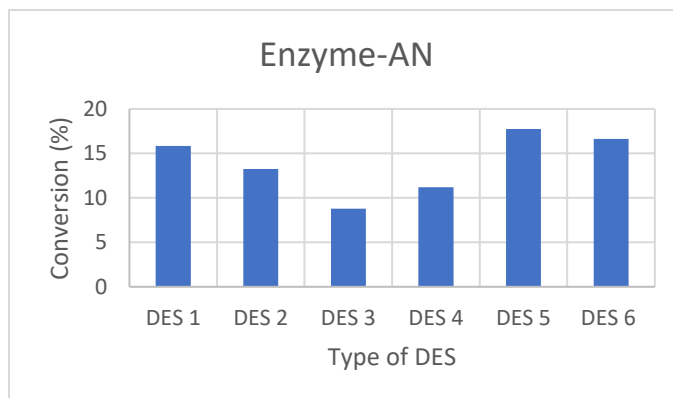


Figure 15. Conversion according with each type of DES for the enzyme Aspergillus niger

Experimental results for BHET system using Immobilized lipase Transenzyme are presented: DES 5 and 6 exhibited maximum conversion of 23.3% and 28.1%. Low conversion was noticed also for DES3.

Experimental results for BHET system using Immobilized lipase Lypozime TL1M were: DES 5 and 6 exhibited maximum conversion of 17.9% and 21.9%. Low conversion was noticed also for DES3

Experimental results for BHET system using Immobilized lipase Novozyme 425 are given: DES 5 and 4 exhibited maximum conversion of 26.9% and 18.5%. Low conversion was noticed for DES 1, 2 and 3.

Experimental results for BHET system using Immobilized lipase Lypozime RMIM were: DES 5 and 6 exhibited maximum conversion of 22.5% and 21.9%. Low conversion was noticed for DES 2 and 4.

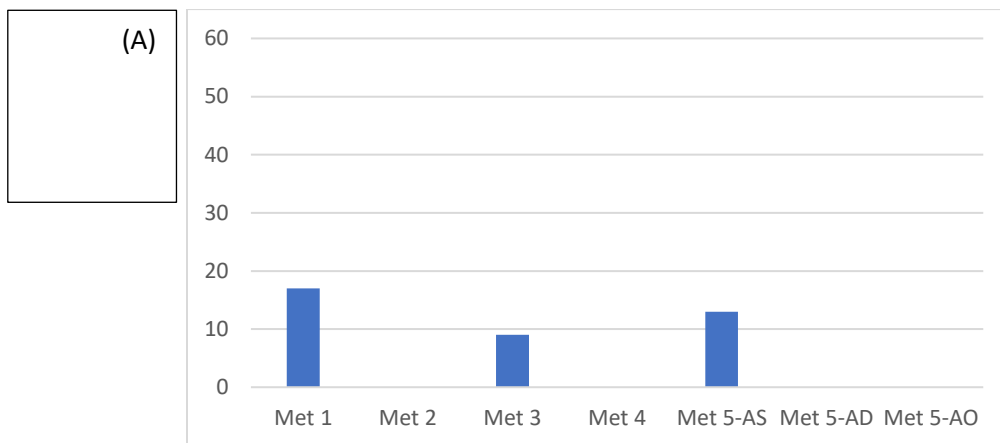
As a general remarks analysing the graphics, it can be seen that the best systems are: DES 1, 3 and 5 with Transenzyme, DES 6 with Lypozime TLIM, DES 5 with Novozyme 425 and DES 5 and 6 with Lypozime RMIM. The reactions with these systems were repeated, but varying the quantity of the enzyme: 2 mg and 5 mg were used instead.

1.3. Choosing the pre-treatment approach

Both pieces of PET and PET powder treated with all 5 pre-treatment methods were put in reactions with DMC and had their liquid phase analysis by HPLC.

Using HPLC, the interest compounds solubilized in the liquid phase that results from the reaction such as terephthalic acid (TA), Bis(β -hydroxyethyl) terephthalate (MHET) and Bis(2-Hydroxyethyl) terephthalate (BHET) were identified.

In the graphs below all the areas of the interest compounds from HPLC have been noted.



(B)

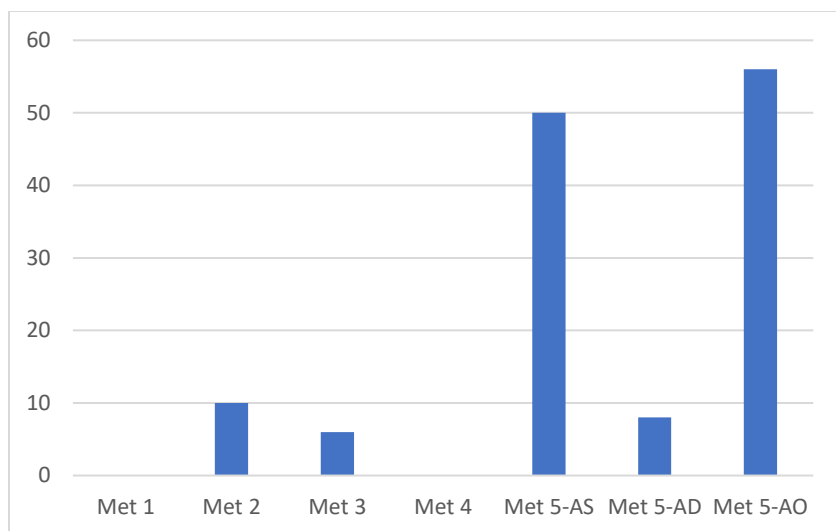


Figure 16. Influence of the pre-treatment approach on the PET derivatization. (A) PET film and (B) PET powder

From the figure 1(A and B), it is obvious that the best results were for PET powder which was pre-treated with method 5 (exposure to UV lamp for several days) in nothing (AS) and in H_2O_2 (AO). The research was continued using these two types of pre-treatment and only using grinding PET.

2.4 Reactions of BHET with thiols

BHET has a structure very similar with PET, so it can mime very well the PET behavior. Before the reaction with PET, a hydrolysis of BHET was tried.

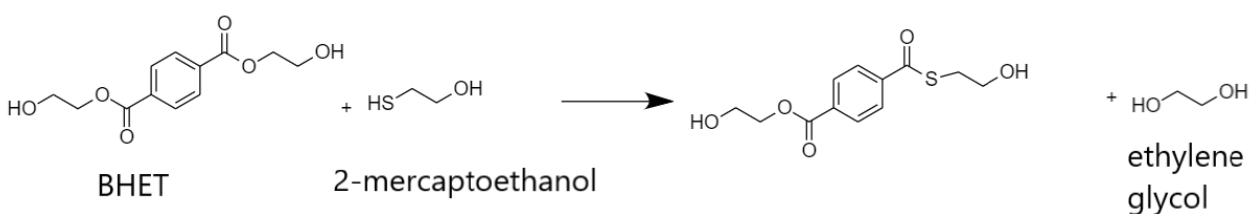


Figure 17. Reaction of BHET with 2-mercaptoethanol

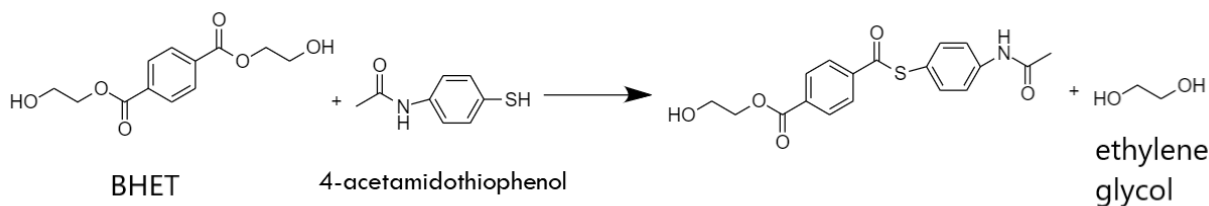


Figure 18. Reaction of BHET with 4-acetamidothiophenol

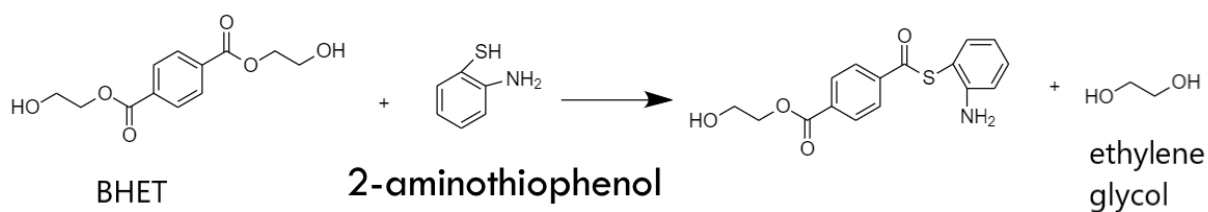
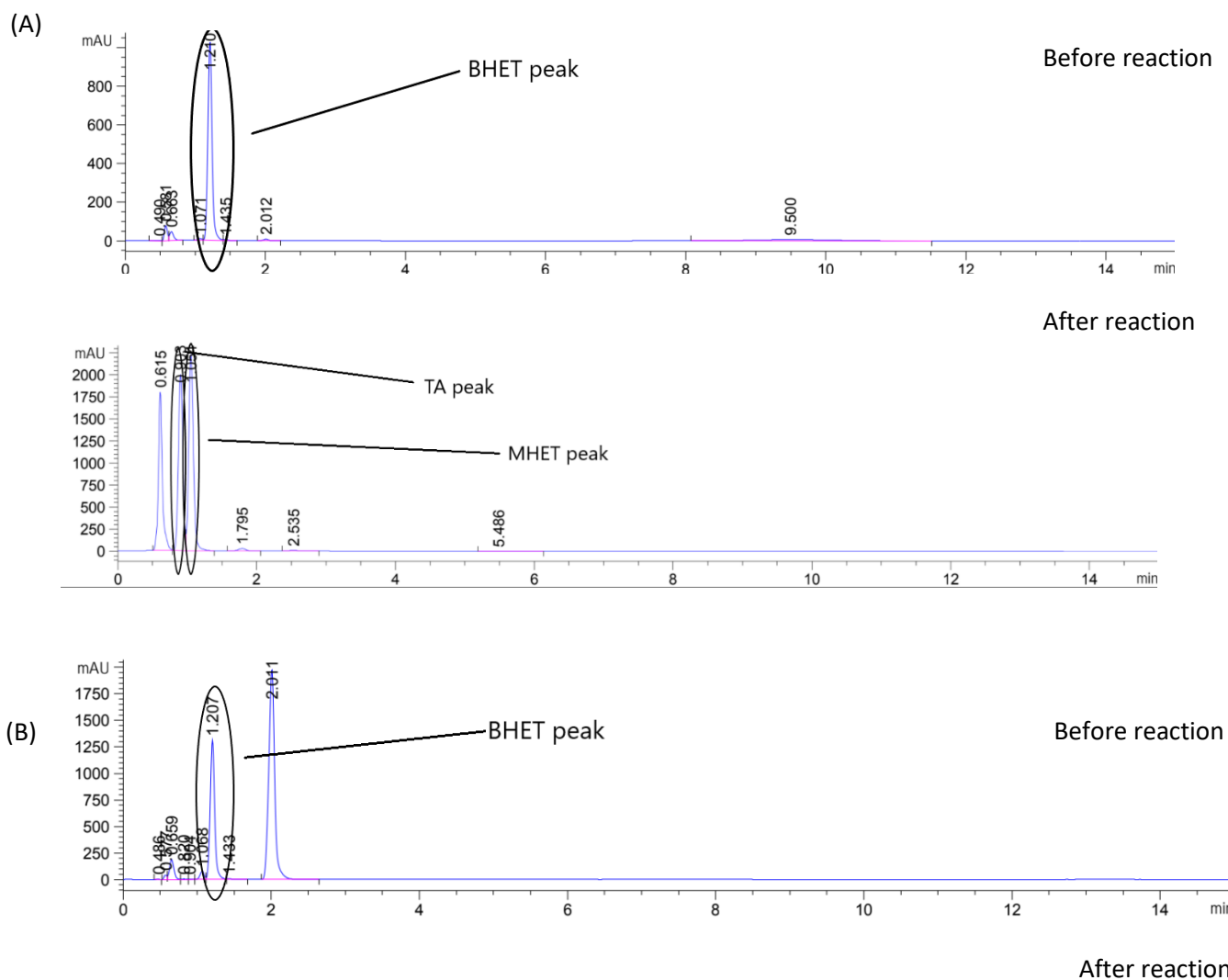


Figure 19. Reaction of BHET with 2-aminothiophenol

BHET was subjected in a reaction with thiols. The liquid phase from the reaction was analyzed using HPLC. For a better analysis of the results, control sample containing the same compounds were also analyzed using HPLC.



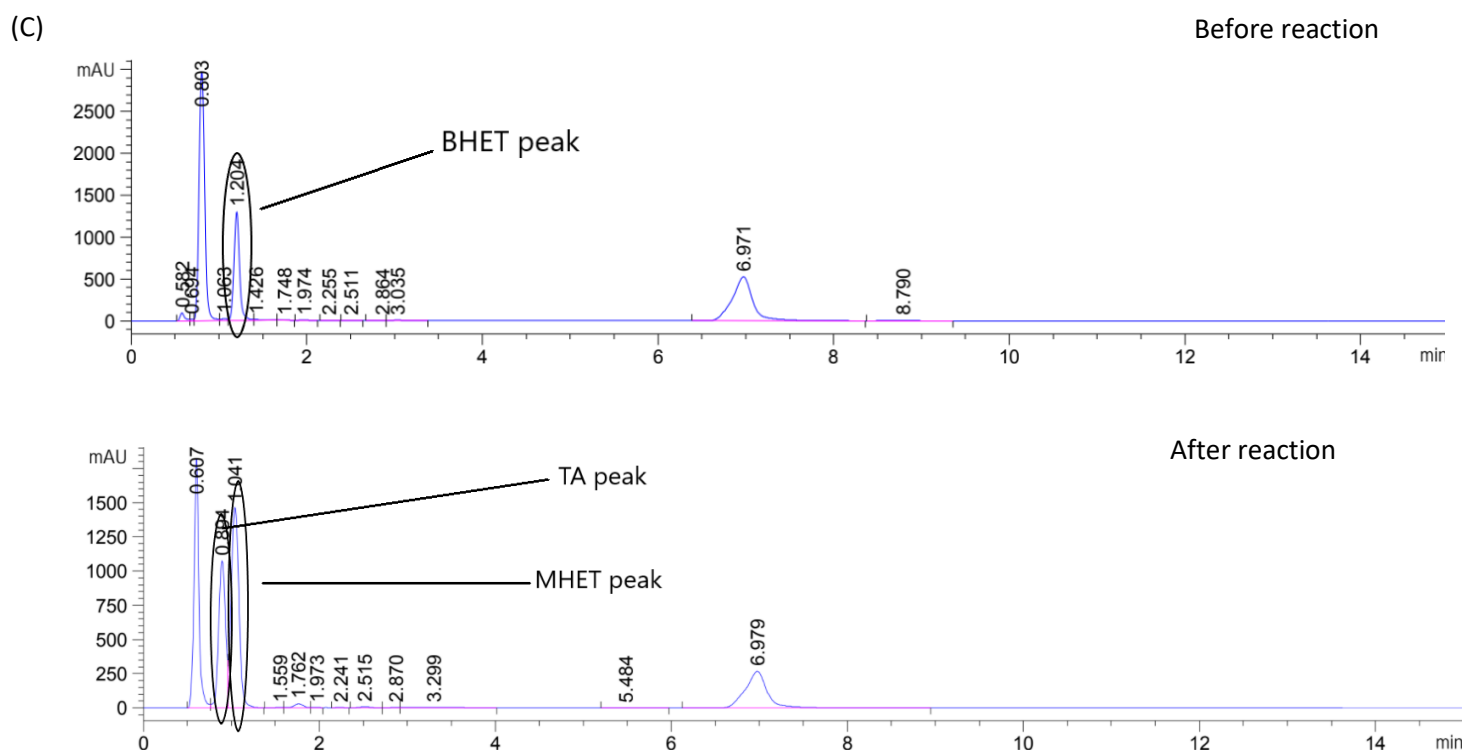
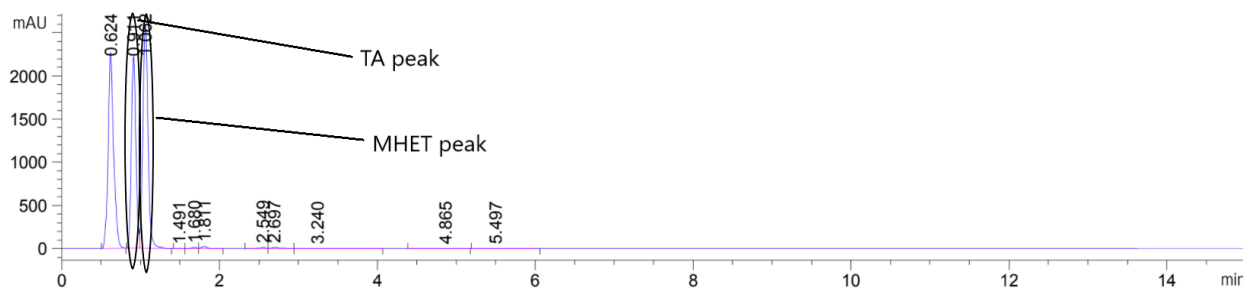


Figure 20. Reaction of BHET with (A) 2-mercaptoethanol, (B) 4-acetamidothiophenol and (C) 2-aminothiophenol

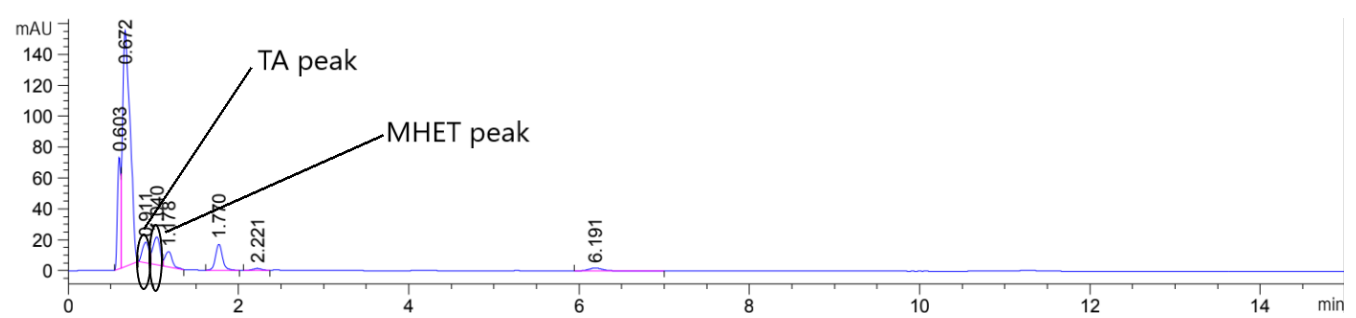
From the control sample chromatograms, it can be observed the BHET peak disappears in the chromatograms realized after the reactions. This has been replaced with the peaks for TA and MHET, its products after the hydrolysis.

After analysing the HPLC chromatograms, it is clear that the hydrolysis of BHET takes place in the presence of thiols so the research was continued with PET.

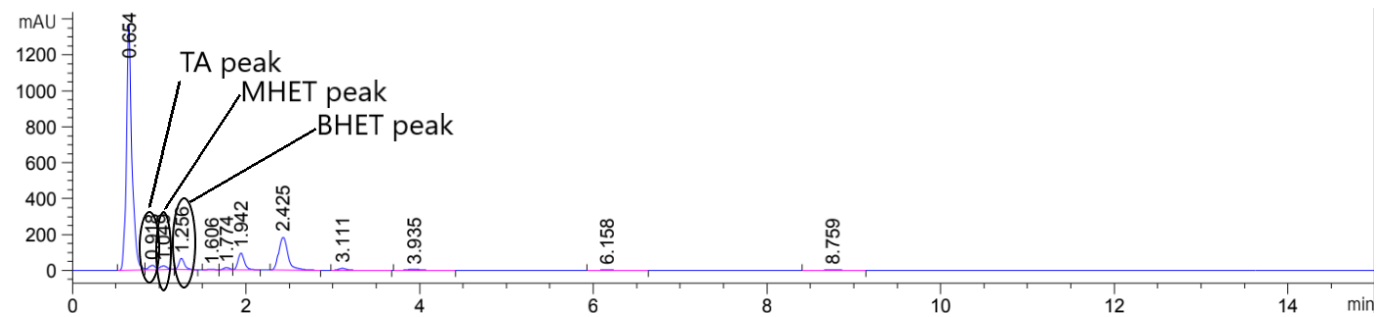
2.5 Reaction of PET with thiols

The liquid phase from the PET reaction with thiols was also analyzed using HPLC.

(A)



(B)



(C)

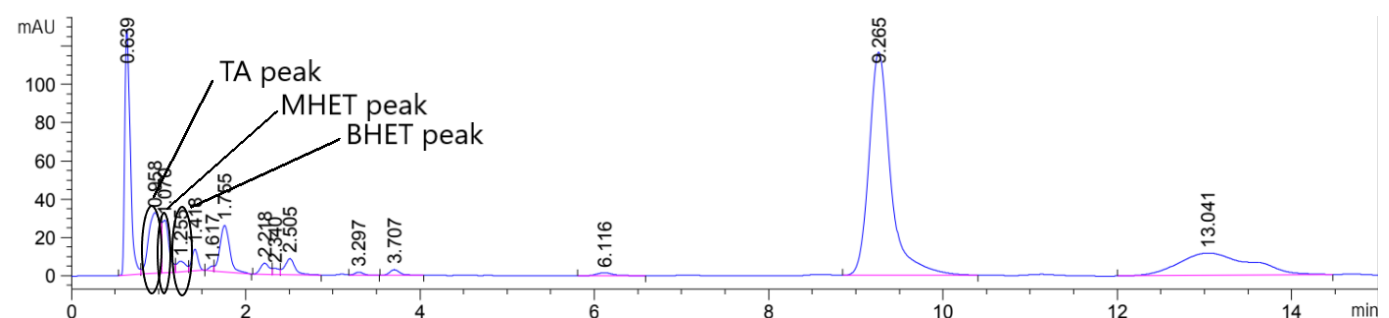
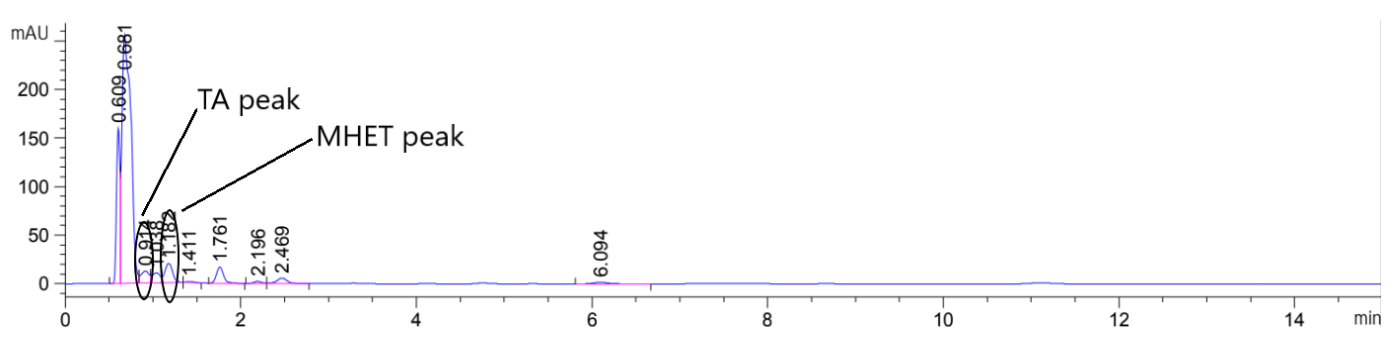
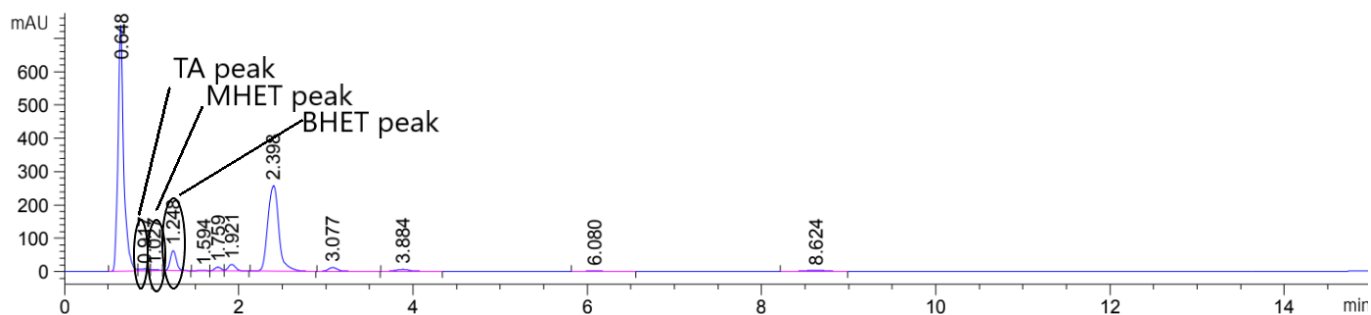


Figure 21. Reaction of PET with (A) 2-mercaptoethanol, (B) 4-acetamidothiophenol and (C) 2-aminothiophenol using method AO of pretreatment

(A)



(B)



(C)

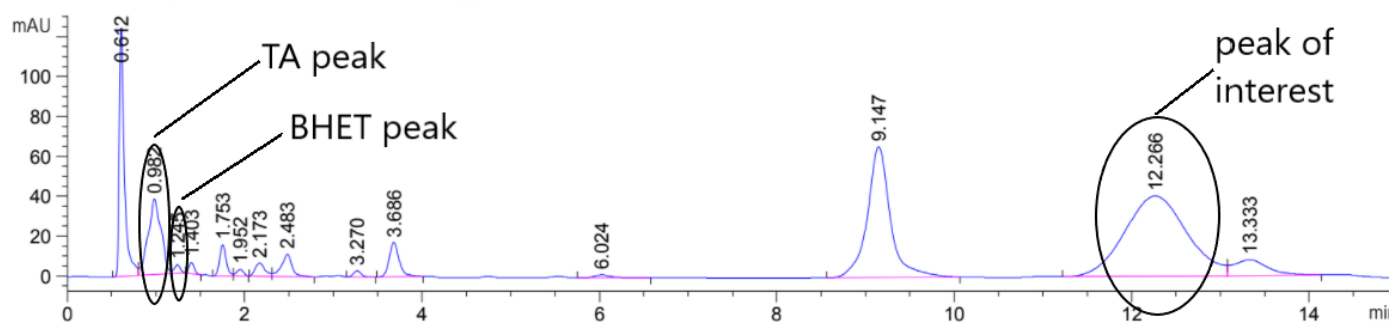


Figure 22. Reaction of PET with (A) 2-mercaptoethanol, (B) 4-acetamidothiophenol and (C) 2-aminothiophenol using method AS of pretreatment

Similar with the BHET reaction, peaks for TA and MHET were observed in the chromatogram meaning the hydrolysis of PET took place. BHET peaks also appeared.

All the chromatograms were examined and the ones with the best results were chosen for FTIR. The second one (the reaction with PET-AO and 4-acetamidothiophenol) due to the high area of the TA, MHET and BHET peaks and the last one (the reaction with PET-AS and 2-aminothiophenol) due to the interesting peak that appeared at the retention time of 12.2 min were the one characterized by FTIR.

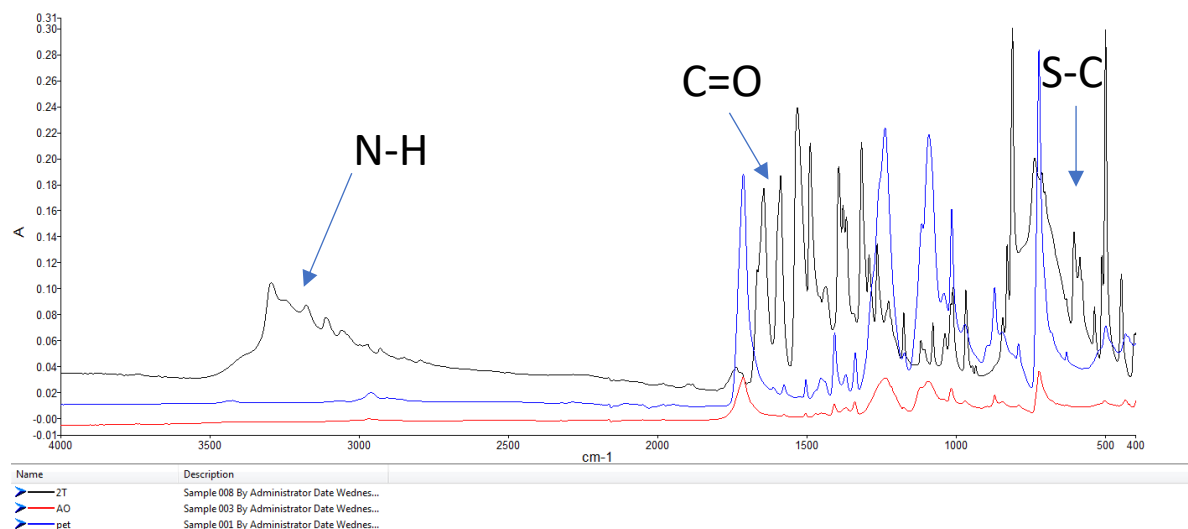


Figure 23. Overlaid spectrums of PET before pre-treatment (blue), PET after pre-treatment (red) and PET after reaction with 4-acetamidothiophenol (black)

New bands can be observed around the wave number 3000-3400 cm^{-1} . These can correspond to N-H stretching. The ones at the wave number 1500-1700 cm^{-1} can be a new bound C=O. The new bands appeared at 500-7000 cm^{-1} can be the bounds S-C that are formed after PET reacted with thiols.

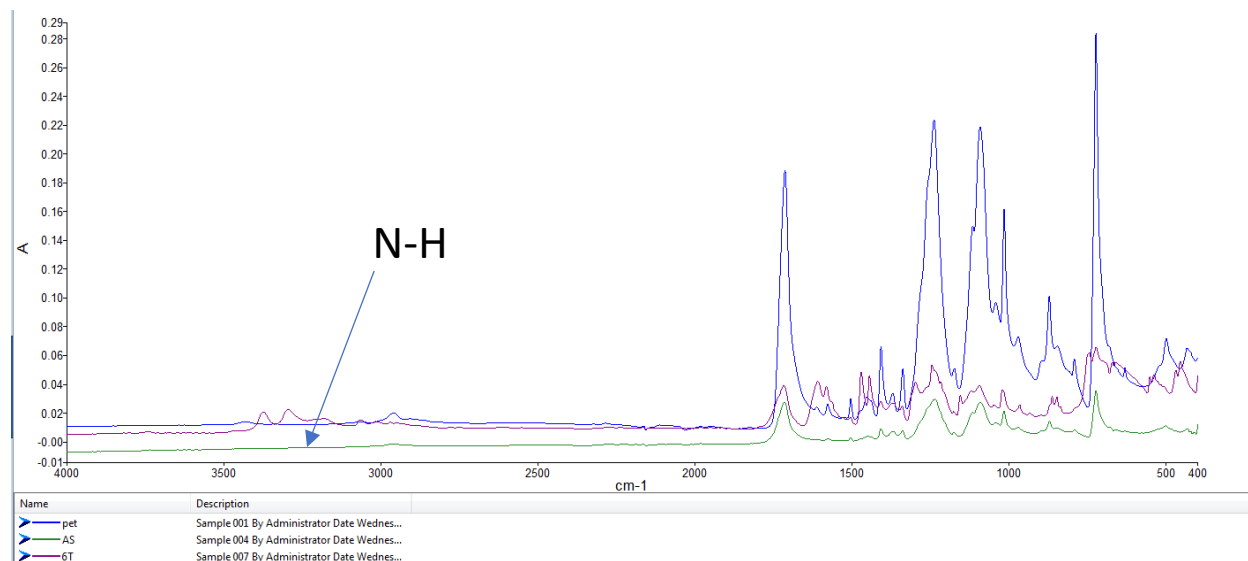


Figure 24. Overlaid spectrums of PET before pre-treatment (blue), PET after pre-treatment (green) and PET after reaction with 2-aminothiophenol (purple)

New bands can be observed around the wave number 3000-3400 cm^{-1} . These can correspond to N-H stretching.

2.6 Reaction of BHET with aniline

The same method with BHET as in 3.4 was used, but this time different peroxidases and aniline were put in the reaction. The liquid phase was analysed using HPLC.

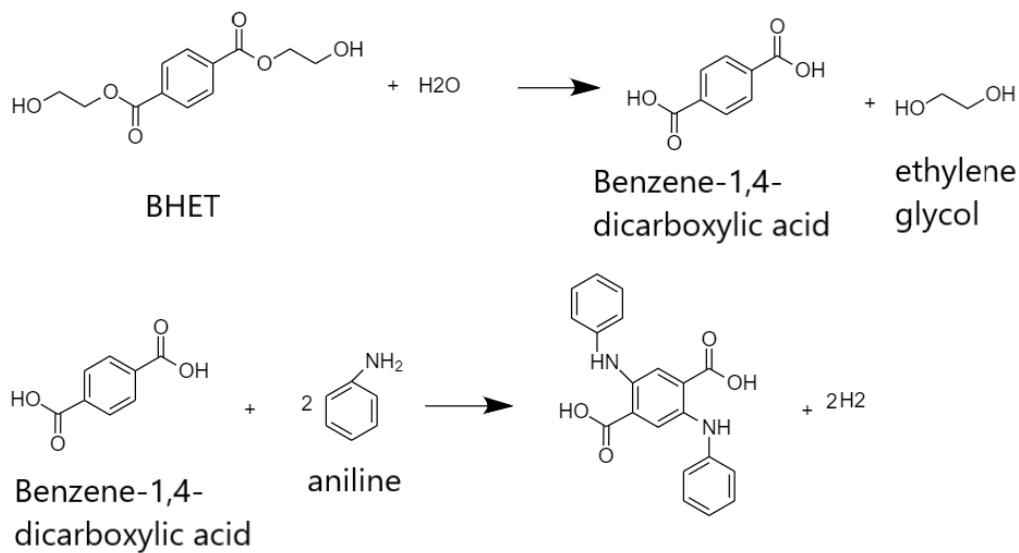


Figure 25. Reaction of BHET and aniline

From the chromatograms, using the area peaks of TA, MHET and BHET, the conversion rate of obtaining TA and MHET was calculated for each peroxidase.

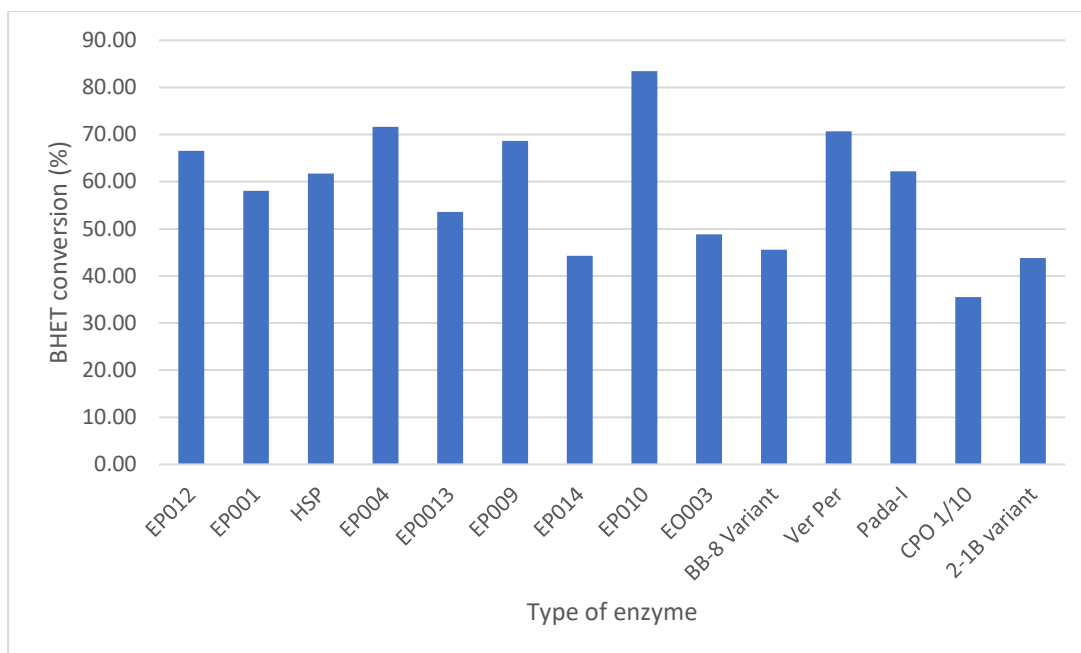


Figure 26. Enzyme effect on the biocatalytic reaction between BHET and aniline. Experimental conditions: 0.001 g BHET (5 mM), 5 μ L H₂O₂, 1 μ L anilina (10 mM), 100 μ L enzyme and 894 μ L Tris hydrochloride for 24 hours at 40° C and 1000 rotation/min

Peroxidase/laccase are catalysts for oxi-polymerization of aniline attached on the PET surface via o/o' benzene positions of TPA or TPA derivatives. The peroxidase with the best conversion rate (EP010, EP004 and Versatile Peroxidase) were chosen for reactions with PET.

2.7 Reaction of PET with aniline

As described previously aniline interacted with PET surface. the reaction was catalysed by three different types of peroxidases. Both liquid phase of the reaction and PET surface were evaluated. The liquid phase was again analyzed with HPLC.

Table 5. Abbreviation of aniline-peroxidase sample

Sample	Abbreviation
Reaction of PET pretreated with method AS with peroxidase EP010	9A-AS
Reaction of PET pretreated with method AO with peroxidase EP010	9A-AO
Reaction of PET pretreated with method AS with Versatile Peroxidase	14A-AS

Reaction of PET pretreated with method AO with Versatile Peroxidase	14A-AO
Reaction of PET pretreated with method AS with Lacase M120	4A-AS
Reaction of PET pretreated with method AO with Lacase M120	4A-AO

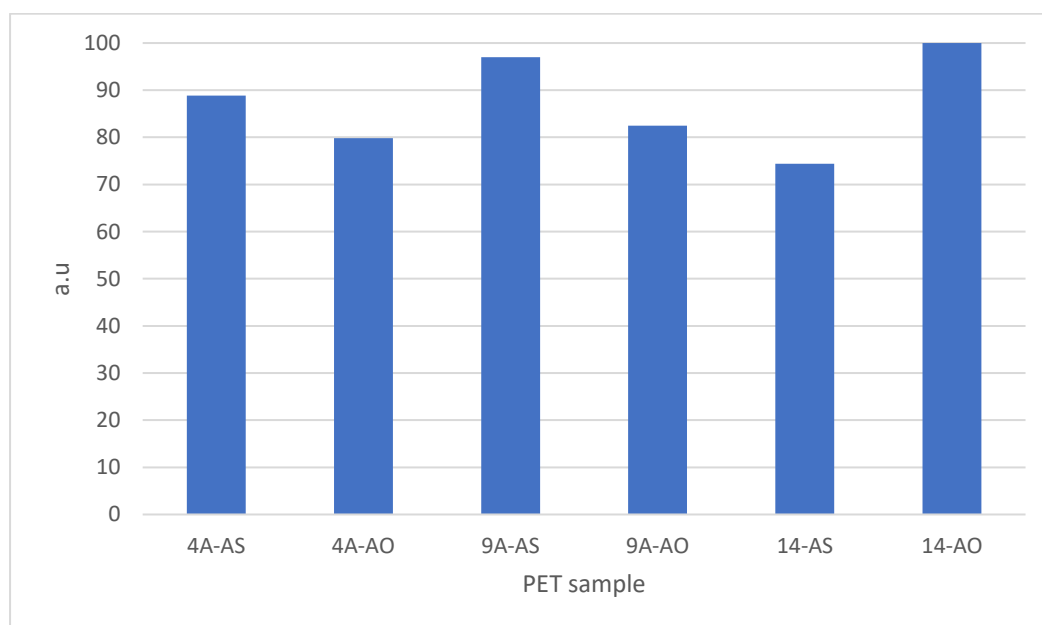


Figure 27. Evaluation of the liquid phase after the reaction between PET and aniline(peroxidase enzyme as biocatalyst). Experimental conditions: 0.01 g PET (45 mM), 5 μ L H₂O₂, 9 μ L anilina, 100 μ L of peroxidase and 884 μ L Tris hydrochloride for 72 hours at 40° C

All the areas from the chromatogram were calculated. Then, the relative area for each one of the reaction was put in the graph from above. It can be seen that the reaction with Versatile Peroxidase using the AO method of pre-treatment had the best results. The sample was characterized with FTIR after.

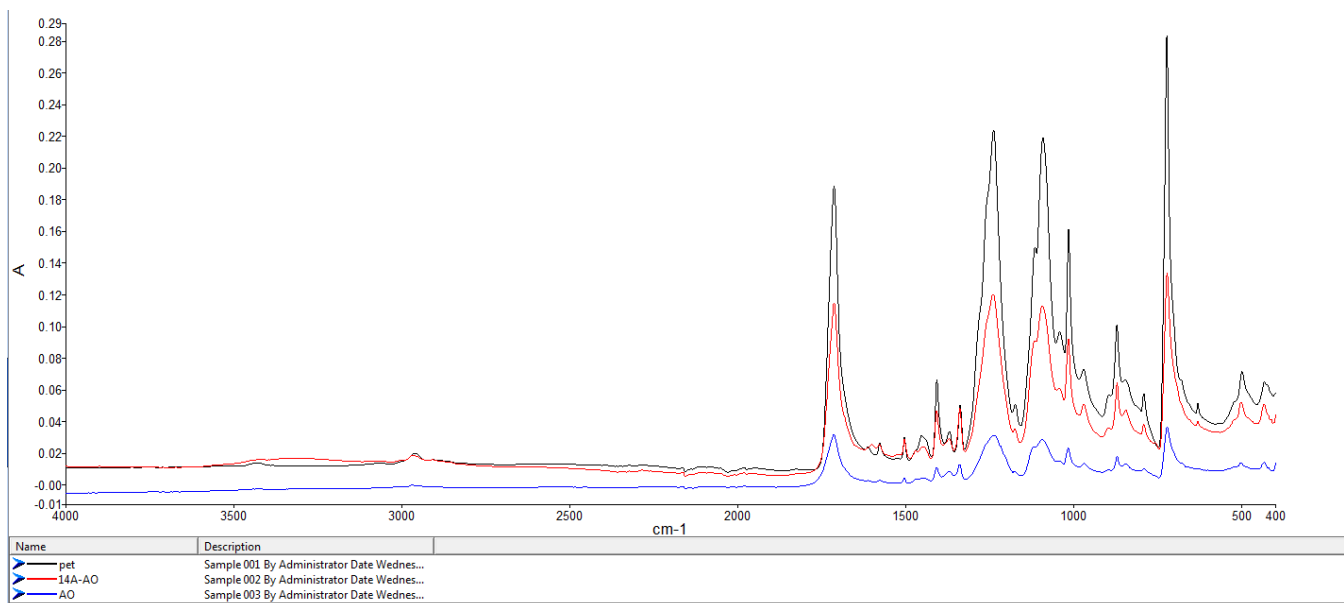


Figure 28. Overlaid spectrums of PET before pre-treatment (black), PET after pre-treatment (blue) and PET after reaction with aniline-peroxidase (red)

The spectrum of PET before pre-treatment and the PET after pre-treatment (AO) was overlaid with the one of the sample after reaction with aniline-peroxidase. Unfortunately, no change can be observed in the spectrum.

2.8 Reaction of PET with DMC

PET reacted with DMC during different periods of time for studying if the reaction time affect in a positive way the final products. The periods of time studied were: 5, 10, 15, 20 and 25 days.

At the end of the reactions, the samples were analyzed using HPLC.

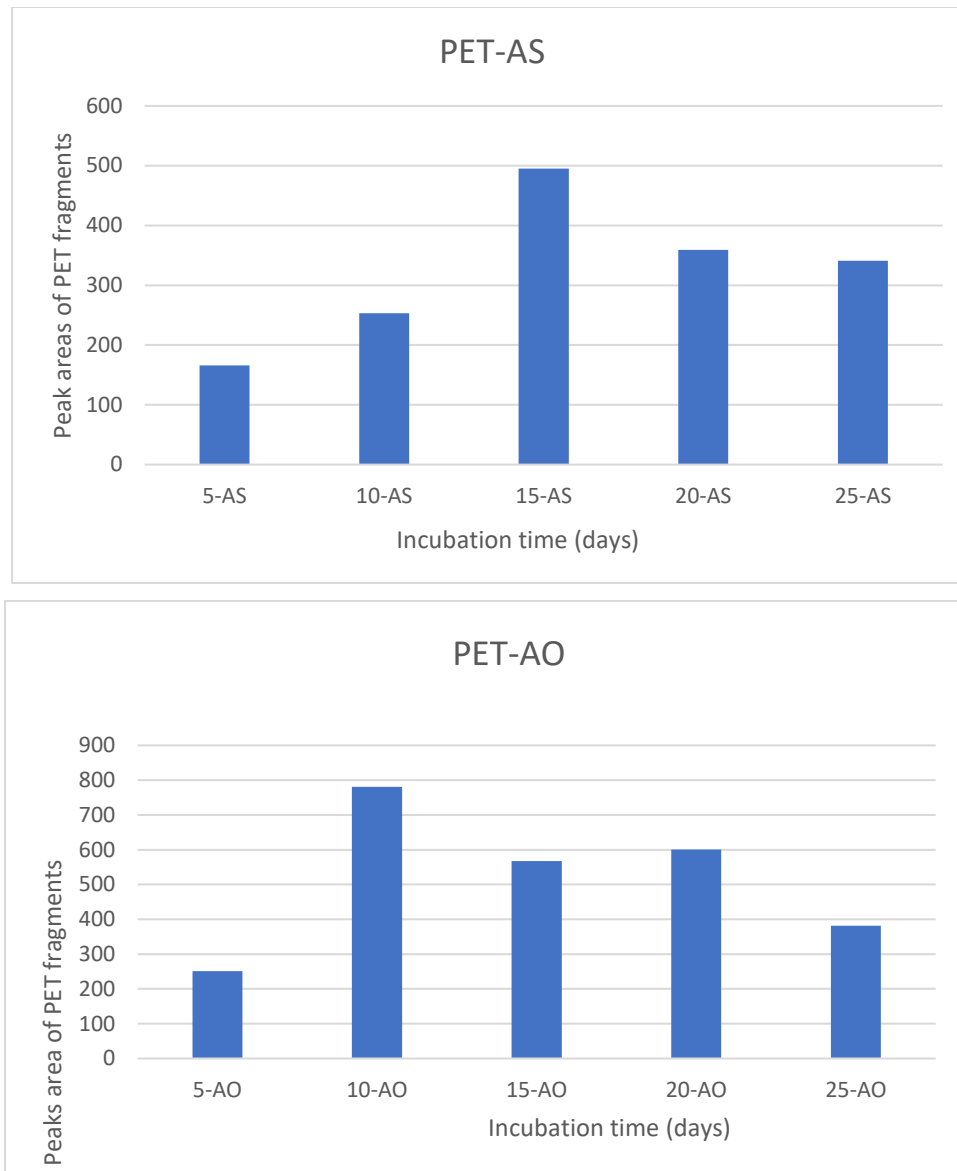


Figure 29. Area of peaks of interest for PET pre-treated using method AO and AS during different periods of time

It can be seen that for the method of pre-treatment AS, the best results were for the reaction left for 15 days and for the method of pre-treatment AO, the best results were for the reaction left for 10 days. FTIR characterization was succeeded by this analysis.

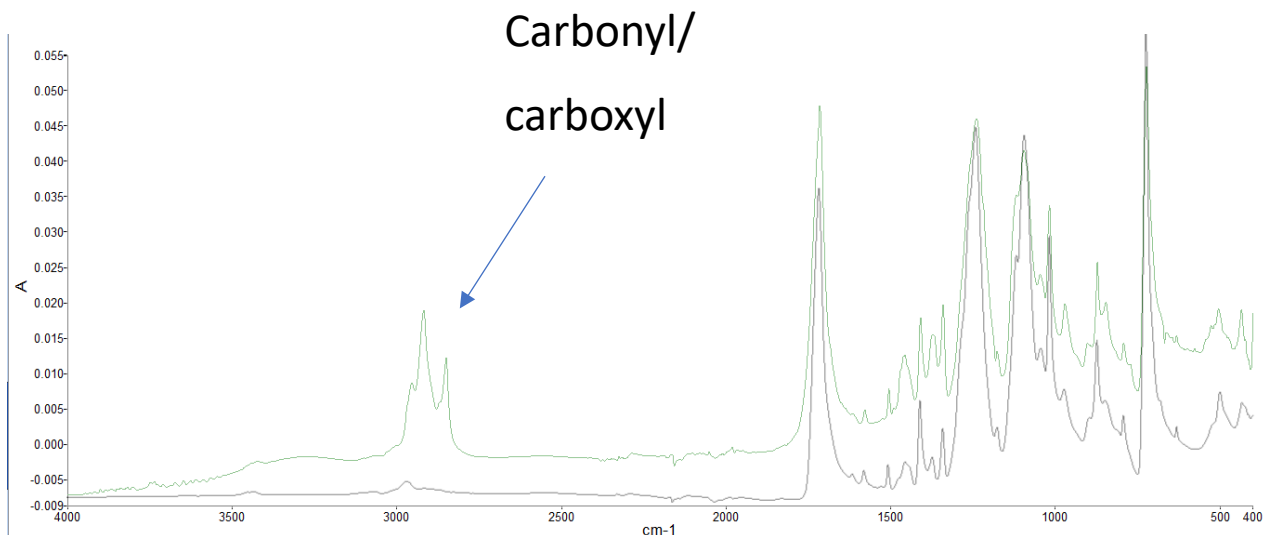


Figure 30. Overlaid spectrum of PET before pre-treatment (gray) and PET after a 15 days reaction with DMC (green)

New bands can be observed around the wave number 2700-3000 cm^{-1} . These can correspond to new aldehydes, carbonyl groups and carboxyl groups that were formed after the reaction with DMC.

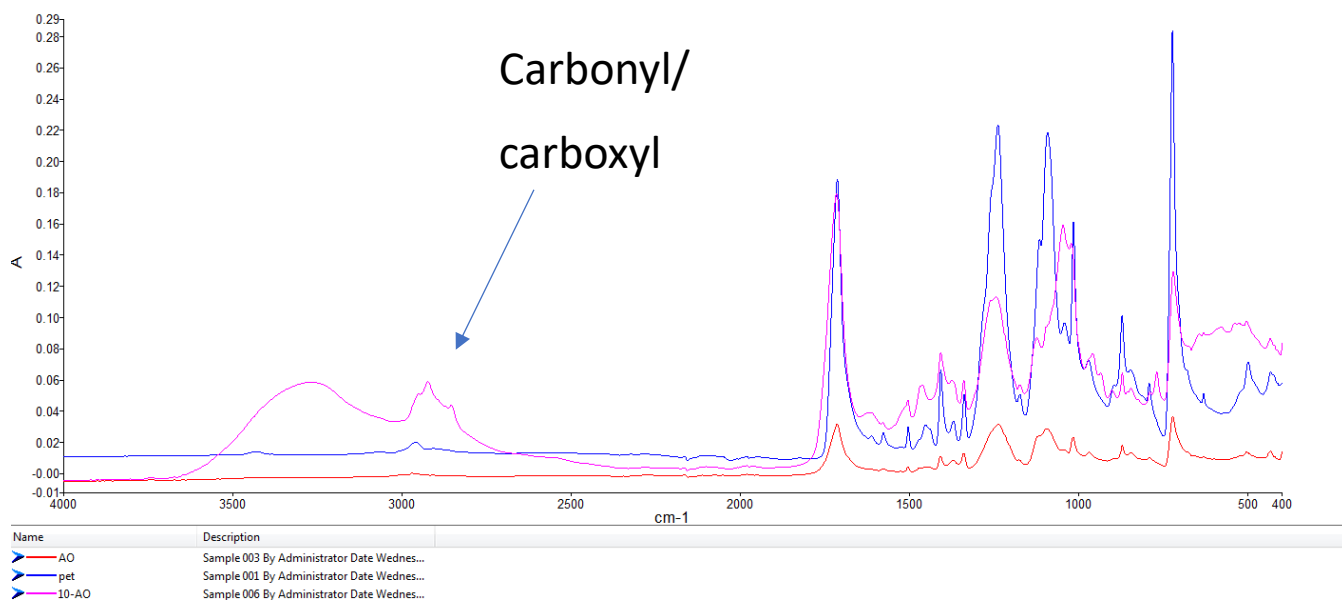


Figure 31. Overlaid spectrum of PET before pre-treatment (blue), PET after pre-treatment (red) and PET after a 10 days reaction with DMC (purple)

New bands can be observed around the wave number 2700-3000 cm^{-1} and a very large and wide one around the wave number 3000-3400 cm^{-1} .

The bands from 2700-3000 cm^{-1} can correspond to aldehydes, carbonyl groups and carboxyl groups that were formed after reaction similar to the previous FTIR spectrum.

2.9 DLS

The PET before pre-treatment was subjected to a DLS characterizations for measuring the dimension of the PET particles after grinding.

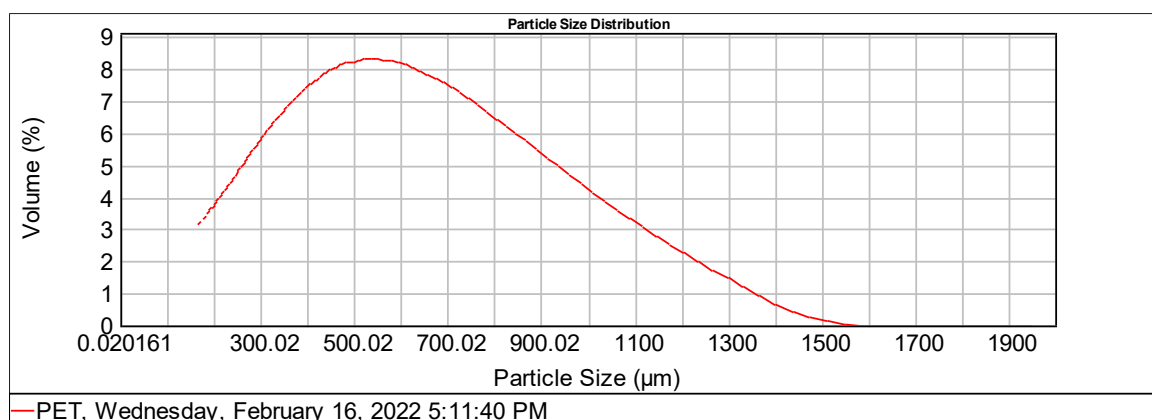


Figure 32. DLS spectrum

Table 6. Results from DSL characterization

Size (µm)	Volume In %	Size (µm)	Volume In %	Size (µm)	Volume In %	Size (µm)	Volume In %	Size (µm)	Volume In %	Size (µm)	Volume In %
0.020	0.00			1.002	0.00	7.096	0.08	50.238	0.83	355.656	5.36
0.022	0.00	0.159	0.00	1.125	0.00	7.962	0.09	56.368	0.95	399.052	5.80
0.025	0.00	0.178	0.00	1.262	0.00	8.934	0.10	63.246	1.08	447.744	6.10
0.028	0.00	0.200	0.00	1.416	0.00	10.024	0.12	70.963	1.22	502.377	6.24
0.032	0.00	0.224	0.00	1.589	0.00	11.247	0.14	79.621	1.37	563.677	6.15
0.036	0.00	0.252	0.00	1.783	0.02	12.619	0.17	89.337	1.52	632.456	5.83
0.040	0.00	0.283	0.00	2.000	0.07	14.159	0.21	100.237	1.67	709.627	5.27
0.045	0.00	0.317	0.00	2.244	0.07	15.887	0.25	112.468	1.82	796.214	4.53
0.050	0.00	0.356	0.00	2.518	0.08	17.825	0.29	126.191	1.98	893.367	3.63
0.056	0.00	0.399	0.00	2.825	0.09	20.000	0.34	141.589	2.16	1002.374	2.71
0.063	0.00	0.448	0.00	3.170	0.09	22.440	0.39	158.866	2.38	1124.683	1.80
0.071	0.00	0.502	0.00	3.557	0.09	25.179	0.43	178.250	2.66	1261.915	0.89
0.080	0.00	0.564	0.00	3.991	0.09	28.251	0.48	200.000	3.00	1415.892	0.09
0.089	0.00	0.632	0.00	4.477	0.08	31.698	0.53	224.404	3.39	1588.656	0.00
0.100	0.00	0.710	0.00	5.024	0.08	35.566	0.58	251.785	3.85	1782.502	0.00
0.112	0.00	0.796	0.00	5.637	0.08	39.905	0.65	282.508	4.35	2000.000	0.00
0.126	0.00	0.893	0.00	6.325	0.08	44.774	0.73	316.979	4.87		
0.142	0.00	1.002	0.00	7.096	0.08	50.238		355.656			

The average dimension of the particles was around 500 µm. The dimension range of all particles started with 2 µm and ended with 1400 µm.

2.10 Enzyme entrapment

Using the method from 2.8, different types of beads were prepared. PET-AO derivatized with 4-acetamidothiophenol, PET-AS derivatized with 2-amicemidothiophenol, PET-AS after 15 days in reaction with DMC and PET-AO after 10 days in reaction with DMC were the reactions with the best results. The PET from these reactions was put in the entrapment formed.

Specific enzymatic activity was calculated for all types of beads, either containing PET or not with the help of para nitrophenyl butyrate. The results from the enzymatic activity were listed in the table below.

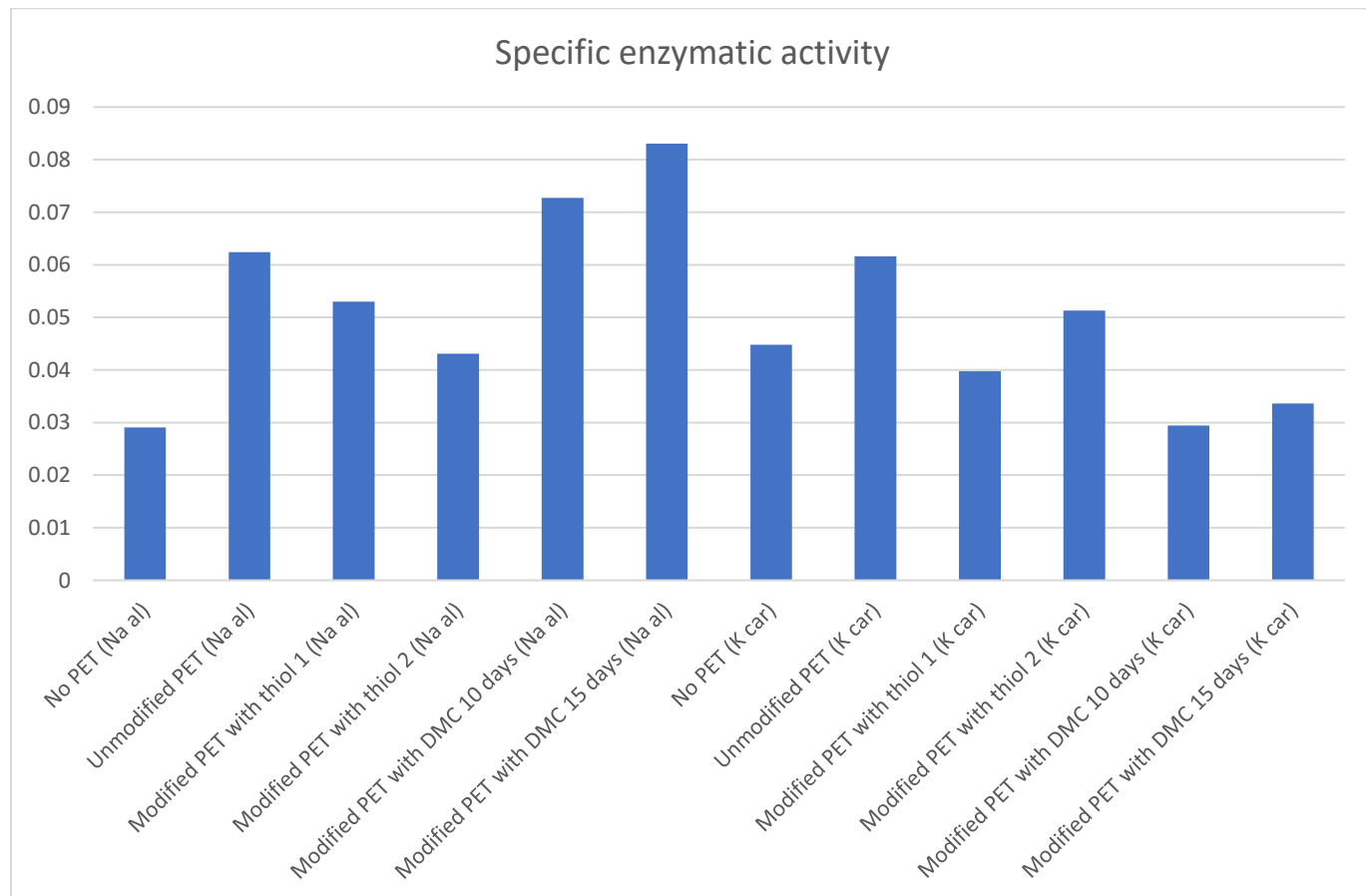


Figure 33. Specific enzymatic activity for different enzyme entrapment

It can be seen that the enzymatic activity raised in most of the cases were Pet was added in the enzyme entrapment. This it is possible due to the fact that the enzyme became more stable after the addition of PET.

For testing the enzymes, these were used in a reaction between sylibin and methyl palmitate with the enzyme cold active.

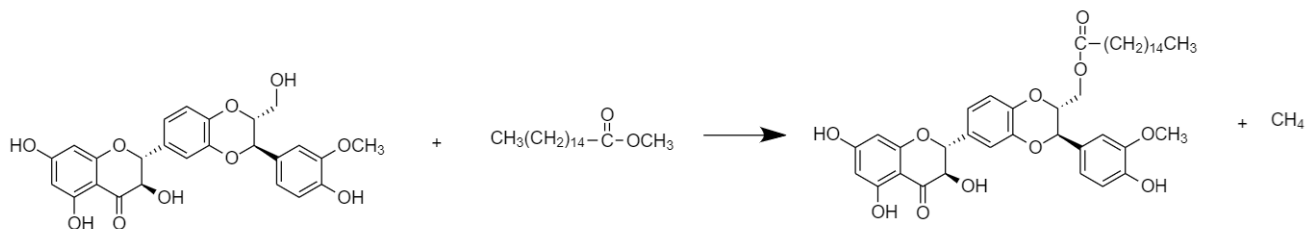


Figure 34. Reaction between sylibin and methyl palmitate

The reaction took place at 25° C for 24 hours in tetrahydrofuran. After the reaction, the liquid phase, after it was dried in an oven, was analyzed using HPLC. All the peaks were calculated and the conversions were listed in the graph below.

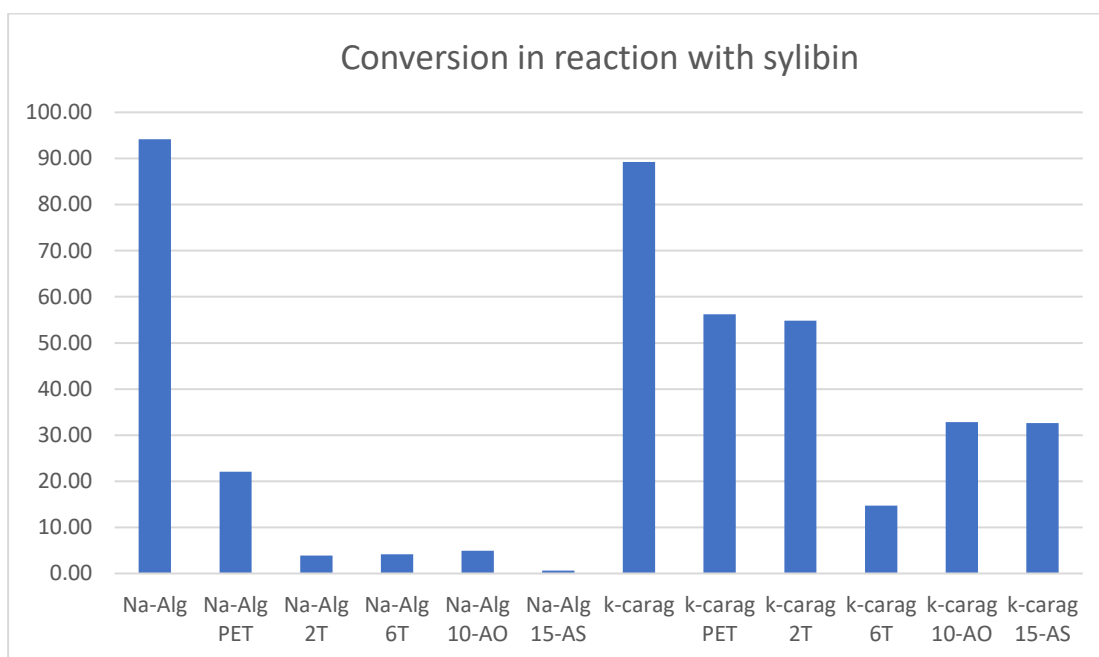


Figure 35. Conversion in reaction with sylibin

In the graph it can be seen that a better conversion rate was for the beads formed with K carrageenan. The study was continued further using only K carrageenan in making the beads.

Another study made followed the changing of the conversion rate after adding three beads in the reaction and not just one. The study also tracked the variation of the conversion rate modifying the temperature.

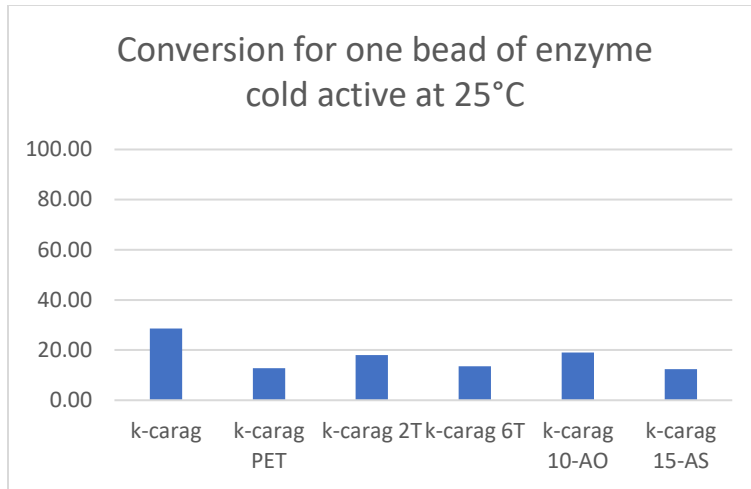


Figure 36. Conversion for one bead of enzyme

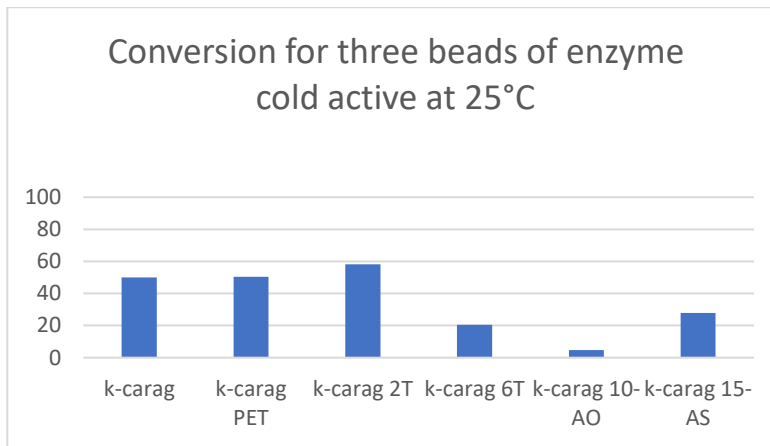


Figure 37. Conversion for three beads of enzyme

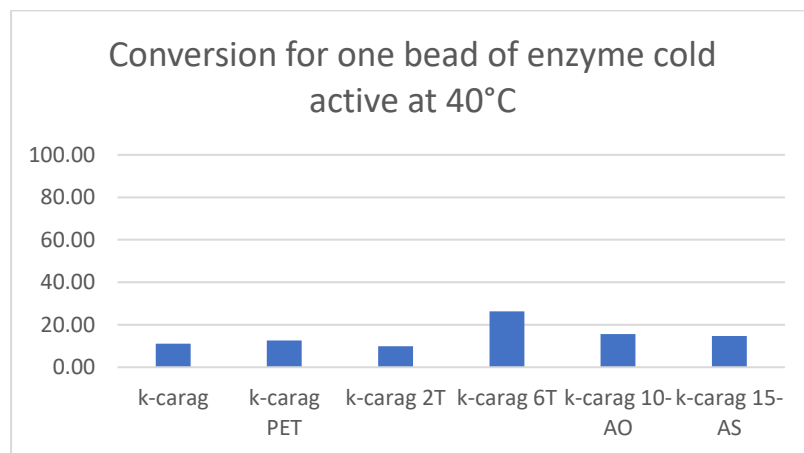


Figure 38. Conversion for one bead of enzyme

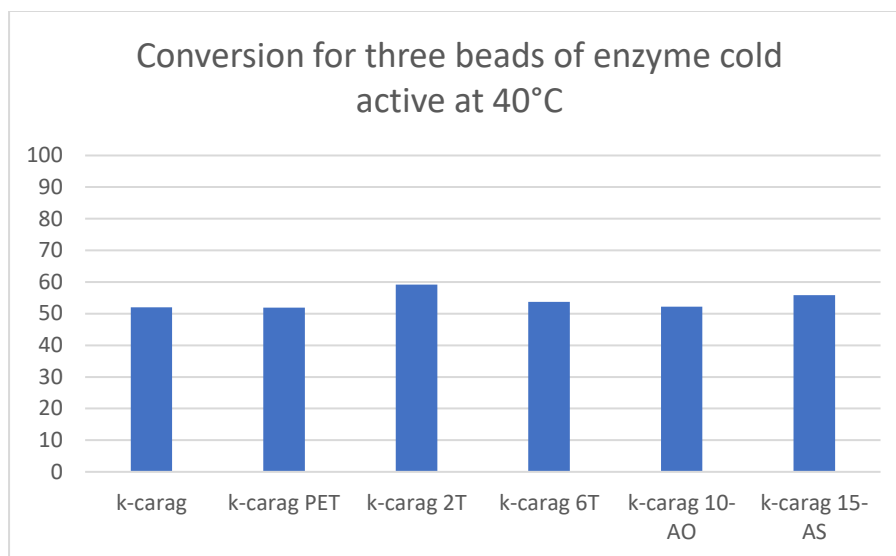


Figure 39. Conversion for three beads of enzyme

As it can be seen from the graphs from above, the conversion rate has increased with the increasing of number of beads in the reaction.

In the initial reaction, 8.1 mg of methyl palmitate, 988 μ L tetrahydrofuran (THF), 1 mg of sylibin and 1 bead of enzyme were used. For getting a better view of the perfect conditions for the reaction, these reactants were changed as in the table from below. The beads with Pet-AO derivatized with 4-acetamidothiophenol(2T) and Pet-AS derivatized with DMC for 15 days were chosen to continue this study with.

Table 7. The name of the reactions when reactants were changed

Type of Pet	Name of the reaction	Reactants
2T	2TA	8.1 mg of methyl palmitate, 988 μ L THF, 1 mg of sylibin and 4 beads of enzyme
2T	2TB	8.1 mg of methyl palmitate, 988 μ L THF, 1 mg of sylibin and 6 beads of enzyme
2T	2TC	8.1 mg of methyl palmitate, 988 μ L THF, 1 mg of sylibin and 8 beads of enzyme
2T	2TD	4 mg of methyl palmitate, 988 μ L THF, 1 mg of sylibin and 4 beads of enzyme
2T	2TE	12 mg of methyl palmitate, 988 μ L THF, 1 mg of sylibin and 4 beads of enzyme

2T	2TF	8.1 mg of methyl laurate, 988 μ L THF, 1 mg of sylibin and 4 beads of enzyme
2T	2TG	8.1 mg of methyl oleate, 988 μ L THF, 1 mg of sylibin and 4 beads of enzyme
2T	2TI	8.1 mg of methyl palmitate, 988 μ L ethanol, 1 mg of sylibin and 4 beads of enzyme
15-AS	15-ASA	8.1 mg of methyl palmitate, 988 μ L THF, 1 mg of sylibin and 4 beads of enzyme
15-AS	15-ASB	8.1 mg of methyl palmitate, 988 μ L THF, 1 mg of sylibin and 6 beads of enzyme
15-AS	15-ASC	8.1 mg of methyl palmitate, 988 μ L THF, 1 mg of sylibin and 8 beads of enzyme
15-AS	15-ASD	4 mg of methyl palmitate, 988 μ L THF, 1 mg of sylibin and 4 beads of enzyme
15-AS	15-ASE	12 mg of methyl palmitate, 988 μ L THF, 1 mg of sylibin and 4 beads of enzyme
15-AS	15-ASF	8.1 mg of methyl laurate, 988 μ L THF, 1 mg of sylibin and 4 beads of enzyme
15-AS	15-ASG	8.1 mg of methyl oleate, 988 μ L THF, 1 mg of sylibin and 4 beads of enzyme
15-AS	15-ASI	8.1 mg of methyl palmitate, 988 μ L ethanol, 1 mg of sylibin and 4 beads of enzyme

All the liquid phases from the reactions was analyzed after using HPLC. The conversion rates were calculated and listed in the graphs from below.

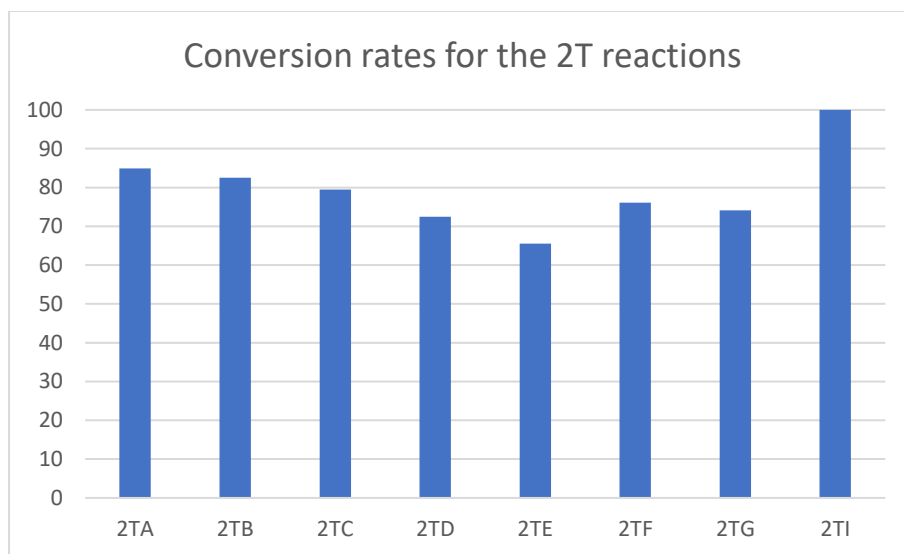


Figure 40. Conversion rated for the 2T reactions

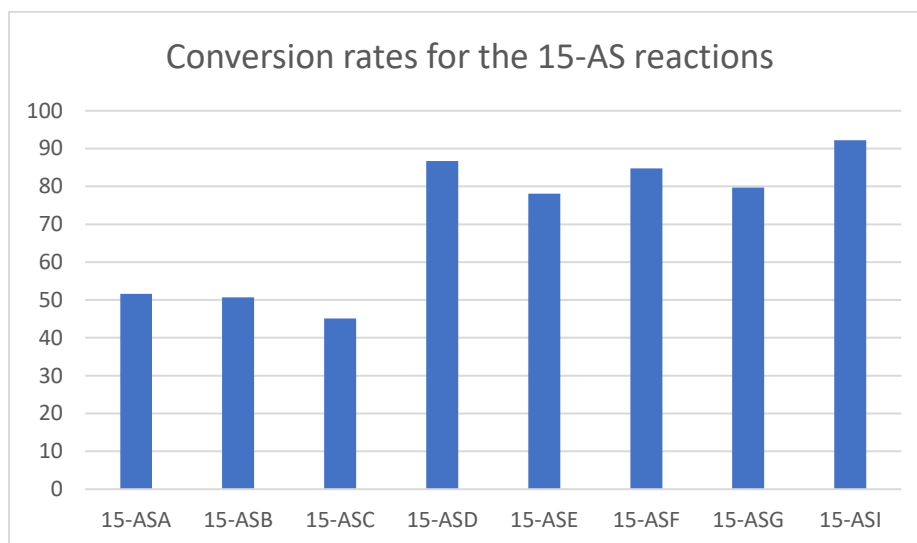


Figure 41. Conversion rated for the 15-AS reactions

From the graphs it can be concluded that after 4 beads, the conversion rate do not increase with the increase of number of beads. It can be seen that the conversion rates start to decrease a little with rising the number of beads. Also, it can be observe that methyl laurate has decent conversion rate results can be used as a substituent for methyl palmitate. Good conversion were also seen in the case when ethanol was used instead of tetrahydrofuran.

3. Conclusions

1. Reaction with thiols

4-acetamidothiophenol and 2-aminothiophenol offered best performance for PET(AO) and PET(AS) derivatization, respectively. FTIR analysis confirmed the thiol insertion on the PET surface.

2. Reaction with aniline

Enzyme screening was performed for BHET and aniline interaction. The best ones Laccase M10, EP010 and Versatile peroxidase were selected. Unfortunately, PET surface cannot be modified using peroxidase biocatalysis.

3. Reaction with DMC

PET derivatization with DMC has been performed. The best results were obtained for PET(AS) at 15 days and for PET(AO) at 10 days. FTIR spectra confirmed the acyl insertion on PET surface.

Modified PET was used as stabilizer for polysaccharide (alginate/carageenan) cavity prepared for enzyme immobilization. Cold active lipase was evaluated for silybin esterification. A solution was the entrapment of the lipase in polysaccharide cavity protecting the proteinic structure against solvent attack. The Pet used for the entrapment was chosen to be the one derivatized with 4-acetamidothiophenol, 2-aminothiophenol and DMC at 10 and 15 days.

Multiple studies were made for seeing if the which were the best parameters and reactans for the enzyme cold active trapped in beads with Pet. It was concluded that the bead with carageenan had the best stability. We also examined if the number of beads that affect the reaction and we saw that with the increasing of beads up to four, the reaction will have a better conversion rate. After four beads, the conversion rate starts to drop.

References

- [1] Lambertini M., Roman-Ramirez A., Wood J., Recycling of Bioplastics: Routes and Benefits. *J. Polym. Environ.*, 28 (2020), 2551:2571
- [2] Ru J., Huo Y.X., Yang Y., Microbial degradation and valorization of plastic wastes. *Front. Microbiol.*, 11 (2019), 230:245
- [3] Carniel A., Valoni E., Nicomedes J., Gomes A., Castro A., Lipase from *Candida antarctica* (CALB) and cutinase from *Humicola insolens* act synergistically for PET hydrolysis to terephthalic acid. *Process Biochem.*, 59(2017), 84:90
- [4] Müller R.J., Schrader H., Profe J., Dresler K., Deckwer W.D., Enzymatic Degradation of Poly(ethylene terephthalate): Rapid Hydrolyse using a Hydrolase from *T. Fusca*. *Macromol. Rapid Commun.*, 26(2005), 1400:1405
- [5] Thiounn T., Smith R., Advances and approaches for chemical recycling of plastic waste. *J Polym Sci*, 58 (2020), 1347:1364
- [6] Moore C.J., Synthetic polymers in the marine environment: A rapidly increasing, long-term threat. *Environ. Res.*, 108 (2008), 131:139
- [7] Cooper I., *Chemical Migration and Food Contact Materials*, Elsevier, 2007, Chapter 10: Plastics and chemical migration into food, Academic Press, 2018, Chapter 14, 228–250
- [8] Tajeddin, B., Ahmadi, B., Sohrab, F., Chenarbon, H. A., Tajeddin, B., Ahmadi, B., Sohrab, F., & Chenarbon, H. A., Plastics and chemical migration into food, Academic Press, 2018, Chapter 14, *Polymers for Modified Atmosphere Packaging Applications*, 457–499
- [9] Kwon B.G., Saido K., Koizumi K., Sato H., Ogawa N., Chung S.Y., Kusui T., Kodera Y., Kogure K., et al., Regional distribution of styrene analogues generated from polystyrene degradation along the coastlines of the North-East Pacific Ocean and Hawaii. *Environ. Pollut.*, 188 (2014), 45:54
- [10] Andrade B., Bezzerá A., Calado C., Adding value to polystyrene waste by chemically transforming it into sulfonated polystyrene, *Materia*, 24 (2019), 120:132
- [11] Thanh H., Roberts T., Lucas S., An overview on biodegradation of polystyrene and modified polystyrene: the microbial approach, *Crit. Rev. in Biotechnol.*, 38 (2017), 308:320
- [12] Maharana T., Negi S., Mohanty B., Recycling of polystyrene. *Polym. Plast. Technol.*, 46 (2017), 729:736

- [13] Maddah, H., Polypropylene as a Promising Plastic: A Review, *Am. J. Polym. Sci.*, 6(2016), 1:11
- [14] Menyhárd, A., Menczel, J. D., & Abraham, T., *Thermal Analysis of Textiles and Fibers*, Woodhead Publishing, 2020, Chapter 12, Polypropylene fibers, 205–222
- [15] Clayman, H. M., Polypropylene. *J. Ophthalmol.*, 88(1981), 959:964
- [16] Geyer, R., Jambeck, J., Law, K., Production, use, and fate of all plastics ever made. *Sci. Adv.*, 3 (2017), 48:62
- [17] Ghatge S., Yang Y., Ahn J., Hur H., Biodegradation of polyethylene: a brief review, *Appl Biol Chem*, 27 (2020), 220:231
- [18] Das, A., & Mahanwar, P., A Brief Discussion on Advances in Polyurethane Applications. *Adv. Ind. Eng. Polym. Res.*, 3(2020), 120:134
- [19] Madhav, H., Singh, N., & Jaiswar, G., *Materials for Biomedical Engineering*, Elsevier, 2019, Chapter 4, Thermoset, bioactive, metal–polymer composites for medical applications, 105–143.
- [20] Koerner, G. R., Koerner, R. M., *Solid Waste Landfilling, Concepts, Process, Technologies*, 2019, Chapter 7.3, Polymeric Geomembrane Components in Landfill Liners, 313–341
- [21] Alla R., Swamy K.N., Conventional and Contemporary polymers for the fabrication of denture prosthesis: part I – Overview, composition and properties, *Int. J. Appl. Dent. Sci.*, 82 (2015), 82:89
- [22] Akovali, G., *Toxicity of Building Materials*, Woodhead Publishing, 2012, Chapter 2, Plastic materials: polyvinyl chloride (PVC)23–53
- [23] Lanaro, M., Booth, L., Powell, S. K., & Woodruff, M. A., *Electrofluidodynamic Technologies (EFDTs) for Biomaterials and Medical Devices*, Woodhead Publishing, 2018, Chapter 3, Electrofluidodynamic technologies for biomaterials and medical devices, 37–69
- [24] Ouellette, R. J., & Rawn, J. D., *Organic Chemistry*, Elsevier, 2018, Chapter 15, Synthetic Polymers, 397–419
- [25] Horvart T., The mechanical properties of polyethylene-terephthalate (PET) and polylactic-acid (PDLLA and PLLA), the influence of material structure on forming, *Conf. Ser.: Mater. Sci. Eng.*, 426(2018), 67:85
- [26] Nisticò, R., Polyethylene terephthalate (PET) in the packaging industry. *Polym Test.*, 90(2020), 340:354

- [27] Niessen W. R., Marks C. H., Sommerlad R. E., *Waste pre-treatment. A Review.*, Environment Agency, 2020, Chapter 1, Introduction, 1-2
- [28] Wi R., Imran M., Lee K., Yoon S., Cho B., Effect of Support Size on the Catalytic Activity of Metal-Oxide-Doped Silica Particles in the Glycolysis of Polyethylene Terephthalate, *J. Nanosci. Nanotechnol.*, 11 (2011), 80:103
- [29] Thiounn T., Smith R., Advances and approaches for chemical recycling of plastic waste. *J. Polym. Sci.*, 58 (2020), 1347:1364
- [30] Sabagh A.M., Yehia F.Z, Eshaq G., Rabie A.M., Elmetwally A.E, Greener routes for recycling of polyethylene terephthalate, *Egypt. J. Pet.*, 25(2016), 53:64
- [31] Kanelli M., Vasilakos S., Nikolaivits E., Ladas S., Christakopoulos P., Topakas E., Surface modification of poly(ethylene terephthalate) (PET) fibers by a cutinase from *Fusarium oxysporum*, *Process Biochem.*, 50 (2015), 1885:1892
- [32] Kim H., Song W., Effects of Triton X-100 and Calcium Chloride on the Porcine Pancreas Lipase Treatment of PET fabrics, *J. Korean Soc. Cloth. Text.*, 6(2008), 911:917
- [33] Gomes D., Matama T., Paulo A., Takaki G., Salgueiro A., Production of heterologous cutinases by *E. coli* and improved enzyme formulation for application on plastic degradation, *Electron. J. Biotechnol.*, 5(2013), 133:143
- [34] Korpecka J., Heumann S., Billig S., Zimmermann W., Zinn M., Ihssen J., Cavaco-Paulo A., Guebitz G., Hydrolysis of Cutin by PET-Hydrolases, *Macromol. Symp.*, 296 (2010), 342:346
- [35] Vertommen M.A., Nierstrasz V.A., van der Veer M., Warmoeskerken M.M., Enzymatic surface modification of poly(ethylene terephthalate), *J. Biotechnol.*, 120 (2005), 376:386
- [36] Falkenstein P., Grasing D., Bielytsky P., Zimmermann W., UV pretreatment impairs the enzymatic degradation of polyethylene terephthalate, *Front. Microbiol.*, 11(2020), 67:76
- [37] Liu Y., Yao X., Yao H., Zhou Q., Xin J., Lu X., Zhang S., Degradation of Poly(ethylene terephthalate) Catalyzed by Metal-free 2 Choline-Based Ionic Liquids. *Green Chem.*, 22(2020), 85:102.